USC
UNIVERSIDADE
DE SANTIAGO
DE COMPOSTELA

INTERNATIONAL DOCTORAL
SCHOOL OF THE USC

Germán
Berrecoso Cuña

PhD Thesis

Nanocapsules containing immunomodulators and monoclonal antibodies for the treatment of lung cancer

Santiago de Compostela, 2023

Doctoral Programme in Drug Research and Development

USC
UNIVERSIDADE
DE SANTIAGO
DE COMPOSTELA

USC
UNIVERSIDADE
DE SANTIAGO
DE COMPOSTELA

DOCTORAL THESIS

NANOCAPSULES CONTAINING IMMUNOMODULATORS AND MONOCLONAL ANTIBODIES FOR THE TREATMENT OF LUNG CANCER

Germán Berrecoso Cuña

INTERNATIONAL PHD SCHOOL OF THE UNIVERSITY OF SANTIAGO DE COMPOSTELA

PHD PROGRAMME IN DRUG RESEARCH AND DEVELOPMENT

SANTIAGO DE COMPOSTELA

2023

USC
UNIVERSIDADE
DE SANTIAGO
DE COMPOSTELA

SUPERVISOR / TUTOR AUTHORIZATION

NANOCAPSULES CONTAINING IMMUNOMODULATORS AND MONOCLONAL ANTIBODIES FOR THE TREATMENT OF LUNG CANCER

Prof. María José Alonso Fernández, Full Professor in the Department of Pharmacology, Pharmacy, and Pharmaceutical Technology at the University of Santiago de Compostela.
Dr. José Crecente Campo, Researcher in the Department of Pharmacology, Pharmacy, and Pharmaceutical Technology at the University of Santiago de Compostela.

STATE:

That this thesis corresponds to the work carried out by Mr. Germán Berrecoso Cuña, under my supervision/ tutoring, and I hereby authorize its presentation, taking into account that it meets all the relevant requirements stated in the Doctoral Studies Regulations of the USC, and as its director it does not incur in the causes of abstention established in the 40/2015 Law.

In accordance with what is stated in the Regulations for Doctoral Studies, it is also declared that this doctoral thesis can be defended based on the modality of monographic with reproduction of publications, in which the participation of the PhD student was decisive for its elaboration and the publications adjust to the Research Plan.

Sgd.: María José Alonso Fernández

Sgd.: José Crecente Campo

Santiago de Compostela. November 18, 2022.

USC
UNIVERSIDADE
DE SANTIAGO
DE COMPOSTELA

PhD CANDIDATE STATEMENT

Mr. **Germán Berrecoso Cuña**

Thesis title: **NANOCAPSULES CONTAINING IMMUNOMODULATORS AND MONOCLONAL ANTIBODIES FOR THE TREATMENT OF LUNG CANCER**

I submit my Doctoral thesis, following the procedure according to the Regulation, stating that:

1) This thesis gathers the results corresponding to my work.
2) When applicable, explicit mention is given to the collaborations this work may have had.
3) I confirm that this thesis does not incur any plagiarism of any other authors or documents I submitted for obtaining other degrees.
4) The present document is the final version submitted for its defense and coincides with the document sent in electronic format.

And I undertake to submit the Supervisory Documentary Commitment in the event that the original is not in the School.

Santiago de Compostela. **December 1, 2022**.

Signature

USC
UNIVERSIDADE
DE SANTIAGO
DE COMPOSTELA

Conflict of interest

The doctoral candidate declares no conflicts of interest related to his thesis.

Santiago de Compostela. **December 1, 2022**.

Sgd.: Germán Berrecoso Cuña

USC
UNIVERSIDADE
DE SANTIAGO
DE COMPOSTELA

USC
UNIVERSIDADE
DE SANTIAGO
DE COMPOSTELA

Á mina xente

USC
UNIVERSIDADE
DE SANTIAGO
DE COMPOSTELA

USC
UNIVERSIDADE
DE SANTIAGO
DE COMPOSTELA

«Escoitar, aprender e compartir»

Dakidarría

USC
UNIVERSIDADE
DE SANTIAGO
DE COMPOSTELA

USC
UNIVERSIDADE
DE SANTIAGO
DE COMPOSTELA

ACKNOWLEDGEMENTS / AGRADECEMENTOS / AGRADECIMIENTOS

USC
UNIVERSIDADE
DE SANTIAGO
DE COMPOSTELA

USC
UNIVERSIDADE
DE SANTIAGO
DE COMPOSTELA

Ante todo, agradecer a confianza e o apoio da miña directora de tese, María José Alonso Fernández e do meu codirector, José Crecente Campo. Grazas a vós desenvolvín calidades como a perseveranza e o pensamento crítico, necesarias na carreira investigadora. Por suposto, grazas por guiarme ao longo dos anos cos vosos coñecementos.

Special thanks to the 2^2-Intratarget collaborators from SINTEF, Norway: Ruth S, Sven B, Geir K, and Simon L, from HYBRIGENICS, France: Jean-Christophe R and Stephanie B, from the University of Navarra: Iván P and Jon A, and from HUMANITAS, Italy: Paola A and Clement A. Without all of you the half of this thesis would not be possible. Also, thanks to mAbxience, León, for the kindly donated bevacizumab.

Grazas a Dolores TL ("*Loli*") e o resto do persoal do programa de doutoramento en Investigación e desenvolvemento de medicamentos pola inmensa axuda coa burocracia ao longo dos anos e, especialmente, durante o depósito da Tese. Grazas á Xunta de Galicia polas axudas predoutorais das cales fun beneficiario, do mesmo xeito que á AECT GNP polo programa IACOBUS. Grazas tamén ao persoal do Servizo de vixilancia da saúde da USC pola amabilidade e dispoñibilidade para a recollida de mostras de sangue.

Por suposto, grazas aos meus compañeiros de laboratorio durante estes anos. A realización desta tese doutoral non sería o mesmo sen a vosa presencia.

Grazas Ovidio C, Lali Z e Desirée TO pola axuda durante os primeiros anos no proxecto de pel. Grazas a Marta RA e a GSK pola oportunidade de traballar cunha "big pharma". É un pracer poder compartir convosco dúas patentes.

Lucía SB, foi un pracer real traballar xunto a ti. Coa túa experiencia coas células e as técnicas bioquímicas fuches a salvadora do proxecto 2^2-Intratarget. Grazas por lembrarme constantemente que os "*nanobodies*" son os meus amigos, aínda que estes empeñásense en non asociarse ás miñas nanocápsulas.

Grazas aos meus maiores, Sara C, Nataliya S, Adriana ML, Irene SR, Belén LB, Andrea G, Sofia S. Que saibades que a tradición dos "*calamardos*" segue en pé. Tamara GD, douche hoxe, que non "Tomorrow", as grazas polo bo ambiente e música, sobre todo durante as limpezas. PD: sabías que en portugués a palabra "*tâmara*" significa dátil? Grazas Ana OF pola túa sinceridade, temperanza e realismo e grazas ao "*duende gallego*" de Iago FM pola limpeza espontánea e organización do laboratorio.

Grazas aos que se foron indo ou vindo e indo: Rosana S, Bhanu T, Carmen TV, Cecília M, Cristina CC, Edilberto OH, Eleni S, Francesco M, Matilde DL, Mireia AD, Sergio DS, Vanessa CL, Vanessa O, Sagi R, Jovana K, Avinash M e máis.

Grazas aos "PichiDi Sharks". Os días foron moitísimo máis amenos convosco. Carmen FV, "*Carmen III*", espero que ás avespas do condado de York non lle gusten tanto os teus vestidos floridos como ás de aquí. Ana LE, "*cochón*" que el futuro te lleve a un lugar en el que haga más sol, haya más negros, puedas realizar mucha lucha canaria y no necesites llevar paraguas, aunque la verdad es que nunca lo has necesitado, e Mireya LB, grazas polos teus debuxos e polos teus dotes artísticos que culminaron na realización do debuxo que deu nome ao grupo e do "*The amazing shrimp-eater lion*" e, ademais, polas risas que nos deches inventando palabras ou escribindo frases de cinco liñas que se poderían resumir en catro palabras. (Nótese que este parágrafo foi escrito adoptando o teu estilo). Deséxoche un futuro no que sexas mesmo máis feliz do que vin que estabas a ser durante a túa estadía en Boston e, polo teu ben, no que non teñas que cubrir moitos papeis. Grazas tamén a Laura PA "*deditos*" pola túa espontaneidade e

por motivarnos a "*Tirar pa' alante, como las gatas (que no hablan)*". De cumprise, todas chegaredes lonxe.

Muito obrigado à menina com as mãos mais habilidosas do laboratório, Catarina A. Boas ELISAS, melhor pessoa. Vou para sempre recordar aqueles momentos em que gritávamos "*Aiii mãe!*" ou fechávamos o Tarasca a cantar o "*Grândola, Vila Morena*".

Moitas grazas ao resto de compañeiros de viaxes "*os polidispersos*", especialmente polas aventuras de Porto, Asturias, Cantabria e Bilbao. Expresións como "*¡Cascada!*" e "*Ah!, toalhitas (para bebés)!*" quedarán para o recordo. Gora polisakabanatu askatuta. Unha aperta a María R e Alexandre CP.

Grazas aos postdocs. Gracias a Gustavo LR por fomentar el hacer picnics en los parques de Santiago para aprovechar el sol (y las Estrellas). Thanks, Shubaash, for all you have taught us during these years. I wish you the best in your current trip in the industry. Gracias a Federico Q por todos los experimentos con el AF4. Grazas Fernando TA polos teus coñecementos de bioloxía celular e por poñer orde entre os colaboradores do proxecto. Grazas tamén a Marta MG, que mesmo co suplicio de traballar coa colistina, sempre fuches capaz coas túas historias de sacarnos un sorriso todos os días. Gracias a Juan LB por volver a animar la sexta planta con tu llegada, aunque lamentablemente fuese por un corto período. Recordos a Patricia GB, que aínda que vai de sinistra, é unha das persoas máis humildes do laboratorio. Moitísimas grazas por toda a axuda coa química e polas túas suxestións de confección desta tese.

Por supuesto, gracias a mis jóvenes "*Padawans*" (alias "*puppies*"). Marta BC, Alberto DP, Ibrahim H y Eugenia SG. Por mi parte, ha sido un placer haberos enseñado un poco de la ciencia recogida en esta tesis doctoral. Espero haber estado a vuestra altura y deseo un futuro lleno de éxito.

Grazas aos novos doutorandos e ao grupo de "*Paddle*" dos domingos no que se facía de todo menos "*Paddle*". Gracias al flipado de Alfonso FB, que tanto te hace un estudio de liberación de meses como un triatlón. Dank dir, Philipp, dem am besten in die spanische Kultur integrierten Deutschen, haben wir gelernt, dass alles „makes sense", wenn man nur genug darüber nachdenkt. Especialmente a vós, aconséllovos que non desesperedes, xa que tamén vos vai a chegar este momento. Grazas tamén a Darío BM que, aínda que caeu en combate, seguiu asistindo a quedadas espontáneas.

Grazie mille Elena G ("*peperoncino*") e Giorgio B. Anche se breve, la tua cultura italiana è stata apprezzata. "*Caffè?*" "*Domenica pizza?*" "*Quanto te la rischi?*". Almeno con la tua partenza abbiamo perso solo una milza. Colgo l'occasione per congratularmi con Anna per essere diventata un investigatore principale. Ti auguro il meglio con i tuoi nuovi progetti, con Elena, e con tutti i nuovi "*Puppies*" che avrai.

Grazas ás "*puretas*". Grazas Purificación DR ("Puri") pola túa inestimable axuda durante este tempo. Grazas Balbina FM pola túa eficiencia co liofilizador e por manter sempre un stock de todos os reactivos do laboratorio na túa mesa, aínda que logo sexan imposibles de atopar. Ola Belén CR, vou ser algo máis orixinal en comparación cos meus "maiores" e non che vou dar a grazas polas túas funcións de terapeuta, conselleira, mantemento do laboratorio ou xestión de pedidos. Citando a Tamara, gracias por ser la pureta más cañera. Aquí déixoche unha cita de Rosendo: "Al final la vida no consiste más que en pasar el tiempo de la manera más agradable posible dentro de tus posibilidades".

USC DE COMPOSTELA

Grazas ás novas técnicas do laboratorio. A Cristina IL por reivindicar o uso do galego no laboratorio e por sempre convidarme a calquera plan teu, aínda que veñan tamén os teus amigos, que igual son 30. Grazas a Ana OL pola túa espontaneidade e actitude de dicir que si ante a vida. Vinme reflectido en ti. Non deixes de ensinarlle castelán e galego a Philipp ou aos teus próximos compañeiros estranxeiros. O único que lamento é que non chegases antes.

Un saludo a las ultimísimas altas en el laboratorio, Inés RP y Elena IM. Aunque actualmente no he podido interactuar con vosotras tanto como quisiera, se os ve buena gente. No tengo pruebas, ni tampoco dudas, que para dentro de unos meses, en el momento de la defensa de esta tesis, tendremos momentos tan remarcables como los mencionados con vuestros compañeros.

Gracias al profesor Wolfgang J Parak y a la doctora Neus Feliu por aceptarme durante mi primera estancia en vuestro laboratorio en Hamburgo. Gracias también a mis compañeros no alemanes Michele C y Nacho L.

Muito obrigado à profesora Ana Paula Pêgo por abrir-me as portas do seu grupo de investigação durante o meu segundo período de formação no estrangeiro. Aí senti-me como em casa. Obrigado à Sofia G pela tua paciência quando me ensinaste a fazer cultura de células. Obrigado à María GL pela tua incrível ajuda com a ImageStream. Espero que a estátua de Fátima continue a benzer os próximos doutorandos. Obrigado também a Ana S, Eva C, Ana M, Sara ZA, Débora M, Beatriz C, Marília T, Victoria L, Miguel M, Gil M, João Pedro C, Francisca C, e Duarte S. Para sempre recordei os nossos almoços em plena época de pandemia desfrutando do sol de julho no jardín do i3s e aquele incrível dia de Paddle surf.

Grazas aos profesores do departamento de Farmacia, Farmacoloxía e Tecnoloxía Farmacéutica. Foi un pracer formar parte do equipo de profesores de Tecnoloxía Farmacéutica, Biofarmacia e Formulación Maxistral e Dermofarmacia, nos mesmos laboratorios pero esta vez do outro lado da bancada. Grazas tamén a Marcos GF e Noemi C.

Grazas aos mellores compañeiros de piso, Tiago M e Rui A. Grazas por esas noites de cervexas, xogos de mesa, “Fall Guys”, “Exploding Kittens” e “camioneta”. Dato curioso, hai xusto un ano que construímos aquela marabillosa árbore de Nadal. Tiago, ánimo cos teus últimos 95 luns de doutoramento. En breves, serás libre como eu. Deséxoche un gran futuro científico e, senón, un moi “o máis belo horizonte” na Foz do Porto. Longa vida á casa do pobo.

Grazas ao resto de amizades cultivadas no CiMUS e no IDIS. Grazas aos meus compañeiros de P2L6 (“os da segunda”), Sheila BE, Maruthi P, Carla GM, Sandra RA, Diego PD, Héctor RA, Saeedeh K., Rocío MC, Sara GG. Grazas polas charlas que tivemos mentres a ultracentrífuga freaba. Muchísimas gracias a SSL7, “*platelet proteomics*”. Agradecer a Ángel García su disponibilidad para debatir los resultados de proteómica. Gracias Lidia HN, por todos tus consejos sobre el depósito de la tesis. Muchísimas gracias a mis amigos de P1L3 y P1L4. Muchísimas gracias a Cristina DR por todos los planes de fin de semana. Saúdos a Saínza LT e Sandra DV.

Ademais de toda a xente que me apoiou desde dentro, tamén hai moita xente de fóra do laboratorio á que quero agradecer todo o seu apoio durante este tempo. Un agradecemento especial a Diego RM, Nuria VM e Mónica MH, os verdadeiros confidentes e, citando a Mónica, as persoas máis importantes do mundo mundial.

Finalmente, grazas aos meus pais, Benito e Charo, porque sen a vosa confianza e apoio non tería chegado ata aquí. Grazas polas chamadas que comezaban con "estás a estudar?" e

continuaban con "non, estou a traballar". Nas próximas páxinas poderedes atopar o que “estaba a estudar”.

Grazas.

USC
UNIVERSIDADE DE SANTIAGO DE COMPOSTELA

LIST OF ABBREVIATIONS

USC
UNIVERSIDADE
DE SANTIAGO
DE COMPOSTELA

USC
UNIVERSIDADE
DE SANTIAGO
DE COMPOSTELA

%0123

%RRES: Percentual relative residuals
1D: One-dimension
2D: Two-dimension
7-AAD: 7-aminoactinomycin D
δ: Chemical shift
ζpot: ζ-potential

A

Ab: Antibody
ACN: Acetonitrile
ActRIIA: Activin receptor type IIA
ActRIIB: Activin receptor type IIB
AE: Association efficiency
AF4: Asymmetric flow field-flow fractionation
AKR1C3: Aldo-keto reductase family 1 member C3
ALK: Anaplastic lymphoma kinase
AMBP: Alpha-1-microglobulin/bikunin precursor
ANOVA: Analysis of variance
ANT3: Antithrombin-III
Apo: Apolipoprotein
APOA2: Apolipoprotein A-II
APOA4: Apolipoprotein A-IV
APOC1: Apolipoprotein C-I
APOC2: Apolipoprotein C-II
APOC3: Apolipoprotein C-III
APOD: Apolipoprotein D
APOE: Apolipoprotein E
APOF: Apolipoprotein F
APOL1: Apolipoprotein L1
APOM: Apolipoprotein M
Apt: Aptamer

B

BAM: *N*-tert-butyl acrylamide
Bb: Activated complement factor B
BBB: Blood-brain barrier
BME: 2 mercaptoethanol
BSA: Bovine serum albumin
BZT: Benzethonium

C

C(−): Negative control
C(+): Positive control
C1q: Complement C1q subcomponent
C1QB: Complement C1q subcomponent subunit B
C1QC: Complement C1q subcomponent subunit C
C1r: Complement C1r subcomponent
C1s: Complement C1s subcomponent
C2: Complement C2
C3(H_2O) Thioester bond-hydrolyzed complement C3
C3: Complement C3
C3a: Complement C3-A
C3b: Complement C3-B
C4: Complement C4
C4a: Complement C4-A
C4B: Complement C4-B
C4bC2a: C4bC2a C3 convertase
C4BPA: C4b-binding protein alpha chain
C4BPB: C4b-binding protein beta chain
C5: Complement C5
C5a: Complement C5-A
C5b: Complement C5-B
C5bC6C7C8C9: Membrane attack complex; Terminal complement complex
C6: Complement C6
C7: Complement C7
C8: Complement C8
C8G: Complement component C8 gamma chain
C9: Complement C9
CBPB2: Carboxypeptidase B2
CCL2: Monocyte chemoattractant protein-1
CD: Cluster of differentiation
cDNA: Complementary desoxyribonucleic acid
CDX: Cyclodextrin
CendR: C-end rule sequence
CFB: Complement factor B
CFD: Complement factor D
CFH: Complement factor H
CFI: Complement factor I
CFP: Properdin
CHAPS: 3-[(3- Cholamidopropyl) dimethylammonio]-1-propanesulfonate
Cl/F: Apparent total body clearance of the drug calculated after extravascular administration
CLL1: C-type lectin-like molecule-1
CLU: Clusterin
CM: Chylomicron
cryo-EM: Cryogenic transmission electron microscopy
CTAB: Hexadecyltrimethylammonium bromide

USC
UNIVERSIDADE
DE SANTIAGO
DE COMPOSTELA

D

DCR: Derived count rate
DDA: Data-dependent acquisition
DF: Dilution factor
DIA: Data-independent acquisition
DiD: 1,1'-Dioctadecyl-3,3,3',3'-Tetramethylindodicarbocyanine, 4-Chlorobenzenesulfonate
DLin-KC2-DMA: 2,2-dilinoleyl-4-dimethylaminoethyl-[1,3]-dioxolane
DLin-MC3-DMA: (6Z,9Z,28Z,31Z)-heptatriacont-6,9,28,31-tetraene-19-yl 4-(dimethylamino)butanoate
DLS: Dynamic light scattering
DMEM: Dulbecco's modified Eagle's medium
DMPC: Dimyristoylphosphatidylcholine
DMPG: 1,2-dimyristoyl-sn-glycero-3-phosphorylglycerol
DMSO: Dimethyl sulfoxide
DNR: Daunorubicin
DOPC: 1,2-dioleoyl-sn–glycero-3-phosphocholine
DOPE: Dioleoyl phosphatidylethanolamine
DOTAP: 1,2-dioleoyl-3-trimethylammonium propane
DP: Declustering potential
DPEG or DSPE-PEG_{2000}: *N*-(carbonyl-methoxy polyethylene glycol 2000)-1,2-distearoyl-sn-glycero-3-phosphoetanolamine
DSPC: Distearoylphosphatidylcholine
DSPE: 1,2-Distearoyl-sn-glycero-3-phosphorylethanolamine
DTAB: Dodecyltrimethylammonium bromide
DTT: Dithiothreitol
DTX: Docetaxel

E

EDTA: Ethylenediaminetetraacetic acid
EGF: Epidermal growth factor
EGFR: Epidermal growth factor receptor
ELISA: Enzyme-linked immunosorbent assay
EMA: European Medicines Agency
EPR: Enhanced Permeation and Retention
ERK: Extracellular signal-regulated kinase
ESI: Electrospray ionization
EU: Europe
EV: Extracellular vesicle
EY: Extraction yield

F

F3: KDEPQRRSARLSAKPAPPKPEPKPKKAPAKK peptide
FACS: Fluorescence-activated cell sorting (flow cytometry)
FBS: Fetal bovine serum

Fc: Antibody fragment crystallizable region
FC: Fold change
FDA: United States Food and Drug Administration
FDR: False discovery rate
FE-SEM: Field emission-scanning electron microscopy
FR: Folate receptor

G

GAK: Cyclin G-associated kinase
Galu.: Galunisertib
GEM: Gemcitabine
GFP: Green-fluorescent protein
GI: Gastrointestinal

H

HA: Hyaluronic acid
HDL: High-density lipoprotein
HEP2: Heparin cofactor 2
HER2: Human epidermal growth factor receptor 2
HILIC: Hydrophilic interaction liquid chromatography
HPA: Heparanase
HPLC: High performance liquid chromatography
HRP: Horseradish peroxidase

I

I: Fibrinogen
iC3b Complement factor I-cleaved C3b
IC_{50}: Half maximal inhibitory concentration
Ig: Immunoglobulin
IGF-1R: Insulin-like growth factor 1 receptor
IGFALS: Insulin like growth factor binding protein acid labile subunit
IgG γ: Immunoglobulin g γ heavy chain
IGHG: Immunoglobulin heavy constant gamma
IGHM: Immunoglobulin heavy constant mu
IGLC2: Immunoglobulin lambda constant 2
II: Coagulation factor II; Prothrombin
III: Coagulation factor III; tissue factor
IL: Interleukin
iMFI: Integrated mean fluorescence intensity
InsR: Insulin receptor
IPSP: Plasma serine protease inhibitor
iRGD: Cyclic CRGDKGPDC peptide
IX: Coagulation factor IX

J

JAK: Janus kinase

K

k_a: Affinity constant
KLKB1: Kallikrein B1
KNG1: Kininogen 1
Kol. HS15: Kolliphor® HS15
KRAS: Kirsten rat sarcoma viral oncogene homolog
KV127: Immunoglobulin kappa variable 1-27

L

LC: Liquid chromatography
LDE: Laser Doppler electrophoresis
LDL: Low-density lipoprotein
LDLR: Low-density lipoprotein receptors
L-DOPA: L-3,4 dihidroxifenilalanina
LoD: Limit of detection
LoQ: Limit of quantification
LPS: Lipopolysaccharides
LRP: Lipoprotein receptor-related protein
LTK: Leukocyte receptor tyrosine kinase
LYVE: Lymphatic vessel endothelial hyaluronic acid receptor

M

M1: Cytotoxic/pro-inflammatory type macrophage
M2: Repair/anti-inflammatory type macrophage
mAb: Monoclonal antibody
Mal: Maleimide
MALS: Multiangle light scattering
MASP1: Mannan-binding lectin serine protease 1
MASP2: Mannan-binding lectin serine protease 2
MBL: Mannan-binding lectin
MEK: Mitogen-activated protein kinase kinase
MET: Mesenchymal-epithelial transition factor
MFI: Mean fluorescence intensity
MINBE: Minimum Information about Nanomaterial Biocorona Experiments
MMP2: Matrix metalloproteinase-2
mPES: Modified polyethersulfone
MRM: Multiple reaction monitoring
MS: Mass spectrometry
MTX: Methotrexate

MW: Molecular weight

N

n.d.: No data
N/A: Not applicable
N/D: Not determined
NC: Nanocapsule
NCT: ClinicalTrials.gov identifier
NE: Nanoemulsion
NIPAM: *N*-isopropylacrylamide
NMR: Nuclear magnetic resonance
NO: Nitric oxide
NP: Nanoparticle
NRP1: Neuropilin-1
NRP2: Neuropilin-2
ns: Not significative
NSCLC: non-small cell lung cancer
NTA: Nanoparticle tracking analysis

P

P/S: Penicillin/Streptomycin
p-: Phosphorilated-
PAA: Polyaspartic acid
pAb: Polyclonal antibody
PAGE: Polyacrylamide gel electrophoresis
PAI-1: Plasminogen activator inhibitor-1
PBCL: Poly-(α-benzyl carboxylate ε-caprolactone)
PBS: Phosphate-buffered saline
PCL: Poly ε-caprolactone
PCs: Phosphatidylcholines
PD-1: Programmed cell death protein 1
PDI: Polydispersity index
PD-L1: Programmed death-ligand 1
PDX: Patient-derived xenograft
PEG: Polyethylene glycol
PEG·PGA: Polyethylene glycol (5 kDa) poly-α-glutamic acid (10 u).
PEO: Poly(ethylene oxide)
PES: Polyethersulfone
PFA: Paraformaldehyde
PGA: Polyglutamic acid
PGMA: Poly(glycidyl methacrylate)
PHDCA: Poly(hexadecyl cyanoacrylate)
PHPMA: Poly[*N*-(2-hydroxypropyl) methacrylamidelactate]
pI: Isoelectric point

PIBCA: Poly(isobutyl cyanoacrylate)
PLA: Poly(D,L-lactic acid)
PLG: Poly(D,L-glycolic acid).
PLGA: Poly(lactic-co-glycolic acid)
PLL: Poly-L-lysine
PLMN: Plasminogen
PLS:6: PLS:6 unidentified protein named by Anderson and Anderson
PON1: Paraoxonasa 1
PPE: Polyphosphoester
PPO: Poly(propylene oxide)
PROC: Vitamin K-dependent protein C
PROS: Vitamin K-dependent protein S
PS: Polystyrene
PSA: Polysialic acid (colominic acid)
PS-COOH: Carboxylic functionalized polystyrene
PseudoMRM: Pseudo-Multiple Reaction Monitoring
PSMA: Prostate-specific membrane antigen
PTX: Paclitaxel
PVDF: Polyvinylidene difluoride
PVP: Poly(N-vinylpyrrolidone)

R

r^2: Lineal coefficient of determination
RAF: Rapidly accelerated fibrosarcoma protein
RE%: Relative differences between concentrations and the actual standard concentrations
RE: Recovery
Ref.: Reference
RES: Reticuloendothelial system
RHAMM: Receptor for Hyaluronan Mediated Motility
RI: Refractive index
ROS: Reactive oxygen species
ROS1: Proto-oncogene tyrosine-protein kinase ROS
RStD%: Relative standard deviation
RT: Room temperature

S

SAA4: Serum Amyloid A4
SCLC: Small cell lung cancer
SD: Solvent displacement
SDS: Sodium dodecyl sulfate
SE: Self-emulsifying
SEM: Scanning electron microscopy
SERPINA10: Serpin family A member 10
SIM: Selected ion monitoring

URG

siRNA: Small interfering ribonucleic acid
SLNPs: Solid lipid nanoparticles
Smad: Suppressor of mothers against decapentaplegic
SOPC: 1-stearoyl-2-oleoyl phosphatidylcholine
SR-BI: Scavenger receptor class B type I
ST8SiaII: ST8 Alpha-*N*-Acetyl-Neuraminide Alpha-2,8-Sialyltransferase 2
ST8SiaIV: ST8 Alpha-*N*-Acetyl-Neuraminide Alpha-2,8-Sialyltransferase 4
STAT: Signal transducer and activator of transcription
StD: Standard deviation
STEM: Scanning transmission electron microscopy
STK22D: Testis-specific serine/threonine-protein kinase 1
STRING: Search Tool for the Retrieval of Interacting Genes/Proteins
SWATH: Sequential Window Acquisition of all Theoretical Mass Spectra

T

$t_{1/2}$: Half-life
TAM: Tumor-associated macrophage
TAT-peptide: GRKKRRQRRRPQ peptide
TAT: Thrombin–antithrombin III complex
TBS: Tris-buffered saline
TBST: Tris-buffered saline with 0.01 % polysorbate 20
TEM: Transmission electron microscopy
TFA: Trifluoroacetic acid
TFF: Tangential flow filtration
TFPI1: Tissue factor pathway inhibitor 1
TfR: Transferrin receptor
TG: Triglyceride
TGF-β: Transforming growth factor beta
TGF-βR: Transforming growth factor beta receptor
Th: T helper cell
TLR: Toll-like receptor
tLyp-1: Truncated form of LyP-1 (sequence: CGNKRTR)
t_{max}: Time of maximum plasmatic drug concentration
TME: Tumor microenvironment
TNBC: Triple-negative breast cancer
TOF: Time of flight
TPGS: D-α-tocopherol polyethylene glycol 1000 succinate
TRBM: Thrombomodulin
Treg: Regulatory T cell

U

U2: U2 unidentified protein named by Golaz *et al.*
UHPLC: Ultra-high performance liquid chromatography
uPAR: Urokinase-type plasminogen activator receptor

USA: United States of America
UV: Ultraviolet

V

V: Coagulation factor V
VEGF: Vascular endothelial growth factor
VII: Coagulation factor VII
VIII: Coagulation factor VIII
Vis: Visible
VLDL: Very low-density lipoprotein
vs.: *versus*
VTN: Vitronectin
VWF: von Willebrand factor
Vz/F: Apparent volume of distribution during the terminal phase after extravascular administration
v/v: volume/volume

W

WHO: World Health Organization
w/v: weight/volume
w/w: weight/weight

X

X: Coagulation factor X
XI: Coagulation factor XI
XII: Coagulation factor XII

USC UNIVERSIDADE DE SANTIAGO DE COMPOSTELA

USC
UNIVERSIDADE
DE SANTIAGO
DE COMPOSTELA

TABLE OF CONTENTS

USC
UNIVERSIDADE
DE SANTIAGO
DE COMPOSTELA

USC
UNIVERSIDADE
DE SANTIAGO
DE COMPOSTELA

Table of contents

Abstract / resumen 35

Resumo *in extenso* 39

Introduction 63

Background, hypothesis, and objectives 89

CHAPTER 1. Characterization of polymeric nanocapsules: chemical composition and physicochemical and biological properties 95

CHAPTER 2. Galunisertib and stattic-loaded polymeric nanocapsules for lung cancer treatment 227

CHAPTER 3. Polymeric nanocapsules for the intracellular delivery of monoclonal antibodies 291

Overall discussion 337

Conclusions 361

Ethical considerations 365

Publications derived from this thesis 371

USC
UNIVERSIDADE DE SANTIAGO DE COMPOSTELA

USC
UNIVERSIDADE
DE SANTIAGO
DE COMPOSTELA

ABSTRACT / RESUMEN

USC
UNIVERSIDADE
DE SANTIAGO
DE COMPOSTELA

USC
UNIVERSIDADE
DE SANTIAGO
DE COMPOSTELA

ABSTRACT

Despite the recent advances in lung cancer immunotherapy, there is a critical need to decrease the off-target toxicities of immunotherapeutic drugs and increase their efficacy. Moreover, mutations of Kirsten rat sarcoma viral oncogene homolog (*KRAS*) are particularly relevant therapeutic targets in lung cancer. However, until now, treatments have been developed for only one mutation of KRAS, whereas the rest remain undruggable.

The main goal of this thesis has been to use nanotechnology to improve the efficacy/toxicity balance of specific immunomodulatory drugs and to enable the intracellular delivery of monoclonal antibodies (mAbs). For this, we have chosen polymeric nanocapsules (NCs), a well-established delivery platform developed in our laboratory, and optimized them according to three principal objectives: i) modulation of the NCs' interaction with plasma proteins (protein corona); ii) encapsulation of two immunomodulatory drugs (stattic and galunisertib) for their use in combination therapy, and iii) encapsulation of anti-$KRAS^{G12V}$ mAb to achieve their intracellular delivery and interaction with the G12V-mutated KRAS protein.

Chapter 1 explores the influence of the composition (oil, surfactant, and polymer) and preparation technique (solvent displacement *versus* self-emulsifying) of six different NCs on their interaction with plasma proteins. The results showed that NCs with higher amounts of polyethylene glycol (PEG), either in the form of PEGylated surfactants or PEGylated polymers, exhibited lower protein adsorptions. Concerning the main adsorbed proteins, NCs containing 1,2-dioleoyl-3-trimethylammonium propane (DOTAP) as the only surfactant adsorbed vitronectin intensely, whereas those containing polysorbate 80 were enriched in complement proteins.

In Chapter 2, two immunomodulators, namely, galunisertib, a transforming growth factor beta (TGF-β) pathway inhibitor, and stattic, a signal transducer and activator of transcription 3 (STAT3) inhibitor, were loaded into a selection of NCs prototypes developed in Chapter 1. The loaded NCs were tested in CMT 167 lung cancer cell lines and RAW 264.7 macrophages to determine their *in vitro* cellular uptake, cytotoxicity, and STAT3 and TGF-β pathways inhibition efficacies.

Finally, in Chapter 3, bevacizumab was used as a model mAb to develop anti-$KRAS^{G12V}$ mAb-loaded NCs and to evaluate their efficiency for the intracellular delivery of mAbs. The target engagement of the anti-$KRAS^{G12V}$ mAb after loading into NCs with the $KRAS^{G12V}$ protein was assessed.

Overall, this work highlights the technological possibilities of polymeric NCs for treating lung cancer by modifying the biodistribution of the drugs, allowing their access to new biological compartments, and potentially reducing their off-target toxicities. These studies will hopefully contribute to advancing a new generation of lung cancer treatments with higher therapeutic outcomes and lower off-target toxicities.

USC
UNIVERSIDADE DE SANTIAGO DE COMPOSTELA

RESUMEN

A pesar de los recientes avances en la inmunoterapia contra el cáncer de pulmón, todavía existe una necesidad crítica de disminuir los efectos adversos de los fármacos inmunoterápicos e incrementar su eficacia. Además, las mutaciones del homólogo de oncogén viral del sarcoma de rata Kirsten (*KRAS*) son dianas terapéuticas particularmente relevantes en el cáncer de pulmón. Sin embargo, hasta la fecha, sólo se han desarrollado tratamientos contra una de las mutaciones de KRAS, mientras que para el resto de ellas no ha sido posible encontrar un tratamiento.

El principal objetivo de esta tesis ha sido el uso de la nanotecnología para mejorar el balance efectividad/toxicidad de ciertos fármacos inmunomoduladores específicos y el permitir la liberación intracelular de anticuerpos monoclonales (mAbs). Para ello, hemos elegido las nanocápsulas (NCs) poliméricas, una plataforma de liberación desarrollada y arraigada en nuestro laboratorio, y las hemos optimizado de acuerdo a tres objetivos principales: i) la modulación de la interacción de las NCs con proteínas plasmáticas (corona proteica); ii) la encapsulación de dos fármacos inmunomoduladores (stattic y galunisertib) para su uso en terapia combinada y iii) la encapsulación de un mAb anti-$KRAS^{G12V}$ para lograr su liberación intracelular e interacción con la proteína KRAS con mutación G12V.

El Capítulo 1 explora la influencia de la composición (aceite, surfactante y polímero) y la técnica de preparación (desplazamiento del solvente frente a auto-emulsificación) de seis NCs diferentes en su interacción con proteínas plasmáticas. Los resultados mostraron que las NCs con mayor cantidad de polietilenglicol (PEG), tanto en la forma de surfactantes o polímeros PEGilados, exhibieron una menor adsorción de proteínas. En cuanto a las principales proteínas adsorbidas, las NCs elaboradas con 1,2-dioleoil-3-trimetilamoniopropano (DOTAP) como único surfactante adsorbieron vitronectina intensamente, mientras que aquellas elaboradas con polisorbato 80 se vieron enriquecidas en proteínas del complemento.

En el Capítulo 2, dos inmunomoduladores, galunisertib, un inhibidor de la vía del factor de crecimiento transformante beta (TGF-β), y stattic, un inhibidor del transductor de señal y activador de la transcripción 3 (STAT3), fueron incorporados en una selección de los prototipos desarrollados en el Capítulo 1. Las NCs cargadas fueron testadas en la línea celular de cáncer de pulmón CMT 167 y en macrófagos RAW 264.7 para determinar su internalización, citotoxicidad y la eficacia de inhibición de las vías de STAT3 y TGF-β *in vitro*.

Finalmente, en el Capítulo 3, bevacizumab fue usado como mAb modelo para desarrollar NCs cargadas con un mAb anti-$KRAS^{G12V}$ y evaluar su eficiencia para la liberación intracelular de mAbs. El reconocimiento de la diana $KRAS^{G12V}$ por parte del mAb anti-$KRAS^{G12V}$ tras su incorporación en las NCs fue evaluada.

En conjunto, este trabajo destaca las posibilidades tecnológicas de las NCs poliméricas para el tratamiento del cáncer de pulmón mediante la modificación de la biodistribución de los fármacos, permitiendo su acceso a nuevos compartimentos biológicos y reduciendo sus efectos adversos. Idealmente, se espera que estos estudios contribuyan al avance de una nueva generación de tratamientos contra el cáncer de pulmón, con mejores resultados terapéuticos y menores efectos adversos.

USC
UNIVERSIDADE DE SANTIAGO DE COMPOSTELA

RESUMO *IN EXTENSO*

USC
UNIVERSIDADE
DE SANTIAGO
DE COMPOSTELA

USC
UNIVERSIDADE
DE SANTIAGO
DE COMPOSTELA

1. INTRODUCIÓN

1.1. SITUACIÓN ACTUAL NO CANCRO DE PULMÓN

O cancro de pulmón é a neoplasia maligna coa taxa de mortalidade máis alta do mundo, sendo responsable do 18 % das mortes causadas por cancros (1,8 millóns de mortes ao ano).[1] O cancro de pulmón non microcítico (NSCLC) representa o 80 %[2] dos cancros de pulmón e presenta unha taxa de supervivencia aos 5 anos do 63 % cando estes se atopan localizados e do 5,2 % cando son metastásicos.[3] As alteracións do homólogo do oncoxene viral do sarcoma de rata Kirsten (KRAS) son as mutacións de ganancia de función máis frecuentes no NSCLC (27,5 %).[4] Nestes casos, as mutacións de KRAS máis habituais son G12C (≈ 40 %), G12V (≈ 20 %) e G12D (≈ 15 %).[4,5]

O tratamento do NSCLC realízase mediante cirurxía, radioterapia, quimioterapia clásica, terapia dirixida e inmunoterapia. A terapia dirixida resérvase para pacientes con alteracións moi específicas, como as do factor de crecemento epidérmico ou a mutación G12C de KRAS. No resto de casos, a quimioterapia clásica, a cal da lugar a efectos secundarios potencialmente severos, é utilizada cun éxito relativamente baixo.[6–9]

1.2. A NANOTECNOLOXÍA NO TRATAMENTO DO CANCRO DE PULMÓN

A nanotecnoloxía é unha estratexia útil para solucionar as limitacións de moitos tratamentos oncolóxicos, tales como a baixa solubilidade, inestabilidade, acceso limitado ás súas dianas terapéuticas ou falta de especificidade,[10–13] implicando unha redución dos efectos adversos.[11–14] De feito 10 nanomedicamentos de quimioterápicos xa foron aprobados en Europa e EE. UU.

En xeral, a acumulación dos nanosistemas no tumor adoita clasificarse en pasiva e activa. A acumulación pasiva depende de propiedades físicas, tales como o tamaño e a rixidez.[15–35] Pola contra, a acumulación activa depende do uso de ligandos contra receptores específicos presentes nos tumores,[17,25,30,36–42] por exemplo, o ligando tLyp-1 e o receptor neuropilin-1.[43,44] Un dos parámetros que máis afecta á acumulación de nanosistemas en tumores é a composición da súa coroa proteica.[17,45]

1.3. A COROA PROTEICA

A coroa proteica é a capa de proteínas que se depositan espontaneamente sobre os nanosistemas tras a súa administración.[46–49] Este recubrimento proteico é moi relevante xa que afecta ao tempo de circulación dos nanosistemas,[47,50–54] acumulación en tecidos,[47,55–59] capacidade de atravesar barreiras biolóxicas,[60–69] toxicidade[60,70–73] e estabilidade coloidal.[50,74–77] Ditas proteínas adoitan clasificarse en opsoninas, se reducen o tempo de circulación, ou disopsoninas, se o prolongan. A composición da coroa proteica depende das características fisicoquímicas dos nanosistemas.[50,52,53,60,72,78–92] A estratexia más empregada para reducir a coroa proteica e aumentar a fracción de disopsoninas é a adición de polietilenglicol (PEG)[69,70,93–95] ou os seus derivados ás nanopartículas. Con todo, o uso do PEG dá lugar a algunhas limitacións potenciais como a ocultación dos ligandos usados para a acumulación activa[94,96–98] ou a opsonización con anticorpos en persoas sensibles ao PEG.[99,100]

1.4. AS NANOCÁPSULAS POLIMÉRICAS

As nanocápsulas (NCs) poliméricas son nanosistemas constituídos por un núcleo oleoso, axentes tensioactivos e unha cuberta polimérica. As NCs son nanosistemas versátiles xa que permiten a incorporación tanto de moléculas hidrofílicas como hidrofóbicas, protexéndoas da súa degradación e modificando o seu perfil de biodistribución e aclaramento plasmático.

O noso grupo de investigación ten unha alta experiencia no desenvolvemento de NCs cargadas con quimioterápicos.[101–103] O primeiro traballo publicado describe a eficacia dunha formulación de NCs recubertas de quitosano e cargadas con docetaxel (DTX).[104] Logo, co obxectivo de aumentar a acumulación no tumor mediante mecanismos pasivos, deseñáronse NCs cubertas con PGA-PEG e cargadas con DTX. Ditas formulacións demostraron unha redución significativa no crecemento de gliomas U87 en ratos, cun subseguinte incremento do seu tempo de supervivencia.[105] Finalmente, ditas NCs demostraron a súa capacidade de actuación no cancro de pulmón metastásico, reducindo de maneira significativa as metástases linfáticas.[106]

Por outra banda, o noso grupo de investigación explorou recentemente a liberación intracelular de anticorpos monoclonais (mAb) como, por exemplo, anti-gasdermina B. Para iso, o mAb foi incorporado en NCs de ácido hialurónico (HA), conseguíndose a inhibición da migración celular *in vitro*, a redución do cancro de mama ortotópico e a redución de metástases pulmonares en ratos.[107]

Mentres que os resultados preclínicos conseguidos coas NCs no contexto do cancro tiveron éxito, non existe información con respecto á coroa proteica das NCs. Por tanto, o primeiro obxectivo desta tese foi a caracterización da coroa proteica de varias NCs tras a incubación con plasma humano, acompañada da caracterización fisicoquímica (tamaño de partícula, carga superficial, composición e morfoloxía) co fin de obter bos candidatos no marco do tratamento do cancro de pulmón.

2. CARACTERIZACIÓN QUÍMICA, FISICOQUÍMICA E BIOLÓXICA DAS NANOCÁPSULAS POLIMÉRICAS

2.1. CARACTERIZACIÓN FISICOQUÍMICA

As NCs son nanotransportadores con prometedoras características para o tratamento do cancro de pulmón. Diferentes polisacáridos como o HA, ácido polisiálico (PSA) e polipéptidos como o ácido poliglutámico conxugado con PEG (PEG·PGA) foron usados como cuberta polimérica das mesmas. Por outra banda, unha gran cantidade de axentes tensioactivos, tanto con rexións de PEG como sen elas, poden empregarse na súa formulación. Adicionalmente, varios métodos de formulación destas están descritos na literatura, sendo o desprazamento de solvente (SD) e a auto emulsificación (SE) dos máis empregados (Ilustración 1).

USC UNIVERSIDADE DE SANTIAGO DE COMPOSTELA

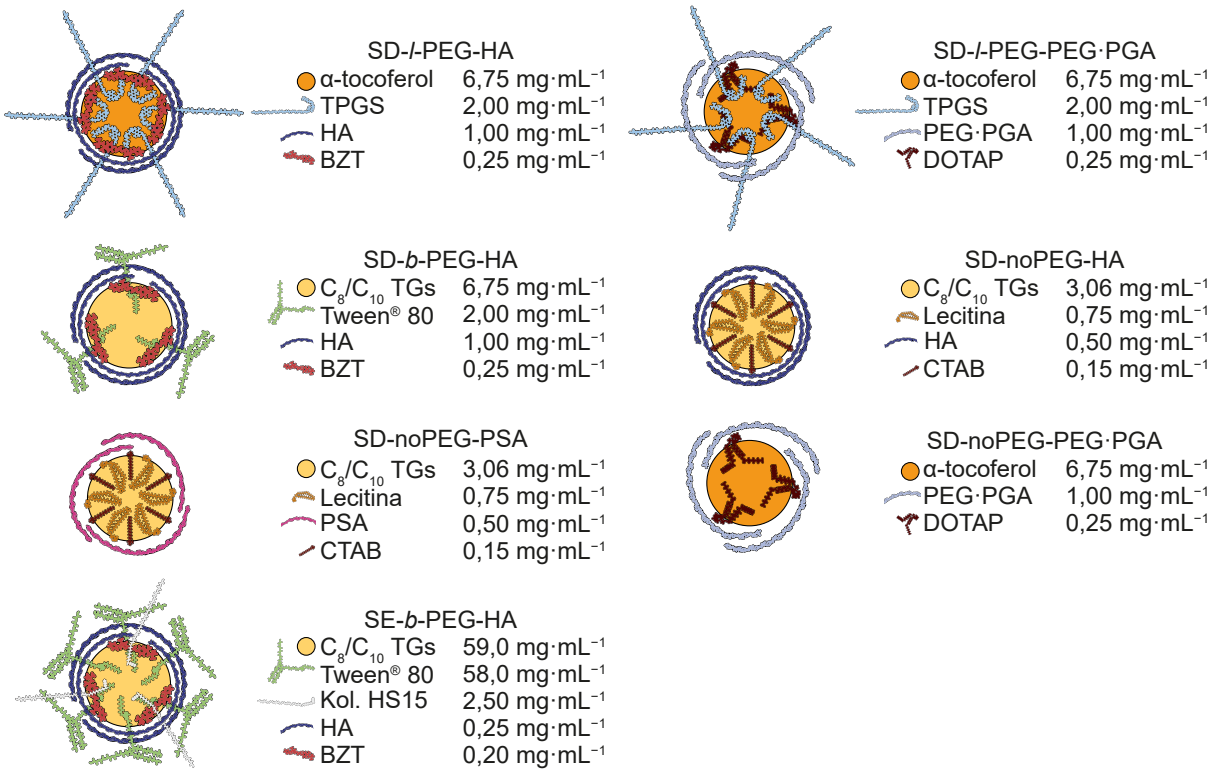


Ilustración 1. Representación esquemática do ordenamento esperado dos compostos presentes nas nanocápsulas e a súa composición teórica

SD-*l*-PEG-HA: Formulación preparada pola técnica de desprazamento do solvente e composta por PEG lineal (TPGS), BZT e cuberta de HA. **SD-*l*-PEG-PEG·PGA**: Formulación preparada pola técnica de desprazamento do solvente e composta por PEG lineal (TPGS), DOTAP e cuberta de PEG·PGA. **SD-*b*-PEG-HA**: formulación preparada pola técnica de desprazamento do solvente e composta de PEG ramificado (polisorbato 80), BZT e cuberta de HA. **SD-noPEG-HA**: Formulación preparada pola técnica do desprazamento do solvente e composta por axentes tensioactivos sen PEG (lecitina), CTAB e cuberta de HA. **SD-noPEG-PSA**: Formulación preparada pola técnica de desprazamento de solvente e composta por axentes tensioactivos sen PEG (lecitina), CTAB e cuberta de PSA. **SD-noPEG-PEG·PGA**: Formulación preparada pola técnica de desprazamento do solvente e composta por axentes tensioactivos sen PEG (DOTAP) e cuberta de PEG·PGA. **SE-*b*-PEG-HA**: Formulación preparada pola técnica de auto emulsificación e composta por PEG ramificado (polisorbato 80), BZT e cuberta de HA. **Abreviaturas**: BZT: cloruro de bencetonio. C_8/C_{10} TGs: triglicéridos de ácidos caprílicos e cápricos. CTAB: bromuro de hexadeciltrimetilamonio. DOTAP: 1,2-dioleoil-3-trimetilamoniopropano. HA: ácido hialurónico. Kol. HS15: Kolliphor® HS15. PEG·PGA: ácido poliglutámico conxugado a polietilenglicol. PSA: ácido polisiálico. TPGS: D-α-tocoferol polietilenglicol 1000 succinato. Adaptada de [108] baixo licenza de Creative Commons.

Para facilitar as comparacións, as NCs foron nomeadas indicando primeiro a técnica de formulación, despois a natureza do axente tensioactivo con PEG predominante e, finalmente, a composición da súa cuberta polimérica.

Co fin de eliminar a fracción de reactivos que non se ensamblaron na estrutura das NCs e, por tanto, permanecen en solución ou formando estruturas micelares, as NCs foron illadas por ultracentrifugación, excepto para a formulación elaborada por SE, a cal foi purificada por filtración de fluxo tanxencial. Neste punto, o estudo da formulación SD-*b*-PEG-HA foi interrompido por adquirir un tamaño maior que o desexado (> 200 nm) tras o seu illamento. Ditas NCs illadas foron caracterizadas polas técnicas de dispersión dinámica de luz (DLS), electroforese láser Doppler e análise de traxectoria de nanopartículas (NTA) (Táboa 1).

Táboa 1. Resumo das propiedades fisicoquímicas das nanocápsulas illadas, incluíndo os seus diámetros hidrodinámicos, cargas superficiais, concentracións, áreas superficiais e pH

	SD-*l*-PEG-HA	SD-*l*-PEG-PEG·PGA	SD-noPEG-HA	SD-noPEG-PSA	SD-noPEG-PEG·PGA	SE-*b*-PEG-HA
Diámetro hidrodinámico (DLS) (nm)	156 ± 8	137 ± 4	135 ± 4	124 ± 7	116 ± 2	113 ± 2
PDI	0,17 ± 0,01	0,08 ± 0,05	0,09 ± 0,02	0,06 ± 0,01	0,11 ± 0,02	0,25 ± 0,01
Potencial ζ (mV)	−39 ± 4	+0 ± 3	−33 ± 5	−38 ± 4	−35 ± 2	−6 ± 1
Diámetro hidrodinámico (NTA) (nm)	125 ± 10	118 ± 13	113 ± 3	107 ± 4	102 ± 2	126 ± 3
Concentración ($\times 10^{11}$ partículas·mL^{-1})	51 ± 10	85 ± 24	88 ± 6	96 ± 9	106 ± 10	71 ± 2
Área superficial (m^2·mL^{-1})	0,25 ± 0,03	0,37 ± 0,03	0,35 ± 0,02	0,35 ± 0,04	0,35 ± 0,04	0,36 ± 0,03
pH	6,0 ± 0,1	6,2 ± 0,1	4,9 ± 0,1	5,3 ± 0,1	6,0 ± 0,1	7,4 ± 0,1

Abreviaturas: DLS: dispersión dinámica de luz. NTA: análise de traxectoria de nanopartículas. PDI: índice de polidispersión. Os valores representan a media ± desviación estándar (n = 3). As composicións de SD-*l*-PEG-HA, SD-*l*-PEG-PEG·PGA, SD-*b*-PEG-HA, SD-noPEG-HA, SD-noPEG-PSA, SD-noPEG-PEG·PGA e SE-*b*-PEG-HA móstranse na Ilustración 1.

Os resultados de DLS e NTA mostraron que as NCs posuían un tamaño inferior a 160 nm. Todas as formulacións elaboradas pola técnica de SD tiñan un índice de polidispersión (PDI) < 0,2. O PDI de SE-*b*-PEG-HA foi maior debido a varias subpoboacións de partículas de tamaño medio maior a 200 nm. Segundo a súa carga superficial, puideron diferenciarse dúas categorías de NCs: cargadas moi negativamente (SD-*l*-PEG-HA, SD-noPEG-HA, SD-noPEG-PSA e SD-noPEG-PEG·PGA) e neutras (SD-*l*-PEG-PEG·PGA e SE-*b*-PEG-HA). A morfoloxía esférica foi confirmada por microscopia electrónica, o cal permitiu calcular a súa área superficial a través da área dunha esfera.

Finalmente, as NCs demostraron ser estables tras 24 h de incubación en 90 % plasma humano a 37 °C.

2.2. CARACTERIZACIÓN QUÍMICA

Para a caracterización química, desenvolvéronse métodos de cromatografía líquida-espectrometría de masas para a totalidade das sustancias empregadas na formulación das NCs. Ditos métodos foron valorados seguindo guías internacionais.

As eficiencias de asociación (AE) variaron para cada substancia e formulación entre o 14 % e 95 %.

Os datos obtidos permitiron a avaliación do contido de PEG e da conformación do mesmo. A densidade de PEG, é dicir, o número de cadeas de PEG por 100 nm^2, foi similar entre SD-noPEG-PEG·PGA, SD-*l*-PEG-PEG·PGA e SD-*l*-PEG-HA. Por outra banda, a densidade de PEG en SE-*b*-PEG-HA foi máis de 20 veces maior, probablemente debido á presenza de PEG

ramificado. En canto á conformación do PEG, todas as NCs demostraron unha conformación en cepillo, a cal é máis axeitada para reducir a interacción con proteínas.

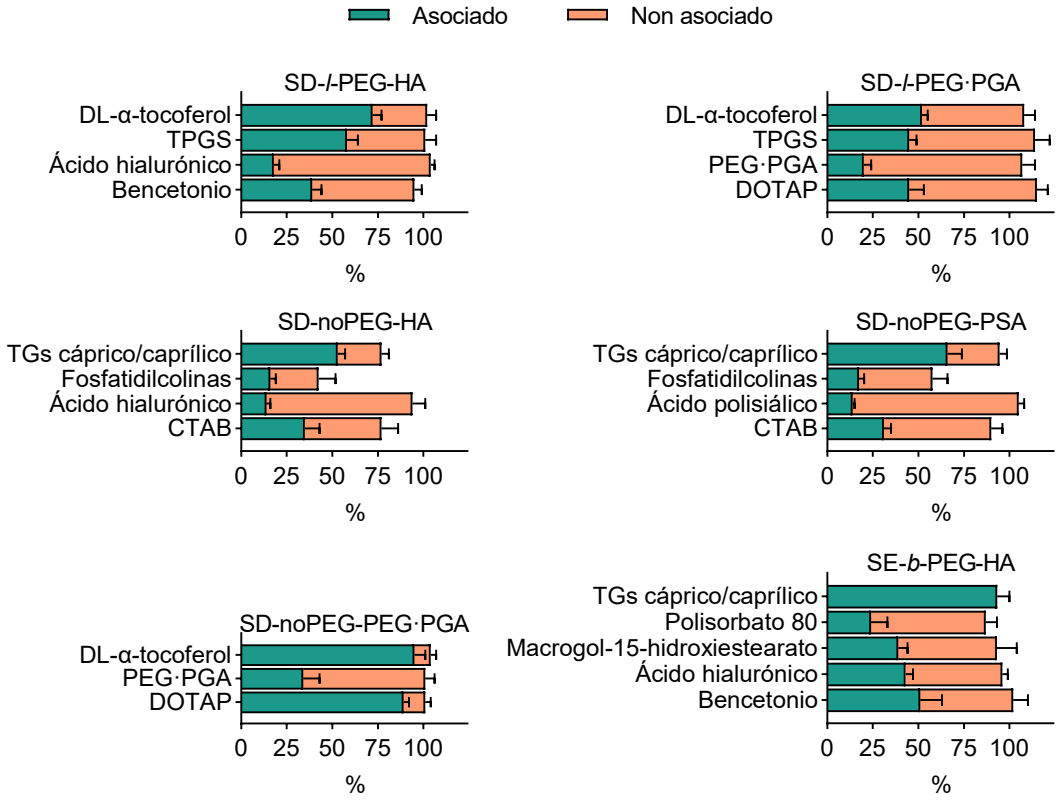


Ilustración 2. Porcentaxe de masa asociada e non asociada da masa total engadida no momento de formular para seis nanocápsulas

Abreviaturas: TGs: triglicéridos. CTAB: bromuro de hexadeciltrimetilamonio. DOTAP: 1,2-dioleoil-3-trimetilamoniopropano. PEG·PGA: ácido poliglutámico conxugado a polietilenglicol. TPGS: D-α-tocoferol polietilenglicol 1000 succinato. As composicións de SD-*l*-PEG-HA, SD-*l*-PEG-PEG·PGA, SD-*b*-PEG-HA, SD-noPEG-HA, SD-noPEG-PSA, SD-noPEG-PEG·PGA e SE-*b*-PEG-HA móstranse na Ilustración 1. Os valores representan a media ± desviación estándar (n = 3). Adaptada de [108] baixo licenza de Creative Commons.

Finalmente, os resultados mostraron que a asociación do polímero foi significativamente menor na formulación de SE (2 mg de polímero por g de aceite) en comparación coas de SD (de 36 a 57 mg de polímero por g de aceite).

2.3. Caracterización biolóxica

Para poder establecer comparacións entre as NCs, a área superficial das mesmas foi estandarizada a 0,25 $m^2 \cdot mL^{-1}$, incubadas durante 1 h en 90 % plasma humano a 37 °C e sometidas a ultracentrifugación nun gradiente triplo de densidade. Dito gradiente permitiu a correcta separación dos nanosistemas, coas respectivas proteínas unidas formando a coroa proteica, das proteínas non unidas ás NCs. As proteínas unidas ás NCs foron visualizadas tras

USC DE SANTIAGO DE COMPOSTELA

electroforese en xeles de poliacrilamida e tintura fluorescente e cuantificadas por cromatografía líquida-espectrometría de masas.

A concentración de proteínas foi máis alta en SD-*l*-PEG-HA debido á alta asociación de apolipoproteína A-IV (Apo A-IV). As NCs elaboradas con axentes tensioactivos sen PEG (SD-no-PEG-HA, SD-noPEG-PSA e SD-noPEG-PEG·PGA) exhibiron unha cantidade total de proteína intermedia. Finalmente, as formulacións coa cantidade máis baixa de proteínas foron SE-*b*-PEG-HA e SD-*l*-PEG-PEG·PGA (Ilustración 3). Estes resultados concordan coa composición química das NCs, dado que SE-*b*-PEG-HA contén a maior densidade de PEG e SD-*l*-PEG-PEG·PGA foi a NC máis axeitada para prover un efecto "escudo" sobre a adsorción de proteínas (conformación en cepillo e peso molecular do PEG superior a 2 kDa).

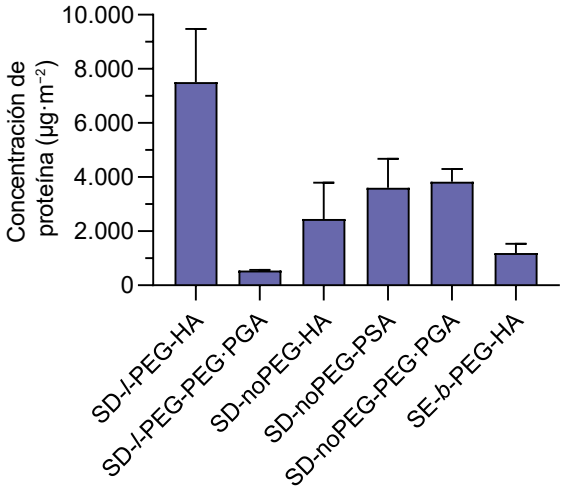


Ilustración 3. Cantidade total de proteínas unidas

As composicións de SD-*l*-PEG-HA, SD-*l*-PEG-PEG·PGA, SD-*b*-PEG-HA, SD-noPEG-HA, SD-noPEG-PSA, SD-noPEG-PEG·PGA e SE-*b*-PEG-HA móstranse na Ilustración 1. Os valores representan a media ± desviación estándar (n = 3).

As apolipoproteínas foron particularmente relevantes na coroa proteica de SD-*l*-PEG-PEG·PGA, SD-noPEG-HA, SD-noPEG-PSA, SD-*l*-PEG-HA e SD-noPEG-PEG·PGA, representado o 99,82, 84,47, 84,34, 75,27 e 50,71 % da masa proteica, respectivamente (Ilustración 4).

Os factores do complemento foron a segunda familia proteica máis relevante nas coroas proteicas, con todo, a súa importancia foi bastante diferente entre os prototipos. De feito, a masa de proteínas do complemento representou o 83,52, 24,05, 14,71, 11,82, 7,05 e 0,18 % da coroa proteica para SE-*b*-PEG-HA, SD-*l*-PEG-HA, SD-noPEG-HA, SD-noPEG-PSA, SD-noPEG-PEG·PGA e SD-*l*-PEG-PEG·PGA, respectivamente.

As inmunoglobulinas só estiveron presentes nas formulacións sen PEG, sendo o 3,52 % da coroa proteica no caso de SD-noPEG-PSA, 2,90 % en SD-noPEG-PEG·PGA e 0,39 % en SD-noPEG-HA.

Outras familias de proteínas foron detectadas en todas as NCs excepto SD-*l*-PEG-PEG·PGA e SE-*b*-PEG-HA. En xeral, estas proteínas presentáronse en porcentaxes baixas

(0,32 – 0,67 %), excepto no caso de SD-noPEG-PEG·PGA, onde representaron o 39,34% da coroa. Este fenómeno debeuse a unha intensa deposición de vitronectina (VTN).

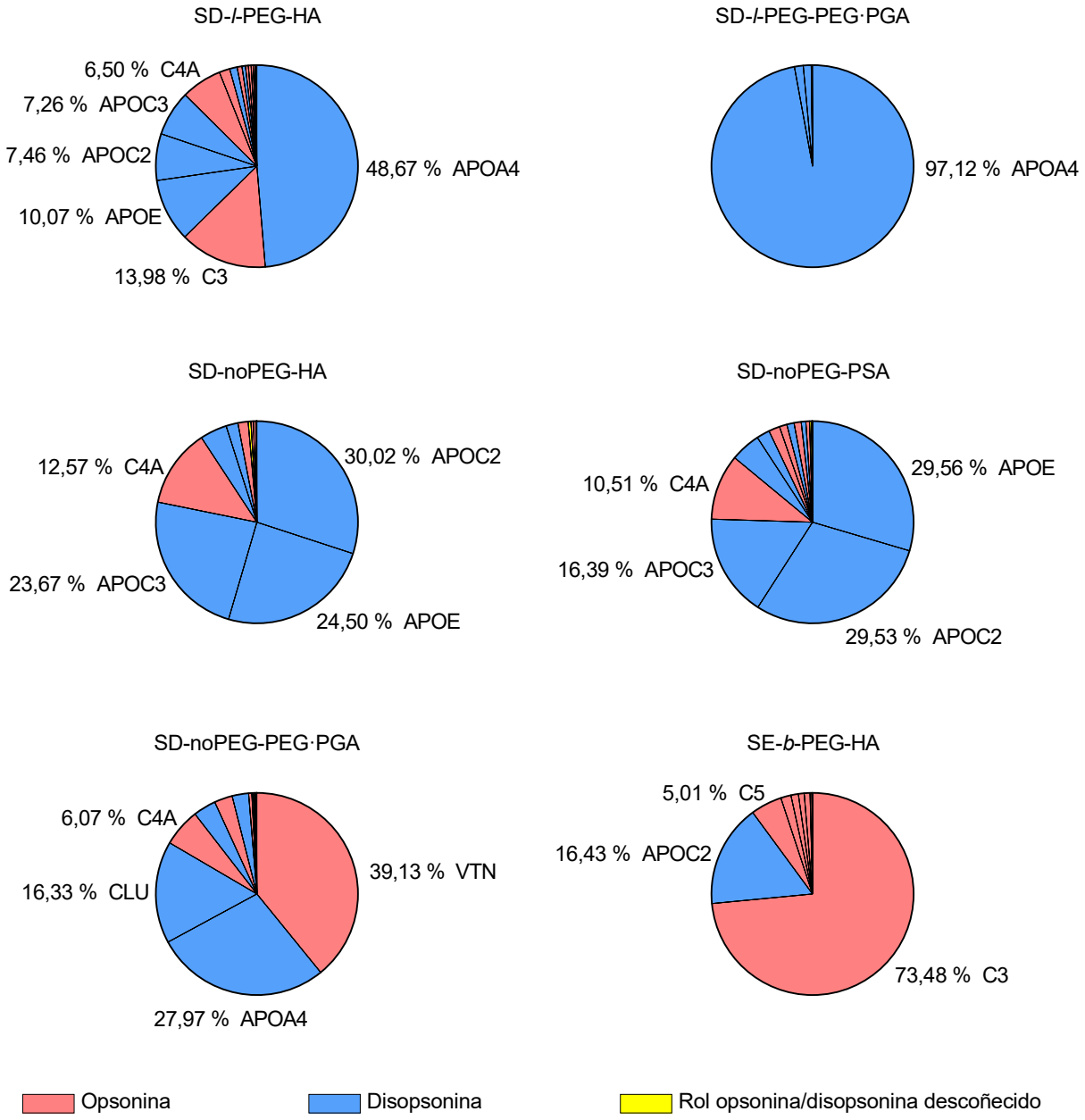


Ilustración 4. Porcentaxe en masa das diferentes proteínas detectadas na coroa proteica das nanocápsulas

Abreviaturas: APOA4: Apolipoproteína A-IV, APOC2: Apolipoproteína C-II, APOC3: Apolipoproteína C-III, APOE: Apolipoproteína E, C3: Complemento C3, C4A: Complemento C4-A, C5: Complemento C5, CLU: Clusterina, VTN: Vitronectina. As composicións de SD-*l*-PEG-HA, SD-*l*-PEG-PEG·PGA, SD-*b*-PEG-HA, SD-noPEG-HA, SD-noPEG-PSA, SD-noPEG-PEG·PGA e SE-*b*-PEG-HA móstranse na Ilustración 1. Os valores representan a media de tres replicados.

A unión de VTN é moi interesante debido a que posúe unha secuencia arxinina-glicina-aspartato, a cal lle permite interactuar cos receptores integrinas como $\alpha_V\beta_3$. Aínda que este receptor non sexa específico de células de cancro,[109] moitos tumores sólidos

sobreexprésano,[109,110] e, de feito, documentouse unha maior internalización *in vitro* de liposomas,[109] lipoplexos de 1,2-dioleoil-3-trimetilamoniopropano (DOTAP)/ADN[111] e nanopartículas lipídicas[111] cunha coroa proteica enriquecida en VTN. A alta unión de VTN neste sistema está relacionada coa presenza de DOTAP, en consonancia co descrito na literatura.[112,113]

A cantidade de Apo A-IV foi extraordinaria no caso de SD-*l*-PEG-HA, detectándose máis de 3,6 $mg \cdot m^{-2}$. Apo A-IV tamén foi relevante para SD-*l*-PEG-PEG·PGA, onde, en moita menor cantidade, representou máis do 97 % da súa coroa proteica. Neste sentido, SD-*l*-PEG-HA podería ser, de entre os nanosistemas testados, o máis prometedor para acumulación hepática, dada a alta densidade de receptores para Apo A-IV en dito órgano. Por outra banda, SD-*l*-PEG-PEG·PGA podería ser o sistema que sufrise a menor fagocitose por parte do sistema inmune.

Finalmente, outras relacións entre a composición das NCs e a coroa proteica foron confirmadas. Por exemplo, os sistemas que conteñen fosfatidilcolina sufriron unha forte unión de apolipoproteínas E e C-II.

Como conclusión deste experimento, as seis NCs estudadas posuíron unha coroa proteica diferente, o cal se pode traducir nun destino biolóxico distinto. SD-noPEG-PEG·PGA foi fortemente recuberta por VTN, mentres que a coroa proteica de SD-*l*-PEG-PEG·PGA foi a menos abundante. Baseándonos nestes resultados, os prototipos SD-noPEG-PEG·PGA e SD-*l*-PEG-PEG·PGA foron elixidos como os máis prometedores para o tratamento do cancro de pulmón.

3. NANOCÁPSULAS CARGADAS CON GALUNISERTIB E STATTIC PARA O TRATAMENTO DO CANCRO DE PULMÓN

A vía de STAT3 está sobreactivada no 70 % dos tumores sólidos humanos, incluíndo o cancro de pulmón.[114,115] Nas células de cancro, a activación de STAT3 induce o aumento do crecemento tumoral, redución da apoptose e desenvolvemento de resistencias.[114,116,117] Por outra banda, a activación de STAT3 en macrófagos promove a súa polarización cara o fenotipo M2, o cal está asociado a funcións reparadoras do tecido e antiinflamatorias, as cales axudan á progresión do cancro.[115,118]

A vía de TGF-β promove o crecemento celular, invasión, diseminación e desenvolvemento de resistencias por parte das células de cancro.[119] E, do mesmo xeito que STAT3, promove a polarización dos macrófagos cara o fenotipo M2.[119]

Varios inhibidores da vía de STAT3 están actualmente en ensaios clínicos en Europa e EE. UU.[120–133] No caso da vía de TGF-β, 5 fármacos atópanse actualmente comercializados.[134–149] Con todo, ditos tratamentos posúen limitacións biofarmacéuticas que comprometen a súa capacidade terapéutica. Por exemplo, notificáronse toxicidades hepáticas, pancreáticas, cerebrais e cardíacas severas tras o tratamento con inhibidores de TGF-β.[134,135,138,140,141,147–149] No caso dos inhibidores de STAT3, a maior preocupación provén das súas posibles toxicidades a nivel cerebral.[150,151] Ditas toxicidades son provocadas pola biodistribución indiscriminada dos fármacos tras a súa administración oral e a presenza ubicua de ditas dianas no organismo.

A encapsulación dos inhibidores de STAT3 e TGF-β supón unha estratexia terapéutica prometedora dado que: (i) a encapsulación dos fármacos modifica o seu perfil de biodistribución, potencialmente reducindo os seus efectos adversos e promovendo a súa acumulación no tumor por mecanismos de acumulación pasiva ou activa; (ii) a terapia combinada pode ter efectos sinérxicos, por tanto, unha maior eficacia terapéutica; (iii) ditos fármacos promoven un ambiente tumoral proinflamatorio, o cal axuda ao sistema inmune a atacar ás células de cancro; (iv) a terapia combinatoria pode reducir a formación de resistencias; e (iv) os inhibidores de TGF-β promoven a penetración de nanopartículas no tumor xa que aumentan a permeabilidade dos vasos sanguíneos.[152,153]

Polo tanto, o obxectivo desta parte do traballo foi a modificación do perfil de biodistribución do fármaco galunisertib (inhibidor de TGF-β, actualmente en ensaios clínicos) e stattic (inhibidor de STAT3, actualmente en fase preclínica). Para iso, ditos fármacos foron incorporados en NCs.

3.1. Deseño e caracterización de nanocápsulas cargadas con galunisertib e stattic

En base aos resultados da sección anterior, desenvolvéronse novos prototipos de NCs. Por simplicidade, xa que todos os prototipos comparten a cuberta polimérica de PEG·PGA, foron nomeados en función da natureza do seu axente tensioactivo (Ilustración 5).

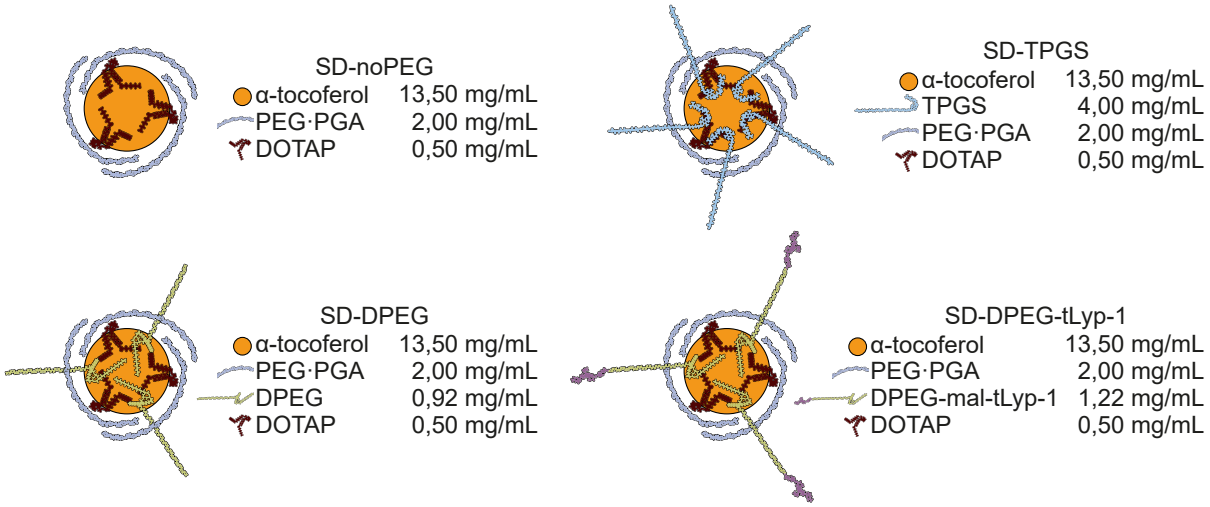


Ilustración 5. Representación esquemática do ordenamento esperado dos compostos presentes nas nanocápsulas e a súa composición teórica

SD-noPEG: Formulación preparada pola técnica de desprazamento do solvente e composta por axentes tensioactivos sen PEG (DOTAP) e cuberta de PEG·PGA. **SD-TPGS**: Formulación preparada pola técnica de desprazamento do solvente e composta por PEG lineal (TPGS), DOTAP e cuberta de PEG·PGA. **SD-DPEG**: formulación preparada pola técnica de desprazamento do solvente e composta por PEG lineal (DPEG) e cuberta de PEG·PGA. **SD-DPEG-tLyp-1**: Formulación preparada pola técnica de desprazamento do solvente e composta por PEG lineal (DPEG-tLyp-1) e cuberta de PEG·PGA. **Abreviaturas**: DOTAP: 1,2-dioleoil-3-trimetilamoniopropano. DPEG: DSPE-PEG_{2000} [*N*-(carbonil-metoxipolietilenglicol-2000)-1,2-distearoil-sn-glicero-3-fosfoetanolamina]. DPEG-tLyp-1: DSPE-PEG_{2000}-maleimida-tLyp-1. PEG·PGA: ácido poliglutámico conxugado a polietilenglicol. TPGS: D-α-tocoferol polietilenglicol 1000 succinato.

USC UNIVERSIDADE DE SANTIAGO DE COMPOSTELA

En resumo, as formulacións desenvolvidas cumpriron as propiedades desexadas en termos de tamaño de partícula (próximas a 100 nm) e carga superficial (potencial ζ próximo á neutralidade ou moderadamente negativo). A carga superficial más negativa deuse na formulación SD-noPEG debido á falta de axentes tensioactivos con PEG. As AE dos fármacos variaron entre o 36 e 75 % para o galunisertib e o 26 e 54 % para o stattic. As AE máis altas presentárona os sistemas SD-noPEG e SD-DPEG. No caso de SD-noPEG, isto debeuse á ausencia de axentes tensioactivos con PEG, xa que estes poden formar micelas coa capacidade de solubilizar parte dos fármacos. Todas as NCs resultaron ser estables en condicións de almacenamento durante 2 meses (Táboa 2).

Táboa 2. Caracterización fisicoquímica das nanocápsulas SD-noPEG, SD-TPGS, SD-DPEG e SD-DPEG-tLyp-1 cargadas con galunisertib e stattic

	SD-noPEG	SD-TPGS	SD-DPEG	SD-DPEG-tLyp-1
[Galunisertib] final ($mg \cdot mL^{-1}$)	1,25	1,25	1,25	1,25
[Stattic] final ($mg \cdot mL^{-1}$)	0,0625	0,0625	0,0625	0,0625
Contido de galunisertib (%)	7,2	5,9	6,9	6,7
Contido de stattic (%)	0,4	0,3	0,3	0,3
Diámetro hidrodinámico (DLS) (nm)	118 ± 3	87 ± 9	98 ± 7	106 ± 14
PDI	0,05 ± 0,03	0,19 ± 0,06	0,09 ± 0,02	0,15 ± 0,05
Potencial ζ (mV)	−21 ± 1	−3 ± 2	−10 ± 2	+5 ± 7
AE de galunisertib (%)	75 ± 11	36 ± 7	71 ± 10	58 ± 12
AE de stattic (%)	50 ± 1	26 ± 12	54 ± 12	38 ± 11
pH	5,5 ± 0,1	5,4 ± 0,1	6,6 ± 0,2	6,1 ± 0,1

As composicións de SD-noPEG, SD-TPGS, SD-DPEG e SD-DPEG-tLyp-1 móstranse na Ilustración 5 **Abreviaturas:** AE: eficiencia de asociación. DLS: dispersión dinámica de luz. PDI: índice de polidispersión. Os valores representan a media ± desviación estándar (n = 3).

3.2. AVALIACIÓN *IN VITRO* DAS NANOCÁPSULAS CARGADAS CON GALUNISERTIB E STATTIC

A estabilidade das formulacións foi confirmada en tampón fosfato salino (PBS) suplementado con 10 % de soro bovino fetal (FBS) a 37 °C durante 24 h e a liberación dos fármacos en ditas condicións foi moi baixa no caso do stattic e alta no do galunisertib. Despois, confirmouse a internalización das NCs nas liñas celulares de cancro (CMT 167) e macrófagos (RAW 264.7). Ditos resultados demostraron unha internalización dependente de temperatura e dose.

A toxicidade das NCs foi estudada nas mesmas liñas celulares. No caso das células de cancro, a toxicidade das NCs cargadas con galunisertib e stattic foi similar á dos fármacos libres. Con todo, o prototipo SD-noPEG demostrou unha toxicidade menor que a dos fármacos libres no caso dos macrófagos.

Finalmente, a eficacia de inhibición das vías de STAT3 e TGF-β foi avaliada, por separado, en macrófagos *in vitro*. As NCs SD-noPEG cargadas con galunisertib ou stattic resultaron efectivas na repolarización de macrófagos cara o fenotipo M1. A encapsulación de galunisertib

USC DE SANTIAGO DE COMPOSTELA

aumentou o seu efecto terapéutico, mentres que se obtivo unha lixeira redución da eficacia por parte do stattic (Ilustración 6).

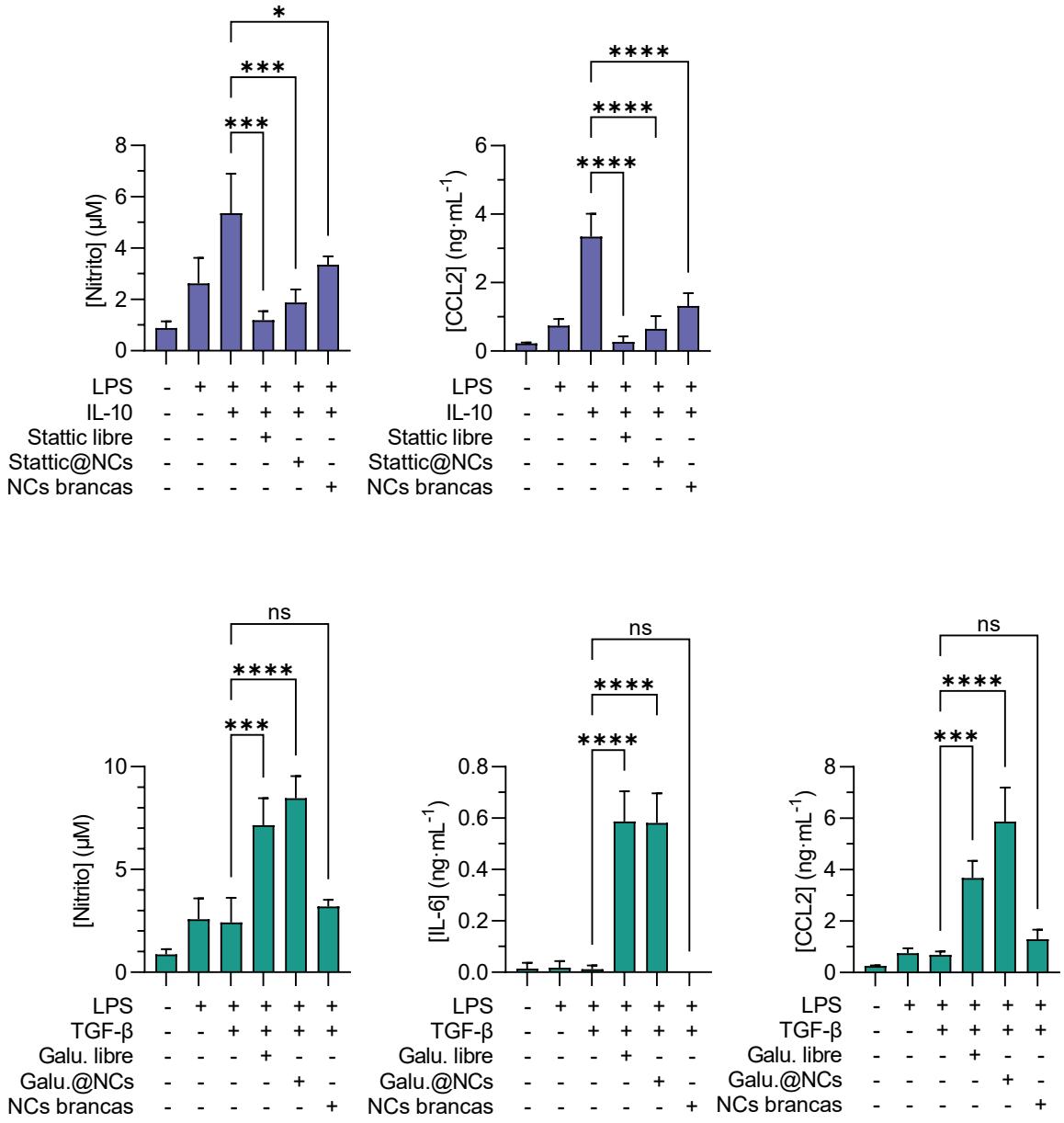


Ilustración 6. Eficacia *in vitro* das NCs SD-noPEG cargadas con stattic ou galunisertib na liña celular de macrófagos RAW 264.7

No caso do estudo da eficacia do stattic, a vía de STAT3 foi activada mediante a adición de LPS e IL-10. Despois, stattic libre ou cargado nas NCs ou as NCs brancas foron engadidos. Comprobouse a redución de nitritos e a produción de CCL2. No caso do galunisertib, a vía do TGF-ß foi activada mediante a adición de LPS e TGF-ß. Despois, galunisertib libre ou cargado nas NCs ou as NCs brancas foron engadidas. Incrementos de nitritos e a produción de IL-6 e CCL2 foron comprobados. As NCs SD-noPEG cargadas con galunisertib ou stattic resultaron efectivas. Mentres que a eficacia das NCs SD-noPEG cargadas con stattic foi menor que a do stattic libre, o efecto contrario foi observado para o galunisertib. **Abreviaturas**: Galu.: galunisertib. IL-6: interleucina 6. IL-10: interleucina 10. LPS: lipopolisacáridos. NCs: nanocápsulas. TGF-ß: factor de crecemento transformante beta. A composición de SD-noPEG móstrase na Ilustración 5. Os valores representan a media mean ± desviación estándar de dous replicados celulares e un replicado das NCs. Análises da varianza (ANOVA) de 1 cola contra os grupos LPS + IL-10 ou LPS + TGF-ß seguido pola proba de Dunnett. Valores $p < 0,05$ foron considerados estatisticamente significativos (*). Ademais, (**) se o valor $p < 0,01$, (***) se o valor $p < 0,001$ e (****) se o valor $p < 0,0001$. ns: non significativo.

Dado que estes fármacos non teñen problemas de permeabilidade de membranas, a redución da eficacia do stattic pode ser debida a súa permanencia na fracción de NCs que non foron internalizadas.

Como conclusións deste traballo, a encapsulación de galunisertib e stattic en NCs preservou a actividade dos fármacos en liñas celulares de cancro mentres que reduciu lixeiramente a súa toxicidade en macrófagos asociados a tumores. Ademais, a formulación SD-noPEG inhibiu con éxito as vías de STAT3 e TGF-β *in vitro*. Por tanto, os beneficios da co-encapsulación en termos de sinerxía e redución de efectos adversos son prometedores para a continuación da súa avaliación *in vivo*.

4. LIBERACIÓN INTRACELULAR DE ANTICORPOS MONOCLONAIS FORMULADOS EN NANOCÁPSULAS

Moitas das dianas oncolóxicas máis relevantes permanecen intratables debido a súa localización intracelular, a cal impide o acceso de mAbs, e a que non posúen rexións de unión a moléculas pequenas ben definidas. Algúns exemplos de ditas dianas son o protooncoxene da mielocitomatose, o protooncoxene da mieloblastose, o factor nuclear-κB, a variante 7 do receptor androxénico, STAT3, ou a proteína supresora de tumores p53. Ademais, o desenvolvemento de terapias contra a familia de oncoxenes máis frecuentemente mutada en cancros humanos, o KRAS, non tivo éxito para moitas das súas mutacións.[154]

Diferentes estratexias terapéuticas foron investigadas en ensaios clínicos para o tratamento das mutacións de KRAS.[155] A maioría de ditos esforzos leváronse a cabo na mutación G12C. Como consecuencia, decenas de inhibidores de $KRAS^{G12C}$ encóntranse actualmente baixo ensaios clínicos e, moi recentemente, a Axencia Europea do Medicamento (EMA) e a Administración de Alimentos e Medicamentos dos Estados Unidos (FDA) aprobaron o uso do Lumakras™ (sotorasib), converténdose no primeiro tratamento contra unha mutación de KRAS.[156] Con todo, é preciso moito máis esforzo para obter tratamentos axeitados contra cancros con outras mutacións de KRAS como a G12V.

Esta sección ten por obxectivo o desenvolvemento dunha plataforma nanotecnolóxica que permita a liberación intracelular de mAbs. Dita plataforma será empregada para inhibir a proliferación do cancro de pulmón en cancros con mutación G12V de KRAS por parte dun mAb anti-$KRAS^{G12V}$.

Como primeiro paso no desenvolvemento de NCs para a liberación intracelular de mAbs, deseñáronse máis formulacións, baseándose naquelas seleccionadas en seccións anteriores e realizouse un cribado destas en base ás súas propiedades fisicoquímicas (tamaño, carga superficial, estabilidade coloidal e eficiencia de asociación do mAb modelo bevacizumab; BVZ). Como resultado, obtivéronse dous novos prototipos, os cales volveron ser optimizados ao substituír o mAb modelo polo terapéutico.

USC UNIVERSIDADE DE SANTIAGO DE COMPOSTELA

4.1. DESEÑO E CARACTERIZACIÓN DE NANOCÁPSULAS CARGADAS CUN ANTICORPO MONOCLONAL ANTI-KRAS^{G12V}

Despois do primeiro cribado con BVZ como proteína modelo, os sistemas cargados co mAb terapéutico anti-KRAS^{G12V} volveron ser optimizados (Ilustración 7).

Ditas NCs exhibiron un diámetro hidrodinámico reducido (< 150 nm), PDI < 0,3, potencial ζ neutro e, no caso de SD-P80, unha alta eficiencia de asociación do mAb (Táboa 3).

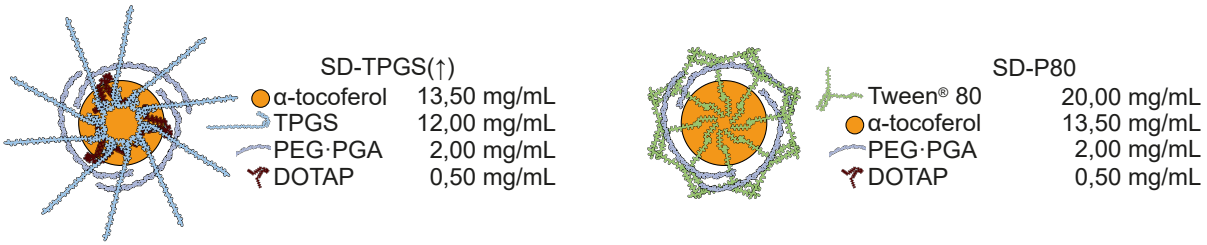


Ilustración 7. Representación esquemática do ordenamento esperado dos compostos presentes nas NCs e a súa composición teórica

SD-TPGS(↑): Formulación preparada pola técnica de desprazamento do solvente e composta por PEG lineal (TPGS; 12 mg·mL^{-1}) e cuberta de PEG·PGA. SD-P80: Formulación preparada por la técnica de desprazamento do solvente e composta por PEG ramificado (polisorbato 80) e cuberta de PEG·PGA. **Abreviaturas:** DOTAP: 1,2-dioleoil-3-trimetilamoniopropano. NCs: nanocápsulas. P80: polisorbato 80. PEG·PGA: ácido poliglutámico conxugado a polietilenglicol. TPGS: D-α-tocoferol polietilenglicol 1000 succinato.

Táboa 3. Propiedades fisicoquímicas das NCs cargadas co mAb anti-KRAS^{G12V}

	SD-TPGS(↑)	SD-P80
Diámetro hidrodinámico (DLS) (nm)	117 ± 5	143 ± 14
PDI	0,20 ± 0,06	0,21 ± 0,05
Potencial ζ (mV)	−5 ± 1	+1 ± 1
Contido de mAb anti-KRAS^{G12V} (%)	6,67	5,26
Eficiencia de asociación do mAb anti-KRAS^{G12V} (%)	11 ± 19	90 ± 6

Abreviaturas: DLS: dispersión dinámica de luz. KRAS: homólogo do oncoxene viral do sarcoma de rata Kirsten. mAb: anticorpo monoclonal. NCs: nanocápsulas. PDI: índice de polidispersión. Os valores representan a media ± desviación estándar (n = 3). As composicións de SD-TPGS(↑) e SD-P80 móstranse na Ilustración 7.

4.2. ESTUDO DO RECOÑECEMENTO INTRACELULAR DA DIANA POR PARTE DE NANOCÁPSULAS CARGADAS CUN ANTICORPO MONOCLONAL ANTI-KRAS^{G12V}

A internalización dos dous sistemas foi avaliada en células de cancro de pulmón con mutación G12V de KRAS (CMT 167) mediante a técnica de tintura intracelular. Dita técnica permite o marcaxe selectivo da fracción do mAb terapéutico que foi internalizado nas células. Os resultados de dito experimento demostraron unha liberación intracelular relevante e dependente de temperatura e dose por parte da formulación SD-P80 (Ilustración 8). Con todo, a internalización foi moito menor no caso de SD-TPGS.

USC UNIVERSIDADE DE SANTIAGO DE COMPOSTELA

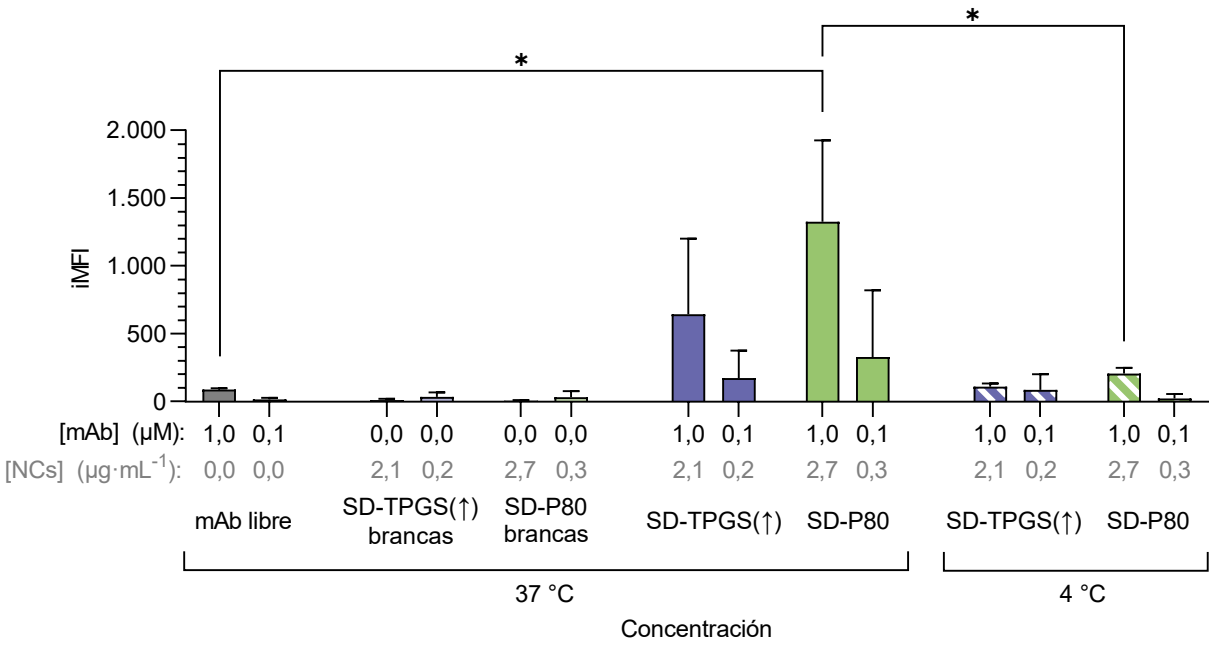


Ilustración 8. Tintura intracelular do mAb anti-KRAS^{G12V} na liña de cancro de pulmón CMT 167 tras incubación de 4 h a 37 °C

SD-P80 liberou significativamente o mAb anti-KRAS^{G12V} na liña de cancro de pulmón CMT 167 tras incubación durante 4 h a 37 °C a unha concentración de mAb de 1 μM. Este efecto demostrou ser dependente de temperatura (t-test *vs.* mAb libre ou NCs brancas). **Abreviaturas:** mAb: anticorpo monoclonal. NCs: nanocápsulas. iMFI: media da intensidade de fluorescencia integrada. As composicións de SD-TPGS(↑) e SD-P80 móstranse na Ilustración 7. Os valores representan a media ± desviación estándar (n = 3).

Tras a comprobación de que o mAb anti-KRAS^{G12V} é capaz de penetrar nas células de cancro de pulmón CMT 167 tras a súa incorporación en SD-P80, realizouse un estudo de recoñecemento intracelular da súa diana. Neste experimento, os mAb anti-KRAS^{G12V} presentes no interior das células foron inmunoprecipitados por unión doutro anticorpo á súa rexión constante e comprobouse se a rexión variable do mAb terapéutico tiña unida a proteína KRAS^{G12V} (Ilustración 9). Os resultados de Western Blot revelaron que o mAb terapéutico conseguiu unirse á súa diana intracelularmente.

Como conclusións desta sección, as nanocápsulas poliméricas representan unha plataforma de liberación de fármacos moi versátil xa que poden ser adaptadas á formulación de anticorpos monoclonais tales como o BVZ ou o anti-KRAS^{G12V}. As formulacións seleccionadas demostraron ter una alta capacidade para asociar anticorpos monoclonais e liberalos a nivel intracelular. Ademais, foi posible observar un recoñecemento da diana por parte do anticorpo monoclonal anti-KRAS^{G12V} liberado dende as nanocápsulas dentro das células. A avaliación dos resultados terapéuticos do mAb anti-KRAS^{G12V} formulado en nanocápsulas deberá ser realizada en futuros estudos *in vivo*.

USC UNIVERSIDADE DE SANTIAGO DE COMPOSTELA

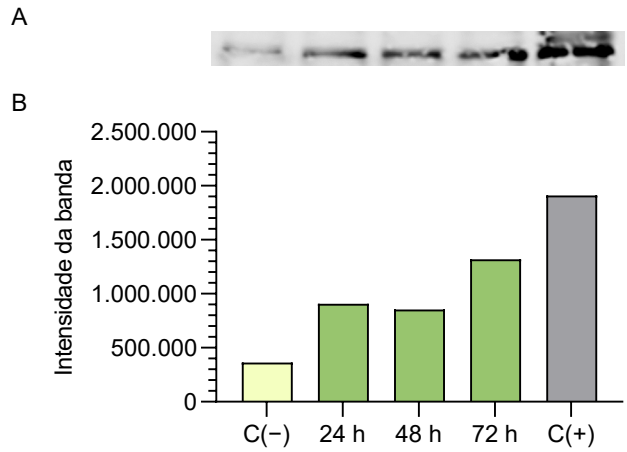


Ilustración 9. Inmunoprecipitación da proteína KRAS^{G12V} polo mAb anti-KRAS^{G12V} cargado nas NCs SD-P80 tras incubación de 24, 48 e 72 h na liña celular CMT 167

(A) Imaxe sen procesar da membrana de WB. **(B)** Intensidade das bandas correspondentes na membrana de WB. Para o control negativo [C(−)], 1 mg de lisado celular de CMT 167 foi immunoprecipitado con perlas de agarosa con anti-mAbs. Para o control positivo [C(+)], 5 µg do mAb anti-KRAS^{G12V} foron engadidos a 1 mg de lisado celular de CMT 167 e immunoprecipitados coas mesmas perlas. **Abreviaturas:** KRAS: homólogo do oncoxene viral do sarcoma de rata Kirsten. mAb: anticorpo monoclonal. NCs: nanocápsulas. A composición de SD-P80 móstrase na Ilustración 7. Os valores representan a media de 1 replicado.

5. REFERENCIAS

[1] Global Cancer Observatory. International Agency for Research on Cancer. https://gco.iarc.fr. Accessed: October 28, 2022.

[2] American Lung Association. Lung Cancer Basics. https://www.lung.org/lung-health-diseases/lung-disease-lookup/lung-cancer/basics/lung-cancer-types. Accessed: October 31, 2022.

[3] American Society of Clinical Oncology (ASCO). Lung Cancer - Non-Small Cell: Statistics | Cancer.Net. https://www.cancer.net/cancer-types/lung-cancer-non-small-cell/statistics. Accessed: October 31, 2022.

[4] J. Judd, N. A. Karim, H. Khan, A. R. Naqash, Y. Baca, J. Xiu, A. M. VanderWalde, H. Mamdani, L. E. Raez, M. Nagasaka, S. G. Pai, M. A. Socinski, J. J. Nieva, C. Kim, A. J. Wozniak, C. Ikpeazu, G. de Lima Lopes, A. I. Spira, W. M. Korn, E. S. Kim, S. V. Liu, H. Borghaei. Characterization of KRAS mutation subtypes in non-small cell lung cancer. *Molecular Cancer Therapeutics*. 20, 2577–2584. (2021). doi: 10.1158/1535-7163.MCT-21-0201.

[5] R. Veluswamy, P. C. Mack, J. Houldsworth, E. Elkhouly, F. R. Hirsch. KRAS G12C–Mutant Non–Small Cell Lung Cancer: Biology, Developmental Therapeutics, and Molecular Testing. *Journal of Molecular Diagnostics*. 23, 507–520. (2021). doi: 10.1016/j.jmoldx.2021.02.002.

[6] H. Mithoowani, M. Febbraro. Non-Small-Cell Lung Cancer in 2022: A Review for General Practitioners in Oncology. *Current Oncology*. 29, 1828–1839. (2022). doi: 10.3390/curroncol29030150.

[7] Y. Barenholz. Doxil® - The first FDA-approved nano-drug: Lessons learned. *Journal of Controlled Release*. 160, 117–134. (2012). doi: 10.1016/j.jconrel.2012.03.020.

[8] National Cancer Institute - NIH. Types of Chemotherapy Drugs. https://training.seer.cancer.gov/treatment/chemotherapy/types.html. Accessed: November 3, 2022.

[9] J. Logie, A. N. Ganesh, A. M. Aman, R. S. Al-awar, M. S. Shoichet. Preclinical evaluation of taxane-binding peptide-modified polymeric micelles loaded with docetaxel in an orthotopic breast cancer mouse model. *Biomaterials*. 123, 39–47. (2017). doi: 10.1016/j.biomaterials.2017.01.026.

[10] A. C. Anselmo, S. Mitragotri. Nanoparticles in the clinic. *Bioengineering & Translational Medicine*. 1, 10–29. (2016). doi: 10.1002/btm2.10003.

[11] J. Shi, P. W. Kantoff, R. Wooster, O. C. Farokhzad. Cancer nanomedicine: progress, challenges and opportunities. *Nature Reviews Cancer*. 17, 20–37. (2017). doi: 10.1038/nrc.2016.108.

[12] J. Wolfram, M. Ferrari. Clinical cancer nanomedicine. *Nano Today*. 25, 85–98. (2019). doi: 10.1016/j.nantod.2019.02.005.

[13] A. Wicki, D. Witzigmann, V. Balasubramanian, J. Huwyler. Nanomedicine in cancer therapy: challenges,

USC UNIVERSIDADE DE SANTIAGO DE COMPOSTELA

opportunities, and clinical applications. *Journal of Controlled Release*. 200, 138–157. (2015). doi: 10.1016/j.jconrel.2014.12.030.
[14] L. Milling, Y. Zhang, D. J. Irvine. Delivering safer immunotherapies for cancer. *Advanced Drug Delivery Reviews*. 114, 79–101. (2017). doi: 10.1016/j.addr.2017.05.011.
[15] Y. Matsumura, H. Maeda. A New Concept for Macromolecular Therapeutics in Cancer Chemotherapy: Mechanism of Tumoritropic Accumulation of Proteins and the Antitumor Agent Smancs. *Cancer Research*. 46, 6387–6392. (1986).
[16] M. Morales-Cruz, Y. Delgado, B. Castillo, C. M. Figueroa, A. Molina, A. Torres, M. Milian, K. Griebenow. Smart Targeting To Improve Cancer Therapeutics. *Drug Design, Development and Therapy*. 13, 3753–3772. (2019). doi: 10.2147/DDDT.S219489.
[17] M. F. Attia, N. Anton, J. Wallyn, Z. Omran, T. F. Vandamme. An overview of active and passive targeting strategies to improve the nanocarriers efficiency to tumour sites. *Journal of Pharmacy and Pharmacology*. 71, 1185–1198. (2019). doi: 10.1111/jphp.13098.
[18] W. Yu, R. Liu, Y. Zhou, H. Gao. Size-Tunable Strategies for a Tumor Targeted Drug Delivery System. *ACS Central Science*. 6, 100–116. (2020). doi: 10.1021/acscentsci.9b01139.
[19] W. Jiang, B. Y. S. Kim, J. T. Rutka, W. C. W. Chan. Nanoparticle-mediated cellular response is size-dependent. *Nature Nanotechnology*. 3, 145–150. (2008). doi: 10.1038/nnano.2008.30.
[20] A. K. Pearce, R. K. O'Reilly. Insights into Active Targeting of Nanoparticles in Drug Delivery: Advances in Clinical Studies and Design Considerations for Cancer Nanomedicine. *Bioconjugate Chemistry*. 30, 2300–2311. (2019). doi: 10.1021/acs.bioconjchem.9b00456.
[21] C. Sarisozen, U. Joshi, L. P. Mendes, V. P. Torchilin. In *Stimuli Responsive Polymeric Nanocarriers for Drug Delivery Applications*. Elsevier. (2019). pp. 269–304.
[22] L. Salvioni, M. A. Rizzuto, J. A. Bertolini, L. Pandolfi, M. Colombo, D. Prosperi. Thirty Years of Cancer Nanomedicine: Success, Frustration, and Hope. *Cancers*. 11, 1855. (2019). doi: 10.3390/cancers11121855.
[23] P. Foroozandeh, A. A. Aziz. Insight into Cellular Uptake and Intracellular Trafficking of Nanoparticles. *Nanoscale Research Letters*. 13, 339. (2018). doi: 10.1186/s11671-018-2728-6.
[24] J. Zhao, M. H. Stenzel. Entry of nanoparticles into cells: The importance of nanoparticle properties. *Polymer Chemistry*. 9, 259–272. (2018). doi: 10.1039/c7py01603d.
[25] J. Yoo, C. Park, G. Yi, D. Lee, H. Koo. Active Targeting Strategies Using Biological Ligands for Nanoparticle Drug Delivery Systems. *Cancers*. 11, 640. (2019). doi: 10.3390/cancers11050640.
[26] A. C. Anselmo, S. Mitragotri. Impact of particle elasticity on particle-based drug delivery systems. *Advanced Drug Delivery Reviews*. 108, 51–67. (2017). doi: 10.1016/j.addr.2016.01.007.
[27] T. Lammers, F. Kiessling, W. E. Hennink, G. Storm. Drug targeting to tumors: Principles, pitfalls and (pre-) clinical progress. *Journal of Controlled Release*. 161, 175–187. (2012). doi: 10.1016/j.jconrel.2011.09.063.
[28] Y. Hui, X. Yi, F. Hou, D. Wibowo, F. Zhang, D. Zhao, H. Gao, C.-X. Zhao. Role of Nanoparticle Mechanical Properties in Cancer Drug Delivery. *ACS Nano*. 13, 7410–7424. (2019). doi: 10.1021/acsnano.9b03924.
[29] O. Kutova, E. Guryev, E. Sokolova, R. Alzeibak, I. Balalaeva. Targeted Delivery to Tumors: Multidirectional Strategies to Improve Treatment Efficiency. *Cancers*. 11, 68. (2019). doi: 10.3390/cancers11010068.
[30] Y. Shi, R. van der Meel, X. Chen, T. Lammers. The EPR effect and beyond: Strategies to improve tumor targeting and cancer nanomedicine treatment efficacy. *Theranostics*. 10, 7921–7924. (2020). doi: 10.7150/thno.49577.
[31] X. Liu, J. Jiang, H. Meng. Transcytosis - An effective targeting strategy that is complementary to "EPR effect" for pancreatic cancer nano drug delivery. *Theranostics*. 9, 8018–8025. (2019). doi: 10.7150/thno.38587.
[32] S. Sindhwani, A. M. Syed, J. Ngai, B. R. Kingston, L. Maiorino, J. Rothschild, P. MacMillan, Y. Zhang, N. U. Rajesh, T. Hoang, J. L. Y. Wu, S. Wilhelm, A. Zilman, S. Gadde, A. Sulaiman, B. Ouyang, Z. Lin, L. Wang, M. Egeblad, W. C. W. Chan. The entry of nanoparticles into solid tumours. *Nature Materials*. 19, 566–575. (2020). doi: 10.1038/s41563-019-0566-2.
[33] S. Wilhelm, A. J. Tavares, Q. Dai, S. Ohta, J. Audet, H. F. Dvorak, W. C. W. W. Chan. Analysis of nanoparticle delivery to tumours. *Nature Reviews Materials*. 1, 16014. (2016). doi: 10.1038/natrevmats.2016.14.
[34] J. I. Hare, T. Lammers, M. B. Ashford, S. Puri, G. Storm, S. T. Barry. Challenges and strategies in anti-cancer nanomedicine development: An industry perspective. *Advanced Drug Delivery Reviews*. 108, 25–38. (2017). doi: 10.1016/j.addr.2016.04.025.
[35] F. T. Andón, E. Digifico, A. Maeda, M. Erreni, A. Mantovani, M. J. Alonso, P. Allavena. Targeting tumor associated macrophages: The new challenge for nanomedicine. *Seminars in Immunology*. 34, 103–113. (2017). doi: 10.1016/j.smim.2017.09.004.
[36] V. P. V. Torchilin, B. B. A. Khaw, V. V. N. Smirnov, E. Haber. Preservation of antimyosin antibody activity after covalent coupling to liposomes. *Biochemical and Biophysical Research Communications*. 89, 1114–1119. (1979). doi: 10.1016/0006-291X(79)92123-5.
[37] P. N. Navya, A. Kaphle, S. P. Srinivas, S. K. Bhargava, V. M. Rotello, H. K. Daima. Current trends and challenges in cancer management and therapy using designer nanomaterials. *Nano Convergence*. 6, 23. (2019). doi: 10.1186/s40580-019-0193-2.
[38] D. Rosenblum, N. Joshi, W. Tao, J. M. Karp, D. Peer. Progress and challenges towards targeted delivery of cancer therapeutics. *Nature Communications*. 9, 1410. (2018). doi: 10.1038/s41467-018-03705-y.
[39] A. K. Barui, J. Y. Oh, B. Jana, C. Kim, J. Ryu. Cancer-Targeted Nanomedicine: Overcoming the Barrier of the Protein Corona. *Advanced Therapeutics*. 3, 1900124. (2020). doi: 10.1002/adtp.201900124.

[40] P. Mi, H. Cabral, K. Kataoka. Ligand-Installed Nanocarriers toward Precision Therapy. *Advanced Materials*. 32, 1902604. (2020). doi: 10.1002/adma.201902604.
[41] N. Dammes, D. Peer. *Monoclonal antibody-based molecular imaging strategies and theranostic opportunities*, Vol. 10, Ivyspring International Publisher, (2020), pp. 938–955.
[42] P. J. Carter, G. A. Lazar. Next generation antibody drugs: Pursuit of the "high-hanging fruit." *Nature Reviews Drug Discovery*. 17, 197–223. (2018). doi: 10.1038/nrd.2017.227.
[43] E. Ruoslahti. Tumor penetrating peptides for improved drug delivery. *Advanced Drug Delivery Reviews*. 110–111, 3–12. (2017). doi: 10.1016/j.addr.2016.03.008.
[44] C. Teijeiro-Valiño, R. Novoa-Carballal, E. Borrajo, A. Vidal, M. Alonso-Nocelo, M. de la Fuente Freire, P. P. P. Lopez-Casas, M. Hidalgo, N. Csaba, M. J. Alonso. A multifunctional drug nanocarrier for efficient anticancer therapy. *Journal of Controlled Release*. 294, 154–164. (2019). doi: 10.1016/j.jconrel.2018.12.002.
[45] G. Berrecoso, J. Crecente-Campo, M. J. Alonso. Unveiling the pitfalls of the protein corona of polymeric drug nanocarriers. *Drug Delivery and Translational Research*. 10, 730–750. (2020). doi: 10.1007/s13346-020-00745-0.
[46] M. Mahmoudi, S. E. Lohse, C. J. Murphy, A. Fathizadeh, A. Montazeri, K. S. Suslick. Variation of protein corona composition of gold nanoparticles following plasmonic heating. *Nano Letters*. 14, 6–12. (2014). doi: 10.1021/nl403419e.
[47] M. Mahmoudi, N. Bertrand, H. Zope, O. C. Farokhzad. Emerging understanding of the protein corona at the nano-bio interfaces. *Nano Today*. 11, 817–832. (2016). doi: 10.1016/j.nantod.2016.10.005.
[48] S. Salameh, M. A. Van Der Veen, M. Kappl, J. R. Van Ommen. Contact forces between single metal oxide nanoparticles in gas-phase applications and processes. *Langmuir*. 33, 2477–2484. (2017). doi: 10.1021/acs.langmuir.6b02982.
[49] V. Pareek, A. Bhargava, V. Bhanot, R. Gupta, N. Jain, J. Panwar. Formation and characterization of protein corona around nanoparticles: a review. *Journal of Nanoscience and Nanotechnology*. 18, 6653–6670. (2018). doi: 10.1166/jnn.2018.15766.
[50] A. Almalik, H. Benabdelkamel, A. Masood, I. O. Alanazi, I. Alradwan, M. A. Majrashi, A. A. Alfadda, W. M. Alghamdi, H. Alrabiah, N. Tirelli, A. H. Alhasan. Hyaluronic acid coated chitosan nanoparticles reduced the immunogenicity of the formed protein corona. *Scientific Reports*. 7, 10542. (2017). doi: 10.1038/s41598-017-10836-7.
[51] S. Nagayama, K. Ogawara, Y. Fukuoka, K. Higaki, T. Kimura. Time-dependent changes in opsonin amount associated on nanoparticles alter their hepatic uptake characteristics. *International Journal of Pharmaceutics*. 342, 215–221. (2007). doi: 10.1016/j.ijpharm.2007.04.036.
[52] R. Gossmann, E. Fahrländer, M. Hummel, D. Mulac, J. Brockmeyer, K. Langer. Comparative examination of adsorption of serum proteins on HSA- and PLGA-based nanoparticles using SDS-PAGE and LC-MS. *European Journal of Pharmaceutics and Biopharmaceutics*. 93, 80–87. (2015). doi: 10.1016/j.ejpb.2015.03.021.
[53] M. P. Monopoli, D. Walczyk, A. Campbell, G. Elia, I. Lynch, F. Baldelli Bombelli, K. A. Dawson. Physical-chemical aspects of protein corona: relevance to in vitro and in vivo biological impacts of nanoparticles. *Journal of the American Chemical Society*. 133, 2525–2534. (2011). doi: 10.1021/ja107583h.
[54] D. Pozzi, G. Caracciolo, A. L. Capriotti, C. Cavaliere, S. Piovesana, V. Colapicchioni, S. Palchetti, A. Riccioli, A. Laganà. A proteomics-based methodology to investigate the protein corona effect for targeted drug delivery. *Molecular BioSystems*. 10, 2815–2819. (2014). doi: 10.1039/C4MB00292J.
[55] V. Mirshafiee, M. Mahmoudi, K. Lou, J. Cheng, M. L. Kraft. Protein corona significantly reduces active targeting yield. *Chemical Communications*. 49, 2557–2559. (2013). doi: 10.1039/c3cc37307j.
[56] V. Mirshafiee, R. Kim, S. Park, M. Mahmoudi, M. L. Kraft. Impact of protein pre-coating on the protein corona composition and nanoparticle cellular uptake. *Biomaterials*. 75, 295–304. (2016). doi: 10.1016/j.biomaterials.2015.10.019.
[57] V. Francia, K. Yang, S. Deville, C. Reker-Smit, I. Nelissen, A. Salvati. Corona composition can affect the mechanisms cells use to internalize nanoparticles. *ACS Nano*. 13, 11107–11121. (2019). doi: 10.1021/acsnano.9b03824.
[58] K. Yang, B. Mesquita, P. Horvatovich, A. Salvati. Tuning liposome composition to modulate corona formation in human serum and cellular uptake. *Acta Biomaterialia*. 106, 314–327. (2020). doi: 10.1016/j.actbio.2020.02.018.
[59] J. Gilleron, W. Querbes, A. Zeigerer, A. Borodovsky, G. Marsico, U. Schubert, K. Manygoats, S. Seifert, C. Andree, M. Stöter, H. Epstein-Barash, L. Zhang, V. Koteliansky, K. Fitzgerald, E. Fava, M. Bickle, Y. Kalaidzidis, A. Akinc, M. Maier, M. Zerial. Image-based analysis of lipid nanoparticle–mediated siRNA delivery, intracellular trafficking and endosomal escape. *Nature Biotechnology*. 31, 638–646. (2013). doi: 10.1038/nbt.2612.
[60] M. P. Monopoli, C. Åberg, A. Salvati, K. A. Dawson. Biomolecular coronas provide the biological identity of nanosized materials. *Nature Nanotechnology*. 7, 779–786. (2012). doi: 10.1038/nnano.2012.207.
[61] I. Lynch, T. Cedervall, M. Lundqvist, C. Cabaleiro-Lago, S. Linse, K. A. Dawson. The nanoparticle–protein complex as a biological entity; a complex fluids and surface science challenge for the 21st century. *Advances in Colloid and Interface Science*. 134–135, 167–174. (2007). doi: 10.1016/j.cis.2007.04.021.
[62] A. Cox, P. Andreozzi, R. Dal Magro, F. Fiordaliso, A. Corbelli, L. Talamini, C. Chinello, F. Raimondo, F. Magni, M. Tringali, S. Krol, P. J. Silva, F. Stellacci, M. Masserini, F. Re. Evolution of nanoparticle protein corona across the blood–brain barrier. *ACS Nano*. 12, 7292–7300. (2018). doi: 10.1021/acsnano.8b03500.
[63] A. L. Barrán-Berdón, D. Pozzi, G. Caracciolo, A. L. Capriotti, G. Caruso, C. Cavaliere, A. Riccioli, S. Palchetti, A. Laganaì. Time evolution of nanoparticle-protein corona in human plasma: relevance for targeted drug delivery. *Langmuir*. 29, 6485–6494. (2013). doi: 10.1021/la401192x.

USC UNIVERSIDADE DE SANTIAGO DE COMPOSTELA

[64] J. Kreuter, T. Hekmatara, S. Dreis, T. Vogel, S. Gelperina, K. Langer. Covalent attachment of apolipoprotein A-I and apolipoprotein B-100 to albumin nanoparticles enables drug transport into the brain. *Journal of Controlled Release*. 118, 54–58. (2007). doi: 10.1016/j.jconrel.2006.12.012.

[65] H. R. Kim, K. Andrieux, S. Gil, M. Taverna, H. Chacun, D. Desmaële, F. Taran, D. Georgin, P. Couvreur. Translocation of poly(ethylene glycol-co-hexadecyl)cyanoacrylate nanoparticles into rat brain endothelial cells: Role of apolipoproteins on receptor-medicted endocytosis. *Biomacromolecules*. 8, 793–799. (2007). doi: 10.1021/bm060711a.

[66] S. Ritz, S. Schöttler, N. Kotman, G. Baier, A. Musyanovych, J. Kuharev, K. Landfester, H. Schild, O. Jahn, S. Tenzer, V. Mailänder. Protein Corona of Nanoparticles: Distinct Proteins Regulate the Cellular Uptake. *Biomacromolecules*. 16, 1311–1321. (2015). doi: 10.1021/acs.biomac.5b00108.

[67] S. Schöttler, K. Landfester, V. Mailänder. Controlling the stealth effect of nanocarriers through understanding the protein corona. *Angewandte Chemie - International Edition*. 55, 8806–8815. (2016). doi: 10.1002/anie.201602233.

[68] K. Prapainop, P. Wentworth. A shotgun proteomic study of the protein corona associated with cholesterol and atheronal-B surface-modified quantum dots. *European Journal of Pharmaceutics and Biopharmaceutics*. 77, 353–359. (2011). doi: 10.1016/j.ejpb.2010.12.026.

[69] S. Schöttler, G. Becker, S. Winzen, T. Steinbach, K. Mohr, K. Landfester, V. Mailänder, F. R. Wurm. Protein adsorption is required for stealth effect of poly(ethylene glycol)- and poly(phosphoester)-coated nanocarriers. *Nature Nanotechnology*. 11, 372–377. (2016). doi: 10.1038/nnano.2015.330.

[70] C. D. Walkey, J. B. Olsen, H. Guo, A. Emili, W. C. W. Chan. Nanoparticle size and surface chemistry determine serum protein adsorption and macrophage uptake. *Journal of the American Chemical Society*. 134, 2139–2147. (2012). doi: 10.1021/ja2084338.

[71] E. Mahon, A. Salvati, F. Baldelli Bombelli, I. Lynch, K. A. Dawson. Designing the nanoparticle-biomolecule interface for "targeting and therapeutic delivery." *Journal of Controlled Release*. 161, 164–174. (2012). doi: 10.1016/j.jconrel.2012.04.009.

[72] I. Capjak, S. Š. Goreta, D. D. Jurašin, I. V. Vrček. How protein coronas determine the fate of engineered nanoparticles in biological environment. *Arhiv za Higijenu Rada i Toksikologiju*. 68, 245–253. (2017). doi: 10.1515/aiht-2017-68-3054.

[73] F. Bertoli, D. Garry, M. P. Monopoli, A. Salvati, K. A. Dawson. The intracellular destiny of the protein corona: a study on its cellular internalization and evolution. *ACS Nano*. 10, 10471–10479. (2016). doi: 10.1021/acsnano.6b06411.

[74] S. Behzadi, V. Serpooshan, R. Sakhtianchi, B. Müller, K. Landfester, D. Crespy, M. Mahmoudi. Protein corona change the drug release profile of nanocarriers: the "overlooked" factor at the nanobio interface. *Colloids and Surfaces B: Biointerfaces*. 123, 143–149. (2014). doi: 10.1016/j.colsurfb.2014.09.009.

[75] K. Abstiens, S. Maslanka Figueroa, M. Gregoritza, A. M. Goepferich. Interaction of functionalized nanoparticles with serum proteins and its impact on colloidal stability and cargo leaching. *Soft Matter*. 15, 709–720. (2019). doi: 10.1039/C8SM02189A.

[76] H. Wang, R. Ma, K. Nienhaus, G. U. Nienhaus. Formation of a monolayer protein corona around polystyrene nanoparticles and implications for nanoparticle agglomeration. *Small*. 15, e1900974. (2019). doi: 10.1002/smll.201900974.

[77] S. B. Gunnarsson, K. Bernfur, A. Mikkelsen, T. Cedervall. Analysis of nanoparticle biomolecule complexes. *Nanoscale*. 10, 4246–4257. (2018). doi: 10.1039/C7NR08696B.

[78] D. F. Moyano, K. Saha, G. Prakash, B. Yan, H. Kong, M. Yazdani, V. M. Rotello. Fabrication of corona-free nanoparticles with tunable hydrophobicity. *ACS Nano*. 8, 6748–6755. (2014). doi: 10.1021/nn5006478.

[79] E. Casals, T. Pfaller, A. Duschl, G. J. Oostingh, V. Puntes. Time evolution of the nanoparticle protein corona. *ACS Nano*. 4, 3623–3632. (2010). doi: 10.1021/nn901372t.

[80] A. Gessner, A. Lieske, B. R. Paulke, R. H. Müller. Influence of surface charge density on protein adsorption on polymeric nanoparticles: Analysis by two-dimensional electrophoresis. *European Journal of Pharmaceutics and Biopharmaceutics*. 54, 165–170. (2002). doi: 10.1016/S0939-6411(02)00081-4.

[81] P. Aggarwal, J. B. Hall, C. B. McLeland, M. A. Dobrovolskaia, S. E. McNeil. Nanoparticle interaction with plasma proteins as it relates to particle biodistribution, biocompatibility and therapeutic efficacy. *Advanced Drug Delivery Reviews*. 61, 428–437. (2009). doi: 10.1016/j.addr.2009.03.009.

[82] C. F. Wang, E. M. Mäkilä, C. Bonduelle, J. Rytkönen, J. Raula, S. Almeida, A. Närvänen, J. J. Salonen, S. Lecommandoux, J. T. Hirvonen, H. A. Santos. Functionalization of alkyne-terminated thermally hydrocarbonized porous silicon nanoparticles with targeting peptides and antifouling polymers: Effect on the human plasma protein adsorption. *ACS Applied Materials and Interfaces*. 7, 2006–2015. (2015). doi: 10.1021/am507827n.

[83] A. Gessner, R. Waicz, A. Lieske, B. R. Paulke, K. Mäder, R. H. Müller. Nanoparticles with decreasing surface hydrophobicities: influence on plasma protein adsorption. *International Journal of Pharmaceutics*. 196, 245–249. (2000).

[84] V. H. Nguyen, B. J. Lee. Protein corona: a new approach for nanomedicine design. *International Journal of Nanomedicine*. 12, 3137–3151. (2017). doi: 10.2147/IJN.S129300.

[85] K. Sempf, T. Arrey, S. Gelperina, T. Schorge, B. Meyer, M. Karas, J. Kreuter. Adsorption of plasma proteins on uncoated PLGA nanoparticles. *European Journal of Pharmaceutics and Biopharmaceutics*. 85, 53–60. (2013). doi: 10.1016/j.ejpb.2012.11.030.

[86] H. Zhang, T. Wu, W. Yu, S. Ruan, Q. He, H. Gao. Ligand size and conformation affect the behavior of nanoparticles

coated with in vitro and in vivo protein corona. *ACS Applied Materials and Interfaces*. 10, 9094–9103. (2018). doi: 10.1021/acsami.7b16096.

[87] K. Saha, M. Rahimi, M. Yazdani, S. T. Kim, D. F. Moyano, S. Hou, R. Das, R. Mout, F. Rezaee, M. Mahmoudi, V. M. Rotello. Regulation of macrophage recognition through the interplay of nanoparticle surface functionality and protein corona. *ACS Nano*. 10, 4421–4430. (2016). doi: 10.1021/acsnano.6b00053.

[88] G. Pulido-Reyes, F. Leganes, F. Fernández-Piñas, R. Rosal. Bio-nano interface and environment: a critical review. *Environmental Toxicology and Chemistry*. 36, 3181–3193. (2017). doi: 10.1002/etc.3924.

[89] D. Bonvin, U. Aschauer, D. T. L. Alexander, D. Chiappe, M. Moniatte, H. Hofmann, M. Mionić Ebersold. Protein corona: impact of lymph versus blood in a complex in vitro environment. *Small*. 13, 1700409. (2017). doi: 10.1002/smll.201700409.

[90] M. Lundqvist, J. Stigler, G. Elia, I. Lynch, T. Cedervall, K. A. Dawson. Nanoparticle size and surface properties determine the protein corona with possible implications for biological impacts. *Proceedings of the National Academy of Sciences of the United States of America*. 105, 14265–70. (2008). doi: 10.1073/pnas.0805135105.

[91] K. Partikel, R. Korte, N. C. Stein, D. Mulac, F. C. Herrmann, H.-U. U. Humpf, K. Langer. Effect of nanoparticle size and PEGylation on the protein corona of PLGA nanoparticles. *European Journal of Pharmaceutics and Biopharmaceutics*. 141, 70–80. (2019). doi: 10.1016/j.ejpb.2019.05.006.

[92] I. Lynch, K. A. Dawson. Protein-nanoparticle interactions. *Nano Today*. 3, 40–47. (2008). doi: 10.1016/S1748-0132(08)70014-8.

[93] M. A. Dobrovolskaia, P. Aggarwal, J. B. Hall, S. E. McNeil. Preclinical studies to understand nanoparticle interaction with the immune system and its potential effects on nanoparticle biodistribution. *Mol Pharm.* 5, 487–495. (2008). doi: 10.1021/mp800032f.Preclinical.

[94] A. Salvati, A. S. Pitek, M. P. Monopoli, K. Prapainop, F. B. Bombelli, D. R. Hristov, P. M. Kelly, C. Åberg, E. Mahon, K. A. Dawson. Transferrin-functionalized nanoparticles lose their targeting capabilities when a biomolecule corona adsorbs on the surface. *Nature Nanotechnology*. 8, 137–143. (2013). doi: 10.1038/nnano.2012.237.

[95] J. Leroux, P. Gravel, L. Balant, B. Volet, B. M. Anner, E. Allémann, E. Doelker, R. Gurny. Internalization of poly(D,L-lactic acid) nanoparticles by isolated human leukocytes and analysis of plasma proteins adsorbed onto the particles. *Journal of Biomedical Materials Research*. 28, 471–481. (1994). doi: 10.1002/jbm.820280410.

[96] N. Samadi, M. J. Van Steenbergen, J. B. Van Den Dikkenberg, T. Vermonden, C. F. Van Nostrum, M. Amidi, W. E. Hennink. Nanoparticles based on a hydrophilic polyester with a sheddable peg coating for protein delivery. *Pharmaceutical Research*. 31, 2593–2604. (2014). doi: 10.1007/s11095-014-1355-x.

[97] X. Zhu, W. Tao, D. Liu, J. Wu, Z. Guo, X. Ji, Z. Bharwani, L. Zhao, X. Zhao, O. C. Farokhzad, J. Shi. Surface de-PEGylation controls nanoparticle-mediated siRNA delivery in vitro and in vivo. *Theranostics*. 7, 1990–2002. (2017). doi: 10.7150/thno.18136.

[98] L. Sanchez, Y. Yi, Y. Yu. Effect of partial PEGylation on particle uptake by macrophages. *Nanoscale*. 9, 288–297. (2017). doi: 10.1039/c6nr07353k.

[99] P. Grenier, I. M. de Oliveira Viana, E. M. Lima, N. Bertrand. Anti-polyethylene glycol antibodies alter the protein corona deposited on nanoparticles and the physiological pathways regulating their fate in vivo. *Journal of Controlled Release*. 287, 121–131. (2018). doi: 10.1016/j.jconrel.2018.08.022.

[100] H. B. Haroon, A. C. Hunter, Z. S. Farhangrazi, S. M. Moghimi. A brief history of long circulating nanoparticles. *Advanced Drug Delivery Reviews*. 188, 114396. (2022). doi: 10.1016/j.addr.2022.114396.

[101] G. R. Rivera-Rodríguez, M. J. Alonso, D. Torres. Poly-l-asparagine nanocapsules as anticancer drug delivery vehicles. *European Journal of Pharmaceutics and Biopharmaceutics*. 85, 481–487. (2013). doi: 10.1016/j.ejpb.2013.08.001.

[102] G. R. Rivera-Rodriguez, G. Lollo, T. Montier, J. P. Benoit, C. Passirani, M. J. Alonso, D. Torres. In vivo evaluation of poly-l-asparagine nanocapsules as carriers for anti-cancer drug delivery. *International Journal of Pharmaceutics*. 458, 83–89. (2013). doi: 10.1016/j.ijpharm.2013.09.038.

[103] G. Lollo, P. Hervella, P. Calvo, P. Avilés, M. J. Guillen, M. Garcia-Fuentes, M. J. Alonso, D. Torres. Enhanced in vivo therapeutic efficacy of plitidepsin-loaded nanocapsules decorated with a new poly-aminoacid-PEG derivative. *International Journal of Pharmaceutics*. 483, 212–219. (2015). doi: 10.1016/j.ijpharm.2015.02.028.

[104] M. V. Lozano, D. Torrecilla, D. Torres, A. Vidal, F. Domínguez, M. J. Alonso. Highly efficient system to deliver taxanes into tumor cells: Docetaxel-loaded chitosan oligomer colloidal carriers. *Biomacromolecules*. 9, 2186–2193. (2008). doi: 10.1021/bm800298u.

[105] G. Lollo, G. R. Rivera-Rodriguez, J. Bejaud, T. Montier, C. Passirani, J. P. Benoit, M. García-Fuentes, M. J. Alonso, D. Torres. Polyglutamic acid-PEG nanocapsules as long circulating carriers for the delivery of docetaxel. *European Journal of Pharmaceutics and Biopharmaceutics*. 87, 47–54. (2014). doi: 10.1016/j.ejpb.2014.02.004.

[106] E. Borrajo, R. Abellan-Pose, A. Soto, M. Garcia-Fuentes, N. Csaba, M. J. M. J. Alonso, A. Vidal. Docetaxel-loaded polyglutamic acid-PEG nanocapsules for the treatment of metastatic cancer. *Journal of Controlled Release*. 238, 263–271. (2016). doi: 10.1016/j.jconrel.2016.07.048.

[107] Á. Molina-Crespo, A. Cadete, D. Sarrio, M. Gámez-Chiachio, L. Martinez, K. Chao, A. Olivera, A. Gonella, E. Díaz, J. Palacios, P. K. Dhal, M. Besev, M. Rodríguez-Serrano, M. L. García Bermejo, J. C. Triviño, A. Cano, M. García-Fuentes, O. Herzberg, D. Torres, M. J. Alonso, G. Moreno-Bueno. Intracellular Delivery of an Antibody Targeting Gasdermin-B Reduces HER2 Breast Cancer Aggressiveness. *Clinical Cancer Research*. 25, 4846–4858. (2019). doi: 10.1158/1078-0432.CCR-18-2381.

[108] G. Berrecoso, J. Crecente-Campo, M. J. Alonso. Quantification of the actual composition of polymeric nanocapsules: a quality control analysis. *Drug Delivery and Translational Research*. 12, 2865–2874. (2022). doi: 10.1007/s13346-

022-01150-5.
[109] S. Palchetti, D. Caputo, L. Digiacomo, A. Capriotti, R. Coppola, D. Pozzi, G. Caracciolo. Protein corona fingerprints of liposomes: new opportunities for targeted drug delivery and early detection in pancreatic cancer. *Pharmaceutics*. 11, 31. (2019). doi: 10.3390/pharmaceutics11010031.
[110] P. Pande, T. A. Mosleh, A. E. Aust. Role of αvβ5 integrin receptor in endocytosis of crocidolite and its effect on intracellular glutathione levels in human lung epithelial (A549) cells. *Toxicology and Applied Pharmacology*. 210, 70–77. (2006). doi: 10.1016/j.taap.2005.07.017.
[111] G. Caracciolo, D. Pozzi, A. L. Capriotti, C. Cavaliere, F. Cardarelli, F. Salomone, A. Lagana. In *Nanotechnology 2013: Bio Sensors, Instruments, Medical, Environment and Energy*. (2013). pp. 247–250.
[112] F. Giulimondi, L. Digiacomo, D. Pozzi, S. Palchetti, E. Vulpis, A. L. Capriotti, R. Z. Chiozzi, A. Laganà, H. Amenitsch, L. Masuelli, M. Mahmoudi, I. Screpanti, A. Zingoni, G. Caracciolo. Interplay of protein corona and immune cells controls blood residency of liposomes. *Nature Communications*. 10, 3686. (2019). doi: 10.1038/s41467-019-11642-7.
[113] G. Caracciolo. Clinically approved liposomal nanomedicines: Lessons learned from the biomolecular corona. *Nanoscale*. 10, 4167–4172. (2018). doi: 10.1039/c7nr07450f.
[114] Y. Verhoeven, S. Tilborghs, J. Jacobs, J. De Waele, D. Quatannens, C. Deben, H. Prenen, P. Pauwels, X. B. Trinh, A. Wouters, E. L. J. Smits, F. Lardon, P. A. van Dam. The potential and controversy of targeting STAT family members in cancer. *Seminars in Cancer Biology*. 60, 41–56. (2020). doi: 10.1016/j.semcancer.2019.10.002.
[115] S. L. Furtek, D. S. Backos, C. J. Matheson, P. Reigan. Strategies and Approaches of Targeting STAT3 for Cancer Treatment. *ACS Chemical Biology*. 11, 308–318. (2016). doi: 10.1021/acschembio.5b00945.
[116] S. Zhuang. Regulation of STAT signaling by acetylation. *Cellular Signalling*. 25, 1924–1931. (2013). doi: 10.1016/j.cellsig.2013.05.007.
[117] Y. Liu, S. Liao, S. Bennett, H. Tang, D. Song, D. Wood, X. Zhan, J. Xu. STAT3 and its targeting inhibitors in osteosarcoma. *Cell Proliferation*. 54, 1–15. (2021). doi: 10.1111/cpr.12974.
[118] S. Zou, Q. Tong, B. Liu, W. Huang, Y. Tian, X. Fu. Targeting STAT3 in Cancer Immunotherapy. *Molecular Cancer*. 19, 145. (2020). doi: 10.1186/s12943-020-01258-7.
[119] R. Derynck, S. J. Turley, R. J. Akhurst. TGFβ biology in cancer progression and immunotherapy. *Nature Reviews Clinical Oncology*. 18, 9–34. (2021). doi: 10.1038/s41571-020-0403-1.
[120] M. B. Sonbol, D. H. Ahn, D. Goldstein, T. Okusaka, J. Tabernero, T. Macarulla, M. Reni, C. P. Li, B. O'Neil, E. Van Cutsem, T. Bekaii-Saab. CanStem111P trial: A Phase III study of napabucasin plus nab-paclitaxel with gemcitabine. *Future Oncology*. 15, 1295–1302. (2019). doi: 10.2217/fon-2018-0903.
[121] D. Han, T. Yu, N. Dong, B. Wang, F. Sun, D. Jiang. Napabucasin, a novel STAT3 inhibitor suppresses proliferation, invasion and stemness of glioblastoma cells. *Journal of Experimental and Clinical Cancer Research*. 38, 1–12. (2019). doi: 10.1186/s13046-019-1289-6.
[122] C. Yoo, J. Kang, H. Y. Lim, J. H. Kim, M. A. Lee, K. H. Lee, T. Y. Kim, B. Y. Ryoo. Phase I dose-finding study of OPB-111077, a novel STAT3 inhibitor, in patients with advanced hepatocellular carcinoma. *Cancer Research and Treatment*. 51, 510–518. (2019). doi: 10.4143/crt.2018.226.
[123] D. Genini, L. Brambilla, E. Laurini, J. Merulla, G. Civenni, S. Pandit, R. D'Antuono, L. Perez, D. E. Levy, S. Pricl, G. M. Carbone, C. V. Catapano. Mitochondrial dysfunction induced by a SH2 domain-Targeting STAT3 inhibitor leads to metabolic synthetic lethality in cancer cells. *Proceedings of the National Academy of Sciences of the United States of America*. 114, E4924–E4933. (2017). doi: 10.1073/pnas.1615730114.
[124] A. L. Wong, R. A. Soo, D. S. Tan, S. C. Lee, J. S. Lim, P. C. Marban, L. R. Kong, Y. J. Lee, L. Z. Wang, W. L. Thuya, R. Soong, M. Q. Yee, T. M. Chin, M. T. Cordero, B. R. Asuncion, B. Pang, S. Pervaiz, J. L. Hirpara, A. Sinha, W. W. Xu, M. Yuasa, T. Tsunoda, M. Motoyama, T. Yamauchi, B. C. Goh. Phase I and biomarker study of OPB-51602, a novel signal transducer and activator of transcription (STAT) 3 inhibitor, in patients with refractory solid malignancies. *Annals of Oncology*. 26, 998–1005. (2015). doi: 10.1093/annonc/mdv026.
[125] M. Ogura, T. Uchida, Y. Terui, F. Hayakawa, Y. Kobayashi, M. Taniwaki, Y. Takamatsu, T. Naoe, K. Tobinai, W. Munakata, T. Yamauchi, A. Kageyama, M. Yuasa, M. Motoyama, T. Tsunoda, K. Hatake. Phase I study of OPB-51602, an oral inhibitor of signal transducer and activator of transcription 3, in patients with relapsed/refractory hematological malignancies. *Cancer Science*. 106, 896–901. (2015). doi: 10.1111/cas.12683.
[126] L. MacDonagh, S. G. Gray, E. Breen, S. Cuffe, S. P. Finn, K. J. O'Byrne, M. P. Barr. BBI608 inhibits cancer stemness and reverses cisplatin resistance in NSCLC. *Cancer Letters*. 428, 117–126. (2018). doi: 10.1016/j.canlet.2018.04.008.
[127] G. P. Nagaraju, B. Farran, M. Farren, G. Chalikonda, C. Wu, G. B. Lesinski, B. F. El-Rayes. Napabucasin (BBI 608), a potent chemoradiosensitizer in rectal cancer. *Cancer*. 126, 3360–3371. (2020). doi: 10.1002/cncr.32954.
[128] A. Kawazoe, Y. Kuboki, E. Shinozaki, H. Hara, T. Nishina, Y. Komatsu, S. Yuki, M. Wakabayashi, S. Nomura, A. Sato, T. Kuwata, M. Kawazu, H. Mano, Y. Togashi, H. Nishikawa, T. Yoshino. Multicenter phase I/II trial of napabucasin and pembrolizumab in patients with metastatic colorectal cancer (EPOC1503/SCOOP Trial). *Clinical Cancer Research*. 26, 5887–5894. (2020). doi: 10.1158/1078-0432.CCR-20-1803.
[129] Y. Li, H. A. Rogoff, S. Keates, Y. Gao, S. Murikipudi, K. Mikule, D. Leggett, W. Li, A. B. Pardee, C. J. Li. Suppression of cancer relapse and metastasis by inhibiting cancer stemness. *Proceedings of the National Academy of Sciences of the United States of America*. 112, 1839–1844. (2015). doi: 10.1073/pnas.1424171112.
[130] D. J. Jonker, L. Nott, T. Yoshino, S. Gill, J. Shapiro, A. Ohtsu, J. Zalcberg, M. M. Vickers, A. C. Wei, Y. Gao, N. C. Tebbutt, B. Markman, T. Price, T. Esaki, S. Koski, M. Hitron, W. Li, Y. Li, N. M. Magoski, C. J. Li, J. Simes, D. Tu, C. J. O'Callaghan. Napabucasin versus placebo in refractory advanced colorectal cancer: a randomised phase 3 trial.

The Lancet Gastroenterology and Hepatology. 3, 263–270. (2018). doi: 10.1016/S2468-1253(18)30009-8.

[131] S. Sau, S. K. Mondal, S. K. Kashaw, A. K. Iyer, R. Banerjee. Combination of cationic dexamethasone derivative and STAT3 inhibitor (WP1066) for aggressive melanoma: a strategy for repurposing a phase I clinical trial drug. *Molecular and Cellular Biochemistry*. 436, 119–136. (2017). doi: 10.1007/s11010-017-3084-z.

[132] J. De Groot, M. Ott, J. Wei, C. Kassab, D. Fang, H. Najem, B. O'Brien, S. P. Weathers, C. K. Matsouka, N. K. Majd, R. A. Harrison, G. N. Fuller, J. T. Huse, J. P. Long, R. Sawaya, G. Rao, T. J. Macdonald, W. Priebe, M. Decuypere, A. B. Heimberger. A first-in-human Phase i trial of the oral p-STAT3 inhibitor WP1066 in patients with recurrent malignant glioma. *CNS Oncology*. 11, (2022). doi: 10.2217/cns-2022-0005.

[133] A. Tolcher, K. Flaherty, G. I. Shapiro, J. Berlin, T. Witzig, T. Habermann, A. Bullock, E. Rock, A. Elekes, C. Lin, D. Kostic, N. Ohi, D. Rasco, K. P. Papadopoulos, A. Patnaik, L. Smith, G. M. Cote. A First-in-Human Phase I Study of OPB-111077, a Small-Molecule STAT3 and Oxidative Phosphorylation Inhibitor, in Patients with Advanced Cancers. *The Oncologist*. 23, 658-e72. (2018). doi: 10.1634/theoncologist.2017-0325.

[134] Y. L. Wu, S. Lu, Y. Lu, J. Zhou, Y. kai Shi, V. Sriuranpong, J. C. M. Ho, C. K. Ong, C. M. Tsai, C. H. Chung, K. D. Wilner, Y. Tang, E. T. Masters, P. Selaru, T. S. Mok. Results of PROFILE 1029, a Phase III Comparison of First-Line Crizotinib versus Chemotherapy in East Asian Patients with ALK-Positive Advanced Non–Small Cell Lung Cancer. *Journal of Thoracic Oncology*. 13, 1539–1548. (2018). doi: 10.1016/j.jtho.2018.06.012.

[135] A. T. Shaw, T. M. Kim, L. Crinò, C. Gridelli, K. Kiura, G. Liu, S. Novello, A. Bearz, O. Gautschi, T. Mok, M. Nishio, G. Scagliotti, D. R. Spigel, S. Deudon, C. Zheng, S. Pantano, P. Urban, C. Massacesi, K. Viraswami-Appanna, E. Felip. Ceritinib versus chemotherapy in patients with ALK-rearranged non-small-cell lung cancer previously given chemotherapy and crizotinib (ASCEND-5): a randomised, controlled, open-label, phase 3 trial. *The Lancet Oncology*. 18, 874–886. (2017). doi: 10.1016/S1470-2045(17)30339-X.

[136] J. Guan, S. Fransson, J. T. Siaw, D. Treis, J. Van Den Eynden, D. Chand, G. Umapathy, K. Ruuth, P. Svenberg, S. Wessman, A. Shamikh, H. Jacobsson, L. Gordon, J. Stenman, P. J. Svensson, M. Hansson, E. Larsson, T. Martinsson, R. H. Palmer, P. Kogner, B. Hallberg. Clinical response of the novel activating ALK-I1171T mutation in neuroblastoma to the ALK inhibitor ceritinib. *Cold Spring Harbor Molecular Case Studies*. 4, 1–24. (2018). doi: 10.1101/mcs.a002550.

[137] K. W. Nassar, J. D. Hintzsche, S. M. Bagby, V. Espinoza, C. Langouët-Astrié, C. M. Amato, T.-S. Chimed, M. Fujita, W. Robinson, A. C. Tan, R. E. Schweppe. Targeting CDK4/6 Represents a Therapeutic Vulnerability in Acquired BRAF/MEK Inhibitor–Resistant Melanoma. *Molecular Cancer Therapeutics*. 20, 2049–2060. (2021). doi: 10.1158/1535-7163.MCT-20-1126.

[138] K. Hotta, T. Hida, H. Nokihara, M. Morise, Y. H. Kim, K. Azuma, T. Seto, Y. Takiguchi, M. Nishio, H. Yoshioka. Final overall survival analysis from the phase III J-ALEX study of alectinib versus crizotinib in ALK inhibitor-naïve Japanese patients with ALK -positive. *ESMO Open*. 7, 100527. (2022). doi: 10.1016/j.esmoop.2022.100527.

[139] W. Wick, S. Dettmer, A. Berberich, T. Kessler, I. Karapanagiotou-Schenkel, A. Wick, F. Winkler, E. Pfaff, B. Brors, J. Debus, A. Unterberg, M. Bendszus, C. Herold-Mende, A. Eisenmenger, A. Von Deimling, D. T. W. Jones, S. M. Pfister, F. Sahm, M. Platten. N 2 M 2 (NOA-20) phase I/II trial of molecularly matched targeted therapies plus radiotherapy in patients with newly diagnosed non-MGMT hypermethylated glioblastoma. *Neuro-Oncology*. 21, 95–105. (2019). doi: 10.1093/neuonc/noy161.

[140] D. W. Kim, M. Tiseo, M. J. Ahn, K. L. Reckamp, K. H. Hansen, S. W. Kim, R. M. Huber, H. L. West, H. J. M. Groen, M. J. Hochmair, N. B. Leighl, S. N. Gettinger, C. J. Langer, L. G. P. A. Rodríguez, E. F. Smit, E. S. Kim, W. Reichmann, F. G. Haluska, D. Kerstein, D. R. Camidge. Brigatinib in patients with crizotinib-refractory anaplastic lymphoma kinase-positive non-small-cell lung cancer: A randomized, multicenter phase II trial. *Journal of Clinical Oncology*. 35, 2490–2498. (2017). doi: 10.1200/JCO.2016.71.5904.

[141] A. T. Shaw, T. M. Bauer, F. de Marinis, E. Felip, Y. Goto, G. Liu, J. Mazieres, D.-W. Kim, T. Mok, A. Polli, H. Thurm, A. M. Calella, G. Peltz, B. J. Solomon. First-Line Lorlatinib or Crizotinib in Advanced ALK -Positive Lung Cancer. *New England Journal of Medicine*. 383, 2018–2029. (2020). doi: 10.1056/nejmoa2027187.

[142] A. Okines, T. Irfan, B. Asare, K. Mohammed, P. Osin, A. Nerurkar, I. E. Smith, M. Parton, A. Ring, S. Johnston, N. C. Turner. Clinical outcomes in patients with triple negative or HER2 positive lobular breast cancer: a single institution experience. *Breast Cancer Research and Treatment*. 192, 563–571. (2022). doi: 10.1007/s10549-021-06432-z.

[143] Y. Li, J. Shi, J. Yang, S. Ge, J. Zhang, R. Jia, X. Fan. Uveal melanoma: progress in molecular biology and therapeutics. *Therapeutic Advances in Medical Oncology*. 12, 1–27. (2020). doi: 10.1177/1758835920965852.

[144] A. Jamieson, T. Bosse, J. N. McAlpine. The emerging role of molecular pathology in directing the systemic treatment of endometrial cancer. *Therapeutic Advances in Medical Oncology*. 13, 1–14. (2021). doi: 10.1177/17588359211035959.

[145] K. T. Flaherty, R. Gray, A. Chen, S. Li, D. Patton, S. R. Hamilton, P. M. Williams, E. P. Mitchell, A. John Iafrate, J. Sklar, L. N. Harris, L. M. McShane, L. V. Rubinstein, D. J. Sims, M. Routbort, B. Coffey, T. Fu, J. A. Zwiebel, R. F. Little, D. Marinucci, R. Catalano, R. Magnan, W. Kibbe, C. Weil, J. V. Tricoli, B. Alexander, S. Kumar, G. K. Schwartz, F. Meric-Bernstam, C. J. Lih, W. McCaskill-Stevens, P. Caimi, N. Takebe, V. Datta, C. L. Arteaga, J. S. Abrams, R. Comis, P. J. O'Dwyer, B. A. Conley, M. Schnall, T. Johnson, F. B. de Abreu, S. J. Deharvengt, T. L. Gallagher, K. Godwin, D. C. Green, C. C. Hain, B. E. Houde, J. D. Peterson, H. B. Steinmetz, G. J. Tsongalis, X. Xiao, B. Giantonio, M. Lou Smith, N. Azad, M. Lambert, L. P. Le, A. Raymond, H. Robinson, K. Vernovsky, D. Hyman, C. Chung, C. Rowe, F. Spina, S. Ansher, J. Cristofaro, P. S. Ivy, I. Lubensky, H. Makhlouf, L. Shankar, J. Wright, L. Yee, L. Lison, M. Anderson, M. Benson, N. Birus, L. Brem, D. Chebattina, H. Donolo, E. Dumene, M. Hammer, M. Hendriksson, S. Kadiyala, J. Lee, A. Lu, T. O'Connor, W. Osman, J. Pumphrey, A. Purkayastha, V.

USC UNIVERSIDADE DE SANTIAGO DE COMPOSTELA

Ramani, J. Scibelli, M. Smith, A. Steinfeld, J. Thompson, S. Vallala, J. Verbeck, C. Winter, S. Yang, Q. Yu, R. Zakharov, C. Bouk, T. C. Chang, A. Fredlock, K. Harper, R. Harrington, C. Karlovich, M. Majano, S. McDermott, E. Mosher, P. Runge, M. Saeed, G. S. Mantha, D. Panditi, K. P. Patel, R. Pepper, L. Rajyalakshmi, N. G. Reddy, R. R. Singh, D. Tripathy, J. Yau, S. Canosa, K. Finberg, J. Huang, K. Ronski, T. Zenta Walther. The molecular analysis for therapy choice (NCI-MATCH) trial: Lessons for genomic trial design. *Journal of the National Cancer Institute*. 112, 1021–1029. (2020). doi: 10.1093/jnci/djz245.

[146] A. S. Mansfield, Z. Wei, R. Mehra, A. T. Shaw, C. H. Lieu, P. M. Forde, A. E. Drilon, E. P. Mitchell, J. J. Wright, N. Takebe, E. Sharon, D. Hovelson, S. Tomlins, J. Zeng, K. Poorman, N. Malik, R. J. Gray, S. Li, L. M. McShane, L. V. Rubinstein, D. Patton, P. M. Williams, S. R. Hamilton, B. A. Conley, C. L. Arteaga, L. N. Harris, P. J. O'Dwyer, A. P. Chen, K. T. Flaherty. Crizotinib in patients with tumors harboring ALK or ROS1 rearrangements in the NCI-MATCH trial. *npj Precision Oncology*. 6, 1–6. (2022). doi: 10.1038/s41698-022-00256-w.

[147] J. C. Soria, D. S. W. Tan, R. Chiari, Y. L. Wu, L. Paz-Ares, J. Wolf, S. L. Geater, S. Orlov, D. Cortinovis, C. J. Yu, M. Hochmair, A. B. Cortot, C. M. Tsai, D. Moro-Sibilot, R. G. Campelo, T. McCulloch, P. Sen, M. Dugan, S. Pantano, F. Branle, C. Massacesi, G. de Castro. First-line ceritinib versus platinum-based chemotherapy in advanced ALK-rearranged non-small-cell lung cancer (ASCEND-4): a randomised, open-label, phase 3 study. *The Lancet*. 389, 917–929. (2017). doi: 10.1016/S0140-6736(17)30123-X.

[148] N. Ochi, N. Takigawa. What can we learn from 3 phase III trials of ASCEND-4: Ceritinib vs. platinum/pemetrexed with pemetrexed maintenance, PROFILE 1004: Crizotinib vs. platinum/pemetrexed, and J-ALEX: Alectinib vs. crizotinib? *Translational Cancer Research*. 6, S515–S518. (2017). doi: 10.21037/tcr.2017.04.20.

[149] D. S. W. Tan, S. Geater, C. J. Yu, C. M. Tsai, T. C. Hsia, J. Chen, M. C. Lin, Y. Lu, V. Sriuranpong, C. T. Yang, P. Sen, F. Branle, M. Shi, Y. L. Wu. Ceritinib Efficacy and Safety in Treatment-Naive Asian Patients With Advanced ALK-Rearranged NSCLC: An ASCEND-4 Subgroup Analysis. *JTO Clinical and Research Reports*. 2, 100131. (2021). doi: 10.1016/j.jtocrr.2020.100131.

[150] T. Okusaka, H. Ueno, M. Ikeda, S. Mitsunaga, M. Ozaka, H. Ishii, O. Yokosuka, Y. Ooka, R. Yoshimoto, Y. Yanagihara, K. Okita. Phase 1 and pharmacological trial of OPB-31121, a signal transducer and activator of transcription-3 inhibitor, in patients with advanced hepatocellular carcinoma. *Hepatology Research*. 45, 1283–1291. (2015). doi: 10.1111/hepr.12504.

[151] S. Verstovsek, R. Hoffman, J. Mascarenhas, J. C. Soria, R. Bahleda, P. McCoon, W. Tang, J. Cortes, H. Kantarjian, V. Ribrag. A phase I, open-label, multi-center study of the JAK2 inhibitor AZD1480 in patients with myelofibrosis. *Leukemia Research*. 39, 157–163. (2015). doi: 10.1016/j.leukres.2014.11.018.

[152] L. Xie, P. E. Bourne. Developing multi-target therapeutics to fine-tune the evolutionary dynamics of the cancer ecosystem. *Frontiers in Pharmacology*. 6, 1–5. (2015). doi: 10.3389/fphar.2015.00209.

[153] Z. Q. Zuo, K. G. Chen, X. Y. Yu, G. Zhao, S. Shen, Z. T. Cao, Y. L. Luo, Y. C. Wang, J. Wang. Promoting tumor penetration of nanoparticles for cancer stem cell therapy by TGF-β signaling pathway inhibition. *Biomaterials*. 82, 48–59. (2016). doi: 10.1016/j.biomaterials.2015.12.014.

[154] Z.-Y. Zhang. Drugging the Undruggable: Therapeutic Potential of Targeting Protein Tyrosine Phosphatases. *Accounts of Chemical Research*. 50, 122–129. (2017). doi: 10.1021/acs.accounts.6b00537.

[155] S. R. Punekar, V. Velcheti, B. G. Neel, K. K. Wong. The current state of the art and future trends in RAS-targeted cancer therapies. *Nature Reviews Clinical Oncology*. 19, 637–655. (2022). doi: 10.1038/s41571-022-00671-9.

[156] E. Cekani, S. Epistolio, G. Dazio, M. Cefalì, L. Wannesson, M. Frattini, P. Froesch. Molecular Biology and Therapeutic Perspectives for K-Ras Mutant Non-Small Cell Lung Cancers. *Cancers*. 14, 1–32. (2022). doi: 10.3390/cancers14174103.

USC UNIVERSIDADE DE SANTIAGO DE COMPOSTELA

INTRODUCTION

USC
UNIVERSIDADE
DE SANTIAGO
DE COMPOSTELA

USC
UNIVERSIDADE
DE SANTIAGO
DE COMPOSTELA

1. INTRODUCTION*,#

This introduction has been partially adapted from:

*The following published review: T. G. Dacoba[a,b,c], S. Anthiya[a,b,c], G. Berrecoso[a,b,c], I. Fernández-Mariño[a,b,c], C. Fernández-Varela[a,b,c], J. Crecente-Campo[a,b,c], D. Teijeiro-Osorio[a,b,c], F. Torres Andón[d], M. J. Alonso[a,b,c]. Nano-Oncologicals: A Tortoise Trail Reaching New Avenues. *Advanced Functional Materials*. 31, 1–36. (2021). doi: 10.1002/adfm.202009860. ISSN: 1616301X.[1]

#The following published review: G. Berrecoso[a,b,c], J. Crecente-Campo[a,b,c], M. J. Alonso[a,b,c]. Unveiling the pitfalls of the protein corona of polymeric drug nanocarriers. *Drug Delivery and Translational Research*. 10, 730–750. (2020). doi: 10.1007/s13346-020-00745-0. ISSN: 2190393X, 21903948.[2]

[a] Center for Research in Molecular Medicine and Chronic Diseases (CiMUS), Universidade de Santiago de Compostela, Santiago de Compostela, 15782, Spain.
[b] IDIS Research Institute, Universidade de Santiago de Compostela, Santiago de Compostela, 15782, Spain.
[c] Department of Pharmacology, Pharmacy and Pharmaceutical Technology, School of Pharmacy, Universidade de Santiago de Compostela, Santiago de Compostela, 15782, Spain.
[d] Laboratory of Cellular Immunology. Humanitas Clinical and Research Center IRCCS, Milan, 20090, Italy.

1.1. CURRENT SITUATION OF LUNG CANCER

The World Health Organization (WHO) defines cancer as "a large group of diseases that can start in almost any organ or tissue of the body when abnormal cells grow uncontrollably, go beyond their usual boundaries to invade adjoining parts of the body and/or spread to other organs".[3] The Global Cancer Observatory of the WHO reported a 7 % rise in new cancer cases from 2018 to 2020. Indeed, only in 2020, 19.3 million new cancer cases and almost 10 million cancer deaths were reported. Moreover, the global cancer burden was estimated to be 28.4 million cases in 2040, representing a 47 % rise from 2020 data.[4]

Lung cancer is the malignant neoplasm with the highest mortality rate worldwide, accounting for 18 % of cancer-related deaths (1.8 million deaths in 2020).[5] Lung cancer is also the leading cause of cancer death both in the European Union (257,000 deaths in 2020)[6] and in the United States of America (USA) (105,000 deaths in 2020).[7] It is well known that the most important risk factor for lung cancer is cigarette smoking. Indeed, it is reported that smoking causes ≈ 90 % of lung cancers. Additional risk factors are secondhand smoking, genetic predisposition, and exposure to chemicals such as radon and asbestos.[8] Lung cancer is mainly divided based on its histology into non-small cell lung cancer (NSCLC) and small cell lung cancer (SCLC). About 80 to 90 % of lung cancers are represented by NSCLC,[9] whose 5-year survival rate is approximately 63 % of patients when localized while only 5.2 % in the case of metastatic NSCLC.[10]

Kirsten rat sarcoma viral oncogene homolog gene (*KRAS*) mutations are the most frequent gain-of-function alterations in patients with advanced NSCLC. Indeed, an analysis of 17,095 human NSCLCs revealed that 27.5 % of them harbored *KRAS* mutations.[11] The most frequent *KRAS* mutations in NSCLC are G12C (≈ 40 %), G12V (≈ 20 %), and G12D (≈ 15 %).[11,12]

In addition, the hyperactivation of the signal transducer and activator of transcription 3 (STAT3) is reported in ≈ 70 % of solid human tumors, including up to 65 % of NSCLC,[13,14] and it is associated with a poor prognosis.[15] Finally, a recent meta-analysis also showed that high expression of transforming growth factor beta (TGF-β) is also an indicator of a poor prognosis in NSCLC patients.[16]

Currently recommended therapeutic approaches for NSCLC treatment involve surgery, radiotherapy, and the administration of classical cytostatics, targeted therapy, and/or immunotherapy. Targeted therapy is preferred in patients harboring mutations in targets such as the epidermal growth factor receptor (EGFR), anaplastic lymphoma kinase (ALK), or G12C-mutated KRAS due to its higher effectiveness and lower off-target effects. In other cases, classical chemotherapy combined with radiotherapy is usually employed.[17] However, this last approach has only a 5-year survival rate of approximately 15 % in advanced NSCLC.

1.1.1. Immunotherapy in NSCLC

PD-1/PD-L1 monotherapy and its combination with chemotherapy, CTLA-4 inhibitors, and angiogenesis inhibitors are some first-line approved treatments for advanced NSCLC.[18] Still, the overall survival with these treatments has only increased to a few months in the most aggressive conditions,[18] indicating the necessity for improved therapies in NSCLC.

Two signaling pathways involved both in cancer and immune cells in many NSCLCs and, therefore, attractive for drug targeting are STAT3 and TGF-β pathways. However, the use of these drug families has been limited by their off-target toxicities. In fact, no direct STAT3 inhibitors have been approved so far, and only two JAK (upstream STAT3) inhibitors were commercialized,[19] while, in the case of the TGF-β pathways, 5 ALK inhibitors (TGF-β pathway) were approved, but with concerns about their toxicity.[20–27]

More detailed, the direct STAT3 inhibitors that entered clinical trials have been discontinued due to important toxicities, such as peripheral sensory neuropathy (Phase I/II; NCT01406574) and leukemia (Phase I; NCT01029509).[28] Preclinical biodistribution of this drug after oral administration also showed indiscriminate biodistribution, with a preferential accumulation in the liver.[28] On the other hand, the approved ALK inhibitors exhibit severe adverse effects in some patients, including neutropenia and toxicity in different organs such as the liver,[29,30] lung, pancreas,[22,24,26,31,32] brain, and heart.[27] In addition, all the abovementioned ALK inhibitors were found to cause potentially life-threatening bradycardia. Some of these toxicities are related to the broad presence of ALK receptors in those organs. In fact, biodistribution analysis in healthy mice after oral administration found an intense distribution of ALK inhibitors into tissues, including the liver, spleen, kidney, pancreas, and brain.[33–35]

Several studies have tried to incorporate these drugs into nanocarriers with the ultimate goal of modifying their biodistribution to reduce those off-target toxicities. Detailed information about these works can be found in Chapter 2. However, to our knowledge, the co-encapsulation of STAT3 and TGF-β pathway inhibitors has not been explored yet.

USC UNIVERSIDADE DE SANTIAGO DE COMPOSTELA

1.1.2. KRAS inhibitors in NSCLC

Despite the intensive effort, to date, KRAS inhibitors (i.e., sotorasib) have been developed for only one KRAS mutation, while the rest remain undruggable. Several authors have claimed that small-drug chemotherapy against non-G12C mutated KRAS is unlikely to happen due to the lack of specific small-molecule binding domains.[36]

Therefore, it is essential to explore other therapeutic approaches for treating those kinds of tumors. One alternative to small-based chemotherapy is the use of siRNA. Recently, extensive research has been conducted with siRNA against non-G12C KRAS mutations, and a few siRNA-loaded systems are currently under clinical trials. Some examples are anti-$KRAS^{G12D}$ exosomes (Phase I, NCT03608631) and $KRAS^{G12D}$ siRNA-loaded PLGA implants in combination with gemcitabine and Abraxane® (Phase II, NCT01676259), both for the treatment of pancreatic cancer.

The use of monoclonal antibodies for targeting cancer-related extracellular structures has become a successful therapeutic strategy in several tumors. However, mAb-based therapies have inherent biopharmaceutical limitations that severely limit their use in the context of KRAS-mutated NSCLC. First, mAbs do not tend to cross biological membranes, making their extravasation, diffusion through tissues, and tumor accumulation difficult. At the same time, this phenomenon makes it impossible to target intracellular structures in cancer cells. Second, their indiscriminate biodistribution might facilitate the appearance of off-target toxicities. Third, the performance of mAb combination therapy with other kinds of antineoplastic drugs might not be optimal as each of the administered drugs might accumulate in different cells, leading to the selection of the most resistant cancer cell clones. Therefore, nanotechnology has been proposed as a strategy to improve the biodistribution profile of mAbs, reduce their off-target toxicities, and allow a more precise combination therapy. However, to the extent of our knowledge, only one work (unpublished) has been carried out with anti-KRAS mAb-loaded nanocarriers.[37]

More information about currently approved mAbs, intracellular delivery of monoclonal antibodies, and the KRAS pathway in lung cancer is detailed in Chapter 3.

1.2. NANOTECHNOLOGY AS A THERAPEUTIC STRATEGY IN CANCER TREATMENT

Nanomedicine is a valuable strategy to solve some of the limitations of oncological treatments, such as poor solubility, high instability, and limited access to their targets.[38–42] In this sense, nanotechnology approaches can be tuned to allow all therapeutic chemical families to benefit from this strategy. So far, classic chemotherapeutics have been the most used drugs for cancer treatment. These molecules present a potent cytotoxic effect on fast-growing and dividing cells, such as tumor cells. However, their poor specificity and general biodistribution lead to severe side effects. For example, doxorubicin causes cardiotoxicity due to its high affinity for the mitochondrial lipid cardiolipin,[43] while taxanes can cause peripheral neuropathy or myelosuppression, among other undesired effects.[44] This high prevalence of secondary effects has fostered the search for safer and more effective treatments. In this sense, nanotechnology can be used to increase the amount of drug that reaches the tumor, reducing their uptake by healthy cells and, ultimately, diminishing the side effects.[45] In general, depending on their characteristics, nanocarriers can improve the accumulation of the drug in the tumor according

USC DE COMPOSTELA

to two different mechanisms named passive and active targeting (Figure 1). In this section, a general introduction to both mechanisms is presented.

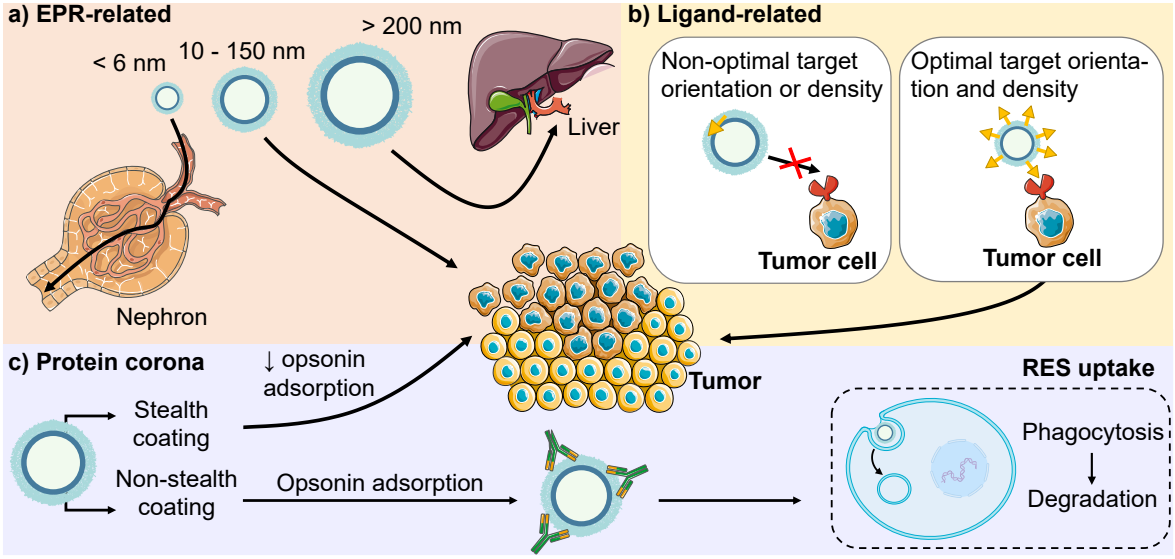


Figure 1. General considerations to achieve an adequate tumor accumulation

(A) Enhanced Permeation and Retention (EPR)-related properties mediate tumor access. For example, small-size particles (< 6 nm) can be excreted through the kidneys, while bigger ones (> 200 nm) tend to be taken up in the liver by macrophages. **(B)** The selection of the correct ligand, its conformation, and its density must be carefully considered when designing an active targeting strategy. **(C)** The protein corona around nanoparticles can promote macrophage uptake and hinder the recognition between decorating ligands and their receptors. Different strategies were developed to reduce the opsonin adsorption and prolong their circulating time. **Abbreviations:** EPR: enhanced permeation and retention. RES: reticuloendothelial system. Some images were adapted and modified from Servier Medical Art (https://smart.servier.com), licensed under Creative Commons Attribution 3.0 (https://creativecommons.org/licenses/by/3.0). Adapted with permission of John Wiley and Sons.[1]

1.2.1. Passive targeting

In 1986, Maeda *et al.* proposed that passive targeting was driven by the Enhanced Permeation and Retention (EPR) effect.[46] This effect suggests that the aberrant hypervascularity, increased blood vessel permeability,[47] and reduced lymphatic drainage facilitate the retention of nanometric particles (such as nanosystems) in the tumor microenvironment (TME). Since then, the EPR effect has been the central dogma to justify the use of nanocarriers in oncology.

Nevertheless, recent reports have questioned the relevance of the EPR effect in humans, as the EPR effect was described as being patient- and tumor-dependent.[48–51] This is especially limiting for tumors that grow for years since they might present a non-aberrant vascularization structure and, thus, a limited EPR effect.[49,50,52,53] Moreover, the high blood vessel permeability and low lymphatic drainage can lead to elevated interstitial fluid pressure, reducing the diffusion of the nanosystem from the blood and its penetration into the tumor.[50,51]

The complexity and variability of the TME make it challenging to define the exact characteristics that nanosystems should have for achieving high passive targeting.[54–56] However, general tendencies regarding particle size, shape, surface charge, and hydrophobicity on protein adsorption have been observed.[57]

Particle size is one of the most relevant parameters regulating the penetration and accumulation of nanosystems at the TME.[58,59] In intravenous administration, nanocarriers bigger than 200 nm are generally accumulated in the liver, spleen, or lungs after being taken up by reticuloendothelial system (RES) macrophages.[60,61] Conversely, nanocarriers smaller than 10 nm tend to leave the tumor through the lymphatic vessels. Finally, particle sizes smaller than 6 nm are usually discarded as they can also be excreted through the kidneys.[57,62] Generally, the preferred particle size for tumor accumulation falls into the range of 10 – 150 nm, which is consistent with the size of approved anti-cancer nanoformulations.

Regarding the influence of the shape, non-spherical particles such as rods were reported to have a lower probability of being taken up by macrophages of the RES, extending their circulation time. However, their non-spherical shape could also compromise their uptake by cancer cells.[63,64] In addition, nanosystems with certain plasticity are more prone to penetrate the tumor tissue[65] than their stiff counterparts due to their deformability and, thus, their ability to extravasate.[66,67]

Finally, the chemical composition, which dictates the surface charge and hydrophobicity of the nanosystems, is well known to strongly influence the circulation time and biodistribution of nanosystems by the different adsorption of proteins ("protein corona") from the surrounding media. In this sense, the preferential adsorption of opsonins, such as complement and immunoglobulins, triggers an increased macrophage uptake, leading to the accumulation of the nanosystems in the liver and spleen. On the contrary, dysopsonins, i.e., apolipoproteins, diminish the recognition by RES macrophages and, thus, increase the circulation time of the nanosystems (Figure 1).[2,57] There are several strategies to modify the protein corona formation, but the generic approach consists of decorating the nanocarriers with polyethylene glycol (PEG), as shown in Table 1. However, there is still an insufficient understanding of the consequences of the nanosystem-proteins interaction and the way to control this process to achieve efficient targeting. The protein corona of polymeric nanosystems is deeply reviewed in Chapter 1.

Table 1. Relevant approved and commercialized nanotherapies containing cytotoxic drugs worldwide[68,69]

Nanosystem type	Name	PEG	Drug	Cancer type	Year of approval	Particle size (nm)
Liposomes	Doxil® / Caelyx®	Yes	Doxorubicin	Breast, myeloma, ovarian, sarcoma	1995 (USA / EU)	90
	DaunoXome®	No	Daunorubicin	Sarcoma	1996 (USA) (*)	45
	DepoCyt®	No	Cytarabine	Lymphomatous meningitis	1996 (USA) (*)	20
	Myocet®	No	Doxorubicin	Breast	2000 (USA / EU)	190
	Mepact®	No	Mifamurtide	Osteosarcoma	2009 (USA / EU)	-
	Marqibo®	No	Vincristine	Leukemia	2012 (USA / EU)	100
	Onivyde®	Yes	Irinotecan	Pancreatic	2015 (USA / EU)	111

USC UNIVERSIDADE DE SANTIAGO DE COMPOSTELA

Table 1. Relevant approved and commercialized nanotherapies containing cytotoxic drugs worldwide[68,69] (continuation)

Nanosystem type	Name	PEG	Drug	Cancer type	Year of approval	Particle size (nm)
	Vyxeos®	No	Daunorubicin & cytarabine	Leukemia	2017 (USA / EU)	100
	Lipusu®	No	Paclitaxel	Ovarian, lung	2006 (China)	400
	Liporaxel®	Yes	Paclitaxel	Gastric	2016 (South Korea)	-
Protein NP	Abraxane®	No	Paclitaxel	Breast, pancreatic, lung	2005 (USA / EU)	130
PVP-based lipid NPs	PICN	No	Paclitaxel	Breast	2014 (India)	100
mPEG·PLA micelles	Genexol®	Yes	Paclitaxel	Breast, lung, ovarian	2006 (South Korea)	20 – 50
PVP-*b*-NIPAM-based micelles	Nanoxel®	No	Paclitaxel	Breast, ovarian, AIDS-related Kaposi's sarcoma	2008 (India)	80 – 100
Vitamin A-derivatives micelles	Apealea® / Paclical®	No	Paclitaxel	Ovarian, peritoneal, fallopian tube	2018 (USA / EU)	20 – 60

(*) Discontinued in Europe. **Abbreviations:** NP: nanoparticle. EU: Europe. PEG: polyethylene glycol. NIPAM: *N*-isopropylacrylamide. PLA: poly(D,L-lactic acid). PVP: poly(*N*-vinylpyrrolidone). USA: United States of America.

The passive targeting capacity of nanocarriers has been extensively applied to small cytotoxic molecules, and many candidates have already made their way to the clinic. Since the first cancer nanotherapy, Doxil®, a liposomal doxorubicin formulation, was approved in 1995, 10 nanotechnology-based formulations containing small molecules have been approved by the United States Food and Drug Administration (FDA) and European Medicines Agency (EMA) (Table 1), and tens are being tested in clinical trials (Table 2).

Of note, most of the passively-targeted nanocarriers have a PEG shell that reduces the adsorption of opsonins, thereby increasing their circulation time and, in principle, their access to the tumor.[70–72] However, as previously mentioned, the use of PEG has its limitations, and, accordingly, several articles have reported the activation of complement elicited by the commercial PEGylated liposomal formulation Doxil®.[73–75] Therefore, there is a need to look for alternative biomaterials that may reduce the protein corona.

USC UNIVERSIDADE DE SANTIAGO DE COMPOSTELA

Table 2. Relevant anti-cancer passively-targeted nanotherapies containing cytotoxic drugs undergoing clinical trials in the USA/EU in the last years

Nanocarrier	PEG	Drug	Cancer type	Particle size (nm)	Last update	Phase / NCT or EudraCT
PEG·PHPMA NP	Yes	DTX	Ovarian	65	2020	IIa / NCT03742713
PLL-based dendrimers	Yes	SN38	Colorectal, pancreatic, ovarian, gastrointestinal, & breast	5 – 15	2019	I/II / 2019-001318-40
	Yes	DTX	Advanced malignant solid tumors	5 – 15	2020	I/II / 2019-004332-36 I/II / 2016-000877-19
	Yes	Cabazitaxel	Advanced solid tumors	5 – 15	2018	I/II / 2017-003424-76
CDX-based cyclodextrin-polymer-drug conjugate	Yes	Camptothecin	Rectal, urothelial, NSCLC, & prostate	30 – 40	2022	I/II / NCT02010567 I/II / NCT02769962
PEG·PAA polymer-drug conjugate	Yes	Epirubicin	Sarcoma	–	2020	Ib/II / NCT03168061
Liposome	No	Cytarabine & Daunorubicin	Leukemia	100	2022	II & III / >30 clinical trials
	No	Lurtotecan	Fallopian tube, ovarian, & peritoneal	–	2020	II / NCT00010179 (3 more in II)
	Yes	Doxorubicin	Hepatic	100	2018	III / NCT02112656 (3 more in III)
	Yes	Vinorelbine	Advanced malignancy	100	2021	I/II / NCT02925000
	No	Annamycin	Leukemia	–	2022	I/II / NCT03388749 I/II / NCT03315039
PEG·PAA polymeric micelle	Yes	Paclitaxel	Breast	85	2019	III / NCT01644890
PEG·PLA polymeric micelle	Yes	Paclitaxel	NSCLC	20	2021	III / NCT02667743
	Yes	Docetaxel	Breast & bladder	25	2022	III / NCT05207514 III / NCT02982395
PEG·PGA polymeric micelle	Yes	Cisplatin	Head and neck, & pancreatic	30	2021	II / NCT03771820 III / NCT02043288
Albumin NPs	No	Rapamycin	Bladder	100	2021	I/II / NCT02009332
Exosomes	No	Curcumin	Colon	50 - 100	2021	I / NCT01294072

Abbreviations: CDX: cyclodextrin. EU: Europe. NP: nanoparticle. NSCLC: non-small cell lung cancer. PEG: polyethylene glycol. PAA: polyaspartic acid. PGA: polyglutamic acid. PLA: poly(D,L-lactic acid). PLL: poly-L-lysine. PHPMA: poly[*N*-(2-hydroxypropyl) methacrylamidelactate]. USA: United States of America.

1.2.2. Active targeting

To increase the efficiency of the targeting capacity of nanocarriers, researchers have functionalized the surface of the carriers with ligands with the capacity to interact with receptors present in specific tissues or cells.[49,65] This approach was first explored in the late 70s when Torchilin showed that the covalently linking of anti-canine cardiac myosin antibodies on the surface of liposomes promoted liposomal accumulation in the heart tissue of infarcted dogs.[76]

The first step in the design of an actively-targeted nanocarrier is the selection of the targeting ligand. Ideally, the ligand should be specific to the intended target; however, since this is an unrealistic scenario, active targeting usually takes advantage of the overexpression of a specific molecule or receptor in diseased tissues compared to healthy ones.[77] Different receptors have been identified on the surface of cancer cells, capillary and lymphatic vessels, and TME.[77] Altogether, the design of active-targeting nanocarriers should also consider the multiple barriers that nanocarriers must overcome before reaching their final target.[78]

In addition, from the design perspective, the presentation of the ligands in an adequate number and a convenient orientation on the surface of the nanocarrier may be critical for successful targeting. Usually, ligands are chemically conjugated to specific components of the nanocarriers, although simple methods involving adsorption have also been explored.[65] In addition, it has been reported that a high ligand density is not necessarily required. In fact, a high ligand density may inhibit the interaction due to steric hindrance.[77] Therefore, identifying the appropriate ligand density for each specific nanosystem, ligand, and target, becomes a critical aspect in the rational design of nanocarriers.

Finally, the protein corona of the actively-targeted delivery nanocarrier upon *in vivo* administration might compromise the active targeting capabilities of the nanosystem. Therefore, the new protein corona composition and the subsequent possible alteration of its targeting capacity should be addressed.[57,79]

So far, less than 10 formulations based on active targeting have reached the clinical phase for cancer treatment.[80] Although most of them successfully completed phase I, they failed to meet the endpoints of phase II. In this regard, some authors have argued that this limited clinical translation might be related to an inadequate choice of animal models in preclinical stages.[80] However, the reason for the complexity of translation is still a matter of debate. One of the main problems that active targeting suffers from is the limited identification of targets that are exclusively expressed at the tumor site or, at least, have negligible expression in healthy tissues compared to tumors.

In general, monoclonal antibodies (i.e., anti-EGFR or anti-HER2),[80–82] polymers, peptides, and small molecules were the most exploited for achieving active nanosystems targeting, and the folate and transferrin receptors represent some of the most commonly studied targets. Some examples of well-studied targeting ligands are summarized in Table 3.

USC UNIVERSIDADE DE SANTIAGO DE COMPOSTELA

Table 3. Examples of active targeting strategies for cancer cells of nanocarriers loading cytotoxic drugs

Ligand	Target	Nanocarrier	Tumor model	Outcome	Ref.
Transferrin	TfR	PEG·PLA DOX-loaded NPs	Glioma (C6, intracranial)	≈ 2-fold tumor growth inhibition and increased survival *vs.* non-targeted NPs	[83]
MTX	FR	PEG·PLGA curcumin & PTX-loaded NPs	Cervix (HeLa; subcutaneous)	Enhanced presence of targeted liposomes in cervix up to 24 h, while no untargeted liposomes were detected after 3 h	[84]
HA	CD44	DTX-loaded HA-coated NPs	Lung (A549; orthotopic)	4-fold accumulation in the tumor *vs.* free DTX	[85]
		HA-coated GEM- & DTX-loaded liposomes	TNBC (MDA-MB-23; subcutaneous)	4-fold tumor reduction *vs.* free drugs	[86]
F3	Nucleolin	PEG-PLA PTX-loaded micelles	Breast (MCF-7; subcutaneous)	2-fold tumor weight reduction in comparison with Taxol®	[87]
tLyP-1	Neuropilin 1/2	HA-tLyP-1 DTX-loaded NCs	Lung (A549; orthotopic)	37-fold higher accumulation in the tumor *vs.* Taxotere®	[88]
CDLRSAAVC	CLL1	DNR-loaded disulfide-crosslinked PEGylated micelles	Acute myeloid leukemia (PDX)	Significantly less acute myeloid leukemia engraftment compared to free DNR	[89]
Apt(S1.5)	HPA	PTX-loaded PEG PLGA NPs decorated with aptamer	TNBC (MDA-MB-231; orthotopic)	Significantly improved tumor regression *vs.* untargeted NPs	[90]

Abbreviations: Apt: aptamer. CLL1: C-type lectin-like molecule-1. DNR: daunorubicin. DTX: docetaxel. F3: KDEPQRRSARLSAKPAPPKPEPKPKKAPAKK peptide. FR: folate receptor. GEM: gemcitabine. HA: hyaluronic acid. HPA: heparanase. MTX: methotrexate. NC: nanocapsule. NP: nanoparticle. PDX: patient-derived xenograft. PEG: polyethylene glycol. PLA: polylactic acid. PLGA: poly(lactic-co-glycolic) acid. PTX: paclitaxel. TfR: transferrin receptor. TNBC: triple-negative breast cancer.

1.2.2.1. Hyaluronic acid

Hyaluronic acid (HA) can be considered an active targeting ligand because it binds to an overexpressed receptor in tumors, the cluster of differentiation (CD) 44. However, HA specificity is limited by the ubiquitous expression of CD44 receptors and the capacity of HA to interact with other receptors expressed by healthy cells, such as the receptor for hyaluronan mediated motility (RHAMM), hyaluronan receptor for endocytosis 1, and the lymphatic vessel endothelial hyaluronic acid receptor (LYVE).[91,92] Despite this, several works have shown that HA-based nanosystems tend to accumulate in the tumor tissue, which could also be caused by its stealth properties or a combined effect of active and passive mechanisms.[93]

The first report in this line showed that HA-coated liposomes encapsulating mitomycin C were more efficacious than the uncoated carriers in different murine cancer models (colon, melanoma, and lung metastasis).[94] This idea has evolved over the years, and a recent interesting combination approach consisted of liposomes loaded with docetaxel (DTX)

and coated by a conjugate of gemcitabine and HA,[86] which led to significant tumor regression in a xenograft breast cancer model.

The group of Professor Alonso has also contributed to this field by developing DTX-loaded HA NCs.[88,95–97] The improved biodistribution provided by the HA coating was translated into a higher efficacy than that of the control (Taxotere®). An additional cell-penetrating peptide (tLyp-1) was subsequently attached to these carriers to enhance their active-targeting capacity.

Overall, besides the limited specificity of the HA receptors in the context of cancer, this biomaterial holds promise for improving the biodistribution of anti-cancer drugs.

1.2.2.2. Tumor-homing peptides

Tumor-homing peptides are short peptides of 3 to 15 amino acids that specifically interact with either tumor cells or other cells present in the TME.

A specific kind of tumor-homing peptide comprises arginine-rich peptides, such as iRGD, or tLyp-1.[98] These peptides have been described to target the tumor vasculature and to facilitate the penetration of drugs and nanoparticles (NPs) across the tumor through the presence of a C-end rule sequence (CendR; R/K/XXR/K sequence at the C-terminus end).[98] In this sense, peptides complying with this rule can interact with the neuropilin-1 and 2 receptors (NRP1 and NRP2), overexpressed in lymphatic vessels and some cancer cells.[98] Indeed, our group has conducted research to exploit this targeting ligand. We hypothesized that the previously mentioned DTX-loaded NCs coated with an HA-tLyP-1 conjugate could improve the efficacy of NSCLC treatment while also targeting the metastatic cells in the surrounding lymphatic vessels.[88] Indeed, the encapsulation of DTX in these targeted NCs resulted in a preferential and dramatic drug accumulation at the tumor site (37-times that of Taxotere®) and a reduced presence in clearance organs such as the liver or spleen, leading to a significant reduction in tumor growth.

1.2.2.3. Small molecules

The functionalization of nanocarriers with a wide variety of small molecules, such as folic, glycyrrhetinic acids, or mannose, has been explored as a targeting strategy.[77,84,106,92,99–105]

One of the most relevant examples of promising targeted therapies was the nanocarrier developed by BIND Therapeutics (acquired by Pfizer in 2016). This formulation consisted of PLGA-PEG NPs functionalized with *S*,*S*-2-[3-[5-amino-1-carboxypentyl]-ureido]-pentanedioic acid, which targets the prostate-specific membrane antigen (PSMA). This targeted delivery carrier encapsulated DTX and demonstrated a dramatic capacity to suppress tumor growth in a xenograft mouse model of human $PSMA^+$ prostate cancer in a preclinical setting.[107] These outstanding data enabled the translation of the technology to clinical trials for several indications. Unfortunately, the clinical development was stopped in phase II due to insufficient evidence of the improved performance of the therapy as compared to the standard of care.[108,109] Although this approach seemed promising, the high effectivity of the standard treatment with DTX was argued to hinder the success of this PSMA-targeted nanocarrier in an

unselected population. Thus, the authors claim that a pre-selection of $PSMA^+$ patients could result in a therapeutic advantage over standard treatment.

1.3. POLYMERIC NCS DESIGN AS A DELIVERY PLATFORM

Polymeric nanocapsules (NCs), originally designed by Al-Kouri, H. Fessi, and coworkers,[110] are made of an oily core and a polymeric shell. They are versatile nanocarriers for delivering hydrophobic and hydrophilic drugs, protecting them from degradation and modulating their biodistribution profile and body clearance.[97,111–116] By adjusting the composition and the preparation technique, it is possible to obtain NCs with very different physicochemical properties and biological behavior.

In this section, we provide the rationale for selecting oils, surfactants, polymers, and formulation techniques for developing small-molecule immunomodulator- and monoclonal antibody-loaded NCs for treating lung cancer.

1.3.1. Components

1.3.1.1. Oil core

NCs oily core composition is usually selected based on the hydrophobicity and the solubility of the hydrophobic drugs to encapsulate in order to achieve a high encapsulation efficiency. Some of the most explored oils in the formulation of NCs are long-chain triglycerides (i.e., soybean oil or castor oil), DL-α-tocopherol, medium-chain triglycerides (i.e., capric/caprylic acid triglycerides), ethyl oleate, and oleic acid.[117]

1.3.1.2. Polymeric coating

Our group has extensive experience in the engineering of NCs made with different biodegradable and biocompatible polymers, i.e., poly-ε-caprolactone-PEG,[118] hyaluronic acid (HA),[95] polysialic acid (PSA),[119] polyarginine,[112] polyglutamic acid-PEG (PEG·PGA),[116,120,121] protamine,[115] and chitosan.[122]

The polymeric coating of NCs is of particular relevance as it is their most exposed part, meaning that it will closely interact with biological fluids and play a critical role in the protein corona composition. We have discarded the use of positively-charged polymers due to their higher protein adsorption. Instead, this work has been focused on the effect of polymers made of substances already present in humans, such as carbohydrates and poly(amino acids), for example, hyaluronic acid, polysialic acid, and polyethylene glycol-polyglutamic acid.

1.3.1.2.1. Hyaluronic acid

HA is an anionic polymer composed of disaccharides of D-glucuronic acid and *N*-acetyl-D-glucosamine, linked by alternating β-(1→4) and β-(1→3) glycosidic bonds (Figure 2). The pK_a of the carboxylic groups of HA is between 3 and 4, meaning that these groups are

USC DE SANTIAGO DE COMPOSTELA

ionized in physiological conditions, having the polymer a net charge of 1 negative charge per 378 Da.

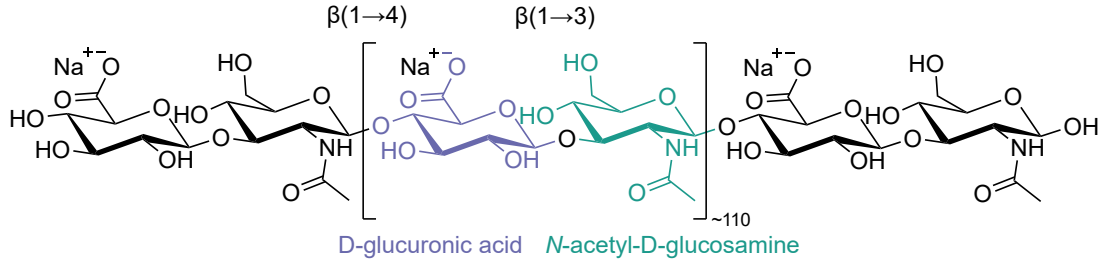


Figure 2. Chemical structure of hyaluronic acid, sodium salt, 45 kDa

Hyaluronic acid is composed of disaccharides of D-glucuronic acid and *N*-acetyl-D-glucosamine, linked by alternating ß-(1→4) and ß-(1→3) glycosidic bonds.

Endogenous HA has a molecular weight (MW) of 1 to 10 MDa and is mainly present in the synovial fluid and extracellular matrix. As such, it is biocompatible and has a low toxicity profile. HA is known to interact with several receptors that are located in all tissues, such as CD44, LYVE-1, RHAMM, and toll-like receptors (TLR).

In healthy cells, the interaction of endogenous high MW HA with CD44 leads to cell migration, proliferation, the preservation of cell and tissue integrity, cell survival, and regulated apoptosis. In addition, the interaction of endogenous HA with LYVE-1, which is expressed on the surface of lymphatic endothelial cells, mediates immune cell migration. Moreover, this HA regulates mitotic processes through the RHAMM receptor and affects innate and adaptative immunity through its interaction with TLRs. Of note, the overexpression of CD44 and RHAMM receptors has been reported for different cancer types such as breast,[123–125] lung,[126–128] melanoma,[129] and stomach,[130] among others. On the contrary, low MW HA fragments are known to stimulate the immune system and polarize macrophages to tumor-associated macrophages and M1 antitumoral macrophages, increasing angiogenesis, cancer progression cell proliferation, and inflammatory processes.

The first work reporting the use of HA as a polymeric coating of nanosystems was performed by the group of Prof. Margalit with HA-modified liposomes.[131] Since then, HA coating has been explored for several nanosystems due to its ability to provide a negative surface charge and target CD44 overexpressing cells. For example, Taetz *et al.* reported that 1,2-dioleoyl-3-trimethylammonium propane (DOTAP) / dioleoyl phosphatidylethanolamine (DOPE) liposomes suffered from a higher uptake when coated with HA when compared to the non-modified ones in A549 lung cancer cells (overexpressing CD44), whereas the same effect was not observed in Calu-3 (CD44-deficient).[132]

However, whether HA can be classified as an active targeting strategy given its low specificity for the targeted cells is still a matter of debate, and the influence of its MW when decorating NPs is not fully understood yet. NPs decorated with low MW HA might be seen as a big HA molecule by HA receptors. Thus, the spatial distribution of the HA moieties on the surface might be more relevant than the MW itself.

Finally, from the regulatory point of view, HA is currently approved for ocular, nasal, pulmonary, and parenteral administration.[133]

1.3.1.2.2. Polysialic acid

Sialic acids are a family of negatively-charged monosaccharides derived from the nine-carbon back-chain monosaccharide neuraminic acid.

Colominic acid is a homopolymer of α(2→8)-linked *N*-acetyl-D-neuraminic acids (Figure 3). The pK_a of the carboxylic groups of colominic acid is approximately 2.6,[134] meaning that these groups are ionized in physiological conditions, having the polymer a net charge of 1 negative charge per 290 Da. In general, colominic acid will be referred to as polysialic acid in this thesis.

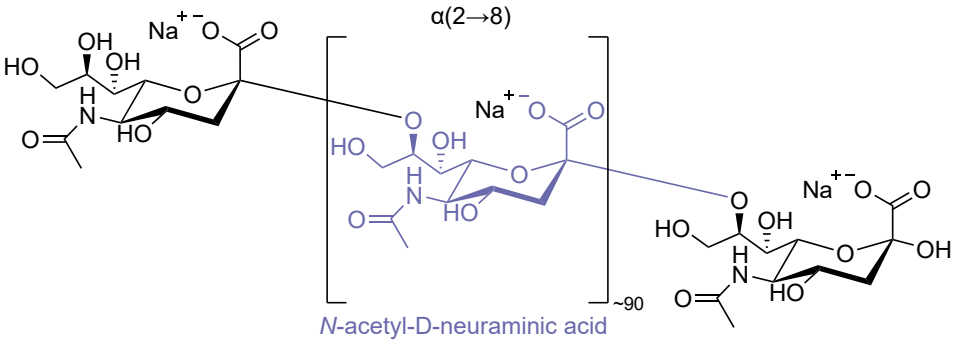


Figure 3. Chemical structure of colominic acid, sodium salt, 26 kDa

Colominic acid is composed of *N*-acetyl-D-neuraminic acids linked by α(2→8) glycosidic bonds.

Polysialic acid is highly expressed during embryonic development.[135] Then, its presence becomes limited to a few cell surface proteins in adults. Polysialylation has been reported for several proteins, such as the neuronal cell adhesion molecule and neuropilin-2 receptor.[136] Polysialylation is mediated by polysialyltransferases (ST8Sia 1 to 6).[136] Of note, the overexpression of polysialic acid has been reported for different cancer types such as lung,[137–139] breast,[135] and pancreatic,[140] and is usually found in SCLC.[138] In this sense, the polysialylation of surface proteins is supposed to diminish the adhesion of tumor cells and promote metastasis.[141] Since PSA is barely expressed in human adults, cancer vaccines for promoting the recognition of PSA by the immune system were developed.[139,141,142] Of note, one of them reached phase II clinical trials (NCT00004249). In this sense, a polysialic acid-coated nanocarrier, including immunostimulants, might be beneficial for SCLC vaccination.

On the other hand, the endogenous existence of PSA receptors is barely described. PSA is known to bind to the brain-derived neurotrophic factor, and the resulting complex becomes a ligand for the tropomyosin receptor kinase B and the p75 neurotrophin receptors. The activation of those receptors increases the growth and/or survival of neuroblastoma cells.[136,143,144] Moreover, PSA was reported to interact with sialic acid-binding immunoglobulin-like lectins, which are mainly found on hematopoietic and immune cells,[145] while also present in HeLa cells.[146] The limited interaction of PSA with human receptors and the protein-repellent properties derived from its strong negative charge at physiological pH led to its use for increasing the circulation time of nanocarriers[119,147–150] and proteins.[151] In fact, the conjugation of PSA to a recombinant Factor VIII provided a similar circulation time compared to the already commercialized PEGylated Factor VIII and has reached phase I in clinical trials for the treatment of hemophilia A.[152]

1.3.1.2.3. Polyaminoacids

Our research group has extensive experience in the use of poly(amino acids) as materials for the elaboration of nanocarriers such as polyarginine,[112,153] polyasparagine,[154] or polyglutamic acid.[113]

Polyglutamic acid (PGA) has been explored as a coating for the delivery of cytostatic drugs. For example, PGA-coated latex NPs were found to be taken up by HGSOC cancer cells by a receptor-mediated mechanism without the necessity of a decorating ligand.[155] More recently, PGA-coated layer-by-layer NPs were found to bind to cells with constitutive STAT3 activation in a PGA- and STAT3-dependent manner.[156]

On the other hand, the covalent linking of PGA to small-molecule chemotherapy was also explored for its controlled release. The most advanced therapy was Xyotax™ (USA) / Opaxio® (EU), a PGA-conjugated paclitaxel (PTX) pro-drug. PGA-PTX was advantageous compared to Cremophor® EL (present in the approved medicine Taxol®) for diminishing the adverse immune reactions.[157] This drug completed phase III clinical trials in the late 2000s to treat ovarian and lung cancer.[158] However, in 2009, regulatory agencies rejected its authorization for the first-line treatment of patients with advanced NSCLC. The major concerns were raised by inadequate comparators, which prevented the demonstration of the efficacy of that treatment.[159]

Besides PGA, PEGylated derivatives of PGA were also explored for cancer treatment. Decoration of 100-nm NCs with PEG·PGA leads to a great accumulation in the lung and lymph nodes.[111] In another experiment, DTX-loaded PEG·PGA NCs demonstrated a total tumor reduction in lungs similar to Taxotere® but without inducing weight loss. However, NCs led to a more significant and sustained reduction in tumor metastasis.[120] The greatest success in chemotherapy treatment using PEG·PGA-based nanocarriers was found for micelles. Cisplatin-loaded PEG·PGA micelles were found to prolong the blood circulation time and tumor accumulation of cisplatin 20 times that of free cisplatin.[160] This 30-nm formulation, called "NC-6004", has entered clinical trials in combination with several drugs.[161] Notably, it has reached phase III clinical trials for the treatment of locally advanced or metastatic pancreatic cancer (NCT02043288) in combination with gemcitabine. The chemical structure of the polyethylene glycol (5 kDa) poly-α-glutamic acid (1.3 kDa), is presented in Figure 4.

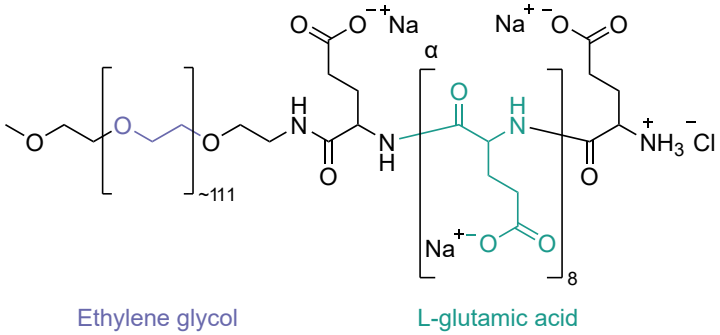


Figure 4. Chemical structure of polyethylene glycol (5 kDa) poly-α-glutamic acid (10 u), sodium and chloride salt

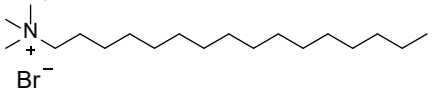
This PGA molecule is composed of approximately 113 units of ethylene glycol and 10 units of glutamic acid, linked by α-amino acid bonds. Of note, other PGAs might be linked by γ-amino acid bonds.

This PEG·PGA molecule is constituted of approximately 113 ethylene glycol units linked to 10 units of glutamic acid, and the pK_a of the carboxyl side chains of PGA is approximately 4.5,[162] meaning it is ionized at physiological conditions, having this polymer a net charge of 1 negative charge per 703 Da.

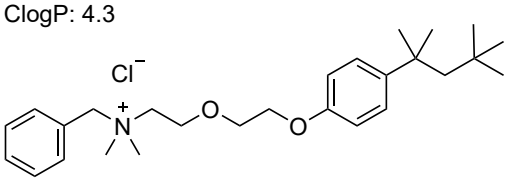
1.3.1.3. Surfactants

Positively charged surfactants were employed to attach the polymeric coating electrostatically to the oil core. CTAB was one of the most explored positively-charged surfactants for the formulation of NCs.[88,95,121,154,163] BZT and especially DOTAP were also explored due to their higher ClogPs, which suggests a more robust interaction of the positively-charged surfactant with the oil core (Figure 5). Moreover, DOTAP has been reported to attract vitronectin to some nanosystems' surfaces, which could be exploited for targeting lung cancer cells.[164–166]

CTAB
Molecular weight (cation): 284.55 Da
ClogP: 2.7



Benzethonium chloride
Molecular weight (cation): 412.64 Da
ClogP: 4.3



DOTAP
Molecular weight (cation): 663.10 Da
ClogP: 12.6

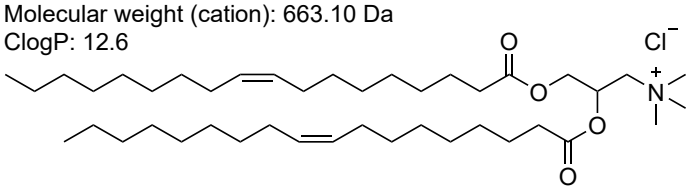


Figure 5. Molecular weight, calculated logP, and chemical structure of the positively-charged surfactants used in the preparation of the NCs of this thesis

ClogP: calculated logP. CTAB: Hexadecyltrimethylammonium bromide. DOTAP: 1,2-dioleoyl-3-trimethylammonium propane. ClogPs were estimated with ChemDraw Professional 21.0.

Finally, the effect of non-PEGylated non-cationic surfactants and PEGylated surfactants was explored based on the most commonly used in NCs formulations. In more detail, we have tested polysorbate 80, D-α-tocopherol polyethylene glycol 1000 succinate (TPGS), Kolliphor® HS15, *N*-(carbonyl-methoxy polyethylene glycol 2000)-1,2-distearoyl-sn-glycero-3-phosphoetanolamine (DSPE-PEG_{2000}), and lecithin (phosphatidylcholines).

1.3.2. Formulation procedures

Several formulation techniques are available for the elaboration of NCs. In this thesis, we will focus on solvent displacement (SD)[163] and self-emulsification (SE),[95] which are easy, fast, and low-energy input techniques. The incorporation of the different components is driven by factors such as the solubility of molecules in the formulation media, the ionic and/or hydrophobic interactions among different molecules, and the self-assembling of amphiphilic substances into micellar structures.

Also, in Chapter 1, we will focus on two limitations, the lack of rigorous characterizations in terms of composition and, more importantly, protein adsorption.

1.3.2.1. Solvent displacement

The solvent displacement method, also known as the nanoprecipitation method, is dictated by the Marangoni effect.[167] It involves mixing a completely water-miscible organic solution, for example, acetone or ethanol, containing the hydrophobic components, and an aqueous solution containing the hydrophilic ones, usually one or more surfactants. The mixing can be fast, done in a dropwise manner, or at a controlled speed, but is usually carried out under moderate stirring. Through rapid solvent diffusion, the hydrophobic components precipitate in a controlled way, and solvents can be removed under reduced pressure. While this method is mainly used for the entrapment of hydrophobic drugs, it can sometimes be employed to incorporate hydrophilic drugs. Depending on their physicochemical characteristics, polymers can be dissolved in the organic or aqueous phase.[168]

The formation of the NPs is immediate and in one step, so it has the advantage of being a rapid and easy operation. The key parameters in the fabrication procedure that greatly influence the solvent displacement method are the organic phase injection rate, the aqueous phase agitation rate, and the oil phase/aqueous phase ratio.[163]

1.3.2.2. Self-emulsification

The self-emulsification method (SE) involves the mixture of a solution of oils and surfactants with an aqueous phase without using organic solvents. Usually, due to the high viscosity of the oily phase, the aqueous phase is introduced under gentle agitation into the oily phase, which then emulsifies spontaneously to form fine oil-in-water emulsions. A self-emulsifying drug delivery system is an efficient and elegant formulation approach for poorly soluble drugs in organic solvents (i.e., proteins and ethanol) and for those requiring a low-energy emulsification technique.

In this thesis, the nanotechnological advantages of NCs will be exploited to improve lung cancer treatment. In this sense, the protein corona of SD and SE NCs will is deeply studied in Chapter 1. Then, that knowledge is applied to the rational development of nanocapsules loaded with immunomodulators (Chapter 2) and monoclonal antibodies (Chapter 3). The technological possibilities of polymeric NCs will hopefully contribute to advancing a new generation of lung cancer treatments with higher therapeutic outcomes and lower off-target toxicities.

2. REFERENCES

[1] T. G. Dacoba, S. Anthiya, G. Berrecoso, I. Fernández-Mariño, C. Fernández-Varela, J. Crecente-Campo, D. Teijeiro-Osorio, F. Torres-Andón, M. J. Alonso. Nano-Oncologicals: A Tortoise Trail Reaching New Avenues. *Advanced Functional Materials*. 31, 1–36. (2021). doi: 10.1002/adfm.202009860.

[2] G. Berrecoso, J. Crecente-Campo, M. J. Alonso. Unveiling the pitfalls of the protein corona of polymeric drug nanocarriers. *Drug Delivery and Translational Research*. 10, 730–750. (2020). doi: 10.1007/s13346-020-00745-0.

[3] World Health Organization. Cancer. https://www.who.int/health-topics/cancer#tab=tab_1. Accessed: October 31, 2022.

[4] H. Sung, J. Ferlay, R. L. Siegel, M. Laversanne, I. Soerjomataram, A. Jemal, F. Bray. Global Cancer Statistics 2020: GLOBOCAN Estimates of Incidence and Mortality Worldwide for 36 Cancers in 185 Countries. *CA: A Cancer Journal for Clinicians*. 71, 209–249. (2021). doi: 10.3322/caac.21660.

[5] Global Cancer Observatory. International Agency for Research on Cancer. https://gco.iarc.fr. Accessed: October 28, 2022.

[6] European Cancer Information System. Cancer burden statistics and trends across Europe | ECIS. https://ecis.jrc.ec.europa.eu/. Accessed: October 30, 2022.

[7] SEER. U.S. National Institutes of Health. Lung and Bronchus Cancer — Cancer Stat Facts. https://seer.cancer.gov/statfacts/html/lungb.html. Accessed: October 31, 2022.

[8] Johns Hopkins Medicine. Lung Cancer Risk Factors. https://www.hopkinsmedicine.org/health/conditions-and-diseases/lung-cancer/lung-cancer-risk-factors. Accessed: October 31, 2022.

[9] American Lung Association. Lung Cancer Basics. https://www.lung.org/lung-health-diseases/lung-disease-lookup/lung-cancer/basics/lung-cancer-types. Accessed: October 31, 2022.

[10] American Society of Clinical Oncology (ASCO). Lung Cancer - Non-Small Cell: Statistics | Cancer.Net. https://www.cancer.net/cancer-types/lung-cancer-non-small-cell/statistics. Accessed: October 31, 2022.

[11] J. Judd, N. A. Karim, H. Khan, A. R. Naqash, Y. Baca, J. Xiu, A. M. VanderWalde, H. Mamdani, L. E. Raez, M. Nagasaka, S. G. Pai, M. A. Socinski, J. J. Nieva, C. Kim, A. J. Wozniak, C. Ikpeazu, G. de Lima Lopes, A. I. Spira, W. M. Korn, E. S. Kim, S. V. Liu, H. Borghaei. Characterization of KRAS mutation subtypes in non-small cell lung cancer. *Molecular Cancer Therapeutics*. 20, 2577–2584. (2021). doi: 10.1158/1535-7163.MCT-21-0201.

[12] R. Veluswamy, P. C. Mack, J. Houldsworth, E. Elkhouly, F. R. Hirsch. KRAS G12C–Mutant Non–Small Cell Lung Cancer: Biology, Developmental Therapeutics, and Molecular Testing. *Journal of Molecular Diagnostics*. 23, 507–520. (2021). doi: 10.1016/j.jmoldx.2021.02.002.

[13] Y. Verhoeven, S. Tilborghs, J. Jacobs, J. De Waele, D. Quatannens, C. Deben, H. Prenen, P. Pauwels, X. B. Trinh, A. Wouters, E. L. J. Smits, F. Lardon, P. A. van Dam. The potential and controversy of targeting STAT family members in cancer. *Seminars in Cancer Biology*. 60, 41–56. (2020). doi: 10.1016/j.semcancer.2019.10.002.

[14] D. Harada, N. Takigawa, K. Kiura. The Role of STAT3 in Non-Small Cell Lung Cancer. *Cancers*. 6, 708–722. (2014). doi: 10.3390/cancers6020708.

[15] S. Parakh, M. Ernst, A. R. Poh. Multicellular Effects of STAT3 in Non-small Cell Lung Cancer: Mechanistic Insights and Therapeutic Opportunities. *Cancers*. 13, 6228. (2021). doi: 10.3390/cancers13246228.

[16] J. Li, C. Shen, X. Wang, Y. Lai, K. Zhou, P. Li, L. Liu, G. Che. Prognostic value of TGF-β in lung cancer: systematic review and meta-analysis. *BMC Cancer*. 19, 691. (2019). doi: 10.1186/s12885-019-5917-5.

[17] H. Mithoowani, M. Febbraro. Non-Small-Cell Lung Cancer in 2022: A Review for General Practitioners in Oncology. *Current Oncology*. 29, 1828–1839. (2022). doi: 10.3390/curroncol29030150.

[18] S. R. Punekar, E. Shum, C. M. Grello, S. C. Lau, V. Velcheti. Immunotherapy in non-small cell lung cancer: Past, present, and future directions. *Frontiers in Oncology*. 12, 1–18. (2022). doi: 10.3389/fonc.2022.877594.

[19] X. Hu, J. li, M. Fu, X. Zhao, W. Wang. The JAK/STAT signaling pathway: from bench to clinic. *Signal Transduction and Targeted Therapy*. 6, (2021). doi: 10.1038/s41392-021-00791-1.

[20] A. Okines, T. Irfan, B. Asare, K. Mohammed, P. Osin, A. Nerurkar, I. E. Smith, M. Parton, A. Ring, S. Johnston, N. C. Turner. Clinical outcomes in patients with triple negative or HER2 positive lobular breast cancer: a single institution experience. *Breast Cancer Research and Treatment*. 192, 563–571. (2022). doi: 10.1007/s10549-021-06432-z.

[21] A. S. Mansfield, Z. Wei, R. Mehra, A. T. Shaw, C. H. Lieu, P. M. Forde, A. E. Drilon, E. P. Mitchell, J. J. Wright, N. Takebe, E. Sharon, D. Hovelson, S. Tomlins, J. Zeng, K. Poorman, N. Malik, R. J. Gray, S. Li, L. M. McShane, L. V. Rubinstein, D. Patton, P. M. Williams, S. R. Hamilton, B. A. Conley, C. L. Arteaga, L. N. Harris, P. J. O'Dwyer, A. P. Chen, K. T. Flaherty. Crizotinib in patients with tumors harboring ALK or ROS1 rearrangements in the NCI-MATCH trial. *npj Precision Oncology*. 6, 1–6. (2022). doi: 10.1038/s41698-022-00256-w.

[22] D. S. W. Tan, S. Geater, C. J. Yu, C. M. Tsai, T. C. Hsia, J. Chen, M. C. Lin, Y. Lu, V. Sriuranpong, C. T. Yang, P. Sen, F. Branle, M. Shi, Y. L. Wu. Ceritinib Efficacy and Safety in Treatment-Naive Asian Patients With Advanced ALK-Rearranged NSCLC: An ASCEND-4 Subgroup Analysis. *JTO Clinical and Research Reports*. 2, 100131. (2021). doi: 10.1016/j.jtocrr.2020.100131.

[23] K. W. Nassar, J. D. Hintzsche, S. M. Bagby, V. Espinoza, C. Langouët-Astrié, C. M. Amato, T.-S. Chimed, M. Fujita, W. Robinson, A. C. Tan, R. E. Schweppe. Targeting CDK4/6 Represents a Therapeutic Vulnerability in Acquired BRAF/MEK Inhibitor–Resistant Melanoma. *Molecular Cancer Therapeutics*. 20, 2049–2060. (2021). doi: 10.1158/1535-7163.MCT-20-1126.

[24] K. Hotta, T. Hida, H. Nokihara, M. Morise, Y. H. Kim, K. Azuma, T. Seto, Y. Takiguchi, M. Nishio, H. Yoshioka.

USC UNIVERSIDADE DE SANTIAGO DE COMPOSTELA

Final overall survival analysis from the phase III J-ALEX study of alectinib versus crizotinib in ALK inhibitor-naïve Japanese patients with ALK -positive. *ESMO Open*. 7, 100527. (2022). doi: 10.1016/j.esmoop.2022.100527.

[25] W. Wick, S. Dettmer, A. Berberich, T. Kessler, I. Karapanagiotou-Schenkel, A. Wick, F. Winkler, E. Pfaff, B. Brors, J. Debus, A. Unterberg, M. Bendszus, C. Herold-Mende, A. Eisenmenger, A. Von Deimling, D. T. W. Jones, S. M. Pfister, F. Sahm, M. Platten. N 2 M 2 (NOA-20) phase I/II trial of molecularly matched targeted therapies plus radiotherapy in patients with newly diagnosed non-MGMT hypermethylated glioblastoma. *Neuro-Oncology*. 21, 95–105. (2019). doi: 10.1093/neuonc/noy161.

[26] D. W. Kim, M. Tiseo, M. J. Ahn, K. L. Reckamp, K. H. Hansen, S. W. Kim, R. M. Huber, H. L. West, H. J. M. Groen, M. J. Hochmair, N. B. Leighl, S. N. Gettinger, C. J. Langer, L. G. P. A. Rodríguez, E. F. Smit, E. S. Kim, W. Reichmann, F. G. Haluska, D. Kerstein, D. R. Camidge. Brigatinib in patients with crizotinib-refractory anaplastic lymphoma kinase-positive non-small-cell lung cancer: A randomized, multicenter phase II trial. *Journal of Clinical Oncology*. 35, 2490–2498. (2017). doi: 10.1200/JCO.2016.71.5904.

[27] A. T. Shaw, T. M. Bauer, F. de Marinis, E. Felip, Y. Goto, G. Liu, J. Mazieres, D.-W. Kim, T. Mok, A. Polli, H. Thurm, A. M. Calella, G. Peltz, B. J. Solomon. First-Line Lorlatinib or Crizotinib in Advanced ALK -Positive Lung Cancer. *New England Journal of Medicine*. 383, 2018–2029. (2020). doi: 10.1056/nejmoa2027187.

[28] T. Okusaka, H. Ueno, M. Ikeda, S. Mitsunaga, M. Ozaka, H. Ishii, O. Yokosuka, Y. Ooka, R. Yoshimoto, Y. Yanagihara, K. Okita. Phase 1 and pharmacological trial of OPB-31121, a signal transducer and activator of transcription-3 inhibitor, in patients with advanced hepatocellular carcinoma. *Hepatology Research*. 45, 1283–1291. (2015). doi: 10.1111/hepr.12504.

[29] Y. L. Wu, S. Lu, Y. Lu, J. Zhou, Y. kai Shi, V. Sriuranpong, J. C. M. Ho, C. K. Ong, C. M. Tsai, C. H. Chung, K. D. Wilner, Y. Tang, E. T. Masters, P. Selaru, T. S. Mok. Results of PROFILE 1029, a Phase III Comparison of First-Line Crizotinib versus Chemotherapy in East Asian Patients with ALK-Positive Advanced Non–Small Cell Lung Cancer. *Journal of Thoracic Oncology*. 13, 1539–1548. (2018). doi: 10.1016/j.jtho.2018.06.012.

[30] A. T. Shaw, T. M. Kim, L. Crinò, C. Gridelli, K. Kiura, G. Liu, S. Novello, A. Bearz, O. Gautschi, T. Mok, M. Nishio, G. Scagliotti, D. R. Spigel, S. Deudon, C. Zheng, S. Pantano, P. Urban, C. Massacesi, K. Viraswami-Appanna, E. Felip. Ceritinib versus chemotherapy in patients with ALK-rearranged non-small-cell lung cancer previously given chemotherapy and crizotinib (ASCEND-5): a randomised, controlled, open-label, phase 3 trial. *The Lancet Oncology*. 18, 874–886. (2017). doi: 10.1016/S1470-2045(17)30339-X.

[31] J. C. Soria, D. S. W. Tan, R. Chiari, Y. L. Wu, L. Paz-Ares, J. Wolf, S. L. Geater, S. Orlov, D. Cortinovis, C. J. Yu, M. Hochmair, A. B. Cortot, C. M. Tsai, D. Moro-Sibilot, R. G. Campelo, T. McCulloch, P. Sen, M. Dugan, S. Pantano, F. Branle, C. Massacesi, G. de Castro. First-line ceritinib versus platinum-based chemotherapy in advanced ALK-rearranged non-small-cell lung cancer (ASCEND-4): a randomised, open-label, phase 3 study. *The Lancet*. 389, 917–929. (2017). doi: 10.1016/S0140-6736(17)30123-X.

[32] N. Ochi, N. Takigawa. What can we learn from 3 phase III trials of ASCEND-4: Ceritinib vs. platinum/pemetrexed with pemetrexed maintenance, PROFILE 1004: Crizotinib vs. platinum/pemetrexed, and J-ALEX: Alectinib vs. crizotinib? *Translational Cancer Research*. 6, S515–S518. (2017). doi: 10.21037/tcr.2017.04.20.

[33] F. Zhao, Y. Wei, Y. Yan, H. Liu, S. Zhou, B. Ren, R. Liu. Determination of Crizotinib in Mouse Tissues by LC-MS/MS and Its Application to a Tissue Distribution Study. *International Journal of Analytical Chemistry*. 2020, (2020). doi: 10.1155/2020/8837254.

[34] European Medicines Agency. Assessent report: Xalkori. https://www.ema.europa.eu/en/documents/product-information/xalkori-epar-product-information_en.pdf. Accessed: November 1, 2022.

[35] European Medicines Agency. Assessent report: Zykadia. https://www.ema.europa.eu/en/documents/assessment-report/zykadia-epar-public-assessment-report_en.pdf. Accessed: November 1, 2022.

[36] E. Cekani, S. Epistolio, G. Dazio, M. Cefalì, L. Wannesson, M. Frattini, P. Froesch. Molecular Biology and Therapeutic Perspectives for K-Ras Mutant Non-Small Cell Lung Cancers. *Cancers*. 14, 1–32. (2022). doi: 10.3390/cancers14174103.

[37] D. Teijeiro-Osorio, C. B. Michalowsky, J. A. Costoya, I. Golán, S. Vicent, M. J. Alonso. In *RAS Targeted Drug Development Summit conference, Boston*. (2019).

[38] A. C. Anselmo, S. Mitragotri. Nanoparticles in the clinic. *Bioengineering & Translational Medicine*. 1, 10–29. (2016). doi: 10.1002/btm2.10003.

[39] J. Shi, P. W. Kantoff, R. Wooster, O. C. Farokhzad. Cancer nanomedicine: progress, challenges and opportunities. *Nature Reviews Cancer*. 17, 20–37. (2017). doi: 10.1038/nrc.2016.108.

[40] J. Wolfram, M. Ferrari. Clinical cancer nanomedicine. *Nano Today*. 25, 85–98. (2019). doi: 10.1016/j.nantod.2019.02.005.

[41] A. Wicki, D. Witzigmann, V. Balasubramanian, J. Huwyler. Nanomedicine in cancer therapy: challenges, opportunities, and clinical applications. *Journal of Controlled Release*. 200, 138–157. (2015). doi: 10.1016/j.jconrel.2014.12.030.

[42] L. Milling, Y. Zhang, D. J. Irvine. Delivering safer immunotherapies for cancer. *Advanced Drug Delivery Reviews*. 114, 79–101. (2017). doi: 10.1016/j.addr.2017.05.011.

[43] Y. Barenholz. Doxil® - The first FDA-approved nano-drug: Lessons learned. *Journal of Controlled Release*. 160, 117–134. (2012). doi: 10.1016/j.jconrel.2012.03.020.

[44] National Cancer Institute - NIH. Types of Chemotherapy Drugs. https://training.seer.cancer.gov/treatment/chemotherapy/types.html. Accessed: November 3, 2022.

[45] J. Logie, A. N. Ganesh, A. M. Aman, R. S. Al-awar, M. S. Shoichet. Preclinical evaluation of taxane-binding peptide-

modified polymeric micelles loaded with docetaxel in an orthotopic breast cancer mouse model. *Biomaterials*. 123, 39–47. (2017). doi: 10.1016/j.biomaterials.2017.01.026.

[46] Y. Matsumura, H. Maeda. A New Concept for Macromolecular Therapeutics in Cancer Chemotherapy: Mechanism of Tumoritropic Accumulation of Proteins and the Antitumor Agent Smancs. *Cancer Research*. 46, 6387–6392. (1986).

[47] M. Morales-Cruz, Y. Delgado, B. Castillo, C. M. Figueroa, A. Molina, A. Torres, M. Milian, K. Griebenow. Smart Targeting To Improve Cancer Therapeutics. *Drug Design, Development and Therapy*. 13, 3753–3772. (2019). doi: 10.2147/DDDT.S219489.

[48] S. K. Golombek, J.-N. May, B. Theek, L. Appold, N. Drude, F. Kiessling, T. Lammers. Tumor targeting via EPR: Strategies to enhance patient responses. *Advanced Drug Delivery Reviews*. 130, 17–38. (2018). doi: 10.1016/j.addr.2018.07.007.

[49] Y. Shi, R. van der Meel, X. Chen, T. Lammers. The EPR effect and beyond: Strategies to improve tumor targeting and cancer nanomedicine treatment efficacy. *Theranostics*. 10, 7921–7924. (2020). doi: 10.7150/thno.49577.

[50] X. Liu, J. Jiang, H. Meng. Transcytosis - An effective targeting strategy that is complementary to "EPR effect" for pancreatic cancer nano drug delivery. *Theranostics*. 9, 8018–8025. (2019). doi: 10.7150/thno.38587.

[51] S. Sindhwani, A. M. Syed, J. Ngai, B. R. Kingston, L. Maiorino, J. Rothschild, P. MacMillan, Y. Zhang, N. U. Rajesh, T. Hoang, J. L. Y. Wu, S. Wilhelm, A. Zilman, S. Gadde, A. Sulaiman, B. Ouyang, Z. Lin, L. Wang, M. Egeblad, W. C. W. Chan. The entry of nanoparticles into solid tumours. *Nature Materials*. 19, 566–575. (2020). doi: 10.1038/s41563-019-0566-2.

[52] T. Lammers, F. Kiessling, W. E. Hennink, G. Storm. Drug targeting to tumors: Principles, pitfalls and (pre-) clinical progress. *Journal of Controlled Release*. 161, 175–187. (2012). doi: 10.1016/j.jconrel.2011.09.063.

[53] O. Kutova, E. Guryev, E. Sokolova, R. Alzeibak, I. Balalaeva. Targeted Delivery to Tumors: Multidirectional Strategies to Improve Treatment Efficiency. *Cancers*. 11, 68. (2019). doi: 10.3390/cancers11010068.

[54] S. Wilhelm, A. J. Tavares, Q. Dai, S. Ohta, J. Audet, H. F. Dvorak, W. C. W. W. Chan. Analysis of nanoparticle delivery to tumours. *Nature Reviews Materials*. 1, 16014. (2016). doi: 10.1038/natrevmats.2016.14.

[55] J. I. Hare, T. Lammers, M. B. Ashford, S. Puri, G. Storm, S. T. Barry. Challenges and strategies in anti-cancer nanomedicine development: An industry perspective. *Advanced Drug Delivery Reviews*. 108, 25–38. (2017). doi: 10.1016/j.addr.2016.04.025.

[56] F. T. Andón, E. Digifico, A. Maeda, M. Erreni, A. Mantovani, M. J. Alonso, P. Allavena. Targeting tumor associated macrophages: The new challenge for nanomedicine. *Seminars in Immunology*. 34, 103–113. (2017). doi: 10.1016/j.smim.2017.09.004.

[57] M. F. Attia, N. Anton, J. Wallyn, Z. Omran, T. F. Vandamme. An overview of active and passive targeting strategies to improve the nanocarriers efficiency to tumour sites. *Journal of Pharmacy and Pharmacology*. 71, 1185–1198. (2019). doi: 10.1111/jphp.13098.

[58] W. Yu, R. Liu, Y. Zhou, H. Gao. Size-Tunable Strategies for a Tumor Targeted Drug Delivery System. *ACS Central Science*. 6, 100–116. (2020). doi: 10.1021/acscentsci.9b01139.

[59] W. Jiang, B. Y. S. Kim, J. T. Rutka, W. C. W. Chan. Nanoparticle-mediated cellular response is size-dependent. *Nature Nanotechnology*. 3, 145–150. (2008). doi: 10.1038/nnano.2008.30.

[60] A. K. Pearce, R. K. O'Reilly. Insights into Active Targeting of Nanoparticles in Drug Delivery: Advances in Clinical Studies and Design Considerations for Cancer Nanomedicine. *Bioconjugate Chemistry*. 30, 2300–2311. (2019). doi: 10.1021/acs.bioconjchem.9b00456.

[61] C. Sarisozen, U. Joshi, L. P. Mendes, V. P. Torchilin. In *Stimuli Responsive Polymeric Nanocarriers for Drug Delivery Applications*. Elsevier. (2019). pp. 269–304.

[62] L. Salvioni, M. A. Rizzuto, J. A. Bertolini, L. Pandolfi, M. Colombo, D. Prosperi. Thirty Years of Cancer Nanomedicine: Success, Frustration, and Hope. *Cancers*. 11, 1855. (2019). doi: 10.3390/cancers11121855.

[63] P. Foroozandeh, A. A. Aziz. Insight into Cellular Uptake and Intracellular Trafficking of Nanoparticles. *Nanoscale Research Letters*. 13, 339. (2018). doi: 10.1186/s11671-018-2728-6.

[64] J. Zhao, M. H. Stenzel. Entry of nanoparticles into cells: The importance of nanoparticle properties. *Polymer Chemistry*. 9, 259–272. (2018). doi: 10.1039/c7py01603d.

[65] J. Yoo, C. Park, G. Yi, D. Lee, H. Koo. Active Targeting Strategies Using Biological Ligands for Nanoparticle Drug Delivery Systems. *Cancers*. 11, 640. (2019). doi: 10.3390/cancers11050640.

[66] A. C. Anselmo, S. Mitragotri. Impact of particle elasticity on particle-based drug delivery systems. *Advanced Drug Delivery Reviews*. 108, 51–67. (2017). doi: 10.1016/j.addr.2016.01.007.

[67] Y. Hui, X. Yi, F. Hou, D. Wibowo, F. Zhang, D. Zhao, H. Gao, C.-X. Zhao. Role of Nanoparticle Mechanical Properties in Cancer Drug Delivery. *ACS Nano*. 13, 7410–7424. (2019). doi: 10.1021/acsnano.9b03924.

[68] U.S. Food and Drug Administration. FDA – Approved Drugs. https://www.accessdata.fda.gov/scripts/cder/daf/index.cfm. Accessed: November 3, 2022.

[69] European Medicines Agency. EMA – Medicines. https://www.ema.europa.eu/en/medicines. Accessed: November 3, 2022.

[70] N. Bertrand, P. Grenier, M. Mahmoudi, E. M. Lima, E. A. Appel, F. Dormont, J. M. Lim, R. Karnik, R. Langer, O. C. Farokhzad. Mechanistic understanding of in vivo protein corona formation on polymeric nanoparticles and impact on pharmacokinetics. *Nature Communications*. 8, 1–8. (2017). doi: 10.1038/s41467-017-00600-w.

[71] E. Samaridou, N. Kalamidas, I. Santalices, J. Crecente-Campo, M. J. Alonso. Tuning the PEG surface density of the PEG-PGA enveloped Octaarginine-peptide Nanocomplexes. *Drug Delivery and Translational Research*. 10, 241–

258. (2020). doi: 10.1007/s13346-019-00678-3.
[72] D. E. Owens, N. A. Peppas. Opsonization, biodistribution, and pharmacokinetics of polymeric nanoparticles. *International Journal of Pharmaceutics*. 307, 93–102. (2006). doi: 10.1016/j.ijpharm.2005.10.010.
[73] P. P. Wibroe, D. Ahmadvand, M. A. Oghabian, A. Yaghmur, S. M. Moghimi. An integrated assessment of morphology, size, and complement activation of the PEGylated liposomal doxorubicin products Doxil®, Caelyx®, DOXOrubicin, and SinaDoxosome. *Journal of Controlled Release*. 221, 1–8. (2016). doi: 10.1016/j.jconrel.2015.11.021.
[74] P. Grenier, I. M. de Oliveira Viana, E. M. Lima, N. Bertrand. Anti-polyethylene glycol antibodies alter the protein corona deposited on nanoparticles and the physiological pathways regulating their fate in vivo. *Journal of Controlled Release*. 287, 121–131. (2018). doi: 10.1016/j.jconrel.2018.08.022.
[75] V. P. Vu, G. B. Gifford, F. Chen, H. Benasutti, G. Wang, E. V. Groman, R. Scheinman, L. Saba, S. M. Moghimi, D. Simberg. Immunoglobulin deposition on biomolecule corona determines complement opsonization efficiency of preclinical and clinical nanoparticles. *Nature Nanotechnology*. 14, 260–268. (2019). doi: 10.1038/s41565-018-0344-3.
[76] V. P. V. Torchilin, B. B. A. Khaw, V. V. N. Smirnov, E. Haber. Preservation of antimyosin antibody activity after covalent coupling to liposomes. *Biochemical and Biophysical Research Communications*. 89, 1114–1119. (1979). doi: 10.1016/0006-291X(79)92123-5.
[77] P. N. Navya, A. Kaphle, S. P. Srinivas, S. K. Bhargava, V. M. Rotello, H. K. Daima. Current trends and challenges in cancer management and therapy using designer nanomaterials. *Nano Convergence*. 6, 23. (2019). doi: 10.1186/s40580-019-0193-2.
[78] D. Rosenblum, N. Joshi, W. Tao, J. M. Karp, D. Peer. Progress and challenges towards targeted delivery of cancer therapeutics. *Nature Communications*. 9, 1410. (2018). doi: 10.1038/s41467-018-03705-y.
[79] A. K. Barui, J. Y. Oh, B. Jana, C. Kim, J. Ryu. Cancer-Targeted Nanomedicine: Overcoming the Barrier of the Protein Corona. *Advanced Therapeutics*. 3, 1900124. (2020). doi: 10.1002/adtp.201900124.
[80] P. Mi, H. Cabral, K. Kataoka. Ligand-Installed Nanocarriers toward Precision Therapy. *Advanced Materials*. 32, 1902604. (2020). doi: 10.1002/adma.201902604.
[81] N. Dammes, D. Peer. *Monoclonal antibody-based molecular imaging strategies and theranostic opportunities*, Vol. 10, Ivyspring International Publisher, (2020), pp. 938–955.
[82] P. J. Carter, G. A. Lazar. Next generation antibody drugs: Pursuit of the "high-hanging fruit." *Nature Reviews Drug Discovery*. 17, 197–223. (2018). doi: 10.1038/nrd.2017.227.
[83] G. Liu, J. Mao, Z. Jiang, T. Sun, Y. Hu, Z. Jiang, C. Zhang, J. Dong, Q. Huang, Q. Lan. Transferrin-modified doxorubicin-loaded biodegradable nanoparticles exhibit enhanced efficacy in treating brain glioma-bearing rats. *Cancer Biotherapy and Radiopharmaceuticals*. 28, 691–696. (2013). doi: 10.1089/cbr.2013.1480.
[84] A. K. T. Thulasidasan, A. P. Retnakumari, M. Shankar, V. Vijayakurup, S. Anwar, S. Thankachan, K. S. Pillai, J. J. Pillai, C. D. Nandan, V. V. Alex, T. J. Chirayil, S. Sundaram, G. S. Vinod Kumar, R. J. Anto. Folic acid conjugation improves the bioavailability and chemosensitizing efficacy of curcumin-encapsulated PLGA-PEG nanoparticles towards paclitaxel chemotherapy. *Oncotarget*. 8, 107374–107389. (2017). doi: 10.18632/oncotarget.22376.
[85] J. Wu, C. Deng, F. Meng, J. Zhang, H. Sun, Z. Zhong. Hyaluronic acid coated PLGA nanoparticulate docetaxel effectively targets and suppresses orthotopic human lung cancer. *Journal of Controlled Release*. 259, 76–82. (2017). doi: 10.1016/j.jconrel.2016.12.024.
[86] Y. Fan, Q. Wang, G. Lin, Y. Shi, Z. Gu, T. Ding. Combination of using prodrug-modified cationic liposome nanocomplexes and a potentiating strategy via targeted co-delivery of gemcitabine and docetaxel for CD44-overexpressed triple negative breast cancer therapy. *Acta Biomaterialia*. 62, 257–272. (2017). doi: 10.1016/j.actbio.2017.08.034.
[87] Y. Cai, Z. Xu, Q. Shuai, F. Zhu, J. Xu, X. Gao, X. Sun. Tumor-targeting peptide functionalized PEG-PLA micelles for efficient drug delivery. *Biomaterials Science*. 8, 2274–2282. (2020). doi: 10.1039/c9bm02036e.
[88] C. Teijeiro-Valiño, R. Novoa-Carballal, E. Borrajo, A. Vidal, M. Alonso-Nocelo, M. de la Fuente Freire, P. P. P. Lopez-Casas, M. Hidalgo, N. Csaba, M. J. Alonso. A multifunctional drug nanocarrier for efficient anticancer therapy. *Journal of Controlled Release*. 294, 154–164. (2019). doi: 10.1016/j.jconrel.2018.12.002.
[89] T. Lin, Y. Zhu, Y. Li, H. Zhang, A.-H. Ma, Q. Long, J. Keck, K. S. Lam, C. Pan, B. A. Jonas. Daunorubicin-containing CLL1-targeting nanomicelles have anti-leukemia stem cell activity in acute myeloid leukemia. *Nanomedicine: Nanotechnology, Biology and Medicine*. 20, 102004. (2019). doi: 10.1016/j.nano.2019.04.007.
[90] T. Duan, Z. Xu, F. Sun, Y. Wang, J. Zhang, C. Luo, M. Wang. HPA aptamer functionalized paclitaxel-loaded PLGA nanoparticles for enhanced anticancer therapy through targeted effects and microenvironment modulation. *Biomedicine and Pharmacotherapy*. 117, 109121. (2019). doi: 10.1016/j.biopha.2019.109121.
[91] J. M. Rios de la Rosa, A. Tirella, N. Tirelli. Receptor-Targeted Drug Delivery and the (Many) Problems We Know of: The Case of CD44 and Hyaluronic Acid. *Advanced Biosystems*. 2, 1–19. (2018). doi: 10.1002/adbi.201800049.
[92] A. Cadete, M. J. Alonso. Targeting cancer with hyaluronic acid-based nanocarriers: Recent advances and translational perspectives. *Nanomedicine*. 11, 2341–2357. (2016). doi: 10.2217/nnm-2016-0117.
[93] G. Mattheolabakis, L. Milane, A. Singh, M. M. M. Amiji. Hyaluronic acid targeting of CD44 for cancer therapy: From receptor biology to nanomedicine. *Journal of Drug Targeting*. 23, 605–618. (2015). doi: 10.3109/1061186X.2015.1052072.
[94] D. Peer, R. Margalit. Loading mitomycin C inside long circulating hyaluronan targeted nano-liposomes increases its antitumor activity in three mice tumor models. *International Journal of Cancer*. 108, 780–789. (2004). doi:

10.1002/ijc.11615.

[95] A. Cadete, A. Olivera, M. Besev, P. K. Dhal, L. Gonçalves, A. J. Almeida, G. Bastiat, J.-P. Benoit, M. de la Fuente, M. Garcia-Fuentes, M. J. Alonso, D. Torres. Self-assembled hyaluronan nanocapsules for the intracellular delivery of anticancer drugs. *Scientific Reports*. 9, 11565. (2019). doi: 10.1038/s41598-019-47995-8.

[96] F. A. Oyarzun-Ampuero, G. R. Rivera-Rodriguez, M. J. Alonso, D. Torres. Hyaluronan nanocapsules as a new vehicle for intracellular drug delivery. *European Journal of Pharmaceutical Sciences*. 49, 483–490. (2013). doi: 10.1016/j.ejps.2013.05.008.

[97] Á. Molina-Crespo, A. Cadete, D. Sarrio, M. Gámez-Chiachio, L. Martinez, K. Chao, A. Olivera, A. Gonella, E. Díaz, J. Palacios, P. K. Dhal, M. Besev, M. Rodríguez-Serrano, M. L. García Bermejo, J. C. Triviño, A. Cano, M. García-Fuentes, O. Herzberg, D. Torres, M. J. Alonso, G. Moreno-Bueno. Intracellular Delivery of an Antibody Targeting Gasdermin-B Reduces HER2 Breast Cancer Aggressiveness. *Clinical Cancer Research*. 25, 4846–4858. (2019). doi: 10.1158/1078-0432.CCR-18-2381.

[98] E. Ruoslahti. Tumor penetrating peptides for improved drug delivery. *Advanced Drug Delivery Reviews*. 110–111, 3–12. (2017). doi: 10.1016/j.addr.2016.03.008.

[99] X. Wang, Z. Chang, X. Nie, Y. Li, Z. P. Hu, J. Ma, W. Wang, T. Song, P. Zhou, H. Wang, Z. Yuan. A conveniently synthesized Pt (IV) conjugated alginate nanoparticle with ligand self-shielded property for targeting treatment of hepatic carcinoma. *Nanomedicine: Nanotechnology, Biology, and Medicine*. 15, 153–163. (2019). doi: 10.1016/j.nano.2018.09.012.

[100] T. Sudha, D. J. Bharali, M. Yalcin, N. H. E. Darwish, M. D. Coskun, K. A. Keating, H. Y. Lin, P. J. Davis, S. A. Mousa. Targeted delivery of cisplatin to tumor xenografts via the nanoparticle component of nano-diamino-tetrac. *Nanomedicine*. 12, 195–205. (2017). doi: 10.2217/nnm-2016-0315.

[101] M. H. Ross, A. K. Esser, G. C. Fox, A. H. Schmieder, X. Yang, G. Hu, D. Pan, X. Su, Y. Xu, D. V. Novack, T. Walsh, G. A. Colditz, G. H. Lukaszewicz, E. Cordell, J. Novack, J. A. J. Fitzpatrick, D. L. Waning, K. S. Mohammad, T. A. Guise, G. M. Lanza, K. N. Weilbaecher. Bone-induced expression of integrin b3 enables targeted nanotherapy of breast cancer metastases. *Cancer Research*. 77, 6299–6312. (2017). doi: 10.1158/0008-5472.CAN-17-1225.

[102] L. Huang, B. Chaurasiya, D. Wu, H. Wang, Y. Du, J. Tu, T. J. Webster, C. Sun. Versatile redox-sensitive pullulan nanoparticles for enhanced liver targeting and efficient cancer therapy. *Nanomedicine: Nanotechnology, Biology, and Medicine*. 14, 1005–1017. (2018). doi: 10.1016/j.nano.2018.01.015.

[103] H. Peng, B. Chen, W. Huang, Y. Tang, Y. Jiang, W. Zhang, Y. Huang. Reprogramming Tumor-Associated Macrophages to Reverse EGFRT790M Resistance by Dual-Targeting Codelivery of Gefitinib/Vorinostat. *Nano Letters*. 17, 7684–7690. (2017). doi: 10.1021/acs.nanolett.7b03756.

[104] C. Shi, T. Liu, Z. Guo, R. Zhuang, X. Zhang, X. Chen. Reprogramming Tumor-Associated Macrophages by Nanoparticle-Based Reactive Oxygen Species Photogeneration. *Nano Letters*. 18, 7330–7342. (2018). doi: 10.1021/acs.nanolett.8b03568.

[105] Y. Song, C. Tang, C. Yin. Combination antitumor immunotherapy with VEGF and PIGF siRNA via systemic delivery of multi-functionalized nanoparticles to tumor-associated macrophages and breast cancer cells. *Biomaterials*. 185, 117–132. (2018). doi: 10.1016/j.biomaterials.2018.09.017.

[106] I. Fernández-Mariño, C. Anfray, J. Crecente-Campo, A. Maeda, A. Ummarino, C. Teijeiro-Valiño, D. Blanco-Martinez, F. Mpambani, L. Poul, J. Devalliere, M. Germain, J. Correa, M. Fernandez-Villamarin, P. Allavena, E. Fernandez-Megia, M. J. Alonso, F. T. Andón. Mannose-modified hyaluronic acid nanocapsules for the targeting of tumor-associated macrophages. *Drug Delivery and Translational Research*. Online ahead of print. (2022). doi: 10.1007/s13346-022-01265-9.

[107] J. Hrkach, D. Von Hoff, M. M. Ali, E. Andrianova, J. Auer, T. Campbell, D. De Witt, M. Figa, M. Figueiredo, A. Horhota, S. Low, K. McDonnell, E. Peeke, B. Retnarajan, A. Sabnis, E. Schnipper, J. J. Song, Y. H. Song, J. Summa, D. Tompsett, G. Troiano, T. V. G. Hoven, J. Wright, P. LoRusso, P. W. Kantoff, N. H. Bander, C. Sweeney, O. C. Farokhzad, R. Langer, S. Zale. Preclinical development and clinical translation of a PSMA-targeted docetaxel nanoparticle with a differentiated pharmacological profile. *Science Translational Medicine*. 4, (2012). doi: 10.1126/scitranslmed.3003651.

[108] D. D. Von Hoff, M. M. Mita, R. K. Ramanathan, G. J. Weiss, A. C. Mita, P. M. Lorusso, H. A. Burris, L. L. Hart, S. C. Low, D. M. Parsons, S. E. Zale, J. M. Summa, H. Youssoufian, J. C. Sachdev. Phase I study of PSMA-targeted docetaxel-containing nanoparticle BIND-014 in patients with advanced solid tumors. *Clinical Cancer Research*. 22, 3157–3163. (2016). doi: 10.1158/1078-0432.CCR-15-2548.

[109] K. A. Autio, R. Dreicer, J. Anderson, J. A. Garcia, A. Alva, L. L. Hart, M. I. Milowsky, E. M. Posadas, C. J. Ryan, R. P. Graf, R. Dittamore, N. A. Schreiber, J. M. Summa, H. Youssoufian, M. J. Morris, H. I. Scher. Safety and Efficacy of BIND-014, a Docetaxel Nanoparticle Targeting Prostate-Specific Membrane Antigen for Patients with Metastatic Castration-Resistant Prostate Cancer: A Phase 2 Clinical Trial. *JAMA Oncology*. 4, 1344–1351. (2018). doi: 10.1001/jamaoncol.2018.2168.

[110] N. Al Khouri Fallouh, L. Roblot-Treupel, H. Fessi, J. P. Devissaguet, F. Puisieux. Development of a new process for the manufacture of polyisobutylcyanoacrylate nanocapsules. *International Journal of Pharmaceutics*. 28, 125–132. (1986). doi: 10.1016/0378-5173(86)90236-X.

[111] R. Abellan-Pose, C. Teijeiro-Valiño, M. J. Santander-Ortega, E. Borrajo, A. Vidal, M. Garcia-Fuentes, N. Csaba, M. J. Alonso. Polyaminoacid nanocapsules for drug delivery to the lymphatic system: Effect of the particle size. *International Journal of Pharmaceutics*. 509, 107–117. (2016). doi: 10.1016/j.ijpharm.2016.05.034.

[112] A. M. Ledo, M. S. Sasso, V. Bronte, I. Marigo, B. J. Boyd, M. Garcia-Fuentes, M. J. Alonso. Co-delivery of RNAi

USC UNIVERSIDADE DE SANTIAGO DE COMPOSTELA

and chemokine by polyarginine nanocapsules enables the modulation of myeloid-derived suppressor cells. *Journal of Controlled Release*. 295, 60–73. (2019). doi: 10.1016/j.jconrel.2018.12.041.

[113] T. Gonzalo, G. Lollo, M. Garcia-Fuentes, D. Torres, J. Correa, R. Riguera, E. Fernandez-Megia, P. Calvo, P. Avilés, M. J. Guillén, M. J. M. J. Alonso. A new potential nano-oncological therapy based on polyamino acid nanocapsules. *Journal of Controlled Release*. 169, 10–16. (2013). doi: 10.1016/j.jconrel.2013.03.037.

[114] J. Crecente-Campo, S. Lorenzo-Abalde, A. Mora, J. Marzoa, N. Csaba, J. Blanco, Á. González-Fernández, M. J. Alonso. Bilayer polymeric nanocapsules: A formulation approach for a thermostable and adjuvanted E. coli antigen vaccine. *Journal of Controlled Release*. 286, 20–32. (2018). doi: 10.1016/j.jconrel.2018.07.018.

[115] S. Reimondez-Troitiño, J. V. González-Aramundiz, J. Ruiz-Bañobre, R. López-López, M. J. Alonso, N. Csaba, M. de la Fuente. Versatile protamine nanocapsules to restore miR-145 levels and interfere tumor growth in colorectal cancer cells. *European Journal of Pharmaceutics and Biopharmaceutics*. 142, 449–459. (2019). doi: 10.1016/j.ejpb.2019.07.016.

[116] G. Lollo, G. R. Rivera-Rodriguez, J. Bejaud, T. Montier, C. Passirani, J. P. Benoit, M. García-Fuentes, M. J. Alonso, D. Torres. Polyglutamic acid-PEG nanocapsules as long circulating carriers for the delivery of docetaxel. *European Journal of Pharmaceutics and Biopharmaceutics*. 87, 47–54. (2014). doi: 10.1016/j.ejpb.2014.02.004.

[117] A. A. Date, N. Desai, R. Dixit, M. Nagarsenker. Self-nanoemulsifying drug delivery systems: Formulation insights, applications and advances. *Nanomedicine*. 5, 1595–1616. (2010). doi: 10.2217/nnm.10.126.

[118] P. Calvo, C. Thomas, M. J. Alonso, J. . Vila-Jato, J. R. Robinson. Study of the mechanism of interaction of poly(ϵ-caprolactone) nanocapsules with the cornea by confocal laser scanning microscopy. *International Journal of Pharmaceutics*. 103, 283–291. (1994). doi: 10.1016/0378-5173(94)90179-1.

[119] L. N. Thwala, A. Beloqui, N. S. Csaba, D. González-Touceda, S. Tovar, C. Dieguez, M. J. Alonso, V. Préat. The interaction of protamine nanocapsules with the intestinal epithelium: A mechanistic approach. *Journal of Controlled Release*. 243, 109–120. (2016). doi: 10.1016/j.jconrel.2016.10.002.

[120] E. Borrajo, R. Abellan-Pose, A. Soto, M. Garcia-Fuentes, N. Csaba, M. J. M. J. Alonso, A. Vidal. Docetaxel-loaded polyglutamic acid-PEG nanocapsules for the treatment of metastatic cancer. *Journal of Controlled Release*. 238, 263–271. (2016). doi: 10.1016/j.jconrel.2016.07.048.

[121] M. Alonso-Nocelo, R. Abellan-Pose, A. Vidal, M. Abal, N. Csaba, M. J. Alonso, R. Lopez-Lopez, M. de la Fuente. Selective interaction of PEGylated polyglutamic acid nanocapsules with cancer cells in a 3D model of a metastatic lymph node. *Journal of Nanobiotechnology*. 14, 1–9. (2016). doi: 10.1186/s12951-016-0207-8.

[122] A. S. Cordeiro, J. Crecente-Campo, B. L. Bouzo, S. F. González, M. de la Fuente, M. J. Alonso. Engineering polymeric nanocapsules for an efficient drainage and biodistribution in the lymphatic system. *Journal of Drug Targeting*. 27, 646–658. (2019). doi: 10.1080/1061186X.2018.1561886.

[123] H. Fang, X. Zhao, X. Gu, H. Sun, R. Cheng, Z. Zhong, C. Deng. CD44-Targeted Multifunctional Nanomedicines Based on a Single-Component Hyaluronic Acid Conjugate with All-Natural Precursors: Construction and Treatment of Metastatic Breast Tumors in Vivo. *Biomacromolecules*. 21, 104–113. (2020). doi: 10.1021/acs.biomac.9b01012.

[124] B. Lu, Y. Li, Z. Wang, B. Wang, X. Pan, W. Zhao, X. Ma, J. Zhang. A dual responsive hyaluronic acid graft poly(ionic liquid) block copolymer micelle for an efficient CD44-targeted antitumor drug delivery. *New Journal of Chemistry*. 43, 12275–12282. (2019). doi: 10.1039/c9nj02608h.

[125] Y. Zhong, K. Goltsche, L. Cheng, F. Xie, F. Meng, C. Deng, Z. Zhong, R. Haag. Hyaluronic acid-shelled acid-activatable paclitaxel prodrug micelles effectively target and treat CD44-overexpressing human breast tumor xenografts in vivo. *Biomaterials*. 84, 250–261. (2016). doi: 10.1016/j.biomaterials.2016.01.049.

[126] E. L. H. Leung, R. R. Fiscus, J. W. Tung, V. P. C. Tin, L. C. Cheng, A. D. L. Sihoe, L. M. Fink, Y. Ma, M. P. Wong. Non-small cell lung cancer cells expressing CD44 are enriched for stem cell-like properties. *PLoS ONE*. 5, 1–13. (2010). doi: 10.1371/journal.pone.0014062.

[127] M. Dohadwala, J. Luo, L. Zhu, Y. Lin, G. J. Dougherty, S. Sharma, M. Huang, M. Põld, R. K. Batra, S. M. Dubinett. Non-small Cell Lung Cancer Cyclooxygenase-2-dependent Invasion is Mediated by CD44. *Journal of Biological Chemistry*. 276, 20809–20812. (2001). doi: 10.1074/jbc.C100140200.

[128] Y. Shi, C. Liu, X. Liu, D. G. Tang, J. Wang. The microRNA miR-34a inhibits non-small cell lung cancer (NSCLC) growth and the CD44hi stem-like NSCLC cells. *PLoS ONE*. 9, 1–8. (2014). doi: 10.1371/journal.pone.0090022.

[129] R. E. Eliaz, J. Szoka. Liposome-encapsulated doxorubicin targeted to CD44: A strategy to kill CD44-overexpressing tumor cells. *Cancer Research*. 61, 2592–2601. (2001).

[130] H. Li, L. Guo, J. W. Li, N. Liu, R. Qi, J. Liu. Expression of hyaluronan receptors CD44 and RHAMM in stomach cancers: relevance with tumor progression. *International journal of oncology*. 17, 927–932. (2000). doi: 10.3892/ijo.17.5.927.

[131] N. Yerushalmi, A. Arad, R. Margalit. Molecular and Cellular Studies of Hyaluronic Acid-Modified Liposomes as Bioadhesive Carriers for Topical Drug Delivery in Wound Healing. *Archives of Biochemistry and Biophysics*. 313, 267–273. (1994). doi: 10.1006/abbi.1994.1387.

[132] S. Taetz, A. Bochot, C. Surace, S. Arpicco, J. M. Renoir, U. F. Schaefer, V. Marsaud, S. Kerdine-Roemer, C. M. Lehr, E. Fattal. Hyaluronic acid-modified DOTAP/DOPE liposomes for the targeted delivery of anti-telomerase siRNA to CD44-expressing lung cancer cells. *Oligonucleotides*. 19, 103–115. (2009). doi: 10.1089/oli.2008.0168.

[133] S. Vasvani, P. Kulkarni, D. Rawtani. Hyaluronic acid: a review on its biology, aspects of drug delivery, route of administrations and a special emphasis on its approved marketed products and recent clinical studies. *International Journal of Biological Macromolecules*. (2019). doi: 10.1016/j.ijbiomac.2019.11.066.

[134] E. R. Vimr, K. A. Kalivoda, E. L. Deszo, S. M. Steenbergen. Diversity of Microbial Sialic Acid Metabolism.

Microbiology and Molecular Biology Reviews. 68, 132–153. (2004). doi: 10.1128/mmbr.68.1.132-153.2004.

[135] X. Wang, X. Li, Y. N. Zeng, F. He, X. M. Yang, F. Guan. Enhanced expression of polysialic acid correlates with malignant phenotype in breast cancer cell lines and clinical tissue samples. *International Journal of Molecular Medicine*. 37, 197–206. (2016). doi: 10.3892/ijmm.2015.2395.

[136] T. M. Villanueva-Cabello, L. D. Gutiérrez-Valenzuela, R. Salinas-Marín, D. V. López-Guerrero, I. Martínez-Duncker. Polysialic Acid in the Immune System. *Frontiers in Immunology*. 12, 1–21. (2022). doi: 10.3389/fimmu.2021.823637.

[137] L. M. Krug, G. Ragupathi, C. Hood, M. G. Kris, V. A. Miller, J. R. Allen, S. J. Keding, S. J. Danishefsky, J. Gomez, L. Tyson, B. Pizzo, V. Baez, P. O. Livingston. Vaccination of patients with small-cell lung cancer with synthetic fucosyl GM-1 conjugated to keyhole limpet hemocyanin. *Clinical Cancer Research*. 10, 6094–6100. (2004). doi: 10.1158/1078-0432.CCR-04-0482.

[138] P. Komminoth, J. Roth, P. M. Lackie, D. Bitter-Suermann, P. U. Heitz. Polysialic acid of the neural cell adhesion molecule distinguishes small cell lung carcinoma from carcinoids. *American Journal of Pathology*. 139, 297–304. (1991).

[139] S. Zhang, H. S. Zhang, C. Cordon-Cardo, G. Ragupathi, P. O. Livingston. Selection of tumor antigens as targets for immune attack using immunohistochemistry: Protein antigens. *Clinical Cancer Research*. 4, 2669–2676. (1998).

[140] K. Kameda, H. Shimada, T. Ishikawa, A. Takimoto, N. Momiyama, S. Hasegawa, K. Misuta, A. Nakano, Y. Nagashima, Y. Ichikawa. Expression of highly polysialylated neural cell adhesion molecule in pancreatic cancer neural invasive lesion. *Cancer Letters*. 137, 201–207. (1999). doi: 10.1016/S0304-3835(98)00359-0.

[141] L. M. Krug, G. Ragupathi, K. K. Ng, C. Hood, H. J. Jennings, Z. Guo, M. G. Kris, V. Miller, B. Pizzo, L. Tyson, V. Baez, P. O. Livingston. Vaccination of small cell lung cancer patients with polysialic acid or N-propionylated polysialic acid conjugated to keyhole limpet hemocyanin. *Clinical Cancer Research*. 10, 916–923. (2004). doi: 10.1158/1078-0432.CCR-03-0101.

[142] L. M. Krug, G. Ragupathi, C. Hood, C. George, F. Hong, R. Shen, L. Abrey, H. J. Jennings, M. G. Kris, P. O. Livingston. Immunization with N-propionyl polysialic acid-KLH conjugate in patients with small cell lung cancer is safe and induces IgM antibodies reactive with SCLC cells and bactericidal against group B meningococci. *Cancer Immunology, Immunotherapy*. 61, 9–18. (2012). doi: 10.1007/s00262-011-1083-6.

[143] M. Korja, A. Jokilammi, T. T. Salmi, H. Kalimo, T. T. Pelliniemi, J. Isola, I. Rantala, H. Haapasalo, J. Finne. Absence of polysialylated NCAM is an unfavorable prognostic phenotype for advanced stage neuroblastoma. *BMC Cancer*. 9, 1–8. (2009). doi: 10.1186/1471-2407-9-57.

[144] Y. Kanato, S. Ono, K. Kitajima, C. Sato. Complex formation of a brain-derived neurotrophic factor and glycosaminoglycans. *Bioscience, Biotechnology and Biochemistry*. 73, 2735–2741. (2009). doi: 10.1271/bbb.90637.

[145] H. Thiesler, J. Beimdiek, H. Hildebrandt. Polysialic acid and Siglec-E orchestrate negative feedback regulation of microglia activation. *Cellular and Molecular Life Sciences*. 78, 1637–1653. (2021). doi: 10.1007/s00018-020-03601-z.

[146] A. Shimoda, Y. Tahara, S. Sawada, Y. Sasaki, K. Akiyoshi. Glycan profiling analysis using evanescent-field fluorescence-assisted lectin array: Importance of sugar recognition for cellular uptake of exosomes from mesenchymal stem cells. *Biochemical and Biophysical Research Communications*. 491, 701–707. (2017). doi: 10.1016/j.bbrc.2017.07.126.

[147] F. Greco, I. Arif, R. Botting, C. Fante, L. Quintieri, C. Clementi, O. Schiavon, G. Pasut. Polysialic acid as a drug carrier: Evaluation of a new polysialic acid-epirubicin conjugate and its comparison against established drug carriers. *Polymer Chemistry*. 4, 1600–1609. (2013). doi: 10.1039/c2py20876h.

[148] R. A. Bader, A. L. Silvers, N. Zhang. Polysialic acid-based micelles for encapsulation of hydrophobic drugs. *Biomacromolecules*. 12, 314–320. (2011). doi: 10.1021/bm1008603.

[149] T. Zhang, Z. She, Z. Huang, J. Li, X. Luo, Y. Deng. Application of sialic acid/polysialic acid in the drug delivery systems. *Asian Journal of Pharmaceutical Sciences*. 9, 75–81. (2014). doi: 10.1016/j.ajps.2014.03.001.

[150] X. Han, T. Zhang, M. Liu, Y. Song, X. Liu, Y. Deng. Polysialic acid modified liposomes for improving pharmacokinetics and overcoming accelerated blood clearance phenomenon. *Coatings*. 10, (2020). doi: 10.3390/coatings10090834.

[151] A. I. Fernandes, G. Gregoriadis. Polysialylated asparaginase: preparation, activity and pharmacokinetics. *Biochimica et Biophysica Acta (BBA) - Protein Structure and Molecular Enzymology*. 1341, 26–34. (1997). doi: 10.1016/S0167-4838(97)00056-3.

[152] A. Tiede, G. Allen, A. Bauer, P. Chowdary, P. Collins, B. Goldstein, H. J. Jiang, K. Köck, I. Takács, M. Timofeeva, M. Wolfsegger, S. Srivastava. SHP656, a polysialylated recombinant factor VIII (PSA-rFVIII): First-in-human study evaluating safety, tolerability and pharmacokinetics in patients with severe haemophilia A. *Haemophilia*. 26, 47–55. (2020). doi: 10.1111/hae.13878.

[153] A. Gonzalez-paredes, D. Torres, M. José. Polyarginine nanocapsules : A versatile nanocarrier with potential in transmucosal drug delivery. *International Journal of Pharmaceutics*. 529, 474–485. (2017). doi: 10.1016/j.ijpharm.2017.07.001.

[154] G. R. Rivera-Rodríguez, M. J. Alonso, D. Torres. Poly-l-asparagine nanocapsules as anticancer drug delivery vehicles. *European Journal of Pharmaceutics and Biopharmaceutics*. 85, 481–487. (2013). doi: 10.1016/j.ejpb.2013.08.001.

[155] S. Correa, N. Boehnke, A. E. Barberio, E. Deiss-Yehiely, A. Shi, B. Oberlton, S. G. Smith, I. Zervantonakis, E. C. Dreaden, P. T. Hammond. Tuning Nanoparticle Interactions with Ovarian Cancer through Layer-by-Layer Modification of Surface Chemistry. *ACS Nano*. 14, 2224–2237. (2020). doi: 10.1021/acsnano.9b09213.

[156] I. Tosic, L. N. Heppler, S. P. Egusquiaguirre, N. Boehnke, S. Correa, D. F. Costa, E. A. Grossman Moore, S. Pal, D.

S. Richardson, A. R. Ivanov, D. A. Haas-Kogan, D. K. Nomura, P. T. Hammond, D. A. Frank. Lipidome-based targeting of STAT3-driven breast cancer cells using poly-l-glutamic acid–coated layer-by-layer nanoparticles. *Molecular Cancer Therapeutics*. 20, 726–738. (2021). doi: 10.1158/1535-7163.MCT-20-0505.

[157] N. d'Avanzo, C. Celia, A. Barone, M. Carafa, L. Di Marzio, H. A. Santos, M. Fresta. Immunogenicity of Polyethylene Glycol Based Nanomedicines: Mechanisms, Clinical Implications and Systematic Approach. *Advanced Therapeutics*. 3, 1–18. (2020). doi: 10.1002/adtp.201900170.

[158] M. E. R. O'Brien, M. A. Socinski, A. Y. Popovich, I. N. Bondarenko, A. Tomova, B. T. Bilynsky, Y. S. Hotko, V. L. Ganul, I. Y. Kostinsky, A. J. Eisenfeld, L. Sandalic, F. B. Oldham, B. Bandstra, A. B. Sandler, J. W. Singer. Randomized phase III trial comparing single-agent paclitaxel poliglumex (CT-2103, PPX) with single-agent gemcitabine or vinorelbine for the treatment of PS 2 patients with chemotherapy-naïve advanced non-small cell lung cancer. *Journal of Thoracic Oncology*. 3, 728–734. (2008). doi: 10.1097/JTO.0b013e31817c6b68.

[159] J. Zhao, E. J. Koay, T. Li, X. Wen, C. Li. A hindsight reflection on the clinical studies of poly(l-glutamic acid)-paclitaxel. *Wiley Interdisciplinary Reviews: Nanomedicine and Nanobiotechnology*. 10, 1–18. (2018). doi: 10.1002/wnan.1497.

[160] N. Nishiyama, S. Okazaki, H. Cabral, M. Miyamoto, Y. Kato, Y. Sugiyama, K. Nishio, Y. Matsumura, K. Kataoka. Novel cisplatin-incorporated polymeric micelles can eradicate solid tumors in mice. *Cancer Research*. 63, 8977 LP – 8983. (2003).

[161] A. Osada. NC-6004, a novel cisplatin nanoparticle, in combination with pembrolizumab for head and neck cancer. *Integrative Clinical Medicine*. 3, 1–2. (2019). doi: 10.15761/icm.1000147.

[162] Y. Zhang, W. Song, Y. Lu, Y. Xu, C. Wang, D. G. Yu, I. Kim. Recent Advances in Poly(α-L-glutamic acid)-Based Nanomaterials for Drug Delivery. *Biomolecules*. 12, (2022). doi: 10.3390/biom12050636.

[163] J. Crecente-Campo, M. J. Alonso. Engineering, on-demand manufacturing, and scaling-up of polymeric nanocapsules. *Bioengineering & Translational Medicine*. 4, 38–50. (2019). doi: 10.1002/btm2.10118.

[164] F. Giulimondi, L. Digiacomo, D. Pozzi, S. Palchetti, E. Vulpis, A. L. Capriotti, R. Z. Chiozzi, A. Laganà, H. Amenitsch, L. Masuelli, M. Mahmoudi, I. Screpanti, A. Zingoni, G. Caracciolo. Interplay of protein corona and immune cells controls blood residency of liposomes. *Nature Communications*. 10, 3686. (2019). doi: 10.1038/s41467-019-11642-7.

[165] G. Caracciolo. Clinically approved liposomal nanomedicines: Lessons learned from the biomolecular corona. *Nanoscale*. 10, 4167–4172. (2018). doi: 10.1039/c7nr07450f.

[166] S. A. Dilliard, Q. Cheng, D. J. Siegwart. On the mechanism of tissue-specific mRNA delivery by selective organ targeting nanoparticles. *Proceedings of the National Academy of Sciences*. 118, e2109256118. (2021). doi: 10.1073/pnas.2109256118.

[167] C. V. Sternling, L. E. Scriven. Interfacial turbulence: Hydrodynamic instability and the marangoni effect. *AIChE Journal*. 5, 514–523. (1959). doi: 10.1002/aic.690050421.

[168] Y. Wang, P. Li, T. T. D. Tran, J. Zhang, L. Kong. Manufacturing techniques and surface engineering of polymer based nanoparticles for targeted drug delivery to cancer. *Nanomaterials*. 6, 1–18. (2016). doi: 10.3390/nano6020026.

USC UNIVERSIDADE DE SANTIAGO DE COMPOSTELA

BACKGROUND, HYPOTHESIS, AND OBJECTIVES

USC
UNIVERSIDADE
DE SANTIAGO
DE COMPOSTELA

USC
UNIVERSIDADE
DE SANTIAGO
DE COMPOSTELA

1. BACKGROUND

Prognosis in some lung cancers, such as metastatic non-small cell lung cancer (NSCLC), is still dramatic, with only a 5.2 % 5-year survival rate in the case of metastatic NSCLC.[1] This low therapeutic success is a consequence of the limited efficacy of chemotherapy and immunotherapy and their high off-target toxicities.[2] Mutations of Kirsten rat sarcoma viral oncogene homolog (*KRAS*) are particularly relevant therapeutic targets in lung cancer. However, only one mutation of KRAS has been confronted until now, whereas the rest remain undruggable.[3]

Polymeric nanocapsules (NCs) made of an oily core and a polymeric shell are versatile nanocarriers for both hydrophobic and hydrophilic drugs, with the capacity to protect them from degradation and modulate their biodistribution profile and body clearance.[4–11] This delivery platform has been developed by our group to deliver cytotoxic drugs and assessed in different tumor models.[4,11–18] The results reported so far have underlined the potential of these delivery vehicles for reducing the toxicity and enhancing the efficacy of some cytotoxic drugs.[12] On the other hand, our group has also adapted this delivery platform for the intracellular delivery of monoclonal antibodies targeting intracellular oncoproteins, such as gasdermin B, which, so far, are considered undruggable.[5]

Despite the attractive features and positive results obtained for these delivery carriers, critical aspects remain to be elucidated. These are: i) the determination of the actual chemical composition of the NCs,[19] and ii) the evaluation of their interaction with plasmatic proteins (protein corona).[20] In this sense, it is broadly accepted in the scientific community that in order to make significant progress in the nano-drug delivery field, it is essential to design the nanocarriers in a rational manner, paying particular attention to the protein corona and its implications in the biological behavior of nanocarriers.[21–23] On the other hand, the potential of NCs for the delivery of immunomodulators and monoclonal antibodies[5] is still in an early stage.

2. HYPOTHESIS

1. The protein corona composition of the polymeric NCs is dependent not only on the components used for the formation of the NC but also on the structural changes caused by different preparation techniques. The nature of the hydrophilic polymer shell may influence the amount and the type of proteins forming the corona.

2. Given their structure and composition, polymeric NCs may be useful nanocarriers for encapsulating hydrophobic immunomodulatory molecules such as inhibitors of signal transducer and activator of transcription 3 (STAT3) and transforming growth factor beta (TGF-β) pathways, which are known to have biopharmaceutical limitations.

3. Following a rational design, polymeric NCs may be useful nanocarriers for the intracellular delivery of anti-KRAS^{G12V} monoclonal antibodies. Based on previous

USC UNIVERSIDADE DE SANTIAGO DE COMPOSTELA

experiments in our laboratory, these encapsulated antibodies are expected to have the potential for the treatment of KRAS-dependent cancers, such as some lung cancers.

3. OBJECTIVES

Based on the background knowledge in the field and the hypothesis above outlined and with the final goal of designing delivery carriers adapted for immunomodulators and monoclonal antibodies in the context of lung cancer, the main experimental objectives of this thesis were, first, to characterize the chemical composition of polymeric NCs and to study their interaction with proteins, following the Minimum Information about Nanomaterial Biocorona Experiments (MINBE) recommendations, second, to study if the biodistribution profile of chemotherapeutics and immunomodulators (STAT3 and TGF-β pathways inhibitors) can be modified by their loading into the optimized NCs, and third, to expand the potential of a delivery platform previously developed in our lab for the intracellular delivery of mAb (bevacizumab as a model mAb, and anti-KRAS^{G12V} mAb as a therapeutic mAb. More precisely, to achieve these objectives, the following experimental activities were undertaken:

1. Chemical analysis of a series of NCs (different compositions and preparation techniques) and their interaction with plasma proteins.

   The results corresponding to this objective are presented in Chapter 1: "Characterization of polymeric nanocapsules: chemical composition and physicochemical and biological properties". Some of the results from this chapter have already been published in the journal article: G. Berrecoso, J. Crecente-Campo, M. J. Alonso. Quantification of the actual composition of polymeric nanocapsules: a quality control analysis. *Drug Delivery and Translational Research.* 12, 2865–2874. (2022). doi: 10.1007/s13346-022-01150-5. ISSN: 2190393X, 21903948.[19]

2. Design, development, and in vitro evaluation of NCs loaded with stattic (anti-STAT3) and galunisertib (anti-TGF-β) for the treatment of lung cancer.

   The results corresponding to this objective are presented in Chapter 2: "Galunisertib and stattic-loaded nanocapsules for lung cancer treatment".

3. Design, development, and in vitro evaluation of NCs loaded with an anti-KRAS^{G12V} monoclonal antibody for the treatment of lung cancer.

   The results corresponding to this objective are presented in Chapter 3: "Nanocapsules for the intracellular delivery of monoclonal antibodies".

4. REFERENCES

[1] American Society of Clinical Oncology (ASCO). Lung Cancer - Non-Small Cell: Statistics | Cancer.Net. https://www.cancer.net/cancer-types/lung-cancer-non-small-cell/statistics. Accessed: October 31, 2022.

[2] H. Mithoowani, M. Febbraro. Non-Small-Cell Lung Cancer in 2022: A Review for General Practitioners in Oncology. *Current Oncology*. 29, 1828–1839. (2022). doi: 10.3390/curroncol29030150.

[3] S. R. Punekar, V. Velcheti, B. G. Neel, K. K. Wong. The current state of the art and future trends in RAS-targeted cancer therapies. *Nature Reviews Clinical Oncology*. 19, 637–655. (2022). doi: 10.1038/s41571-022-00671-9.

[4] M. V. Lozano, D. Torrecilla, D. Torres, A. Vidal, F. Domínguez, M. J. Alonso. Highly efficient system to deliver taxanes into tumor cells: Docetaxel-loaded chitosan oligomer colloidal carriers. *Biomacromolecules*. 9, 2186–2193. (2008). doi: 10.1021/bm800298u.

[5] Á. Molina-Crespo, A. Cadete, D. Sarrio, M. Gámez-Chiachio, L. Martinez, K. Chao, A. Olivera, A. Gonella, E. Díaz, J. Palacios, P. K. Dhal, M. Besev, M. Rodríguez-Serrano, M. L. García Bermejo, J. C. Triviño, A. Cano, M. García-Fuentes, O. Herzberg, D. Torres, M. J. Alonso, G. Moreno-Bueno. Intracellular Delivery of an Antibody Targeting Gasdermin-B Reduces HER2 Breast Cancer Aggressiveness. *Clinical Cancer Research*. 25, 4846–4858. (2019). doi: 10.1158/1078-0432.CCR-18-2381.

[6] R. Abellan-Pose, C. Teijeiro-Valiño, M. J. Santander-Ortega, E. Borrajo, A. Vidal, M. Garcia-Fuentes, N. Csaba, M. J. Alonso. Polyaminoacid nanocapsules for drug delivery to the lymphatic system: Effect of the particle size. *International Journal of Pharmaceutics*. 509, 107–117. (2016). doi: 10.1016/j.ijpharm.2016.05.034.

[7] A. M. Ledo, M. S. Sasso, V. Bronte, I. Marigo, B. J. Boyd, M. Garcia-Fuentes, M. J. Alonso. Co-delivery of RNAi and chemokine by polyarginine nanocapsules enables the modulation of myeloid-derived suppressor cells. *Journal of Controlled Release*. 295, 60–73. (2019). doi: 10.1016/j.jconrel.2018.12.041.

[8] T. Gonzalo, G. Lollo, M. Garcia-Fuentes, D. Torres, J. Correa, R. Riguera, E. Fernandez-Megia, P. Calvo, P. Avilés, M. J. Guillén, M. J. M. J. Alonso. A new potential nano-oncological therapy based on polyamino acid nanocapsules. *Journal of Controlled Release*. 169, 10–16. (2013). doi: 10.1016/j.jconrel.2013.03.037.

[9] J. Crecente-Campo, S. Lorenzo-Abalde, A. Mora, J. Marzoa, N. Csaba, J. Blanco, Á. González-Fernández, M. J. Alonso. Bilayer polymeric nanocapsules: A formulation approach for a thermostable and adjuvanted E. coli antigen vaccine. *Journal of Controlled Release*. 286, 20–32. (2018). doi: 10.1016/j.jconrel.2018.07.018.

[10] S. Reimondez-Troitiño, J. V. González-Aramundiz, J. Ruiz-Bañobre, R. López-López, M. J. Alonso, N. Csaba, M. de la Fuente. Versatile protamine nanocapsules to restore miR-145 levels and interfere tumor growth in colorectal cancer cells. *European Journal of Pharmaceutics and Biopharmaceutics*. 142, 449–459. (2019). doi: 10.1016/j.ejpb.2019.07.016.

[11] G. Lollo, G. R. Rivera-Rodriguez, J. Bejaud, T. Montier, C. Passirani, J. P. Benoit, M. García-Fuentes, M. J. Alonso, D. Torres. Polyglutamic acid-PEG nanocapsules as long circulating carriers for the delivery of docetaxel. *European Journal of Pharmaceutics and Biopharmaceutics*. 87, 47–54. (2014). doi: 10.1016/j.ejpb.2014.02.004.

[12] E. Borrajo, R. Abellan-Pose, A. Soto, M. Garcia-Fuentes, N. Csaba, M. J. M. J. Alonso, A. Vidal. Docetaxel-loaded polyglutamic acid-PEG nanocapsules for the treatment of metastatic cancer. *Journal of Controlled Release*. 238, 263–271. (2016). doi: 10.1016/j.jconrel.2016.07.048.

[13] D. Torrecilla, M. V. Lozano, E. Lallana, J. I. Neissa, R. Novoa-Carballal, A. Vidal, E. Fernandez-Megia, D. Torres, R. Riguera, M. J. Alonso, F. Dominguez. Anti-tumor efficacy of chitosan-g-poly(ethylene glycol) nanocapsules containing docetaxel: Anti-TMEFF-2 functionalized nanocapsules vs. non-functionalized nanocapsules. *European Journal of Pharmaceutics and Biopharmaceutics*. 83, 330–337. (2013). doi: 10.1016/j.ejpb.2012.10.017.

[14] M. V. Lozano, H. Esteban, J. Brea, M. I. Loza, D. Torres, M. J. Alonso. Intracellular delivery of docetaxel using freeze-dried polysaccharide nanocapsules. *Journal of Microencapsulation*. 30, 181–188. (2013). doi: 10.3109/02652048.2012.714411.

[15] B. L. Bouzo, S. Lores, R. Jatal, S. Alijas, M. J. Alonso, I. Conejos-Sánchez, M. de la Fuente. Sphingomyelin nanosystems loaded with uroguanylin and etoposide for treating metastatic colorectal cancer. *Scientific Reports*. 11, 17213. (2021). doi: 10.1038/s41598-021-96578-z.

[16] A. Cadete, A. Olivera, M. Besev, P. K. Dhal, L. Gonçalves, A. J. Almeida, G. Bastiat, J.-P. Benoit, M. de la Fuente, M. Garcia-Fuentes, M. J. Alonso, D. Torres. Self-assembled hyaluronan nanocapsules for the intracellular delivery of anticancer drugs. *Scientific Reports*. 9, 11565. (2019). doi: 10.1038/s41598-019-47995-8.

[17] C. Teijeiro-Valiño, R. Novoa-Carballal, E. Borrajo, A. Vidal, M. Alonso-Nocelo, M. de la Fuente Freire, P. P. P. Lopez-Casas, M. Hidalgo, N. Csaba, M. J. Alonso. A multifunctional drug nanocarrier for efficient anticancer therapy. *Journal of Controlled Release*. 294, 154–164. (2019). doi: 10.1016/j.jconrel.2018.12.002.

[18] M. Alonso-Nocelo, R. Abellan-Pose, A. Vidal, M. Abal, N. Csaba, M. J. Alonso, R. Lopez-Lopez, M. de la Fuente. Selective interaction of PEGylated polyglutamic acid nanocapsules with cancer cells in a 3D model of a metastatic lymph node. *Journal of Nanobiotechnology*. 14, 1–9. (2016). doi: 10.1186/s12951-016-0207-8.

[19] G. Berrecoso, J. Crecente-Campo, M. J. Alonso. Quantification of the actual composition of polymeric nanocapsules: a quality control analysis. *Drug Delivery and Translational Research*. 12, 2865–2874. (2022). doi: 10.1007/s13346-022-01150-5.

[20] G. Berrecoso, J. Crecente-Campo, M. J. Alonso. Unveiling the pitfalls of the protein corona of polymeric drug nanocarriers. *Drug Delivery and Translational Research*. 10, 730–750. (2020). doi: 10.1007/s13346-020-00745-0.

[21] T. A. Faunce, J. White, K. I. Matthaei. Integrated research into the nanoparticle–protein corona: a new focus for safe, sustainable and equitable development of nanomedicines. *Nanomedicine*. 3, 859–866. (2008). doi: 10.2217/17435889.3.6.859.

[22] M. Mahmoudi. Protein corona: The golden gate to clinical applications of nanoparticles. *International Journal of Biochemistry and Cell Biology*. 75, 141–142. (2016). doi: 10.1016/j.biocel.2016.03.016.

[23] V. H. Nguyen, B. J. Lee. Protein corona: a new approach for nanomedicine design. *International Journal of*

USC UNIVERSIDADE DE SANTIAGO DE COMPOSTELA

Nanomedicine. 12, 3137–3151. (2017). doi: 10.2147/IJN.S129300.

USC
UNIVERSIDADE
DE SANTIAGO
DE COMPOSTELA

CHAPTER 1

Characterization of polymeric nanocapsules: chemical composition and physicochemical and biological properties

USC
UNIVERSIDADE
DE SANTIAGO
DE COMPOSTELA

USC
UNIVERSIDADE
DE SANTIAGO
DE COMPOSTELA

Chapter 1: Characterization of polymeric nanocapsules: chemical composition and physicochemical and biological properties*,#

This work have been done under the frame of the 2^2-INTRATARGET project. The cryo-EM image capture, process, and interpretation work have been made in collaboration with Abrescia's Lab (CIC bioGUNE - Centro de Investigación Cooperativa en Biociencias, Derio, Spain).

*The introduction of this chapter has been partially adapted from the published review: G. Berrecoso[a,b,c], J. Crecente-Campo[a,b,c], M. J. Alonso[a,b,c]. Unveiling the pitfalls of the protein corona of polymeric drug nanocarriers. *Drug Delivery and Translational Research*. 10, 730–750. (2020). doi: 10.1007/s13346-020-00745-0. ISSN: 2190393X, 21903948.[1]

#Some of the results from this chapter have already been published in the journal article: G. Berrecoso[a,b,c], J. Crecente-Campo[a,b,c], M. J. Alonso[a,b,c]. Quantification of the actual composition of polymeric nanocapsules: a quality control analysis. *Drug Delivery and Translational Research*. 12, 2865–2874. (2022). doi: 10.1007/s13346-022-01150-5. ISSN: 2190393X, 21903948.[2]

[a] Center for Research in Molecular Medicine and Chronic Diseases (CiMUS), Universidade de Santiago de Compostela, Santiago de Compostela, 15782, Spain.
[b] IDIS Research Institute, Universidade de Santiago de Compostela, Santiago de Compostela, 15782, Spain.
[c] Department of Pharmacology, Pharmacy and Pharmaceutical Technology, School of Pharmacy, Universidade de Santiago de Compostela, Santiago de Compostela, 15782, Spain.

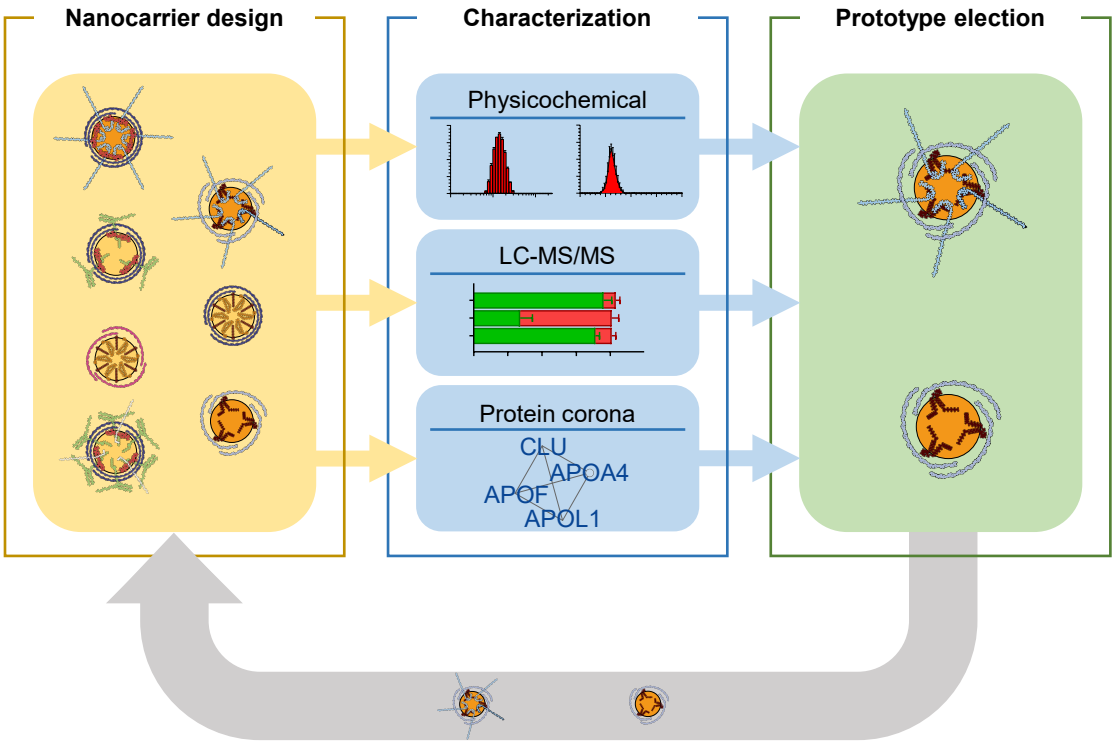
ABSTRACT

Nanocapsules (NCs) are drug-delivery nanosystems composed of an oily core, one or more stabilizing surfactants, and a surrounding polymeric shell. This chapter highlights the importance of performing an exhaustive physicochemical and biological characterization of nanocarriers to understand the *in vitro* and *in vivo* behavior of NCs. The results of the quantification of the NCs' components by liquid chromatography-mass spectrometry (LC-MS) indicated that their incorporation into the NCs structure depended on their chemical nature and the preparation technique. With regard to their interaction with plasma proteins, the results showed that the protein corona of NCs consisted mainly of apolipoproteins and complement factors. More detailed, the NCs containing polyethylene glycol (PEG) showed a reduced protein corona, except for the prototype (SD-*l*-PEG-HA) with the lowest PEG mass ratio, which exhibited an intense apolipoprotein (Apo) A-IV adsorption. On the other hand, a prototype containing 1,2-dioleoyl-3-trimethylammonium propane (DOTAP) exhibited an important interaction with vitronectin, an RGD motif-containing protein. Finally, immunoglobulins were adsorbed onto the surface of non-PEGylated systems. Overall, this information was taken into consideration for the definition of the NCs' candidates to be used for the loading of drugs for lung cancer treatment (Chapters 2 and 3).

USC UNIVERSIDADE DE SANTIAGO DE COMPOSTELA

USC
UNIVERSIDADE
DE SANTIAGO
DE COMPOSTELA

GRAPHICAL ABSTRACT



USC
UNIVERSIDADE DE SANTIAGO DE COMPOSTELA

USC
UNIVERSIDADE
DE SANTIAGO
DE COMPOSTELA

1. INTRODUCTION

Despite the attractive features of the NCs reported in the literature, critical issues remain to be investigated. Two of these issues are i) the determination of their actual chemical composition and ii) the evaluation of their interaction with plasmatic proteins. Here we describe in detail these critical matters using a series of NCs prototypes which differ in their composition and fabrication technique.

1.1. QUANTIFICATION OF THE ACTUAL COMPOSITION OF NANOCAPSULES

Solvent displacement (SD)[3] and self-emulsifying (SE)[4] are the most commonly reported techniques for the fabrication of NCs. They stand out for their easiness and low time and energy requirements. Components of these NCs, notably surfactants and polymers forming the shell, are typically added in excess so that their exact chemical composition is unknown, leading to NCs' production yields significantly lower than 100 %.[5–7] This fact is of great importance as it means that all the compounds might be present in the NCs in lower amounts than expected. Nevertheless, most of the published works in the nano-drug delivery field only evaluate the association efficiency (AE) of the most-relevant components for each study, which usually are the ones with biological activity (drugs) or targeting capabilities (active ligands), while the NCs' final composition has not ever been reported.

Many analytical techniques are available to quantify typical components of the NCs. For example, DL-α-tocopherol can be quantified by ultraviolet-visible (UV-Vis) spectrophotometry at $\lambda = 285$ nm. Also, reactions and derivatization processes can be applied to some compounds to allow their colorimetric-based quantification, such as the Bradford assay for proteins ($\lambda = 595$ nm) or the reaction products of carbohydrates and carbazole/H_2SO_4, with a wavelength of 530 nm.[8] However, while these techniques are appropriate for highly pure analytes, interference from the complex formulation matrixes usually occurs.

As an alternative, some authors have chemically modified NCs' components, such as polymers, to add fluorescent groups to determine their AE quickly, though this method assumes that incorporating the fluorophore will not affect the association efficiency, which might be erroneous.

Chromatographic-based separation techniques such as ultra-high performance liquid chromatography (UHPLC) are very appropriate for quantifying the actual composition of NCs as they can separate the NCs components from each other, diminishing the possible interferences. In addition, several detectors can be coupled to UHPLC equipment. However, since NCs components are very diverse, their quantification by an analytical technique that allows robustness of high specificity for a set of different compounds, such as mass spectrometry, is recommended.

Overall, for the abovementioned reasons, UHPLC-MS/MS is presented as an ideal methodology to face the NCs' composition characterization challenge.

USC UNIVERSIDADE DE SANTIAGO DE COMPOSTELA

1.2. PROTEIN CORONA

When nanocarriers are dispersed in biological fluids, they become surrounded by various biomolecules, such as proteins, carbohydrates, lipids, and nucleic acids.[9] These molecules can interact with the nanosystems,[10–12] leading to a biomolecular corona.

The composition of the corona depends on the physicochemical characteristics of the nanosystems and the surrounding biomolecules. Proteins are the most relevant biomolecules forming part of the biomolecular corona. Therefore, protein corona is usually studied. Despite the clinical relevance of this protein corona, there is still much to be learned about its potential control.[13]

Protein corona studies started in the late 70s. In 1977, Tyrell *et al.* found that albumin and the α- and β-globulin fractions of serum interact with liposomes, affecting the *in vivo* uptake of these systems.[14] Soon later, in 1987, Kiwada *et al.* found that some serum proteins facilitate the *in vivo* uptake of liposomes.[15] However, it was not until 2007, after Kenneth A. Dawson and his team coined the term "protein corona",[16] that the protein adsorption originated after nanosystems dispersion in biological samples was intensively studied.[17]

Currently, the protein corona field is continuously growing and evolving, with almost 300 publications per year (Figure 1).

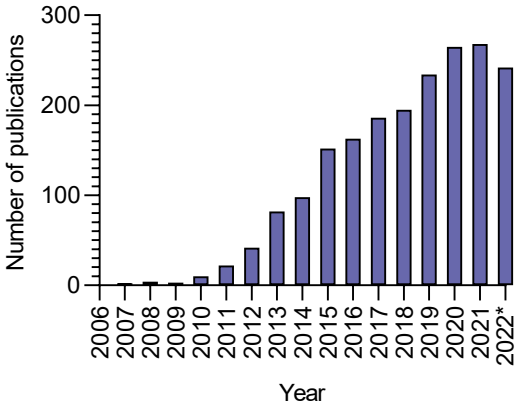


Figure 1. Scientific articles focused on the study of nanosystem's protein corona

Quantity of published articles containing the words "protein corona" and "nanoparticle" in their title, abstract, or keywords since the coining of the term in 2007. (*) Data retrieved at the time of writing (November 2022) from Scopus® (https://www.scopus.com) with the following search options: TITLE-ABS-KEY ("protein corona" AND "nanoparticle*"). Adapted with permission of Springer Nature from [1].

Protein adsorption onto nanosystems' surfaces is a remarkably selective process. Although there are more than 3,700 different proteins in the human plasma, only 100 – 300 proteins were reported as components of protein coronae.[18] Moreover, only tens are usually abundant in the protein corona (Table 1).[13,19,20]

USC UNIVERSIDADE DE SANTIAGO DE COMPOSTELA

USC

Table 1. Summary of the protein corona of different human plasma-incubated polymeric nanosystems

Main polymer	Functionalization / polymer surface	Particle size ζ-potential	Relevant proteins	Ref.
PS	Unfunctionalized	140 nm n.d.	Fibrinogen (38 %), Albumin (20 %), IgG γ (9 %) PLS:6 (5 %), Clusterin (2 %), IgM (2 %), Ig light chain (2 %)	[21]
	With 2-hydroxyethyl acrylate	650 nm n.d.	Fibrinogen (50 %), PLS:6* (15 %), IgG γ (13 %), Ig light chain (3 %), IgM (2 %), Apo C-III (2 %)	[21]
	With hydroxyethyl methacrylate	90 nm n.d.	Fibrinogen (25 %), Albumin (23 %), IgG γ (15 %), Ig light chain (4 %), U2 (4 %), Clusterin (3 %), α-1-antitrypsin (2 %), IgM (2 %)	[21]
	With (dimethylamino)ethyl methacrylate	90 nm n.d.	Fibrinogen (56 %), Albumin (8 %), IgM (2 %), α-1-antitrypsin (2 %), IgD (2 %), C3 ß (2 %)	[21]
	Carboxyl functionalized (-COOH)	150 nm −4 mV	Ig γ-1 chain C (21 %), Ig κ chain C (20 %), Clusterin (17 %), Apo A-I (13 %), Antithrombin III (3 %), Ig λ-like polypeptide 5 (2 %), Apo C-III (2 %), Ig heavy chain V-III (2 %) [a]	[22]
		130 nm −30 mV	Vitronectin (≈ 28 %), Clusterin (≈ 18 %), Apo A-I (≈ 18 %), ß2-glicoprotein 1 (≈ 16 %), Apo E (≈ 14 %)	[23]
		140 nm −10 mV	Ig γ-1 chain C (24 %), Ig κ chain C (21 %), Vitronectin (11 %), Apo A-I (3 %), Antithrombin-III (3 %), Ig γ-3 chain C (3 %), Apo E (3 %), Prothrombin (3 %) [a]	[22]
		120 nm −60 mV	CD5 antigen-like (12 %), Ceruloplasmin (11 %), Prothrombin (6 %), Complement C1r subcomponent (6 %), Haptoglobin (4 %), Haptoglobin-related protein (3 %), Coagulation factor IX (3 %), Coagulation factor X (3 %)	[18]
		230 nm −70 mV	Albumin (36 %), Ig κ chain C region (6 %), Apo E (6 %), Ig γ-1 chain C region (6 %), Fibrinogen γ chain (5 %), Kininogen-1 (4 %), Vitronectin (4 %), Fibrinogen ß chain (3 %)	[24]
	- COOH + IgG-depleted plasma	160 nm −15 mV	Fibrinogen γ chain (≈ 22 %), Vitronectin (≈ 22 %), Fibrinogen ß chain (≈ 20 %), Fibrinogen α chain (≈ 18 %), Clusterin (≈ 16 %)	[23]
	-COOH covalently linked to CD63	230 nm −30 mV	Albumin (43 %), Ig κ chain C region (7 %), Ig γ-1 chain C region (6 %), Clusterin (4 %), Complement C3 (3 %), Apo A-I (3 %), Apo B-100 (3 %)	[24]
	-COOH precoated with CD63	230 nm −40 mV	Albumin (33 %), Ig κ chain C region (9 %), Ig γ-1 chain C region (9 %), Ig μ chain C region (7 %), Complement C3 (4 %), Clusterin (3 %)	[24]
	-COOH covalently linked to IgG	230 nm −30 mV	Albumin (24 %), Ig μ chain C region (10 %), Ig κ chain C region (8 %), Ig γ-1 chain C region (5 %), Complement C3 (4 %), Complement C1q subcomponent subunit ß (4 %), Apo A-I (4 %), Clusterin (4 %)	[24]

Table 1. Summary of the protein corona of different human plasma-incubated polymeric nanosystems (continuation)

Main polymer	Functionalization / polymer surface	Particle size ζ-potential	Relevant proteins	Ref.
	-COOH covalently linked to IgG	230 nm −30 mV	Albumin (24 %), Ig μ chain C region (10 %), Ig κ chain C region (8 %), Ig γ-1 chain C region (5 %), Complement C3 (4 %), Complement C1q subcomponent subunit B (4 %), Apo A-I (4 %), Clusterin (4 %)	[24]
	Amine functionalized ($-NH_2$)	150 nm +5 mV	Clusterin (≈ 30 %), Antithrombin III (≈ 14 %), Apo A-I (≈ 14 %), Albumin (≈ 14 %), Vitronectin (≈ 14 %)	[23]
		120 nm +50 mV	Keratin type II cuticular Hb6 (30 %), CD5 antigen-like (7 %), Ceruloplasmin (6 %), Coagulation factor XIII A chain (5 %), Prothrombin (4 %), Complement C1r subcomponent (3 %), Haptoglobin (3 %), Haptoglobin-related protein (2 %)	[18]
		150 nm +10 mV	Ig γ-1 chain C (27 %), Ig κ chain C (22 %), Clusterin (14 %), Apo A-I (9 %), Ig γ-2 chain C (3 %), Ig γ-3 chain C (3 %), Keratin (2 %), Ig heavy chain V-III (2 %) [a]	[22]
		150 nm +5 mV	Clusterin (63 %), Apo A-I (14 %), Albumin (6 %), Apo E (3 %), Apo A-IV (3 %)	[24]
		150 nm +10 mV	Ig γ -1 chain C (27 %), Ig κ chain C (22 %), Clusterin (14 %), Apo A-I (9 %), Ig γ -2 chain C (3 %), Ig γ-3 chain C (3 %), Keratin (2 %), Ig heavy chain V-III (2 %) [a]	[22]
	$-NH_2$ + IgG-depleted plasma	160 nm −30 mV	Clusterin (≈ 30 %), Hemopexin (≈ 18 %), Albumin (≈ 14 %), Antithrombin III (≈ 14 %), Vitronectin (≈ 14 %)	[23]
	PEGylated surfactant	130 nm −15 mV	Clusterin (31 %), Apo A-I (11 %), Ig κ chain C region (10 %), Ig γ-1 chain C region (7 %), Albumin (3 %), Apo E (3 %), Ig λ-like polypeptide 5 (2 %), Zinc finger protein basonuclin-2 (2 %)	[25]
	PEGylated surfactant	130 nm −10 mV	Albumin (16 %), Ig κ chain C (11 %), Ig γ-1 chain C region (9 %), Ig μ chain c region (3 %), Haptoglobin (3 %), Ig γ-3 chain c region (2 %), Ig α-1 chain C region (2 %), Ig γ-4 chain C region (2 %) [c]	[25]
	Polyglycerol/ cholesterol	560 nm −30 mV	Clusterin (60 %), Complement C3 (14 %), Immunoglobulins (< 10 %) [e]	[26]
	Phosphonylated polyglycerol/ cholesterol	340 nm −66 mV	Immunoglobulins (25 %), Clusterin (20 %), Fibrinogen (18 %) [e]	[26]
PLA	Unfunctionalized	300 nm	IgG γ chains (25 %), Antithrombin III (24 %), Apo E (5 %), Fibrinogen γ chain (5 %), Ig light chains (4 %), Apo A-I (2 %), Albumin (2 %) [a]	[27]

Table 1. Summary of the protein corona of different human plasma-incubated polymeric nanosystems (continuation)

Main polymer	Functionalization / polymer surface	Particle size ζ-potential	Relevant proteins	Ref.
	PEG	160 - 270 nm −55 - −10 mV	Albumin, IgG, Apo E, Apo A-I, Clusterin, Apo A-IV, α-1-antitrypsin, Fibrinogen, Apo C-III	[28]
PLGA	Unfunctionalized	170 nm −25 mV	Apo E, Albumin, Ig κ chain C, Ig Heavy Constant γ, Apo A-I [f]	[29]
			Albumin, Fibrinogen, Ig heavy constant α, GFP1 [d,f]	[29]
	Didodecyldimethyl-ammonium bromide	70 nm +45 mV	Albumin, Apo A-I, Apo A-II, Apo C-III, Apo E, Apo D, Complement C3, Complement C4, Complement factor H, α-2-HS-glycoprotein, Hemoglobin subunit α, Hemoglobin fetal subunit β, α-2-macroglobulin, α-1-antiproteinase, AMBP protein, Inter-α-trypsin inhibitor heavy chain H1-H3, Prothrombin, Antithrombin-III, Clusterin, Pigment epithelium-derived factor, Lumican [b]	[30]
PCL	Unfunctionalized	200 nm −60 mV	Ig light chain > IgG γ chain > Apo A-I > Apo C-III > Apo E > Apo C-II	[31]
	Dextran 5 kDa	140 nm −20 mV	Ig light chain > IgG γ chain > Apo A-IV > Apo A-I > Haptoglobin β chain > Fibrinogen γ chain > C3a	[31]
	Dextran 40 kDa	150 nm −5 mV	Apo A-I > Ig light chain > Apo A-IV > IgG γ chain > Apo E	[31]
	PEG	220 nm −10 mV	Ig light chain > Apo A-I > Apo E > Apo A-IV > IgG γ chain > Fibrinogen γ chain	[31]
PIBCA	Dextran coated	215 nm −15 mV	Fibrinogen > Apo A-I > Albumin > IgG > Apo C-III	[32]
	Heparin coated	90 nm −50 mV	IgG > Fibrinogen > Apo A-I > Albumin	[32]
	Dextran-Heparin coated	190 nm −25 mV	Fibrinogen > IgG > Serotransferrin	[32]
NIPAM/BAM	Unfunctionalized	70 - 200 nm	Albumin, Apo A-IV, Apo E, Apo A-I, Apo A-II	[33]
PCL	Unfunctionalized	200 nm −60 mV	Ig light chain > IgG γ chain > Apo A-I > Apo C-III > Apo E > Apo C-II	[31]

Table 1. Summary of the protein corona of different human plasma-incubated polymeric nanosystems (continuation)

Main polymer	Functionalization / polymer surface	Particle size ζ-potential	Relevant proteins	Ref.
PHDCA	Unfunctionalized	165 nm −20 mV	IgG γ chain > Albumin > IgM μ chain > Apo A-I > Ig light chain > Apo A-IV > α1-antitrypsin > Clusterin > Apo C-III > Apo C-II	[34]
	PEG	170 nm −20 mV	Albumin > IgM μ chain > Ig light chain > IgG γ chain > Apo A-I > α1-Antitrypsin > Apo A-IV > α2-HS-glycoprotein	[34]
PGMA	Unfunctionalized	140 nm +10 mV	Apo A-I > Albumin > Ig κ chain > α-1-antitrypsin > Apo E	[35]
	PEG	180 nm +20 mV	Albumin > Apo A-I > Serotransferrin > Ig κ chain > Antithrombin-III	[35]

Unless indicated otherwise, the isolation and separation steps were ultracentrifugation followed by sodium dodecyl sulfate addition and polyacrylamide gel electrophoresis, and the protein analysis method was liquid chromatography coupled to mass spectroscopy. **Abbreviations:** AMBP: Alpha-1-microglobulin/bikunin precursor. n.d.: no data. GFP: green-fluorescent protein. NIPAM/BAM: *N*-isopropylacrylamide / *N*-tert-butyl acrylamide. PCL: Poly ε-caprolactone. PEG: polyethylene glycol. PGMA: Poly(glycidyl methacrylate). PHDCA: Poly(hexadecyl cyanoacrylate). PIBCA: poly(isobutyl cyanoacrylate). PLA: Polylactic acid. PLGA: Poly(lactic-co-glycolic acid). PS: polystyrene. [a]: incubated in serum. [b]: incubated in fetal bovine serum. [c]: isolated by asymmetric flow field-flow fractionation. [d]: isolated by size exclusion chromatography. [e]: separated by urea, thiourea + 3-[(3- cholamidopropyl) dimethylammonio]-1-propanesulfonate (CHAPS). [f]: separated by lysis buffer. Adapted with permission of Springer Nature from [1].

1.2.1. Mechanisms behind the protein corona formation

Protein adsorption onto nanosystems' surfaces is a spontaneous process that starts immediately after the nanosystems contact biological media.[9,10,20] This process is driven mainly by five attractive intermolecular forces: Van der Waals, hydrogen bonding, disulfide interactions, and electrostatic and hydrophobic forces.[10–12,36,37]

The protein binding and protein exchange occurring at the nanosystem's surface level is dictated by the Vroman effect.[38] First mentioned in 1962, it describes how the adsorption of blood proteins onto a surface is time-dependent. Initially, proteins with the highest diffusion rates, that is, of small size and higher concentrations, are the first ones to interact with the nanoparticles (NPs), as in the case of albumin and globulins. Afterward, they are gradually displaced by proteins with a higher affinity constant (k_a) to the nanosystem surface.[10,20,37,39] The laxest bound proteins maintain a rapid dynamic exchange rate with other biomolecules in the blood (Figure 2).[33,40]

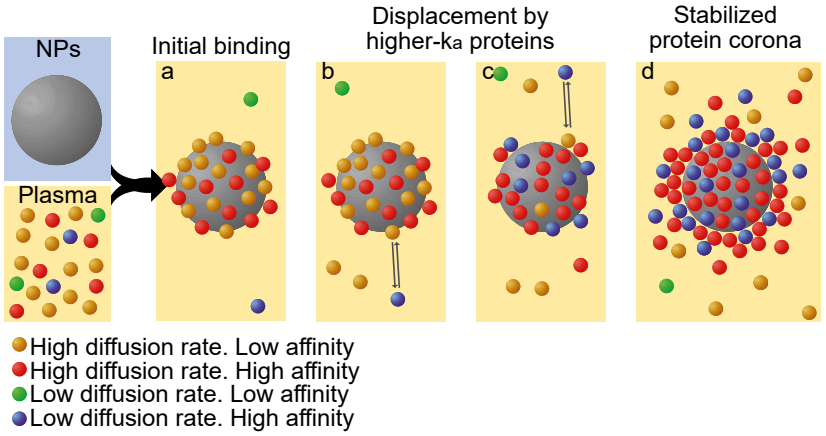


Figure 2. Formation mechanism of the protein corona

(**a**) Upon contact with the plasma, nanoparticles are initially coated by proteins with the highest diffusion rate. (**b**) Then, bound low-affinity proteins are exchanged with proteins with a higher affinity constant (k_a). (**c**) The protein corona evolves until it reaches its equilibrium state. (**d**) Stabilized protein corona. Adapted with permission of Springer Nature from [1].

The time it takes for a stable protein corona to be formed depends on the nanosystems' physicochemical properties. Some systems can reach a stable protein corona composition within 5 minutes,[18,41] while others need more than an hour.[27] Generally, 1 h is the commonly accepted time required for a protein corona to be stable. Once stabilized, the protein corona fingerprint has been reported to remain constant for hours or even days.[42,43]

Even when the protein corona is stabilized, any subsequent exposure to a new environment with different biomolecules may change its fingerprint, which is especially relevant in the case of non-intravenous administrations such as the subcutaneous or pulmonary routes. For example, nanoparticles recovered from blood after pulmonary administration might preserve mucus proteins. In this sense, the biomolecules from other environments remaining on the NP surface can be considered a "memory" of the NPs' journey through the biological system.[37]

USC DE COMPOSTELA

Some researchers differentiate two layers in the protein corona: the "hard" and the "soft" corona.[10,20,37] The "hard" corona is usually considered responsible for the biological fate of the nanocarriers, while the "soft" corona is commonly seen as a bunch of non-relevant proteins that are quickly exchanged between the "hard" corona and the medium. However, the relevance of the loosely bound proteins is not completely clear yet. For instance, different authors reported that the cellular uptake of polystyrene (PS) NPs was modified[22] or unaltered[25] after the removal of the "soft" corona layer. Nevertheless, the separation between these two layers is mainly theoretical since, ultimately, it is determined by the separation method.

The composition of the protein corona depends on: i) the nanosystem's chemical and physicochemical properties (i.e., surface composition, size, and shape) and ii) the composition (i.e., proteins, lipids, and nucleic acids) and characteristics of the biological environment (i.e., ionic strength, pH, and temperature).[44,45]

1.2.2. Protein corona of polymeric nanoparticles

Most of the protein corona studies reported in the literature have been performed with metallic nanosystems, such as gold and silver NPs (Figure 3). This could be explained by the great attention that these particles have recently received, their stability, and their easy isolation and detection. Many protein corona studies have also been reported for liposomes, the most successful delivery carriers from the translational perspective.

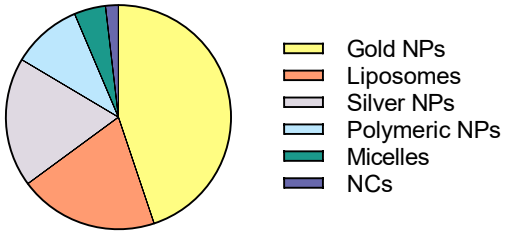


Figure 3. Percentage of research articles studying the protein corona for different nanosystems

Data retrieved at the time of writing (November 2022) from Scopus® (https://www.scopus.com) with the following search options: TITLE-ABS-KEY ("protein corona" AND gold AND nanoparticle*); TITLE-ABS-KEY ("protein corona" AND silver AND nanoparticle*); TITLE-ABS-KEY ("protein corona" AND polymeric AND nanoparticle*); TITLE-ABS-KEY ("protein corona" AND liposom*); TITLE-ABS-KEY ("protein corona" AND nanocapsul*) and TITLE-ABS-KEY ("protein corona" AND micelle*), respectively for gold NPs, silver NPs, polymeric NPs, liposomes, micelles, and NCs. **Abbreviations:** NCs: nanocapsules. NPs: nanoparticles. Adapted with permission of Springer Nature from [1].

In some cases, a correlation between the composition of nanosystems and adsorbed proteins has also been successfully established. For example, liposomes and lipid NPs containing 1,2-dioleoyl-3-trimethylammonium propane (DOTAP) were found to specifically interact with vitronectin,[46,47] whereas those containing dioleoyl phosphatidylethanolamine (DOPE) showed an affinity towards apolipoproteins.[48]

Biocompatible polymeric NPs, such as NCs, have gained significant interest because of their versatility. First, they can be used to design a great variety of nanostructures. Second, the available polymer diversity can help tune their physicochemical properties to increase their

ability to cross biological barriers and tissues, their stability in contact with biological fluids, and their drug loading and release kinetics.[49] Despite these appealing properties, their affinity towards plasma proteins has not been investigated systematically, thus making it very difficult to establish a relationship between their composition and their protein corona. A summary of the protein corona of different human plasma-incubated polymeric nanosystems is included in Table 1. Notably, most of the studies in the literature refer to model PS NPs.

Data in Table 1 shows a high presence of immunoglobulins, albumin, and clusterin on PS NPs. Notoriously, albumin was detected as one of the protein corona components in all the studied poly(lactic-co-glycolic acid) (PLGA)-based NPs, while Apo A-I was detected in all the abovementioned PLC NPs. Finally, no clear correlation was detected between PEG presence and the protein corona identity.

1.2.3. Biological relevance of the protein corona

Protein adsorption can modify the behavior of pristine nanosystems, such as their targeting, biodistribution, clearance, and toxicity. These changes may explain why most *in vitro* and *in vivo* studies do not correlate as expected.[10,50,51]

1.2.3.1. Circulation time and clearance

Changes in the circulation time and clearance of nanosystems mediated by protein adsorption can be due to physical and biological reasons.

In general, protein adsorption increases the particle size of the nanosystems and modifies their surface charge. However, in the case of flexible nanosystems, such as liposomes, a decrease in size after contact with plasma may happen.[52,53] This shrinkage has been attributed to the high osmotic pressure of the biological media.[52] While this size variation is mild, it might modify the nanosystem's clearance by the immune cells in the bloodstream and tissues.[54–57]

More importantly, the nature of the adsorbed proteins also impacts the nanosystems' clearance.[41,53] Adsorbed proteins are usually classified into opsonins and dysopsonins, depending on their effect on the circulation time and immune system interaction. Opsonins, such as complement factors and immunoglobulins, tend to induce a higher uptake by the mononuclear phagocytic system,[10,20,30] while dysopsonins, such as apolipoproteins, promote the opposite effect.[58] The opsonin/dysopsonin role of some of the most common corona proteins is shown in Table 2.

Most of the work in the protein corona field has been focused on reducing opsonin adsorption by designing negatively charged hydrophilic carriers containing stealth polymers such as PEG. However, even in that case, achieving a total lack of adsorbed proteins is very unusual. Moreover, the new protein corona formed after PEG incorporation might alter the tissue accumulation profile of nanocarriers rather than exclusively extending their circulation time.

USC UNIVERSIDADE

The opsonin/dysopsonin behavior of the adsorbed proteins may be altered if the last ones are partially denatured. For example, a new secondary structure of bovine serum albumin

was formed after its interaction with positively charged PS NPs, which led to a scavenger receptor activation instead of its recognition by albumin receptors.[59]

Glycan moieties are also involved in the dysopsonin effect of some plasma proteins.[60] Generally speaking, protein deglycosylation increases NP uptake by macrophages and leads to pro-inflammatory cytokine secretion.[60,61] In this regard, Ghazaryan *et al.* demonstrated that the incubation of PS NPs with several deglycosylated proteins (clusterin, −also known as Apo J−, low-density lipoprotein −LDL−, and very low-density lipoprotein −VLDL− components) led to a notable increase in their uptake by murine macrophage-like cells. However, in other cases (such as with Apo A-I), where glycans seem necessary for receptor binding, a decrease in the NPs uptake could be observed after the deglycosylation process.[60]

Finally, protein orientation also plays a critical role in opsonization. Exposure to some domains, like the Fc fragments of antibodies, may trigger an immune response. In contrast, complement activation may be limited if this Fc region is hidden due to its interaction with an NP.[62]

Table 2. Proteins on the protein corona that may impact the nanosystems' clearance

Role	Protein	Ref.
Opsonin	α-2-HS-glycoprotein	[30]
	Apo H (ß2-glycoprotein 1)	[63]
	C-reactive protein	[15,64]
	Complement proteins (C3, C3b, C4, C4b, C4BPA, C5)	[10,20,30,40,41,63,65-67]
	Fetuin	[68]
	Fibrinogen	[20,40,41,65]
	Fibronectin	[15,20,41,64]
	Galectin-3-binding protein	[30]
	Hemoglobin	[55]
	Immunoglobulins (IgA, IgG)	[15,40,65]
	Laminin	[64]
	Type I collagen	[64]
	Vitronectin	[20,41]
Dysopsonin	Apo A-I, Apo A-IV, Apo C-III and Apo J (clusterin)	[30,44,63,69]
	Apo A-IV	[63]
	Apo C-III	[63]
	CD47	[63]
	Human serum albumin	[30,63,66,69,70]
	IGLC2	[10,65]

Opsonins are molecules that enhance phagocytosis by marking an antigen to trigger an immune response and promoting an accelerated plasma clearance through specific recognition by macrophages, leading to the accumulation of NPs in the liver and spleen. Dysopsonins have the opposite effect. **Abbreviations:** Apo: alpolipoprotein. CD: cluster of differentiation. IGLC2: immunoglobulin lambda constant 2. Adapted with permission of Springer Nature from [1].

USC UNIVERSIDADE DE SANTIAGO DE COMPOSTELA

1.2.3.2. Targeting and accumulation

The protein corona can act as a "blanket", covering and hiding potential ligands on the NPs' surface and, hence, their interaction with their receptors.[10,50,71] Instead, adsorbed proteins are susceptible to interacting with host receptors.[72,73] If the protein moieties are preserved and accessible, it is evident that their biological receptors might recognize them through a typical mechanism. In this sense, the protein corona may facilitate the accumulation of the nanosystems in areas where specific receptors for these proteins are overexpressed, modifying their biodistribution profile. For example, adsorbed Apo E leads to the accumulation of nanosystems in the liver, where low-density lipoprotein receptors (LDLR) and lipoprotein receptor-related proteins (LRPs) are highly present.[74] On the other hand, Dawson *et al.* have recently reported that, in some cases, the protein corona can trigger an atypical receptor-mediated uptake,[75] a fact that opens new avenues for identifying new ligand-receptor interactions.

1.2.3.3. Crossing biological barriers

Among the different plasma proteins usually present in the protein corona of the nanosystems, apolipoproteins have the highest impact on the nanosystems' capacity to cross biological barriers.[13,37,76] Apo B is the main component of low-density lipoproteins (LDLs), endogenous nanostructures that are known to cross the BBB. Moreover, Apo A-I, along with Apo A-II, Apo E, lipids, and cholesterol, form the HDL particles, which are also present in the brain.[77] In this sense, it has been shown that the presence of Apo A-I, Apo E, and Apo B-100 improves the trafficking of NPs into the central nervous system.[78,79]

Clusterin (Apo J) is usually the most abundant apolipoprotein reported in the protein corona studies of polymeric nanosystems. This anti-inflammatory protein, involved in lipid transport, has a crucial impact on preventing macrophage uptake.[68,80] However, a study has shown that coating NPs with only this protein was insufficient to reduce macrophage uptake and that the combination with other proteins, such as Apo A-IV, Apo C-III, or Apo D, was necessary to achieve the full stealth effect.[69]

1.2.3.4. Toxicity

Several mechanisms may be involved in protein corona-related toxicity. For instance, the macrophage uptake of NPs may lead to the release of toxic substances, such as pro-inflammatory cytokines, the reduction of the host defense capability, and their accumulation in organs such as the liver or the spleen.[56] In other cases, the adsorbed proteins were found to undergo structural changes that triggered inflammatory signals[40] or promoted the formation of reactive oxygen species, causing oxidative damage.[81] It has also been argued that pristine surfaces can aggressively steal biomolecules from cell membranes and other biological entities, causing cell damage.[37,82] Moreover, the internalization of the extracellular proteins bound to the particles may trigger different intracellular pathways and cause changes in cell performance. Finally, the deposition and cleavage of complement proteins can trigger the activation of the complement system, which not only promotes the uptake of the NPs by the immune system but also produces anaphylatoxins which may induce adverse reactions such as complement activation-related pseudoallergy.

USC DE SANTIAGO DE COMPOSTELA

1.2.3.5. Physical stability and release of the cargo

The protein corona may also affect the controlled release of drugs by the nanosystems. As described by Mahmoudi *et al.* for some synthetic nanosystems and Abraxane®, the formation of thick protein layers can delay the release of the nanosystem's cargo.[83] A steric hindrance phenomenon may easily explain this since the protein corona represents an extra barrier between the inner part of the nanosystem and the medium. In other studies, the protein attachment destabilized the nanocarrier, causing a burst release[84] and particle agglomeration.[53,85,86]

1.2.4. Influence of the nanosystems characteristics on the protein corona composition

Since protein corona composition depends on the nanosystems' characteristics, tuning different parameters of the NPs can help alter or minimize the formation of the protein corona. However, it is essential to remember that the protein corona might not be entirely suppressed.[69]

1.2.4.1. Size and morphology

The influence of the particle size on the resulting protein corona has been confirmed for different nanosystems,[37,45,87] including polymeric NPs made of PS,[20,44] PLGA,[88] or acrylamide.[33,44] Smaller particles have a higher specific surface area and, as a rule, adsorb more proteins.[53] In addition, they have a lower curvature degree, providing more binding sites for the proteins and allowing a better interaction between large proteins and the nanosystem surface.[16] In contrast, extremely small nanosystems (< 10 nm), exposed to proteins of a similar size, may entirely avoid protein adsorption[39,89,90] or attach to only one single protein.[91] However, in the latest case, their minimal size makes their use as drug delivery systems difficult. Regarding morphology, non-spherical systems may also behave differently from spherical nanosystems. For example, Chithrani *et al.* found that nanorods with an almost flat surface might allow proteins to establish stronger interactions with the nanosystem surface.[92]

1.2.4.2. Surface charge

Electrostatic forces also play a crucial role in protein adsorption onto nanomaterials.[93] Nanosystems with a ζ-potential close to neutrality tend to adsorb fewer proteins than charged ones.[19] Alkaline proteins (isoelectric point, pI > 5.5) preferentially bind to negatively charged particle surfaces, while acidic ones (pI < 5.5) tend to bind to positively charged surfaces.[30] In addition, positively charged NPs usually have a thicker protein corona than negatively charged ones due to the higher abundance of negatively charged proteins in plasma.[53,94] Surface charge modifications can selectively enrich the presence of one specific protein. For instance, Gessner *et al*. used PS NPs of similar size and hydrophobicity but different charges, finding that clusterin concentration increased in the negatively charged NPs.[95]

1.2.4.3. Surface hydrophobicity

In general, hydrophobic nanosystems attach more proteins than hydrophilic ones.[81,96,97] Furthermore, hydrophobic NP surfaces tend to establish interactions with

hydrophobic protein domains. Apolipoproteins are lipophilic proteins highly present in the protein corona of hydrophobic nanosystems,[63,98,99] such as PLGA[100] and acrylamide-based copolymer NPs.[101] Nevertheless, a general correlation between the adsorption of opsonins or dysopsonins and the hydrophobicity of the nanosystems cannot be established.[65,95,99,102,103]

1.2.4.4. Surface decoration

The functionalization of NPs with different molecules, such as antibodies, proteins, and peptides, may considerably impact the protein corona of the nanosystem. Different ligand properties (i.e., nature, size, and conformation) may change the original protein corona composition.[20,104,105] For example, Zhang *et al.* evaluated the effect of three different ligands for the transferrin receptor [two different 1-kDa peptides and transferrin; molecular weight (MW) of 77 kDa] in the formation of the protein corona of PS NPs. The resulting *in vivo* protein corona was quantitatively altered, especially in the case of α-globin, Apo E, Apo A-IV, whose amount was reduced in the functionalized NPs compared to the non-functionalized ones.[104] Similarly, Fornaguera *et al.* described that the decoration of peptide-conjugated poly(beta aminoester):mRNA NPs with retinol caused a retinol-driven protein corona enrichment in Apo D and Apo A-II after incubation in FBS, which was correlated with a decrease in the spleen and increase in the liver accumulations *in vivo*.[106]

Moreover, an adsorbed protein layer on the nanosystems' surface can hinder the interaction between targeting ligands and receptors. For example, in the previously mentioned work of Zhang *et al.*, the *in vitro* formation of a protein corona led to the loss of the targeting capacity for the three decorated NPs.[104] However, this phenomenon does not always occur, as the targeting capacity of other systems was reported not to be altered by their protein corona.[24,107]

An alteration of the protein corona has also been reported in the case of nanosystems decorated with fluorescent dyes. In this sense, linking rhodamine B to the surface of PS NPs led to a 3-fold decrease and a 2-fold increase in the adsorption of fibrinogen and IgG, respectively. Consequently, the uptake of the nanosystem by human HL60 cells was strongly reduced.[103] This highlights the importance of using adequate labeling strategies to prevent surface attachment of the markers in biodistribution studies of NPs.

1.2.4.5. Polymeric coating

1.2.4.5.1. PEGylation

Grafting nanomaterials with PEG moieties is the most widely applied strategy to increase the circulation time and reduce their clearance by phagocytes.[55,56,69,108,109] PEG chains create a highly hydrophilic environment, hindering the interactions between particles and the most hydrophobic molecules. Furthermore, they also create a steric hindrance, preventing molecules from approaching the NPs' surface.

While the presence of PEG is generally accepted to decrease protein adsorption in comparison with the non-PEGylated counterparts, a correlation between PEG presence and the identity of the adsorbed proteins has not yet been established. On the other hand, a strict correlation between the characteristics of the PEG shell in terms of length, density, and

disposition and the protein corona fingerprint could not be established either. Also, the nanosystems' core components might influence the adsorbed proteins onto PEGylated systems.

The PEG stealth effect depends on the number of PEG chains per surface area of the nanosystem (PEG density) and, to some extent, on their length (PEG MW).[56] At low PEG densities, the PEG mushroom conformation is the most stable from a thermodynamic point of view, providing more space for protein interactions. Greater PEG densities (> 7 – 20 PEG chains/100 nm^2) lead to a PEG brush conformation, making protein interactions more difficult.[110,111] Once all PEG chains are arranged in a brush conformation, increasing the PEG density does not further decrease protein adsorption. Regarding PEG MW, it has been shown that PEG molecules with MWs above 5 kDa have similar stealth properties. At lower MW values (< ≈ 5 kDa), the stealth effect increases with the length of the PEG chain since bigger PEG chains form a thicker barrier between the NP's surface and the free proteins. However, an MW of approximately 2 kDa was reported to be the threshold length for the stealth effect.[64] The influence of these parameters in the PEG coating has been proved for different types of nanosystems, among which poly(glycidyl methacrylate) (PGMA),[35] PLA,[28] PLGA,[28,88,110] and PCL[28] NPs. Still, it is essential to remember that PEGylation does not entirely prevent protein adsorption, and some proteins, preferentially dysopsonins, can still be detected on PEGylated surfaces.[28,37,56]

Despite its advantages, PEGylation may also present some limitations. For instance, PEGylation may interfere with the target-receptor recognition of ligand-functionalized nanosystems. Different approaches have been studied to minimize this phenomenon. For example, targeting ligands can be attached to the end of the PEG chain, providing flexibility to the conjugated molecules and preventing protein adsorption, thus facilitating targeting.[108] Another approach to facilitate the exposure of the targeting ligands relies on the controlled *in vivo* degradation of the PEG-NP linker and subsequent detachment of PEG molecules. PEG linkers can be enzymatically or pH-dependently cleaved, exposing the hidden ligands.[112,113] In a different scenario, some PEGylated lipids bound to siRNA-loaded PLGA NPs through hydrophobic interactions were found to be progressively displaced from the NP core by albumin, prolonging the circulation time at short times while facilitating their cellular uptake after de-PEGylation.[113] Finally, coupling PEG and anti-CD3 antibodies in different hemispheres of Janus particles, which are characterized by surface regions with different compositions, was found to prevent macrophage uptake while still allowing T-cell targeting.[114]

Another concern about PEGylation is the potential anti-PEG IgM response. It has been reported that IgMs are susceptible to being included in the corona of PEGylated nanosystems, which would increase the activation of the complement.[115,116] To bypass this issue, the administration of a PEG solution to saturate the circulating Igs was proposed.[117] Nevertheless, the relevance of this activation has been questioned. For example, complement activation was found for micelles composed of poloxamers 188 and 407 but not for similar systems made of PEGylated phospholipids, suggesting that this phenomenon does not exclusively rely on the presence of ethylene oxide moieties.[118–121]

USC UNIVERSIDADE DE SANTIAGO DE COMPOSTELA

1.2.4.5.2. PEG-derivative coating

Poloxamers and poloxamines are constituted by poly(ethylene oxide) (PEO) and poly(propylene oxide) (PPO) regions. Poloxamers are constituted by PEO and PPO blocks,

while poloxamines have additional ethylenediamine residues. Some of these compounds are temperature- and pH-sensitive.[122] Their amphiphilic nature allows them to interact with hydrophobic surfaces. For example, the addition of poloxamer 407 in PS NPs extended their circulation time[123] and decreased the number of adsorbed proteins due to an enrichment in clusterin and Apo C-III.[124] On the other hand, polysorbates are amphiphilic sorbitan derivatives containing PEO residues and hydrophobic chains. Some polysorbates (20, 40, 60, and 80) were found to help cross the blood-brain barrier (BBB) through a preferential Apo A-I, Apo B, or Apo E binding.[34,78,97,125] As an example, coating poly(butyl cyanoacrylate) NPs with polysorbate 80 (P80) increased BBB crossing through preferential adsorption of Apo E.[19,40]

1.2.4.5.3. Polyphosphoesters coating

Polyphosphoesters (PPEs) are molecules similar in structure to nucleic and teichoic acids,[126] whose degradation and hydrophilicity can be chemically adjusted. Highly hydrophilic PPEs were found to have a stealth effect comparable to that of PEG.[126–128]

The stealth effects of PPE and PEG were compared in the case of amine-functionalized PS NPs. PPEylation was able to reverse and drastically change the surface potential of the particles (from +46 to approximately –10 mV) compared to PEGylation (approximately +10 mV). Regarding the protein corona composition, clusterin was the most abundant protein in both cases, especially in PPEylated systems (77 %). On the other hand, Apo A-I was also a significant component of the PEGylated NPs but not of the PPEylated corona.[69]

1.2.4.5.4. Polysaccharide coating

Polysialic acid (PSA) was used to extend the circulation time and reduce the accelerated blood clearance and IgM production of liposomes.[129] Moreover, exosomes coated with PSA were recognized and internalized by sialic acid-binding immunoglobulin-like lectin receptors in HeLa cells,[130] and PLGA NPs coated with sialic acids decreased the production of pro-inflammatory cytokines.[131]

Hyaluronic acid (HA) coating was reported to prevent the aggregation of chitosan NPs after contact with serum[53] and to reduce the adsorption of pro-inflammatory proteins.[53] However, the HA shielding effect has generated some controversy as some authors have found that its interaction with proteins, and subsequent immunogenicity, may depend on its molecular weight.[132]

Finally, the potential stealth effect of a dextran coating was studied in poly(isobutyl cyanoacrylate) NPs. However, such an effect could not be established due to the attachment of IgG, fibrinogen, and complement C3.[32]

1.2.4.5.5. Zwitterionic coating

The decoration with zwitterionic coatings can lead to a significant reduction in protein adsorption.[90,133] Zwitterionic molecules, such as sulfobetaine, phosphorylcholine, poly(acrylic acid), and poly(maleic anhydride-alt-1-alkene) derivatives, have both positively and negatively charged groups, which are stabilized among themselves, leading to a neutral net

charge and an absence of counterions, which strongly reduces the possibility of establishing ionic bonds with surrounding proteins.[133] However, despite being studied for metallic NPs, the use of zwitterionic coating for polymeric nanosystems has not been deeply explored.

From the information gathered in this section and Table 1, we can agree that the interplay between the different parameters makes it difficult to draw a conclusion about the protein corona composition for a specific material. Instead, it is necessary to analyze the different types of nanosystems in a case-by-case manner.[20]

1.2.5. Grafting an artificial protein corona

Precoating the pristine NP surface with specific high-affinity proteins is another way to modulate the protein corona. Pre-incubation with the appropriate proteins would result in different *in vivo* coronae enriched in those specific proteins, thereby altering certain processes, such as the cellular uptake by the target cells or the BBB crossing (i.e., Apo E adsorption). Pre-incubation of acid-functionalized PS NPs with the dysopsonins Apo A-IV and Apo C-III decreased their uptake by mesenchymal stem cells (used as a model for healthy human cells) while precoating with β2-glycoprotein 1 had the opposite effect.[63] These results suggest that Apo A-IV and Apo C-III might help decrease the nonspecific cellular uptake. In another experiment, the incubation of NPs with clusterin almost entirely prevented their nonspecific uptake.[69] Alternatively, precoating can be achieved by incubating the NPs with plasma depleted of unwanted proteins.[23] Following this last idea, Sobczynski *et al.* incubated PLGA NPs with IgA- and IgM-depleted plasma, which promoted the adhesion of the particles to endothelial cells, an interaction that would not happen in the presence of those proteins.[134]

As a limitation of these findings, proteins were found to establish new interactions with other plasma proteins, spreading the initial protein corona.[10,71] For example, Mirshafiee *et al*. precoated NPs with γ-globulins to enhance macrophage uptake. However, additional protein adsorption hindered the interaction between γ-globulins and macrophage Fc receptors.[71] For this reason, it is crucial to incubate pre-coated NPs in plasma before performing *in vitro* studies.[135]

1.2.6. Influence of the biological system on the protein corona

The characteristics of the biological environment that surrounds the nanosystems strongly influence the protein corona composition. Thus, the protein corona may vary depending on the individual phenotypes and environmental factors, such as geographical location and diet.[136] Besides, temperature variations may change the protein corona composition even within the physiological range (35 – 40 °C), meaning that fever and the own temperature of the targeted body region should always be considered.[9]

Another relevant physical factor to be taken into consideration is blood flow. Blood moves at speeds from 0.085 $cm \cdot s^{-1}$ in capillaries to a maximum of 60 $cm \cdot s^{-1}$ inside the aorta. In general, protein adsorption increases with higher blood flow. Although the mechanisms governing this process are not fully understood, it has been hypothesized that the higher protein adsorption may be due to increased encounters between proteins and NPs.[137] Also, high flow rates create shear stress on the nanosystem surface, which removes smoothly adsorbed proteins and may facilitate their interaction with others of higher affinity. This may lead to a specific

protein enrichment, as it is described for plasminogen and PS NPs.[138] Furthermore, the blood flow can modify the conformational structure of free proteins, such as plasminogen or the von Willebrand factor. Different conformations can lead to different interactions with the nanosystems and, thus, to different protein corona compositions.[138]

In addition, diseases may modify the protein corona of a nanosystem.[136] For example, Hajipour *et al.* studied the role of protein deficiencies related to common diseases and medical conditions in modifying protein corona on PS NPs,[136] and concluded that the protein corona significantly differed among diseases, underscoring the importance and difficulty of recreating an accurate biological environment.

1.2.7. Critical aspects of performing a protein corona assay

1.2.7.1. *In vitro* protein corona characterization

The output of the protein corona characterization is the average protein content calculated from all the analyzed NPs. However, it should be highlighted that the protein corona composition also changes between particles in the same sample, as recently demonstrated using stochastic optical reconstruction microscopy.[139] In general, *in vitro* protein corona characterization experiments include four main steps: i) incubation with the medium, ii) isolation of the NP-protein corona, iii) protein separation, and iv) protein analysis (Figure 4). Some critical aspects of each step are detailed hereafter.

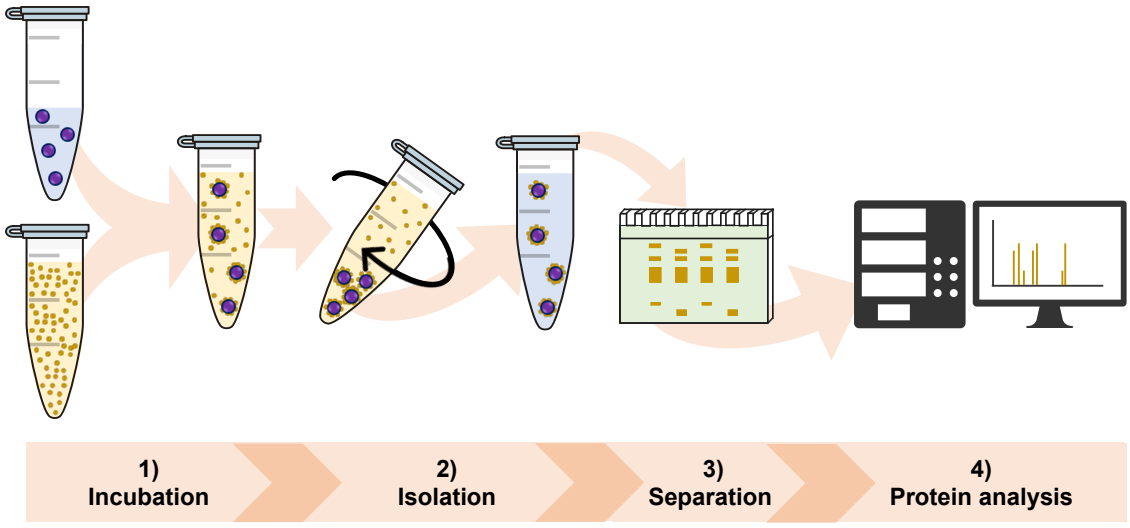


Figure 4. *In vitro* protein corona characterization procedure

The first step in the *in vitro* protein corona characterization involves mixing the nanosystems with the biological medium (incubation). After a fixed time, an isolation method, such as centrifugation, separates the desired protein-nanosystem complexes from the unbound proteins. Finally, a protein determination assay, such as mass spectrometry or direct comparison using a reference polyacrylamide gel, is needed to determine which proteins were adsorbed onto the nanosystems. During the *in vivo* characterization process, incubation is replaced by the administration and subsequent recovery of the nanosystems from the living organism. Adapted with permission of Springer Nature from [1].

USC
UNIVERSIDADE DE SANTIAGO DE COMPOSTELA

1.2.7.1.1. Incubation with biological media

First, a medium that mimics the *in vivo* biological conditions must be carefully selected, i.e., the biological medium most similar to the target animal species or, even more specifically, to animals with the same disease or conditions present in the potential final users of the nanosystem.[135] In this regard, the protein corona of amine- and carboxyl-functionalized PS NPs was studied after incubation with the plasma of different animal species.[140] The immunoglobulin content differed depending on the plasma origin: approximately 13 % for humans, 7 % for rabbits, and 1 % for mice. In the case of human and mouse plasma, significant differences were observed in the main adsorbed proteins: for unmodified PS NPs, clusterin (49 %), Apo A-I (9 %), and Apo A-IV were the most abundant proteins in the corona after human plasma incubation, while Apo A-I (15 %), Apo E (17 %) and Apo A-IV (12 %) were the most common ones after mouse plasma incubation. In another experiment, PLGA NPs were found to bind more immune-related proteins when using human samples than when using murine ones.[100] These differences strongly compromise the transferability of the *in vivo* human-targeted nanomedicine results carried out in mice.

The adequate incubation medium for protein corona experiments of human-targeted intravenously-administered NPs is whole human plasma, but specific proteins can be used to study their relative affinity. The use of serum is not recommended since it does not include coagulation proteins, which may be present in the *in vivo* protein corona.[135] Fetal bovine serum (FBS) should also be avoided because it lacks coagulation proteins and varies among species.[30,135]

Clotting has to be avoided using an anticoagulant, which should be carefully selected since it may interfere with protein adsorption.[44,135] The use of heparin is not recommended as it interacts with several plasmatic proteins, including fibronectin, apolipoproteins, complement C1, C3, C4b, C5b67, factor H, and antithrombin, which may induce changes in the protein corona fingerprint of the nanosystems.[141,142] In addition, heparin has been described as a complement inhibitor at high concentrations but as an activator at low concentrations. Calcium-chelator anticoagulants, such as ethylenediaminetetraacetic acid (EDTA) or sodium citrate, are commonly used in the clinical environment. Their mechanism of action relies on the sequestration of the calcium ions needed to activate factors IX and X and for the transformation of prothrombin into thrombin.[143] Sodium citrate is preferred over EDTA as the latest can withdraw other divalent cations, such as magnesium, inhibiting the complement cascade's three activation pathways. Finally, using the recombinant protein lepirudin or natural hirudin, which are direct thrombin inhibitors, would be an excellent option for protein corona assays since they are very specific factor II inhibitors, preserving the integrity of the complement system.[144,145] However, their use is limited by their price and market availability. Interactions between the abovementioned anticoagulants and the main proteins involved in the coagulation and complement cascade are detailed in Supplementary Figure 1.

Then, the ratio "NP surface area/volume of plasma" or "NP surface area/amount of proteins" should be kept constant for all the studied nanosystems to establish comparisons.[86] Furthermore, the plasma protein levels must be in excess related to the available particle surface area to mimic the bloodstream environment.[19,146] This way, proteins will have to compete for a reduced number of binding places, resulting in the preferential attachment of those with higher affinity.[147]

USC UNIVERSIDADE DE SANTIAGO DE COMPOSTELA

Regarding blood flow, some authors have used agitation and flow rates of about 50 $cm \cdot s^{-1}$, which are consistent with the flow rates inside the thickest human blood vessels.[96,137,148] A microfluidic approach was also proposed for dynamic flow simulation.[149]

The incubation time should be adjusted to the estimated time required for protein corona stabilization and the expected circulation time *in vivo*. For these reasons, most authors choose to incubate the nanosystems for 1 h.[44,150–152] In addition, kinetic assays can be performed to characterize the composition evolution through time and to confirm the complete protein corona formation at the end of the incubation time.[27]

Moreover, the results of *in vitro* studies in human plasma should be extrapolated with extreme care because the *in vivo* whole blood/lymph composition, the circulation flux, and the NPs clearance by macrophages are challenging to simulate.

1.2.7.1.2. Isolation of the NP-protein corona complexes

The isolation process aims to separate the protein-NP complexes from the unbound proteins and should be done without disrupting the protein corona or inducing additional protein binding.[16] Furthermore, confirming the absence of free proteins after the isolation process is essential.[135]

Different methods can be used to isolate protein-NP complexes. Some examples reported in the literature are ultracentrifugation, asymmetric flow field-flow fractionation (AF4), size exclusion chromatography, hydrodynamic chromatography, and capillary electrophoresis. The advantages and disadvantages of ultracentrifugation and AF4 are discussed in this section.

Consecutive ultracentrifugation is the most widely employed method for separating the protein-NP complexes from unbound proteins in protein corona assays.[16,153] The isolated complexes are washed and recentrifuged repeatedly to ensure that the free proteins are removed.[44] Three centrifugation cycles of 15 – 120 min at 15,000 - 30,000 g at 4 °C with phosphate-buffered saline (PBS) washes are commonly used in the literature.[21,23–25,146] However, nanosystems with different compositions may require different centrifugation parameters. The use of ultracentrifugation as a protein corona isolation method presents some limitations. In general, the higher the centrifugation time, speed, dilution, and washings, the higher the desorption of the bound proteins. On the contrary, insufficient washing will not remove all the free proteins in suspension and will overestimate the adsorbed proteins, mainly albumin. Besides, large proteins and protein aggregates can sediment at high speeds and be mixed with the high-density protein-NP complexes, becoming false positives. Also, this methodology is not helpful for nanosystems with an apparent density lower than plasma, such as NCs, as they will tend to accumulate on the top part of the vial, making impossible the decantation of the unbound proteins and also the extraction of the nanosystems without taking part of the unbound protein fraction. In fact, since the protein concentration in plasma is expected to be thousands higher than in the corona, contaminating volumes as low as ≈ 1 µL of plasma in 1000 µL of sample would hinder the protein corona results. Finally, a relatively high sample quantity may be needed to visualize the pellet or cream formed. Due to all these restrictions of the ultracentrifugation method and to exclude false positives, it is highly recommended to validate the isolation process by other methods.[19]

USC DE COMPOSTELA

One-step ultracentrifugation appeared as an alternative to washing steps. Generally, it involves the use of a high-density cushion solution.[154] The protein-NP complexes are placed on top of the cushion. High-density nanosystems will pellet across the cushion when centrifuged, while free proteins will remain on top of the high-density solution. This methodology was also valuable for studying the protein corona formation kinetics. In this case, the cushion can prevent the interaction between the free proteins and the still-free binding sites of NPs. Also, discrete gradients can be used to facilitate the ultracentrifugation isolation of low-density nanosystems. For example, Amiji *et al.* recently developed a methodology of this kind using an iodixanol gradient.[147] After centrifugation, the protein-NP complexes were displaced to the top of the vial, while free proteins remained at the bottom.

AF4 is a chromatographic technique in which a parabolic-shaped main flow pushes forward the sample while a perpendicular cross-flow is applied. As a result, bigger particles will be pushed farther from the center of the main flow than smaller ones. Consequently, the smaller particles travel faster and, therefore, are eluted sooner. AF4 can be coupled to several detectors useful for protein corona characterization, such as UV-Vis spectrophotometers for free protein detection, multiangle light scattering (MALS) for NPs detection, and MS/MS detectors for the identification and quantification of the adsorbed proteins. The main advantage of this isolation technique is the theoretical smoothness of the resolving forces, which allows the isolation of more loosely-bound proteins than other methods.[25,154] In this sense, AF4 and centrifugation isolation techniques were recently compared using PS NPs. The results obtained by AF4 indicated that the protein corona was mainly composed of albumin and IgGs, while the most prevalent proteins detected after centrifugation were apolipoproteins. In the latter case, albumin and IgGs were supposed to be removed during the ultracentrifugation process. Therefore, the authors claimed that AF4 is adequate for detecting more loosely-bound proteins, although proper controls with free proteins that would have been detached during ultracentrifugation were missing.[25] Other advantages of this technique are that it usually requires a minimal sample volume (< 100 µL) and that the fractionation does not depend on the surface composition or charge of the nanosystem.[155]

However, AF4 also presents a series of limitations. First, since it relies on salt-enriched mobile phases, it might be incompatible with unstable formulations in protein-free salt-containing media. Second, part of the sample might adhere to the filtration membrane,[156] reducing the amount of recovered NCs and underestimating the adsorbed protein amount. More importantly, protein desorption may occur due to the high dilution while samples pass through the fractionating channel.[155] Also, proteins with fast dissociation rates might be washed off by the flow and separated accordingly to their size, preventing their re-association with the particles.[157–159] Finally, like in the ultracentrifugation technique, a control consisting of plasma subjected to the same fractionation method is needed as a blank to ensure that the identified proteins are indeed attached to the particles, and not contaminants, protein aggregates, or co-separating proteins.

The use of AF4 as a fractionation technique for isolating protein corona-coated NPs from their incubating medium has already been reported in the literature by several authors.[25,160–164] As an example, Weber *et al.*[164] have compared the protein corona of human plasma-incubated PS NPs subjected to AF4 and the classical isolating ultracentrifugation technique involving three cycles of washes and centrifugation. The AF4-isolated protein corona was composed mainly of albumin and IgGs, while clusterin and Apo A-I were the most predominant proteins in the case of the ultracentrifuged systems. However, absolute protein

quantity results were not provided, and the abovementioned controls were not run. To the extent of our knowledge, only a recent work from Alberg *et al*.[163] has considered it. Notoriously, they demonstrated that most of the more relevant proteins found in the corona of three different polymeric micelles, such as albumin, did, indeed, co-separate with the particles, being the actual protein corona of these systems almost neglectable.

1.2.7.1.3. Separation

The objective of this step is to separate the bound proteins from the NPs so that they can be subsequently identified. There are two main strategies of separation: desorption and direct digestion.[97]

The desorption process aims to separate the adsorbed proteins from the NPs' surface. Sodium dodecyl sulfate (SDS), an anionic and denaturing surfactant, is preferred because of its high protein solubilizing properties. Different times (5 min – 2 h), temperatures (50 – 95 °C), and SDS concentrations (2 – 20 %) are reported in the literature.[30,79,146,165] Furthermore, a reducing agent such as dithioerythritol, dithiothreitol (DTT), or 2-mercaptoethanol (BME) must be added to prevent the oxidation of the thiol groups and the formation of disulfide bonds between cysteine residues from the proteins.[28,146] A disadvantage of this process is that SDS may not be able to desorb some tightly-bound proteins, which some authors call "interfacial protein corona".[109,166] After SDS incubation, the addition of acetonitrile (ACN) and KCl solutions can lead to additional protein detachment, but these solutions alone have a lower desorption power than SDS. Finally, since SDS is an anionic detergent, it is not suitable for 2D- polyacrylamide gel electrophoresis (PAGE) analysis, where the separation in one dimension depends on the proteins' charge.[166,167] Other explored solutions include urea[30] and detergents such as 3-[(3-cholamidopropyl)dimethylammonio]-1-propanesulfonate (CHAPS; zwitterionic and non-denaturing), 2-[4-(2,4,4-trimethylpentan-2-yl)phenoxy]ethanol (Triton X-100; non-ionic and non-denaturing), and dodecyltrimethylammonium bromide (DTAB; cationic and denaturing). The effect of these detergents was studied for PS NPs, where both ionic detergents desorbed most of the attached proteins, while the use of CHAPS and TritonX-100 resulted in an inefficient detachment.[165] Techniques such as LC-MS may sometimes require the removal of the NPs from the sample, which can be accomplished by ultracentrifugation after detergent treatment or by excision of protein bands from PAGE gels. Additional centrifugation cycles may be needed until no more unbound proteins can be detected.[146]

The less explored direct digestion involves adding a lysis buffer (such as trypsin) directly to the isolated protein-NP complexes. Then, the solution is centrifuged, and the digested protein fraction is recovered.[97,146] In general, direct digestion presents more limitations than desorption. For example, trypsin might not be able to attack some protein domains if they are hidden from the accessible surface.[168] Also, some protein fragments might interact with the nanosystems and, as they are withdrawn from the analytical solution, will be underestimated in the corona.[169] Finally, since the proteins are digested, the sample is no longer suitable for any analysis that relies on MW or global charge, such as PAGE. Thus, it is necessary to perform LC-MS analysis afterward.

USC UNIVERSIDADE DE SANTIAGO DE COMPOSTELA

1.2.7.1.4. Identification and quantification

One-dimension (1D)- and two-dimension (2D)- PAGE have been widely used as semiquantitative methods for protein analysis.[21,34] However, quantitative data can be obtained after scanning the gel and analyzing the spot or band intensity with image software like ImageJ.[86] Nevertheless, this technique has numerous limitations: a) the spots or bands of the less abundant proteins can be shielded by the intensity of the most abundant ones, such as albumin, b) comparison with the standard map reference may lead to misinterpretation, especially with overlapped spots or close bands,[97] c) some proteins, such as apolipoprotein B-100 (550 kDa), have an MW too high for PAGE analysis and will barely move from the sample well,[34] d) in the case of 2D-PAGE, problems with extreme hydrophobicities and isoelectric points have also been described,[153] e) in 2D-PAGE, desorption cannot be performed with charged detergents such as SDS, f) the individual variability of the donors can alter the plasma protein gel map.[19]

Mass spectrometry (MS) has been proven effective for the characterization of proteins and analysis of complex protein samples due to its capacity to determine a wide range of MWs and isoelectric points and its sensitivity in detecting small amounts of proteins.[170] Depending on the technique used, proteins can be fragmented inside the spectrometer (top-down analysis), making it possible to differentiate isoforms and post-translational modifications, or pre-digested before the LC-MS analysis (bottom-up analysis). Notably, top-down analyses must be done right after the desorption process, while bottom-up analyses require direct digestion or the combination of desorption followed by digestion. In the latest case, two types of digestion can be carried out after desorption: in-solution digestion and in-gel digestion. In the in-solution digestion, trypsin is added to the desorbed protein solution. While this procedure is faster as it does not involve the cast of a PAGE gel, an additional isolation step might be required to remove the extracting agents if they interfere with trypsin. In the in-gel digestion, desorbed proteins are loaded into a 1D-PAGE gel, thus being separated from the remaining nanosystems and desorption agents. Then, bands can be excised for identifying single proteins, or the whole lane can be excised for a general characterization of all the adsorbed proteins.[147] Afterward, gel fragments are dried, and proteins are extracted and digested with trypsin.

1.2.7.1.5. Data quality and necessary controls

Negative controls are critical when studying protein adsorption to nanosystems. The control consisting of the biological medium, e.g., plasma, and the nanosystems incubated with that biological medium should follow the same treatment. Ideally, no protein should be detected when the nanosystems are not present, which would confirm that all the quantified proteins in the original experiment come from the corona of the nanosystem. However, if this is not the case, the isolation methods may lead to enrichment in some specific proteins, causing their overestimation. In that case, it is necessary to subtract the amount of these free proteins from the protein corona profile.

Galmarini *et al.* investigated the importance of running the appropriate controls.[171] In that experiment, they detected 35 proteins adsorbed onto the nanosystem surface with a prevalence higher than 1 % without running a negative control. However, when they ran the control without the NPs, 6 of those proteins were also detected. These results indicate that

the presence of 60 % of the detected proteins was not statistically significant, which strongly compromises the validity of the data obtained without following these recommendations.

Finally, if correlations between the NPs composition and the adsorbed proteins are intended to be established, a complete characterization of the nanosystems' composition should be performed, especially for those with production yields distant from 100 %.

1.2.7.2. *In vivo* protein corona characterization

The possibility of determining the protein corona of NPs after *in vivo* administration is exciting but challenging. The general workflow of *in vivo* protein corona characterization consists of administering the desired system and recovering the administered nanosystem from the living organism.

The usual way to administer the nanoformulations intravenously in mice is by injection in the tail vein[172–175] or the subclavian vein.[110] Circulating times between 5 min and 6 h were studied for different nanosystems to determine protein corona formation kinetics. Afterward, blood is recovered through a cardiac puncture or the saphenous vein (30 µL – 1 mL) and subjected to centrifugation cycles to separate the protein-nanosystems from the blood cells.[172] Subsequently, the workflow explained in the *in vitro* section is applied.

Recently, Hadjidemetriou and coworkers conducted the first human *in vivo* protein corona characterization experiment in patients treated with Caelyx® (PEGylated doxorubicin-encapsulated liposomes).[176] Blood was extracted after perfusing the liposomes for up to 90 min, and their protein corona composition was determined. Surprisingly, the results showed that cDNA clone CS0DD006YL02 protein was the most abundant protein in the protein corona despite its limited plasmatic concentration, followed by Ig µ chain C, α-2-macroglobulin, fibrinogen β and α chains, and Apo B.

The *in vivo* protein corona determination has the additional shortcoming of not recovering the total number of administered NPs. Logically, since the protein corona varies from particle to particle, those proteins adsorbed onto the particles that are preferentially internalized, cleared, and accumulated in an organ will be underestimated.

Furthermore, different authors have compared *in vivo* and *in vitro* protein adsorption and found the correlation of these data to be scarce.[172,175,176] Therefore, further studies are required to determine how relevant the *in vitro* protein corona determination is for predicting the nanosystems' biological fate.

1.2.8. Future perspectives

Currently, the search for models that might predict the protein corona composition and the consequences that such corona might have on the *in vivo* fate of the nanosystems is under consideration. For example, some authors are trying to develop *in silico* protein corona predictor models,[151] which might represent the final piece of the puzzle for an accurate *in vitro/in vivo* extrapolation.[171] However, an entirely accurate protein corona predictive model has not been achieved yet.

USC UNIVERSIDADE DE SANTIAGO DE COMPOSTELA

On the other hand, the protein corona has been proposed as an indicator of an early stage of diseases such as early central nervous system tumors,[177] melanoma, and lung cancer.[178] The disease-driven protein alterations may be so subtle that they cannot be detected with standard blood tests. However, it has been hypothesized that, since the protein corona would act as a concentrator of the proteins of interest, it will allow their evaluation. Nevertheless, this attractive idea has some limitations. First, it is necessary to rationally design a nanosystem that would tend to recruit the specific proteins whose circulating levels are altered in that disease.[179] Second, the nanosystems and trapped proteins would need to be recovered from the bloodstream accurately to perform the proteomic analysis. Hence, research in this field would have to advance before assessing the value of this diagnostics approach.

1.3. OBJECTIVES

The objective of this work has been the physicochemical characterization of blank NCs by dynamic light scattering (DLS), laser Doppler electrophoresis (LDE), nanoparticle tracking analysis (NTA), electronic microscopy, and AF4, the quantitative analysis of their composition by LC-MS/MS, and the protein corona characterization after incubation with human plasma under the Minimum Information about Nanomaterial Biocorona Experiments (MINBE) recommendations.

Altogether, this exhaustive characterization of the NCs, never performed until now, was critical for selecting suitable candidates for loading therapeutic agents for lung cancer treatment (Chapters 2-3).

2. MATERIALS AND METHODS

2.1. PREPARATION OF NANOCAPSULES

NCs were prepared by solvent displacement (SD)[3] or self-emulsifying (SE)[4] techniques using the following materials: 1,2-dioleoyl-3-trimethylammonium-propane chloride (DOTAP; Avanti Polar Lipids, Alabaster, AL, USA), acetone (Thermo Fisher Scientific, Waltham, MA, USA), benzethonium chloride (BZT; Spectrum Chemical Mfg. Corp., New Brunswick, NJ, USA), caprylic/capric triglyceride (Miglyol® 812N; IOI Oleo GmbH, Hamburg, Germany), D-α-tocopherol polyethylene glycol 1000 succinate (TPGS; Antares Health Products, Jonesborough, TN, USA), DL-α-tocopherol (MilliporeSigma, Burlington, MA, USA), ethanol absolute (Scharlau, Barcelona, Spain), hexadecyltrimethylammonium bromide (CTAB; Sigma-Aldrich, St. Louis, MO, USA), hyaluronic acid 41 – 65 kDa (HA; Lifecore Biomedical, Chaska, MN, USA), Kolliphor® HS15 (BASF SE, Ludwigshafen, Germany), lecithin (Epikuron™ 145V; phosphatidylcholine content: 51.7 % w/w; Cargill, Wayzata, MN, USA), phosphate buffered saline tablets (Thermo Fisher Scientific, Waltham, MA, USA), polyethylene glycol (5 kDa) poly-α-glutamic acid (10 u) (PEG·PGA; Polypeptide Therapeutic Solutions, Paterna, Spain), polysialic acid 26 kDa (PSA; Serum Institute of India, Pune, India), and polysorbate 80 (P80; Tween® 80; Merck KGaA, Darmstadt, Germany).

For SD-*l*-PEG-HA, 500 µL of oil phase (27 $mg \cdot mL^{-1}$ DL-α-tocopherol, 8 $mg \cdot mL^{-1}$ TPGS, and 1 $mg \cdot mL^{-1}$ BZT in ethanol) were poured onto 1.5 mL of aqueous phase (1.33 $mg \cdot mL^{-1}$ HA) under magnetic stirring at 700 rpm. Stirring was kept until NCs' volume was lower than

1.5 mL. Then, it was raised to 2 mL using ultrapure water. If isolation was necessary, the sample was ultracentrifuged at an average of 110,000 g (40,000 rpm) for 1 h at 15 °C in an Optima^{TM} L-90 K Ultracentrifuge equipped with a 70.1 Ti rotor and 10 mL open-top thickwall polycarbonate tubes 16 × 76 mm (Beckman Coulter, Brea, CA, USA). The infranatant was removed using a syringe and discarded. Finally, the supernatant volume was raised to 750 µL with ultrapure water.

For SD-*l*-PEG-PEG·PGA, 900 µL of oil phase (15 mg·mL^{-1} DL-α-tocopherol, 4.44 mg·mL^{-1} TPGS, and 0.56 mg·mL^{-1} DOTAP in ethanol) were poured onto 2.231 mL of PEG·PGA 0.89 mg·mL^{-1} in water under magnetic stirring at 700 rpm. Stirring was kept until the NCs' volume was lower than 1.0 mL. Then, it was raised to 2 mL using ultrapure water. If isolation was necessary, it was ultracentrifuged at ≈ 110,000 g (40,000 rpm) for 1 h at 15 °C. Next, the infranatant was removed using a syringe and kept separately. Finally, the supernatant volume was raised to 750 µL by adding ultrapure water.

For SD-*b*-PEG-HA, 500 µL of oil phase (27 mg·mL^{-1} caprylic/capric triglyceride, 8 mg·mL^{-1} P80, and 1 mg·mL^{-1} BZT in ethanol) were poured onto 1.5 mL of aqueous phase (1.33 mg·mL^{-1} HA) under magnetic stirring at 700 rpm. Stirring was kept until the NCs' volume was lower than 1.5 mL. Then, it was raised to 2 mL using ultrapure water. If isolation was necessary, the sample was ultracentrifuged at ≈ 110,000 g (40,000 rpm) for 1 h at 15 °C. The infranatant was removed using a syringe and discarded. Finally, the supernatant volume was raised to 750 µL by adding ultrapure water.

For SD-noPEG-HA and SD-noPEG-PSA, 5 mL of oil phase (2.96 mg·mL^{-1} of caprylic/capric triglyceride, 0.75 mg·mL^{-1} of lecithin, and 0.15 mg·mL^{-1} of CTAB in a mixture of acetone and ethanol 19:1) were added dropwise using a Pasteur pipette to 10 mL of a 0.25 mg·mL^{-1} aqueous solution of the polymer (HA or PSA) under magnetic stirring at 700 rpm. Acetone was removed using a rotavapor until the sample volume was 5 mL. If isolation was necessary, it was ultracentrifuged at ≈ 43,000 g (25,000 rpm) for 30 min at 15 °C. The infranatant was removed using a syringe and discarded. Finally, the supernatant volume was raised to 750 µL by adding ultrapure water.

For SD-noPEG-PEG·PGA, 1070 µL of oil phase (12.62 mg·mL^{-1} DL-α-tocopherol and 0.47 mg·mL^{-1} DOTAP in ethanol) were poured onto 2.907 mL of water under magnetic stirring at 700 rpm. After 10 min, 66.67 µL of PEG·PGA 30 mg·mL^{-1} in water were added to the formulation. Stirring was kept until the NCs' volume was lower than 2.0 mL. Then, it was raised to 2 mL using ultrapure water. If isolation was necessary, it was ultracentrifuged at ≈ 110,000 g (40,000 rpm) for 1 h at 15 °C. Next, the infranatant was removed using a syringe and kept separately. Finally, the supernatant volume was raised to 750 µL by adding ultrapure water.

For SE-*b*-PEG-HA, 4.375 mL of aqueous phase (0.286 mg·mL^{-1} of HA and 2.86 mg·mL^{-1} of macrogol-15-hydroxystearate in PBS 1 ×) were quickly poured over the oil phase (295 mg of caprylic/capric triglyceride, 290 mg of P80, and 1 mg of BZT) at 1100 rpm using a micropipette. If isolation was necessary, it was subjected to tangential flow filtration (TFF) (KrosFlo® KR2i, Repligen, Waltham, MA, USA) with a 500 kDa-cut off modified polyethersulfone (mPES) column. The resulting ≈ 5 mL NCs solution was continuously diafiltered until three original volumes were collected as permeate with PBS as exchanging buffer at 9 mL·min^{-1}. With these conditions, the transmembrane pressure was kept below 0.2 bar, taking approximately 50 min for the filtration to complete.

USC DE SANTIAGO DE COMPOSTELA

2.2. CHARACTERIZATION OF THE SIZE, Z-POTENTIAL, PH, AND MORPHOLOGY OF NANOCAPSULES

Dynamic light scattering (Zetasizer® Nano ZS, Malvern Instruments, Malvern, UK) was used to characterize the nanosystems' hydrodynamic diameter and polydispersity index. The derived count rate (DCR), a measurement of the number of photons reaching the Zetasizer's photodiode detector in the absence of the laser attenuation filter, namely, a measurement of the global scattering intensity of the sample, was also taken into account. ζ-potential was measured by laser Doppler electrophoresis with the same equipment. Unless indicated otherwise, measurements were done after diluting the samples 10 × in ultrapure water, with an automatic run number and length at 25 °C. pH was measured with a Sartorius Docu-pHmeter equipped with a HANNA Instruments HI1330 electrode. Nanoparticle tracking analysis (NanoSight® NS300, Malvern Instruments, Malvern, UK) was used for additional hydrodynamic diameter characterization and for determining the concentration of NCs. Three replicates of NCs (10,000 ×-diluted in their formulating buffer) were analyzed. Measurements consisted of 5 60 s videos, recorded at 25 °C and subsequent processing with NanoSight NTA software v3.2. The superficial area was calculated using Equation 1:

$$A = 10^{-18} \cdot \pi \cdot \bar{d}^2 \cdot \bar{c}$$

Where A is the area per volume of formulation in $m^2 \cdot mL^{-1}$. $\bar{d}$ is the average hydrodynamic diameter measured by DLS in nm. And $\bar{c}$ is the average of the concentrations obtained from each NTA replicate in particles$\cdot mL^{-1}$.

Equation 1. Calculation of the surface area of NCs

Scanning electron microscopy (SEM) and scanning transmission electron microscopy in SEM (STEM-in-SEM) images were used for examining the NCs morphology by an Ultra Plus (Zeiss, Oberkochen, Germany) field emission-scanning electron microscope (FE-SEM) incorporating an in-lens secondary electron detector, a dedicated STEM detector, and a 12-TEM grids SEM sample stage that allows STEM-in-SEM imaging. Images were acquired with SmartSEM software (Zeiss, Oberkochen, Germany). The working distances were kept between 2.8 and 3.1 mm. Samples were diluted 100 – 10,000 × and, due to the low contrast of NCs in EM, mixed 1:1 with a phosphotungstic acid aqueous solution (2 % w/v) (Sigma-Aldrich, St. Louis, MO, USA) to perform a negative stain of the preparation. Next, 1 µL of the suspension was placed on copper grids with carbon films (CF400-CU, Electron Microscopy Sciences, Hatfield, PA, USA) and dried in a ventilated environment. The phosphotungstic acid excess on the grids was washed dropwise with 1000 µL of ultrapure water. Grids were dried before observation.

For the cryo-EM preparation, SD-noPEG-PEG·PGA and SE-*b*-PEG-HA were diluted 3 × in ultrapure water and PBS, respectively, and pipetted onto 200-mesh Quantifoil R 2/2 graphene oxide-coated grids. Grids were vitrified using a Vitrobot (Mark III; FEI) and visualized in a JEM-2200FS 200 kV TEM (JEOL, Ltd.) equipped with a K 2 direct detection camera at 30,000 × magnification.

USC UNIVERSIDADE DE SANTIAGO DE COMPOSTELA

2.3. PLASMA PREPARATION

Human blood from healthy donors was collected by venipuncture in Vacutainer citrated (3.8 %) vials at the University of Santiago de Compostela (Spain), with the approval of the Santiago and Lugo research ethic committee (Reference 2019_466). Citrated plasma was separated from the other blood components by centrifugation at 1,200 g for 10 min (Eppendorf™ 5702 centrifuge, Eppendorf AG, Hamburg, Germany) in the 2 h following collection. Then, plasma was pooled to avoid inter-individual differences, aliquoted, and stored at –80 °C. Before each experiment, plasma aliquots were thawed overnight at 4 °C and centrifuged at 20,000 g for 1 h at 4 °C (Eppendorf™ 5430 R centrifuge, Eppendorf AG, Hamburg, Germany). If cream-like supernatant or pellet were present, they were discarded. Once thawed, plasma was used within the next 24 h.

2.4. COLLOIDAL STABILITY

The colloidal stability of the different NCs in plasma was evaluated by incubating 10 % of NCs with 90 % of human plasma at 37 °C. Then, the samples were diluted 10 × before measuring their hydrodynamic diameter, PDI, and DCR at different time points by DLS, as indicated in the section "2.2. Characterization of the size, Z-potential, pH, and morphology of nanocapsules".

The NCs' colloidal stability in inorganic solutions of different ionic strengths and pHs was studied after diluting the nanosystems 100 × in the corresponding media and incubating at room temperature (RT). NaCl was purchased from Acofarma (Terrassa, Spain). Citric acid, sodium hydrogen phosphate dihydrate, sodium carbonate, and sodium hydrogen carbonate were purchased from Sigma-Aldrich (St. Louis, MO, USA).

In all cases, samples were subjected to mild horizontal shaking during the whole incubation time (300 rpm, Heidolph Titramax/Inkubator 1000, Heidolph Instruments, Schwabach, Germany).

2.5. SIZE CHARACTERIZATION AND HA ASSOCIATION EFFICIENCY BY AF4

2.5.1. Equipment

Separation by asymmetric flow field-flow fractionation (AF4) was performed using an AF2000 separation system (Postnova Analytics, Landsberg, Germany) equipped with a PN1130 isocratic pump and degasser, an inline PVDF filter 0.1 µm (Millipore, MA, USA), and an autosampler with an injection loop of 103 µL. Data were evaluated with AF2000Control version 2.1.0.4 software (Postnova Analytics, Landsberg, Germany). The separation was performed on a channel composed of a regenerated cellulose membrane (molecular weight cut-off of 1 kDa) and a polytetrafluoroethylene spacer of 350 µm thickness. The AF4 equipment was coupled to a UV-Vis spectrophotometer (PN3211) set up at λ = 280 nm, a multi-angle laser light scattering (MALS, PN3609), and a refractive index detector (RI, PN3150).

USC UNIVERSIDADE DE SANTIAGO DE COMPOSTELA

2.5.2. Fractionation methods

Different fractionation methods were used to quantify HA in each sample and based on the classic method for quantifying the extent of PEGylation developed by Zillies *et al.*.[180]

The amount of HA associated with the NCs was quantified at a low ionic strength (1 mM) using the refractive index (RI) detector.

For SD-*b*-PEG-HA, the method consisted of 1 mM NaCl as the carrier fluid, injection volume of 40 µL (approx. total concentration 10 $mg \cdot mL^{-1}$), injection flow of 0.2 $mL \cdot min^{-1}$, and outlet flow of 0.5 $mL \cdot min^{-1}$. The cross-flow program was: 1.5 $mL \cdot min^{-1}$ during injection (6 min), transition (1 min), and the first 10 min of elution. Then, it was lowered from 3 to 0.5 $mL \cdot min^{-1}$ in 5 min, from 0.5 to 0.05 $mL \cdot min^{-1}$ in 13 min, and from 0.05 to 0 $mL \cdot min^{-1}$ in 15 min. The cross-flow was then kept at 0 for 10 min to ensure complete sample elution. A 1 $mg \cdot mL^{-1}$ HA solution was analyzed instead of the nanosystem as a standard.

For SE-*b*-PEG-HA, the method consisted of 1 mM NaCl as the carrier fluid, injection volume of 2 – 3 µL (approx. total concentration 119 $mg \cdot mL^{-1}$), injection flow of 0.2 $mL \cdot min^{-1}$, and outlet flow of 0.5 $mL \cdot min^{-1}$. The cross-flow program was: 1.5 $mL \cdot min^{-1}$ during injection (6 min) and transition (1 min). Then, it was lowered from 1.5 to 0.5 $mL \cdot min^{-1}$ in 10 min, from 0.5 to 0.1 $mL \cdot min^{-1}$ in 20 min, from 0.1 to 0.01 $mL \cdot min^{-1}$ in 10 min, and finally from 0.01 to 0 $mL \cdot min^{-1}$ in 35 min. The cross-flow was kept constant at 0 for 10 min to ensure complete sample elution. A 0.25 $mg \cdot mL^{-1}$ HA solution was analyzed instead of the nanosystem as a standard.

Calibration curves were built at 4 calibrating levels in duplicate in the range of 20 – 50 µg using the area under the curve of the RI detector in the time window between the end of the first peak and the starting of the micelle/NCs peak. Samples were analyzed in triplicate, with two injections per replicate, using the AF2000Control version 2.1.0.4 software (Postnova Analytics, Landsberg, Germany).

2.6. ANALYSIS OF THE COMPOSITION OF NANOCAPSULES BY LC-MS/MS

2.6.1. Equipment

The isolated nanosystems' actual compositions were characterized by LC-MS using the Waters Acquity H-Class UHPLC equipment (Waters Corporation, Milford, MA, USA) equipped with a 50 µL extension loop and a Waters Xevo TQD detector. For all tested molecules but PEG·PGA, a Kinetex® 1.7 µm C18 100 Å 50 × 2.1 mm column was used. In the latest case, a Kinetex® 1.7 µm hydrophilic interaction liquid chromatography (HILIC) 100 Å 50 × x 2.1 mm column was used instead (Phenomenex, Torrance, CA, USA). Experimental procedures were done accordingly to the work of Berrecoso *et al.*.[2]

UHPLC-MS/MS analysis is a robust technique for quantifying a wide variety of different molecules. First, the high resolving power of UHPLC allows the separation of the compounds in a relatively low time. Second, the MS/MS detector offers high sensitivity and selectivity. Our equipment consisted of an electrospray ionization source and a triple quadrupole detector, which can operate in mainly two quantitative detection modes: selected ion monitoring (SIM) and multiple reaction monitoring (MRM). In both cases, the original molecules are ionized in the MS source (Q0) by high declustering potential, becoming the parent ions. Then, the first

quadrupole mass filter (Q1) is used to select the parents of interest. In the case of MRM, parents are subjected to a controlled collision with argon in the quadrupole collision cell (Q2). Different collision energies will produce different fragmentation patterns, and the fragments (daughters) of interest are selected in the second quadrupole mass filter (Q3). Finally, selected ions reach the photomultiplier detector, where they are quantified. MRM provides better signals and higher signal-to-noise ratios than SIM due to its higher specificity. However, there are some cases where the use of SIM might be more indicated than MRM. For example, sometimes parents cannot be fragmented into any daughter. On other occasions, the intensity of the generated daughters is not stable or concentration-dependent. Also, some parents can be simultaneously fragmented into a high number of daughters, making each daughter's signal significantly weaker than the parent's signal, increasing the LoD and LoQ. Lastly, in some cases, using a pseudoMRM technique, in which the quadrupoles Q1 and Q3 are used to quantify the same parent ion, can lead to higher intensities or signal/noise ratios than SIM.

2.6.2. Sample preparation

The total concentration of the NCs' components was analyzed before isolation. Then, the bound and unbound component concentrations were calculated by analyzing the isolated fraction containing the purified NCs (cream-like supernatant or retentate) and the waste fraction (infranatant or permeate). Bound and unbound concentrations were compared to the total detected concentration before isolation.

For each NCs prototype, the compositional analysis was carried out with two different sample treatments.

In the first analysis, all the molecules but the polymer were quantified after dilution in ACN. The dilution factors varied with each sample to fit the analyte concentrations in their calibrating range. In the case of SD-*l*-PEG-HA, the non-isolated formulations and the infranatant solutions were diluted 3,750 ×. The SD-*l*-PEG-HA cream-like supernatant was diluted 10,000 × instead. In the case of SD-noPEG-HA and SD-noPEG-PSA, the formulations were diluted 500 × before rotary evaporation, while the infranatant solutions were diluted 667 × after ultracentrifugation, and the cream-like supernatants were diluted 5,000 ×. For SE-*b*-PEG-HA, the formulations before tangential flow filtration and the retentates were diluted 25,000 ×, while the permeates were diluted 8,333 ×. Finally, in the case of SD-noPEG-PEG·PGA and SD-*l*-PEG-PEG·PGA, the non-isolated formulations and the infranatant solutions after ultracentrifugation were diluted 4,000 ×, while the cream-like supernatants were diluted 10,000 ×.

During the second analysis, the analytes were mixed with strong acids to digest the polymers. On the one hand, the carbohydrate-containing formulations (coated with HA or PSA) were digested in H_2SO_4. In the case of SD-*l*-PEG-HA, 60 µL of the samples (non-isolated formulation, infranatant, or cream-like supernatant) were mixed with 40 µL of ethanol and heated in a water bath at 68 °C in a 2-mL microtube. For SD-noPEG-HA and SD-noPEG-PSA, 69.5 µL of formulation were mixed with 16.8 µL of ethanol and 13.7 µL of water before centrifugation, while the cream-like supernatants and infranatants were treated as in the SD-*l*-PEG-HA formulation. In the case of SE-*b*-PEG-HA, 60 µL of non-isolated formulation and retentate were mixed with 40 µL of ethanol, while 180 µL of permeate were mixed with 20 µL of ethanol. In all the previous cases but the permeate of SE-*b*-PEG-HA, 125 µL of 4 M H_2SO_4 (prepared from H_2SO_4 96 %, Panreac Química, Castellar del Vallès, Spain) pre-heated at 68 °C

were added to each tube. Digestions were carried out for exactly 60 s; then the acid was neutralized with 1 mL of 1 M aqueous solution of NaOH (prepared from solid NaOH, Sigma-Aldrich, St. Louis, MO, USA), shaken for 10 min at 2,000 rpm, and centrifuged at 20,817 g, 10 min, 20 °C. In the case of the permeate of SE-*b*-PEG-HA, where more sample volume was needed due to the low HA concentration, 250 µL of 4 M aqueous H_2SO_4 and 400 µL of NaOH 5 M were used instead. Consequently, monomers, dimers, and oligomers of these carbohydrates were generated. On the other hand, polyaminoacid-containing formulations (coated with PEG·PGA) were digested in HCl. In the case of SD-noPEG-PEG·PGA and SD-*l*-PEG-PEG·PGA, 85 µL of formulations before ultracentrifugation, infranatants, and 1.63 × diluted cream-like supernatants in ultrapure water were mixed with 15 µL of ethanol and 100 µL of 37 % HCl (Panreac Química, Castellar del Vallès, Spain) in a screw-capped 1.5-mL microtube. Tubes were shaken and put in an oil bath at 110 °C for 24 h. Then, 800 µL of NaOH 1.5 M were added to each vial. PEG·PGA samples were shaken and centrifuged as abovementioned for other polymers.

All digested samples, independently of their carbohydrate- or polyaminoacid-coating, were filtered through Millex® - GV 0.22 µm PVDF filter units (Merck, Darmstadt, Germany) after their first dilution with ACN or after the centrifugation step performed following the polymer digestion.

Analytes were injected three times per replicate. A total of 3 different NCs' replicates were performed.

2.6.3. Standard preparation

The calibration curves of the NCs' components were constructed from mixtures in the same ratio as the theoretical composition. 8 concentration levels were used for calibration except for polymers, where 6 levels were used instead. Calibrating samples were filtered through 0.22 µm PVDF filters after their first dilution with ACN or after neutralizing their acidic digestion. Standards were injected thrice, and a new calibration curve was done with each NCs' replicate.

Calibration curves for non-polymeric compounds were prepared by mixing the compounds to be analyzed at this stage and the polymeric coating at their maximum theoretical concentration to mimic the sample. Calibration curves for polymeric compounds (HA, PSA, and PEG·PGA) were done by digesting a final volume of 100 µL (except for the permeate of SE-*b*-PEG-HA, which was 200 µL) containing all the other compounds present in the samples. In the case of the bound and free fraction analysis, artificial matrixes were built considering the results obtained after the quantification of the non-polymeric compounds. The standard solvent ratios were matched with the ones of the analytes, with a 3:2 (v/v) water:ethanol mixture in all cases of carbohydrate quantification but two samples. These exceptions were the non-isolated SD-noPEG formulations, whose solvent was 30:11:9 (v/v) water:acetone:ethanol, and the permeate of SE-*b*-PEG-HA, which was 9:1 water:ethanol. The ethanol percentage of the calibrating solutions for PEG·PGA was 15 % (v/v). The digestion and following steps were carried out as abovementioned. Calibrating ranges for each substance are detailed in Supplementary Table 1.

USC UNIVERSIDADE DE SANTIAGO DE COMPOSTELA

2.6.4. Mass spectrometry method

The MS/MS detector was tuned differently for the non-polymeric substances, the carbohydrates, and the polyaminoacids. In the first case, the parameters were used as follows. Ionization mode: positive electrospray ionization [ESI (+)]. Source capillary voltage: 3.50 kV. Desolvation temperature: 600 °C. Source temperature: 150 °C. Desolvation gas flow: 900 $L \cdot h^{-1}$. Cone gas flow: 10 $L \cdot h^{-1}$. In the case of HA and PSA, the following parameters were used instead. Source capillary voltage: 3.20 kV. Desolvation temperature: 450 °C. Desolvation gas flow: 350 $L \cdot h^{-1}$. MS parameters for PEG·PGA analysis were the following. Source capillary voltage: 1.00 kV. Desolvation temperature: 550 °C. Desolvation gas flow: 1000 $L \cdot h^{-1}$. Cone gas flow: 50 $L \cdot h^{-1}$. The conditions used for quantifying each molecule are summarized in Table 3.

Table 3. MS or MS/MS methods for quantifying all the molecules present in the NCs

Substance	Method
DL-α-tocopherol	MRM, *m/z* 431.4 → 165.0, DP: 40 V, CE: 18 eV
Benzethonium chloride	MRM, *m/z* 412.3 → 91.0, DP: 45 V, CE: 44 eV
D-α-tocopherol polyethylene glycol 1000 succinate	MRM, *m/z* 557.4 → 99.0, DP: 50 V, CE: 30 eV
Hexadecyltrimethylammonium bromide	MRM, *m/z* 284.3 → 60.1, DP: 2 V, CE: 28 eV
1,2-dioleoyl-3-trimethylammonium propane chloride	MRM, *m/z* 662.6 → 603.5, DP: 54 V, CE: 30 eV
Miglyol® 812N	MRM, *m/z* 488.4 → 327.2, DP: 30 V, CE: 14 eV
	MRM, *m/z* 516.4 → 355.3, DP: 32 V, CE: 16 eV
	MRM, *m/z* 544.5 → 355.3, DP: 34 V, CE: 18 eV
	MRM, *m/z* 572.5 → 383.3, DP: 36 V, CE: 18 eV
Phosphatidylcholines (Epikuron™ 145V)	MRM, *m/z* 756.6 → 184.1, DP: 50 V, CE: 30 eV
	MRM, *m/z* 758.6 → 184.1, DP: 50 V, CE: 30 eV
	MRM, *m/z* 780.6 → 184.1, DP: 50 V, CE: 30 eV
	MRM, *m/z* 782.5 → 184.1, DP: 50 V, CE: 30 eV
Macrogol-15-hydroxystearate (Kolliphor® HS15)	PseudoMRM, *m/z* 309.3 → 309.3, DP: 90 V, CE: 5 eV
Polysorbate 80	MRM, *m/z* 804.6 → 309.3, DP: 30 V, CE: 40 eV
Digested hyaluronic acid	SIM, *m/z* 759.2, DP: 100 V
Digested polysialic acid	SIM, *m/z* 274.1, DP: 100 V
Digested polyethylene glycol poly-α-glutamic acid	MRM, *m/z* 148.1 → 84.1, DP: 18 V, CE: 16 eV

CE: collision energy. DP: declustering potential. MRM: multiple reaction monitoring. MS: mass spectrometry. PseudoMRM: pseudo-multiple reaction monitoring. SIM: Selected ion monitoring. Adaptation from [2] licensed under a Creative Commons CC BY license.

2.6.5. Chromatographic method

Chromatographic methods for all the compounds but the polymers and the polymeric coatings were developed for each NCs prototype. In the first case, all the compounds but the polymers were analyzed with the following solvents: Solvent A: 50 mM formic acid (HCOOH) (VWR International, Radnor, PA, USA) and 2 mM ammonium formate (NH_4HCOO) (Sigma-Aldrich, St. Louis, MO, USA) aqueous solution. Solvent B: 95 % ACN (Scharlau, Barcelona, Spain) and 5 % water containing 50 mM HCOOH and 2 mM NH_4HCOO (v/v). Solvent C: water. Solvent D: isopropyl alcohol (VWR International, Radnor, PA, USA). The injection

volume was 5 μL, the column temperature was 50 °C, the sample temperature was 20 °C, and the flow rate was 0.400 $mL \cdot min^{-1}$. The chromatographic method for the non-polymeric substances of each formulation is detailed in Table 4.

Table 4. Chromatographic method for the analysis of non-polymeric substances by UHPLC-MS/MS

Formulation	Time (min)	Solvent A (%)	Solvent B (%)	Solvent C (%)	Solvent D (%)
SD-*l*-PEG-HA	0.00	90	10	0	0
	1.00	70	30	0	0
	1.10	0	100	0	0
	6.90	0	100	0	0
	7.00	0	0	100	0
	10.40	0	0	100	0
	10.50	70	30	0	0
	12.00	70	30	0	0
SD-*l*-PEG-PEG·PGA	0.00	70	30	0	0
	1.00	70	30	0	0
	1.10	0	100	0	0
	8.00	0	100	0	0
	8.10	0	0	100	0
	10.00	0	0	100	0
	10.10	70	30	0	0
	12.00	70	30	0	0
SD-noPEG-HA and SD-noPEG-PSA	0.00	90	10	0	0
	0.10	90	10	0	0
	0.11	0	40	0	60
	2.90	0	40	0	60
	2.95	0	0	100	0
	4.00	0	0	100	0
	4.05	90	10	0	0
	5.00	90	10	0	0
SD-noPEG-PEG·PGA	0.00	70	30	0	0
	1.00	70	30	0	0
	1.10	0	50	0	50
	3.00	0	50	0	50
	3.10	0	0	100	0
	4.50	0	0	100	0
	4.60	70	30	0	0
	6.00	70	30	0	0
SE-*b*-PEG-HA	0.00	70	30	0	0
	0.20	70	30	0	0
	0.30	40	60	0	0
	5.30	24	76	0	0
	6.80	0	100	0	0

USC UNIVERSIDADE DE SANTIAGO DE COMPOSTELA

Table 4. Chromatographic method for the analysis of non-polymeric substances by UHPLC-MS/MS (continuation)

Formulation	Time (min)	Solvent A (%)	Solvent B (%)	Solvent C (%)	Solvent D (%)
	8.50	0	30	0	70
	9.50	0	30	0	70
	9.60	0	0	100	0
	14.00	0	0	100	0
	14.10	70	30	0	0
	16.00	70	30	0	0

Solvent A: 50 mM formic acid and 2 mM ammonium formate in water. Solvent B: 95 % acetonitrile and 5 % 2 mM ammonium formate aqueous solution (v/v) 50 mM formic acid. Solvent C: water. Solvent D: isopropyl alcohol. **Abbreviations:** UHPLC-MS: ultra-performance liquid chromatography-mass spectrometry. The compositions of SD-*l*-PEG-HA, SD-*l*-PEG-PEG·PGA, SD-noPEG-HA, SD-noPEG-PSA, SD-noPEG-PEG·PGA, and SE-*b*-PEG-HA are shown in Figure 5. Adaptation from [2] licensed under a Creative Commons CC BY license.

The carbohydrates fragments were analyzed based on the work of Vigliano *et al.*.[181] Solvent A was 50 mM HCOOH and 2 mM NH_4HCOO aqueous solution; solvent B was methanol (Thermo Fisher Scientific, Waltham, MA, USA). The injection volume was 50 µL. The column and sample temperatures were not modified, and the flow rate was 0.200 $mL \cdot min^{-1}$. The chromatographic method was equal for HA and PSA (Table 5). The flow was diverted to waste during the first 3.9 min to prevent the non-volatile salt Na_2SO_4 from entering the detector.

In the case of PEG·PGA, solvent A was 75 mM HCOOH and 5 mM NH_4HCOO aqueous solution, and solvent B was 90 % ACN and 10 % water (v/v) containing 75 mM HCOOH and 5 mM NH_4HCOO (Table 6). The injection volume was 5 µL. The column temperature was 35 °C, and the flow rate was 0.300 $mL \cdot min^{-1}$. The flow was diverted to waste during the first 9 min to avoid the non-volatile salt Na_2SO_4 from entering the detector.

Table 5. Chromatographic method for the analysis of digested hyaluronic and polysialic acids by UHPLC-MS/MS

Time (min)	Solvent A (%)	Solvent B (%)
0.00	98	2
2.00	98	2
3.00	60	40
4.00	60	40
4.10	20	80
8.00	20	80
9.00	98	2
13.00	98	2

Solvent A: 50 mM formic acid and 2 mM ammonium formate in water. Solvent B: methanol. **Abbreviations:** UHPLC-MS: ultrahigh-performance liquid chromatography-mass spectrometry. Adaptation from [2] licensed under a Creative Commons CC BY license.

USC UNIVERSIDADE DE SANTIAGO DE COMPOSTELA

Table 6. Chromatographic method for the analysis of digested PEG·PGA by UHPLC-MS/MS

Time (min)	Solvent A (%)	Solvent B (%)
0.00	0	100
6.00	0	100
6.10	5.9	94.1
10.00	17.6	82.4
12.00	29.4	70.6
12.10	0	100
15.50	0	100

Solvent A: 75 mM formic acid and 5 mM ammonium formate in water. Solvent B: 75 mM formic acid and 5 mM ammonium formate in acetonitrile (90 %) and water (10 %) mixture (v/v). **Abbreviations:** UHPLC-MS: ultrahigh-performance liquid chromatography-mass spectrometry. Adaptation from [2] licensed under a Creative Commons CC BY license.

2.6.6. Processing method and data interpretation

Chromatographic peaks were smoothed using the Savitzky-Golay method prior to integration. The calibration curves for linear fit were obtained after 1/x weighting of the obtained areas.

The recovery before isolation was calculated as in Equation 2.

$$Compound's\ recovery\ before\ isolation\ (\%) = \frac{[Compound]_t \cdot DF_t}{[Compound]_{theoretical}} \cdot 100$$

Where the $[Compound]_t$ is the experimental concentration of that compound determined by LC-MS before subjecting the NCs to their isolating methodology. DF_t is the dilution factor applied during the sample processing of the non-isolated NCs. And $[Compound]_{theoretical}$ is the total theoretical concentration of that compound in the formulation.

Equation 2. Calculation of the compound's recovery before isolation (%)

The association efficiency (AE) of each compound was calculated as in Equation 3:

$$AE\ (\%) = \frac{[Compound]_i \cdot DF_i \cdot V_i}{[Compound]_t \cdot DF_t \cdot V_t} \cdot 100$$

Where the $[Compound]_i$ is the experimental concentration of that compound in the fraction containing the isolated particles. $[Compound]_t$ is the experimental concentration of that compound determined by LC-MS before subjecting the NCs to their isolating methodology. DF_i is the dilution factor applied during the sample processing of the isolated fraction of the NCs. DF_t is the dilution factor applied during the sample processing of the non-isolated NCs. V_i is the experimental volume of the isolated fraction of NCs after isolation. And V_t is the theoretical volume of the non-isolated formulations.

Equation 3. Calculation of the compound's AE (%)

USC UNIVERSIDADE DE SANTIAGO DE COMPOSTELA

The compounds' free percentage (unbound fraction) was calculated as in Equation 4:

$$Compound's\ unbound\ fraction\ (\%) = \frac{[Compound]_w \cdot DF_w \cdot V_w}{[Compound]_t \cdot DF_t \cdot V_t} \cdot 100$$

Where the $[Compound]_w$ is the experimental concentration of that compound in the fraction that did not contain the isolated particles (infranatant or permeate). $[Compound]_t$ is the experimental concentration of that compound determined by LC-MS before subjecting the NCs to the isolating methodology. DF_w is the dilution factor applied during the processing of the infranatants or permeates. DF_t is the dilution factor applied during the processing of the non-isolated NCs. V_w is the theoretical volume of the infranatants and the experimental volume of the permeates. And V_t is the theoretical volume of the non-isolated NCs.

Equation 4. Calculation of the compound's unbound fraction (%)

Finally, the production yield, which gives information about the mass of reagents incorporated into the NCs compared to the initial mass, was calculated as in Equation 5.

$$Production\ yield\ (\%) = \frac{\sum AE_{compound} \cdot [Compound]_{theoretical}}{\sum [Compound]_{theoretical}}$$

Equation 5. Calculation of the production yield (%)

2.6.7. Method validation

Method validation was performed following ICH guidelines.[182] Specificity was confirmed by subjecting each compound to the other LC-MS/MS methods and checking that there was no signal in those chromatograms. Linearity was assessed by the coefficients of determination (r^2) (Equation 6) and the percentual relative residuals (%RRES) (Equation 7).

$$r^2 = \frac{\sum_{i=1}^{I} (\hat{y}_i - \bar{y})^2}{\sum_{i=1}^{I} (y_i - \bar{y})^2}$$

Where r^2 is the coefficient of determination. y_i is the value of the experimental responses used to build the calibration curve for a calibrating point i. $\hat{y}_i$ is the value of the responses predicted by the calibration curve for the concentration of y_i. $\bar{y}_i$ is the average of all the experimental responses used to build the calibration curve. And I is the number of calibrating points.

Equation 6. Calculation of the coefficients of determination (r^2)

$$\%RRES\ (\%) = \frac{y_i - \hat{y}_i}{\hat{y}_i} \cdot 100$$

Where $\%RRES$ is the percentual relative residuals. y_i is the value of the experimental responses used to build the calibration curve for a calibrating point i. And $\hat{y}_i$ is the value of the responses predicted by the calibration curve for the concentration of y_i.

Equation 7. Calculation of the percentual relative residuals (%RRES)

USC UNIVERSIDADE DE SANTIAGO DE COMPOSTELA

The quantification limit was calculated as in Equation 8.

$$LoQ = 10 \cdot \sigma_x \cdot S^{-1}$$

Where LoQ is the limit of quantification. σ_x is the standard deviation of the response of 10 blank injections. And S is the slope of the calibration curve.

Equation 8. Calculation of the limit of quantification (LoQ)

Precision and accuracy were proved at three calibration levels (low, medium, and high), by three injections of three different vials, through the pooled relative standard deviations of the signals (pooled RStD%, Equation 9) and the relative differences between the estimated and actual concentrations (RE%; Equation 10) of the standards, respectively.

$$pooled\ RStD\%\ (\%) = \frac{\sum_{l=1}^{L}\left(\sqrt{\frac{\sum_{n=1}^{N}\left[(r-1)_n \cdot \left(\frac{\sigma_{\hat{x}}}{\bar{\hat{x}}}\right)^2_n\right]}{\sum_{n=1}^{N}(r-1)_n}}\right)_l}{L}$$

Where $pooled\ RStD\%$ is the pooled relative standard deviations of the signals. $\sigma_{\hat{x}}$ is the standard deviation of the estimated concentrations for a calibration level l and curve n. $\bar{\hat{x}}$ is the average of the estimated concentrations for a calibration level l and curve n. r is the number of replicates for a calibrating level l on a curve n. N is the number of calibration curves. And L is the number of calibration levels.

Equation 9. Calculation of the pooled RStD%

$$RE\%\ (\%) = \left|1 - \frac{\bar{\hat{x}}}{x}\right| \cdot 100$$

Where $RE\%$ is the relative difference between the estimated and actual concentrations. $\bar{\hat{x}}$ is the average of the estimated concentrations for a calibration level. And x is the concentration used to build the calibration curve.

Equation 10. Calculation of the relative difference between the estimated and actual concentrations (RE%)

Complementarily, the amount of each substance in the formulation before isolation was checked and confirmed to match the theoretical composition. The same determination was also carried out for the two fractions generated after isolation.

2.7. ANALYSIS OF THE PEG DENSITY OF NANOCAPSULES

The amount of attached PEGylated substances, calculated by LC-MS/MS, was used along with the hydrodynamic diameter, measured by DLS, and particle concentration, measured by NTA, for the evaluation of the thickness and disposition of the PEG in the selected NCs. A monodisperse population of NCs with a perfectly spherical shape was assumed. Equations 11 – 17 were extracted from the literature.[111,183,184]

The molar amount of PEGylated molecules per particle for each PEGylated compound was calculated following Equation 11.

$$M_{PEGylated\ molecule}\ (\text{moles per NP}) = \frac{[PEGylated\ molecule]}{[NCs] \cdot MW_{PEGylated\ molecule}} \cdot 100$$

Where $[PEGylated\ molecule]$ is the concentration of the PEGylated molecule in g·mL^{-1}. $MW_{PEGylated\ molecule}$ is the molecular weight of the PEGylated molecule in g per mol. And $[NCs]$ is the NCs concentration, measured by NTA in particles·mL^{-1}.

Equation 11. Calculation of the molar amount of PEGylated molecules

The PEG surface density (Γ) is defined as the number of PEGylated molecules per 100 nm^2 of NCs' surface area. It can be calculated following Equation 12.

$$\Gamma\ (\text{PEG chain}/100\ \text{nm}^2) = \frac{mole_{PEGylated\ molecule} \cdot N_A}{4 \cdot \pi \cdot \left(\frac{d}{2}\right)^2} \cdot 100$$

Where $mole_{PEGylated\ molecule}$ is the amount of PEG chains per particle, in moles. N_A is the Avogadro constant ($N_A = 6.022 \cdot 10^{23}\ \text{mol}^{-1}$). And d is the NCs' hydrodynamic diameter, measured by DLS, in nm.

Equation 12. Calculation of the PEG surface density

The Flory radius (R_F) indicates the polymer size when its surface density is weak. It depends on the number of monomers per polymer chain, the ramifications (branches) of the polymer, and the length of one monomer. The Flory radius of the PEG motifs of linear PEGylated molecules can be calculated as in Equation 13:

$$R_{F_{lineal\ PEG}}\ (\text{nm}) = \alpha \cdot n^{\frac{3}{5}}$$

Where α is the ethylene glycol length (≈ 0.35 nm) and n the number of ethylene glycol monomers.

Equation 13. Calculation of the Flory radius of linear PEG molecules

The Flory radius of the PEG motifs of branched PEGylated molecules can be calculated as in Equation 14:

$$R_{F_{branched\ PEG}}\ (\text{nm}) = \alpha \cdot f^{\frac{2}{5}} \cdot (f \cdot n)^{\frac{3}{5}}$$

Where α is the length of ethylene glycol (≈ 0.35 nm), f is the number of PEG branches, and n is the number of ethylene glycol monomers on each branch.

Equation 14. Calculation of the Flory radius of branched PEG molecules

USC UNIVERSIDADE DE SANTIAGO DE COMPOSTELA

The area occupied by each PEG chain (A) can be calculated as in Equation 15:

$$A\ (\mathrm{nm^2}) = \frac{6 \cdot 10^{-21} \cdot MW_{PEGylated\ molecule}}{d \cdot N_A \cdot w_{PEG/NCs} \cdot q}$$

Where $MW_{PEGylated\ molecule}$ is the molecular weight of the PEGylated molecule. d is the NCs' hydrodynamic diameter, measured by DLS, in nm. N_A is the Avogadro constant ($N_A = 6.022 \cdot 10^{23}\ \mathrm{mol^{-1}}$). $w_{PEG/NCs}$ is the mass fraction of the PEGylated molecule in the NCs, calculated from the concentrations detected by LC-MS/MS. And q is the density of the NCs in $\mathrm{g \cdot mL^{-1}}$.

Equation 15. Calculation of the area occupied by each PEGylated molecule

The distance between PEG molecules (D) was calculated as in Equation 16:

$$D\ (\mathrm{nm}) = 2 \cdot \left(\frac{A}{\pi}\right)^{\frac{1}{2}}$$

Where A is the area occupied by each PEG chain in $\mathrm{nm^2}$.

Equation 16. Calculation of the distance between PEG molecules

The thickness of the PEG layer (L) was calculated as in Equation 17:

$$L\ (\mathrm{nm}) = \frac{f \cdot n \cdot \alpha^{\frac{5}{3}}}{D^{\frac{2}{3}}}$$

Where α is the monomer's length (≈ 0.35 nm). f is the number of PEG branches ($f = 1$ for lineal PEG chains). n is the number of PEG monomers (on each branch, in the case of branched PEGs). And D is the distance between PEG molecules in nm.

Equation 17. Calculation of the thickness of the PEG layer

2.8. PROTEIN CORONA EXPERIMENTS

In the case of the protein characterization experiments, the incubation was performed by mixing 990 µL of undiluted citrated plasma with 110 µL of the nanosystem with the lowest surface area. For the other systems, a volume < 110 µL containing the same superficial area was added to a solution containing 990 µL of undiluted plasma and enough volume to achieve a final volume of 1,100 µL. Consequently, the "plasma volume/NP area" ratio, the available protein amount, and the final volume remained constant. Then, the resulting 1,100 µL were mixed and incubated at 37 °C, with mild shaking of 300 rpm for 1 h (Tritamax 1000, Heidolph Instruments, Schwabach, Germany).

USC UNIVERSIDADE DE SANTIAGO DE COMPOSTELA

2.8.1 Isolation of nanocapsules and their bound proteins

2.8.1.1. Ultracentrifugation

In the separation by ultracentrifugation, 1 mL of incubated sample was mixed with 1 mL of 40 % sucrose solution and placed on the bottom of an ultracentrifuge tube. The sucrose gradient was completed by pouring 2 mL of a 10 % sucrose solution and then 2 mL of ultrapure water. The gradient was ultracentrifuged at ≈ 110,000 g (40,000 rpm) for 1 h at 15 °C with the same equipment of section "2.1. Preparation of nanocapsules". Then, the isolated NCs with their bound proteins were collected by taking 1 mL from the surface of the gradient with a syringe. The rest of the gradient was discarded.

2.8.1.2. AF4

AF4 equipment can be consulted in section "2.3. Plasma preparation". Samples of 90 % human plasma and 10 % SD-*l*-PEG-HA were subjected to AF4 separation. The UV-Vis spectrophotometer was set up at 280 nm, the eluents consisted of 0.9 % aqueous NaCl, and the injection volume was 20 µL. The whole run lasted 43 min and was composed of an initial delay of 2.5 min, followed by a focus step of 4 min at an injection flow of 0.2 $mL \cdot min^{-1}$, cross-flow of 2 $mL \cdot min^{-1}$, and focus pump at 2.3 $mL \cdot min^{-1}$. Then, 1 minute of transition time was set. The elution step consisted of a 5-minute cross-flow gradient from 2 $mL \cdot min^{-1}$ to 1 $mL \cdot min^{-1}$, followed by a 20-minute gradient from 1 $mL \cdot min^{-1}$ cross-flow to 0.5 $mL \cdot min^{-1}$, a 2.5-min gradient from 0.5 $mL \cdot min^{-1}$ to 0 $mL \cdot min^{-1}$, and 10 min of stabilization without cross-flow. 2-mL fractions were recovered, dried in a Genevac miVac Centrifugal Duo Concentrator Quattro Pump (SP Scientific, Gardiner, NY, USA), and resuspended to 80 µL with ultrapure water.

2.8.1.3. Pressure-driven membrane filtration

Two types of pressure-driven membrane filtration mechanisms were evaluated for the isolation of NCs protein corona: a stirred cell and a tangential flow filtration machine.

First, an Amicon® stirred cell of 3 mL (Model 8003) was used with a piece of a Biomax® 500 kDa polyethersulfone ultrafiltration disc (Merck, Darmstadt, Germany). Incubated samples or plasma were diluted 16 × with ultrapure water. 1.2 mL were introduced into the cell and filtered at 4 °C under an N_2 pressure of 2 bars at 200 rpm until 1 mL was recovered. Then, discontinuous diafiltration was performed by washing the retentate with 1 mL of cold PBS and filtering it two more times. Finally, the retentate volume was raised to 1.2 mL with cold PBS and transferred to a microtube.

For the tangential flow filtration procedure, the same equipment as in section "2.1. Preparation of nanocapsules" was used but equipped with a 750 kDa cut-off mPES membrane. 5 mL of 16 × diluted 90 % human plasma in PBS was continuously diafiltered a maximum of five times at a flow rate of 18 $mL \cdot min^{-1}$.

USC UNIVERSIDADE DE SANTIAGO DE COMPOSTELA

2.8.2. Protein solubilization

Samples containing isolated NCs with their bound proteins were mixed 1:1 with 2 × Laemmli sample buffer [25 % stacking buffer 0.5 M Tris-HCl pH 6.8 (Bio-Rad, Hercules, CA, USA), 20 % glycerol (Fagron Ibérica, Terrassa, Spain), 10 % BME, 4.1 % SDS, and 0.0025 % bromophenol blue sodium salt (Sigma-Aldrich, St. Louis, MO, USA)] and boiled at 100 °C for 5 min. In all cases, the incubation with the 2 × sample buffer and subsequential boiling led to the complete solubilization of the NCs' components as the DCR was decreased by more than 98 %. Since the particles no longer exist, the desorption of all the proteins was assured.

2.8.3. Acrylamide-based electrophoresis

10-well 1.5-mm-thick gels were cast using Bio-Rad mini-PROTEAN® 3 Cell. Each gel was composed of 7 mL of resolving gel [33 % of 30 % Acrylamide/Bis solution 37.5:1 and 25 % of resolving buffer 1.5 M Tris-HCl pH 8.8 (Bio-Rad, Hercules, CA, USA), 0.4 % SDS, 0.1 % ammonium persulfate, and 0.04 % *N*,*N*,*N*′,*N*′-tetramethylethylenediamine (Sigma-Aldrich, St. Louis, MO, USA). Gelation was achieved by placing isopropanol over the resolving buffer. Isopropanol was removed, and the stacking buffer (15 % of 30 % Acrylamide/Bis solution 37.5:1, 28 % of stacking buffer 0.5 M Tris-HCl pH 6.8, 0.4 % SDS, 0.1 % ammonium persulfate and 0.1 % *N*,*N*,*N*′,*N*′-tetramethylethylenediamine) was filled until overflow. Unless indicated otherwise, 5 µL of PageRuler Broad Range Unstained Protein Ladder (Thermo Fisher Scientific, Waltham, MA, USA) were used as a reference for molecular weight, and a volume of 25 µL of each sample were added to each well.

Gels were run at 100 V until bromophenol blue reached the bottom (approximately 90 min). Proteins were fixed to the gel by immersion in 40 % methanol (Panreac Applichem, Barcelona, Spain) and 10 % acetic acid (Scharlau, Barcelona, Spain) in water for 1 h with mild agitation. The fixation solution was washed with ultrapure water, and proteins were fluorescently stained with SYPRO® Ruby Protein Gel Stain (Bio-Rad, Hercules, CA, USA) for 18 h in the dark, under the same agitation conditions. Gels were washed with ultrapure water for 5 min and scanned with a Gel Doc XR+ molecular imager (Bio-Rad, Hercules, CA, USA).

2.8.4. Protein digestion

Prior to the proteomic LC-MS/MS, the adsorbed proteins were purified from non-proteic substances, such as residual sucrose, oils, surfactants, and polymers. 12 µL of 1,000 × diluted human plasma, negative control, and samples were mixed 1:1 with 2 × Laemmli buffer, boiled at 100 °C for 5 min, and loaded into a 10-well 10 %-acrylamide PAGE gel, which was run at a constant voltage of 100 V until the front dye penetrated ≈ 3 mm into the resolving gel. Next, gels were stained with Coomassie brilliant blue R250 staining solution (Bio-Rad; Hercules, CA, USA) to show a unique band containing all the proteins. This band was manually excised from each lane and transferred to a low-binding microtube.

Gel fragments were washed twice with 25 mM NH_4HCO_3 (Fluka, Steinheim, Germany) and then with ACN (Scharlau, Barcelona, Spain) until the gel fragments were fully dehydrated. The cysteines of the proteins in the dehydrated gel fragments were reduced with 10 mM DL-dithiothreitol (DTT; Bio-Rad; Hercules, CA, USA) in 50 mM NH_4HCO_3 aqueous solution at 56 °C for 30 min. The reduced cysteines were subsequentially alkylated by iodoacetamide

(Merck, Darmstadt, Germany) in 50 mM NH_4HCO_3 for 20 min in the dark. Samples were dehydrated again with ACN. 30 µL of trypsin (Merck, Darmstadt, Germany) (20 ng·µL^{-1} in 20 mM NH_4HCO_3) were added to each sample and were incubated for 16 h at RT. The first extracted peptides' supernatant was transferred to a new low-binding microtube. The remaining peptides were further extracted using a 50 % (v/v) ACN/water solution containing 0.1 % (v/v) trifluoroacetic acid (TFA, Scharlau, Barcelona, Spain) three times. Finally, the extracts were pooled together and dehydrated with ACN before storing them at –20 °C.

2.8.5. Mass spectrometry of the adsorbed proteins

The mass spectrometry of the adsorbed proteins was carried out by microLC-MS/MS in an Eskpert nLC425 micro-LC system (Eksigen, Dublin, CA, USA), equipped with a trap column [YMC-TRIART C18 reversed-phase column (particle size: 3 µm; pore size: 120 Å)] and an analytical column [Chrom XP C18 reversed-phase column (dimensions: 150 × 0.30 mm; particle size: 3 µm; pore size: 120 Å)], coupled to a microsource and a TripleTOF® 6600 detector (Sciex, Redwood City, CA, USA). Sciex Analyst TF, version 1.7.1, was used to control the chromatographic and mass spectrometry equipment. 0.1 % formic acid in water (A) and 0.1 % formic acid in ACN (B) were used as mobile phases (Scharlau, Barcelona, Spain). In all analyses, the flow rate was set at 5 µL·min^{-1}, and the oven temperature was 40 °C.

First, 4 µL of an equal mixture of all the analytes (protein corona samples, negative control, and a 1,000 ×-diluted plasma solution in PBS) were analyzed by data-dependent acquisition (DDA). The chromatographic method for the DDA analysis consisted of a gradient of 80 min from 2 % B to 90 % B, followed by 5 min of 90 % B and a gradient of 5 min from 90 % B to 2 % B. The microsource potential was tuned at 2,600 V to ionize the peptides, and the TripleTOF® detector was set up in positive ion mode. The curtain gas (N_2) was kept at 25 psi; the collision energy was set to 10 eV, and the ion source gas was 1 to 25 psi. The MS method consisted of consecutive MS scans of 250 ms from 400 to 1250 *m/z*. The top 65 precursor ions detected during each scan were subjected to MS/MS scans of 25 ms from 100 to 1500 *m/z*. Protein Pilot software (version 5.0.1, Sciex) was used to identify peptides and proteins from the DDA analysis by using the Human-specific UniProt database (50,590 proteins) and specifying iodoacetamide as cysteine alkylation. The oxidation of methionines was considered a variable modification. The false discovery rate (FDR) was set to 1 % for peptides and proteins.

Second, the MS/MS spectra of the identified proteins by DDA were used to generate the spectral library for Sequential Window Acquisition of all Theoretical Mass Spectra (SWATH-MS) peak extraction using the add-in for PeakView Sofware (version 2.2, Sciex). Also, the spectral library was used to optimize the 100 SWATH-MS detection windows according to the detected ion density using the SWATH-MS variable window calculator worksheet from Sciex.

Third, a data-independent acquisition (DIA) was performed by SWATH-MS after the injection of 4 µL of each analyte. The chromatographic method for the DIA analysis consisted of a gradient of 35 min from 5 % B to 95 % B, followed by 5 min of a gradient to 90 % B, 5 min of 90 % B, and a gradient of 5 min from 90 % B to 5 % B. The MS method consisted of an initial TOF MS scan (400 to 1500 *m/z*, 50 ms acquisition time), followed by sequential precursor isolation using 100 isolation widows of variable width (with 1 *m/z* of overlap), covering the 400 to 1250 *m/z* mass range, and then, 100 TOF MS/MS scans (400 to 1500 *m/z*; high sensitivity mode, 50 ms acquisition time). The entire cycle lasted 6.3 s and was repeated during the whole run.

Fourth, the ion fragments listed on the DDA-generated library were extracted from all the detected fragments on the SWATH-MS runs using PeakView (version 2.2, Sciex) and SWATH-MS Acquisition MicroApp (version 2.0, Sciex). Up to 10 peptides per protein and 7 fragments per peptide were selected based on signal intensity; any shared and modified peptides were excluded from the processing. Five-minute windows and 30 ppm widths were used to extract the ion chromatograms. The final peak areas for the peptides were obtained by summing the peak areas from the corresponding fragment ions. PeakView computed an FDR and a score for each assigned peptide according to the chromatographic and spectral components only peptides with an FDR below 1 % were used for protein quantification.

The sample's raw ion peak areas were not subjected to normalization and were exported to a Microsoft Excel (Redmond, WA, USA) datasheet. Two-tailed homoscedastic Student's t-tests of the final peak areas of the protein corona samples *vs.* the negative control were performed. Protein concentrations were considered statistically significant if the p-value < 0.1. Next, fold changes (FCs) were calculated between the mean areas of the proteins in the samples and the negative control. Proteins with an FC > 1.5 were chosen as enriched in the corona of the NCs. Then, the mean area in the negative control was subtracted from the sample areas for all the proteins that matched the previously stated parameters. Later, an FC between the adjusted mean area of the samples and the mean areas of the 1,000 ×-diluted plasma was calculated. The FCs were transformed into concentration considering the plasmatic concentration of the detected proteins in healthy conditions, consulted on the Plasma Proteome Database (http://plasmaproteomedatabase.org). Last, the protein mass percentage was calculated based on these results. The experimental protocol is summarized in Supplementary Table 2.

2.9. ACTIVATION OF COMPLEMENT

Zymosan A was purchased from Sigma-Aldrich (St. Louis, MO, USA) and dispersed in water at 0.3 $mg \cdot mL^{-1}$. Taxol®-like NPs were formulated by mixing Cremophor® EL (BASF SE, Ludwigshafen, Germany) and a 2 $mg \cdot mL^{-1}$ citric acid solution in ethanol at a 1:1 (v/v) ratio under magnetic stirring and 10 ×-dilution in PBS. 10 µL of Zymosan A, Taxol®-like NPs, PBS, or NCs were mixed with 10 µL of veronal buffer 1 × (Lonza, Basel, Switzerland) and 10 µL of non-pooled citrated human plasma and incubated at 37 °C for 1 h with mild agitation. 300 µL of 2 × Laemmli buffer and 270 µL of water were added to the vial and boiled for 5 min at 100 °C. PAGE was performed as in section "2.8.3. Acrylamide-based electrophoresis". 5 µL of pre-stained protein ladder (Thermo Fisher Scientific, Waltham, MA, USA) and 5 µL of samples were loaded on the gel. Proteins were subjected to a wet transfer to a methanol-activated Immobilon-FL polyvinylidene difluoride (PVDF) protein blotting membrane (Merck, Darmstadt, Germany) at 4 °C overnight in a mini-protean 3 cell tank (Bio-Rad, Hercules, CA, USA) at an intensity of 35 mA. Transfer buffer containing 20 % methanol was prepared from commercial Novex® tris-glycine transfer buffer 25 × (Thermo Fisher Scientific, Waltham, MA, USA). Membranes were stained with 50 mL of Ponceau S (SERVA Electrophoresis, Heidelberg, Germany) 1 $mg \cdot mL^{-1}$ in 5 % acetic acid aqueous solution for 5 min. Then, they were washed twice with 50 mL of ultrapure water for 10 min and tris-buffered saline (TBST; Thermo Fisher Scientific, Waltham, MA, USA) with 0.01 % polysorbate 20 (Merck, Darmstadt, Germany) for 15 min, and incubated with 10 mL of blocking buffer [5 % bovine serum albumin (BSA; Sigma-Aldrich, St. Louis, MO, USA) and 0.1 % NaN_3 (Scharlau, Barcelona, Spain) in TBST] for 1 h at RT, followed by incubation with 10 mL of anti-Complement 3 Goat pAb (Merck, Darmstadt, Germany) 1:2,000 in blocking buffer for 90 min

at RT. Membranes were washed 3 times for 10 min with 50 mL of TBST and incubated with 10 mL of anti-goat IgG horseradish peroxidase (HRP) (Mouse. Clone eB270) (Rockland Immunochemicals, Pottstown, PA, USA) 1:10,000 in blocking buffer at 4 °C for 1 h. Then, they were washed 5 times with 50 mL of TBST for 10 min and incubated with 2 mL of UniGlow® One component chemiluminescent substrate (Rockland Immunochemicals, Pottstown, PA, USA) for 2 min. Membranes were wrapped in transparent plastic films, and X-ray films (Fujifilm, Tokyo, Japan) were exposed to the membrane for < 5 min. Then, they were immersed in a developing solution [20 % G-150 Developer / Replenisher for medical X-Ray film processing; (Afga, Mortsel, Belgium) and 80 % ultrapure water (v/v)], rinsed in water, fixed with 10 % G-354 manual fixing bath for medical X-Ray film processing water solution and dried in a ventilated environment.

2.10. DATA PRESENTATION AND STATISTICAL ANALYSIS

Unless indicated otherwise, data are presented as the mean or the mean ± standard deviation of 3 replicates, GraphPad Prism version 9.4.1 (GraphPad, San Diego, CA, USA) was used for data analysis, type I errors (α) were fixed to 0.05, and *p*-values < 0.05 were considered statistically significant (*). Also, (**) if *p*-value < 0.01, (***) if *p*-value < 0.001 and (****) if *p*-value < 0.0001.

For the evaluation of the size preservation after the separating techniques, comparisons were performed by two-tailed paired parametric t-tests. For the protein corona studies, two-tailed homoscedastic Student's t-tests of the final peak areas of the protein corona samples *vs.* the negative control were performed. Protein concentrations were considered statistically significant if the *p*-value < 0.1.

Analyses requiring normality were performed after passing the Kolmogorov-Smirnov test, with the Dallal-Wilkinson-Lilliefor corrected *p*-value.

3. RESULTS AND DISCUSSION

3.1. DEVELOPMENT OF POLYMERIC NCS

We have extensively characterized the physicochemical properties, composition, and protein corona of a set of seven different negatively charged or neutral NCs formulations. To facilitate their comparison, the NCs were referred to according to a tri-block code, indicating their formulation technique, the nature of their predominant PEGylated surfactant, and the composition of their polymeric coating (Figure 5).

Six formulations of NCs were prepared using the solvent displacement (SD) technique (SD-*l*-PEG-HA, SD-*l*-PEG-PEG·PGA, SD-*b*-PEG-HA, SD-noPEG-HA, and SD-noPEG-PEG·PGA) while one prototype was produced using the self-emulsifying (SE) technique (SE-*b*-PEG-HA).

The principal PEGylated surfactant of each formulation was classified depending on the disposition of their PEG residues. "*l*-PEG" formulations have linear PEG residues, while "*b*-PEG" refers to branched PEG. Two of the prototypes were "*l*-PEG" (SD-*l*-PEG-HA and SD-*l*-

PEG-PEG·PGA) containing, in both cases, TPGS, which has a linear polyethylene oxide (PEO) chain (*l*-PEG) of approximately 22 monomers. Two other prototypes (SD-*b*-PEG-HA and SE-*b*-PEG-HA) contained P80 instead, with 4 PEG chains in a branched disposition (*b*-PEG) with 20 PEO monomers. Moreover, three prototypes did not contain any PEGylated surfactant (noPEG) (SD-noPEG-HA, SD-noPEG-PSA, and SD-noPEG-PEG·PGA). Finally, we have also explored three different negatively charged polymeric coatings: HA, polyethylene glycol poly-α-glutamic acid (PEG·PGA), and polysialic acid (PSA).

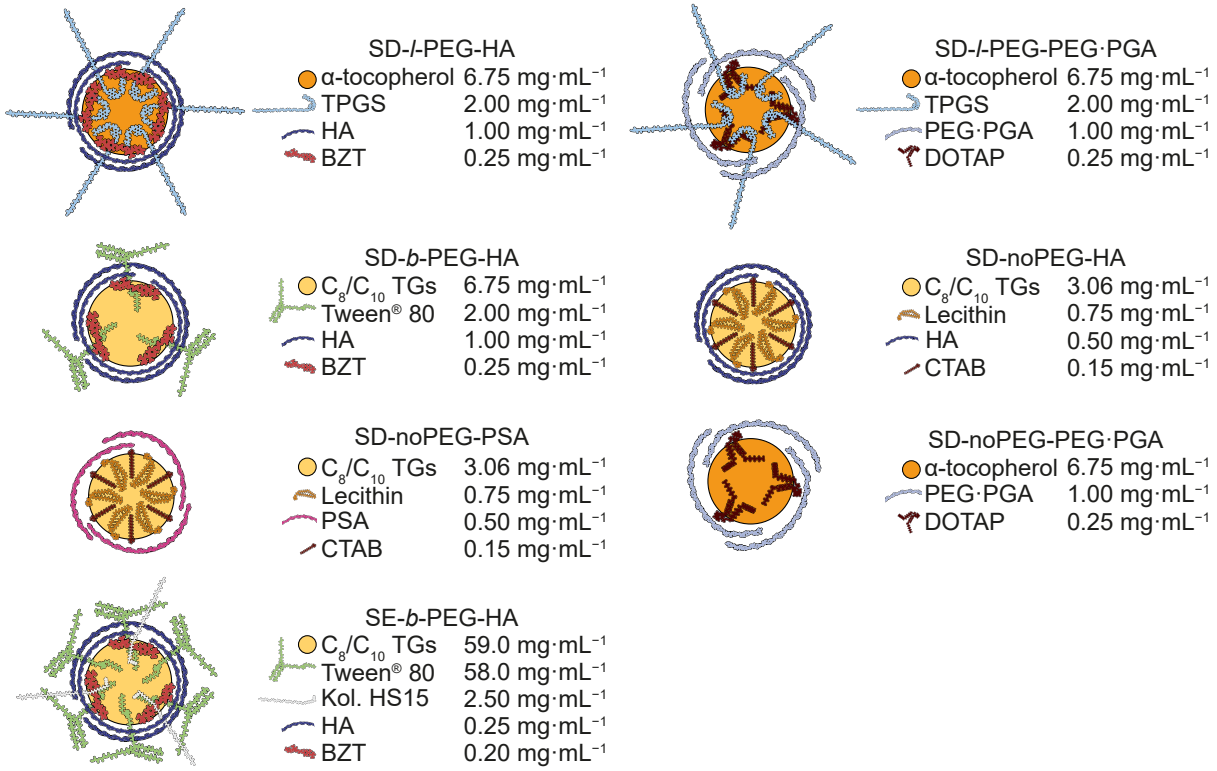


Figure 5. Schematic representation of the expected NCs' compound arrangement and their theoretical composition

SD-*l*-PEG-HA: Formulation prepared by solvent displacement technique and composed of lineal PEG (TPGS), BZT, and HA shell. **SD-*l*-PEG-PEG·PGA**: Formulation prepared by solvent displacement technique and composed of lineal PEG (TPGS), DOTAP, and PEG·PGA shell. **SD-*b*-PEG-HA**: Formulation prepared by solvent displacement technique and composed of branched PEG (polysorbate 80), BZT, and HA shell. **SD-noPEG-HA**: Formulation prepared by solvent displacement technique and composed of non-PEGylated surfactants (lecithin), CTAB, and HA shell. **SD-noPEG-PSA**: Formulation prepared by displacement technique and composed of non-PEGylated surfactant (lecithin), CTAB, and PSA shell. **SD-noPEG-PEG·PGA**: Formulation prepared by solvent displacement technique and composed of non-PEGylated surfactants (DOTAP) and PEG·PGA shell. **SE-*b*-PEG-HA**: Formulation prepared by self-emulsifying technique and composed of branched PEG (polysorbate 80), BZT, and HA shell. **Abbreviations**: BZT: benzethonium chloride. C_8/C_{10} TGs: caprylic/capric triglycerides. CTAB: hexadecyltrimethylammonium bromide. DOTAP: 1,2-dioleoyl-3-trimethylammonium propane. HA: hyaluronic acid. Kol. HS15: Kolliphor® HS15. PEG·PGA: polyethylene glycol polyglutamic acid. PSA: polysialic acid. TPGS: D-α-tocopherol polyethylene glycol 1000 succinate. Adaptation from [2] licensed under a Creative Commons CC BY license.

USC UNIVERSIDADE DE SANTIAGO DE COMPOSTELA

3.2. CHARACTERIZATION OF NON-ISOLATED NANOCAPSULES

The particle size and morphology of non-isolated NCs were characterized using different techniques.

DLS measurements revealed hydrodynamic diameters between 121 and 171 nm (Table 7, Supplementary Figure 2). The hydrodynamic diameters measured by NTA matched DLS results, although values were generally slightly lower. The differences might be due to the intensity-based nature of the DLS results, which may have led to an overestimation of the proportion of bigger particles (Table 7). All solvent displacement formulated NCs exhibited a PDI < 0.2. However, SE-*b*-PEG-HA formulation PDI was 0.33, suggesting a broad range of hydrodynamic diameters (Table 7). The NTA results indicated that all SD formulations were mainly monodisperse in the 60 – 1000 nm range, while SE-*b*-PEG-HA presented several subpopulations of an average size of more than 200 nm (Supplementary Figure 3).

Regarding the ζ-potential, we can classify the systems into three categories: strongly negative (SD-noPEG-PSA, SD-noPEG-HA, SD-*b*-PEG-HA, SD-*l*-PEG-HA, and SD-noPEG-PEG·PGA, with −55, −53, −41, −37, and −22 mV, respectively), slightly negative (SE-*b*-PEG-HA, −10 mV) and neutral or slightly positive (SD-*l*-PEG-PEG·PGA, +6 mV) (Table 7).

The spherical morphology of the NCs was confirmed by SEM / STEM-in-SEM (Figure 6). Generally, NCs were well defined as individual entities, except for the formulation SD-*b*-PEG-HA, where clusters of particles could be observed. The main benefit of STEM-in-SEM is that it operates at lower voltages, approximately 20 to 30 kV, compared to STEM and TEM (usually 100 to 300 kV). While the reduced voltage limits the resolution of the images, it enhances the contrast for molecules constituted by atoms of low atomic number, becoming a good technique for the visualization of NCs from 100 to 200 nm. However, the size distribution detected by FE-SEM did not fully match the one obtained by DLS and NTA. The detected NCs' size variations could be attributed to physical changes during the staining or dehydration steps. Therefore, cryo-EM, where unaltered liquid samples are quickly frozen by cold ethane, resulting in the vitrification and, thus, preservation of the original status of the sample, was used for visualizing the natural structure of NCs. Two NCs were selected for cryo-EM visualization: SD-noPEG-PEG·PGA and SE-*b*-PEG-HA (Figure 7). Cryo-EM results indicate that all NCs were in the range of 100 nm, with a spherical shape. In the case of SD-noPEG-PEG·PGA, most of the counted NCs exhibited a particle diameter between 80 and 120 nm, and 40 – 80 nm in the case of SE-*b*-PEG-HA. This reduction in the particle size, in comparison to the DLS results, could be attributed to the presence of micelles of a size smaller than 40 nm (Table 7, Supplementary Figure 4).

NCs' surface area was calculated using the sphere's area mathematical formula with the hydrodynamic diameters measured by DLS and the particle concentration measured by NTA. SE-*b*-PEG-HA showed the highest surface area, at 0.98 $m^2 \cdot mL^{-1}$. The rest of the nanosystems exhibited a similar surface area, between 0.23 and 0.59 $m^2 \cdot mL^{-1}$ (Table 7).

USC UNIVERSIDADE DE SANTIAGO DE COMPOSTELA

Table 7. Physicochemical characterization of NCs, including particle diameter, PDI, ζ potential, concentration, surface area, and pH

	SD-*l*-PEG-HA	SD-*l*-PEG-PEG·PGA	SD-*b*-PEG-HA	SD-noPEG-HA	SD-noPEG-PSA	SD-noPEG-PEG·PGA	SE-*b*-PEG-HA
Hydrodynamic diameter (DLS) (nm)	135 ± 4	143 ± 1	171 ± 12	158 ± 12	150 ± 10	121 ± 3	147 ± 5
PDI	0.09 ± 0.02	0.10 ± 0.01	0.14 ± 0.01	0.10 ± 0.01	0.06 ± 0.01	0.13 ± 0.01	0.33 ± 0.04
ζ-potential (mV)	−33 ± 5	+6 ± 1	−41 ± 2	−53 ± 16	−55 ± 1	−22 ± 1	−10 ± 1
Hydrodynamic diameter (NTA) (nm)	120 ± 1	137 ± 11	134 ± 11	124 ± 8	129 ± 6	121 ± 14	127 ± 5
Particle diameter (TEM) (nm)	94 ± 19 (n = 50)	156 ± 25 (n = 50)	148 ± 60 (n = 50)	83 ± 29 (n = 50)	92 ± 22 (n = 50)	76 ± 13 (n = 50)	110 ± 41 (n = 50)
Particle diameter (cryo-EM) (nm)	-	-	-	-	-	95 ± 52 (n = 67)	77 ± 117 (n = 240)
Concentration ($\times 10^{11}$ particles·mL^{-1})	51 ± 2	70 ± 7	49 ± 9	80 ± 2	113 ± 40	82 ± 19	193 ± 46
Surface area (m^2·mL^{-1})	0.23 ± 0.01	0.41 ± 0.05	0.28 ± 0.04	0.39 ± 0.06	0.59 ± 0.13	0.38 ± 0.01	0.98 ± 0.17
pH	4.9 ± 0.1	5.4 ± 0.1	7.0 ± 0.2	5.2 ± 0.3	5.4 ± 0.2	6.6 ± 0.3	7.4 ± 0.1

Abbreviations: DLS: dynamic light scattering. NTA: nanoparticle tracking analysis. TEM: transmission electron microscopy. The compositions of SD-*l*-PEG-HA, SD-*l*-PEG-PEG·PGA, SD-*b*-PEG-HA, SD-noPEG-HA, SD-noPEG-PSA, SD-noPEG-PEG·PGA, and SE-*b*-PEG-HA are shown in Figure 5. Values represent the mean ± standard deviation (n = 3 unless indicated otherwise).

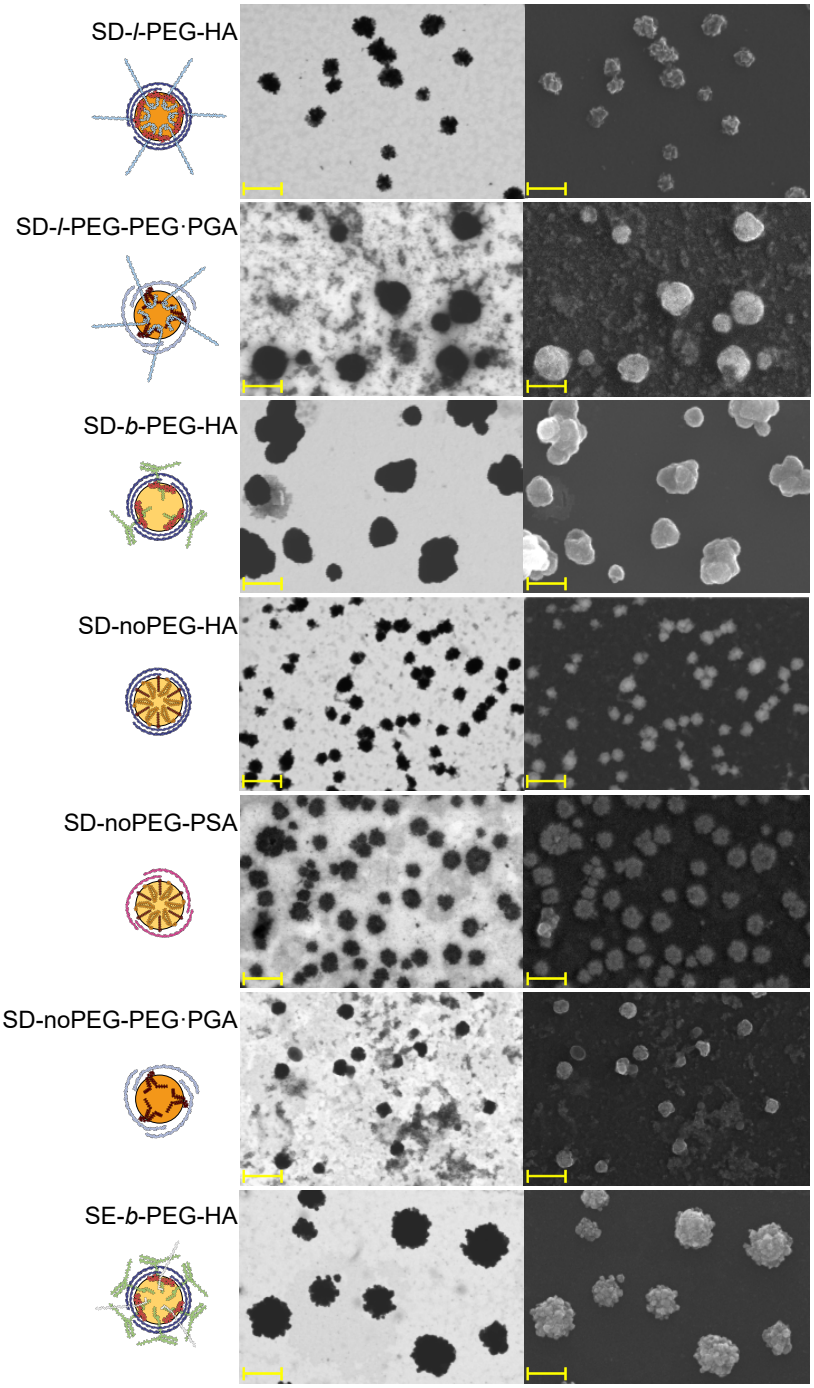


Figure 6. Representative FE-SEM images of different non-isolated NCs

Images were taken using the STEM (left) and In-lens secondary electron (right) detectors. The compositions of SD-*l*-PEG-HA, SD-*l*-PEG-PEG·PGA, SD-*b*-PEG-HA, SD-noPEG-HA, SD-noPEG-PSA, SD-noPEG-PEG·PGA, and SE-*b*-PEG-HA are shown in Figure 5. Scale bars indicate 200 nm.

USC UNIVERSIDADE DE SANTIAGO DE COMPOSTELA

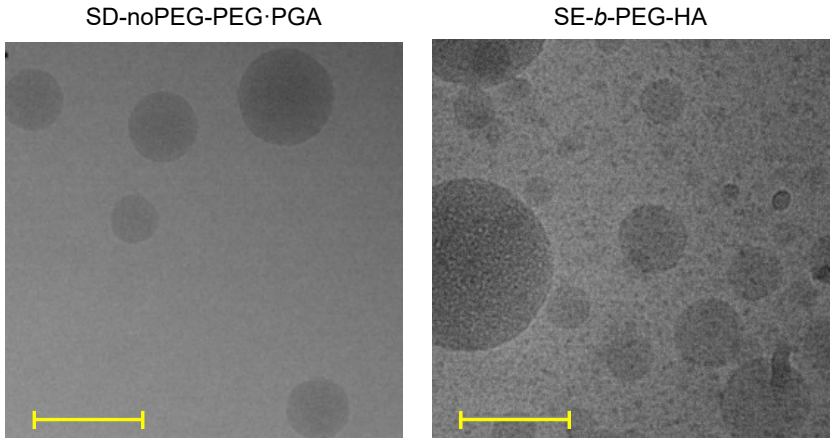


Figure 7. Representative cryo-EM images of different non-isolated NCs

The compositions of SD-noPEG-PEG·PGA and SE-*b*-PEG-HA are shown in Figure 5. Scale bars indicate 100 nm.

3.3. HA INTERACTION BY AF4

For the HA interaction analysis, we have selected the SD-*b*-PEG-HA and SE-*b*-PEG-HA NCs, which, despite sharing the same polymer and PEGylated surfactant, were formulated by different techniques and exhibited different surfactant concentrations. NCs were stable during the AF4 separation, as the Z-average hydrodynamic diameters measured by MALS were 262 ± 2 and 164 ± 4 nm for SD-*b*-PEG-HA and SE-*b*-PEG-HA, respectively. The results in Figure 8 indicated that the HA AE was 22 and 31 % for SD-*b*-PEG-HA and SE-*b*-PEG-HA, respectively.

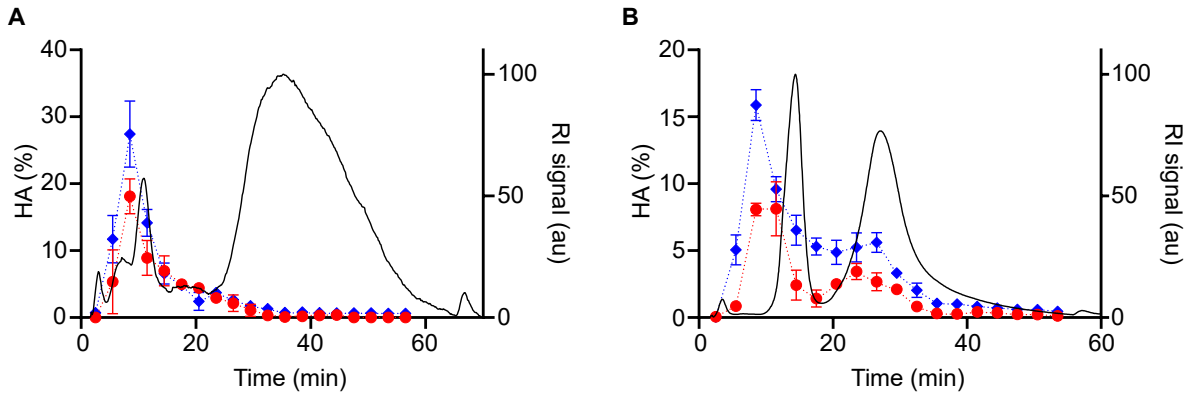


Figure 8. Association of HA to two different NCs studied by AF4

Black lines: NCs fractogram by the refractive index (RI) detector. **Red symbols:** % content of HA in the fractions of NCs. **Blue symbols:** % content of HA in the fractions of a HA standard solution in ultrapure water (1 mg·mL^{-1}). **(A)** SD-*b*-PEG-HA. **(B)** SE-*b*-PEG-HA. **Abbreviations:** AF4: asymmetric flow field-flow fractionation. HA: hyaluronic acid. RI: refractive index. The compositions of SD-*b*-PEG-HA and SE-*b*-PEG-HA are shown in Figure 5.

HA association studies were carried out using NaCl 1 mM as the carrier solution for separating the free compounds and micelles from the NCs. In general, carrier solutions with reduced background electrolyte concentrations are not recommended, as they enhance the

solute-membrane interactions.[185] In our case, though, they were required due to two reasons. First, a high ionic strength media might promote the dissociation of HA from the NCs. Second, the quantification of HA was hindered by high ionic strength media such as PBS, being the bound and free HA fractions under the RI detection range in that case.

3.4. CHARACTERIZATION OF ISOLATED NANOCAPSULES

NCs were isolated by ultracentrifugation except for SE formulations, which were found to aggregate in the experimental conditions explored for ultracentrifugation. Also, we decided to discontinue the characterization of the isolated SD-*b*-PEG-HA formulation, whose mean hydrodynamic diameter was beyond the targeted size (< 200 nm).

The results in Table 8 show a slight reduction in the hydrodynamic diameter, statistically significant (unpaired t-test) for SE-*b*-PEG-HA, which could be attributed to the re-organization or partial detachment of the polymeric shells (Supplementary Figures 5 and 6).

Probably, for the same reason, the ζ-potential of SD-noPEG-PSA and SD-noPEG-PEG·PGA changed significantly (unpaired t-test), now being roughly −35 mV.

Table 8. Summary of the physicochemical properties of the isolated NCs, including hydrodynamic diameter, PDI, ζ potential, concentration, surface area, and pH

	SD-*l*-PEG-HA	SD-*l*-PEG-PEG·PGA	SD-noPEG-HA	SD-noPEG-PSA	SD-noPEG-PEG·PGA	SE-*b*-PEG-HA
Hydrodynamic diameter (DLS) (nm)	156 ± 8	137 ± 4	135 ± 4	124 ± 7	116 ± 2	113 ± 2
PDI	0.17 ± 0.01	0.08 ± 0.05	0.09 ± 0.02	0.06 ± 0.01	0.11 ± 0.02	0.25 ± 0.01
ζ-potential (mV)	−39 ± 4	+0 ± 3	−33 ± 5	−38 ± 4	−35 ± 2	−6 ± 1
Hydrodynamic diameter (NTA) (nm)	125 ± 10	118 ± 13	113 ± 3	107 ± 4	102 ± 2	126 ± 3
Concentration ($\times 10^{11}$ particles·mL^{-1})	51 ± 10	85 ± 24	88 ± 6	96 ± 9	106 ± 10	71 ± 2
Surface area (m^2·mL^{-1})	0.25 ± 0.03	0.37 ± 0.03	0.35 ± 0.02	0.35 ± 0.04	0.35 ± 0.04	0.36 ± 0.03
pH	6.0 ± 0.1	6.2 ± 0.1	4.9 ± 0.1	5.3 ± 0.1	6.0 ± 0.1	7.4 ± 0.1

Abbreviations: DLS: dynamic light scattering. NTA: nanoparticle tracking analysis. PDI: polydispersity index. Values represent the mean ± standard deviation (n = 3). The compositions of SD-*l*-PEG-HA, SD-*l*-PEG-PEG·PGA, SD-*b*-PEG-HA, SD noPEG HA, SD-noPEG-PSA, SD-noPEG-PEG·PGA, and SE-*b*-PEG-HA are shown in Figure 6.

3.5. CHARACTERIZATION OF THE CHEMICAL COMPOSITION OF NANOCAPSULES

We have analyzed each compound's total, bound, and unbound fractions for the 6 formulations mentioned in the section "3.4. Characterization of isolated nanocapsules".

USC UNIVERSIDADE DE SANTIAGO DE COMPOSTELA

3.5.1. Development of the MS and MS/MS methods

The development of MRM methods for DL-α-tocopherol,[186,187] BZT,[188,189] DOTAP,[190] and CTAB[191] was straightforward as they are fragmentable molecules with a unique and defined structure. However, the analysis of the rest of the components was more challenging.

For example, Epikuron™ 145V, Miglyol® 812N, and Kolliphor® HS15 are mixtures of different molecules. Epikuron™ 145V is a lecithin mainly composed of phosphatidylcholines (PCs) of several molecular weights (MW). Luckily, all PCs have phosphocholine (*m/z* 184.1) as a common daughter.[192,193] A parent scan for phosphatidylcholine showed that our most predominant PCs had MWs of 756.6, 758.6, 780.6, and 782.5 Da. Since we did not have any information about their ratio, an equal contribution of the four molecules was assumed. Miglyol® 812N is a mixture of four triglyceride molecules (C_8-C_8-C_8, C_8-C_8-C_{10}, C_8-C_{10}-C_{10}, and C_{10}-C_{10}-C_{10} triglycerides). However, in this case, no parent molecules could be detected without NH_4HCOO-enriched mobile phases. NH_4HCOO promotes the formation of an ammonium adduct with the triglycerides, allowing their detection at an *m/z* shifted up in 18 units.[194] In this case, we also assumed an equal contribution of the four molecules. Kolliphor® HS15 comprises approximately 70 % macrogol-15-hydroxystearate and 30 % unconjugated polyethylene glycols of different molecular weights. Macrogol-15-hydroxystearate is a labile molecule that inevitably breaks down in the ESI source, detecting an in-source fragment of *m/z* 309.3, which was used for quantification by the pseudoMRM transition *m/z* 309.3 → 309.3,[195] as it was not possible to fragment this molecule further.

Molecules such as TPGS can be in-source fragmented and then fragmented again in the collision cell into granddaughters of the molecule of interest. Consequently, we have quantified TPGS by an MRM transition between the daughter ion *m/z* 557.4 and the granddaughter *m/z* 99.0. The quantification of PEG is well described in the literature,[196] but we have excluded its analysis as, due to its high hydrophilicity, it improbably forms part of the NCs.

P80 is composed of molecules with slightly different molecular weights. Thus, its MS spectrum contained many different *m/z* signals, among which *m/z* 804.6 was the most intense. Consequently, we have used an MRM transition between this parent and its predominant daughter (*m/z* 309.3)[197] for quantification.

Finally, the quantification of the polymers was particularly challenging since their MW was higher than the operating range of our detector (*m/z* 2 to 2048). Hence, HA, PSA, and PEG·PGA were broken down into smaller fragments, which could be quantified. Lysis of carbohydrates and proteins can occur by several mechanisms, including enzymatic, ultrasonic, thermal, oxidant, acidic, and alkali-driven.[198] H_2SO_4 is known for hydrolyzing glycosidic linkages at a high yield and low monomer degradation.[199] We digested HA and PSA with H_2SO_4 to form, predominantly, HA dimers of *m/z* 759.2[181,198,200] and dehydrated sialic acid monomers of *m/z* 274.1.[201,202] We have quantified these fragments by SIM, as a stable transition could not be found. On the other hand, peptidic bonds can be hydrolyzed in acidic conditions, i.e., 6 M HCl at a high temperature (110 °C) for a long time (24 h).[203] The quantification of poly-γ-glutamic acid in these conditions has been reported in the literature,[204] but to our knowledge, no work has been published on polyethylene glycol poly-α-glutamic acid ESI (+) LC-MS/MS quantification. The amino acids resulting from the PEG·PGA digestion were quantified based on previous works for underivatized glutamic acid.[205,206] The structures of the parent and daughter molecules can be consulted in Table 9. The MS and MS/MS spectra of each molecule can be consulted in Supplementary Table 6 of Berrecoso *et al.*.[2]

Table 9. Structure of the parent and daughter molecules of each component of NCs

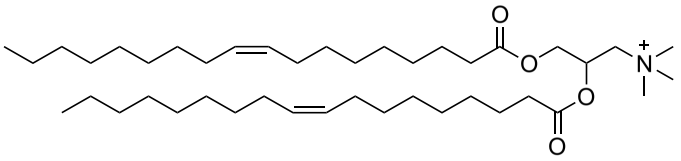
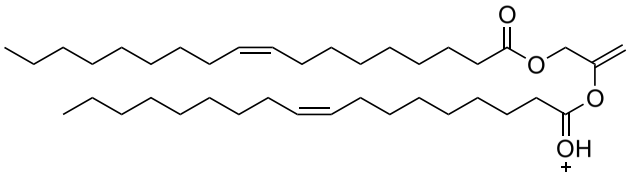
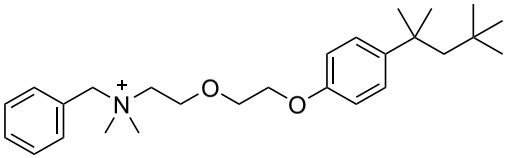
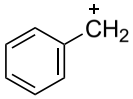
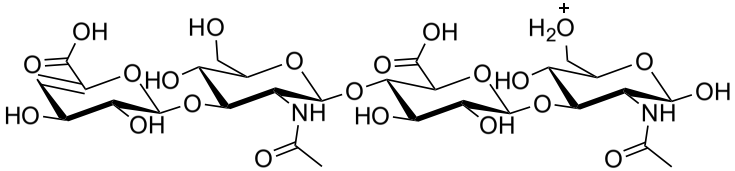
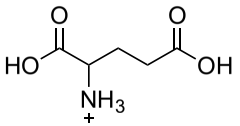
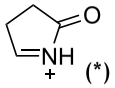
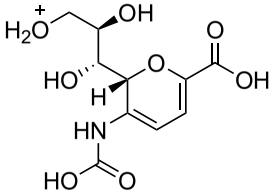
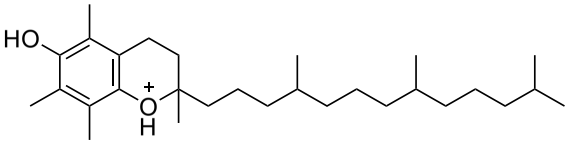
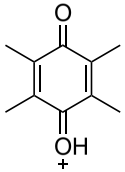
Substance	Parent structure	Daughter structure	Ref.
1,2-dioleoyl-3-trimethyl-ammonium-propane chloride			[190]
Benzethonium chloride			[188,189]
Digested hyaluronic acid		N/A	[181,200]
Digested polyethylene glycol poly-α-glutamic acid		 (*)	[206]
Digested polysialic acid		N/A	[201,202]
DL-α-tocopherol			[186,187]

Table 9. Structure of the parent and daughter molecules of each component of NCs (continuation)

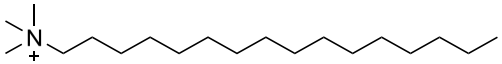
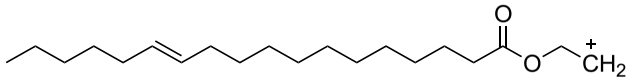
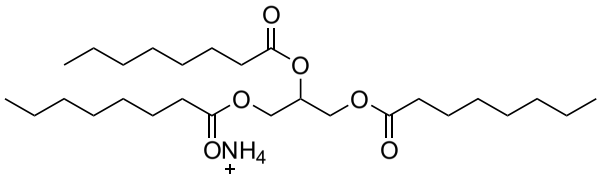
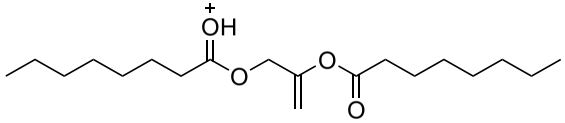
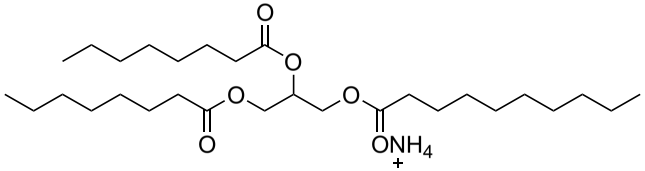
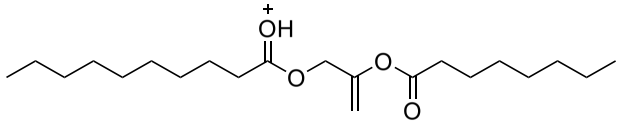
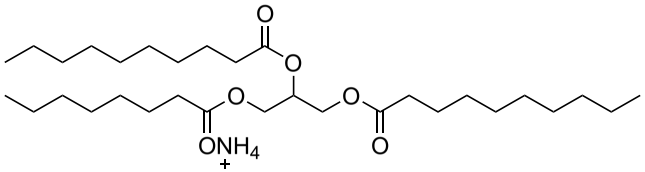
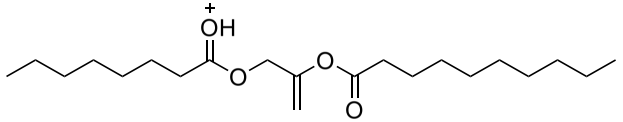
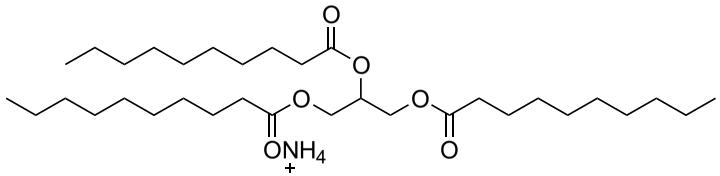
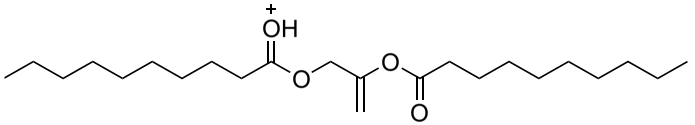
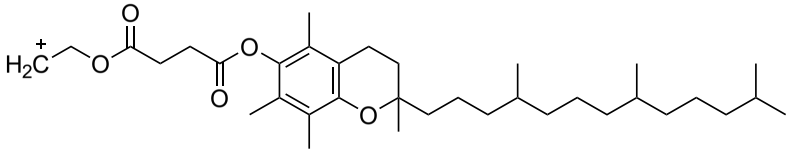
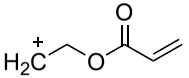
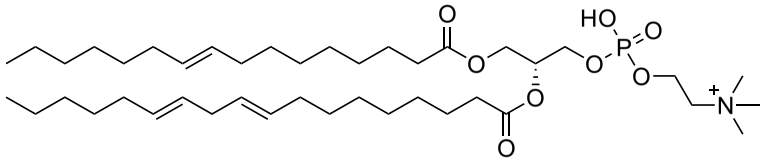
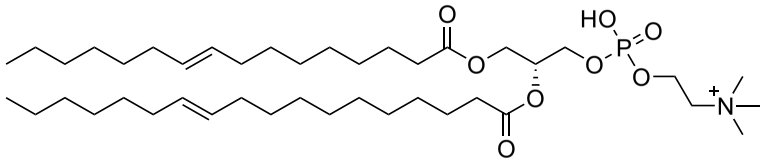
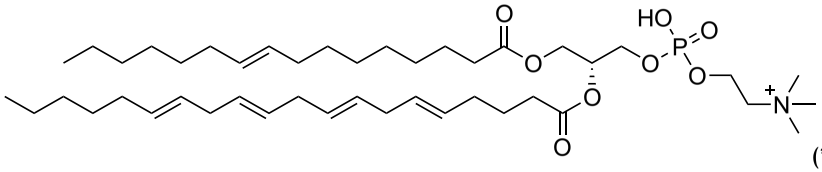
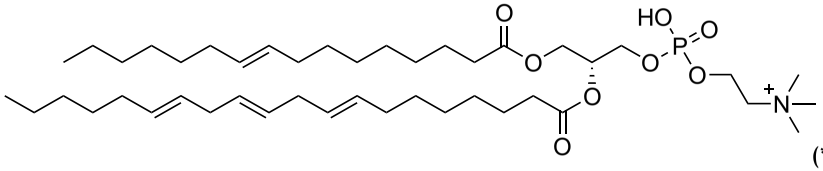
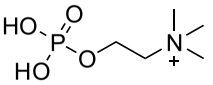
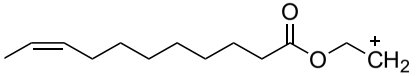
Substance	Parent structure	Daughter structure	Ref.
Hexadecyltri-methyl-ammonium bromide			-
Macrogol-15-hydroxystearate (Kolliphor® HS15)		N/A	-
Miglyol® 812N			[194]
			[194]
			[194]
			[194]

Table 9. Structure of the parent and daughter molecules of each component of NCs (continuation)

Substance	Parent structure	Daughter structure	Ref.
D-α-tocopherol polyethylene glycol 1000 succinate			-
Phosphatidylcholines (Epikuron™ 145V)	 (*)  (*)  (*)  (*)		[193]
Polysorbate 80	N/D		[197]

Abbreviations: N/A: not applicable. N/D: not determined. (*): A possible structure, other molecules with the same *m/z* may co-exist. Adaptation from [2] licensed under a Creative Commons CC BY license.

3.5.2. Development of the chromatographic methods

The chromatographic methods were developed considering each molecule's logP value and achieved an excellent separation for all the molecules in each formulation. Examples can be consulted in Supplementary Table 5 of the publication of Berrecoso *et al.*[2] for all NCs but SD-*l*-PEG-PEG·PGA (Supplementary Table 3).

3.5.3. Method validation

Calibration curves were found to be linear, with an average r^2 of 0.985 (all r^2 were within 0.9383 and 0.9997) and percentual relative residuals (%RRES) for each calibration level of less than ± 20 % (Supplementary Table 8 of the publication of Berrecoso *et al.*[2] and Supplementary Table 4, the latest for SD-*l*-PEG-PEG·PGA). The quantification limits (LoQs) were lower than the concentrations of the calibrating standards. Notably, the LoQs of BZT and CTAB were extraordinarily low, in the range of 200 – 700 $pg \cdot L^{-1}$. Also, repeatability and accuracy were assessed since all intraday pooled RStD% were lower than 9 % and the RE% lower than 13 % (Supplementary Table 1).

The recoveries of all substances tested after the formulation of NCs, were close to 100 % of the theoretical composition, indicating no material losses, including deposition onto the container walls. Also, except for the phosphatidylcholines and medium-chain triglycerides of SD-noPEG-HA and SD-noPEG-PSA, the sum of the associated and non-associated fractions was roughly 100 %. However, this precipitation was systematic, as the association efficiencies were constant in all triplicates.

3.5.4. Actual composition of the isolated NCs

Besides being just solubilized in the formulating media, unbound molecules might generate micellar structures or form complexation products. The latest might be probable for polymers and counter-charged surfactants, as described, for example, for CTAB and PGA.[207]

The actual composition of the NCs after isolation is shown in Supplementary Table 5 and Figure 9. The association efficiencies varied for each substance and formulation, ranging from 14 % to 95 %. From these data, the production yield of each formulation could be calculated. No correlation with the formulation technique or PEG presence was observed, but SD-noPEG-PEG·PGA resulted in the formulation with the highest production yield (Table 10).

The study of the associated proportion is crucial as it might prove that a compound of interest is bound in a lower amount than expected. However, an excess of one or several components is sometimes necessary to promote the auto-emulsification of NCs or avoid particle aggregation. For example, the SE process requires increasing the surfactant concentration to 30 – 60 % (w/w).[208] Consequently, components put far in excess will present lower mass association percentages in the isolated fraction, while the bound compound quantity could be high in absolute mass. To compare the composition of different NCs, the amounts of surfactant and polymer per isolated particle, the mass and molar ratio between these substances, and the oils in the isolated formulation, were studied instead (Table 11).

USC
UNIVERSIDADE
DE SANTIAGO
DE COMPOSTELA

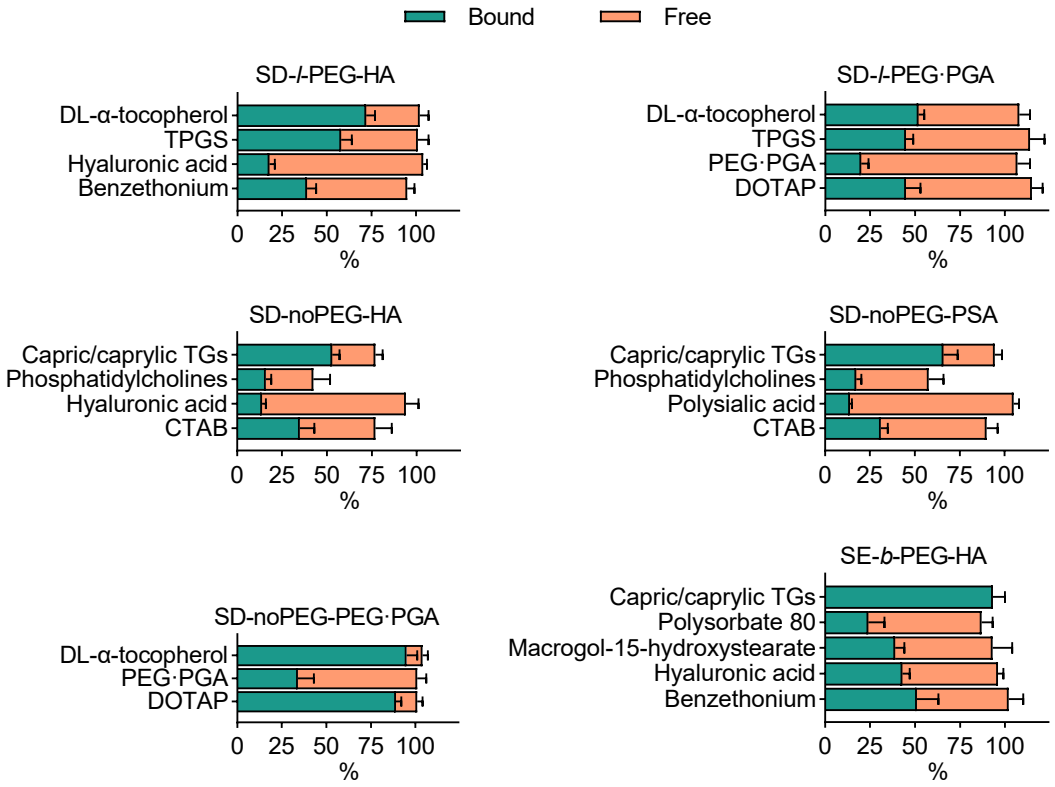


Figure 9. Associated (bound) and non-associated (free) mass percentages referred to the total added mass of each component of the six tested NCs

Abbreviations: TPGS: D-α-tocopherol polyethylene glycol 1000 succinate. TGs: triglycerides. CTAB: Hexadecyltrimethylammonium. DOTAP: 1,2-dioleoyl-3-trimethylammonium-propane chloride. PEG·PGA: Polyethylene glycol poly-α-glutamic acid. The compositions of SD-*l*-PEG-HA, SD-*l*-PEG-PEG·PGA, SD-noPEG-HA, SD-noPEG-PSA, SD-noPEG-PEG·PGA, and SE-*b*-PEG-HA are shown in Figure 5. Values represent the mean ± standard deviation (n = 3). Adaptation from [2] licensed under a Creative Commons CC BY license.

Table 10. Production yields for the selected NCs

Formulation	Production yield (%)
SD-*l*-PEG-HA	63 ± 5
SD-*l*-PEG-PEG·PGA	47 ± 4
SD-noPEG-HA	42 ± 4
SD-noPEG-PSA	51 ± 6
SD-noPEG-PEG·PGA	87 ± 6
SE-*b*-PEG-HA	59 ± 8

The compositions of SD-*l*-PEG-HA, SD-*l*-PEG-PEG·PGA, SD-noPEG-HA, SD-noPEG-PSA, SD-noPEG-PEG·PGA, and SE-*b*-PEG-HA are shown in Figure 5. Values represent the mean ± standard deviation (n = 3).

While not significant (two-way ANOVA), the total amount of surfactant exhibited a trend for higher amounts in the formulations containing PEGylated surfactants than in those incorporating non-PEGylated surfactants.

USC UNIVERSIDADE DE SANTIAGO DE COMPOSTELA

PEG moieties are relevant in providing the NCs with stealth properties in protein adsorption. The PEG amount, length, and disposition were reported to affect the protein corona of nanosystems in terms of protein variety and amount.[1]

Table 11. Mass and molar ratios of PEGylated surfactants, non-PEGylated surfactants, and polymers referred to the quantity of oil

Formulation	Mass ratio (mg per g of oil)			Molar ratio (mmol per mol of oil)		
	PEGylated surfactants	Non-PEGylated surfactants	Polymer	PEGylated surfactants	Non-PEGylated surfactants	Polymer
SD-*l*-PEG-HA	238 ± 40	20 ± 4	36 ± 8	68.31 ± 11.48	20.89 ± 4.18	0.27 ± 0.06
SD-*l*-PEG-PEG·PGA	254 ± 37	32 ± 8	57 ± 13	72.86 ± 10.61	20.67 ± 5.17	3.90 ± 0.89
SD-noPEG-HA	N/A	73 ± 20	45 ± 9	N/A	86.64 ± 23.74	0.40 ± 0.08
SD-noPEG-PSA	N/A	58 ± 15	34 ± 7	N/A	64.94 ± 16.79	0.52 ± 0.11
SD-noPEG-PEG·PGA	N/A	35 ± 3	53 ± 18	N/A	22.45 ± 1.92	3.64 ± 1.24
SE-*b*-PEG-HA	265 ± 118	2 ± 1	2 ± 0	105.62 ± 47.03	2.26 ± 1.13	0.02 ± 0.00

Abbreviations: N/A: not applicable. The compositions of SD-*l*-PEG-HA, SD-*l*-PEG-PEG·PGA, SD-noPEG-HA, SD-noPEG-PSA, SD-noPEG-PEG·PGA, and SE-*b*-PEG-HA are shown in Figure 5. Values represent the mean ± standard deviation (n = 3). Adaptation from [2] licensed under a Creative Commons CC BY license.

The PEG content was evaluated in terms of mass, density, conformation, and thickness. The highest PEG mass content was found in SD-*l*-PEG-PEG·PGA, with 215 mg of PEG per g of oil (Table 12). PEG density was 19, 200, 320, and 6,814 PEG chains/100 nm^2 for SD-noPEG-PEG·PGA, SD-*l*-PEG-PEG·PGA, SD-*l*-PEG-HA, and SE-*b*-PEG-HA, respectively. Of note, the high PEG density of SE-*b*-PEG-HA is related to the short PEG chains of P80. The lowest PEG density was found for SD-noPEG-PEG·PGA, in agreement with its low PEG mass content. Overall, all cases exhibited a PEG density higher than the usually reported for the stealth effect to appear (> 7 – 20 PEG chains/100 nm^2).

For the study of the PEG conformation, the PEG chains' radius in a relaxed status, that is, the Flory Radius (F_R), and the distance between PEG chains (D) were compared. If $D > F_R$, there will be enough space for the PEG chains to be relaxed and present in the mushroom conformation. Oppositely, when $D < F_R$, the PEG chains are forced to acquire a brush conformation. In the case of all the tested NCs, $D < F_R$, adopting the PEG a brush conformation. For the calculus of D, the particle density was assumed between the density of the oil (0.95 $mg \cdot mL^{-1}$ for Vitamin E and 0.93 $mg \cdot mL^{-1}$ for capric/caprylic triglycerides) and 1 $mg \cdot mL^{-1}$, based on the fact that NCs tend to accumulate on the top of the water when centrifuged in ultrapure water.

USC UNIVERSIDADE DE SANTIAGO DE COMPOSTELA

Table 12. Total PEG mass, density, and thickness, considering both surfactant and polymer PEG moieties, of the different NCs

Formulation	PEG mass ratio (mg of PEG per g of oil)	Γ (PEG chains / 100 nm^2)	F_R (nm)	A (nm^2)	D (nm)	L (nm)	Configuration
SD-*l*-PEG-HA	159 ± 27	320 ± 133	2.24 (TPGS)	0.5 ± 0.1 (TPGS)	0.83 ± 0.06	4.3 ± 0.2	Brush
SD-*l*-PEG-PEG·PGA	215 ± 35	200 ± 86	2.24 (TPGS) 5.91 (PEG·PGA)	0.6 ± 0.1 (TPGS) 11.1 ± 3.5 (PEG·PGA)	1.19 ± 0.86	4.1 ± 3.4	Brush
SD-noPEG-HA	N/A	N/A	N/A	N/A	N/A	N/A	N/A
SD-noPEG-PSA	N/A	N/A	N/A	N/A	N/A	N/A	N/A
SD-noPEG-PEG·PGA	42 ± 14	19 ± 8	5.91 (PEG·PGA)	11.4 ± 4.6	3.81 ± 0.43	7.9 ± 0.6	Brush
SE-*b*-PEG-HA	188 ± 84	9,038 ± 3,893	3.68 (P80) 1.78 (m15OHSt)	0.6 ± 0.3 (P80) 8.9 ± 3.0 (m15OHSt)	0.97 ± 0.73	3.5 ± 3.3	Brush

Abbreviations: Γ: PEG density. F_R: Flory radius. A: area occupied by each PEG chain. D: distance between PEG molecules. L: PEG layer thickness. TPGS: D-α-tocopherol polyethylene glycol 1000 succinate. m15OHSt: macrogol-15-hydroxystearate. P80: polysorbate 80. The compositions of SD-*l*-PEG-HA, SD-*l*-PEG-PEG·PGA, SD-noPEG-HA, SD-noPEG-PSA, SD-noPEG-PEG·PGA, and SE-*b*-PEG-HA are shown in Figure 5. Values represent the mean ± standard deviation (n = 3).

The average thickness of the PEGylated layer depended on the length of the PEGylated molecules and their disposition. SD-noPEG-PEG·PGA presented the largest average thickness due to its high amount of 5-kDa-PEG PEG·PGA. Oppositely, SE-*b*-PEG-HA, the one containing the PEGylated molecule with the shortest PEG chain (P80), was the one with the less thick PEG layer.

Finally, the stealth effect is usually reported for > 7 – 20 PEG chains per 100 nm^2 with an MW > 2 kDa. While all NCs fulfilled the first requirement, only those containing PEG·PGA exhibited a PEG chain higher than 2 kDa. Overall, based on this information, we expect that the SD-*l*-PEG·PGA formulation, with a high PEG density and molecular weight, would be less taken up by macrophages and have a longer circulating time than the other PEGylated NCs.

The polymers forming the shell of the NCs may have different roles, such as the protection of their cargo from instability or degradation (i.e., PEG·PGA envelopment of mRNA nanocomplexes),[209] the increase of their circulation time, and the modification of their biodistribution,[210] as well as their interaction with specific receptors (i.e., HA and CD44).[4] Moreover, polymers can be modified to include ligands for other receptors (i.e., tLyp1-HA and neuropilin receptors).[211] Due to the tremendous importance of this layer, it is of crucial importance to quantify the amount of polymer attached to the NCs. Results showed that the polymer AE was significantly lower in the SE formulations with 2 mg per g of oil (equivalent to 0.02 mmol per mol of oil) than in the ones formulated by SD, with similar values ranging from 36 to 57 mg of polymer per g of oil (or, in molar ratio, from 0.27 to 3.90 mmol per mol of oil) (two-way ANOVA).

Considering all of this, the importance of reporting the actual composition of NCs is evident, considering the number of components that are part of the nanostructure and those that may be solubilized or forming micelles in the medium. Unfortunately, as discussed above, most of the works only report on the total amount of each component, independently of whether they are bound or unbound, which can be misleading, making it difficult to draw clear conclusions. Therefore, the actual composition of the isolated NCs before plasma incubation and quantified by LC-MS is presented in Table 13.

Table 13. NCs composition after their purification

Formulation	Compound	Concentration ($mg \cdot mL^{-1}$)
SD-*l*-PEG-HA	DL-α-tocopherol	12.99 ± 0.84
	D-α-tocopherol polyethylene glycol 1000 succinate	3.09 ± 0.32
	Hyaluronic acid	0.47 ± 0.08
	Benzethonium	0.26 ± 0.03
SD-*l*-PEG-PEG·PGA	DL-α-tocopherol	9.42 ± 0.59
	D-α-tocopherol polyethylene glycol 1000 succinate	2.39 ± 0.20
	DOTAP	0.30 ± 0.06
	PEG·PGA	0.54 ± 0.09
SD-noPEG-HA	Medium-chain triglycerides	10.55 ± 0.77
	Hyaluronic acid	0.47 ± 0.06
	Phosphatidylcholines	0.42 ± 0.08
	Hexadecyltrimethylammonium	0.35 ± 0.08

USC UNIVERSIDADE DE SANTIAGO DE COMPOSTELA

Table 13. NCs composition after their purification (continuation)

Formulation	Compound	Concentration (mg·mL^{-1})
SD-noPEG-PSA	Medium-chain triglycerides	13.20 ± 1.60
	Phosphatidylcholines	0.46 ± 0.07
	Polysialic acid	0.45 ± 0.04
	Hexadecyltrimethylammonium	0.31 ± 0.04
SD-noPEG-PEG·PGA	DL-α-tocopherol	17.07 ± 1.03
	DOTAP	0.59 ± 0.02
	PEG·PGA	0.91 ± 0.25
SE-*b*-PEG-HA	Medium-chain triglycerides	55.01 ± 4.22
	Polysorbate 80	13.90 ± 5.26
	Macrogol-15-hydroxystearate	0.69 ± 0.09
	Benzethonium	0.10 ± 0.02
	Hyaluronic acid	0.11 ± 0.01

The compositions of SD-*l*-PEG-HA, SD-*l*-PEG-PEG·PGA, SD-noPEG-HA, SD-noPEG-PSA, SD-noPEG-PEG·PGA, and SE-*b*-PEG-HA are shown in Figure 5. Values represent the mean ± standard deviation (n = 3). Adaptation from [2] licensed under a Creative Commons CC BY license.

3.6. STABILITY OF NANOCAPSULES IN RELEVANT BIOLOGICAL FLUIDS

When the NCs were in contact with human plasma, no aggregation or relevant tendency in their hydrodynamic diameter size was noticeable (Figure 10).

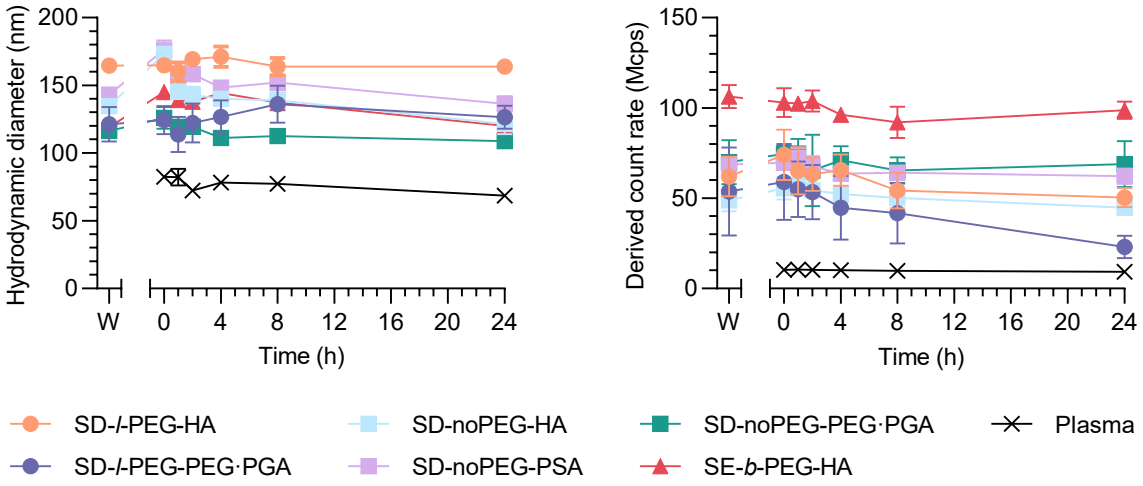


Figure 10. Hydrodynamic diameter and derived count rate variation of NCs when incubated in 90 % human plasma at 37 °C for 24 h

Abbreviations: W: NCs dispersed in water. Plasma: control consisting of phosphate-buffered saline instead of NCs'. The size increase was statistically significant for SD-noPEG-HA at t = 0 h and SE-*b*-PEG-HA at times 0 h to 4 h (two-way ANOVA *versus* NCs dispersed in water). All NCs' DCRs were not statistically significant (two-way ANOVA *vs.* NCs dispersed in water). The compositions of SD-*l*-PEG-HA, SD-*l*-PEG-PEG·PGA, SD-noPEG-HA, SD-noPEG-PSA, SD-noPEG-PEG·PGA, and SE-*b*-PEG-HA are shown in Figure 5. Values represent the mean ± standard deviation (n = 3).

USC UNIVERSIDADE DE SANTIAGO DE COMPOSTELA

However, a slight size increase was observed for all NCs' when the size measurement was performed just after mixing the NCs with plasma (t = 0 h). However, this size increase was only statistically significant for SD-noPEG-HA (+ 40 nm) and SE-*b*-PEG-HA (+ 26 nm) (two-way ANOVA *vs.* NCs dispersed in water). Additionally, SE-*b*-PEG-HA size variation was significant compared to water for the following 4 h. However, this difference was even lower than at 0 h and non-significant at higher timer points.

To further explore the mechanistic of the NCs' size increase tendency in the moment of incubation with plasma (t = 0 h) and complete the NCs' stability profile, NCs were incubated in protein-free media of different ionic strength and pHs.

Except for the three noPEG NCs, the particle sizes remained unaltered after incubation in NaCl solutions of 75 mM, 154 mM, and 300 mM for 24 h. Notably, non-PEGylated NCs were stabilized by their protein corona since SD-noPEG-HA and SD-noPEG-PSA were not stable in NaCl 75 – 300 mM (Figure 11), pH 6, PBS, and pH 9.2 (Figure 12) but stable in human plasma.

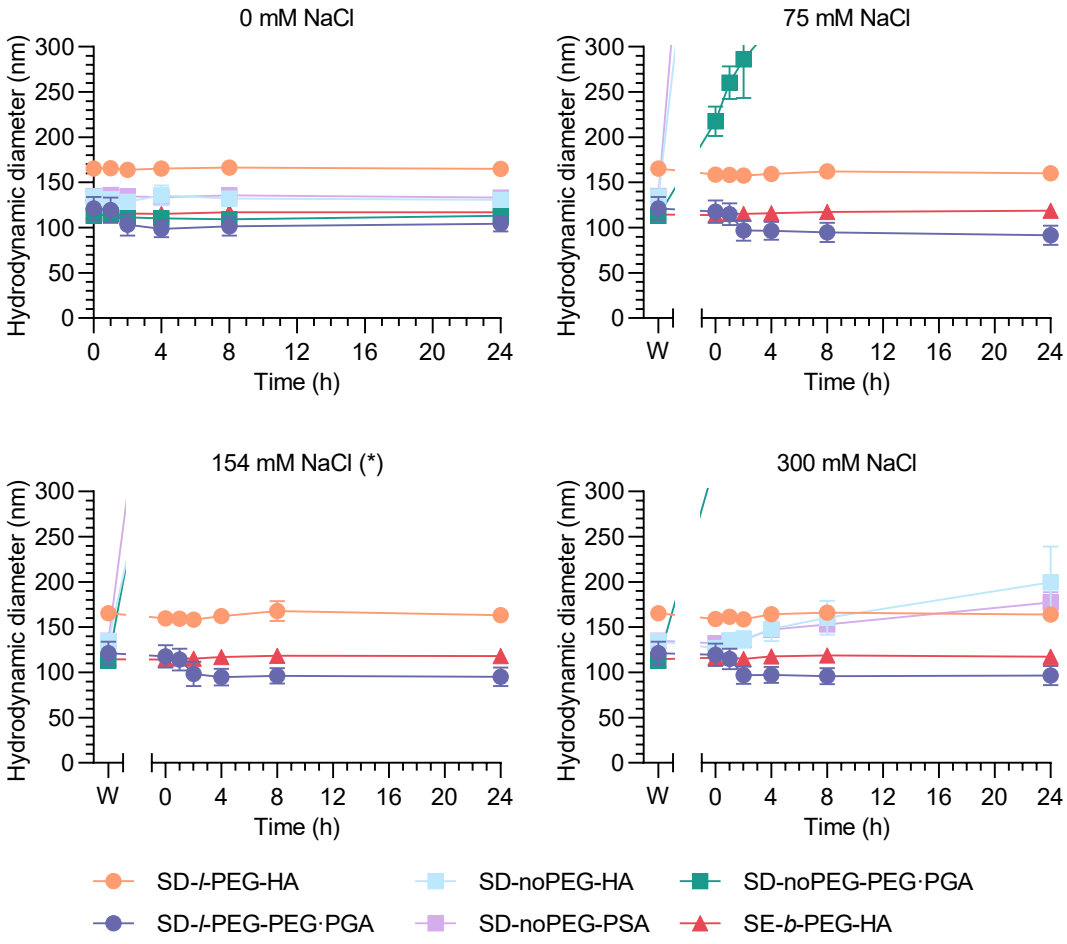


Figure 11. Stability data of SD-*l*-PEG-HA, SD-*l*-PEG-PEG·PGA, SD-noPEG-HA, SD-noPEG-PSA, SD-noPEG-PEG·PGA, and SE-*b*-PEG-HA in different ionic forces (0, 75, 154*, and 300 mM NaCl)

(*) Physiological conditions. The compositions of SD-*l*-PEG-HA, SD-*l*-PEG-PEG·PGA, SD-noPEG-HA, SD-noPEG-PSA, SD-noPEG-PEG·PGA, and SE-*b*-PEG-HA are shown in Figure 5. Values represent the mean ± standard deviation (n = 3).

USC UNIVERSIDADE DE SANTIAGO DE COMPOSTELA

Moreover, the size variation detected at t = 0 h after plasma incubation did not occur when the systems were dispersed in these inorganic solutions, suggesting that the size increment was somehow due to the interaction with proteins.

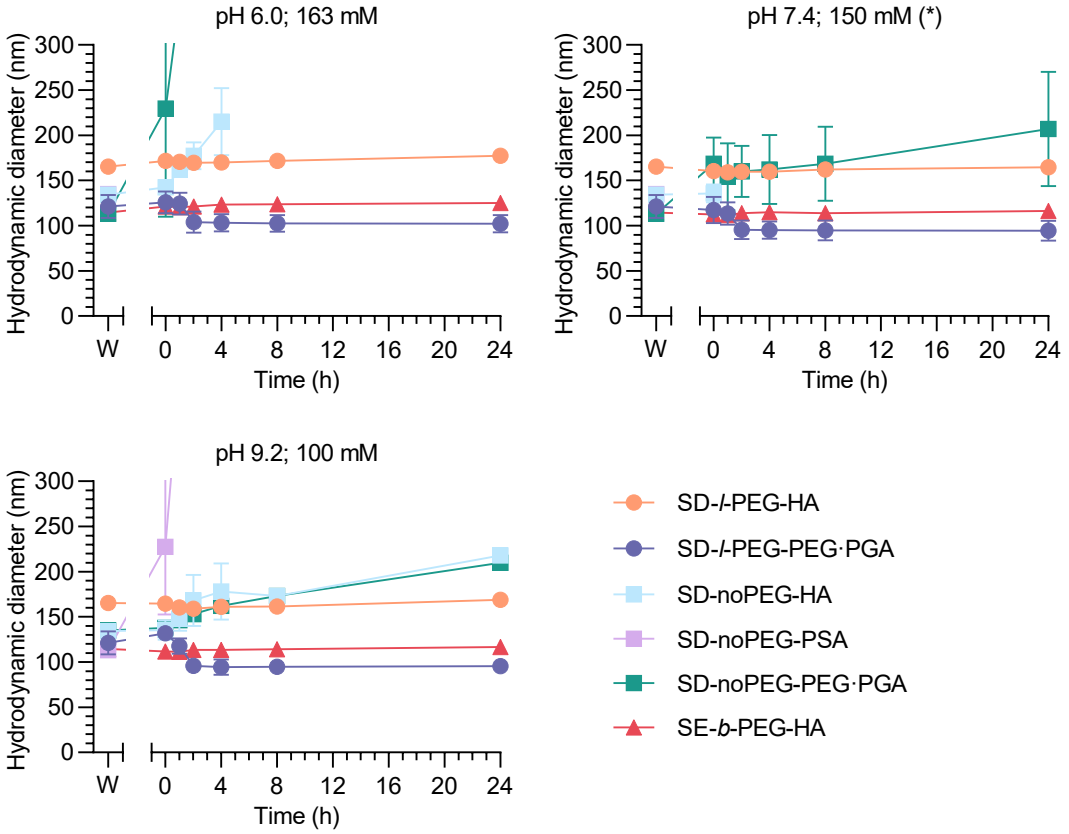


Figure 12. Stability data of SD-*l*-PEG-HA, SD-*l*-PEG-PEG·PGA, SD-noPEG-HA, SD-noPEG-PSA, SD-noPEG-PEG·PGA, and SE-*b*-PEG-HA in different pHs (6.0, 7.4*, and 9.2)

(*) Physiological conditions. The compositions of SD-*l*-PEG-HA, SD-*l*-PEG-PEG·PGA, SD-noPEG-HA, SD-noPEG-PSA, SD-noPEG-PEG·PGA, and SE-*b*-PEG-HA are shown in Figure 5. Values represent the mean ± standard deviation (n = 3).

3.7. Determination of the protein corona of NCs

3.7.1. Experimental incubation conditions in plasma

The surface areas of NCs were standardized to 0.25 $m^2 \cdot mL^{-1}$, as mentioned in section "2.2. Characterization of the size, Z-potential, pH, and morphology of nanocapsules". For this, the NCs suspensions were diluted in different volumes of water or PBS (Table 14).

Once correctly diluted, NCs were incubated in citrated human plasma, with a final 90 % plasma composition, at 37 °C under mild agitation and in the dark. In these conditions, the plasma volume/NP area ratio resulted in approximately 35 mL plasma·m^{-2} of nanosystem. For a rough estimation of the surface area ratio between the NCs and the plasmatic proteins, we have assumed a plasma protein concentration of 70 $mg \cdot mL^{-1}$ and that plasmatic proteins had the same molecular weight (66.5 kDa) and hydrodynamic diameter (4.2 nm) of the main

protein, albumin. As a result, the surface ratio was approximately 1,230 m^2 of plasmatic proteins *versus* 1 m^2 of particles, confirming the plasma excess compared to the NCs. In the literature, incubation ratios are usually 1 – 20 mL of plasma·m^{-2} of nanosystems.[28,140,212–214] High plasma volume/surface area ratios are more similar to the *in vivo* situation. If the ratio is too low, the amount of the set of proteins with higher affinity will not be enough to fill all the protein binding sites, and consequently, abundant proteins, such as albumin, will be adsorbed even if their affinity is relatively low.[215] The incubation time was fixed to 1 h following most of the published works,[1] and the equilibrium of the protein corona was presumed.

Table 14. Standardization of the surface area to 35 mL·m^{-2}

Formulation	Ultrapure water or PBS 1 × volume (µL)	NCs volume (µL)	Plasma volume (µL)
SD-*l*-PEG-HA	0 (water)	110	990
SD-*l*-PEG-PEG·PGA	36 (water)	74	990
SD-noPEG-HA	32 (water)	78	990
SD-noPEG-PSA	31 (water)	79	990
SD-noPEG-PEG·PGA	30 (water)	80	990
SE-*b*-PEG-HA	33 (PBS)	77	990

Abbreviations: PBS: phosphate-buffered saline. The compositions of SD-*l*-PEG-HA, SD-*l*-PEG-PEG·PGA, SD-noPEG-HA, SD-noPEG-PSA, SD-noPEG-PEG·PGA, and SE-*b*-PEG-HA are shown in Figure 5.

3.7.2. Separation of NCs from unbound proteins

The isolation of the nanosystems-protein corona from the free proteins still present in the surrounding media is the most critical step when characterizing protein corona.

The most common procedure involves consecutive ultracentrifugation cycles, physical filtration, AF4 separation, and, if suitable, magnetic-based separation.

We have explored ultracentrifugation, AF4, filtration under N_2 positive pressure, and TFF as isolating techniques for the protein-coated NCs. The best results were obtained with ultracentrifugation. AF4 was able to separate the unbound proteins from the protein corona-coated NCs, but the protein amount was too low to be appropriately detected by SDS-PAGE. Finally, the pressure-driven membrane filtration methods (Amicon® stirred cell and TFF) were not suitable for isolating protein corona of NCs, as NCs suspension fouled these filters, leading to the detection of unbound proteins.

3.7.2.1. Ultracentrifugation-based separation

We have decided to explore ultracentrifugation as a protein corona isolation technique as it is the most employed methodology in the literature. However, to solve the inherent problems of consecutive ultracentrifugation, mentioned in section "1.2.7.1.2. Isolation of the NP-protein corona complexes", we have developed a discrete 3-layer sucrose gradient (Figure 13).

USC UNIVERSIDADE DE SANTIAGO DE COMPOSTELA

In our procedure, NCs were mixed with a concentrated sucrose solution and placed on the bottom of the centrifugation vial. Then, two more layers of decreasing density were placed

on top of the first one, acting as spacers to reduce the interference from free proteins in the bottom layer. When centrifuged, NCs moved from the bottom to the top layer, forming a cream-like supernatant due to their low density.

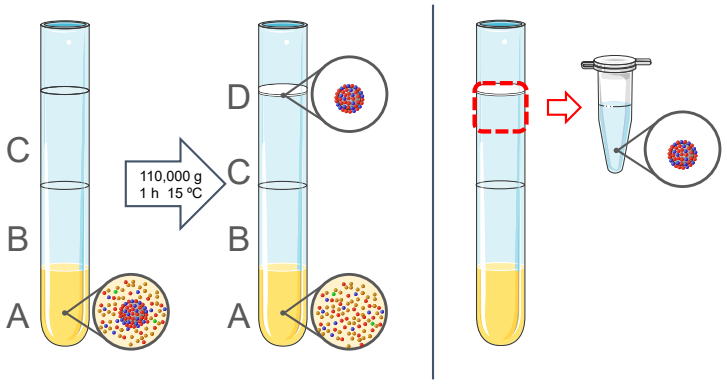


Figure 13. Schematic representation of the developed sucrose gradient based-ultracentrifugation isolation techniques

For the gradient elaboration, 1 mL of 90 % plasma and 10 % surface area-normalized NCs were mixed with 1 mL of concentrated sucrose solution to form the **A** layer (20 % sucrose). 2 mL of a less concentrated sucrose solution (**B**) were placed on top of **A**, followed by a third layer of ultrapure water or PBS (**C**). Visually, layer **A** was yellowish since it consisted of approximately 45 % of plasma. After centrifugation, if NCs were present, a thin cream layer (**D**) was formed on top of layer **C**. 1 mL was withdrawn from the surface with a syringe, taking all the cream with it, and placed in a low-binding microtube. **Abbreviations:** NCs: nanocapsules. PBS: phosphate-buffered saline. Images of tubes and microtubes were reproduced (adapted and modified) from Servier Medical Art (https://smart.servier.com), licensed under Creative Commons Attribution 3.0 (https://creativecommons.org/licenses/by/3.0).

Visually, the bottom layer remained yellowish after ultracentrifugation, indicating that most proteins remained still and the phases unmixed. Then, the top 1000 µL of the gradient, including the cream-like supernatant if present, were collected using a syringe.

We have designed six different gradient conditions and evaluated their isolation performance for plasma-incubated SD-l-PEG-HA (Table 15).

The six different gradients led to similar protein adsorption profiles (Figure 15). A 45-kDa protein was the most intense for the six conditions, followed by proteins of approximately 25 and 35 kDa. The elaboration of the mildest gradients (10 % sucrose / 5 % sucrose / 0 % sucrose in water or PBS; conditions 3 and 6 of Table 15) was harsh, as their tendency to remain unmixed is lower than in the other cases. Indeed, a band of ≈ 70 kDa appeared in these conditions. We believe the most probable explanation is the contamination of the top layer with plasma since the molecular weight of albumin, the most abundant protein, matches with the band exclusively detected in these conditions.

The addition of PBS did not show any relevant difference compared to the sucrose-exclusive solutions except for the appearance of a strange band of more than 250 kDa in some replicates. More importantly, since SD-noPEG-HA and SD-noPEG-PSA were not stable in the presence of salts, we discarded the use of PBS-containing gradients (conditions 4, 5, and 6) as they might aggregate at the highest layers, where the protein content is low.

USC DE SANTIAGO DE COMPOSTELA

The most favorable gradient conditions were the first and second ones. Condition 2 was chosen as the final gradient composition since it had a lower sucrose percentage than Condition 1 while still allowing a good separation.

Table 15. Summary of all the explored conditions during the optimization of the sucrose gradient-based ultracentrifugation isolation technique

Condition	Bottom layer	Middle layer	Top layer
1	30 % sucrose (1 mL sample + 1 mL 60 % sucrose) Density: 1.10	15 % sucrose Density: 1.05	0 % sucrose Density: 1.00
2	20 % sucrose (1 mL sample + 1 mL 40 % sucrose) Density: 1.07	10 % sucrose Density: 1.03	0 % sucrose Density: 1.00
3	10 % sucrose (1 mL sample + 1 mL 20 % sucrose) Density: 1.03	5 % sucrose Density: 1.01	0 % sucrose Density: 1.00
4	30 % sucrose 1 × PBS (1 mL sample + 1 mL 60 % sucrose 1 × PBS) Density: 1.12	15 % sucrose 1 × PBS Density: 1.06	0 % sucrose 1 × PBS Density: 1.01
5	20 % sucrose 1 × PBS (1 mL sample + 1 mL 40 % sucrose 1 × PBS) Density: 1.09	10 % sucrose 1 × PBS Density: 1.05	0 % sucrose 1 × PBS Density: 1.01
6	10 % sucrose 1 × PBS (1 mL sample + 1 mL 20 % sucrose 1 × PBS) Density: 1.05	5 % sucrose 1 × PBS Density: 1.03	0 % sucrose 1 × PBS Density: 1.01

Abbreviations: PBS: phosphate-buffered saline. Density values are indicated in $g \cdot mL^{-1}$.

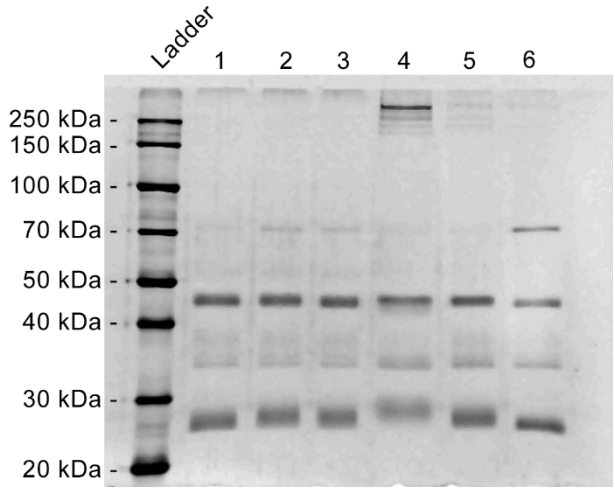


Figure 14. Representative SDS-PAGE of adsorbed proteins of plasma-incubated SD-*l*-PEG-HA subjected to different sucrose-based gradient ultracentrifugation methods

Condition 1: 30 % sucrose/15 % sucrose/0 % sucrose in water. Condition 2: 20 % sucrose/10 % sucrose / 0 % sucrose in water. Condition 3: 10 % sucrose / 5 % sucrose / 0 % sucrose in water. Condition 4: 30 % sucrose/15 % sucrose/0 % sucrose in PBS. Condition 5: 20 % sucrose/10 % sucrose / 0 % sucrose in PBS. Condition 6: 10 % sucrose / 5 % sucrose / 0 % sucrose in PBS. **Abbreviations:** PBS: phosphate-buffered saline. The composition of SD-*l*-PEG-HA is shown in Figure 5.

The preservation of the NCs integrity during the three-layer sucrose-based gradient ultracentrifugation method was assessed in a protein-free media (Table 16). The same kind of approach was recently reported for the analysis of the protein corona of lipid NPs.[147]

Table 16. Physicochemical characterization of the pristine NCs before and after the sucrose gradient-based ultracentrifugation technique

Formulation	SD-*l*-PEG-HA	SD-*l*-PEG-PEG·PGA	SD-noPEG-HA	SD-noPEG-PSA	SD-noPEG-PEG·PGA	SE-*b*-PEG-HA
Particle size (nm) before isolation by ultracentrifugation	156 ± 8	118 ± 9	135 ± 4	124 ± 7	140 ± 6	113 ± 2
PDI before isolation by ultracentrifugation	0.17 ± 0.01	0.07 ± 0.01	0.09 ± 0.02	0.06 ± 0.01	0.02 ± 0.01	0.25 ± 0.01
Particle size (nm) after isolation by ultracentrifugation	160 ± 11	123 ± 2	129 ± 4	131 ± 10	124 ± 8	119 ± 4
PDI after isolation by ultracentrifugation	0.10 ± 0.01	0.08 ± 0.01	0.07 ± 0.02	0.07 ± 0.01	0.05 ± 0.03	0.22 ± 0.02
Particle size significantly different (p-value < 0.05)? (Paired t-test)	No	No	No	No	No	No

The compositions of SD-*l*-PEG-HA, SD-*l*-PEG-PEG·PGA, SD-noPEG-HA, SD-noPEG-PSA, SD-noPEG-PEG·PGA, and SE-*b*-PEG-HA are shown in Figure 5. Values represent the mean ± standard deviation (n = 3).

As explained in the introduction section, proper controls should be performed during the isolation of the NP-protein corona complexes, as free proteins might still be present after the isolating step.

Our optimized sucrose-based gradient centrifugation method allowed the separation of protein-coated NCs from free proteins due to their differences in size and density. However, interference may come from biological nanostructures present in plasma. Indeed, chylomicrons (CM), with a low density and a size higher than 100 nm, could accumulate in the same region of the gradient as the tested NCs, leading to an overestimation of their protein corona (Figure 15).[216] However, the signal of CMs can be easily subtracted from the protein corona results by comparing the detected protein profile of each tested NCs with an NCs-free plasmatic solution. Other endogenous nanostructures such as HDLs, LDLs, and extracellular vesicles (EVs) will tend to move to lower layers of the gradient, and VLDLs are not expected to accumulate at the top of the gradient due to their small size.

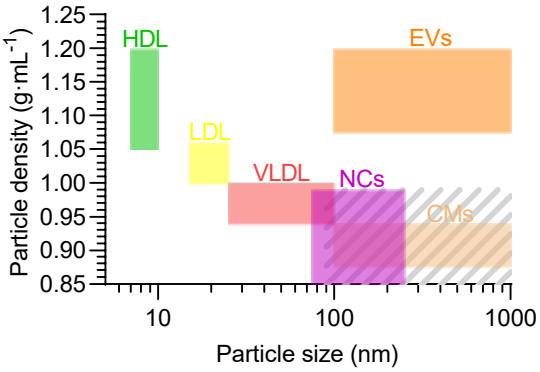


Figure 15. Schematic representation of the particle sizes and densities of biological nanostructures present in plasma (extracellular vesicles, lipoproteins, and chylomicrons) and NCs

NCs size was plotted based on the NTA hydrodynamic diameter results. NCs density was presumed to be lower than 1 g·mL^{-1} as they form a cream-like supernatant when centrifuged in water (1 g·mL^{-1} of density). The grey-shaded area represents the size range that allows the particles' accumulation on top of our optimized sucrose-based gradient ultracentrifugation method. Adapted from Simonsen *et al.*[216] with permission from John Wiley and Sons (License number: 5420271196711).

3.7.2.2. AF4

The AF4 technique was explored to study the protein corona of SD-l-PEG-HA formulation as an alternative to ultracentrifugation. Other formulations, i.e., SD-noPEG-HA, SD-noPEG-PSA, and SD-noPEG-PEG·PGA, had to be excluded from this study because they were unstable in the saline solution required for the technique.

As disclosed in Figure 16, AF4 led to an excellent separation of the free proteins from the NCs detected by the UV-Vis spectrophotometer at 5 – 20 min post-injection, while NCs did elute after 30 – 40 min, as detected by the 90° MALS.

USC UNIVERSIDADE DE SANTIAGO DE COMPOSTELA

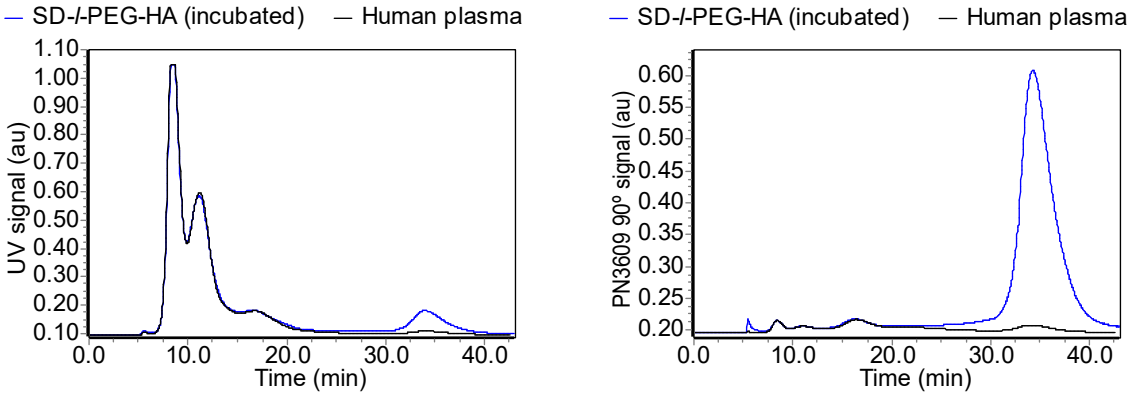


Figure 16. Representative fractograms of incubated SD-*l*-PEG-HA (blue) and human plasma (black) after being subjected to the same separation method and detected by UV-Vis spectrometry (280 nm) (left) and MALS (90°) (right)

The composition of SD-*l*-PEG-HA is shown in Figure 5. **Abbreviations:** MALS: multi-angle light scattering. UV: ultraviolet. Vis: visible.

Fractions of SD-*l*-PEG-HA incubated with plasma were collected every few minutes and analyzed by SYPRO® Ruby-stained SDS-PAGE gels (Figure 17). In agreement with the UV-Vis spectrophotometer, free proteins were eluted in the first 25 min. However, no protein was detected when NCs eluted (fractions 8 – 10, equivalent to 29 – 41 min). Based on these results, we chose ultracentrifugation as the most advantageous method for separating protein-coated NCs from unbound proteins.

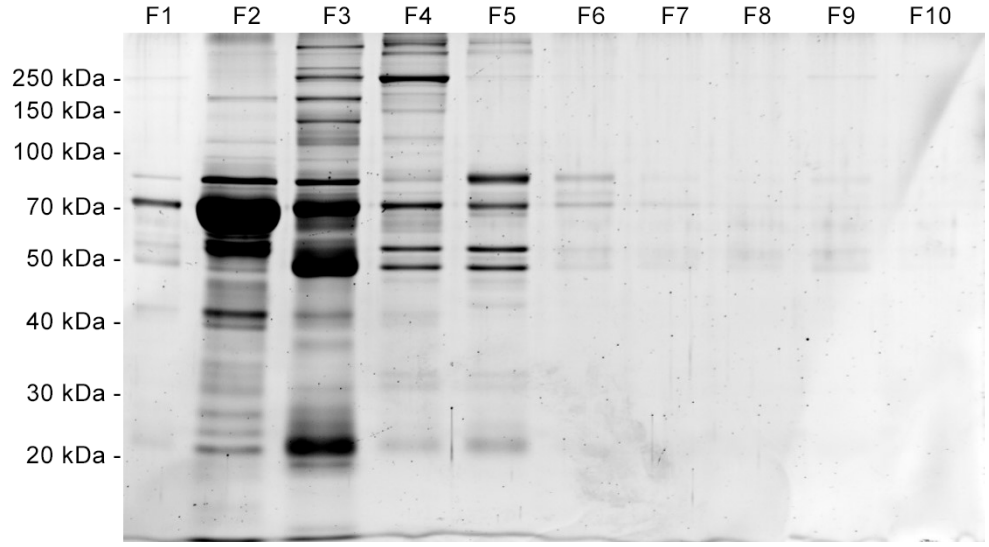


Figure 17. Representative SDS-PAGE of different fractions collected after AF4 separation of incubated SD-*l*-PEG-HA

F1: Fraction 1 (0 – 5 min). F2: Fraction 2 (5 – 9 min). F3: Fraction 3 (9 – 13 min). F4: Fraction 4 (13 – 17 min). F5: Fraction 5 (17 – 21 min). F6: Fraction 6 (21 – 25 min). F7: Fraction 7 (25 – 29 min). F8: Fraction 8 (29 – 33 min). F9: Fraction 9 (33 – 37 min). F10: Fraction 10 (37 – 41 min).

USC UNIVERSIDADE DE SANTIAGO DE COMPOSTELA

3.7.3. Protein identification and quantification

3.7.3.1. SDS-PAGE

The polyacrylamide gel electrophoresis (PAGE) showed different protein adsorption (Figure 18) for different nanosystems. In the second lane, we included 1,000 × diluted plasma as a mass and molecular weight reference. A control consisting of pristine NCs resulted in a gel without any band, confirming the absence of proteins in the formulations before plasma incubation. The negative control only contained a few proteins, probably due to contamination with the incubation media (i.e., mixing the gradient phases) or co-separation with the protein-coated nanosystems (i.e., biological nanostructures with low density). In any case, the LC-MS results of the NCs were compared to the negative control to avoid protein overestimation from co-separating proteins.

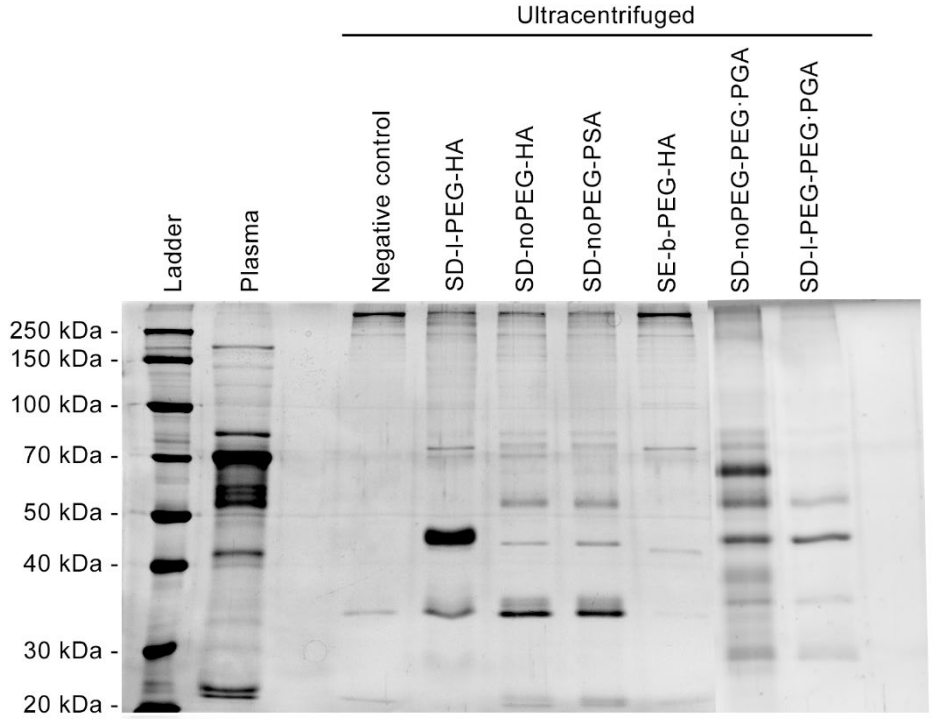


Figure 18. Representative SDS-PAGE of the protein corona of the six tested NCs

Lane 1: ladder. Lane: 2. Whole human plasma diluted 1,000 × in phosphate-buffered saline. Lane 3: Empty. Lane 4: Negative control (Plasma subjected to the sucrose-based gradient ultracentrifugation method). Lanes 5 – 10: Isolated NCs using the sucrose-based gradient ultracentrifugation method [in order: SD-*l*-PEG-HA, SD-noPEG-HA, SD-noPEG-PSA, SE-*b*-PEG-HA, SD-noPEG-PEG·PGA, and SD-*l*-PEG-PEG·PGA]. The compositions of SD-*l*-PEG-HA, SD-*l*-PEG-PEG·PGA, SD-noPEG-HA, SD-noPEG-PSA, SD-noPEG-PEG·PGA, and SE-*b*-PEG-HA are shown in Figure 5. Of note, the last two formulations were run in a different gel.

The SDS-PAGE revealed extraordinary adsorption of a protein of approximately 45 kDa to the SD-*l*-PEG-HA. Non-PEGylated systems exhibited a more diverse corona, as they exhibited more protein bands than PEGylated NCs. SD-noPEG-HA and SD-noPEG-PSA, only differing in their polymeric composition, presented very similar protein coronae in terms of the number and intensity of the protein bands. The lowest protein adsorption seemed to occur on SE-*b*-PEG-HA and SD-*l*-PEG-PEG·PGA. Finally, while bands at ≈ 45 kDa and ≈ 35 kDa were present in most formulations, albumin, the most abundant protein in plasma, (MW ≈ 67 kDa),

was not the main component of any coronae, suggesting that the incubation was performed in a realistic *in vivo* situation and the layers of the gradient were not mixed. The protein identity was further studied by LC-MS.

3.7.3.2. LC-MS

Proteins were digested into peptides before the LC-SWATH-MS analysis using the in-gel digestion approach. SWATH-MS is adequate to study the adsorption of proteins on the NCs' surface as the quantification of all the peptides present in the library, created from the protein corona and plasma samples, is performed unbiasedly, independently of their abundance.

A total of 155 proteins were identified. For each protein, the detected areas of the samples were compared to the detected areas of the control. Sample and control adsorbed protein areas with p-values < 0.1 were chosen as statistically significantly different from the control, and adsorbed proteins with an FC > 1.5 were considered enriched in the corona. As a result, the protein coronas of SD-*l*-PEG-HA, SD-*l*-PEG-PEG·PGA, SD-noPEG-HA, SD-noPEG-PSA, SD-noPEG-PEG·PGA, and SE-*b*-PEG-HA were composed of 22, 7, 15, 17, 16, and 10 proteins, respectively. A volcano plot of the $-\log(p\text{-value})$ and their $\log_2(\text{FC})$ compared to the control is included in Supplementary Figures 7 – 12, while protein identity and FCs related to the plasma control are summarized in Supplementary Tables 6 - 11.

Overall, we identified 13 complement related proteins (complement C1q subcomponent subunit B, complement C1q subcomponent subunit C, complement C1s subcomponent, complement C3, complement C4-A, complement C4-B, C4b-binding protein alpha chain, complement C5, complement component C6, complement component C7, complement component C8 gamma chain, complement component C9, and properdin), 11 different apolipoproteins (apolipoprotein A-II, apolipoprotein A-IV, apolipoprotein C-I, apolipoprotein C-II, apolipoprotein C-III, apolipoprotein D, apolipoprotein E, apolipoprotein F, apolipoprotein L1, apolipoprotein M, and clusterin), several immunoglobulin fragments (Ig heavy constant gamma 1, Ig heavy constant gamma 3, Ig heavy constant mu, and Ig kappa variable 1-27), and other more diverse proteins (aldo-keto reductase family 1 member C3, insulin-like growth factor-binding protein complex acid labile subunit, protein Z-dependent protease inhibitor, serum amyloid A-4 protein, serum paraoxonase/arylesterase 1, and vitronectin) among the protein corona of the different NCs.

The use of the relative FCs against the negative control helps establish comparisons between the tested NCs. For example, the adsorption of Apo A-IV in SD-*l*-PEG-HA resulted in approximately 3.4-fold of SD-noPEG-PEG·PGA, 6.9-fold of SD-*l*-PEG-PEG·PGA, 20.5-fold of SD-noPEG-PSA, and 70.4-fold of SD-noPEG-HA.

However, these FCs are not suitable for comparing the amounts of different proteins in the same corona, as FCs vary not only with the protein amount in the sample but also with its amount on the negative control. To properly compare the amounts of proteins in a sample, we have calculated the FC between the areas of the proteins statistically enriched in the corona of each sample and the areas of these proteins in a 1,000 ×-diluted plasma standard sample (Supplementary Tables 6 - 11).

USC UNIVERSIDADE DE SANTIAGO

Results from the FC of the areas of the adsorbed proteins *versus* the 1,000 ×-diluted plasma sample agreed with the SDS-PAGE. For example, apolipoprotein A-IV in the SD-*l*-

PEG-HA and vitronectin in the SD-noPEG-PEG·PGA exhibited the highest concentrations among all the proteins detected in the tested NCs, with 3.66 and 1.50 mg·m^{-2}, respectively.

A protein-protein interactome between the detected proteins in the NCs coronas was built using the Search Tool for the Retrieval of Interacting Genes/Proteins (STRING) (https://string-db.org/) to identify the enriched functional associations. Only protein interactions with high confidence (> 0.7) were plotted. The protein concentration and opsonin/dysopsonin role were also indicated by the node size and color, respectively (Figure 19).

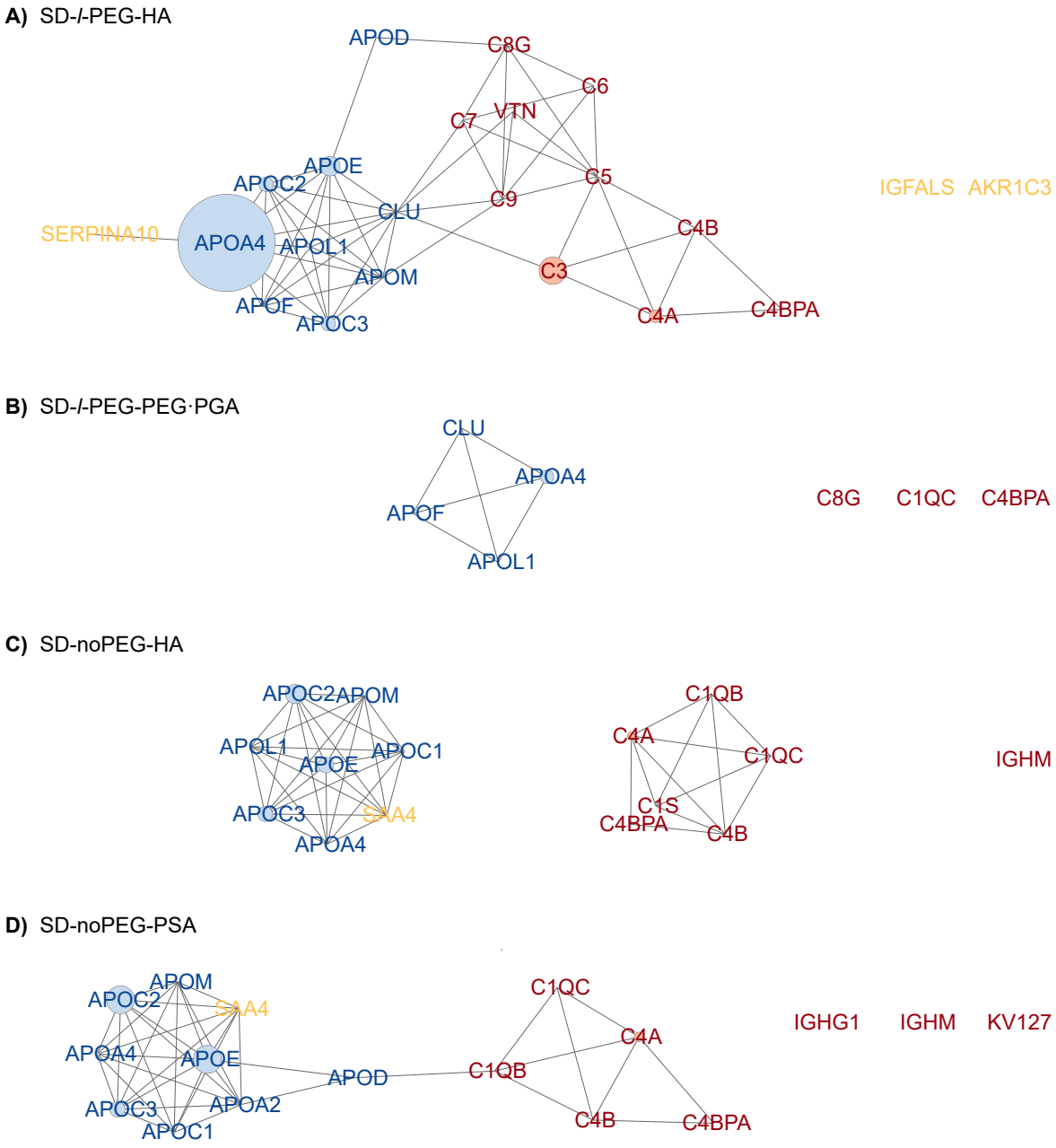


Figure 19. Protein-protein interactome of the detected proteins in the corona of each NC

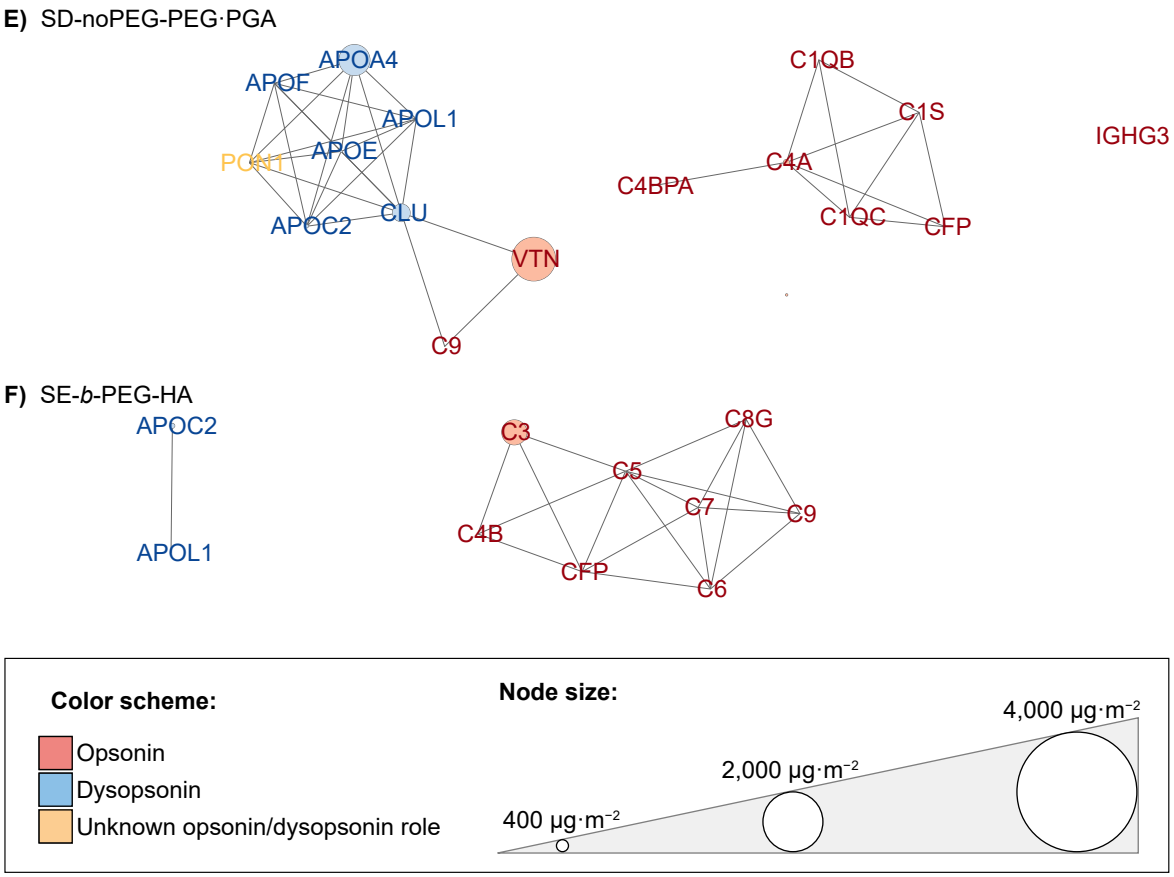


Figure 19. Protein-protein interactome of the detected proteins in the corona of each NC (continuation)

The network nodes represent proteins. The node name indicates the encoding gene name for the detected protein, and the presence of lines implies interactions between proteins. Only interactions with confidence > 70 % were plotted. Node size is linearly correlated with the protein concentration. Opsonins, mainly complement proteins and immunoglobulins, are represented in red. Dysopsonins, mostly apolipoproteins, in blue, and other proteins with unknown opsonin/dysopsonin behavior, in yellow. Overall, two protein interaction clusters of apolipoproteins and complement proteins can be seen. Figure generated by Cytoscape 3.9.1 with stringApp 1.7.0 and yFiles Organic Edge Router Layout Algorithms 1.2. The compositions of SD-*l*-PEG-HA, SD-*l*-PEG-PEG·PGA, SD-noPEG-HA, SD-noPEG-PSA, SD-noPEG-PEG·PGA, and SE-*b*-PEG-HA are shown in Figure 5. **Abbreviations:** AKR1C3: Aldo-keto reductase family 1 member C3, APOA2: Apolipoprotein A-II, APOA4: Apolipoprotein A-IV, APOC1: Apolipoprotein C-I, APOC2: Apolipoprotein C-II, APOC3: Apolipoprotein C-III, APOD: Apolipoprotein D, APOE: Apolipoprotein E, APOF: Apolipoprotein F, APOL1: Apolipoprotein L1, APOM: Apolipoprotein M, C1QB: Complement C1q subcomponent subunit B, C1QC: Complement C1q subcomponent subunit C, C1S: Complement C1s subcomponent, C3: Complement C3, C4A: Complement C4-A, C4B: Complement C4-B, C4BPA: C4b-binding protein alpha chain, C5: Complement C5, C6: Complement component C6, C7: Complement component C7, C8G: Complement component C8 gamma chain, C9: Complement component C9, CFP: Properdin, CLU: Clusterin, IGFALS: Insulin-like growth factor-binding protein complex acid labile subunit, IGHG1: Immunoglobulin heavy constant gamma 1, IGHG3: Immunoglobulin heavy constant gamma 3, IGHM: Immunoglobulin heavy constant mu, IGKV127: Immunoglobulin kappa variable 1-27, PON1: Serum paraoxonase/arylesterase, SAA4: Serum amyloid A-4 protein, SERPINA10: Protein Z-dependent protease inhibitor, VTN: Vitronectin. Values represent the mean of three replicates.

The interactome showed mainly two types of protein networks: apolipoproteins and complement factors. Also, while complement proteins were detected in all NCs, their presence was only marginally notorious in the case of SE-*b*-PEG-HA and SD-*l*-PEG-HA. On the other hand, the presence of apolipoproteins was highly relevant in SD-*l*-PEG-HA and moderated in the case of SD-noPEG-HA, SD-noPEG-PSA, and SD-noPEG-PEG·PGA.

The total protein amount in each system was calculated from Supplementary Tables 6 − 11 data. As illustrated in Figure 20, SD-*l*-PEG-HA showed the highest protein adsorption (due to the high apolipoprotein A-IV adsorption). The NCs made of non-PEGylated surfactants (SD-no-PEG-HA, SD-noPEG-PSA, and SD-noPEG-PEG·PGA) exhibited an intermediate total protein amount. Finally, the formulations with the lowest protein adsorption were SE-*b*-PEG-HA and SD-*l*-PEG-PEG·PGA. These results agree with the ones from section "3.5.4. Actual composition of the isolated NCs", as SE-*b*-PEG-HA was the one with the highest PEG surface density, and SD-*l*-PEG-PEG·PGA the one with a PEG density and MW more likely to provide a stealth effect to the NCs.

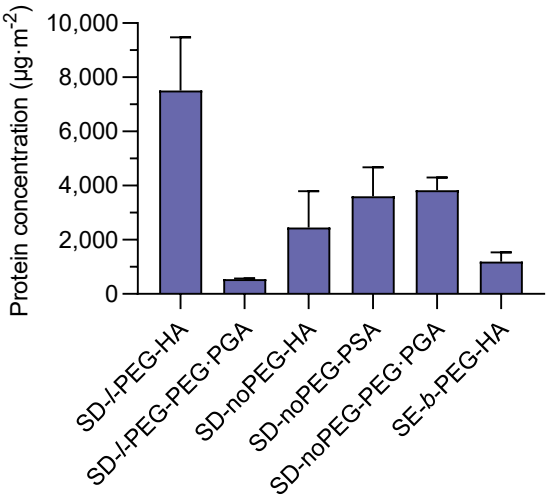


Figure 20. NCs' total adsorbed protein amount

The compositions of SD-*l*-PEG-HA, SD-*l*-PEG-PEG·PGA, SD-noPEG-HA, SD-noPEG-PSA, SD-noPEG-PEG·PGA, and SE-*b*-PEG-HA are shown in Figure 5. Values represent the mean ± standard deviation (n = 3).

A dysopsonin-enriched protein corona usually leads to long-circulating properties. Reduced protein coronas can be beneficial for attaching targeting ligands to drive NCs to specific tissues deliberately. In this sense, SD-*l*-PEG-PEG·PGA and SE-*b*-PEG-HA may be the most adequate for active-targeting strategies. On the other hand, SD-*l*-PEG-HA exhibited the highest corona protein content.

Apolipoproteins were particularly relevant in the protein corona of SD-*l*-PEG-PEG·PGA, SD-noPEG-HA, SD-noPEG-PSA, SD-*l*-PEG-HA, and SD-noPEG-PEG·PGA, reaching values of the main adsorbed proteins in the corona of the tested NCs, representing 99.82, 84.47, 84.34, 75.27, and 50.71 %, respectively (Figure 21).

Complement factors were the second most relevant protein family in the protein coronae, although their significance was very different for the various prototypes. In fact, the mass of complement proteins represented 83.52 %, 24.05 %, 14.71 %, 11.82 %, 7.05 %, and 0.18 % of the protein corona for SE-*b*-PEG-HA, SD-*l*-PEG-HA, SD-noPEG-HA, SD-noPEG-PSA, SD-noPEG-PEG·PGA, and SD-*l*-PEG-PEG·PGA, respectively.

Immunoglobulins were only present in the no-PEG formulations, being 3.52 % of the corona of SD-noPEG-PSA, 2.90 % of the SD-noPEG-PEG·PGA, and 0.39 % of SD-noPEG-HA.

USC UNIVERSIDADE DE SANTIAGO DE COMPOSTELA

Other protein families were detected for all systems but SD-*l*-PEG-PEG·PGA and SE-*b*-PEG-HA. However, these proteins were generally present in low percentages (0.32 – 0.67 %), except in SD-noPEG-PEG·PGA, where they represented 39.34 % of the corona, mainly due to intense vitronectin deposition.

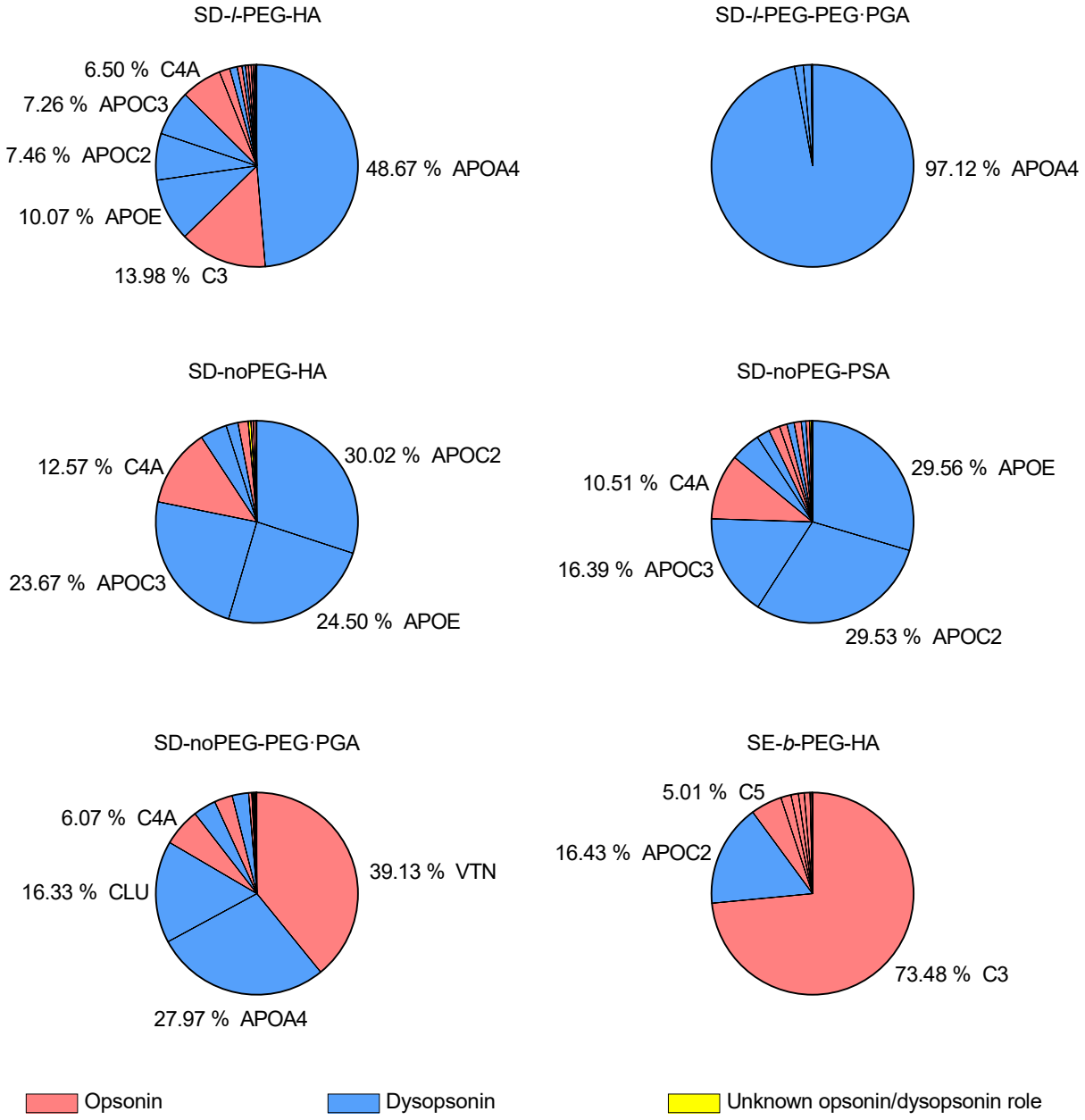


Figure 21. Protein mass percentage of the different proteins detected in the NCs' corona

Abbreviations: APOA4: Apolipoprotein A-IV, APOC2: Apolipoprotein C-II, APOC3: Apolipoprotein C-III, APOE: Apolipoprotein E, C3: Complement C3, C4A: Complement C4-A, C5: Complement C5, CLU: Clusterin, VTN: Vitronectin. The compositions of SD-*l*-PEG-HA, SD-*l*-PEG-PEG·PGA, SD-noPEG-HA, SD-noPEG-PSA, SD-noPEG-PEG·PGA, and SE-*b*-PEG-HA are shown in Figure 5. Values represent the mean of three replicates.

USC UNIVERSIDADE DE SANTIAGO DE COMPOSTELA

3.7.3.3. Relevant proteins detected in the protein corona of NCs

In 2016, Palchetti *et al.* correlated the protein corona fingerprint of 16 different liposomes with their uptake and membrane attachment to human cervical cancer HeLa cells. They found that vitronectin was the most determinant protein promoting the interaction between liposomes and those cell membranes, followed by Apo A-I, Apo A-II, Apo B, Apo C-II, and, to a lesser extent, Ig heavy chain V-III region BRO, vitamin K-dependent protein, and Integrin β3.[96,217] In another study, high cellular uptake of PS NPs by human mesenchymal stem cells was observed for the NPs whose functionalization promoted the adsorption of prothrombin, antithrombin III, and vitronectin, as well as inter-α-trypsin-inhibitor heavy chain H4, platelet factor 4, and Apo H, to a lesser extent.[63]

In this study, we have identified three particularly relevant proteins (vitronectin, Apo A-II, and Apo C-III) in the corona of the investigated NCs prototypes.

3.7.3.3.1. Vitronectin

Vitronectin is a liver-produced 75-kDa glycoprotein that regulates the coagulation cascade, innate immune response, and cell adhesion.[218] Residues 1 to 43 are known for binding to plasminogen activator inhibitor-1 (PAI-1) and urokinase-type plasminogen activator receptor (uPAR), which are involved in the coagulation cascade (Supplementary Figure 1). Vitronectin stabilizes PAI-1 active form, decreasing fibrin lysis and stabilizing thrombus.[219] Also, in addition to fibronectin and laminin,[220] vitronectin is one of plasma's primary cell adhesion proteins.[217] Vitronectin has an Arg-Gly-Asp (RGD) sequence located in residues 45 to 47, allowing vitronectin recognition by cell integrin receptors ($\alpha_V\beta_1$, $\alpha_V\beta_3$, $\alpha_V\beta_5$, $\alpha_V\beta_6$, $\alpha_V\beta_8$, and $\alpha_{IIb}\beta_3$). In this regard, vitronectin promotes cell adhesion and migration in tissue repairing and regeneration. The third binding site is located in residues 53 to 64, allowing vitronectin to interact with the thrombin–antithrombin III complex (TAT) and collagen. Residues 51 – 310 act as binding sites to complement proteins C5b – C7 and C9, blocking the terminal lytic step of the complement cascade. Finally, the polycationic heparin-binding domain-3 site of vitronectin (residues 346 – 361) can interact with perforin, inhibiting the perforin-mediated cytolysis caused by cytolytic T-lymphocytes.[218,221]

The presence of DOTAP is known to promote vitronectin binding to nanosystems' surfaces.[47,48] DOTAP-containing lipid NPs exhibited an average vitronectin protein corona abundance of 12.2 %.[222] However, other compositions can also lead to a vitronectin-enriched corona, such as uncoated PS-COOH NPs, which presented a corona composed of approximately 33 % vitronectin,[23] PLGA NPs,[223,224] and ovalbumin-based polymeric NPs of PEG of high density and MW.[225]

While $\alpha_V\beta_3$ integrin receptors are not cancer-specific,[226] many solid tumors and tumor neovasculature overexpress $\alpha_V\beta_3$ integrins.[226,227] Liposomes,[226] DOTAP/DNA lipoplexes,[228] and lipid NPs[228] with a protein corona enriched in vitronectin were found to have high and vitronectin-dependant *in vitro* uptakes. Some examples of $\alpha_V\beta_3$ integrin-overexpressing human cancer cell lines are U87 (primary glioblastoma), MDA-MB-231 (breast cancer), A549 (lung cancer), and HepG2 (liver cancer), with an integrin $\alpha_V\beta_3$ expression approximately 4.5-, 4-, 3-, and 2-fold of L02 human healthy hepatocytes, respectively.[227] In another study, vitronectin-enriched lipid NPs were found to accumulate in the lung after administration in healthy C57BL/6 mice.

Overall, considering the $\alpha_v\beta_3$ integrin-mediated internalization and the tendency for lung accumulation of vitronectin-coated nanocarriers, we could speculate that SD-noPEG-PEG·PGA might be a good candidate for lung cancer treatment.

3.7.3.3.2. Apolipoprotein A-IV

Apolipoprotein A-IV (Apo A-IV) is involved in lipid metabolism, reverse cholesterol transport, atherosclerosis, platelet aggregation, and thrombosis prevention.[229] Apo A-IV is taken up by hepatocytes through an unidentified receptor interaction. Once internalized, the Apo A-IV binds to NR1D1 and NR4A1 nuclear receptors and regulates glucose metabolism.[229] Apo A-IV dysopsonin behavior was confirmed by Ritz *et al.* after observing that the cellular uptake of carboxy-functionalized PS NPs by human mesenchymal stem cells decreased as the number of Apo A-IV molecules on their surface increased.[63]

In our case, Apo A-IV was one of the most abundant proteins of the protein corona of all the tested SD NCs, being especially relevant for SD-*l*-PEG-HA (Figure 21), with a detected concentration of more than 3.6 $mg \cdot m^{-2}$ and for SD-*l*-PEG-PEG·PGA where, while its concentration was really low, represented more than a 97 % of its corona.

Apo A-IV was detected as a predominant protein for polyethylene carbonate NPs,[230] cross-linked NPs of *N*-isopropylacrylamide (NIPAM), and *N*-tert-butylacrylamide (BAM) copolymers,[33] solid lipid NPs (SLNPs),[231] and PS NPs, to a lesser extent.[95,230]

Different attempts were made to correlate the Apo A-IV presence on the corona of polymeric NPs with their physicochemical characteristics.[95] For example, Göppert *et al.* reported an inverse correlation between Apo A-IV adsorption and the poloxamers' PEO length on cetyl palmitate SLNPs. In that study, poloxamer 184, exposing two 13-PEO chains, led to an intense Apo A-IV deposition, representing 22 % of the protein corona, while it was reduced to 7 % when poloxamer 338, with two chains of 128 PEO, was used.[231] A similar correlation between Apo A-IV deposition and PEG presence was also found for SiO_2 NCs.[232]

However, in our case, the main parameters driving Apo A-IV adsorption were the formulation methodology and/or the type of PEGylated surfactants rather than the PEG mass, density, or thickness. More detailed, Apo A-IV was present in all solvent displacement formulations, including the non-PEGylated NCs, and not in the one formulated by SE. Also, high percentages of Apo A-IV were found for *l*-PEG formulations, meaning that TPGS might also be promoting this adsorption. However, to our knowledge, no other protein corona characterization has been performed with polymeric systems containing TPGS and Vitamin E, and such intense Apo A-IV adsorption was not described, even for other PEGylated NPs. In this sense, SD-*l*-PEG-HA might be the most promising tested carrier for achieving a reduced phagocytic uptake and a preferential hepatic accumulation, while SD-*l*-PEG-PEG·PGA might be the one with the lowest phagocytic uptake.

Finally, Apo E and Apo C-II, proteins that are known to interact with Apo A-IV, were discarded as the reason for the intense Apo A-IV deposition on the SD-*l*-PEG-HA as they were also detected on some of the other SD NCs in similar amounts.

USC UNIVERSIDADE DE SANTIAGO DE COMPOSTELA

3.7.3.3.3. Apolipoprotein E

The biological role of apolipoprotein E (Apo E) is to transport cholesterol and triglycerides in the blood and the brain. Apo E is known to interact with LDLRs,[233] scavenger receptor class B type I (SR-BI),[234] LRP1, and heparan sulfate proteoglycan, which are widely expressed on the human body, mainly in the liver but also in the brain.[235]

Apo E is usually present in the protein corona of lipid-based NPs, especially when their PEG density is low.[110] Nanosystems with a protein corona enriched in Apo E have been explored for active targeting of hepatocytes.[236] The recently FDA-approved drug patisiran [Onpattro®, a double-stranded small interfering RNA encapsulated in a lipid NP mainly composed of the DLin-MC3-DMA, distearoylphosphatidylcholine (DSPC), biotin-lipid, cholesterol, and 1,2-dimyristoyl-sn-glycero-3-phosphoethanolamine to treat hereditary transthyretin-mediated amyloidosis][237] relies on a gradual PEG loss and consequent adsorption of Apo E for achieving a high hepatocyte uptake.[238] In fact, the presence of ionizable cationic lipids such as 1,2-dioleoyl-3-dimethylammonium propane,[222] DLin-KC2-DMA,[239,240] and DLin-MC3-DMA[240,241] promoted the adsorption of Apo E. Also, the nature of the helper lipids is essential for Apo E adsorption and efficacy of the NPs. For example, Zhang *et al.* found that transfection efficiencies in HeLa cells were higher when the phospholipid DOPE was used instead of phosphatidylcholines such as SOPC, 1,2-dioleoyl-sn–glycero-3-phosphocholine (DOPC), and DSPC. However, in all cases, the uptake mechanisms were Apo E-dependent, as these formulations were ineffective in an Apo E-free media.[242]

Several studies have explored the possibility of corona-mediated brain targeting as circulating Apo E and A-I are known to cross the BBB via receptor-mediated transcytosis. For example, a 45-fold tumor accumulation was described for liposomes decorated with an Apo A-I- and Apo E-recruiter peptide compared to the uncoated liposomes in a glioblastoma multiforme xenograft model.[243] Other approaches, such as Apo E-functionalized SLNPs, were explored for BBB crossing.[244] However, in some cases, these brain-targeted Apo E-functionalized particles might suffer from intense blood clearance at the liver.

Finally, the SR-BI and LDLRs were also described to be overexpressed in ovarian[245] and pancreatic cancers.[245,246]

In our study, Apo E was present in the corona of all formulations but SD-*l*-PEG-PEG·PGA and SE-*b*-PEG-HA, which contained the highest PEG content (Table 12). Also, the non-PEGylated PSA- and HA-coated NCs, which had phosphatidylcholines as surfactants, had the highest Apo E adsorption, representing 30 and 24 % of their corona, respectively (Figure 21).

These results agree with the phosphatidylcholine and low-PEG Apo E-binding dependency described in the literature and suggest that SD-noPEG-HA and SD-noPEG-PSA might be the most appropriate of the tested NCs for liver targeting with the drawback of being also captured by the immune system. The use of these NCs for pancreatic tumor-targeting might also be interesting to explore.

3.7.3.3.4. Other apolipoproteins

Apo C-II is another apolipoprotein involved in lipid transport. As Apo E does, it also interacts with the LDLRs and the scavenger receptor SRBI. Apo C-II was a major protein

of DOPC-containing liposomes[73,247] and promoted NP adhesion and internalization to HeLa cells.[217] Like Apo E, the highest Apo C-II adsorption was found for SD-noPEG-HA and PSA (approximately 30 % of their coronae), which might be due to phosphatidylcholines' presence.

Finally, clusterin (CLU; also known as Apolipoprotein J) is a C5b-9 complement complex inhibitor[248] reported to decrease the macrophage uptake of nanocarriers when present in their corona.[69,249] Clusterin was detected in the protein corona of three NCs, SD-*l*-PEG-HA, SD-*l*-PEG-PEG·PGA, and SD-noPEG-PEG·PGA, being a relevant component of the corona only for the latest system, and suggesting a reduced phagocytic uptake.

3.7.3.3.5. Complement

Complement proteins were detected in the corona of all the tested NCs. Generally, they were not found in high amounts, except for C3 in SD-*l*-PEG-HA (1051 $\mu g \cdot m^{-2}$; 14 % of its corona) and SE-*b*-PEG-HA (875 $\mu g \cdot m^{-2}$; 73 % of its corona), and C4A in SD-noPEG-PSA (380 $\mu g \cdot m^{-2}$; 11 % of its corona) and SD-noPEG-HA (308 $\mu g \cdot m^{-2}$; 13 % of its corona). In this sense, the abovementioned formulations might be good candidates for targeting immune cells and might be of interest for vaccination of regulation of inflammation.[250] Contrarily, the lowest complement deposition was found in the prototype with the highest PEGylation (SD-*l*-PEG-PEG·PGA).

While the central role of complement proteins is to facilitate the uptake and destruction of pathogens, non-specific adsorption of unactivated complement factors on nanocarriers can occur. Knowing whether a nanocarrier does or does not activate the complement system is crucial not only because the resulting opsonization would lead to its uptake by phagocytic cells and consequently reduced circulation time but also because of the production of the anaphylatoxins C3a, C4a, and C5a, which may induce adverse reactions such as complement activation-related pseudoallergy.[251] In fact, complement activation was reported in polymer-based NCs like PLA NCs, PLA-poloxamer NCs, PLA·PEG NCs,[252] and commercialized nanomedicines such as Doxil® and Taxol®.[253]

3.8. *IN VITRO* COMPLEMENT ACTIVATION

To elucidate whether the complement system was activated by the tested NCs, we have performed a qualitative analysis of complement factor I-cleaved C3b (iC3b) by Western blot (WB) after incubation of the NCs with plasma. C3 is a central protein in the complement cascade, meaning that iC3b fragments will be present independently of the triggered activation pathway.[254] However, since we have used sodium citrate as an anticoagulant, only the alternative pathway is still subjectable to activation.[255]

The C3 protein is composed of two chains, C3-α chain and C3-β chain, with an MW of ≈ 115 and ≈ 75 kDa, respectively. Therefore, detecting only these two bands in the WB proves that C3 was not activated. On the other hand, if C3 is cleaved, fragments of ≈ 43 kDa would be detected. We used Zymosan, a polysaccharide that activates the complement system through the alternative complement pathway, and Taxol-like NPs as positive controls. Notably, patients treated with Taxol® often experience mild to severe hypersensitivity reactions.

USC UNIVERSIDADE DE SANTIAGO DE COMPOSTELA

Our results indicate a mild complement activation for the tested NCs (Figure 22).

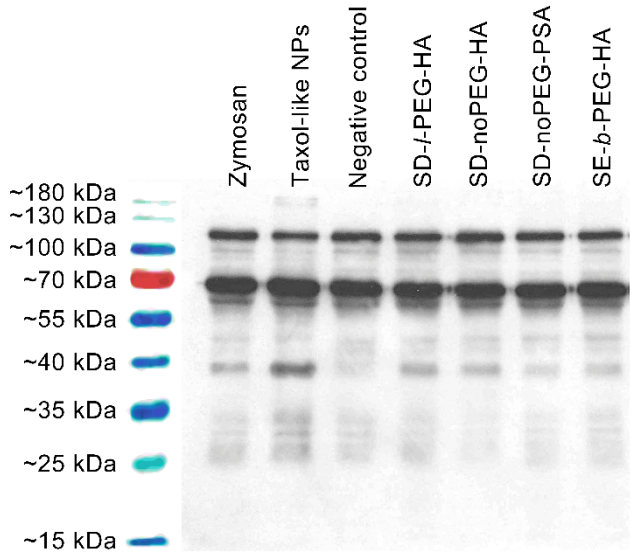


Figure 22. Representative Western blot of C3 and its fragments

Complement activation was confirmed by the presence of C3 fragments with an MW ≈ 43 kDa. Positive controls were Zymosan (0.3 mg·mL^{-1}) and Taxol-like NPs (diluted 10 × in PBS). In the negative control, nanosystems were replaced by PBS. The tested NCs (SD-*l*-PEG-HA, SD-noPEG-HA, SD-noPEG-PSA, and SE-*b*-PEG-HA) activated the complement system. **Abbreviations:** PBS: phosphate-buffered saline. The compositions of SD-*l*-PEG-HA, SD-*l*-PEG-PEG·PGA, SD-noPEG-HA, SD-noPEG-PSA, SD-noPEG-PEG·PGA, and SE-*b*-PEG-HA are shown in Figure 5.

3.9. ANALYSIS OF THE DIFFERENCES AND SIMILARITIES BETWEEN PROTEIN FINGERPRINTS

A protein corona pairwise comparison between NCs (Supplementary Figure 13) revealed that SD-noPEG-HA and SD-noPEG-PSA exhibited the most similar protein adsorption behavior, as they shared 13 proteins out of 15 and 17 proteins, respectively, that is, 68.4 % of shared proteins, indicating that the polymeric shell had low influence altering the protein corona. Of note, it seems that HA promoted the adsorption of Complement C1s subcomponent and apolipoprotein L1. In contrast, the interaction of the SD-noPEG-PSA with the immunoglobulin kappa variable 1-27, apolipoprotein A-II, immunoglobulin heavy constant gamma 1, and apolipoprotein D was probably driven by PSA. Furthermore, none of the unshared proteins could be found among the five most significant proteins detected on the corona of these systems.

SD-noPEG-PSA and SE-*b*-PEG-HA were the NCs that differed the most, with only two shared proteins (8 % out of their total proteins). These systems differed in their surfactant and polymer composition while their oil core composition was constant, suggesting the low influence of the oily core.

The rest of the NCs posed an intermediate situation, with shared protein percentages ranging from 13.3 to 40.9 %.

Also, paying attention to the incidence of each protein in the prototype set (Supplementary Figure 14), we can see that, in general, most of the detected proteins are only shared by a few of the tested formulations. In fact, out of the 33 detected proteins, 25 were found in no more than 3 prototypes, while only 8 were found in the corona of 4 or more systems. More detailed,

8 proteins were found exclusively in one of the prototypes, while 10 in two prototypes, 7 in three prototypes, 4 in 4 prototypes, 4 in 5 prototypes, and none was present in all tested NCs.

The unique proteins found in SD-*l*-PEG-HA were Aldo-keto reductase family 1 member C3, Insulin-like growth factor-binding protein complex acid labile subunit, and Protein Z-dependent protease inhibitor. In the case of SD-noPEG-PSA, Apolipoprotein A-II, Immunoglobulin heavy constant gamma 1, Immunoglobulin kappa variable 1-27. Finally, for SD-noPEG-PEG·PGA, Immunoglobulin heavy constant gamma 3, and Serum paraoxonase/arylesterase 1.

Also, we can see that SD-*l*-PEG-HA and SE-*b*-PEG-HA behaved differently from the other NCs as they recruited four specific proteins of themselves (Complement C3, C5, C6, and C7) as well as SD-noPEG-HA and SD-noPEG-PSA, with three specific proteins (Apolipoprotein C-I, Immunoglobulin heavy constant mu, Serum amyloid A-4 protein). These data suggest that the abovementioned systems differ from the others, which might be attributed to the presence of PEGylation and HA for the first two and the influence of phosphatidylcholines for SD-noPEG-HA and PSA.

Two proteins were present in all the formulations made by solvent displacement but not in the one made by the self-emulsifying technique: apolipoprotein A-IV and C4b-binding protein alpha chain, while no proteins were exclusive to the SE NCs.

Finally, no protein was present in the corona of all NCs. The most repetitive proteins were Apo A-IV, Apo C-II, Apo L1, and C4b-binding protein alpha chain, as they were found in the corona of five out of the six tested NCs.

Among the different prototypes, whose key properties studied in this Chapter are illustrated in Table 17, SD-noPEG-PEG·PGA might be particularly promising for targeting the lung. Indeed, due to the adsorption of vitronectin, it is expected that this formulation will accumulate in the lung. On the other hand, clusterin, another adsorbed protein, is known to extend the circulation time of nanosystems, reducing its uptake by immune cells and increasing the chances of the particles reaching the lung.

SD-*l*-PEG-PEG·PGA is also attractive due to its irrelevant Apo A-IV corona. This prototype might be a good candidate for decoration by targeting ligands.

SD-*l*-PEG-HA might be helpful in liver targeting due to its extraordinary Apo A-IV adsorption.

In the next chapter, SD-*l*-PEG-HA, SD-*l*-PEG-PEG·PGA, and SD-noPEG-PEG·PGA will be used as templates for designing nanocarriers for lung cancer treatment.

USC
UNIVERSIDADE DE SANTIAGO DE COMPOSTELA

Table 17. Summary of the different studied physicochemical and biological parameters studied during this chapter

Formulation	SD-*l*-PEG-HA	SD-*l*-PEG-PEG·PGA	SD-noPEG-HA	SD-noPEG-PSA	SD-noPEG-PEG·PGA	SE-*b*-PEG-HA
Hydrodynamic diameter (DLS) (nm)	135 ± 4	143 ± 1	158 ± 12	150 ± 10	121 ± 3	147 ± 5
ζ-potential (mV)	−33 ± 5	+6 ± 1	−53 ± 16	−55 ± 1	−22 ± 1	−10 ± 1
Morphology (TEM/Cryo-EM)	Spherical	Spherical	Spherical	Spherical	Spherical	Spherical
Stable in NaCl / PBS	Yes	Yes	No	No	No	Yes
Stable in plasma	Yes	Yes	Yes	Yes	Yes	Yes
Polymer attachment	Low	High	Low	Low	High	Low
PEG length	1 kDa	1 – 5 kDa	N/A	N/A	5 kDa	< 1 kDa
PEG density (chains / 100 nm^2)	320 ± 133	200 ± 86	N/A	N/A	19 ± 8	9,038 ± 3,893
PEG conformation	Brush	Brush	N/A	N/A	Brush	Brush
Protein corona	+++	+	++	++	++	+
Main protein adsorption	Apo A-IV, Comp.	Apo A-IV	Apolipoproteins, Comp.	Apolipoproteins, Comp.	Vitronectin, apolipoproteins	Comp.
Expected biodistribution profile	Liver / spleen	Liver	Liver / spleen	Liver / spleen	Lung	Liver / spleen
Expected circulation time	Intermediate	Long	Intermediate	Intermediate	Intermediate / long	Intermediate / short
Comp. activation	Yes (mild activation)	Not tested	Yes (mild activation)	Yes (mild activation)	Not tested	Yes (mild activation)

Abbreviations: Comp: complement. The compositions of SD-*l*-PEG-HA, SD-*l*-PEG-PEG·PGA, SD-noPEG-HA, SD-noPEG-PSA, SD-noPEG-PEG·PGA, and SE-*b*-PEG-HA are shown in Figure 5.

4. CONCLUSIONS

In the present study, we have investigated the relationship between the chemical composition and the protein corona of different NC prototypes.

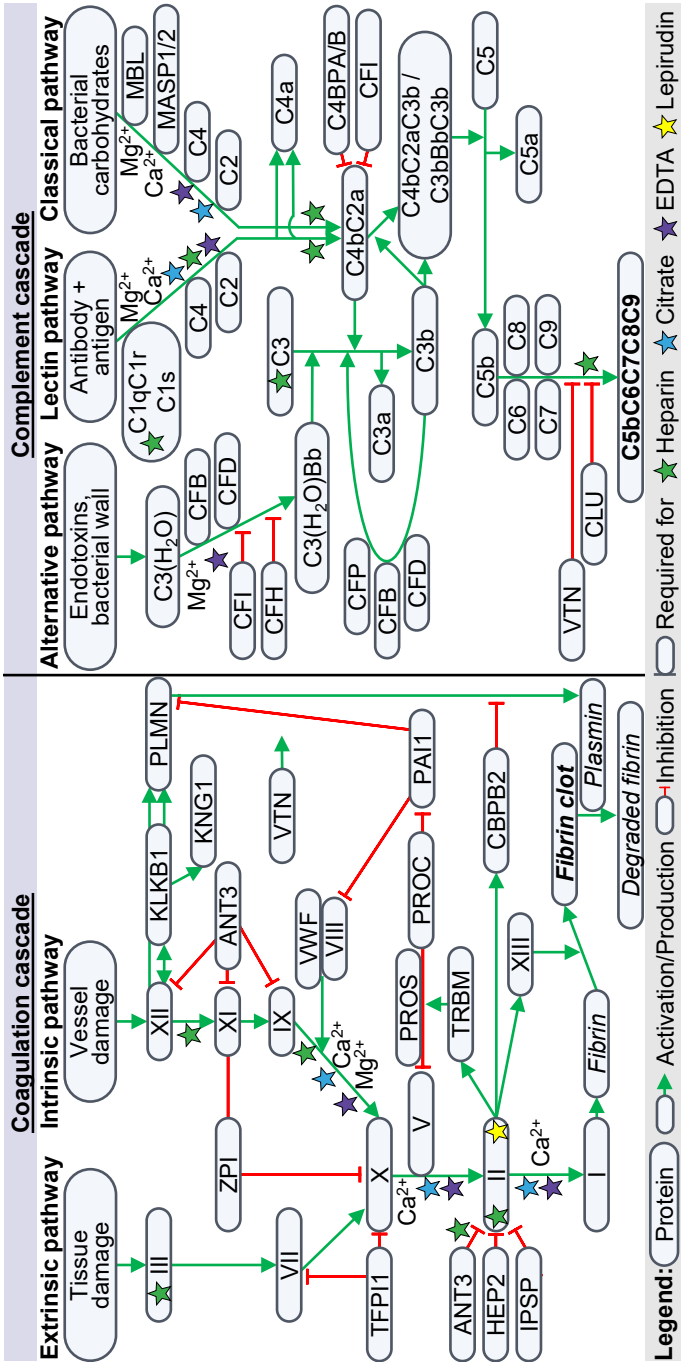
The six tested polymeric NCs exhibited different protein corona fingerprints, which may translate into different biological fates. SD-noPEG-PEG·PGA suffered from intense vitronectin adsorption, while SD-*l*-PEG-PEG·PGA exhibited the thinnest protein corona.

SD-noPEG-PEG·PGA and SD-*l*-PEG-PEG·PGA were identified as the most promising candidates for loading therapeutic agents for lung cancer treatment.

Further *in vitro* and *in vivo* studies would be necessary to evaluate whether the NCs prototypes' behavior matched the predicted internalization, circulation time, and biodistribution.

USC
UNIVERSIDADE
DE SANTIAGO
DE COMPOSTELA

5. SUPPLEMENTARY INFORMATION



Supplementary Figure 1. Effect of heparin, citrate, EDTA, and lepirudin over the coagulation and complement cascades

Heparin binds to several proteins in the coagulation cascade and the three complement activation pathways. Citrate, a Ca^{2+}-chelator, blocks the coagulation cascade at different levels and the classical and lectin complement activation pathways.[143] EDTA, which chelates more divalent cations than Ca^{2+}, also blocks the alternative pathway. Lepirudin, a recombinant version of hirudin, only blocks the coagulation factor II, but its use is not usual in protein corona studies.[144] **Abbreviations:** ANT3: antithrombin-III. Bb: activated complement factor B. C1q: complement component 1, q subcomponent. C1r: complement component 1, r subcomponent. C1s: complement component 1, s subcomponent. C2: complement component 2. C2a: complement C2a fragment. C3: complement C3. $C3(H_2O)$: hydrolyzed complement component C3. C3a: C3a anaphylatoxin. C3b: complement C3 beta chain + alpha' chain. C4: complement C4. C4a: complement C4a fragment. C4b: complement C4b fragment. C4BPA: C4b-binding protein alpha chain. C4BPB: C4b-binding protein beta chain. C5: complement C5. C5a: C5a anaphylatoxin. C5b: complement C5 beta chain + alpha' chain. C6: complement component C6. C7: complement component C7. C8: complement component C8. C9: complement component C9. CBPB2: carboxypeptidase B2. CFB: complement factor B. CFD: complement factor D. CFH: complement factor H. CFI: complement factor I. CLU: clusterin. EDTA: Ethylenediaminetetraacetic acid. HEP2: heparin cofactor 2. I: fibrinogen (coagulation factor I). II: prothrombin (coagulation factor II). III: tissue factor (coagulation factor III). IPSP: plasma serine protease inhibitor. IX: coagulation factor IX. KLKB1: plasma kallikrein. KNG1: kininogen-1. MASP1: mannan-binding lectin serine protease 1. MASP2: mannan-binding lectin serine protease 2. MBL: mannose-binding protein. PAI1: plasminogen activator inhibitor 1. PLMN: plasminogen. PROC: Vitamin K-dependent protein C. PROS: Vitamin K-dependent protein S. TFPI1: tissue factor pathway inhibitor. TRBM: thrombomodulin. V: coagulation factor V. VII: coagulation factor VII. VIII: coagulation factor VIII. VTN: vitronectin. VWF: von Willebrand factor. X: coagulation factor X. XI: coagulation factor XII. XII: coagulation factor XII. XIII: coagulation factor XIII. ZPI: protein Z-dependent protease inhibitor.

USC UNIVERSITAT DE SANTIAGO DE COMPOSTELA

Supplementary Table 1. Validation of the calibration curves for each quantified substance and formulation

Formulation	Molecule	Calibration curve range (ppb)	r^2 (mean ± StD)	Precision (pooled RStD%) (%)	Accuracy (RE%) (%) (low; mid; high range)	LoQ (ppb) (mean ± StD)
SD-*l*-PEG-HA	Benzethonium chloride	8.0 – 80.0	0.9959 ± 0.0016	4.4	3.9; −0.3; 2.4	0.70 ± 0.38
	TPGS	64.0 – 640.0	0.9854 ± 0.0040	8.6	1.9; −1.0; 2.5	1.90 ± 0.86
	DL-α-tocopherol	216.0 – 2160.0	0.9948 ± 0.0040	4.9	−1.6; 2.6; 0.0	1.16 ± 0.47
	Hyaluronic acid (whole)	19,590.0 – 68,570.0	0.9897 ± 0.0009	4.0	3.5; 1.0; 1.0	22.51 ± 9.16
	Hyaluronic acid (supernatant)	15,670.0 – 78,370.0	0.9889 ± 0.0039	4.3	5.3; 3.6; 3.6	26.65 ± 6.62
	Hyaluronic acid (infranatant)	17,140.0 – 58,780.0	0.9840 ± 0.0056	4.8	5.6; 1.7; 1.7	34.42 ± 14.95
SD-*l*-PEG-PEG·PGA	DL-α-tocopherol	202.5 – 2,025.0	0.9940 ± 0.0024	3.4	−3.7; 1.3; −0.5	3.92 ± 4.27
	TPGS	60.0 – 600.0	0.9939 ± 0.0025	4.8	3.4; −2.1; 2.3	15.42 ± 18.8
	1,2-dioleoyl-3-trimethylammonium propane chloride	7.5 – 75.0	0.9984 ± 0.0010	4.9	−0.9; 0.4; 0.1	0.39 ± 0.30
	PEG·PGA (whole)	47,220.0 – 226,667.0	0.9955 ± 0.0006	1.7	3.5; 2.7; 2.7	11,660.83 ± 3,535.07
	PEG·PGA (supernatant)	15,410.0 – 292,740.0	0.9945 ± 0.0034	2.3	15.2; 6.0; 6.0	7,373.02 ± 7,045.28
	PEG·PGA (infranatant)	18,890.0 – 226,667.0	0.9960 ± 0.0020	1.6	2.3; 5.1; 5.1	5,410.25 ± 2,939.91
SD-noPEG-HA	CTAB	43.2 – 144.0	0.9985 ± 0.0009	1.0	2.0; −0.2; 1.1	0.27 ± 0.13
	C_8-C_8-C_8 Triglyceride	881.3 – 2937.6 (*)	0.9880 ± 0.0016	3.2	5.9; −2.7; 3.4	5.99 ± 2.76
	C_8-C_8-C_{10} Triglyceride	881.3 – 2937.6 (*)	0.9859 ± 0.0040	3.0	6.1; −2.0; 4.3	8.22 ± 2.40
	C_8-C_{10}-C_{10} Triglyceride	881.3 – 2937.6 (*)	0.9852 ± 0.0031	3.7	5.6; −3.5; 3.7	8.18 ± 1.66
	C_{10}-C_{10}-C_{10} Triglyceride	881.3 – 2937.6 (*)	0.9792 ± 0.0036	5.0	4.2; −2.7; 3.1	1.63 ± 0.31
	Phosphatidylcholine 756.6 Da	216.0 – 720.0 (**)	0.9887 ± 0.0074	1.6	2.8; 5.4; −4.7	0.62 ± 0.44
	Phosphatidylcholine 758.6 Da	216.0 – 720.0 (**)	0.9812 ± 0.0018	3.4	4.2; 5.3; −4.1	0.14 ± 0.01
	Phosphatidylcholine 780.6 Da	216.0 – 720.0 (**)	0.9908 ± 0.0052	1.2	1.8; 4.8; −4.2	0.24 ± 0.19
	Phosphatidylcholine 782.5 Da	216.0 – 720.0 (**)	0.9880 ± 0.0086	1.2	2.6; 6.1; −4.9	0.06 ± 0.01

Supplementary Table 1. Validation of the calibration curves for each quantified substance and formulation (continuation)

Formulation	Molecule	Calibration curve range (ppb)	r^2 (mean ± StD)	Precision (pooled RStD%) (%)	Accuracy (RE%) (%) (low; mid; high range)	LoQ (ppb) (mean ± StD)
SD-noPEG-HA	Hyaluronic acid (whole)	6,120.0 – 10,200.0	0.9383 ± 0.0652	4.0	3.7; 1.3; 1.3	19.18 ± 2.49
	Hyaluronic acid (supernatant)	20,000.0 – 98,000.0	0.9876 ± 0.0039	4.8	8.1; 6.0; 6.0	32.28 ± 9.41
	Hyaluronic acid (infranatant)	10,000.0 – 29,000.0	0.9852 ± 0.0052	4.3	1.8; 2.4; 2.4	15.35 ± 1.82
SD-noPEG-PSA	CTAB	43.2 – 144.0	0.9952 ± 0.0015	1.5	3.7; −0.2; 0.5	0.20 ± 0.01
	C_8-C_8-C_8 Triglyceride	881.3 – 2937.6 (*)	0.9814 ± 0.0025	3.3	8.5; −1.6; 2.5	6.46 ± 1.65
	C_8-C_8-C_{10} Triglyceride	881.3 – 2937.6 (*)	0.9801 ± 0.0017	3.8	8.4; −2.1; 2.8	9.44 ± 2.86
	C_8-C_{10}-C_{10} Triglyceride	881.3 – 2937.6 (*)	0.9848 ± 0.0008	4.0	5.2; −0.8; 2.3	7.59 ± 1.38
	C_{10}-C_{10}-C_{10} Triglyceride	881.3 – 2937.6 (*)	0.9697 ± 0.0165	5.9	4.6; −2.8; 3.1	1.08 ± 0.05
	Phosphatidylcholine 756.6 Da	216.0 – 720.0 (**)	0.9611 ± 0.0100	2.9	7.8; 4.7; −11.6	0.91± 0.14
	Phosphatidylcholine 758.6 Da	216.0 – 720.0 (**)	0.9552 ± 0.0114	4.7	8.1; 3.2; −11.9	0.15± 0.02
	Phosphatidylcholine 780.6 Da	216.0 – 720.0 (**)	0.9720 ± 0.0092	1.7	7.1; 4.8; −9.1	0.31 ± 0.14
	Phosphatidylcholine 782.5 Da	216.0 – 720.0 (**)	0.9628 ± 0.0116	2.2	8.0; 4.8; −11.8	0.08 ± 0.01
	Hyaluronic acid (whole)	6,150.0 – 10,870.0	0.9788 ± 0.0115	1.4	2.4; 0.7; 0.7	86.30 ± 32.47
	Hyaluronic acid (supernatant)	4,900.0 – 81,630.0	0.9867 ± 0.0061	2.8	3.6; 12.8; 12.8	413.54 ± 424.46
	Hyaluronic acid (infranatant)	7,350.0 – 29,390.0	0.9929 ± 0.0054	1.7	3.6; 3.6; 3.6	245.55 ± 134.63
SD-noPEG-PEG·PGA	DL-α-tocopherol	288.8 – 2,887.5	0.9958 ± 0.0009	2.5	−7.5; 2.8; −3.5	6.33 ± 0.58
	1,2-dioleoyl-3-trimethylammonium propane chloride	7.5 – 75.0	0.9984 ± 0.0010	1.7	−2.5; −0.3; −0.8	1.26 ± 0.49
	PEG·PGA (whole)	23,700.0 – 132,200.0	0.9978 ± 0.0012	1.1	3.8; 1.0; 1.0	432.10 ± 360.61
	PEG·PGA (supernatant)	7,700.0 – 184,800.0	0.9976 ± 0.0017	1.3	2.8; 4.6; 4.6	666.06 ± 970.38
	PEG·PGA (infranatant)	4,800.0 – 113,300.0	0.9984 ± 0.0012	1.9	2.5; 1.1; 1.1	69.37 ± 39.55

USC UNIVERSITAT DE SANTIAGO DE COMPOSTELA

Supplementary Table 1. Validation of the calibration curves for each quantified substance and formulation (continuation)

Formulation	Molecule	Calibration curve range (ppb)	r^2 (mean ± StD)	Precision (pooled RStD%) (%)	Accuracy (RE%) (%) (low; mid; high range)	LoQ (ppb) (mean ± StD)
SE-*b*-PEG-HA	Benzethonium chloride	1.0 – 9.6	0.9997 ± 0.0002	1.1	0.5; −4.7; 0.1	0.24 ± 0.03
	Macrogol-15-hydroxystearate	6.0 – 120.0 (***)	0.9992 ± 0.0001	2.0	−1.8; −0.6; −1.5	2.25 ± 1.74
	Polysorbate 80	487.2 – 2784.0	0.9990 ± 0.0002	0.8	3.9; −1.6; 1.4	11.61 ± 0.36
	C_8-C_8-C_8 Triglyceride	849.6 – 2832.0 (*)	0.9939 ± 0.0028	2.5	3.0; −2.1; 1.1	3.32 ± 1.59
	C_8-C_8-C_{10} Triglyceride	849.6 – 2832.0 (*)	0.9895 ± 0.0027	3.8	3.9; −1.5; 1.0	2.51 ± 1.14
	C_8-C_{10}-C_{10} Triglyceride	849.6 – 2832.0 (*)	0.9895 ± 0.0030	3.7	4.8; 4.7; 0.7	2.15 ± 1.82
	C_{10}-C_{10}-C_{10} Triglyceride	849.6 – 2832.0 (*)	0.9889 ± 0.0046	3.6	2.5; −4.4; 2.1	1.88 ± 1.17
	Hyaluronic acid (whole)	6,730.0 – 17,140.0	0.9863 ± 0.0004	2.4	3.2; 1.7; 1.7	15.53 ± 6.42
	Hyaluronic acid (retentate)	2,450.0 – 9,180.0	0.9658 ± 0.0164	3.3	8.7; 8.4; 8.4	14.21 ± 5.29
	Hyaluronic acid (permeate)	7,000.0 – 28,000.0	0.9901 ± 0.0049	3.9	4.0; 1.1; 1.1	35.22 ± 3.82

Abbreviations: CTAB: Hexadecyltrimethylammonium bromide. LoQ: limit of quantification. PEG·PGA: polyethylene glycol polyglutamic acid. RE%: relative differences between the estimated concentrations and the actual standard concentration. RStD%: Relative standard deviation of the responses for each concentration level. StD: standard deviation. TG: triglyceride. TPGS: D-α-tocopherol polyethylene glycol 1000 succinate. VitE: DL-α-tocopherol. (*): C_8-C_8-C_8, C_8-C_8-C_{10}, C_8-C_{10}-C_{10}, and C_{10}-C_{10}-C_{10} TGs calibration curves were built based on the amount of Miglyol® 812N. (**): Phosphatidylcholines' calibration curves were built based on the amount of Epikuron™ 145V. (***): macrogol-15-hydroxystearate calibration curves were built based on the amount of Kolliphor® HS15. Values represent the mean for pooled RStD% and RE% and mean ± standard deviation for r^2 and LoQ (n = 3). The compositions of SD-*l*-PEG-HA, SD-*l*-PEG-PEG·PGA, SD-noPEG-HA, SD-noPEG-PSA, SD-noPEG-PEG·PGA, and SE-*b*-PEG-HA are shown in Figure 5. Adaptation from [2] licensed under a Creative Commons CC BY license.

Supplementary Table 2. Reporting information for corona characterization based on the Minimum information about Nanomaterial Biocorona Experiments (MINBE)

Reporting component	Description
Biofluid processing	
Collection organisms	Blood from male/female healthy adult volunteers.
Collection approach	Venipuncture in the upper limb in citrated (3.8 %) vials.
Processing	Blood was centrifuged at 1,200 g for 10 min in the following 2 h post-collection. Plasma was collected, pooled, and aliquoted.
Storage	−80 °C, in low-binding plastic microtubes. No more than 2 years. Before each experiment, plasma aliquots were thawed overnight at 4 °C and centrifuged at 20,000 g for 1 h at 4 °C. If cream or pellets were present, they were discarded. Once thawed, plasma was kept at 4° C and not used for more than 24 h.
Reaction conditions	
Dosimetrics	10 % of NCs with a superficial area of 0.25 $m^2 \cdot mL^{-1}$ (or PBS in the case of the control) + 90 % undiluted plasma (final volume 1,100 µL). Plasma volume/NP area ratio of 35 $mL \cdot m^{-2}$
Sample conditions	Incubation at 37 °C for 1 h. Dark. Mild agitation.
Replicates	NPs: n = 3. Pooled plasma: n = 1.
Nanomaterial characterization	
Provenance	SD-*l*-PEG-HA: 500 µL of 27 $mg \cdot mL^{-1}$ VitE, 8 $mg \cdot mL^{-1}$ TPGS, and 1 $mg \cdot mL^{-1}$ BZT in ethanol were poured onto 1.5 mL of aqueous HA 1.33 $mg \cdot mL^{-1}$ under magnetic stirring at 700 rpm. The stirring was kept until the final volume was lower than 1.5 mL. NCs' volume was raised to 2 mL with ultrapure water. NCs were ultracentrifuged at ≈ 110,000 g for 1 h at 15 °C. The supernatant was resuspended to 750 µL with ultrapure water. SD-*l*-PEG-PEG·PGA, 900 µL of 15 $mg \cdot mL^{-1}$ VitE, 4.44 $mg \cdot mL^{-1}$ TPGS, and 0.56 $mg \cdot mL^{-1}$ DOTAP in ethanol were poured onto 2.231 mL of PEG·PGA 0.89 $mg \cdot mL^{-1}$ in water under magnetic stirring at 700 rpm. The stirring was kept until the final volume was lower than 1.0 mL. NCs' volume was raised to 2 mL using ultrapure water. NCs were ultracentrifuged at ≈ 110,000 g for 1 h at 15 °C. The supernatant was resuspended to 750 µL with ultrapure water. SD-noPEG-HA and SD-noPEG-PSA: 5 mL of 2.96 $mg \cdot mL^{-1}$ of MCTs, 0.75 $mg \cdot mL^{-1}$ of PCs, and 0.15 $mg \cdot mL^{-1}$ of CTAB in acetone and ethanol 19:1 were added to 10 mL of a 0.25 $mg \cdot mL^{-1}$ aqueous solution of the polymer (HA or PSA) dropwise using a Pasteur pipette under magnetic stirring at 700 rpm. Acetone was removed using a rotavapor until the sample volume was 5 mL. NCs were ultracentrifuged at ≈ 43,000 g for 30 min at 15 °C. The supernatant was resuspended to 750 µL with ultrapure water. SD-noPEG-PEG·PGA: 1070 µL of 12.62 $mg \cdot mL^{-1}$ VitE and 0.47 $mg \cdot mL^{-1}$ DOTAP in ethanol were poured onto 2.907 mL of water under magnetic stirring at 700 rpm. After 10 min, 66.67 µL of PEG·PGA 30 $mg \cdot mL^{-1}$ in water were added to the formulation. The stirring was kept until the final volume was lower than 2.0 mL. NCs' volume was raised to 2 mL using ultrapure water. NCs were ultracentrifuged at ≈ 110,000 g for 1 h at 15 °C. The supernatant was resuspended to 750 µL with ultrapure water. SE-*b*-PEG-HA: 4.375 mL of 0.286 $mg \cdot mL^{-1}$ of HA and 2.86 $mg \cdot mL^{-1}$ of HS15 in PBS 1 × were quickly poured over 295 mg of MCTs, 290 mg of P80, and 1 mg of BZT at 1100 rpm using a micropipette. NCs were diafiltered thrice by TFF (KrosFlo® KR2i, Repligen, Waltham, MA, USA) with a 500 kDa-cut-off mPES column with PBS at 9 $mL \cdot min^{-1}$.

USC UNIVERSIDADE DE SANTIAGO DE COMPOSTELA

Supplementary Table 2. Reporting information for corona characterization based on the Minimum information about Nanomaterial Biocorona Experiments (MINBE) (continuation)

Reporting component	Description
Nanomaterial characterization (continuation)	
Synthesized properties and agglomeration state	SD-*l*-PEG-HA. Hydrodynamic diameter: 156 ± 8 nm. PDI: 0.17 ± 0.01. ζ-pot.: −39 ± 4 mV. Surface area: 0.25 ± 0.03 $m^2 \cdot mL^{-1}$. SD-*l*-PEG-PEG·PGA. Hydrodynamic diameter: 137 ± 4 nm. PDI: 0.08 ± 0.05. ζ-pot.: +0 ± 3 mV. Surface area: 0.37 ± 0.03 $m^2 \cdot mL^{-1}$. SD-noPEG-HA. Hydrodynamic diameter: 135 ± 4 nm. PDI: 0.09 ± 0.02. ζ-pot.: −33 ± 5 mV. Surface area: 0.35 ± 0.02 $m^2 \cdot mL^{-1}$. SD-noPEG-PSA. Hydrodynamic diameter: 124 ± 7 nm. PDI: 0.06 ± 0.01. ζ-pot.: −38 ± 4 mV. Surface area: 0.35 ± 0.04 $m^2 \cdot mL^{-1}$. SD-noPEG-PEG·PGA. Hydrodynamic diameter: 116 ± 2 nm. PDI: 0.11 ± 0.02. ζ-pot.: −35 ± 2 mV. Surface area: 0.35 ± 0.04 $m^2 \cdot mL^{-1}$. SE-*b*-PEG-HA. Hydrodynamic diameter: 113 ± 2 nm. PDI: 0.25 ± 0.01. ζ-pot.: −6 ± mV. Surface area: 0.36 ± 0.03 $m^2 \cdot mL^{-1}$.
Surface chemistry	No chemical modifications after NCs preparation and isolation.
Separation techniques and processing	
Corona separation	Mix 1 mL sample with 1 mL 40 % sucrose in the centrifugation tube. Add 2 mL of sucrose 10 % on top of it. Complete the gradient with 2 mL of ultrapure water. Ultracentrifuge at 110,000 g for 1 h at 15 °C. Collect the top 1000 µL.
Sample clean-up	24 µL of the sample were loaded into a 10 %-acrylamide PAGE gel. Electrophoresis was run until proteins entered ≈ 3 mm in the resolving gel. Gels were stained with Coomassie blue. The unique band of each lane containing all the proteins was manually excised and transferred to a low-binding microtube. Then, gel pieces were washed twice with 25 mM ammonium bicarbonate, dehydrated with ACN, and reduced with DTT 10 mM in ammonium bicarbonate 50 mM at 56 °C for 30 min. Then, it was alkylated with iodoacetamide in 50 mM ammonium bicarbonate for 20 min in the dark.
Protein digestion	Samples were incubated with 30 µL of trypsin (20 $ng \cdot \mu L^{-1}$ in ammonium bicarbonate 20 mM) for 16 h at RT. The supernatant containing the first extracted peptides was transferred to a new low-binding microtube. The remaining peptides were further extracted using 50 % (v/v) ACN/0.1 % (v/v) TFA aqueous solution thrice. Then, samples were dehydrated with ACN and stored at -20 °C.
LC-MS/MS analysis of protein	
LC platform	Eskpert nLC425 micro-LC system, Analyst TF, version 1.7.1 (Sciex).
MS/MS platform	TripleTOF® 6600 detector (Sciex, Redwood City, CA, USA), Sciex Analyst TF, version 1.7.1.
LC column	Trap column: YMC-TRIART C18 reversed-phase column (particle size: 3 µm; pore size: 120 Å). Analytical column: Eksigent Nano Chrom XP C18 reversed-phase column (dimensions: 150 × 0.30 mm; particle size: 3 µm; pore size: 120 Å).
LC gradient	Flow rate: 5 $\mu L \cdot min^{-1}$. Temperature: 40 °C. DDA: 0 min: 98 % A; 2 % B, 80 min:10 % A; 90 % B, 85 min: 10 % A; 90 % B, 90 min: 98 % A; 2 % B. SWATH-MS: 0 min: 95 % A; 5 % B, 35 min 5 % A; 95 % B, 40 min: 10 % A; 90 % B, 45 min: 10 % A; 90 % B, 50 min: 95 % A; 5 % B.
LC solvents	0.1 % TFA in water (A), 0.1 % TFA in acetonitrile (B) (Scharlau, Barcelona, Spain).
Injection volume	4 µL (DDA and SWATH-MS).

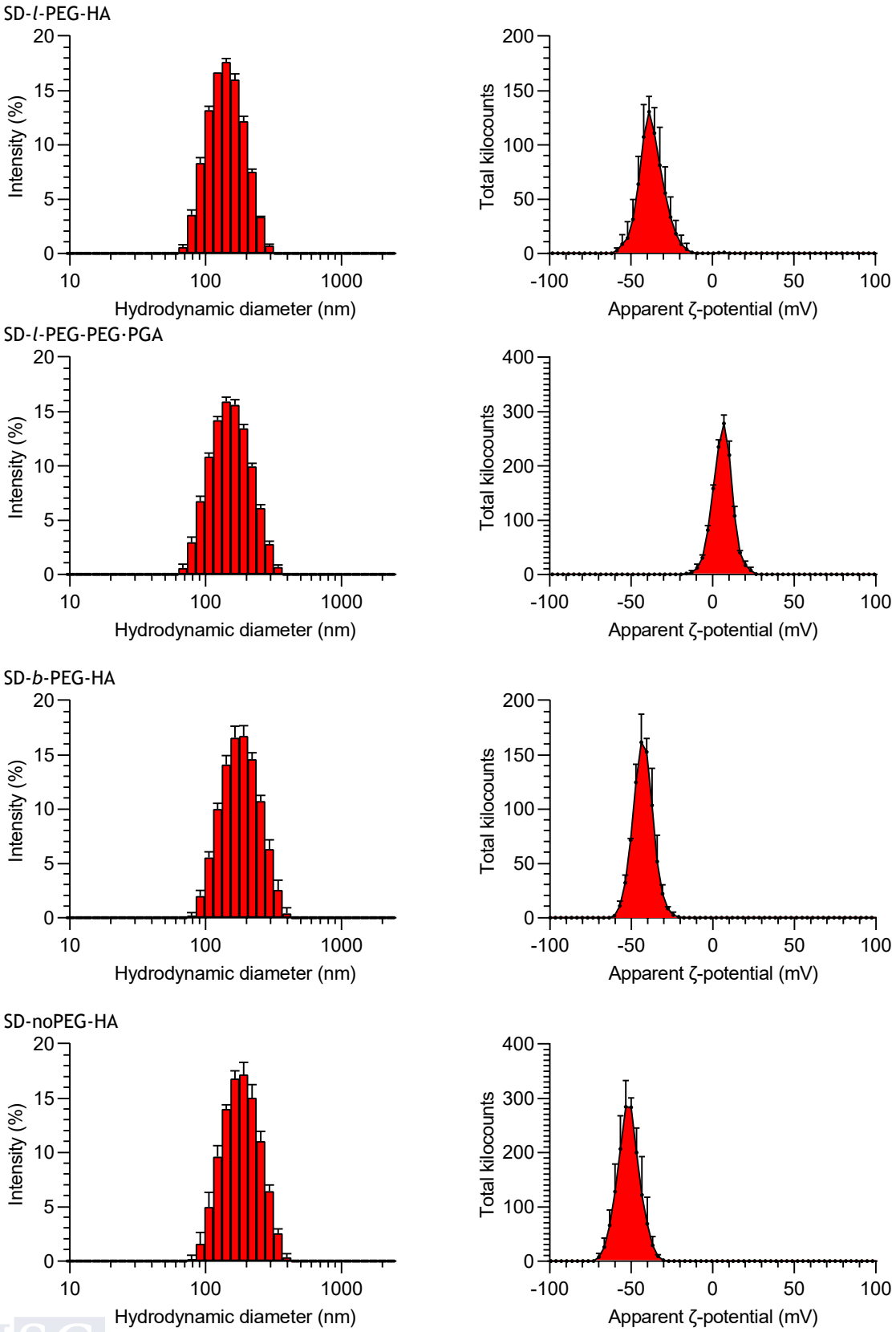
USC UNIVERSIDADE DE SANTIAGO DE COMPOSTELA

Supplementary Table 2. Reporting information for corona characterization based on the Minimum information about Nanomaterial Biocorona Experiments (MINBE) (continuation)

Reporting component	Description
LC-MS/MS analysis of protein (continuation)	
MS source settings	Microsource potential (ionization voltage): 2600 V. Ionization mode: positive ion mode. N_2 gas flow: 24.1 psi. Interface temperature 150 °C.
MS mass analyzer settings and fragmentation method	DDA: Calibration solution: 4 µL of a mixture of an equal composition of all samples. *m/z* and accumulation time: MS scans of 250 ms duration from 400 to 1250 *m/z*. The top 65 precursor ions detected during each scan were subjected to MS/MS scans of 25 ms from 100 to 1500 *m/z*. SWATH: 1 TOF MS scan (400 to 1500 *m/z*, 50 ms acquisition time) followed by 100 TOF MS/MS scans (400 to 1500 *m/z*, 50 ms) of overlapping sequential precursor isolation windows of variable width (1 *m/z* overlap) along the 400 – 1250 *m/z* mass range. For each sample set, the width of the 100 variable windows was optimized according to the ion density found in the DDA runs using a SWATH variable window calculator worksheet from Sciex. Mass resolution: ± 0.001 *m/z*.
Protein identification and quantification	
Database	Protein Pilot software (version 5.0.1, Sciex, Framingham, MA, USA) with a Human Uniprot database (50,590 proteins). Restrictions: iodoacetamide as alkylation of the cysteines; oxidation of methionines.
Accession number	**SD-*l*-PEG-HA:** P06727, P02748, P01024, P04004, P0C0L5, P0C0L4, P01031, P10909, P35858, P07360, Q13790, P02649, P10643, O14791, P02655, P05090, Q9UK55, O95445, P13671, O95445, P04003, P42330. **SD-*l*-PEG-PEG·PGA:** P06727, Q13790, P02747, P04003, P10909, O14791, P07360. **SD-noPEG-HA:** P04003, P02747, P06727, P02655, P0C0L4, P02649, P02654, P09871, P0C0L5, P02656, O95445, O14791, P35542, P02746, P01871. **SD-noPEG-PSA:** P06727, P04003, P02747, P02655, P02649, P0C0L4, O95445, P0C0L5, P02654, P02656, P01871, P35542, P02746, P05090, P01857, P02652, A0A075B6S5. **SD-noPEG-PEG·PGA:** P04004, P06727, P10909, P02747, P04003, P02746, Q13790, P09871, P0C0L4, O14791, P01860, P27169, P02748, P27918, P02655, P02649. **SE-*b*-PEG-HA:** P01024, P01031, P07360, P27918, O14791, P02748, P10643, P02655, P13671, P0C0L5.
Confidence in protein identification	FDR: < 1 %
Validation	Statistical analysis of two-tailed homoscedastic Student's t-test analysis of the final peak areas between sample and control. All samples were prepared in triplicate.

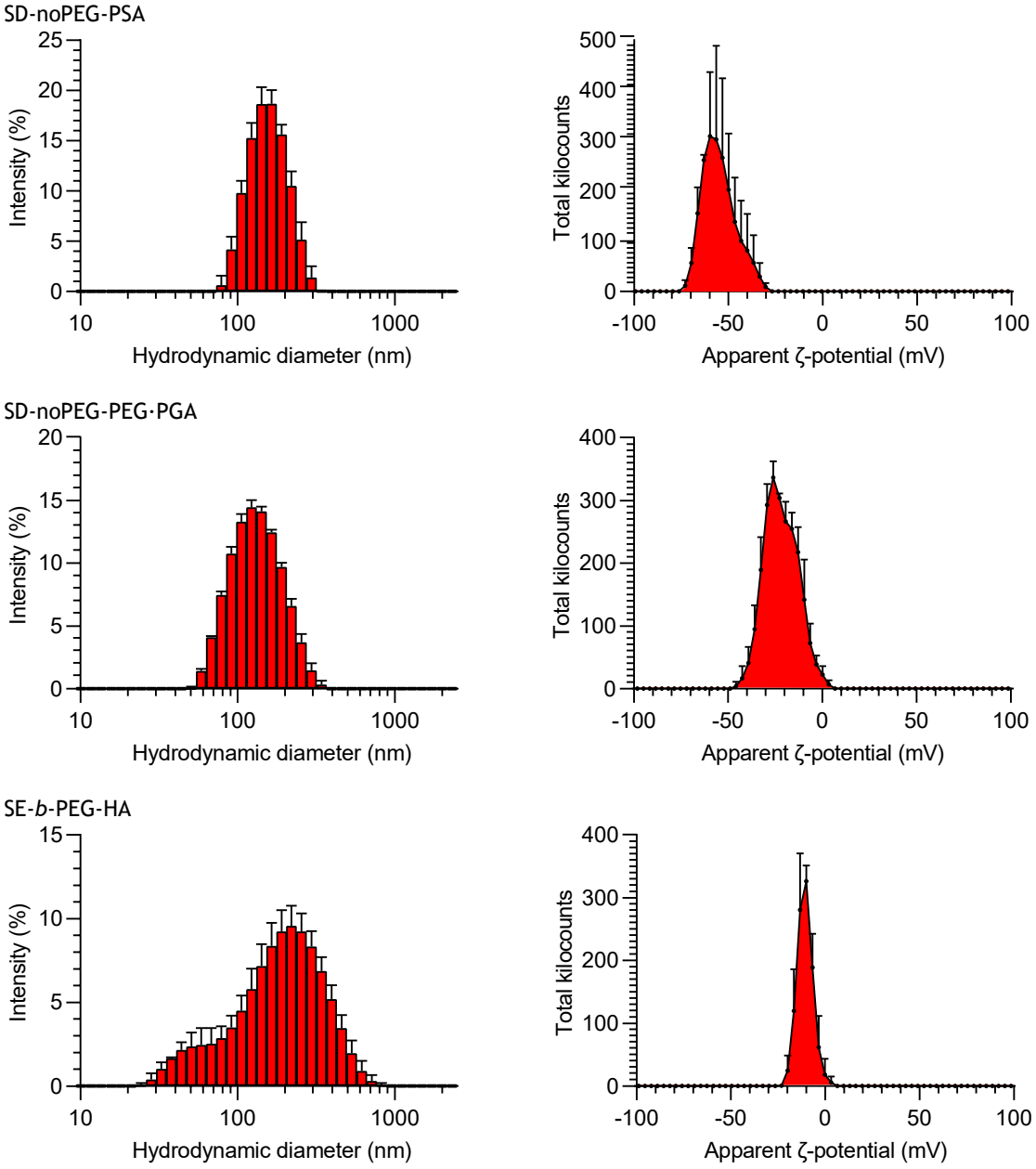
Abbreviations: ACN: acetonitrile. BZT: benzethonium chloride. CTAB: hexadecyltrimethylammonium bromide. DDA: data-dependent acquisition. DOTAP: 1,2-dioleoyl-3-trimethylammonium propane. DTT: dithiothreitol FDR: false discovery rate. HA: hyaluronic acid. PC: phosphatidylcholine. PDI: polydispersity index. PBS: phosphate-buffered saline. PEG·PGA: polyethylene glycol polyglutamic acid. PSA: polysialic acid. MCT: medium-chain triglyceride. mPES: modified polyethersulfone. MS: mass spectrometry. NC: nanocapsule. NP: nanoparticle. TFA: trifluoroacetic acid. TFF tangential flow filtration. TOF: time-of-flight. TPGS: D-α-tocopherol polyethylene glycol 1000 succinate. SWATH-MS: sequential window acquisition of all theoretical mass spectra. VitE: DL-α-tocopherol. ζ-pot: ζ-potential. The compositions of SD-*l*-PEG-HA, SD-*l*-PEG-PEG·PGA, SD-noPEG-HA, SD-noPEG-PSA, SD-noPEG-PEG·PGA, and SE-*b*-PEG-HA are shown in Figure 5.

UNIVERSIDADE DE SANTIAGO DE COMPOSTELA



Supplementary Figure 2. Representative DLS hydrodynamic diameter distributions and ζ-potential of different non-isolated NCs

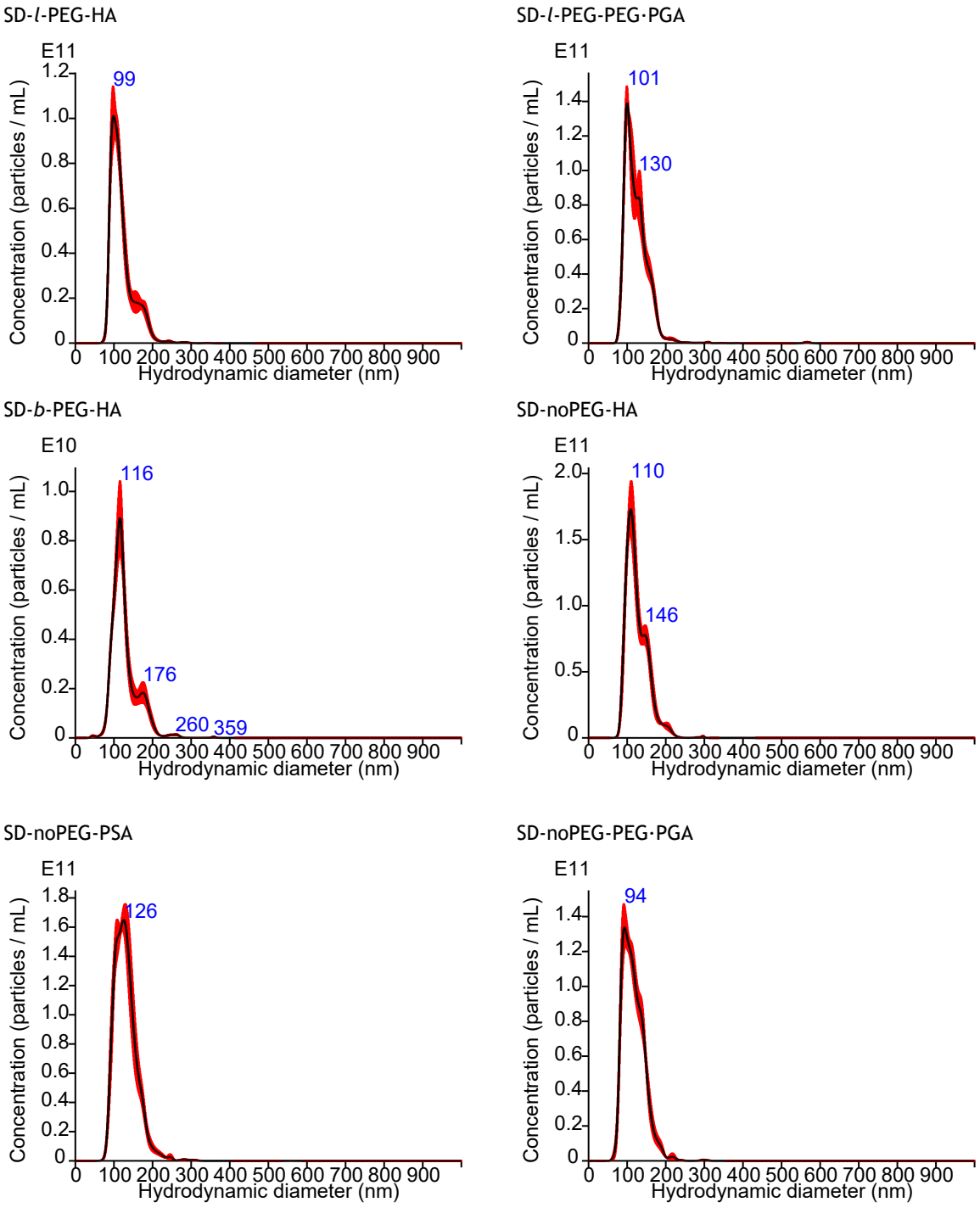
USC UNIVERSIDADE DE SANTIAGO DE COMPOSTELA



Supplementary Figure 2. Representative DLS hydrodynamic diameter distributions and ζ-potential of different non-isolated NCs (continuation)

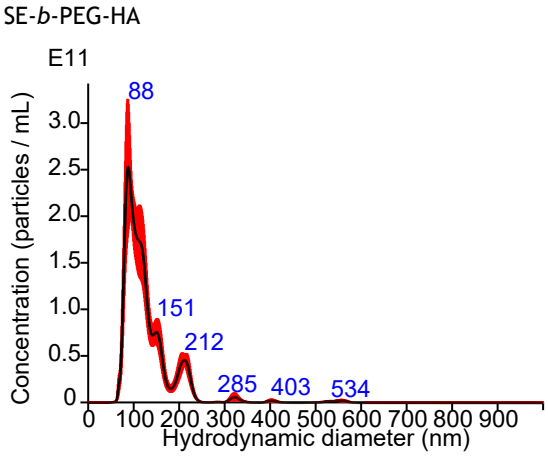
The compositions of SD-*l*-PEG-HA, SD-*l*-PEG-PEG·PGA, SD-*b*-PEG-HA, SD-noPEG-HA, SD-noPEG-PSA, SD-noPEG-PEG·PGA, and SE-*b*-PEG-HA are shown in Figure 5. **Abbreviations:** DLS: dynamic light scattering. NCs: nanocapsules. Values represent the mean ± standard deviation of 3 runs (1 measurement).

USC UNIVERSIDADE DE SANTIAGO DE COMPOSTELA



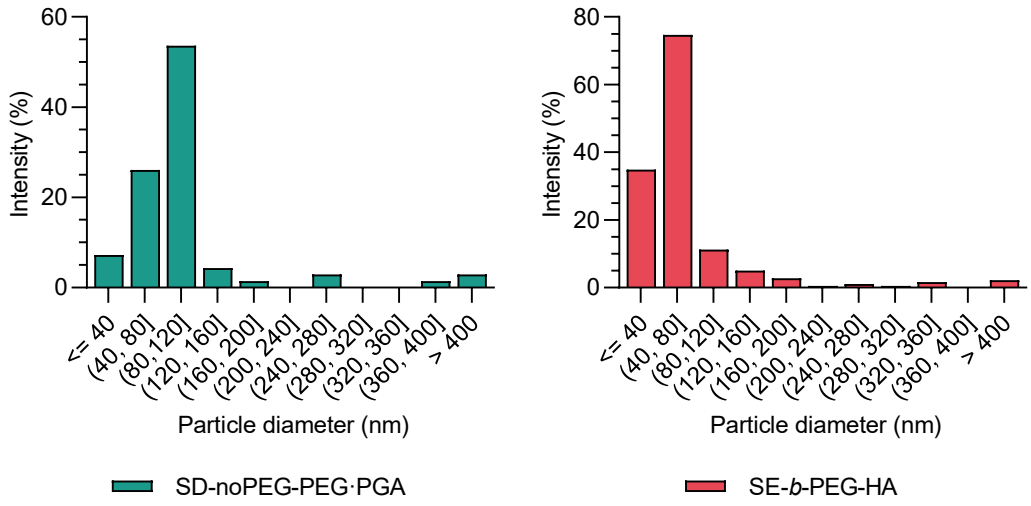
Supplementary Figure 3. Representative NTA hydrodynamic diameter distributions of different non-isolated NCs

USC UNIVERSIDADE DE SANTIAGO DE COMPOSTELA



Supplementary Figure 3. Representative NTA hydrodynamic diameter distributions of different non-isolated NCs (continuation)

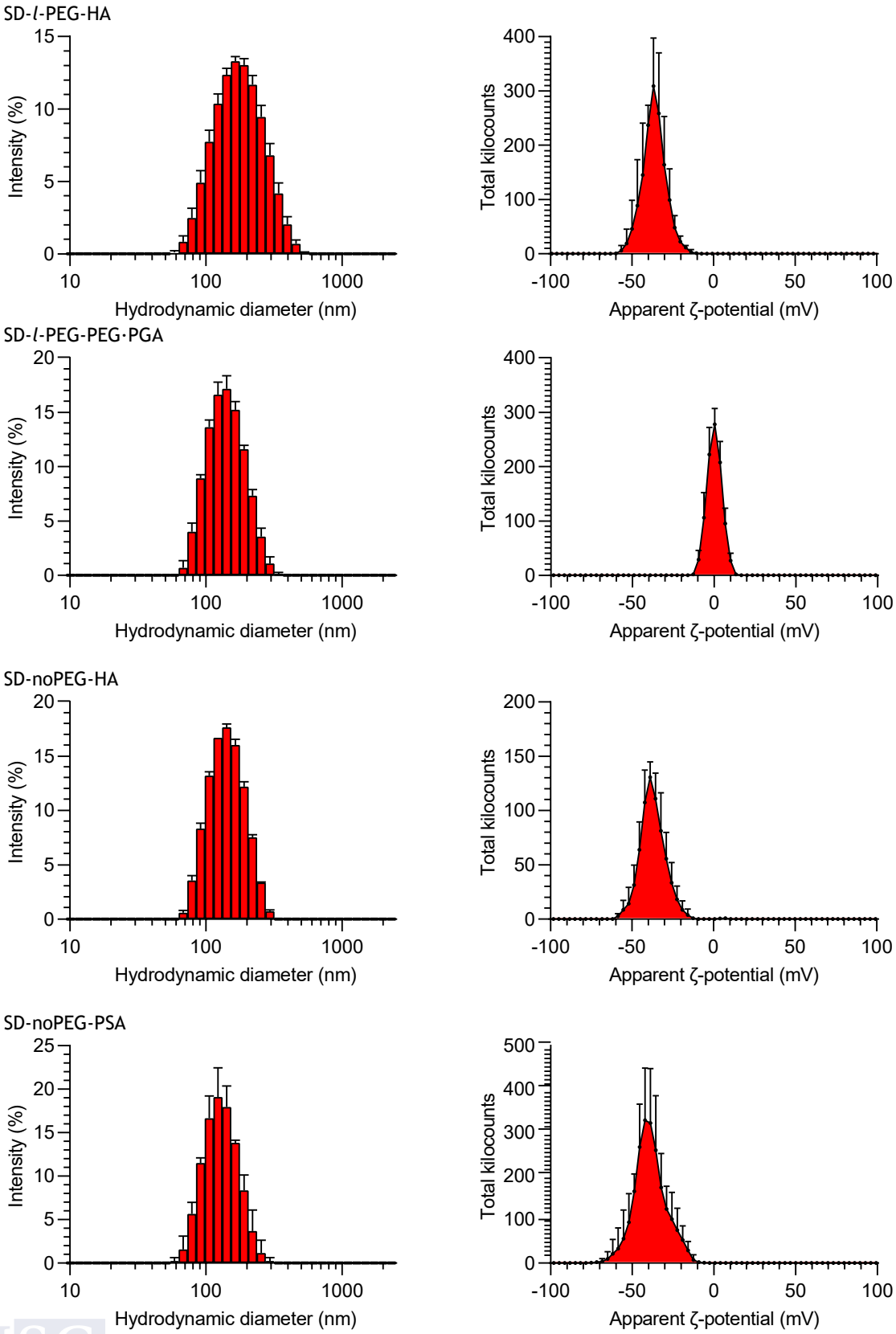
Black: mean particle concentration, in particles·mL^{-1}. Red: standard deviation. The compositions of SD-*l*-PEG-HA, SD-*l*-PEG-PEG·PGA, SD-*b*-PEG-HA, SD-noPEG-HA, SD-noPEG-PSA, SD-noPEG-PEG·PGA, and SE-*b*-PEG-HA are shown in Figure 5.



Supplementary Figure 4. Particle diameter histogram of SD-noPEG-PEG·PGA and SE-*b*-PEG-HA by cryo-EM

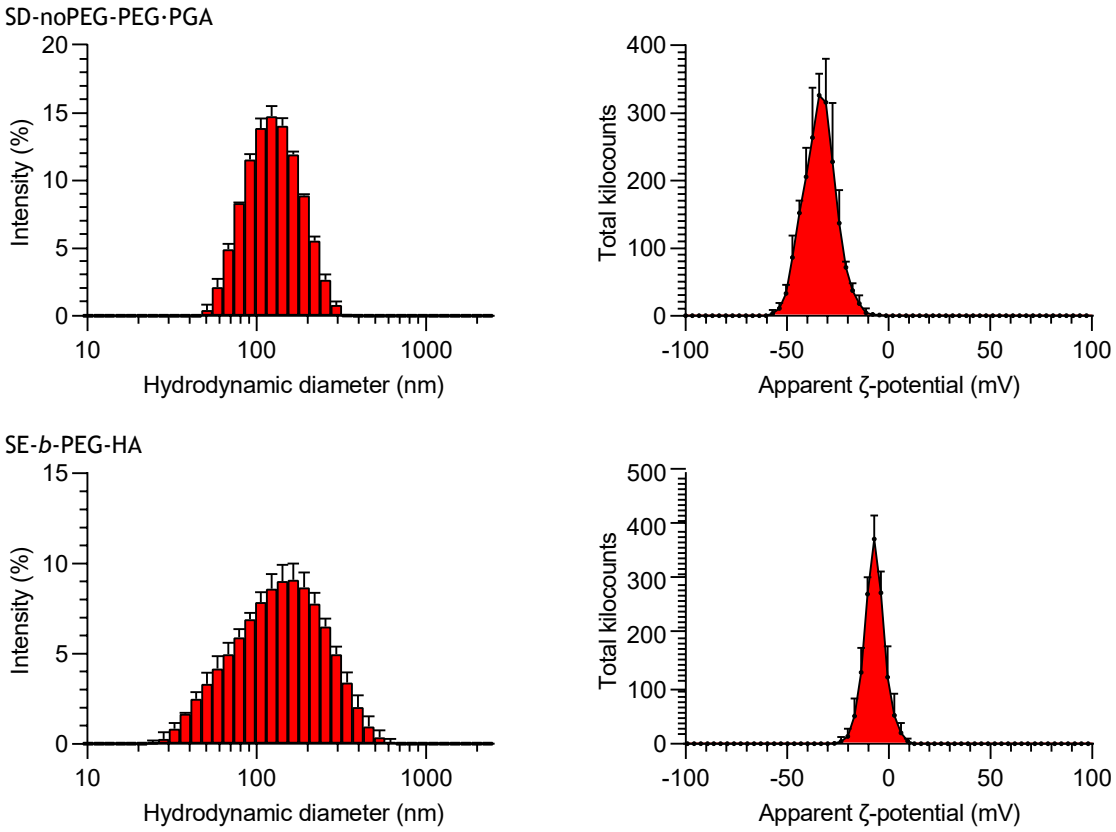
The compositions of SD-noPEG-PEG·PGA and SE-*b*-PEG-HA are shown in Figure 5.

USC UNIVERSIDADE DE SANTIAGO DE COMPOSTELA



Supplementary Figure 5. Representative DLS hydrodynamic diameter and ζ-potential of different isolated NCs

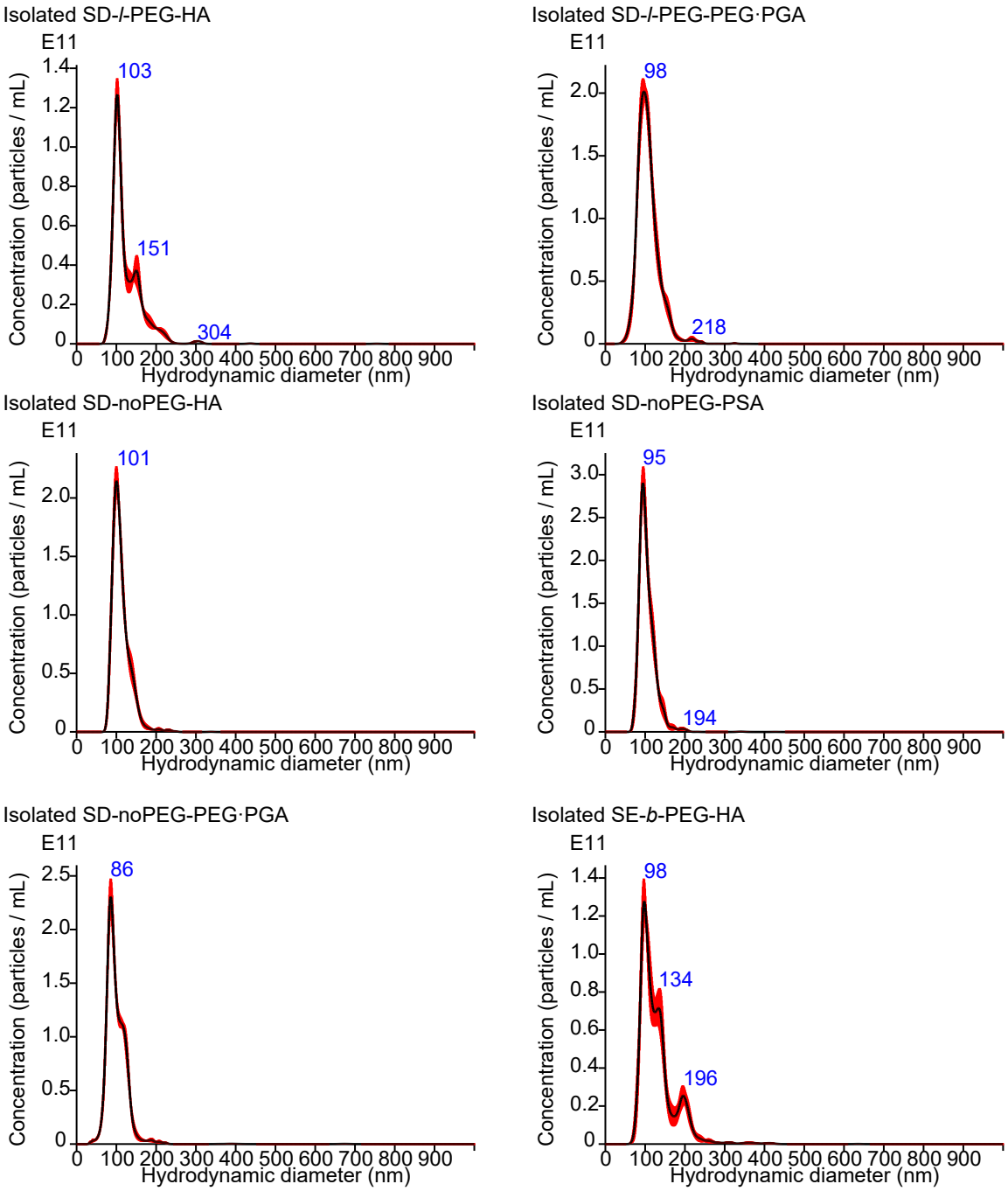
USC UNIVERSIDADE DE SANTIAGO DE COMPOSTELA



Supplementary Figure 5. Representative DLS hydrodynamic diameter and ζ-potential of different isolated NCs (continuation)

The compositions of SD-*l*-PEG-HA, SD-*l*-PEG-PEG·PGA, SD-noPEG-HA, SD-noPEG-PSA, SD-noPEG-PEG·PGA, and SE-*b*-PEG-HA are shown in Figure 5. **Abbreviations:** DLS: dynamic light scattering. NCs: nanocapsules. Values represent the mean ± standard deviation of 3 runs (1 measurement).

USC UNIVERSIDADE DE SANTIAGO DE COMPOSTELA

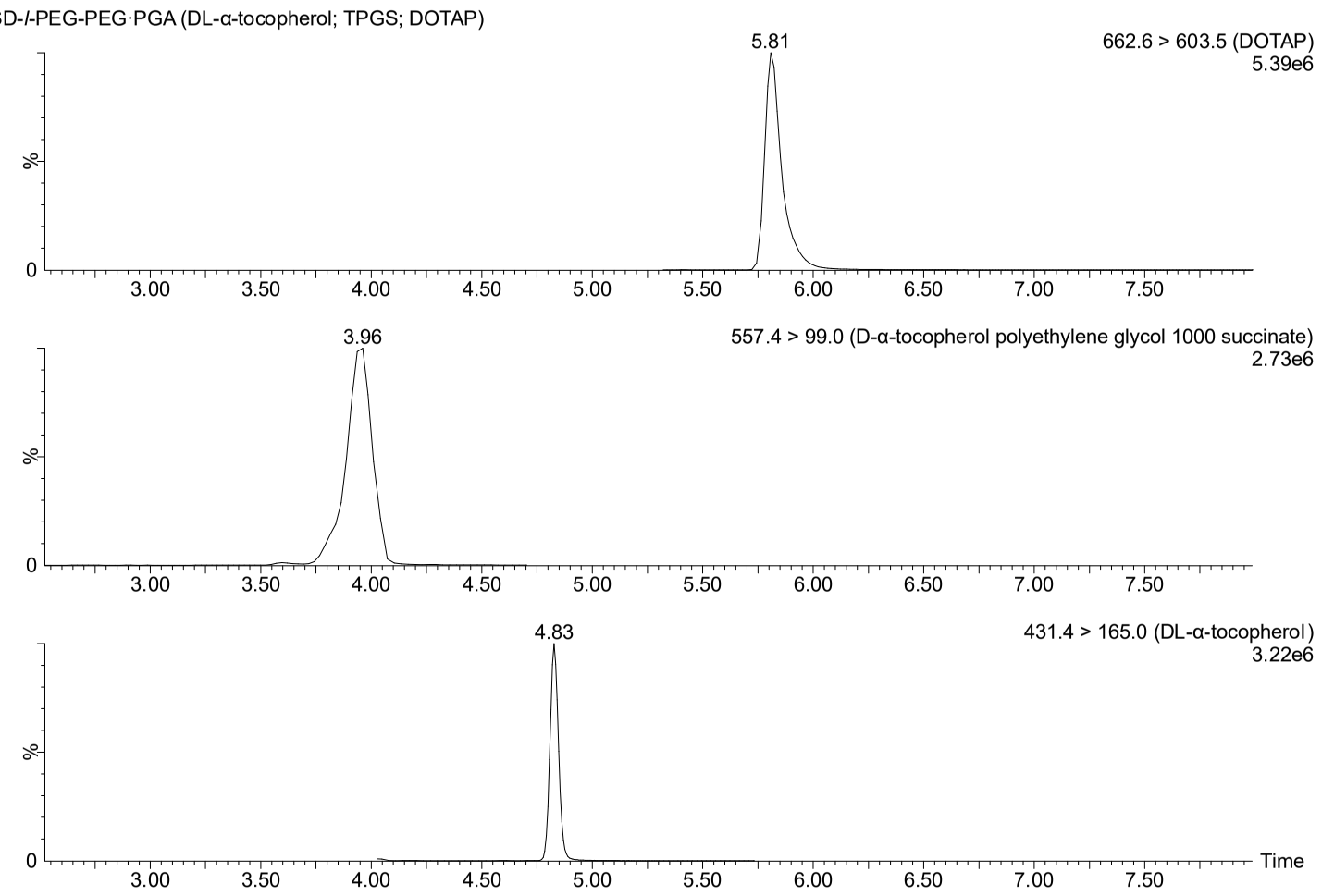


Supplementary Figure 6. Representative NTA hydrodynamic diameter distributions of different NCs after their isolation

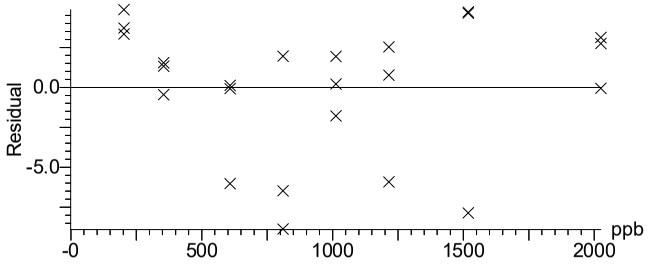
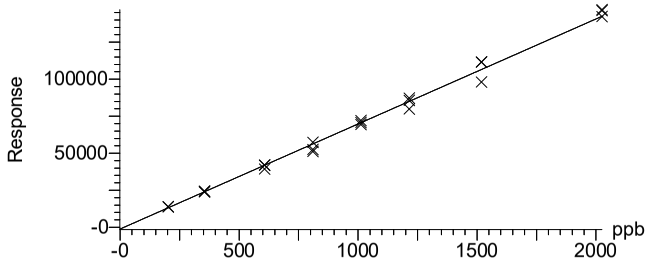
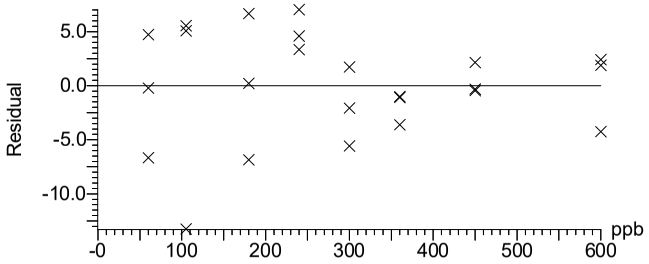
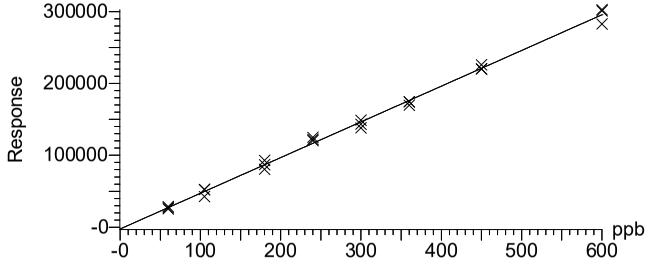
Black: mean particle concentration, in particles·mL^{-1}. Red: standard deviation. The compositions of SD-*l*-PEG-HA, SD-*l*-PEG-PEG·PGA, SD-noPEG-HA, SD-noPEG-PSA, SD-noPEG-PEG·PGA, and SE-*b*-PEG-HA are shown in Figure 5. **Abbreviations:** NCs: nanocapsules. NTA: nanoparticle tracking analysis. Values represent the mean ± standard deviation of 5 videos (1 measurement).

USC UNIVERSIDADE DE SANTIAGO DE COMPOSTELA

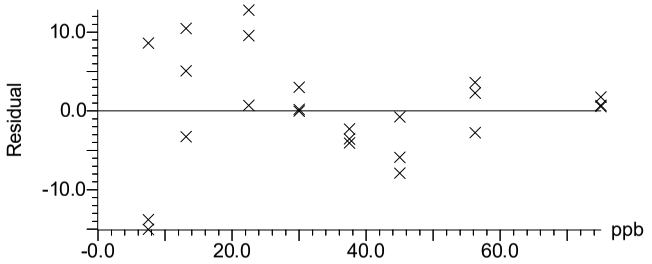
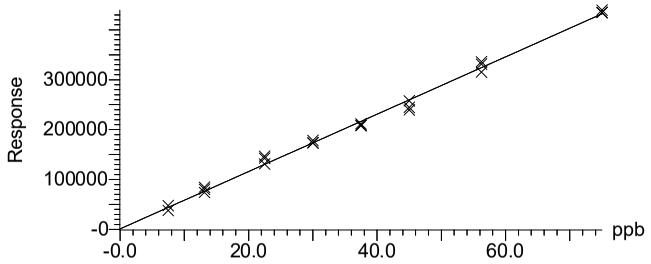
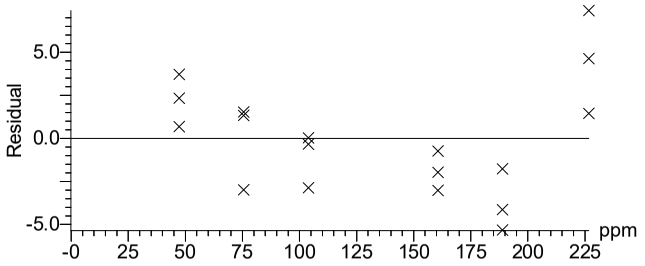
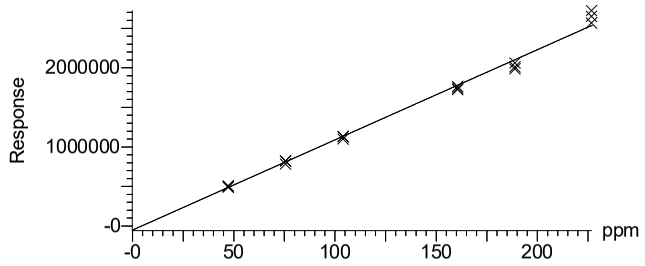
Supplementary Table 3. Example of chromatogram of the hydrophobic substances of SD-*l*-PEG-PEG·PGA

Method	Chromatogram
Hydrophobic substances of SD-*l*-PEG-PEG·PGA	

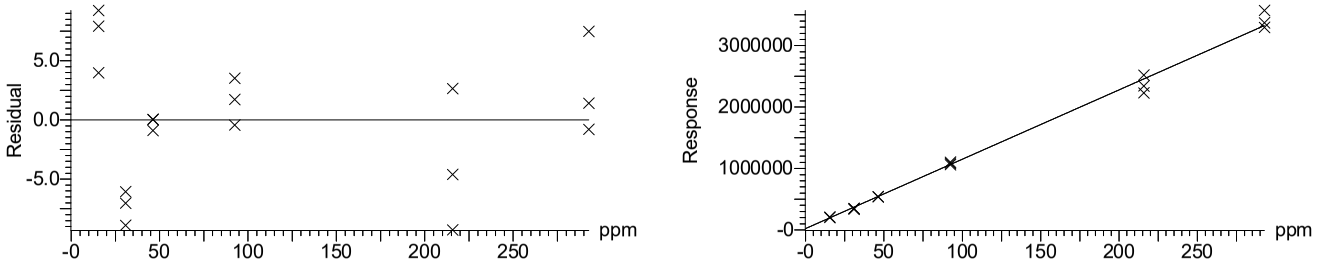
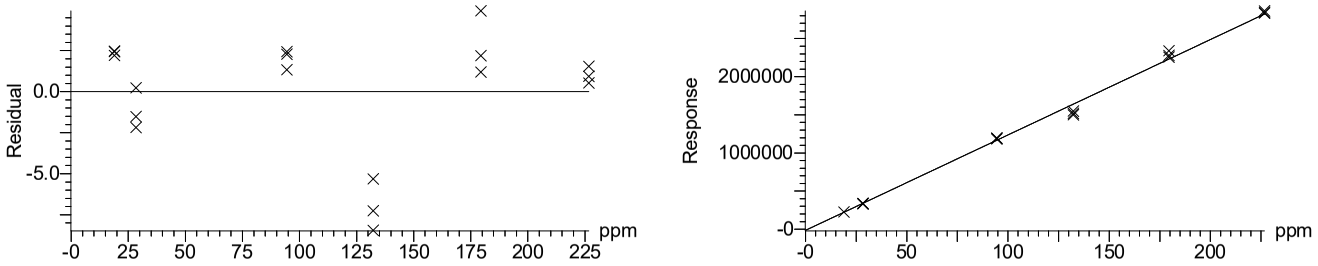
Supplementary Table 4. Calibration curves and residual plots of all the quantified substances in SD-*l*-PEG-PEG·PGA formulation

Molecule	Residual plots and calibration curves
DL-α-tocopherol	Compound name: DL-α-tocopherol Correlation coefficient: r = 0.997880, r^2 = 0.995765 Calibration curve: 70.9223 * x + -1159 Response type: External Std, Area Curve type: Linear, Origin: Exclude, Weighting: 1/x, Axis trans: None  
D-α-tocopherol polyethylene glycol 1000 succinate	Compound name: D-α-tocopherol polyethylene glycol 1000 succinate Correlation coefficient: r = 0.998157, r^2 = 0.996318 Calibration curve: 496.618 * x + -2486.64 Response type: External Std, Area Curve type: Linear, Origin: Exclude, Weighting: 1/x, Axis trans: None  

Supplementary Table 4. Calibration curves and residual plots of all the quantified substances in SD-l-PEG-PEG·PGA formulation (continuation)

Molecule	Residual plots and calibration curves
DOTAP	Compound name: 1,2-dioleoyl-3-trimethylammoniumpropane Correlation coefficient: r = 0.997193, r^2 = 0.994393 Calibration curve: 5744.68 * x + 1087.9 Response type: External Std, Area Curve type: Linear, Origin: Exclude, Weighting: 1/x, Axis trans: None  
PEG·PGA (whole)	Compound name: Digested polyethylene glycol polyglutamic acid Correlation coefficient: r = 0.997376, r^2 = 0.994759 Calibration curve: 11393.1 * x + -50818.9 Response type: External Std, Area Curve type: Linear, Origin: Exclude, Weighting: 1/x, Axis trans: None  

Supplementary Table 4. Calibration curves and residual plots of all the quantified substances in SD-l-PEG-PEG·PGA formulation (continuation)

Molecule	Residual plots and calibration curves
PEG·PGA (supernatant)	Compound name: Digested polyethylene glycol polyglutamic acid Correlation coefficient: r = 0.998039, r^2 = 0.996082 Calibration curve: 11283.4 * x + 22023.8 Response type: External Std, Area Curve type: Linear, Origin: Exclude, Weighting: 1/x, Axis trans: None 
PEG·PGA (infranatant)	Compound name: Digested polyethylene glycol polyglutamic acid Correlation coefficient: r = 0.998736, r^2 = 0.997474 Calibration curve: 12502.6 * x + -14752.4 Response type: External Std, Area Curve type: Linear, Origin: Exclude, Weighting: 1/x, Axis trans: None 

Abbreviations: DOTAP: 1,2-dioleoyl-3-trimethylammonium propane. PEG·PGA: polyethylene glycol polyglutamic acid.. A weighting factor of 1/x was applied. The %RRES triplicates average for each concentration level was found to be within –20 % to 20 %, confirming the linearity of the calibration curves. In general, residuals followed a random distribution around the value %RRES = 0.

Supplementary Table 5. Mass percentage detected in each fraction relative to the theoretical amount added to the formulation

Formulation	Substance	Recovery before isolation (%)	Association efficiency (%)	Unbound fraction (%)	Sum of associated and unbound fractions (%)
SD-*l*-PEG-HA	Benzethonium	92 ± 10	39 ± 5	56 ± 4	95 ± 9
	DL-α-tocopherol	106 ± 10	72 ± 5	30 ± 5	102 ± 10
	D-α-tocopherol polyethylene glycol 1000 succinate	103 ± 10	58 ± 6	43 ± 6	101 ± 12
	Hyaluronic acid	100 ± 5	18 ± 3	86 ± 2	104 ± 5
SD-*l*-PEG-PEG·PGA	DL-α-tocopherol	92 ± 6	52 ± 3	56 ± 6	109 ± 9
	D-α-tocopherol polyethylene glycol 1000 succinate	91 ± 6	45 ± 4	69 ± 8	113 ± 11
	1,2-dioleoyl-3-trimethylammonium propane	95 ± 10	45 ± 8	70 ± 6	115 ± 14
	PEG·PGA	119 ± 10	20 ± 4	87 ± 7	107 ± 10
SD-noPEG-HA	Hexadecyltrimethylammonium	99 ± 19	35 ± 8	42 ± 9	77 ± 16
	C8-C8-C8 Triglyceride	113 ± 8	52 ± 3	24 ± 3	75 ± 6
	C8-C8-C10 Triglyceride	109 ± 7	53 ± 4	25 ± 4	78 ± 7
	C8-C10-C10 Triglyceride	109 ± 8	53 ± 4	24 ± 4	77 ± 7
	C10-C10-C10 Triglyceride	110 ± 10	54 ± 5	23 ± 4	77 ± 9
	Phosphatidylcholine 756.5 Da	96 ± 14	16 ± 3	27 ± 9	43 ± 11
	Phosphatidylcholine 758.5 Da	98 ± 18	16 ± 3	27 ± 9	43 ± 12
	Phosphatidylcholine 780.5 Da	97 ± 12	16 ± 3	25 ± 10	42 ± 13
	Phosphatidylcholine 782.5 Da	97 ± 14	16 ± 3	27 ± 9	44 ± 12
	Hyaluronic acid	105 ± 7	14 ± 2	80 ± 7	95 ± 8
SD-noPEG-PSA	Hexadecyltrimethylammonium	103 ± 11	31 ± 4	59 ± 6	90 ± 9
	C8-C8-C8 Triglyceride	101 ± 10	68 ± 8	28 ± 5	95 ± 13
	C8-C8-C10 Triglyceride	100 ± 12	66 ± 8	28 ± 5	94 ± 13
	C8-C10-C10 Triglyceride	99 ± 11	66 ± 8	28 ± 4	94 ± 13
	C10-C10-C10 Triglyceride	98 ± 12	64 ± 7	30 ± 5	94 ± 12
	Phosphatidylcholine 756.5 Da	96 ± 8	17 ± 3	40 ± 8	57 ± 11
	Phosphatidylcholine 758.5 Da	94 ± 9	18 ± 3	40 ± 8	58 ± 11
	Phosphatidylcholine 780.5 Da	98 ± 9	18 ± 2	41 ± 9	59 ± 11
	Phosphatidylcholine 782.5 Da	97 ± 7	17 ± 3	40 ± 8	58 ± 11
	Polysialic acid	103 ± 2	14 ± 1	91 ± 3	104 ± 4
SD-noPEG-PEG·PGA	DL-α-tocopherol	96 ± 4	95 ± 6	9 ± 3	103 ± 8
	1,2-dioleoyl-3-trimethylammonium propane	84 ± 8	89 ± 3	12 ± 3	101 ± 6
	PEG·PGA	109 ± 11	34 ± 9	67 ± 5	101 ± 15

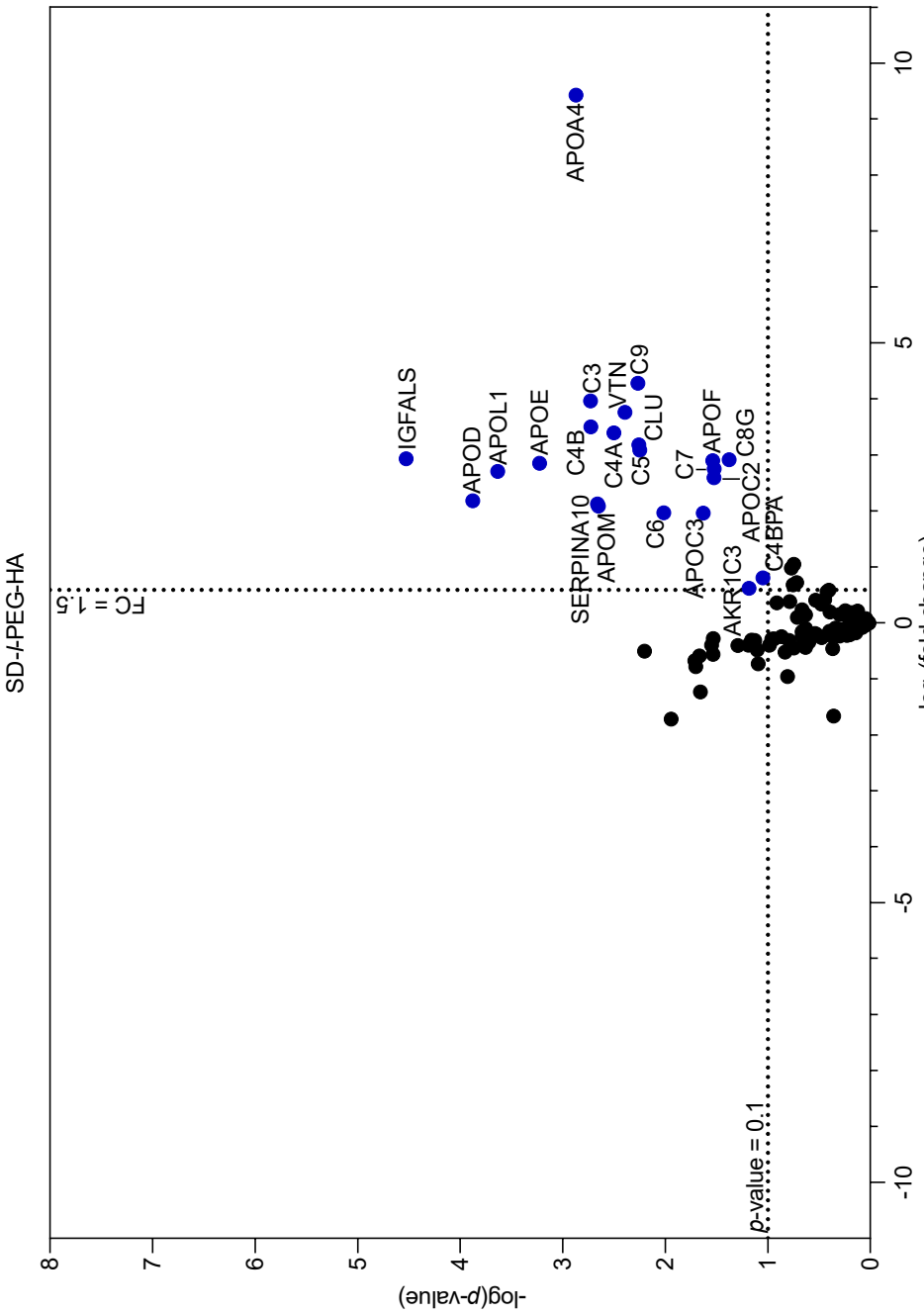
USC UNIVERSIDADE DE SANTIAGO DE COMPOSTELA

Supplementary Table 5. Mass percentage detected in each fraction relative to the theoretical amount added to the formulation (continuation)

Formulation	Substance	Recovery before isolation (%)	Association efficiency (%)	Unbound fraction (%)	Sum of associated and unbound fractions (%)
SE-*b*-PEG-HA	Benzethonium	109 ± 4	51 ± 12	51 ± 8	102 ± 20
	Macrogol-15-hydroxystearate	99 ± 6	39 ± 5	54 ± 11	93 ± 16
	Polysorbate 80	111 ± 4	24 ± 9	63 ± 6	87 ± 15
	C8-C8-C8 Triglyceride	106 ± 5	95 ± 7	< 10	N/A
	C8-C8-C10 Triglyceride	108 ± 6	95 ± 6	< 10	N/A
	C8-C10-C10 Triglyceride	107 ± 6	94 ± 6	< 10	N/A
	C10-C10-C10 Triglyceride	104 ± 10	89 ± 8	< 10	N/A
	Hyaluronic acid	91 ± 3	43 ± 4	53 ± 3	96 ± 7

Abbreviations: N/A: not applicable. Values represent the mean ± standard deviation (n = 3). The compositions of SD-*l*-PEG-HA, SD-*l*-PEG-PEG·PGA, SD-noPEG-HA, SD-noPEG-PSA, SD-noPEG-PEG·PGA, and SE-*b*-PEG-HA are shown in Figure 5. Adaptation from [2] licensed under a Creative Commons CC BY license.

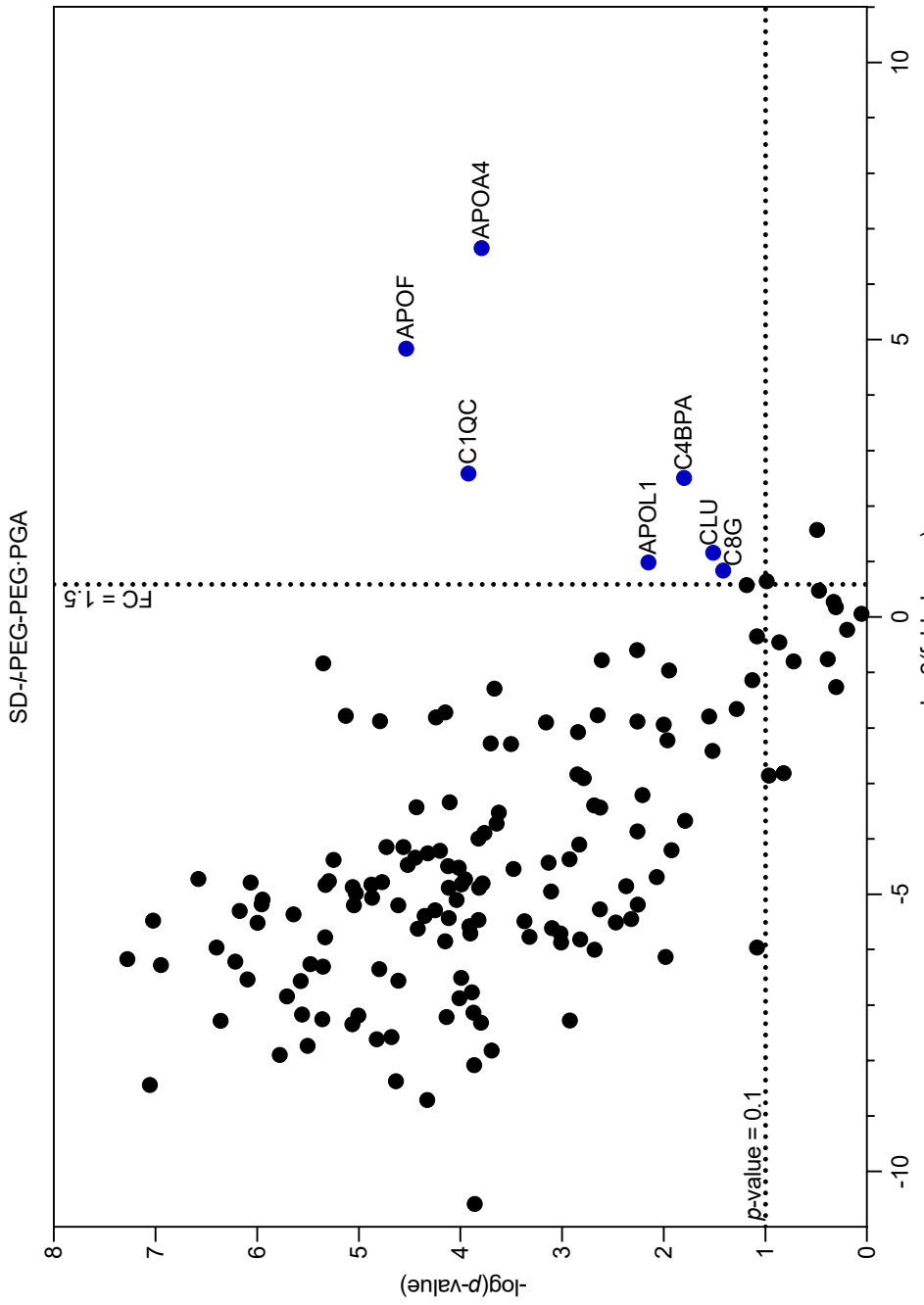
USC UNIVERSIDADE DE SANTIAGO DE COMPOSTELA



Supplementary Figure 7. Volcano plot of the proteins detected in the corona of SD-*l*-PEG-HA

–log(*p*-value) is represented *versus* $\log_2$(fold change *versus* plasma control). Representative proteins (*p*-value < 0.1 and FC > 1.5) were colored in blue and named similarly to their gene name. The compositions of SD-*l*-PEG-HA is shown in Figure 5. Values represent the mean of three replicates.

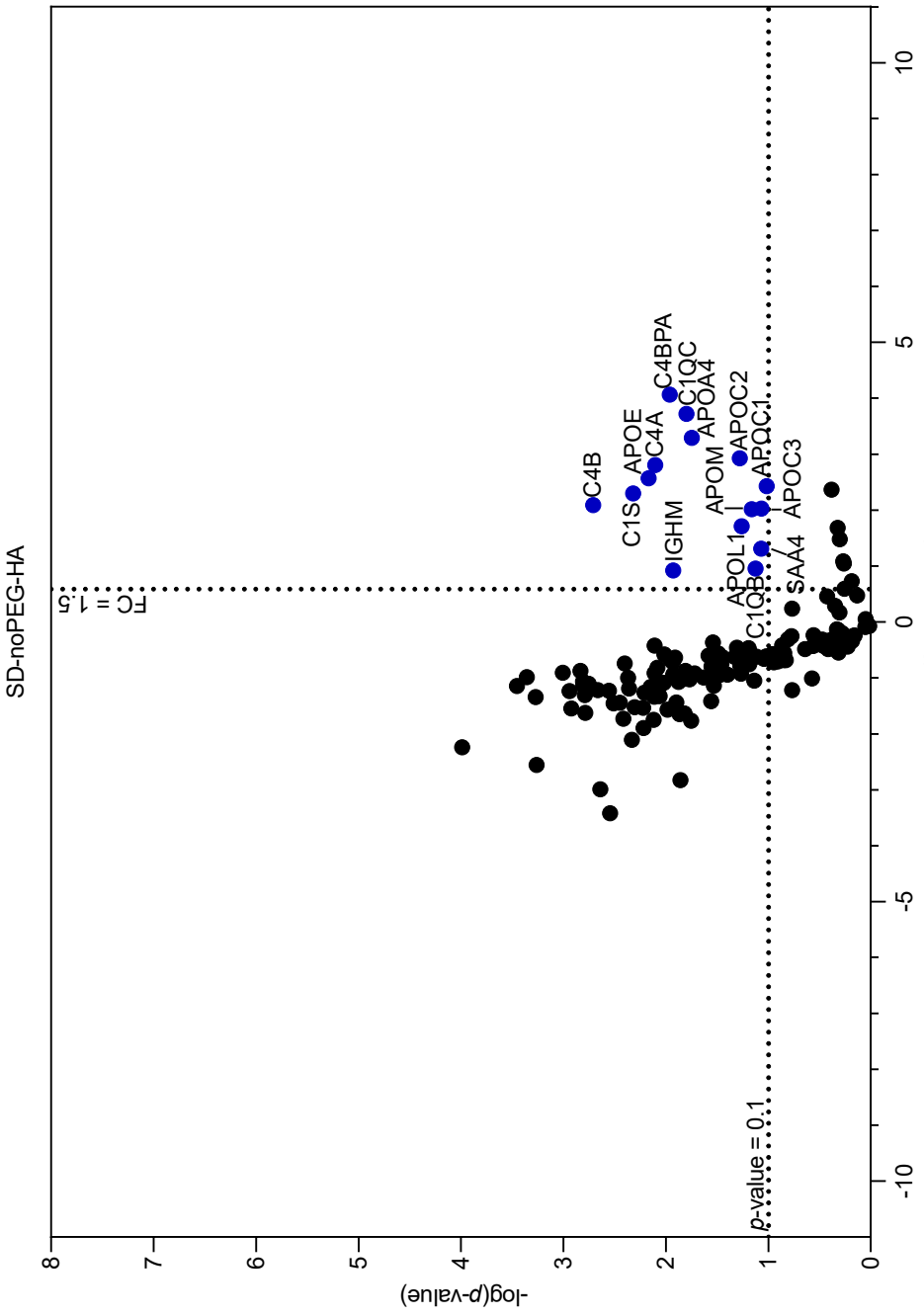
USC UNIVERSIDADE DE SANTIAGO DE COMPOSTELA



Supplementary Figure 8. Volcano plot of the proteins detected in the corona of SD-/-PEG-PEG·PGA

−log(*p*-value) is represented *versus* $\log_2$(fold change *versus* plasma control). Representative proteins (*p*-value < 0.1 and FC > 1.5) were colored in blue and named similarly to their gene name. The compositions of SD-/-PEG-PEG·PGA is shown in Figure 5. Values represent the mean of three replicates.

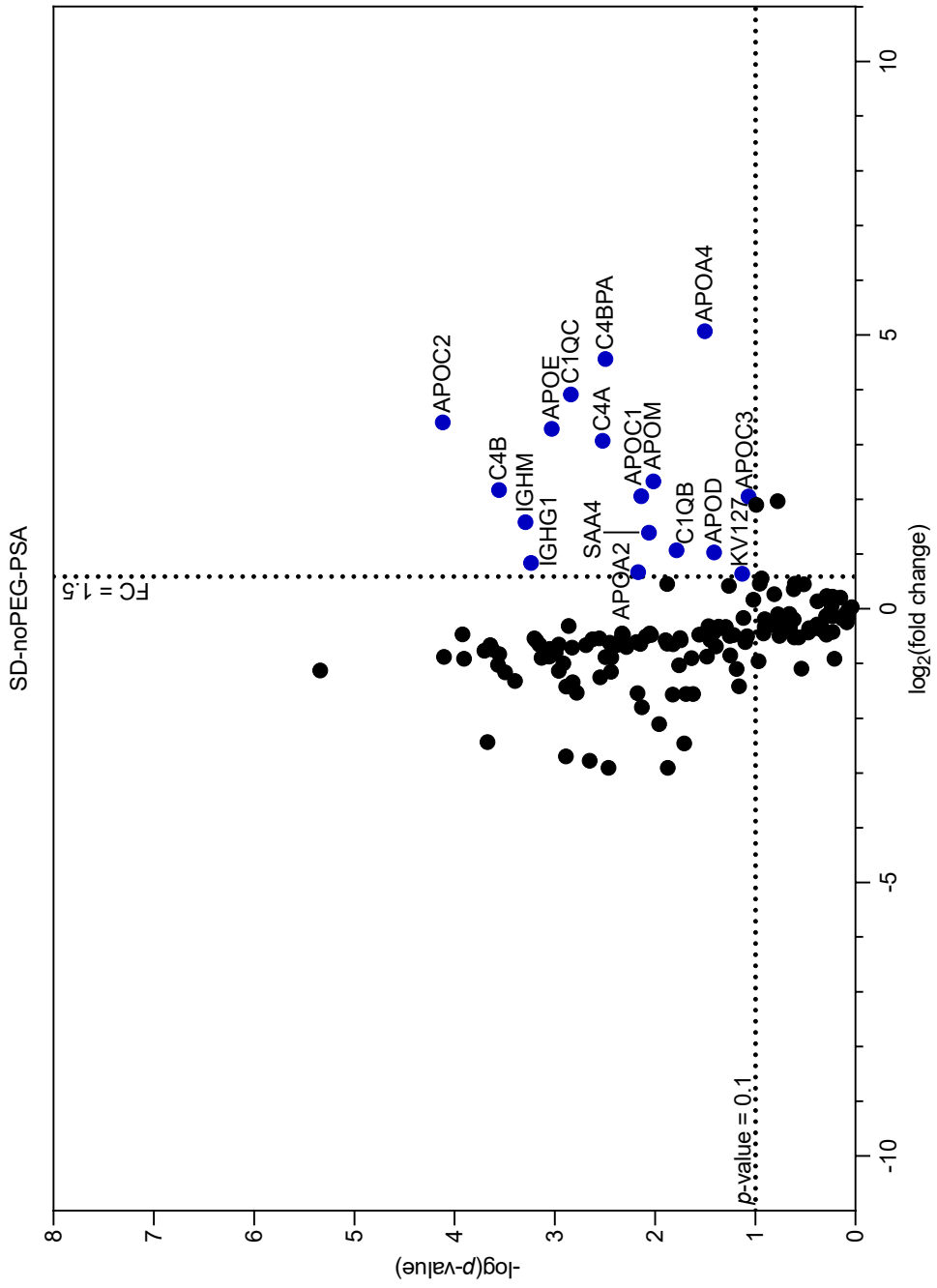
USC UNIVERSIDADE DE SANTIAGO DE COMPOSTELA



Supplementary Figure 9. Volcano plot of the proteins detected in the corona of SD-noPEG-HA

−log(*p*-value) is represented *versus* $\log_2$(fold change *versus* plasma control). Representative proteins (*p*-value < 0.1 and FC > 1.5) were colored in blue and named similarly to their gene name. The composition of SD-noPEG-HA is shown in Figure 5. Values represent the mean of three replicates.

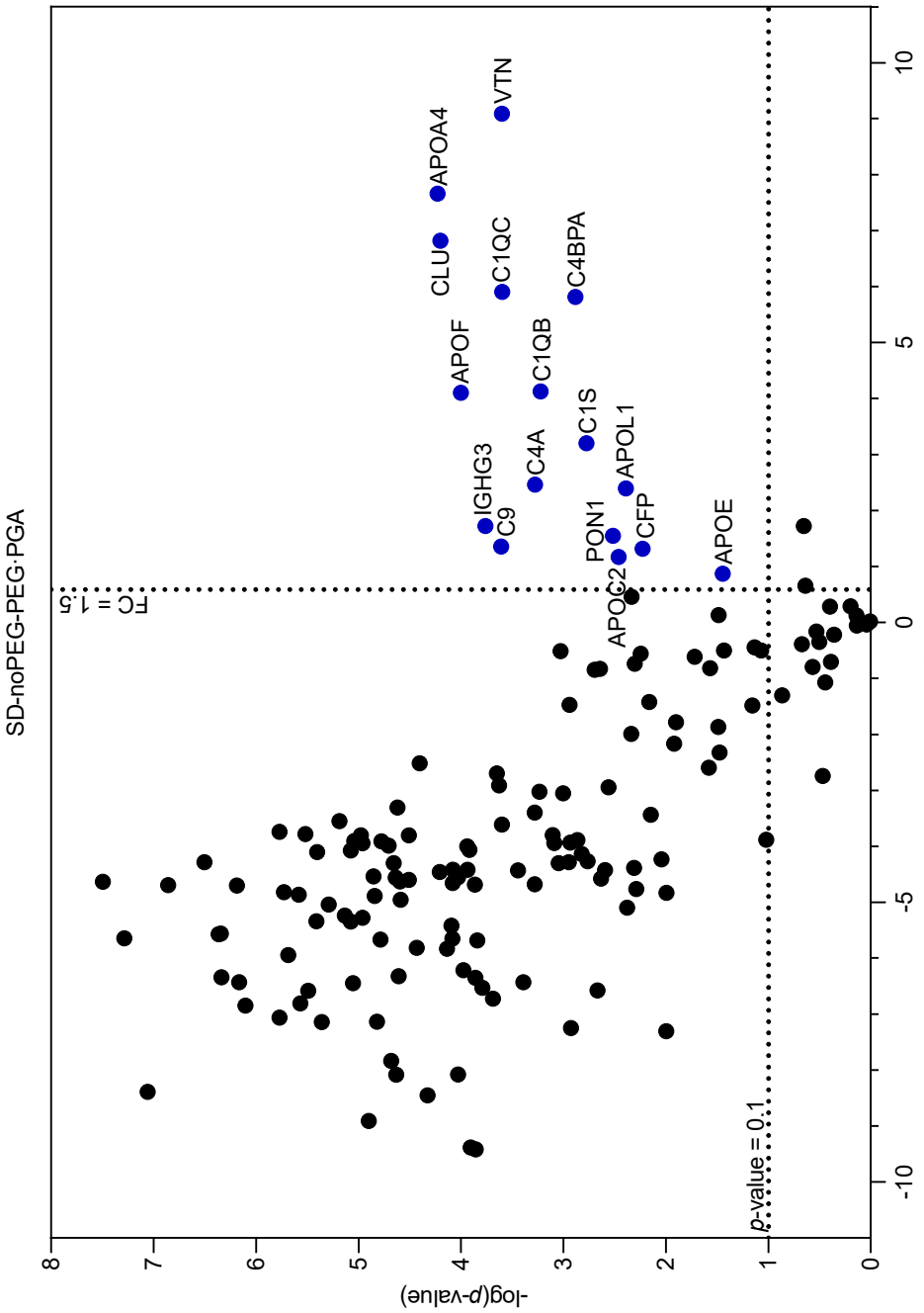
USC UNIVERSIDADE DE SANTIAGO DE COMPOSTELA



Supplementary Figure 10. Volcano plot of the proteins detected in the corona of SD-noPEG-PSA

–log(*p*-value) is represented *versus* $\log_2$(fold change *versus* plasma control). Representative proteins (*p*-value < 0.1 and FC > 1.5) were colored in blue and named similarly to their gene name. The composition of SD-noPEG-PSA is shown in Figure 5. Values represent the mean of three replicates.

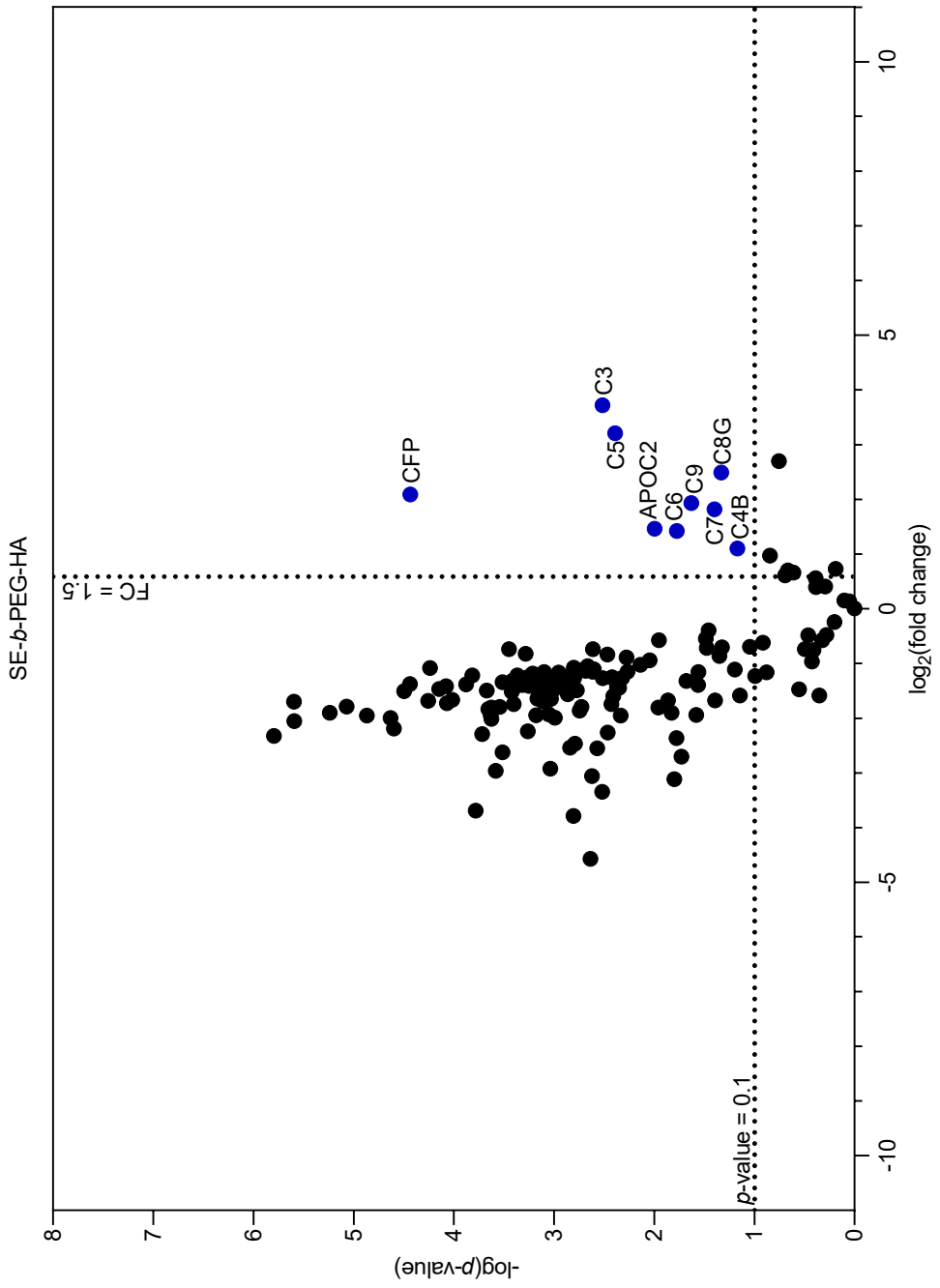
USC UNIVERSIDADE DE SANTIAGO DE COMPOSTELA



Supplementary Figure 11. Volcano plot of the proteins detected in the corona of SD-noPEG-PEG·PGA

−log(*p*-value) is represented *versus* $\log_2$(fold change *versus* plasma control). Representative proteins (*p*-value < 0.1 and FC > 1.5) were colored in blue and named similarly to their gene name. The composition of SD-noPEG-PEG·PGA is shown in Figure 5. Values represent the mean of three replicates.

USC UNIVERSIDADE DE SANTIAGO DE COMPOSTELA



Supplementary Figure 12. Volcano plot of the proteins detected in the corona of SE-*b*-PEG-HA

−log(*p*-value) is represented *versus* $\log_2$(fold change *versus* plasma control). Representative proteins (*p*-value < 0.1 and FC > 1.5) were colored in blue and named similarly to their gene name. The composition of SE-*b*-PEG-HA is shown in Figure 5. Values represent the mean of three replicates.

USC UNIVERSIDADE DE SANTIAGO DE COMPOSTELA

Supplementary Table 6. Detected proteins in the protein corona of SD-*l*-PEG-HA by SWATH-MS LC-MS (n = 3, *p*-value < 0.1)

Protein	Short name (gene name)	UniProtKB accession number	FC	Concentration ($\mu g \cdot m^{-2}$)
Apolipoprotein A-IV	APOA4	P06727	688.51	3,656.820
Complement C3	C3	P01024	15.61	1,050.532
Apolipoprotein E	APOE	P02649	7.21	756.362
Apolipoprotein C-II	APOC2	P02655	6.03	560.640
Apolipoprotein C-III	APOC3	O95445	3.89	545.375
Complement C4-A	C4A	P0C0L4	10.49	488.307
Complement C4-B	C4B	P0C0L5	11.33	127.867
Apolipoprotein D	APOD	P05090	4.53	90.133
Complement C5	C5	P01031	9.05	58.255
Clusterin	CLU	P10909	8.46	41.710
Vitronectin	VTN	P04004	13.55	34.561
Complement component C6	C6	P13671	3.90	33.594
Complement component C7	C7	P10643	6.73	25.014
Complement component C9	C9	P02748	19.43	22.374
Insulin-like growth factor-binding protein complex acid labile subunit	IGFALS	P35858	7.63	14.590
Apolipoprotein F	APOF	Q13790	7.44	1.782
Protein Z-dependent protease inhibitor	SERPINA10	Q9UK55	4.35	1.509
Apolipoprotein M	APOM	O95445	4.24	1.186
Complement component C8 gamma chain	C8G	P07360	7.53	1.101
Apolipoprotein L1	APOL1	O14791	6.53	0.953
C4b-binding protein alpha chain	C4BPA	P04003	1.74	0.124
Aldo-keto reductase family 1 member C3	AKR1C3	P42330	1.53	< 0.001

FC: fold change. The composition of SD-*l*-PEG-HA is shown in Figure 5. Values represent the mean of three replicates.

Supplementary Table 7. Detected proteins in the protein corona of SD-*l*-PEG-PEG·PGA by SWATH-MS LC-MS (n = 3, *p*-value < 0.1)

Protein	Short name (gene name)	UniProtKB accession number	FC	Concentration ($\mu g \cdot m^{-2}$)
Apolipoprotein A-IV	APOA4	P06727	100.42	528.808
Apolipoprotein F	APOF	Q13790	28.57	7.624
Clusterin	CLU	P10909	2.23	6.897
C4b-binding protein alpha chain	C4BPA	P04003	5.68	0.781
Apolipoprotein L1	APOL1	O14791	1.98	0.169
Complement component C8 gamma chain	C8G	P07360	1.78	0.132
Complement C1q subcomponent subunit C	C1QC	P02747	6.01	0.061

FC: fold change. The composition of SD-*l*-PEG-PEG·PGA is shown in Figure 5. Values represent the mean of three replicates.

Supplementary Table 8. Detected proteins in the protein corona of SD-noPEG-HA by SWATH-MS LC-MS (n = 3, *p*-value < 0.1)

Protein	Short name (gene name)	UniProtKB accession number	FC	Concentration ($\mu g \cdot m^{-2}$)
Apolipoprotein C-II	APOC2	P02655	7.60	736.063
Apolipoprotein E	APOE	P02649	5.93	600.704
Apolipoprotein C-III	APOC3	P02656	4.07	580.201
Complement C4-A	C4A	P0C0L4	6.99	308.126
Apolipoprotein C-I	APOC1	P02654	5.39	105.666
Apolipoprotein A-IV	APOA4	P06727	9.78	46.696
Complement C4-B	C4B	P0C0L5	4.25	40.208
Serum amyloid A-4 protein	SAA4	P35542	2.48	10.669
Immunoglobulin heavy constant mu	IGHM	P01871	1.89	9.575
Complement C1s subcomponent	C1S	P09871	4.92	9.368
C4b-binding protein alpha chain	C4BPA	P04003	16.71	2.624
Apolipoprotein M	APOM	O95445	4.04	1.113
Apolipoprotein L1	APOL1	O14791	3.27	0.392
Complement C1q subcomponent subunit C	C1QC	P02747	13.18	0.149
Complement C1q subcomponent subunit B	C1QB	P02746	1.94	0.043

FC: fold change. The composition of SD-noPEG-HA is shown in Figure 5. Values represent the mean of three replicates.

Supplementary Table 9. Detected proteins in the protein corona of SD-noPEG-PSA by SWATH-MS LC-MS (n = 3, *p*-value < 0.1)

Protein	Short name (gene name)	UniProtKB accession number	FC	Concentration ($\mu g \cdot m^{-2}$)
Apolipoprotein E	APOE	P02649	9.76	1,067.297
Apolipoprotein C-II	APOC2	P02655	10.57	1,066.381
Apolipoprotein C-III	APOC3	P02656	4.13	591.886
Complement C4-A	C4A	P0C0L4	8.38	379.576
Apolipoprotein A-IV	APOA4	P06727	33.61	173.448
Apolipoprotein C-I	APOC1	P02654	4.16	75.987
Immunoglobulin kappa variable 1-27	KV127	A0A075B6S5	1.56	64.550
Complement C4-B	C4B	P0C0L5	4.50	43.326
Apolipoprotein A-II	APOA2	P02652	1.58	42.079
Immunoglobulin heavy constant gamma 1	IGHG1	P01857	1.78	41.194
Apolipoprotein D	APOD	P05090	2.04	26.517
Immunoglobulin heavy constant mu	IGHM	P01871	2.99	21.269
Serum amyloid A-4 protein	SAA4	P35542	2.62	11.666
C4b-binding protein alpha chain	C4BPA	P04003	23.63	3.781
Apolipoprotein M	APOM	O95445	5.02	1.472

USC DE SANTIAGO

Supplementary Table 9. Detected proteins in the protein corona of SD-noPEG-PSA by SWATH-MS LC-MS (n = 3, p-value < *0.1*) (continuation)

Protein	Short name (gene name)	UniProtKB accession number	FC	Concentration ($\mu g \cdot m^{-2}$)
Complement C1q subcomponent subunit C	C1QC	P02747	15.03	0.172
Complement C1q subcomponent subunit B	C1QB	P02746	2.10	0.050

FC: fold change. The composition of SD-noPEG-PSA is shown in Figure 5. Values represent the mean of three replicates.

Supplementary Table 10. Detected proteins in the protein corona of SD-noPEG-PEG·PGA by SWATH-MS LC-MS (n = 3, *p*-value < 0.1)

Protein	Short name (gene name)	UniProtKB accession number	FC	Concentration ($\mu g \cdot m^{-2}$)
Vitronectin	VTN	P04004	544.97	1,497.533
Apolipoprotein A-IV	APOA4	P06727	202.21	1,070.199
Clusterin	CLU	P10909	112.78	625.015
Complement C4-A	C4A	P0C0L4	5.52	232.448
Apolipoprotein C-II	APOC2	P02655	2.25	139.443
Immunoglobulin heavy constant gamma 3	IGHG3	P01860	3.30	110.922
Apolipoprotein E	APOE	P02649	1.83	100.772
Complement C1s subcomponent	C1S	P09871	9.18	19.538
C4b-binding protein alpha chain	C4BPA	P04003	56.20	9.223
Serum paraoxonase/arylesterase 1	PON1	P27169	2.92	7.899
Properdin	CFP	P27918	2.48	5.069
Apolipoprotein F	APOF	Q13790	17.21	4.483
Complement component C9	C9	P02748	2.56	1.896
Complement C1q subcomponent subunit B	C1QB	P02746	17.46	0.756
Apolipoprotein L1	APOL1	O14791	5.26	0.734
Complement C1q subcomponent subunit C	C1QC	P02747	59.93	0.721

FC: fold change. The composition of SD-noPEG-PEG·PGA is shown in Figure 5. Values represent the mean of three replicates.

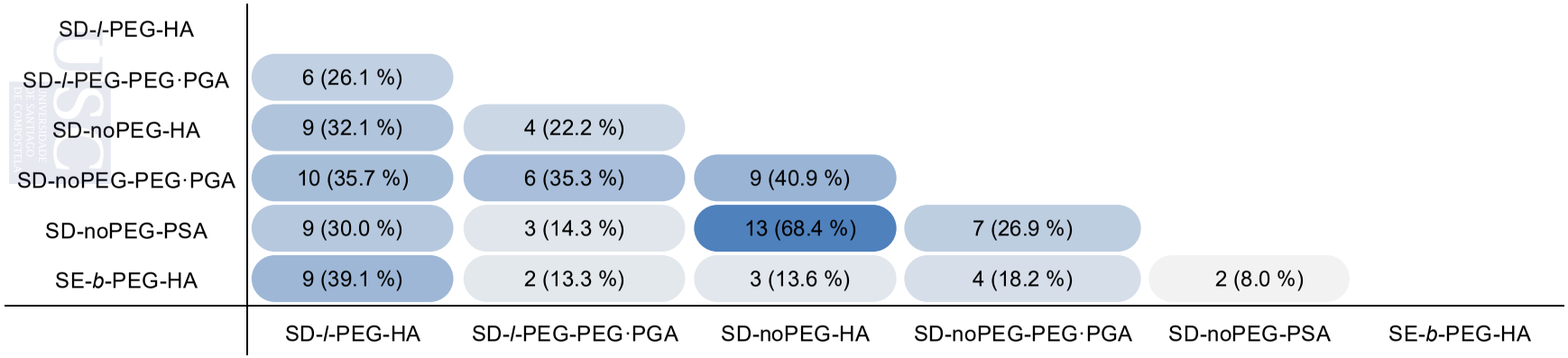
USC UNIVERSIDADE DE SANTIAGO DE COMPOSTELA

Supplementary Table 11. Detected proteins in the protein corona of SE-*b*-PEG-HA by SWATH-MS LC-MS (n = 3, *p*-value < 0.1)

Protein	Short name (gene name)	UniProtKB accession number	FC	Concentration ($\mu g \cdot m^{-2}$)
Complement C3	C3	P01024	13.17	875.081
Apolipoprotein C-II	APOC2	P02655	2.76	195.698
Complement C5	C5	P01031	9.24	59.641
Complement component C6	C6	P13671	2.68	19.468
Complement C4-B	C4B	P0C0L5	2.14	14.154
Properdin	CFP	P27918	4.25	11.098
Complement component C7	C7	P10643	3.53	11.039
Complement component C9	C9	P02748	3.81	3.413
Complement component C8 gamma chain	C8G	P07360	5.61	0.778
Apolipoprotein L1	APOL1	O14791	4.02	0.520

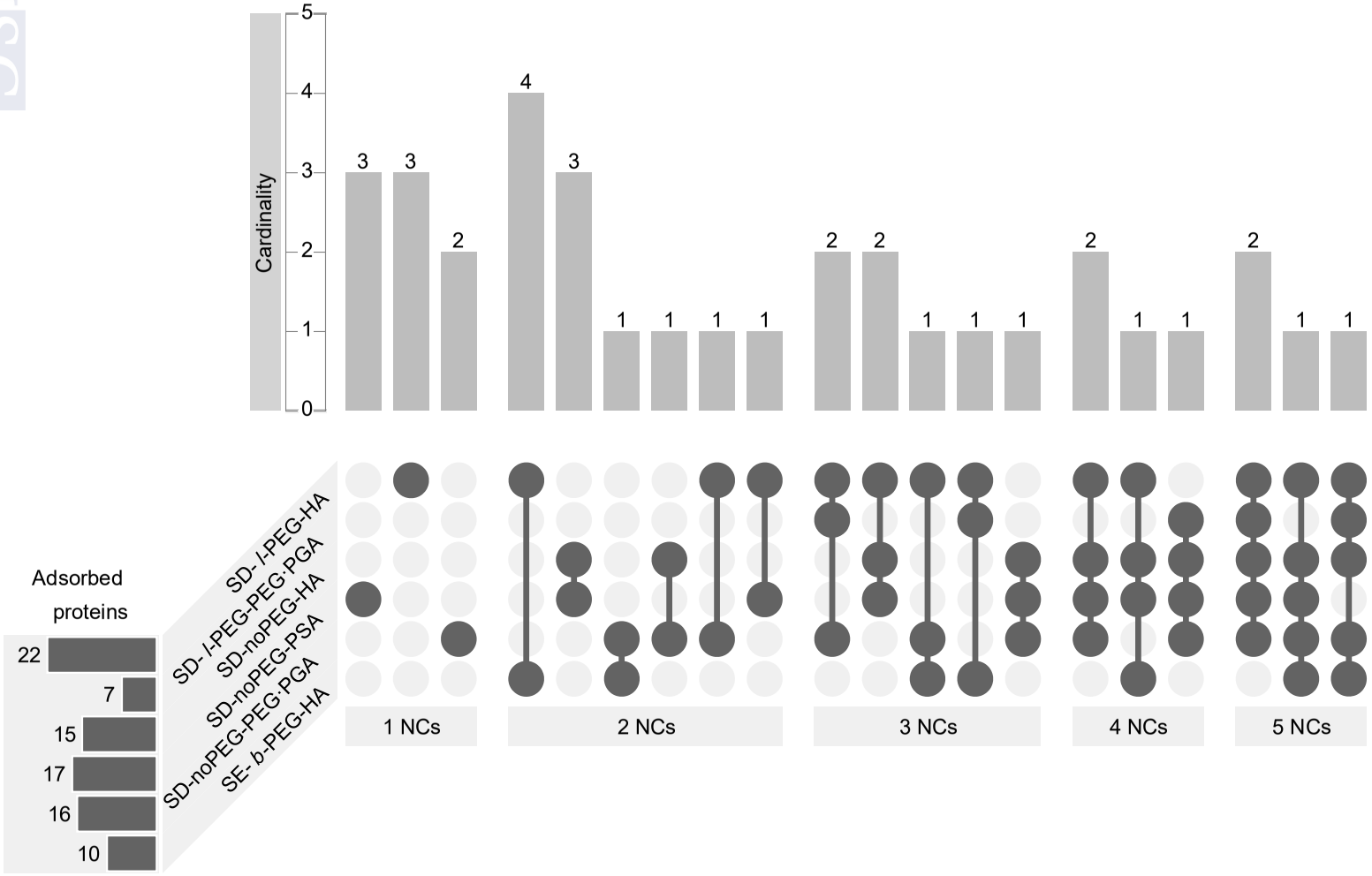
FC: fold change. The composition of SE-*b*-PEG-HA is shown in Figure 5. Values represent the mean of three replicates.

USC UNIVERSIDADE DE SANTIAGO DE COMPOSTELA



Supplementary Figure 13. Shared proteins between different pairs of NCs in number and percentage after 1 h incubation with human plasma

Numbers outside brackets represent the number of shared proteins between two NCs. Percentages, in brackets, represent the ratio between the common proteins and the total number of different proteins detected between the two NCs. On the one hand, SD-noPEG-HA and SD-noPEG-PSA exhibited the most similar protein coronas, sharing 13 proteins (68.4 %). On the other hand, SD-noPEG-PSA and SE-*b*-PEG-HA were the NCs with the less common proteins (2 shared proteins; 8 %). The compositions of SD-*l*-PEG-HA, SD-*l*-PEG-PEG·PGA, SD-noPEG-HA, SD-noPEG-PSA, SD-noPEG-PEG·PGA, and SE-*b*-PEG-HA are shown in Figure 5.



Supplementary Figure 14. Incidence of each protein in the set of tested NCs prototypes

The cardinality (above) represents the number of proteins shared between the systems marked with dark dots (below). The total number of proteins for each system is also represented (below, left). In general, most proteins were shared by a few NCs. Specific proteins for three different NCs were found. Two proteins were exclusive of SD NCs while none of SE. No common protein was detected for all NCs. The compositions of SD-*l*-PEG-HA, SD-*l*-PEG-PEG·PGA, SD-noPEG-HA, SD-noPEG-PSA, SD-noPEG-PEG·PGA, and SE-*b*-PEG-HA are shown in Figure 5. Data generated with Upset.[256]

6. ACKNOWLEDGMENTS

This work was supported by the Spanish Ministry of Economy and Industry under the grant agreement with reference: MINECO- PCIN-2017-129/ AEI (Project “Nano-Inmunoterapia: Targeting Intracelular de Células Tumorales y TAMs” 2-INTRATARGET) under the frame of "EuroNanoMed III", by the 2^2-INTRATARGET project, which received funding from Instituto de Salud Carlos III (ISCIII) with reference A20/00028 under the umbrella of the ERA NET EuroNanoMed GA N 723770 of the EU Horizon 2020 Research and Innovation Programme, by FEDER/Spanish Ministry of Science, Innovation, and Universities (Ref.: SAF2017-86634-R), and by the Competitive Reference Groups, Consellería de Educación e Ordenación Universitaria, Xunta de Galicia, with Ref: ED431C 2017/09. G. Berrecoso acknowledged the financial support by the Xunta de Galicia through the “Axudas de apoio á etapa predoutoral 2018” grant, co-funded by the European Social Fund “FSE Galicia 2014-2020” (Ref.: ED481A-2018/047).

Cryo-EM images were collected in collaboration with Prof. Nicola G. A. Abrescia (Bizkaia Science and Technology Park, Derio, 48160, Spain).

Blood extractions were performed in the Universidade de Santiago de Compostela, Santiago de Compostela, 15782, Spain, in collaboration with María del Carmen Pardiñas, MD.

For the separation of plasma from blood, samples were centrifuged using the equipment from the laboratory of Prof. Ángel García, Center for Research in Molecular Medicine and Chronic Diseases (CiMUS), Universidade de Santiago de Compostela, Santiago de Compostela, 15782, Spain.

Proteomics LC-MS/MS analysis was carried out at the IDIS Research Institute, Universidade de Santiago de Compostela, Santiago de Compostela, 15782, Spain, in collaboration with Susana Bravo, Ph.D.

7. REFERENCES

[1] G. Berrecoso, J. Crecente-Campo, M. J. Alonso. Unveiling the pitfalls of the protein corona of polymeric drug nanocarriers. *Drug Delivery and Translational Research*. 10, 730–750. (2020). doi: 10.1007/s13346-020-00745-0.

[2] G. Berrecoso, J. Crecente-Campo, M. J. Alonso. Quantification of the actual composition of polymeric nanocapsules: a quality control analysis. *Drug Delivery and Translational Research*. 12, 2865–2874. (2022). doi: 10.1007/s13346-022-01150-5.

[3] J. Crecente-Campo, M. J. Alonso. Engineering, on-demand manufacturing, and scaling-up of polymeric nanocapsules. *Bioengineering & Translational Medicine*. 4, 38–50. (2019). doi: 10.1002/btm2.10118.

[4] A. Cadete, A. Olivera, M. Besev, P. K. Dhal, L. Gonçalves, A. J. Almeida, G. Bastiat, J.-P. Benoit, M. de la Fuente, M. Garcia-Fuentes, M. J. Alonso, D. Torres. Self-assembled hyaluronan nanocapsules for the intracellular delivery of anticancer drugs. *Scientific Reports*. 9, 11565. (2019). doi: 10.1038/s41598-019-47995-8.

[5] M. L. Lorenzo-Lamosa, C. Remuñán-López, J. L. Vila-Jato, M. J. Alonso. Design of microencapsulated chitosan microspheres for colonic drug delivery. *Journal of Controlled Release*. 52, 109–118. (1998). doi: 10.1016/S0168-3659(97)00203-4.

[6] D. Teijeiro-Osorio, C. Remuñán-López, M. J. Alonso. New generation of hybrid poly/oligosaccharide nanoparticles as carriers for the nasal delivery of macromolecules. *Biomacromolecules*. 10, 243–249. (2009). doi: 10.1021/bm800975j.

[7] D. F. de Andrade, B. Vukosavljevic, J. B. Hoppe, A. R. Pohlmann, S. S. Guterres, M. Windbergs, I. Külkamp-Guerreiro, C. G. Salbego, R. C. R. Beck. Redispersible Spray-Dried Powder Containing Nanoencapsulated Curcumin: the Drying Process Does Not Affect Neuroprotection In vitro. *AAPS PharmSciTech*. 20, 1–10. (2019). doi: 10.1208/s12249-019-1501-1.

[8] J. M. Song, J. H. Im, J. H. Kang, D. J. Kang. A simple method for hyaluronic acid quantification in culture broth.

Carbohydrate Polymers. 78, 633–634. (2009). doi: 10.1016/j.carbpol.2009.04.033.

[9] M. Mahmoudi, S. E. Lohse, C. J. Murphy, A. Fathizadeh, A. Montazeri, K. S. Suslick. Variation of protein corona composition of gold nanoparticles following plasmonic heating. *Nano Letters*. 14, 6–12. (2014). doi: 10.1021/nl403419e.

[10] M. Mahmoudi, N. Bertrand, H. Zope, O. C. Farokhzad. Emerging understanding of the protein corona at the nano-bio interfaces. *Nano Today*. 11, 817–832. (2016). doi: 10.1016/j.nantod.2016.10.005.

[11] S. Salameh, M. A. Van Der Veen, M. Kappl, J. R. Van Ommen. Contact forces between single metal oxide nanoparticles in gas-phase applications and processes. *Langmuir*. 33, 2477–2484. (2017). doi: 10.1021/acs.langmuir.6b02982.

[12] V. Pareek, A. Bhargava, V. Bhanot, R. Gupta, N. Jain, J. Panwar. Formation and characterization of protein corona around nanoparticles: a review. *Journal of Nanoscience and Nanotechnology*. 18, 6653–6670. (2018). doi: 10.1166/jnn.2018.15766.

[13] I. Lynch, T. Cedervall, M. Lundqvist, C. Cabaleiro-Lago, S. Linse, K. A. Dawson. The nanoparticle–protein complex as a biological entity; a complex fluids and surface science challenge for the 21st century. *Advances in Colloid and Interface Science*. 134–135, 167–174. (2007). doi: 10.1016/j.cis.2007.04.021.

[14] D. A. Tyrrell, V. J. Richardson, B. E. Ryman. The effect of serum protein fractions on liposome cell interactions in cultured cells and the perfused rat liver. *Biochimica et Biophysica Acta*. 497, 469–480. (1977). doi: https://doi.org/10.1016/0304-4165(77)90204-5.

[15] H. Kiwada, T. Miyajima, Y. Kato. Studies on the uptake mechanism factor of liposomes for liver by perfused uptake in serum rat liver. II. An indispensable factor for liver uptake in serum. *Chemical and Pharmaceutical Bulletin*. 35, 1189–1195. (1987). doi: 10.1248/cpb.35.1189.

[16] T. Cedervall, I. Lynch, S. Lindman, T. Berggård, E. Thulin, H. Nilsson, K. A. Dawson, S. Linse, T. Berggard, E. Thulin, H. Nilsson, K. A. Dawson, S. Linse. Understanding the nanoparticle-protein corona using methods to quantify exchange rates and affinities of proteins for nanoparticles. *Proceedings of the National Academy of Sciences*. 104, 2050–2055. (2007). doi: 10.1073/pnas.0608582104.

[17] M. Hadjidemetriou, K. Kostarelos. Nanomedicine: evolution of the nanoparticle corona. *Nature Nanotechnology*. 12, 288–290. (2017). doi: 10.1038/nnano.2017.61.

[18] S. Tenzer, D. Docter, J. Kuharev, A. Musyanovych, V. Fetz, R. Hecht, F. Schlenk, D. Fischer, K. Kiouptsi, C. Reinhardt, K. Landfester, H. Schild, M. Maskos, S. K. Knauer, R. H. Stauber. Rapid formation of plasma protein corona critically affects nanoparticle pathophysiology. *Nature Nanotechnology*. 8, 772–781. (2013). doi: 10.1038/nnano.2013.181.

[19] P. Aggarwal, J. B. Hall, C. B. McLeland, M. A. Dobrovolskaia, S. E. McNeil. Nanoparticle interaction with plasma proteins as it relates to particle biodistribution, biocompatibility and therapeutic efficacy. *Advanced Drug Delivery Reviews*. 61, 428–437. (2009). doi: 10.1016/j.addr.2009.03.009.

[20] M. P. Monopoli, D. Walczyk, A. Campbell, G. Elia, I. Lynch, F. Baldelli Bombelli, K. A. Dawson. Physical-chemical aspects of protein corona: relevance to in vitro and in vivo biological impacts of nanoparticles. *Journal of the American Chemical Society*. 133, 2525–2534. (2011). doi: 10.1021/ja107583h.

[21] M. Luck, B.-R. Paulke, W. Schroder, T. Blunk, R. H. Müller. Analysis of plasma protein adsorption on polymeric nanoparticles with different surface characteristics. *Journal of Biomedical Materials Research*. 39, 478–485. (1998). doi: 10.1002/(SICI)1097-4636(19980305)39:3<478::AID-JBM19>3.0.CO;2-6.

[22] M. Kokkinopoulou, J. Simon, K. Landfester, V. Mailänder, I. Lieberwirth. Visualization of the protein corona: towards a biomolecular understanding of nanoparticle-cell-interactions. *Nanoscale*. 9, 8858–8870. (2017). doi: 10.1039/C7NR02977B.

[23] J. Simon, L. K. Müller, M. Kokkinopoulou, I. Lieberwirth, S. Morsbach, K. Landfester, V. Mailänder. Exploiting the biomolecular corona: pre-coating of nanoparticles enables controlled cellular interactions. *Nanoscale*. 10, 10731–10739. (2018). doi: 10.1039/C8NR03331E.

[24] M. Tonigold, J. Simon, D. Estupiñán, M. Kokkinopoulou, J. Reinholz, U. Kintzel, A. Kaltbeitzel, P. Renz, M. P. Domogalla, K. Steinbrink, I. Lieberwirth, D. Crespy, K. Landfester, V. Mailänder. Pre-adsorption of antibodies enables targeting of nanocarriers despite a biomolecular corona. *Nature Nanotechnology*. 13, 862–869. (2018). doi: 10.1038/s41565-018-0171-6.

[25] C. Weber, J. Simon, V. Mailänder, S. Morsbach, K. Landfester. Preservation of the soft protein corona in distinct flow allows identification of weakly bound proteins. *Acta Biomaterialia*. 76, 217–224. (2018). doi: 10.1016/j.actbio.2018.05.057.

[26] A. Danner, S. Schöttler, E. Alexandrino, S. Hammer, K. Landfester, V. Mailänder, S. Morsbach, H. Frey, F. R. Wurm. Phosphonylation controls the protein corona of multifunctional polyglycerol-modified nanocarriers. *Macromol Biosci.* 19, e1800468. (2019). doi: 10.1002/mabi.201800468.

[27] E. Allémann, P. Gravel, J. C. Leroux, L. Balant, R. Gurny. Kinetics of blood component adsorption on poly(D,L-lactic acid) nanoparticles: Evidence of complement C3 component involvement. *Journal of Biomedical Materials Research*. 37, 229–234. (1997). doi: 10.1002/(SICI)1097-4636(199711)37:2<229::AID-JBM12>3.0.CO;2-9.

[28] R. Gref, M. Lück, P. Quellec, M. Marchand, E. Dellacherie, S. Harnisch, T. Blunk, R. H. Müller. "Stealth" corona-core nanoparticles surface modified by polyethylene glycol (PEG): influences of the corona (PEG chain length and surface density) and of the core composition on phagocytic uptake and plasma protein adsorption. *Colloids and Surfaces B: Biointerfaces*. 18, 301–313. (2000). doi: 10.1016/S0927-7765(99)00156-3.

[29] F. Pederzoli, G. Tosi, F. Genovese, D. Belletti, M. A. Vandelli, A. Ballestrazzi, F. Forni, B. Ruozi. Qualitative and

USC UNIVERSIDADE DE SANTIAGO DE COMPOSTELA

semiquantitative analysis of the protein coronas associated to different functionalized nanoparticles. *Nanomedicine*. 13, 407–422. (2018). doi: 10.2217/nnm-2017-0250.

[30] R. Gossmann, E. Fahrländer, M. Hummel, D. Mulac, J. Brockmeyer, K. Langer. Comparative examination of adsorption of serum proteins on HSA- and PLGA-based nanoparticles using SDS-PAGE and LC-MS. *European Journal of Pharmaceutics and Biopharmaceutics*. 93, 80–87. (2015). doi: 10.1016/j.ejpb.2015.03.021.

[31] C. Lemarchand, R. Gref, C. Passirani, E. Garcion, B. Petri, R. Müller, D. Costantini, P. Couvreur. Influence of polysaccharide coating on the interactions of nanoparticles with biological systems. *Biomaterials*. 27, 108–118. (2006). doi: 10.1016/j.biomaterials.2005.04.041.

[32] D. Labarre, C. Vauthier, C. Chauvierre, B. Petri, R. Müller, M. M. Chehimi. Interactions of blood proteins with poly(isobutylcyanoacrylate) nanoparticles decorated with a polysaccharidic brush. *Biomaterials*. 26, 5075–5084. (2005). doi: 10.1016/j.biomaterials.2005.01.019.

[33] T. Cedervall, I. Lynch, M. Foy, T. Berggård, S. C. Donnelly, G. Cagney, S. Linse, K. A. Dawson. Detailed identification of plasma proteins adsorbed on copolymer nanoparticles. *Angewandte Chemie - International Edition*. 46, 5754–5756. (2007). doi: 10.1002/anie.200700465.

[34] H. R. Kim, K. Andrieux, C. Delomenie, H. Chacun, M. Appel, D. Desmaële, F. Taran, D. Georgin, P. Couvreur, M. Taverna. Analysis of plasma protein adsorption onto PEGylated nanoparticles by complementary methods: 2-DE, CE and Protein Lab-on-chip® system. *Electrophoresis*. 28, 2252–2261. (2007). doi: 10.1002/elps.200600694.

[35] P. S. R. Naidu, M. Norret, N. M. Smith, S. A. Dunlop, N. L. Taylor, M. Fitzgerald, K. S. Iyer. The protein corona of PEGylated PGMA-based nanoparticles is preferentially enriched with specific serum proteins of varied biological function. *Langmuir*. 33, 12926–12933. (2017). doi: 10.1021/acs.langmuir.7b02568.

[36] F. Charbgoo, M. Nejabat, K. Abnous, F. Soltani, S. M. Taghdisi, M. Alibolandi, W. T. Shier, T. W. J. Steele, M. Ramezani. Gold nanoparticle should understand protein corona for being a clinical nanomaterial. *Journal of Controlled Release*. 272, 39–53. (2018). doi: 10.1016/j.jconrel.2018.01.002.

[37] M. P. Monopoli, C. Åberg, A. Salvati, K. A. Dawson. Biomolecular coronas provide the biological identity of nanosized materials. *Nature Nanotechnology*. 7, 779–786. (2012). doi: 10.1038/nnano.2012.207.

[38] L. Vroman, A. L. Adams, G. C. Fischer, P. C. Munoz. Interaction of high molecular weight kininogen, factor XII, and fibrinogen in plasma at interfaces. *Blood*. 55, 156–159. (1980).

[39] E. Casals, T. Pfaller, A. Duschl, G. J. Oostingh, V. Puntes. Time evolution of the nanoparticle protein corona. *ACS Nano*. 4, 3623–3632. (2010). doi: 10.1021/nn901372t.

[40] E. Mahon, A. Salvati, F. Baldelli Bombelli, I. Lynch, K. A. Dawson. Designing the nanoparticle-biomolecule interface for "targeting and therapeutic delivery." *Journal of Controlled Release*. 161, 164–174. (2012). doi: 10.1016/j.jconrel.2012.04.009.

[41] S. Nagayama, K. Ogawara, Y. Fukuoka, K. Higaki, T. Kimura. Time-dependent changes in opsonin amount associated on nanoparticles alter their hepatic uptake characteristics. *International Journal of Pharmaceutics*. 342, 215–221. (2007). doi: 10.1016/j.ijpharm.2007.04.036.

[42] H. Wang, Y. Lin, K. Nienhaus, G. U. Nienhaus. The protein corona on nanoparticles as viewed from a nanoparticle-sizing perspective. *WIREs Nanomed Nanobiotechnol.* 10, e1500. (2018). doi: 10.1002/wnan.1500.

[43] C. Corbo, R. Molinaro, A. Parodi, N. E. Toledano Furman, F. Salvatore, E. Tasciotti. The impact of nanoparticle protein corona on cytotoxicity, immunotoxicity and target drug delivery. *Nanomedicine*. 11, 81–100. (2016). doi: 10.2217/nnm.15.188.

[44] M. Lundqvist, J. Stigler, G. Elia, I. Lynch, T. Cedervall, K. A. Dawson. Nanoparticle size and surface properties determine the protein corona with possible implications for biological impacts. *Proceedings of the National Academy of Sciences of the United States of America*. 105, 14265–70. (2008). doi: 10.1073/pnas.0805135105.

[45] G. Pulido-Reyes, F. Leganes, F. Fernández-Piñas, R. Rosal. Bio-nano interface and environment: a critical review. *Environmental Toxicology and Chemistry*. 36, 3181–3193. (2017). doi: 10.1002/etc.3924.

[46] G. Caracciolo, F. Cardarelli, D. Pozzi, F. Salomone, G. Maccari, G. Bardi, A. L. Capriotti, C. Cavaliere, M. Papi, A. Laganà. Selective targeting capability acquired with a protein corona adsorbed on the surface of 1,2-dioleoyl-3-trimethylammonium propane/dna nanoparticles. *ACS Applied Materials and Interfaces*. 5, 13171–13179. (2013). doi: 10.1021/am404171h.

[47] F. Giulimondi, L. Digiacomo, D. Pozzi, S. Palchetti, E. Vulpis, A. L. Capriotti, R. Z. Chiozzi, A. Laganà, H. Amenitsch, L. Masuelli, M. Mahmoudi, I. Screpanti, A. Zingoni, G. Caracciolo. Interplay of protein corona and immune cells controls blood residency of liposomes. *Nature Communications*. 10, 3686. (2019). doi: 10.1038/s41467-019-11642-7.

[48] G. Caracciolo. Clinically approved liposomal nanomedicines: Lessons learned from the biomolecular corona. *Nanoscale*. 10, 4167–4172. (2018). doi: 10.1039/c7nr07450f.

[49] B. Mandal, H. Bhattacharjee, N. Mittal, H. Sah, P. Balabathula, L. A. Thoma, G. C. Wood. Core-shell-type lipid-polymer hybrid nanoparticles as a drug delivery platform. *Nanomedicine: NBM*. 9, 474–491. (2013). doi: 10.1016/j.nano.2012.11.010.

[50] V. Mirshafiee, M. Mahmoudi, K. Lou, J. Cheng, M. L. Kraft. Protein corona significantly reduces active targeting yield. *Chemical Communications*. 49, 2557–2559. (2013). doi: 10.1039/c3cc37307j.

[51] P. Jain, R. S. Pawar, R. S. Pandey, J. Madan, S. Pawar, P. K. Lakshmi, M. S. Sudheesh. In-vitro in-vivo correlation (IVIVC) in nanomedicine: is protein corona the missing link? *Biotechnology Advances*. 35, 889–904. (2017). doi: 10.1016/j.biotechadv.2017.08.003.

[52] J. Wolfram, K. Suri, Y. Yang, J. Shen, C. Celia, M. Fresta, Y. Zhao, H. Shen, M. Ferrari. Shrinkage of pegylated and

non-pegylated liposomes in serum. *Colloids and Surfaces B: Biointerfaces*. 114, 294–300. (2014). doi: 10.1016/j.colsurfb.2013.10.009.

[53] A. Almalik, H. Benabdelkamel, A. Masood, I. O. Alanazi, I. Alradwan, M. A. Majrashi, A. A. Alfadda, W. M. Alghamdi, H. Alrabiah, N. Tirelli, A. H. Alhasan. Hyaluronic acid coated chitosan nanoparticles reduced the immunogenicity of the formed protein corona. *Scientific Reports*. 7, 10542. (2017). doi: 10.1038/s41598-017-10836-7.

[54] N. Hoshyar, S. Gray, H. Han, G. Bao. The effect of nanoparticle size on in vivo pharmacokinetics and cellular interaction. *Nanomedicine*. 11, 673–692. (2016). doi: 10.2217/nnm.16.5.

[55] M. A. Dobrovolskaia, P. Aggarwal, J. B. Hall, S. E. McNeil. Preclinical studies to understand nanoparticle interaction with the immune system and its potential effects on nanoparticle biodistribution. *Mol Pharm.* 5, 487–495. (2008). doi: 10.1021/mp800032f.Preclinical.

[56] C. D. Walkey, J. B. Olsen, H. Guo, A. Emili, W. C. W. Chan. Nanoparticle size and surface chemistry determine serum protein adsorption and macrophage uptake. *Journal of the American Chemical Society*. 134, 2139–2147. (2012). doi: 10.1021/ja2084338.

[57] B. D. Chithrani, W. C. W. Chan. Elucidating the mechanism of cellular uptake and removal of protein-coated gold nanoparticles of different sizes and shapes. *Nano Letters*. 7, 1542–1550. (2007). doi: 10.1021/nl070363y.

[58] D. Pozzi, G. Caracciolo, A. L. Capriotti, C. Cavaliere, S. Piovesana, V. Colapicchioni, S. Palchetti, A. Riccioli, A. Laganà. A proteomics-based methodology to investigate the protein corona effect for targeted drug delivery. *Molecular BioSystems*. 10, 2815–2819. (2014). doi: 10.1039/C4MB00292J.

[59] C. C. Fleischer, C. K. Payne. Secondary structure of corona proteins determines the cell surface receptors used by nanoparticles. *The Journal of Physical Chemistry B*. 118, 14017–14026. (2014). doi: 10.1021/jp502624n.

[60] A. Ghazaryan, K. Landfester, V. Mailänder. Protein deglycosylation can drastically affect the cellular uptake. *Nanoscale*. 11, 10727–10737. (2019). doi: 10.1039/C8NR08305C.

[61] S. Wan, P. M. Kelly, E. Mahon, H. Stöckmann, P. M. Rudd, F. Caruso, K. A. Dawson, Y. Yan, M. P. Monopoli. The "Sweet" side of the protein corona: effects of glycosylation on nanoparticle–cell interactions. *ACS Nano*. 9, 2157–2166. (2015). doi: 10.1021/nn506060q.

[62] V. P. Vu, G. B. Gifford, F. Chen, H. Benasutti, G. Wang, E. V. Groman, R. Scheinman, L. Saba, S. M. Moghimi, D. Simberg. Immunoglobulin deposition on biomolecule corona determines complement opsonization efficiency of preclinical and clinical nanoparticles. *Nature Nanotechnology*. 14, 260–268. (2019). doi: 10.1038/s41565-018-0344-3.

[63] S. Ritz, S. Schöttler, N. Kotman, G. Baier, A. Musyanovych, J. Kuharev, K. Landfester, H. Schild, O. Jahn, S. Tenzer, V. Mailänder. Protein Corona of Nanoparticles: Distinct Proteins Regulate the Cellular Uptake. *Biomacromolecules*. 16, 1311–1321. (2015). doi: 10.1021/acs.biomac.5b00108.

[64] D. E. Owens, N. A. Peppas. Opsonization, biodistribution, and pharmacokinetics of polymeric nanoparticles. *International Journal of Pharmaceutics*. 307, 93–102. (2006). doi: 10.1016/j.ijpharm.2005.10.010.

[65] K. Furumoto, K. Ogawara, S. Nagayama, Y. Takakura, M. Hashida, K. Higaki, T. Kimura. Important role of serum proteins associated on the surface of particles in their hepatic disposition. *J. Controlled Release*. 83, 89–96. (2002). doi: 10.1016/S0168-3659(02)00196-7.

[66] G. Caracciolo, S. Palchetti, V. Colapicchioni, L. Digiacomo, D. Pozzi, A. L. Capriotti, G. La Barbera, A. Laganà. Stealth effect of biomolecular corona on nanoparticle uptake by immune cells. *Langmuir*. 31, 10764–10773. (2015). doi: 10.1021/acs.langmuir.5b02158.

[67] J. B. Coty, E. Eleamen Oliveira, C. Vauthier. Tuning complement activation and pathway through controlled molecular architecture of dextran chains in nanoparticle corona. *International Journal of Pharmaceutics*. 532, 769–778. (2017). doi: 10.1016/j.ijpharm.2017.04.048.

[68] S. Schöttler, K. Landfester, V. Mailänder. Controlling the stealth effect of nanocarriers through understanding the protein corona. *Angewandte Chemie - International Edition*. 55, 8806–8815. (2016). doi: 10.1002/anie.201602233.

[69] S. Schöttler, G. Becker, S. Winzen, T. Steinbach, K. Mohr, K. Landfester, V. Mailänder, F. R. Wurm. Protein adsorption is required for stealth effect of poly(ethylene glycol)- and poly(phosphoester)-coated nanocarriers. *Nature Nanotechnology*. 11, 372–377. (2016). doi: 10.1038/nnano.2015.330.

[70] L. Landgraf, C. Christner, W. Storck, I. Schick, I. Krumbein, H. Dähring, K. Haedicke, K. Heinz-Herrmann, U. Teichgräber, J. R. Reichenbach, W. Tremel, S. Tenzer, I. Hilger. A plasma protein corona enhances the biocompatibility of Au@Fe3O4 janus particles. *Biomaterials*. 68, 77–88. (2015). doi: 10.1016/j.biomaterials.2015.07.049.

[71] V. Mirshafiee, R. Kim, S. Park, M. Mahmoudi, M. L. Kraft. Impact of protein pre-coating on the protein corona composition and nanoparticle cellular uptake. *Biomaterials*. 75, 295–304. (2016). doi: 10.1016/j.biomaterials.2015.10.019.

[72] V. Francia, K. Yang, S. Deville, C. Reker-Smit, I. Nelissen, A. Salvati. Corona composition can affect the mechanisms cells use to internalize nanoparticles. *ACS Nano*. 13, 11107–11121. (2019). doi: 10.1021/acsnano.9b03824.

[73] K. Yang, B. Mesquita, P. Horvatovich, A. Salvati. Tuning liposome composition to modulate corona formation in human serum and cellular uptake. *Acta Biomaterialia*. 106, 314–327. (2020). doi: 10.1016/j.actbio.2020.02.018.

[74] J. Gilleron, W. Querbes, A. Zeigerer, A. Borodovsky, G. Marsico, U. Schubert, K. Manygoats, S. Seifert, C. Andree, M. Stöter, H. Epstein-Barash, L. Zhang, V. Koteliansky, K. Fitzgerald, E. Fava, M. Bickle, Y. Kalaidzidis, A. Akinc, M. Maier, M. Zerial. Image-based analysis of lipid nanoparticle–mediated siRNA delivery, intracellular trafficking and endosomal escape. *Nature Biotechnology*. 31, 638–646. (2013). doi: 10.1038/nbt.2612.

USC UNIVERSIDADE DE SANTIAGO DE COMPOSTELA

[75] S. Lara, A. Perez-Potti, L. M. Herda, L. Adumeau, K. A. Dawson, Y. Yan. Differential Recognition of Nanoparticle Protein Corona and Modified Low-Density Lipoprotein by Macrophage Receptor with Collagenous Structure. *ACS Nano*. 12, 4930–4937. (2018). doi: 10.1021/acsnano.8b02014.

[76] A. Cox, P. Andreozzi, R. Dal Magro, F. Fiordaliso, A. Corbelli, L. Talamini, C. Chinello, F. Raimondo, F. Magni, M. Tringali, S. Krol, P. J. Silva, F. Stellacci, M. Masserini, F. Re. Evolution of nanoparticle protein corona across the blood–brain barrier. *ACS Nano*. 12, 7292–7300. (2018). doi: 10.1021/acsnano.8b03500.

[77] E. Hellstrand, I. Lynch, A. Andersson, T. Drakenberg, B. Dahlbäck, K. A. Dawson, S. Linse, T. Cedervall. Complete high-density lipoproteins in nanoparticle corona. *FEBS Journal*. 276, 3372–3381. (2009). doi: 10.1111/j.1742-4658.2009.07062.x.

[78] J. Kreuter, T. Hekmatara, S. Dreis, T. Vogel, S. Gelperina, K. Langer. Covalent attachment of apolipoprotein A-I and apolipoprotein B-100 to albumin nanoparticles enables drug transport into the brain. *Journal of Controlled Release*. 118, 54–58. (2007). doi: 10.1016/j.jconrel.2006.12.012.

[79] H. R. Kim, K. Andrieux, S. Gil, M. Taverna, H. Chacun, D. Desmaële, F. Taran, D. Georgin, P. Couvreur. Translocation of poly(ethylene glycol-co-hexadecyl)cyanoacrylate nanoparticles into rat brain endothelial cells: Role of apolipoproteins on receptor-medicted endocytosis. *Biomacromolecules*. 8, 793–799. (2007). doi: 10.1021/bm060711a.

[80] K. Prapainop, P. Wentworth. A shotgun proteomic study of the protein corona associated with cholesterol and atheronal-B surface-modified quantum dots. *European Journal of Pharmaceutics and Biopharmaceutics*. 77, 353–359. (2011). doi: 10.1016/j.ejpb.2010.12.026.

[81] I. Capjak, S. Š. Goreta, D. D. Jurašin, I. V. Vrček. How protein coronas determine the fate of engineered nanoparticles in biological environment. *Arhiv za Higijenu Rada i Toksikologiju*. 68, 245–253. (2017). doi: 10.1515/aiht-2017-68-3054.

[82] F. Bertoli, D. Garry, M. P. Monopoli, A. Salvati, K. A. Dawson. The intracellular destiny of the protein corona: a study on its cellular internalization and evolution. *ACS Nano*. 10, 10471–10479. (2016). doi: 10.1021/acsnano.6b06411.

[83] S. Behzadi, V. Serpooshan, R. Sakhtianchi, B. Müller, K. Landfester, D. Crespy, M. Mahmoudi. Protein corona change the drug release profile of nanocarriers: the "overlooked" factor at the nanobio interface. *Colloids and Surfaces B: Biointerfaces*. 123, 143–149. (2014). doi: 10.1016/j.colsurfb.2014.09.009.

[84] K. Abstiens, S. Maslanka Figueroa, M. Gregoritza, A. M. Goepferich. Interaction of functionalized nanoparticles with serum proteins and its impact on colloidal stability and cargo leaching. *Soft Matter*. 15, 709–720. (2019). doi: 10.1039/C8SM02189A.

[85] H. Wang, R. Ma, K. Nienhaus, G. U. Nienhaus. Formation of a monolayer protein corona around polystyrene nanoparticles and implications for nanoparticle agglomeration. *Small*. 15, e1900974. (2019). doi: 10.1002/smll.201900974.

[86] S. B. Gunnarsson, K. Bernfur, A. Mikkelsen, T. Cedervall. Analysis of nanoparticle biomolecule complexes. *Nanoscale*. 10, 4246–4257. (2018). doi: 10.1039/C7NR08696B.

[87] D. Bonvin, U. Aschauer, D. T. L. Alexander, D. Chiappe, M. Moniatte, H. Hofmann, M. Mionić Ebersold. Protein corona: impact of lymph versus blood in a complex in vitro environment. *Small*. 13, 1700409. (2017). doi: 10.1002/smll.201700409.

[88] K. Partikel, R. Korte, N. C. Stein, D. Mulac, F. C. Herrmann, H.-U. U. Humpf, K. Langer. Effect of nanoparticle size and PEGylation on the protein corona of PLGA nanoparticles. *European Journal of Pharmaceutics and Biopharmaceutics*. 141, 70–80. (2019). doi: 10.1016/j.ejpb.2019.05.006.

[89] I. Lynch, K. A. Dawson. Protein-nanoparticle interactions. *Nano Today*. 3, 40–47. (2008). doi: 10.1016/S1748-0132(08)70014-8.

[90] D. F. Moyano, K. Saha, G. Prakash, B. Yan, H. Kong, M. Yazdani, V. M. Rotello. Fabrication of corona-free nanoparticles with tunable hydrophobicity. *ACS Nano*. 8, 6748–6755. (2014). doi: 10.1021/nn5006478.

[91] D. Glancy, Y. Zhang, J. L. Y. Wu, B. Ouyang, S. Ohta, W. C. W. Chan. Characterizing the protein corona of sub-10 nm nanoparticles. *Journal of Controlled Release*. 304, 102–110. (2019). doi: 10.1016/j.jconrel.2019.04.023.

[92] B. D. Chithrani, A. A. Ghazani, W. C. W. Chan. Determining the size and shape dependence of gold nanoparticle uptake into mammalian cells. *Nano Letters*. 6, 662–668. (2006). doi: 10.1021/nl052396o.

[93] A. Gessner, A. Lieske, B. R. Paulke, R. H. Müller. Influence of surface charge density on protein adsorption on polymeric nanoparticles: Analysis by two-dimensional electrophoresis. *European Journal of Pharmaceutics and Biopharmaceutics*. 54, 165–170. (2002). doi: 10.1016/S0939-6411(02)00081-4.

[94] C. F. Wang, E. M. Mäkilä, C. Bonduelle, J. Rytkönen, J. Raula, S. Almeida, A. Närvänen, J. J. Salonen, S. Lecommandoux, J. T. Hirvonen, H. A. Santos. Functionalization of alkyne-terminated thermally hydrocarbonized porous silicon nanoparticles with targeting peptides and antifouling polymers: Effect on the human plasma protein adsorption. *ACS Applied Materials and Interfaces*. 7, 2006–2015. (2015). doi: 10.1021/am507827n.

[95] A. Gessner, R. Waicz, A. Lieske, B. R. Paulke, K. Mäder, R. H. Müller. Nanoparticles with decreasing surface hydrophobicities: influence on plasma protein adsorption. *International Journal of Pharmaceutics*. 196, 245–249. (2000).

[96] V. H. Nguyen, B. J. Lee. Protein corona: a new approach for nanomedicine design. *International Journal of Nanomedicine*. 12, 3137–3151. (2017). doi: 10.2147/IJN.S129300.

[97] K. Sempf, T. Arrey, S. Gelperina, T. Schorge, B. Meyer, M. Karas, J. Kreuter. Adsorption of plasma proteins on uncoated PLGA nanoparticles. *European Journal of Pharmaceutics and Biopharmaceutics*. 85, 53–60. (2013). doi:

10.1016/j.ejpb.2012.11.030.
[98] C. Vogt, M. Pernemalm, P. Kohonen, S. Laurent, K. Hultenby, M. Vahter, J. Lehtiö, M. S. Toprak, B. Fadeel. Proteomics analysis reveals distinct corona composition on magnetic nanoparticles with different surface coatings: Implications for interactions with primary human macrophages. *PLoS ONE*. 10, 1–20. (2015). doi: 10.1371/journal.pone.0129008.
[99] C. D. Walkey, W. C. W. Chan. Understanding and controlling the interaction of nanomaterials with proteins in a physiological environment. *Chem. Soc. Rev.* 41, 2780–2799. (2012). doi: 10.1039/C1CS15233E.
[100] K. Partikel, R. Korte, D. Mulac, H. Humpf, K. Langer. Serum type and concentration both affect the protein-corona composition of PLGA nanoparticles. *Beilstein Journal of Nanotechnology*. 10, 1002–1015. (2019). doi: 10.3762/bjnano.10.101.
[101] R. Rai, S. Alwani, I. Badea. Polymeric nanoparticles in gene therapy: New avenues of design and optimization for delivery applications. *Polymers*. 11, 745. (2019). doi: 10.3390/polym11040745.
[102] T. Blunk, D. F. Hochstrasser, J.-C. Sanchez, B. W. Müller, R. H. Müller. Colloidal carriers for intravenous drug targeting: Plasma protein adsorption patterns on surface-modified latex particles evaluated by two-dimensional polyacrylamide gel electrophoresis. *Electrophoresis*. 14, 1382–1387. (1993). doi: 10.1002/elps.11501401214.
[103] R. H. Müller, D. Rühl, M. Lück, B. R. Paulke. Influence of fluorescent labelling of polystyrene particles on phagocytic uptake, surface hydrophobicity, and plasma protein adsorption. *Pharmaceutical Research*. 14, 18–24. (1997).
[104] H. Zhang, T. Wu, W. Yu, S. Ruan, Q. He, H. Gao. Ligand size and conformation affect the behavior of nanoparticles coated with in vitro and in vivo protein corona. *ACS Applied Materials and Interfaces*. 10, 9094–9103. (2018). doi: 10.1021/acsami.7b16096.
[105] K. Saha, M. Rahimi, M. Yazdani, S. T. Kim, D. F. Moyano, S. Hou, R. Das, R. Mout, F. Rezaee, M. Mahmoudi, V. M. Rotello. Regulation of macrophage recognition through the interplay of nanoparticle surface functionality and protein corona. *ACS Nano*. 10, 4421–4430. (2016). doi: 10.1021/acsnano.6b00053.
[106] C. Fornaguera, M. Guerra-Rebollo, M. Á. Lázaro, A. Cascante, N. Rubio, J. Blanco, S. Borrós. In Vivo Retargeting of Poly(beta aminoester) (OM-PBAE) Nanoparticles is Influenced by Protein Corona. *Advanced Healthcare Materials*. 8, 1900849. (2019). doi: 10.1002/adhm.201900849.
[107] M. Mahmoudi. Antibody orientation determines corona mistargeting capability. *Nature Nanotechnology*. 13, 775–776. (2018). doi: 10.1038/s41565-018-0147-6.
[108] A. Salvati, A. S. Pitek, M. P. Monopoli, K. Prapainop, F. B. Bombelli, D. R. Hristov, P. M. Kelly, C. Åberg, E. Mahon, K. A. Dawson. Transferrin-functionalized nanoparticles lose their targeting capabilities when a biomolecule corona adsorbs on the surface. *Nature Nanotechnology*. 8, 137–143. (2013). doi: 10.1038/nnano.2012.237.
[109] J. Leroux, P. Gravel, L. Balant, B. Volet, B. M. Anner, E. Allémann, E. Doelker, R. Gurny. Internalization of poly(D,L-lactic acid) nanoparticles by isolated human leukocytes and analysis of plasma proteins adsorbed onto the particles. *Journal of Biomedical Materials Research*. 28, 471–481. (1994). doi: 10.1002/jbm.820280410.
[110] N. Bertrand, P. Grenier, M. Mahmoudi, E. M. Lima, E. A. Appel, F. Dormont, J. M. Lim, R. Karnik, R. Langer, O. C. Farokhzad. Mechanistic understanding of in vivo protein corona formation on polymeric nanoparticles and impact on pharmacokinetics. *Nature Communications*. 8, 1–8. (2017). doi: 10.1038/s41467-017-00600-w.
[111] E. Samaridou, N. Kalamidas, I. Santalices, J. Crecente-Campo, M. J. Alonso. Tuning the PEG surface density of the PEG-PGA enveloped Octaarginine-peptide Nanocomplexes. *Drug Delivery and Translational Research*. 10, 241–258. (2020). doi: 10.1007/s13346-019-00678-3.
[112] N. Samadi, M. J. Van Steenbergen, J. B. Van Den Dikkenberg, T. Vermonden, C. F. Van Nostrum, M. Amidi, W. E. Hennink. Nanoparticles based on a hydrophilic polyester with a sheddable peg coating for protein delivery. *Pharmaceutical Research*. 31, 2593–2604. (2014). doi: 10.1007/s11095-014-1355-x.
[113] X. Zhu, W. Tao, D. Liu, J. Wu, Z. Guo, X. Ji, Z. Bharwani, L. Zhao, X. Zhao, O. C. Farokhzad, J. Shi. Surface de-PEGylation controls nanoparticle-mediated siRNA delivery in vitro and in vivo. *Theranostics*. 7, 1990–2002. (2017). doi: 10.7150/thno.18136.
[114] L. Sanchez, Y. Yi, Y. Yu. Effect of partial PEGylation on particle uptake by macrophages. *Nanoscale*. 9, 288–297. (2017). doi: 10.1039/c6nr07353k.
[115] P. Grenier, I. M. de Oliveira Viana, E. M. Lima, N. Bertrand. Anti-polyethylene glycol antibodies alter the protein corona deposited on nanoparticles and the physiological pathways regulating their fate in vivo. *Journal of Controlled Release*. 287, 121–131. (2018). doi: 10.1016/j.jconrel.2018.08.022.
[116] H. B. Haroon, A. C. Hunter, Z. S. Farhangrazi, S. M. Moghimi. A brief history of long circulating nanoparticles. *Advanced Drug Delivery Reviews*. 188, 114396. (2022). doi: 10.1016/j.addr.2022.114396.
[117] S. M. Moghimi. Re-establishing the long circulatory behaviour of poloxamine-coated particles after repeated intravenous administration: Applications in cancer drug delivery and imaging. *Biochimica et Biophysica Acta - General Subjects*. 1472, 399–403. (1999). doi: 10.1016/S0304-4165(99)00157-9.
[118] N. d'Avanzo, C. Celia, A. Barone, M. Carafa, L. Di Marzio, H. A. Santos, M. Fresta. Immunogenicity of Polyethylene Glycol Based Nanomedicines: Mechanisms, Clinical Implications and Systematic Approach. *Advanced Therapeutics*. 3, 1–18. (2020). doi: 10.1002/adtp.201900170.
[119] S. Moein Moghimi, I. Hamad, T. L. Andresen, K. Jørgensen, J. Szebeni, S. Moein Moghimi, I. Hamad, T. L. Andresen, K. Jørgensen, J. Szebeni. Methylation of the phosphate oxygen moiety of phospholipid-methoxy(polyethylene glycol) conjugate prevents PEGylated liposome-mediated complement activation and anaphylatoxin production. *The FASEB Journal*. 20, 2591–2593. (2006). doi: 10.1096/fj.06-6186fje.
[120] S. M. Moghimi, J. Szebeni. Stealth liposomes and long circulating nanoparticles: Critical issues in pharmacokinetics,

opsonization and protein-binding properties. *Progress in Lipid Research*. 42, 463–478. (2003). doi: 10.1016/S0163-7827(03)00033-X.

[121] S. M. Moghimi, A. C. Hunter, C. M. Dadswell, S. Savay, C. R. Alving, J. Szebeni. Causative factors behind poloxamer 188 (Pluronic F68, Flocor™)- induced complement activation in human sera. A protective role against poloxamer-mediated complement activation by elevated serum lipoprotein levels. *Biochimica et Biophysica Acta - Molecular Basis of Disease*. 1689, 103–113. (2004). doi: 10.1016/j.bbadis.2004.02.005.

[122] M. Almeida, M. Magalhães, F. Veiga, A. Figueiras. Poloxamers, poloxamines and polymeric micelles: Definition, structure and therapeutic applications in cancer. *Journal of Polymer Research*. 25, 31. (2018). doi: 10.1007/s10965-017-1426-x.

[123] J. C. Neal, S. Stolnik, E. Schacht, E. R. Kenawy, M. C. Garnett, S. S. Davis, L. Illum. In vitro displacement by rat serum of adsorbed radiolabeled poloxamer and poloxamine copolymers from model and biodegradable nanospheres. *Journal of Pharmaceutical Sciences*. 87, 1242–1248. (1998). doi: 10.1021/js970462j.

[124] S. Stolnik, B. Daudali, A. Arien, J. Whetstone, C. R. Heald, M. C. Garnett, S. S. Davis, L. Illum. The effect of surface coverage and conformation of poly(ethylene oxide) (PEO) chains of poloxamer 407 on the biological fate of model colloidal drug carriers. *Biochimica et Biophysica Acta - Biomembranes*. 1514, 261–279. (2001). doi: 10.1016/S0005-2736(01)00376-5.

[125] J. Kreuter. Influence of the surface properties on nanoparticle-mediated transport of drugs to the brain. *Journal of Nanoscience and Nanotechnology*. 4, 484–488. (2004). doi: 10.1166/jnn.2003.077.

[126] M. Elsabahy, S. Zhang, F. Zhang, Z. J. Deng, Y. H. Lim, H. Wang, P. Parsamian, P. T. Hammond, K. L. Wooley. Surface charges and shell crosslinks each play significant roles in mediating degradation, biofouling, cytotoxicity and immunotoxicity for polyphosphoester-based nanoparticles. *Scientific Reports*. 3, 3313. (2013). doi: 10.1038/srep03313.

[127] Z. Zhao, J. Wang, H. Q. Mao, K. W. Leong. Polyphosphoesters in drug and gene delivery. *Advanced Drug Delivery Reviews*. 55, 483–499. (2003). doi: 10.1016/S0169-409X(03)00040-1.

[128] J. Simon, T. Wolf, K. Klein, K. Landfester, F. R. Wurm, V. Mailänder. Hydrophilicity regulates the stealth properties of polyphosphoester-coated nanocarriers. *Angewandte Chemie - International Edition*. 57, 5548–5553. (2018). doi: 10.1002/anie.201800272.

[129] X. Han, T. Zhang, M. Liu, Y. Song, X. Liu, Y. Deng. Polysialic acid modified liposomes for improving pharmacokinetics and overcoming accelerated blood clearance phenomenon. *Coatings*. 10, (2020). doi: 10.3390/coatings10090834.

[130] A. Shimoda, Y. Tahara, S. Sawada, Y. Sasaki, K. Akiyoshi. Glycan profiling analysis using evanescent-field fluorescence-assisted lectin array: Importance of sugar recognition for cellular uptake of exosomes from mesenchymal stem cells. *Biochemical and Biophysical Research Communications*. 491, 701–707. (2017). doi: 10.1016/j.bbrc.2017.07.126.

[131] S. Spence, M. K. Greene, F. Fay, E. Hams, S. P. Saunders, U. Hamid, M. Fitzgerald, J. Beck, B. K. Bains, P. Smyth, E. Themistou, D. M. Small, D. Schmid, C. M. O'Kane, D. C. Fitzgerald, S. M. Abdelghany, J. A. Johnston, P. G. Fallon, J. F. Burrows, D. F. McAuley, A. Kissenpfennig, C. J. Scott. Targeting Siglecs with a sialic acid-decorated nanoparticle abrogates inflammation. *Science Translational Medicine*. 7, 1–13. (2015). doi: 10.1126/scitranslmed.aab3459.

[132] A. Cadete, M. J. Alonso. Targeting cancer with hyaluronic acid-based nanocarriers: Recent advances and translational perspectives. *Nanomedicine*. 11, 2341–2357. (2016). doi: 10.2217/nnm-2016-0117.

[133] K. P. García, K. Zarschler, L. Barbaro, J. A. Barreto, W. O'Malley, L. Spiccia, H. Stephan, B. Graham. Zwitterionic-coated "stealth" nanoparticles for biomedical applications: recent advances in countering biomolecular corona formation and uptake by the mononuclear phagocyte system. *Small*. 10, 2516–2529. (2014). doi: 10.1002/smll.201303540.

[134] D. J. Sobczynski, O. Eniola-Adefeso. IgA and IgM protein primarily drive plasma corona-induced adhesion reduction of PLGA nanoparticles in human blood flow. *Bioengineering & Translational Medicine*. 2, 180–190. (2017). doi: 10.1002/btm2.10064.

[135] M. Mahmoudi. Debugging nano–bio interfaces: systematic strategies to accelerate clinical translation of nanotechnologies. *Trends in Biotechnology*. 36, 755–769. (2018). doi: 10.1016/j.tibtech.2018.02.014.

[136] M. J. Hajipour, S. Laurent, A. Aghaie, F. Rezaee, M. Mahmoudi. Personalized protein coronas: a "key" factor at the nanobiointerface. *Biomaterials Science*. 2, 1210. (2014). doi: 10.1039/C4BM00131A.

[137] N. J. Braun, M. C. DeBrosse, S. M. Hussain, K. K. Comfort. Modification of the protein corona–nanoparticle complex by physiological factors. *Mater Sci Eng C Mater Biol Appl.* 64, 34–42. (2016). doi: 10.1016/j.msec.2016.03.059.

[138] D. T. Jayaram, S. M. Pustulka, R. G. Mannino, W. A. Lam, C. K. Payne. Protein corona in response to flow: effect on protein concentration and structure. *Biophysical Journal*. 115, 209–216. (2018). doi: 10.1016/j.bpj.2018.02.036.

[139] J.-B. Coty, C. Vauthier. Characterization of nanomedicines: a reflection on a field under construction needed for clinical translation success. *Journal of Controlled Release*. 275, 254–268. (2018). doi: 10.1016/j.jconrel.2018.02.013.

[140] L. K. Müller, J. Simon, C. Rosenauer, V. Mailänder, S. Morsbach, K. Landfester. The Transferability from Animal Models to Humans: Challenges Regarding Aggregation and Protein Corona Formation of Nanoparticles. *Biomacromolecules*. 19, 374–385. (2018). doi: 10.1021/acs.biomac.7b01472.

[141] D. J. Sobczynski, O. Eniola-Adefeso. Effect of anticoagulants on the protein corona-induced reduced drug carrier adhesion efficiency in human blood flow. *Acta Biomaterialia*. 48, 186–194. (2017). doi: 10.1016/j.actbio.2016.10.023.

[142] C. Salvador-Morales, L. Zhang, R. Langer, O. C. Farokhzad. Immunocompatibility properties of lipid–polymer hybrid

nanoparticles with heterogeneous surface functional groups. *Biomaterials*. 30, 2231–2240. (2009). doi: 10.1016/j.biomaterials.2009.01.005.

[143] M. S. Fawzy, E. A. Toraih. Data supporting the structural and functional characterization of Thrombin-Activatable Fibrinolysis Inhibitor in breast cancer. *Data in Brief*. 5, 981–989. (2015). doi: 10.1016/j.dib.2015.10.043.

[144] T. E. Mollnes, O.-L. Brekke, M. Fung, H. Fure, D. Christiansen, G. Bergseth, V. Videm, K. T. Lappegård, J. D. Lambris. Essential role of the C5a receptor in E coli–induced oxidative burst and phagocytosis revealed by a novel lepirudin-based human whole blood model of inflammation. *Blood*. 100, 1869–1877. (2002). doi: 10.1182/blood-2002-08-2595.

[145] S. M. Moghimi, D. Simberg. Critical issues and pitfalls in serum and plasma handling for complement analysis in nanomedicine and bionanotechnology. *Nano Today*. 44, 101479. (2022). doi: 10.1016/j.nantod.2022.101479.

[146] D. Docter, U. Distler, W. Storck, J. Kuharev, D. Wünsch, A. Hahlbrock, S. K. Knauer, S. Tenzer, R. H. Stauber. Quantitative profiling of the protein coronas that form around nanoparticles. *Nature Protocols*. 9, 2030–2044. (2014). doi: 10.1038/nprot.2014.139.

[147] D. Chen, S. Ganesh, W. Wang, M. Amiji. The role of surface chemistry in serum protein corona-mediated cellular delivery and gene silencing with lipid nanoparticles. *Nanoscale*. 11, 8760–8775. (2019). doi: 10.1039/c8nr09855g.

[148] S. Palchetti, D. Pozzi, A. L. Capriotti, G. La Barbera, R. Z. Chiozzi, L. Digiacomo, G. Peruzzi, G. Caracciolo, A. Laganà. Influence of dynamic flow environment on nanoparticle-protein corona: from protein patterns to uptake in cancer cells. *Colloids and Surfaces B: Biointerfaces*. 153, 263–271. (2017). doi: 10.1016/j.colsurfb.2017.02.037.

[149] A. L. Capriotti, C. Cavaliere, S. Piovesana. Liposome protein corona characterization as a new approach in nanomedicine. *Analytical and Bioanalytical Chemistry*. 411, 4313–4326. (2019). doi: 10.1007/s00216-019-01656-x.

[150] R. R. Arvizo, K. Giri, D. Moyano, O. R. Miranda, B. Madden, D. J. McCormick, R. Bhattacharya, V. M. Rotello, J. P. Kocher, P. Mukherjee. Identifying new therapeutic targets via modulation of protein corona formation by engineered nanoparticles. *PLoS ONE*. 7, 1–8. (2012). doi: 10.1371/journal.pone.0033650.

[151] C. D. Walkey, J. B. Olsen, F. Song, R. Liu, X. H. Guo, D. W. H. Olsen, Y. Cohen, X. A. Emili, W. C. W. Chan. Protein corona fingerprinting predicts the cellular interaction of gold and silver nanoparticles. *ACS Nano*. 8, 2439–2455. (2014). doi: 10.1021/nn406018q.

[152] R. Frost, C. Langhammer, T. Cedervall. Real-time in situ analysis of biocorona formation and evolution on silica nanoparticles in defined and complex biological environments. *Nanoscale*. 9, 3620–3628. (2017). doi: 10.1039/C6NR06399C.

[153] A. L. Capriotti, G. Caracciolo, G. Caruso, C. Cavaliere, D. Pozzi, R. Samperi, A. Laganà. Analysis of plasma protein adsorption onto DC-Chol-DOPE cationic liposomes by HPLC-CHIP coupled to a Q-TOF mass spectrometer. *Analytical and Bioanalytical Chemistry*. 398, 2895–2903. (2010). doi: 10.1007/s00216-010-4104-y.

[154] C. Weber, S. Morsbach, K. Landfester. Possibilities and limitations of different separation techniques for the analysis of the protein corona. *Angewandte Chemie - International Edition*. 58, 12787–12794. (2019). doi: 10.1002/anie.201902323.

[155] Y. Wang, S. V. Olesik. Separation of PEGylated gold nanoparticles by micellar enhanced electrospun fiber based ultrathin layer chromatography. *Analytical Chemistry*. 90, 2662–2670. (2018). doi: 10.1021/acs.analchem.7b04442.

[156] A. Chetwynd, E. Guggenheim, S. Briffa, J. Thorn, I. Lynch, E. Valsami-Jones. Current application of capillary electrophoresis in nanomaterial characterisation and its potential to characterise the protein and small molecule corona. *Nanomaterials*. 8, 99. (2018). doi: 10.3390/nano8020099.

[157] J. Ashby, S. Schachermeyer, S. Pan, W. Zhong. Dissociation-based screening of nanoparticle-protein interaction via flow field-flow fractionation. *Analytical Chemistry*. 85, 7494–7501. (2013). doi: 10.1021/ac401485j.

[158] J. Ashby, S. Pan, W. Zhong. Size and surface functionalization of iron oxide nanoparticles influence the composition and dynamic nature of their protein corona. *ACS Applied Materials and Interfaces*. 6, 15412–15419. (2014). doi: 10.1021/am503909q.

[159] U. Hansen, A. F. Thünemann. Characterization of Silver Nanoparticles in Cell Culture Medium Containing Fetal Bovine Serum. *Langmuir*. 31, 6842–6852. (2015). doi: 10.1021/acs.langmuir.5b00687.

[160] T. K. Mudalige, H. Qu, S. W. Linder. Asymmetric flow-field flow fractionation hyphenated ICP-MS as an alternative to cloud point extraction for quantification of silver nanoparticles and silver speciation: application for nanoparticles with a protein corona. *Analytical Chemistry*. 87, 7395–7401. (2015). doi: 10.1021/acs.analchem.5b01592.

[161] R. Rampado, S. Crotti, P. Caliceti, S. Pucciarelli, M. Agostini. Recent Advances in Understanding the Protein Corona of Nanoparticles and in the Formulation of "Stealthy" Nanomaterials. *Frontiers in Bioengineering and Biotechnology*. 8, (2020). doi: 10.3389/fbioe.2020.00166.

[162] I. Alberg, S. Kramer, C. Leps, S. Tenzer, R. Zentel. Effect of Core-Crosslinking on Protein Corona Formation on Polymeric Micelles. *Macromolecular Bioscience*. 21, (2021). doi: 10.1002/mabi.202000414.

[163] I. Alberg, S. Kramer, M. Schinnerer, Q. Hu, C. Seidl, C. Leps, N. Drude, D. Möckel, C. Rijcken, T. Lammers, M. Diken, M. Maskos, S. Morsbach, K. Landfester, S. Tenzer, M. Barz, R. Zentel. Polymeric Nanoparticles with Neglectable Protein Corona. *Small*. 16, (2020). doi: 10.1002/smll.201907574.

[164] C. Weber, M. Voigt, J. Simon, A.-K. Danner, H. Frey, V. Mailänder, M. Helm, S. Morsbach, K. Landfester. Functionalization of Liposomes with Hydrophilic Polymers Results in Macrophage Uptake Independent of the Protein Corona. *Biomacromolecules*. 20, 2989–2999. (2019). doi: 10.1021/acs.biomac.9b00539.

[165] D. Maiolo, P. Bergese, E. Mahon, K. A. Dawson, M. P. Monopoli. Surfactant titration of nanoparticle–protein corona. *Analytical Chemistry*. 86, 12055–12063. (2014). doi: 10.1021/ac5027176.

[166] H. Zhang, J. Peng, X. Li, S. Liu, Z. Hu, G. Xu, R. Wu. A nano-bio interfacial protein corona on silica nanoparticle.

USC UNIVERSIDADE DE SANTIAGO DE COMPOSTELA

Colloids and Surfaces B: Biointerfaces. 167, 220–228. (2018). doi: 10.1016/j.colsurfb.2018.04.021.
[167] T. Rabilloud, C. Lelong. Two-dimensional gel electrophoresis in proteomics: a tutorial. *Journal of Proteomics*. 74, 1829–1841. (2011). doi: 10.1016/j.jprot.2011.05.040.
[168] F. Pederzoli, G. Tosi, M. A. Vandelli, D. Belletti, F. Forni, B. Ruozi. Protein corona and nanoparticles: how can we investigate on? *Wiley Interdisciplinary Reviews: Nanomedicine and Nanobiotechnology*. 9, e1467. (2017). doi: 10.1002/wnan.1467.
[169] J. Kruszewska, J. Zajda, M. Matczuk. How to effectively prepare a sample for bottom-up proteomic analysis of nanoparticle protein corona? A critical review. *Talanta*. 226, 122153. (2021). doi: 10.1016/j.talanta.2021.122153.
[170] Y. V Karpievitch, A. D. Polpitiya, G. A. Anderson, R. D. Smith, A. R. Dabney. Liquid chromatography mass spectrometry-based proteomics: biological and technological aspects. *Annals of Applied Statistics*. 4, 1797–1823. (2011). doi: 10.1214/10-AOAS341.
[171] S. Galmarini, U. Hanusch, M. Giraud, N. Cayla, D. Chiappe, N. von Moos, H. Hofmann, L. Maurizi. Beyond unpredictability: the importance of reproducibility in understanding the protein corona of nanoparticles. *Bioconjugate Chemistry*. 29, 3385–3393. (2018). doi: 10.1021/acs.bioconjchem.8b00554.
[172] R. García-Álvarez, M. Hadjidemetriou, A. Sánchez-Iglesias, L. M. Liz-Marzán, K. Kostarelos. In vivo formation of protein corona on gold nanoparticles. The effect of their size and shape. *Nanoscale*. 10, 1256–1264. (2018). doi: 10.1039/C7NR08322J.
[173] M. Hadjidemetriou, Z. Al-Ahmady, K. Kostarelos. Time-evolution of in vivo protein corona onto blood-circulating PEGylated liposomal doxorubicin (DOXIL) nanoparticles. *Nanoscale*. 8, 6948–6957. (2016). doi: 10.1039/C5NR09158F.
[174] C. Corbo, R. Molinaro, F. Taraballi, N. E. Toledano Furman, K. A. Hartman, M. B. Sherman, E. De Rosa, D. K. Kirui, F. Salvatore, E. Tasciotti. Unveiling the in vivo protein corona of circulating leukocyte-like carriers. *ACS Nano*. 11, 3262–3273. (2017). doi: 10.1021/acsnano.7b00376.
[175] A. Amici, G. Caracciolo, L. Digiacomo, V. Gambini, C. Marchini, M. Tilio, A. L. Capriotti, V. Colapicchioni, R. Matassa, G. Familiari, S. Palchetti, D. Pozzi, M. Mahmoudi, A. Laganà. In vivo protein corona patterns of lipid nanoparticles. *RSC Advances*. 7, 1137–1145. (2017). doi: 10.1039/C6RA25493D.
[176] M. Hadjidemetriou, S. McAdam, G. Garner, C. Thackeray, D. Knight, D. Smith, Z. Al-Ahmady, M. Mazza, J. Rogan, A. Clamp, K. Kostarelos. The human in vivo biomolecule corona onto PEGylated liposomes: a proof-of-concept clinical study. *Advanced Materials*. 31, 1–9. (2019). doi: 10.1002/adma.201803335.
[177] M. Papi, V. Palmieri, S. Palchetti, D. Pozzi, L. Digiacomo, E. Guadagno, M. del Basso De Caro, M. Di Domenico, S. Ricci, R. Pani, M. Mahmoudi, A. Di Carlo, G. Caracciolo. Exploitation of nanoparticle-protein interactions for early disease detection. *Applied Physics Letters*. 114, 163702. (2019). doi: 10.1063/1.5098081.
[178] M. Hadjidemetriou, Z. Al-ahmady, M. Buggio, J. Swift, K. Kostarelos. A novel scavenging tool for cancer biomarker discovery based on the blood-circulating nanoparticle protein corona. *Biomaterials*. 188, 118–129. (2019). doi: 10.1016/j.biomaterials.2018.10.011.
[179] S. Palchetti, D. Pozzi, M. Mahmoudi, G. Caracciolo. Exploitation of nanoparticle–protein corona for emerging therapeutic and diagnostic applications. *Journal of Materials Chemistry B*. 4, 4376–4381. (2016). doi: 10.1039/C6TB01095D.
[180] J. C. Zillies, K. Zwiorek, G. Winter, C. Coester. Method for quantifying the PEGylation of gelatin nanoparticle drug carrier systems using asymmetrical flow field-flow fractionation and refractive index detection. *Analytical Chemistry*. 79, 4574–4580. (2007). doi: 10.1021/ac062135e.
[181] M. Vigliano, A. Bianchera, R. Bettini, L. Elviri. Determination of hyaluronic acid in a chitosan-based formulation by RP C18 and HILIC LC-ESI-MS: An evaluation of matrix effect. *Chromatographia*. 76, 1761–1766. (2013). doi: 10.1007/s10337-013-2533-4.
[182] International Conference on Harmonisation of Technical Requirements for Registration of Pharmaceuticals for Human Use. Validation of Analytical Procedures: Methodology Q2(R1). https://database.ich.org/sites/default/files/Q2(R1) Guideline.pdf. Accessed: May 4, 2021.
[183] J. L. Perry, K. G. Reuter, M. P. Kai, K. P. Herlihy, S. W. Jones, J. C. Luft, M. Napier, J. E. Bear, J. M. Desimone. PEGylated PRINT nanoparticles: The impact of PEG density on protein binding, macrophage association, biodistribution, and pharmacokinetics. *Nano Letters*. 12, 5304–5310. (2012). doi: 10.1021/nl302638g.
[184] K. L. Lee, S. Shukla, M. Wu, N. R. Ayat, C. E. El Sanadi, A. M. Wen, J. F. Edelbrock, J. K. Pokorski, U. Commandeur, G. R. Dubyak, N. F. Steinmetz. Stealth filaments: Polymer chain length and conformation affect the in vivo fate of PEGylated potato virus X. *Acta Biomaterialia*. 19, 166–179. (2015). doi: 10.1016/j.actbio.2015.03.001.
[185] C. Arfvidsson, K. G. Wahlund. Mass overloading in the flow field-flow fractionation channel studied by the behaviour of the ultra-large wheat protein glutenin. *Journal of Chromatography A*. 1011, 99–109. (2003). doi: 10.1016/S0021-9673(03)01145-2.
[186] T. Inoue, S. Tatemori, N. Muranaka, Y. Hirahara, S. Homma, T. Nakane, A. Takano, Y. Nomi, Y. Otsuka. The identification of vitamin e homologues in medicinal plant samples using ESI(+)-LC-MS3. *Journal of Agricultural and Food Chemistry*. 60, 9581–9588. (2012). doi: 10.1021/jf302425z.
[187] K. Jiang, G. Gachumi, A. Poudel, B. Shurmer, Z. Bashi, A. El-Aneed. The Establishment of Tandem Mass Spectrometric Fingerprints of Phytosterols and Tocopherols and the Development of Targeted Profiling Strategies in Vegetable Oils. *Journal of the American Society for Mass Spectrometry*. 30, 1700–1712. (2019). doi: 10.1007/s13361-019-02242-2.
[188] R. F. LeBouf, M. A. Virji, A. Ranpara, A. B. Stefaniak. Air and surface sampling method for assessing exposures to

quaternary ammonium compounds using liquid chromatography tandem mass spectrometry. *Annals of Work Exposures and Health*. 61, 724–736. (2017). doi: 10.1093/annweh/wxx037.

[189] H. Dang, D. Liu, X. Hou, Y. Wu, B. Wang, H. Dong, Y. Xian. One-step extraction prior to two-step detection by ultra high performance liquid chromatography tandem mass spectrometry (UHPLC-MS/MS) to determine different groups of antibacterial agents in infant disposable hygiene products. *Analytical Methods*. 9, 482–489. (2017). doi: 10.1039/c6ay03220f.

[190] R. Koeber, A. Pappas, U. Michaelis, B. Schulze. Extraction and quantification of the cationic lipid 1,2-dioleoyl-3-trimethylammonium propane from human plasma. *Analytical Biochemistry*. 363, 157–159. (2007). doi: 10.1016/j.ab.2007.01.001.

[191] B. J. Heyde, A. Barthel, J. Siemens, I. Mulder. A fast and robust method for the extraction and analysis of quaternary alkyl ammonium compounds from soil and sewage sludge. *PLoS ONE*. 15, 1–16. (2020). doi: 10.1371/journal.pone.0237020.

[192] C. M. Spickett, A. Reis, A. R. Pitt. Identification of oxidized phospholipids by electrospray ionization mass spectrometry and LC-MS using a QQLIT instrument. *Free Radical Biology and Medicine*. 51, 2133–2149. (2011). doi: 10.1016/j.freeradbiomed.2011.09.003.

[193] B. J. Molloy. LipidQuan-R for Diacyl-Phosphatidylcholines in Human Serum: A Rapid, Targeted UPLC-MS/MS Method for Lipidomic Research Studies. https://www.waters.com/content/dam/waters/en/app-notes/2020/720006935/720006935-en.pdf. Accessed: November 10, 2020.

[194] A. M. McAnoy, C. C. Wu, R. C. Murphy. Direct qualitative analysis of triacylglycerols by electrospray mass spectrometry using a linear ion trap. *Journal of the American Society for Mass Spectrometry*. 16, 1498–1509. (2005). doi: 10.1016/j.jasms.2005.04.017.

[195] V. V. Bhaskar, A. Middha, P. Srivastava, S. Rajagopal. Liquid chromatography/tandem mass spectrometry method for quantitative estimation of solutol HS15 and its applications. *Journal of Pharmaceutical Analysis*. 5, 120–129. (2015). doi: 10.1016/j.jpha.2014.09.002.

[196] V. Vijaya Bhaskar, A. Middha, S. Tiwari, S. Shivakumar. Liquid chromatography/tandem mass spectrometry method for quantitative estimation of polyethylene glycol 400 and its applications. *Journal of Chromatography B: Analytical Technologies in the Biomedical and Life Sciences*. 926, 68–76. (2013). doi: 10.1016/j.jchromb.2013.02.021.

[197] E. Hvattum, W. L. Yip, D. Grace, K. Dyrstad. Characterization of polysorbate 80 with liquid chromatography mass spectrometry and nuclear magnetic resonance spectroscopy: Specific determination of oxidation products of thermally oxidized polysorbate 80. *Journal of Pharmaceutical and Biomedical Analysis*. 62, 7–16. (2012). doi: 10.1016/j.jpba.2011.12.009.

[198] R. Stern, G. Kogan, M. J. Jedrzejas, L. Šoltés. The many ways to cleave hyaluronan. *Biotechnology Advances*. 25, 537–557. (2007). doi: 10.1016/j.biotechadv.2007.07.001.

[199] C. Chemistry. In *Biermann's Handbook of Pulp and Paper (Third Edition)*. (2018). pp. 363–371.

[200] A. V. Kühn, K. Raith, V. Sauerland, R. H. H. Neubert. Quantification of hyaluronic acid fragments in pharmaceutical formulations using LC-ESI-MS. *Journal of Pharmaceutical and Biomedical Analysis*. 30, 1531–1537. (2003). doi: 10.1016/S0731-7085(02)00544-7.

[201] S. Toghi Eshghi, W. Yang, Y. Hu, P. Shah, S. Sun, X. Li, H. Zhang. Classification of Tandem Mass Spectra for Identification of N- and O-linked Glycopeptides. *Scientific Reports*. 6, 1–8. (2016). doi: 10.1038/srep37189.

[202] H. Jiang, H. Desaire, V. Y. Butnev, G. R. Bousfield. Glycoprotein profiling by electrospray mass spectrometry. *Journal of the American Society for Mass Spectrometry*. 15, 750–758. (2004). doi: 10.1016/j.jasms.2004.01.009.

[203] A. Tsugita, J.-J. Scheffler. A Rapid Method for Acid Hydrolysis of Protein with a Mixture of Trifluoroacetic Acid and Hydrochloric Acid. *European Journal of Biochemistry*. 124, 585–588. (2005). doi: 10.1111/j.1432-1033.1982.tb06634.x.

[204] W. Yu, Z. Chen, H. Ye, P. Liu, Z. Li, Y. Wang, Q. Li, S. Yan, C. Zhong, N. He. Effect of glucose on poly-γ-glutamic acid metabolism in Bacillus licheniformis. *Microbial Cell Factories*. 16, 1–10. (2017). doi: 10.1186/s12934-017-0642-8.

[205] H. C. M. T. Prinsen, B. G. M. Schiebergen-Bronkhorst, M. W. Roeleveld, J. J. M. Jans, M. G. M. de Sain-van der Velden, G. Visser, P. M. van Hasselt, N. M. Verhoeven-Duif. Rapid quantification of underivatized amino acids in plasma by hydrophilic interaction liquid chromatography (HILIC) coupled with tandem mass-spectrometry. *Journal of Inherited Metabolic Disease*. 39, 651–660. (2016). doi: 10.1007/s10545-016-9935-z.

[206] X. Ma, S. Dagan, Á. Somogyi, V. H. Wysocki, P. Y. Scaraffia. Low mass MS/MS fragments of protonated amino acids used for distinction of their 13C- isotopomers in metabolic studies. *Journal of the American Society for Mass Spectrometry*. 24, 622–631. (2013). doi: 10.1007/s13361-012-0574-9.

[207] B. Halmschlag, S. P. Putri, E. Fukusaki, L. M. Blank. Identification of Key Metabolites in Poly-γ-Glutamic Acid Production by Tuning γ-PGA Synthetase Expression. *Frontiers in Bioengineering and Biotechnology*. 8, 1–14. (2020). doi: 10.3389/fbioe.2020.00038.

[208] R. N. Gursoy, S. Benita. Self-emulsifying drug delivery systems (SEDDS) for improved oral delivery of lipophilic drugs. *Biomedicine and Pharmacotherapy*. 58, 173–182. (2004). doi: 10.1016/j.biopha.2004.02.001.

[209] E. Samaridou, H. Walgrave, E. Salta, D. M. Álvarez, V. Castro-López, M. Loza, M. J. Alonso. Nose-to-brain delivery of enveloped RNA - cell permeating peptide nanocomplexes for the treatment of neurodegenerative diseases. *Biomaterials*. 230, 119657. (2020). doi: 10.1016/j.biomaterials.2019.119657.

[210] S. Vicente, B. A. Goins, A. Sanchez, M. J. Alonso, W. T. Phillips. Biodistribution and lymph node retention of polysaccharide-based immunostimulating nanocapsules. *Vaccine*. 32, 1685–1692. (2014). doi:

10.1016/j.vaccine.2014.01.059.
[211] C. Teijeiro-Valiño, R. Novoa-Carballal, E. Borrajo, A. Vidal, M. Alonso-Nocelo, M. de la Fuente Freire, P. P. P. Lopez-Casas, M. Hidalgo, N. Csaba, M. J. Alonso. A multifunctional drug nanocarrier for efficient anticancer therapy. *Journal of Controlled Release*. 294, 154–164. (2019). doi: 10.1016/j.jconrel.2018.12.002.
[212] M. Lundqvist, C. Augustsson, M. Lilja, K. Lundkvist, B. Dahlbäck, S. Linse, T. Cedervall. The nanoparticle protein corona formed in human blood or human blood fractions. *PLOS ONE*. 12, e0175871. (2017). doi: 10.1371/journal.pone.0175871.
[213] J. Müller, D. Prozeller, A. Ghazaryan, M. Kokkinopoulou, V. Mailänder, S. Morsbach, K. Landfester. Beyond the protein corona – lipids matter for biological response of nanocarriers. *Acta Biomaterialia*. 71, 420–431. (2018). doi: 10.1016/j.actbio.2018.02.036.
[214] S. Tenzer, D. Docter, S. Rosfa, A. Wlodarski, J. Kuharev, A. Rekik, S. K. Knauer, C. Bantz, T. Nawroth, C. Bier, J. Sirirattanapan, W. Mann, L. Treuel, R. Zellner, M. Maskos, H. Schild, R. H. Stauber. Nanoparticle size is a critical physicochemical determinant of the human blood plasma corona: a comprehensive quantitative proteomic analysis. *ACS Nano*. 5, 7155–7167. (2011). doi: 10.1021/nn201950e.
[215] D. Dell'Orco, M. Lundqvist, S. Linse, T. Cedervall. Mathematical modeling of the protein corona: implications for nanoparticulate delivery systems. *Nanomedicine*. 9, 851–858. (2014). doi: 10.2217/nnm.14.39.
[216] J. B. Simonsen, R. Münter. Pay Attention to Biological Nanoparticles when Studying the Protein Corona on Nanomedicines. *Angewandte Chemie - International Edition*. 59, 12584–12588. (2020). doi: 10.1002/anie.202004611.
[217] S. Palchetti, L. Digiacomo, D. Pozzi, G. Peruzzi, E. Micarelli, M. Mahmoudi, G. Caracciolo. Nanoparticles-cell association predicted by protein corona fingerprints. *Nanoscale*. 8, 12755–12763. (2016). doi: 10.1039/c6nr03898k.
[218] Y. C. Su, K. Riesbeck. In *The Complement FactsBook: Second Edition*. Elsevier. (2018). pp. 351–360.
[219] Ö. B. Ekmekçi, H. Ekmekçi. Vitronectin in atherosclerotic disease. *Clinica Chimica Acta*. 368, 77–83. (2006). doi: 10.1016/j.cca.2005.12.015.
[220] J. Yoo, C. Park, G. Yi, D. Lee, H. Koo. Active Targeting Strategies Using Biological Ligands for Nanoparticle Drug Delivery Systems. *Cancers*. 11, 640. (2019). doi: 10.3390/cancers11050640.
[221] J. Tschopp, D. Masson, S. Schäfer, M. Peitsch, K. T. Preissner. The Heparin Binding Domain of S-Protein/Vitronectin Binds to Complement Components C7, C8, and C9 and Perforin from Cytolytic T-Cells and Inhibits Their Lytic Activities. *Biochemistry*. 27, 4103–4109. (1988). doi: 10.1021/bi00411a029.
[222] S. A. Dilliard, Q. Cheng, D. J. Siegwart. On the mechanism of tissue-specific mRNA delivery by selective organ targeting nanoparticles. *Proceedings of the National Academy of Sciences*. 118, e2109256118. (2021). doi: 10.1073/pnas.2109256118.
[223] D. J. Sobczynski, P. Charoenphol, M. J. Heslinga, P. J. Onyskiw, K. Namdee, A. J. Thompson, O. Eniola-Adefeso. Plasma protein corona modulates the vascular wall interaction of drug carriers in a material and donor specific manner. *PLoS ONE*. 9, 1–12. (2014). doi: 10.1371/journal.pone.0107408.
[224] G. Caracciolo. Liposome–protein corona in a physiological environment: challenges and opportunities for targeted delivery of nanomedicines. *Nanomedicine: Nanotechnology, Biology and Medicine*. 11, 543–557. (2015). doi: 10.1016/j.nano.2014.11.003.
[225] M. Li, S. Jiang, J. Simon, D. Paßlick, M. L. Frey, M. Wagner, V. Mailander, D. Crespy, K. Landfester. Brush conformation of polyethylene glycol determines the stealth effect of nanocarriers in the low protein adsorption regime. *Nano Letters*. 21, 1591–1598. (2021). doi: 10.1021/acs.nanolett.0c03756.
[226] S. Palchetti, D. Caputo, L. Digiacomo, A. Capriotti, R. Coppola, D. Pozzi, G. Caracciolo. Protein corona fingerprints of liposomes: new opportunities for targeted drug delivery and early detection in pancreatic cancer. *Pharmaceutics*. 11, 31. (2019). doi: 10.3390/pharmaceutics11010031.
[227] P. Pande, T. A. Mosleh, A. E. Aust. Role of αvβ5 integrin receptor in endocytosis of crocidolite and its effect on intracellular glutathione levels in human lung epithelial (A549) cells. *Toxicology and Applied Pharmacology*. 210, 70–77. (2006). doi: 10.1016/j.taap.2005.07.017.
[228] G. Caracciolo, D. Pozzi, A. L. Capriotti, C. Cavaliere, F. Cardarelli, F. Salomone, A. Lagana. In *Nanotechnology 2013: Bio Sensors, Instruments, Medical, Environment and Energy*. (2013). pp. 247–250.
[229] J. Qu, C. Ko, P. Tso, A. Bhargava. Apolipoprotein A-IV: A Multifunctional Protein Involved in Protection against Atherosclerosis and Diabetes. *Cells*. 8, 319. (2019). doi: 10.3390/cells8040319.
[230] N. Bege, T. Renette, M. Jansch, R. Reul, O. Merkel, H. Petersen, C. Curdy, R. H. Müller, T. Kissel. Biodegradable poly(ethylene carbonate) nanoparticles as a promising drug delivery system with "stealth" potential. *Macromolecular Bioscience*. 11, 897–904. (2011). doi: 10.1002/mabi.201000496.
[231] T. M. Göppert, R. H. Müller. Protein adsorption patterns on poloxamer- and poloxamine-stabilized solid lipid nanoparticles (SLN). *European Journal of Pharmaceutics and Biopharmaceutics*. 60, 361–372. (2005). doi: 10.1016/j.ejpb.2005.02.006.
[232] S. Jiang, D. Prozeller, J. Pereira, J. Simon, S. Han, S. Wirsching, M. Fichter, M. Mottola, I. Lieberwirth, S. Morsbach, V. Mailänder, S. Gehring, D. Crespy, K. Landfester. Controlling protein interactions in blood for effective liver immunosuppressive therapy by silica nanocapsules. *Nanoscale*. 12, 2626–2637. (2020). doi: 10.1039/c9nr09879h.
[233] Z. Li, J. Zhu, Y. Wang, M. Zhou, D. Li, S. Zheng, C. Luo, H. Zhang, L. Zhong, W. Li, J. Wang, S. Gui, B. Cai, Y. Wang, J. Sun. In situ apolipoprotein E-enriched corona guides dihydroartemisinin-decorating nanoparticles towards LDLr-mediated tumor-homing chemotherapy. *Asian Journal of Pharmaceutical Sciences*. (2019). doi: 10.1016/j.ajps.2019.05.002.
[234] S. Bultel-Brienne, S. Lestavel, A. Pilon, I. Laffont, A. Tailleux, J. C. Fruchart, G. Siest, V. Clavey. Lipid free

apolipoprotein E binds to the class B type I scavenger receptor I (SR-BI) and enhances cholesteryl ester uptake from lipoproteins. *Journal of Biological Chemistry*. 277, 36092–36099. (2002). doi: 10.1074/jbc.M201943200.

[235] Y. Fu, J. Zhao, Y. Atagi, H. M. Nielsen, C. C. Liu, H. Zheng, M. Shinohara, T. Kanekiyo, G. Bu. Apolipoprotein e lipoprotein particles inhibit amyloid-β uptake through cell surface heparan sulphate proteoglycan. *Molecular Neurodegeneration*. 11, 1–11. (2016). doi: 10.1186/s13024-016-0099-y.

[236] V. Francia, R. M. Schiffelers, P. R. Cullis, D. Witzigmann. The Biomolecular Corona of Lipid Nanoparticles for Gene Therapy. *Bioconjugate Chemistry*. 31, 2046–2059. (2020). doi: 10.1021/acs.bioconjchem.0c00366.

[237] ONPATTRO® (patisiran) | Treatment for the Polyneuropathy of hATTR Amyloidosis. https://www.onpattro.com/. Accessed: March 30, 2022.

[238] I. Urits, D. Swanson, M. C. Swett, A. Patel, K. Berardino, A. Amgalan, A. A. Berger, H. Kassem, A. Kaye, O. Viswanath. A Review of Patisiran (ONPATTRO®) for the Treatment of Polyneuropathy in People with Hereditary Transthyretin Amyloidosis. *Neurology and Therapy*. 9, 301–315. (2020). doi: 10.1007/s40120-020-00208-1.

[239] A. Akinc, W. Querbes, S. De, J. Qin, M. Frank-Kamenetsky, K. N. Jayaprakash, M. Jayaraman, K. G. Rajeev, W. L. Cantley, J. R. Dorkin, J. S. Butler, L. Qin, T. Racie, A. Sprague, E. Fava, A. Zeigerer, M. J. Hope, M. Zerial, D. W. Sah, K. Fitzgerald, M. A. Tracy, M. Manoharan, V. Koteliansky, A. De Fougerolles, M. A. Maier. Targeted delivery of RNAi therapeutics with endogenous and exogenous ligand-based mechanisms. *Molecular Therapy*. 18, 1357–1364. (2010). doi: 10.1038/mt.2010.85.

[240] J. A. Kulkarni, J. L. Myhre, S. Chen, Y. Y. C. Tam, A. Danescu, J. M. Richman, P. R. Cullis. Design of lipid nanoparticles for in vitro and in vivo delivery of plasmid DNA. *Nanomedicine: Nanotechnology, Biology, and Medicine*. 13, 1377–1387. (2017). doi: 10.1016/j.nano.2016.12.014.

[241] D. Chen, N. Parayath, S. Ganesh, W. Wang, M. Amiji. The role of apolipoprotein- and vitronectin-enriched protein corona on lipid nanoparticles for in vivo targeted delivery and transfection of oligonucleotides in murine tumor models. *Nanoscale*. 11, 18806–18824. (2019). doi: 10.1039/C9NR05788A.

[242] R. Zhang, R. El-Mayta, T. J. Murdoch, C. C. Warzecha, M. M. Billingsley, S. J. Shepherd, N. Gong, L. Wang, J. M. Wilson, D. Lee, M. J. Mitchell. Helper lipid structure influences protein adsorption and delivery of lipid nanoparticles to spleen and liver. *Biomaterials Science*. 9, 1449–1463. (2021). doi: 10.1039/d0bm01609h.

[243] Z. Zhang, J. Guan, Z. Jiang, Y. Yang, J. Liu, W. Hua, Y. Mao, C. Li, W. Lu, J. Qian, C. Zhan. Brain-targeted drug delivery by manipulating protein corona functions. *Nature Communications*. 10, 3561. (2019). doi: 10.1038/s41467-019-11593-z.

[244] A. R. Neves, J. F. Queiroz, S. A. C. Lima, S. Reis. Apo E-Functionalization of Solid Lipid Nanoparticles Enhances Brain Drug Delivery: Uptake Mechanism and Transport Pathways. *Bioconjugate Chemistry*. 28, 995–1004. (2017). doi: 10.1021/acs.bioconjchem.6b00705.

[245] C. Neyen, A. Plüddemann, S. Mukhopadhyay, E. Maniati, M. Bossard, S. Gordon, T. Hagemann. Macrophage Scavenger Receptor A Promotes Tumor Progression in Murine Models of Ovarian and Pancreatic Cancer. *The Journal of Immunology*. 190, 3798–3805. (2013). doi: 10.4049/jimmunol.1203194.

[246] S. Vasseur, F. Guillaumond. LDL Receptor: An open route to feed pancreatic tumor cells. *Molecular and Cellular Oncology*. 3, 1–3. (2016). doi: 10.1080/23723556.2015.1033586.

[247] L. Digiacomo, F. Cardarelli, D. Pozzi, S. Palchetti, M. A. Digman, E. Gratton, A. L. Capriotti, M. Mahmoudi, G. Caracciolo. An apolipoprotein-enriched biomolecular corona switches the cellular uptake mechanism and trafficking pathway of lipid nanoparticles. *Nanoscale*. 9, 17254–17262. (2017). doi: 10.1039/C7NR06437C.

[248] S. Moein Moghimi, D. Simberg, T. Skotland, A. Yaghmur, A. Christy Hunter, S. M. Moghimi, D. Simberg, T. Skotland, A. Yaghmur, C. Hunter. The interplay between blood proteins, complement, and macrophages on nanomedicine performance and responses. *Journal of Pharmacology and Experimental Therapeutics*. 370, 581–592. (2019). doi: 10.1124/jpet.119.258012.

[249] M. Aoyama, K. Hata, K. Higashisaka, K. Nagano, Y. Yoshioka, Y. Tsutsumi. Clusterin in the protein corona plays a key role in the stealth effect of nanoparticles against phagocytes. *Biochemical and Biophysical Research Communications*. 480, 690–695. (2016). doi: 10.1016/j.bbrc.2016.10.121.

[250] D. Chen, S. Ganesh, W. Wang, M. Amiji. Protein Corona-Enabled Systemic Delivery and Targeting of Nanoparticles. *AAPS Journal*. 22, 1–9. (2020). doi: 10.1208/s12248-020-00464-x.

[251] T. J. Anchordoquy, Y. Barenholz, D. Boraschi, M. Chorny, P. Decuzzi, M. A. Dobrovolskaia, Z. S. Farhangrazi, D. Farrell, A. Gabizon, H. Ghandehari, B. Godin, N. M. La-Beck, J. Ljubimova, S. M. Moghimi, L. Pagliaro, J. H. Park, D. Peer, E. Ruoslahti, N. J. Serkova, D. Simberg. Mechanisms and Barriers in Cancer Nanomedicine: Addressing Challenges, Looking for Solutions. *ACS Nano*. 11, 12–18. (2017). doi: 10.1021/acsnano.6b08244.

[252] V. C. F. Mosqueira, P. Legrand, A. Gulik, O. Bourdon, R. Gref, D. Labarre, G. Barratt. Relationship between complement activation, cellular uptake and surface physicochemical aspects of novel PEG-modified nanocapsules. *Biomaterials*. 22, 2967–2979. (2001). doi: 10.1016/S0142-9612(01)00043-6.

[253] J. Szebeni, F. Muggia, A. Gabizon, Y. Barenholz. Activation of complement by therapeutic liposomes and other lipid excipient-based therapeutic products: Prediction and prevention. *Advanced Drug Delivery Reviews*. 63, 1020–1030. (2011). doi: 10.1016/j.addr.2011.06.017.

[254] B. W. Neun, M. A. Dobrovolskaia. Qualitative analysis of total complement activation by nanoparticles. *Methods in molecular biology (Clifton, N.J.)*. 697, 237–245. (2011). doi: 10.1007/978-1-60327-198-1_25.

[255] R. Snyderman, M. C. Pike. Interaction of complex polysaccharides with the complement system: effect of calcium depletion on terminal component consumption. *Infection and Immunity*. 11, 273–279. (1975). doi: 10.1128/iai.11.2.273-279.1975.

USC UNIVERSIDADE DE SANTIAGO DE COMPOSTELA

[256] A. Lex, N. Gehlenborg, H. Strobelt, R. Vuillemot, H. Pfister. UpSet: Visualization of intersecting sets. *IEEE Transactions on Visualization and Computer Graphics*. 20, 1983–1992. (2014). doi: 10.1109/TVCG.2014.2346248.

USC
UNIVERSIDADE
DE SANTIAGO
DE COMPOSTELA

CHAPTER 2

Galunisertib and stattic-loaded polymeric nanocapsules for lung cancer treatment

USC
UNIVERSIDADE
DE SANTIAGO
DE COMPOSTELA

USC
UNIVERSIDADE
DE SANTIAGO
DE COMPOSTELA

Chapter 2: Galunisertib and stattic-loaded polymeric nanocapsules for lung cancer treatment

This work has been done in collaboration with Humanitas Research Hospital (Milano, Italy) and SINTEF AS (Norway) under the frame of the 2^2-INTRATARGET project.

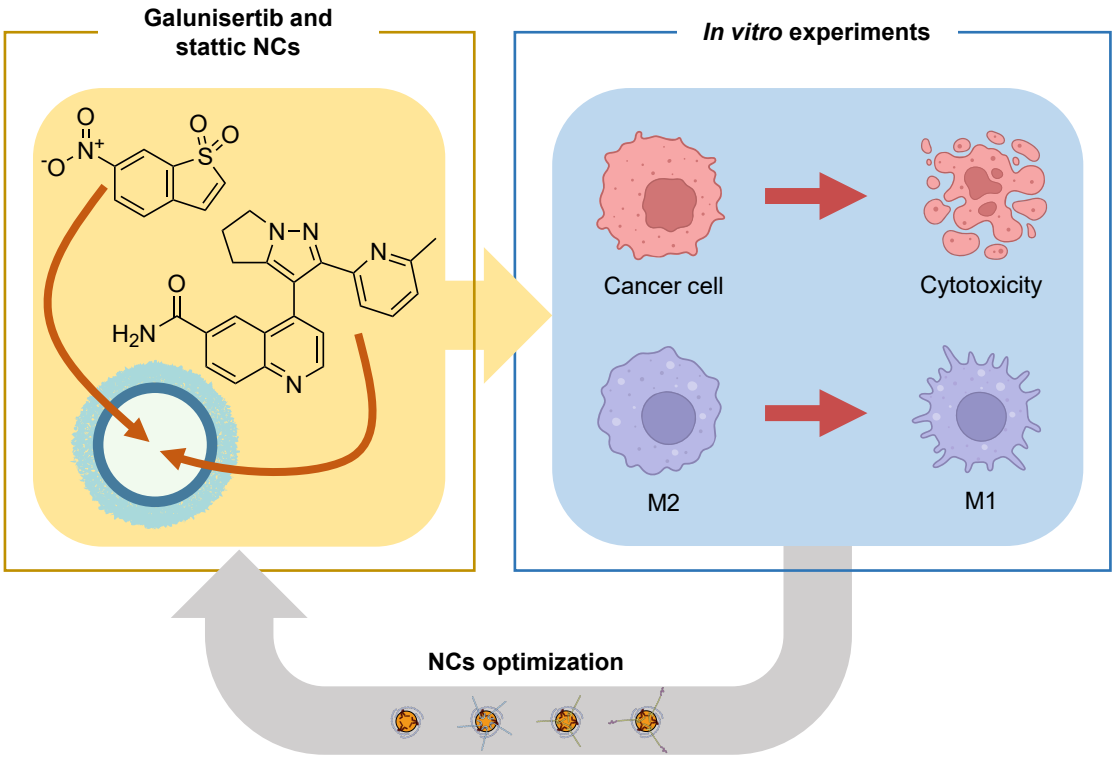
ABSTRACT

Despite the recent success achieved in the treatment of some types of lung cancers, the majority of them still have, unfortunately, a limited prognosis. Two signaling pathways involved in many tumors and, therefore, attractive for drug targeting, are the signal transducer and activator of transcription 3 (STAT3) and the transforming growth factor beta (TGF-β). However, the efficacy of these families of drugs is limited by their severe adverse effects. Intending to solve these issues, we have developed galunisertib (TGF-β pathway inhibitor)- and stattic (STAT3 inhibitor)-loaded NCs with the aim of reducing their off-target toxicities and studying their potential synergistic effect. *In vitro* results showed that the encapsulation of galunisertib and stattic in one NC prototype preserved the cytotoxicity in cancer cells while reducing it in tumor-associated macrophages. The reduction in adverse effects should be evaluated in further *in vivo* experiments.

USC
UNIVERSIDADE DE SANTIAGO DE COMPOSTELA

USC
UNIVERSIDADE
DE SANTIAGO
DE COMPOSTELA

GRAPHICAL ABSTRACT



Created with https://biorender.com.

USC
UNIVERSIDADE
DE SANTIAGO
DE COMPOSTELA

USC
UNIVERSIDADE
DE SANTIAGO
DE COMPOSTELA

1. INTRODUCTION

Inhibiting the signal transducer and activator of transcription (STAT) 3 and transforming growth factor beta (TGF-β) pathways might be promising strategies for treating lung cancers. However, the off-target toxicities of small-molecule STAT3 and TGF-β inhibitors limit their therapeutic outcome. In this section, the physiological and pathological role of the STAT3 and TGF-β pathways, the limitations of the current treatments targeting those pathways, and the benefits of nanotechnology as a tool for delivering those drugs are reviewed.

1.1. THE STAT FAMILY

The STAT protein family is a group of transcription factors that regulate the expression of several genes related to the cell cycle (proliferation, apoptosis, and differentiation) and the immune response. The STAT protein family consists of seven proteins: STAT1, STAT2, STAT3, STAT4, STAT5a, STAT5b, and STAT6.[1–3]

STAT3 was discovered in 1994 by Akira *et al.*[4] and Zhong *et al.*.[5] Several activation modalities are described for STAT3. Predominantly, this activation occurs through the Janus kinase (JAK)-STAT pathway. In this sense, the STAT3 signaling pathway is activated by several cytokines such as interferons or the interleukins IL-6, IL-10, or IL-11, growth factors epidermal growth factor (EGF), fibroblast growth factor, and vascular endothelial growth factor (VEGF), and hormones after their binding to their membrane receptor. More detailed, the ligand binding cause the dimerization of the receptor, which, after some intermediate steps, recruits the JAK proteins, which activate STAT3 by phosphorylation (p-STAT3).[3,6] Once activated, the p-STAT3 dimer migrates from the receptor to the nucleus, triggering the transcription of several genes.

1.2. THE TGF-B SIGNALING PATHWAY

TGF-β is a superfamily composed of 35 dimeric protein factors which regulate the proliferation and differentiation of many cell types, including cardiac development and angiogenesis, and immune system activity. The members of the TGF-β superfamily are subdivided into (i) TGF-β proteins (TGF-β1 to TGF-β3), (ii) activins/inhibins, (iii) bone morphogenetic proteins and growth and differentiation factors, and (iv) glial cell line-derived neurotrophic factor ligands. These ligands are recognized by a transmembrane structure consisting of two type-I and two type-II TGF-β receptors. Type-I TGF-β receptors are also known as anaplastic lymphoma kinases (ALKs) and include ALK1 to ALK7. Meanwhile, the TGF-β receptor 2 (TGF-βRII), activin receptor type IIA (ActRIIA), activin receptor type IIB (ActRIIB), bone morphogenetic protein receptor II, and anti-mullerian hormone receptor type 2 conform the type-II TGF-β receptor family. We will focus on the role of TGF-β1, TGF-β2, and TGF-β3 cytokines. TGF-β1, 2, and 3 are secreted by macrophages, other immune cells, and some malignant tumor cells, and physiologically, they regulate cell growth, cell proliferation, cell differentiation, and apoptosis through their interaction with combinations of ALK4, ALK5, ALK7, TGFRII, ActRIIA, and ActRIIB receptors.[7–9] The activation of these receptors by TGF-β1-3 and activins led to the phosphorylation of the suppressor of mothers against decapentaplegic (Smad)

2 and 3. Then, these Smad complexes recruit Smad4, are translocated to the nucleus, and regulate gene expression.

1.3. USE OF STAT3 INHIBITORS AND TGF-B SIGNALING PATHWAY INHIBITORS IN CANCER

1.3.1. STAT3 in cancer

STAT3 hyperactivation is reported in a wide variety of tumors, including lung cancer.[6] In fact, approximately 70 % of solid human tumors have a constitutively active STAT3 compared to normal cells.[3] Interestingly, p-STAT3 is involved in various mechanisms that promote cancer progression in cancer cells and immune cells.

In cancer cells, p-STAT3 prevents p53-mediated growth control and apoptosis, leading to increased proliferation.[10] Also, it promotes the expression of VEGF and other factors, which stimulate angiogenesis and the production of matrix metalloproteinases that are known to facilitate metastasis.[6,11] STAT3 also regulates autophagy and is known to be involved in drug resistance mechanisms.[11]

Moreover, the activation of STAT3 in other tumor microenvironment cells is also crucial for tumor development. An extensive review of the role of STAT3 on the different immune cells can be found in the literature.[12] Briefly, STAT3 affects both $CD4^+$ (Th1, Th2, Th17, Treg, Tfh, Th9) and $CD8^+$ T-Cells, macrophages, dendritic cells, and myeloid-derived suppressor cells.[12] Tumor-associated macrophages' phenotype changes depending on microenvironmental stimuli, allowing their classification into M1 (cytotoxic/pro-inflammatory type) and M2 (repair/anti-inflammatory type) macrophages. M1 macrophages exhibit a higher expression of nitric oxide synthase and class II major histocompatibility complex and produce more NO, IL-12, IL-8, and CCL2. On the contrary, M2 macrophages produce more anti-inflammatory mediators involved in repairing functions, such as arginase/ornithine, EGF, VEGF, and TGF-β, and overexpress mannose receptors.[13,14] In the case of macrophages, the sustained activation of STAT3 polarizes macrophages toward the M2 phenotype.[3,15] Consequently, the alterations in the immune cells caused by STAT3 activation lead to an immunosuppressive environment, facilitating tumor cell proliferation, survival, angiogenesis, and metastatic processes, which is translated into higher tumor growth and invasion capabilities.[15,16]

Several approaches have been explored in order to block the JAK/STAT signaling pathway. Among them, JAK inhibitors[17] and STAT inhibitors have been the most exploited approaches. By this approach, the inhibitors of JAK/STAT can be considered both chemotherapeutics, since they could directly hamper tumor proliferation, and immunotherapeutics, as they can restore the tumor microenvironment to a pro-inflammatory situation. An extensive review of the STAT3 inhibitors can be found in a book chapter from Bharadwaj *et al.*,[18] as well as in some more recent publications.[19,20] More than 40 different STAT3 inhibitors have been studied so far.

Of note, the JAK inhibitors (upstream STAT3) ruxolitinib and fedratinib were approved by the FDA/EMA in 2011/2012 and 2019/2020, respectively, for the treatment of intermediate or high-risk myelofibrosis, including primary myelofibrosis, post-polycythemia vera myelofibrosis, and post-essential thrombocythemia myelofibrosis. Additionally, several STAT3 inhibitors are currently undergoing clinical trials in the USA and EU (napabucasin, WP1066, OPB-111077, OPB-51602, and danvatirsen) (Table 1).

Table 1. Relevant small-molecule STAT3 and upstream STAT3 inhibitors approved by FDA/EMA or undergoing clinical trials in the US/EU in the last years

Drug	Target	Tumor type	Phase/NCT (Last update)	Limitations/Results	Ref.
Napabucasin (BBI-608)	Multiple oncogenic cellular pathways, including STAT3 (synthesis and activation)	Lung (+ paclitaxel)	III / NCT02826161 (2022)	Moderate toxicity. Encouraging efficacy in combination therapy	[21-27]
		Pancreatic (+ paclitaxel and gemcitabine)	III / NCT02993731 (2022)		
		Gastric (+ paclitaxel)	III / NCT02178956 (2022)		
		Colorectal	III / NCT01830621 (2022)		
		Colorectal (+ fluorouracil, leucovorin, and irinotecan)	III / NCT03522649 (2019)		
		Pancreatic (+ paclitaxel and gemcitabine)	III / NCT03721744 (2019)		
		Colorectal (+ BNC105)	II / NCT03647839 (2021)		
		Liver	I / NCT02358395 (2022)		
WP1066	JAK2/STAT3	Brain	I / NCT01904123 (2022) and I / NCT04334863 (2022)	Limited monotherapy efficacy	[28,29]
OPB-111077	STAT3	Nasopharyngeal	IIa / NCT03158324 (2017)	Limited monotherapy efficacy	[28,30,31]
		Lymphoma (+ bendamustine and rituximab)	I / NCT04049825 (2021)		
		Leukemia (+ decitabine and venetoclax)	I / NCT03063944 (2022)		
OPB-51602	STAT3. Not fully elucidated	Leukemia	I / NCT01344876 (2015)	Insufficient efficacy. Terminated due to severe toxicity	[32-34]
		Nasopharyngeal	I / NCT02058017 (2015)		

Abbreviations: EMA: European Medicines Agency. FDA: Food and Drug Administration. JAK: Janus kinase. NCT: ClinicalTrials.gov identifier. Ref.: reference. STAT: signal transducer and activator of transcription.

1.3.2. TGF-β signaling pathway in cancer

In cancer cells, TGF-β promotes cell growth, invasion, and dissemination. Additionally, it stimulates extracellular matrix production and angiogenesis. TGF-β is also known to be involved in drug resistance mechanisms.[35]

Moreover, the presence of TGF-β in the tumor microenvironment also affects immune cells.[35] An extensive review of the role of TGF-β on the different immune cells can be found in the literature.[36] Briefly, TGF-β affects both $CD4^+$ (Th1, Th2, Th17, Treg, and Th9) and $CD8^+$ T-Cells, macrophages, dendritic cells, B-cells, neutrophils, and NK cells. Also, TGF-β promotes angiogenesis by endothelial cells. In the presence of TGF-β, tumor-associated macrophages are polarized into the M2 phenotype. Overall, as in the case of p-STAT3, the alterations in the immune cells caused by the presence of TGF-β lead to an immunosuppressive environment, facilitating tumor cell proliferation, survival, angiogenesis, and metastatic processes, which is translated into higher tumor growth and invasion capabilities.[35]

Several approaches have been explored for blocking the TGF-β signaling pathway, including TGF-β synthesis inhibitors, TGF-β neutralizing antibodies, ligand traps, and small-molecule inhibitors. The use of TGF-β receptor inhibitors, especially ALKs and TGF-βRII inhibitors, is the most exploited approach. In this sense, the inhibitors of TGF-β receptors can be considered chemotherapeutics since they could directly hamper tumor proliferation and immunotherapeutics as they can restore the tumor microenvironment to a pro-inflammatory situation.[37,38] Currently, 5 small-molecule TGF-β receptor inhibitors are approved (Table 2). However, most of these treatments led to a moderate reduction in tumor growth, with the main advantage of just prolonging the survival time of the patients with ALK or ROS1-positive tumors.

USC UNIVERSIDADE DE SANTIAGO DE COMPOSTELA

Table 2. Relevant small-molecule drugs inhibiting TGF-β receptors FDA/EMA-approved or undergoing clinical trials in the US/EU in the last years

Drug	Target	Tumor type	Phase/NCT (Last update)	Limitations/Results	Ref.
Crizotinib [Xalkori® (US/EU)]	ALKs / MET / ROS-1	Lung	Approved by FDA/EMA in 2011/2012	Common GI toxicity and transaminitis. Significant tumor reduction	[39-45]
		Breast	II / NCT03620643 (2021)		
		Uveal melanoma	II / NCT02223819 (2022)		
		Endometrial	II / NCT04030429 (2022)		
		Lymphoma	II / NCT04439253 (2022)		
Ceritinib [Zykaldia® (US/EU)	ALKs / IGF-1R / InsR / STK22D	Lung	Approved by FDA/EMA in 2014/2015	GI and liver toxicity. Effective treatment. Significant progression-free survival	[46-50]
		Cholangiocarcinoma	II / NCT02374489 (2018)		
		Neuroblastoma	II / NCT02559778 (2022)		
		Melanoma	II / NCT02645149 (2022)		
Alectinib [Alecensa® (US/EU)]	ALKs / GAK / LTK	Lung	Approved by FDA/EMA in 2015/2017	Significant survival improvement. Lower GI toxicity than crizotinib	[51,52]
		Glioblastoma	II / NCT03158389 (2022)		
		Breast	II / NCT05238831 (2022)		
		Renal	II / NCT04644432 (2022)		
Brigatinib [Alunbrig® (US/EU)]	ALKs / ROS1	Lung	Approved by FDA/EMA in 2017/2018	GI and pulmonary toxicity. Significant progression-free survival	[53]
		Lymphoma	II / NCT04925609 (2022)		
Lorlatinib [Lorbrena™ (US) / Lorviqua® (EU)]	ALKs / ROS1	Lung	Approved by FDA/EMA 2018/2019	Significant tumor progression reduction *vs.* crizotinib. Brain toxicity	[54]
		Lymphoma	II / NCT03505554 (2022)		

Table 2. Relevant small-molecule drugs inhibiting TGF-β receptors FDA/EMA-approved or undergoing clinical trials in the US/EU in the last years (continuation)

Drug	Target	Tumor type	Phase/NCT (Last update)	Limitations/Results	Ref.
Galunisertib (LY2157299)	ALK5/ALK2	Myelodysplastic syndromes	II/III NCT02008318 (2019)	GI toxicity. Severe toxicities, including GI, low neutrophil count, and cardiac toxicity in patients with pre-existing conditions	[55]
		Prostate (+ enzalutamide)	II / NCT02452008 (2022)	Tumor growth suppression	[56]
		Rectal (+ capecitabine or fluorouracil)	II / NCT02688712 (2022)	GI and hematological toxicity. Improvement in the complete response rate	[57]
		Liver	II / NCT02178358 (2022) and II / NCT01246986 (2021)	Anemia, neutropenia, and embolism as toxicities	[58]
		Lung (+ nivolumab)	II / NCT02423343 (2021)	Terminated early due to low enrollment	-
		Glioblastoma	II / NCT01582269 (2021)	Lower hematologic toxicities compared to lomustine. No cardiac toxicity	[59]
		Nasopharyngeal	II / NCT04605562 (2021)	-	-
		Pancreas (+abemaciclib)	II / NCT02981342 (2019)	Terminated due to low enrollment	-
LY3200882	ALK5	Colorectal	I/II / NCT04031872 (2019)	No observed dose-limiting toxicities. No cardiotoxicity	[60]
Vactosertib (TEW-7197)	ALK5	Gastric	II / NCT04656002 (2022)	Stroke (1 patient)	[61,62]
		Myeloproliferative neoplasm	II / NCT04103645 (2021)	-	-
		Pancreatic	I/II / NCT03666832 (2022)	-	-

Abbreviations: ALKs: anaplastic lymphoma kinases. ALK2: anaplastic lymphoma kinase 2. ALK5: anaplastic lymphoma kinase 5. EMA: European Medicines Agency. FDA: Food and Drug Administration. GAK: Cyclin G-associated kinase. GI: gastrointestinal. IGF-1R: Insulin-like growth factor 1 receptor. InsR: insulin receptor. LTK: Leukocyte receptor tyrosine kinase. MET: mesenchymal-epithelial transition factor. NCT: ClinicalTrials.gov identifier. Ref.: reference. ROS1: proto-oncogene tyrosine-protein kinase ROS. STK22D: Testis-specific serine/threonine-protein kinase 1. TGF-β: transforming growth factor beta. TGF-βRII: TGF-β receptor 2.

1.4. BIOPHARMACEUTICAL LIMITATIONS OF STAT3 AND TGF-B INHIBITORS

As shown in Table 1 and Table 2, one of the most relevant limitations of the STAT3 and TGF-β pathways inhibitors is their off-target toxicity.

Currently approved ALK inhibitors (TGF-β pathway) exhibit severe adverse effects, including neutropenia and toxicity in different organs such as the liver,[39,40] lung, pancreas,[46–48,51,53] brain, and heart.[54] In addition, all the abovementioned drugs were found to cause potentially life-threatening bradycardia. Some of these toxicities are related to the broad presence of ALK receptors in those organs. In fact, biodistribution analysis in healthy mice after oral administration found an intense distribution of ALK inhibitors into tissues, including the liver, spleen, kidney, pancreas, and brain.[63–65] In healthy humans, the galunisertib maximum observed drug concentration was detected at a time (t_{max}) of 0.5 h, meaning the rapid absorption of this drug. The half-life associated with the terminal rate constant in non-compartmental analysis ($t_{1/2}$) was 8.61 h, the apparent total body clearance of the drug calculated after extravascular administration (Cl/F) was 40.9 $L \cdot h^{-1,}$ and the apparent volume of distribution during the terminal phase after extravascular administration (V_Z/F) was 508 L, indicating fast metabolism and high tissue distribution. Also, approximately 33 % of the radioactivity of ^{14}C-galunisertib after oral administration was recovered in urine in less than 24 h and nearly 66 % in feces in less than 96 h.[66]

On the other hand, no direct STAT3 inhibitors have been approved so far, but several clinical trials failed and led to the discontinuation of the development of the assayed drug due to off-target toxicities. For example, OPB-31121 led to peripheral sensory neuropathy (Phase I/II; NCT01406574) and leukemia (Phase I; NCT01029509).[67] Preclinical biodistribution of this drug after oral administration also showed indiscriminate biodistribution, with a preferential accumulation in the liver.[67] Finally, upstream STAT3 inhibitors were also compromised in terms of off-target toxicities. For example, AZD1480, with therapeutic use in myelofibrosis and solid tumor treatments (Phase I; NCT00910728, NCT01112397, and NCT01219543), was discontinued due to neurological toxicity.[68]

1.5. APPLICATION OF NANOTECHNOLOGY TO IMPROVE THE BIODISTRIBUTION OF STAT3 AND TGF-B INHIBITORS

1.5.1. Nanoformulations of STAT3 inhibitors

Many different STAT3 inhibitors have been identified as promising, and some of them are in clinical trials. However, their high toxicity and poor water solubility are limiting their exploitation. Therefore, future therapeutic strategies must rely on the selective inhibition of STAT3 through the use of targeted delivery carriers. Table 3 summarizes the current literature on drug delivery of stattic and other STAT3 inhibitors. Overall, these reports refer to the decrease in tumor volume and the increase in survival time achieved with a variety of formulations. In the case of lung cancer, results were more discreet, as the encapsulation of fedratinib together with erlotinib in PEG – PLA polymeric NPs increased the survival time of the treated mice from 52 days to 60 days.[69] Still, in general, an important observation is a notorious increase in the effectiveness of the treatment and survival rate when using combination nanotherapies.

USC UNIVERSIDADE DE SANTIAGO DE COMPOSTELA

Table 3. Drug delivery systems of STAT3 inhibitors

Drug	Nanocarrier	Physicochemical characterization	Tumor model	Outcome	Ref.
Stattic	Liposomes (DOPE/DOPC/Cholesterol)	Size: 118 ± 1 nm PDI: 0.14 ± 0.05 ζpot: −20 ± 5 mV	Breast cancer (various cell lines) *in vitro* / *in vivo* (orthotopic)	58 and 80 % reduction in tumor volume for stattic-loaded liposomes and stattic-loaded liposomes in combination with anti-PD-L1 mAb, respectively, compared to non-relevant IgG	[70]
	DSPE-PEG-(Anti-IL20RA-mAb) decorated liposomes (DOPE/DOPC/Cholesterol)	Size: 120 ± 3 nm PDI: 0.23 ± 0.03 ζpot: −11 ± 1 mV			
	Polymeric NPs (Polymer: cabazitaxel-docosahexaenoic acid)	Size: 162 ± 2 nm AE: 74 %	Melanoma (B16/F0) *in vitro* / *in vivo* (subcutaneous)	37 % more tumor volume reduction in comparison with free stattic	[71]
	Polymeric NPs (Polymer: chitosan-coated-PLGA)	Size: 142 ± 2 nm PDI: 0.19 ± 0.01 ζpot: +4 ± 1 mV AE: 54 ± 4 %	Breast cancer (4T1) *in vitro* / *in vivo* (orthotopic)	50 % reduction in the number of metastatic foci in lungs and 75 % size reduction of lung metastasis in comparison with free stattic	[72]
	Polymeric NPs (Polymers: resiquimod- and ovalbumin-CSSVVR-modified docosahexaenoic acid)	Size: ≈ 100 nm ζpot: +41 ± 2 mV	Melanoma (B16/F10-OVA) *in vitro* and *in vivo* (subcutaneous)	Survival of 32 days for stattic-loaded micelles + anti-PD-1 Ab *vs.* ≈ 27 days for the monotherapies	[73]
	SLNPs (Oils: Compritol 888 ATO + Miglyol 812N)	Size: 67 – 115 nm PDI: 0.24 ζpot: +30 mV	Melanoma (B16/F10) *in vitro*	20 % reduction in cell proliferation when encapsulated *vs.* free drug	[74]
	Polymeric micelles [Polymer: modified polyacrylamide]	Size: 164 ± 13 nm PDI: 0.33 ± 0.04 ζpot: −48 ± 1 mV AE: 52 %	Breast cancer (various cell lines) *in vitro*	30 to 90-fold decrease in cytotoxicity IC_{50} values in comparison with free stattic	[75]
	Albumin NPs	Size: 151 ± 7 nm PDI: 0.25 ± 0.05 ζpot: −24 ± 5 mV AE: 53 ± 2 %	Breast cancer (MDA-MB-231) *in vitro*	Stattic IC_{50} value decreased by 2.5-fold when associated with the NPs	[76]
Fedratinib and erlotinib (co-deliver)	Polymeric NPs (Polymer: PEG – PLA)	Size: 120 nm	Lung cancer (H1650) *in vitro* / *in vivo* (subcutaneous)	Tumor growth almost stopped with the co-delivered drugs. Survival was of 60 days *vs.* 52 days for the free drug combination	[69]

Table 3. Drug delivery systems of STAT3 inhibitors (continuation)

Drug	Nanocarrier	Physicochemical characterization	Tumor model	Outcome	Ref.
Fedratinib and SAR302503 (co-deliver)	Polymeric micelles (Polymer: Alendronate – PEG – PLA) Polymeric micelles (Polymer: PEG – PLA)	Size: 26 ± 7 nm ζpot: −23 ± 2 mV Size: 24 ± 4 nm ζpot: −4 ± 1 mV	Leukemia (BaF3/T315I) *in vitro* / *in vivo* (orthotopic)	Survival of 44 days in comparison with untargeted micelles (35 days) and untreated mice (20 days)	[77]
Napabucasin	Polymeric NPs (Polymer: tridecanoyl-modified Lys05)	Size: 110 nm PDI: 0.10 ζpot: +40 ± 2 mV AE: 85 %	Pancreatic cancer (Patient-derived pancreatic cancer stem cells) *in vitro* / *in vivo* (subcutaneous)	73 % reduction of tumor volume. Free drug caused no antitumoral effect (≈ 3 % tumor volume reduction).	[78]
	Polymeric NPs (Polymer: PEG-azobenzene-PLA and iRGD- azobenzene-PLA)	Size: 188 nm	Pancreatic cancer (BxPC-3) *in vitro* / *in vivo* (orthotopic)	Decrease of tumor volume by 84 % of the untreated control. The free drug led to a 39 % reduction in tumor volume.	[79]
WP1066	Liposomes (DSPE-PEG-NH_2 and hydrophobic-modified L-DOPA)	Size: 119 ± 7 nm PDI: 0.25 ζpot: +11 ± 7 mV	Glioblastoma (GL261) *in vitro* / *in vivo* (orthotopic)	Survival increased by ~ 60 % compared to that of the untreated mouse group	[80]
	Liposomes (DSPE-PEG-NH_2 and nicotinylated amphiphiles)	Size: 126 ± 4 nm PDI: 0.17 ζpot: +12 ± 2 mV	Glioblastoma (GL261) *in vitro* / *in vivo* (orthotopic)	≈ 2-fold reduction in tumor size with WP1066-loaded liposomes. Survival of 48 days *vs.* untreated group (20 days). Survival of 110 days when co-administered with TRP2 plasmid-loaded liposomes	[81]
WP1066 and STAT3 siRNA (co-delivered)	Liposomes (DSPE-PEG-NH_2/DOPC/Cholesterol and palmitoylated RGDK peptide)	Size: 139 ± 6 nm PDI: 0.17 ζpot: +9 ± 1 mV	Glioblastoma (GL261) *in vitro* / *in vivo* (orthotopic)	Survival of 67 days in co-loaded liposomes in comparison with ≈ 45 days of single-loaded liposomes	[82]
S3I-1757	Polymeric NPs (Polymer: Anti-CD38-PEO-b-PBCL)	Size: 91 ± 9 nm PDI: 0.37 ± 0.02 AE: 82 ± 7 %	Myeloma (U266) *in vitro* / *in vivo* (orthotopic)	Tumor volume was 16.8 times lower in the S31-1751-loaded NPs in comparison with untreated control	[83]

Abbreviations: Ab: antibody. AE: association efficiency. DOPC: dipalmitoylphosphatidylcholine. DOPE: dioleoyl phosphatidylethanolamine. DSPE: 1,2-Distearoyl-sn-glycero-3-phosphorylethanolamine. IgG: immunoglobulin gamma. L-DOPA: L-3,4 dihidroxifenilalanina. NPs: nanoparticles. PDI: polydispersity index. PEG: polyethylene glycol. PEO: polyethylene oxide. PLA: polylactic acid. PLGA: poly(lactic-co-glycolic) acid. ζpot: ζ-potential. mAb: monoclonal antibody. PBCL: poly-(α-benzyl carboxylate ε-caprolactone). PD-1: Programmed cell death protein 1. PD-L1: programmed death-ligand 1. Ref.: reference. SLNPs: solid lipid nanoparticles.

1.5.2. Nanoformulations of TGF-β inhibitors

TGF-β inhibitors are promising drug entities for the treatment of several tumors, as it was demonstrated by the fact of being five different drugs currently approved by the FDA and EMA. However, TGF-β small molecule inhibitors are associated with severe off-target toxicities, especially cardiotoxicity and GI toxicity.[84–87] Also, mAb-based monotherapy (i.e., fresolimumab) did not show improvement regarding the current therapies,[88–90] and synthetic peptides derived from TGF-β receptors were withdrawn in phase II clinical trials.[91–94] Therefore, as in the case of p-STAT3, the aim of future therapeutic strategies should be directed to deliver TGF-β inhibitors selectively to the tumor microenvironment in order to reduce their toxicity. Table 4 summarizes the current literature on drug delivery of TGF-β inhibitors. In the case of lung cancer, monotherapy resulted in moderate tumor growth inhibition as, for example, alectinib-loaded NPs containing smaller Fe_3O_4 particles decreased tumor growth by only 30 % after NPs treatment and magnetic guidance.[95] On the other hand, combination therapy did significantly increase the therapeutic effects, as demonstrated for liposomal LY3200882 and PD-L1 siRNA. In that study, the combination therapy led to almost tumor eradication.[96]

USC UNIVERSIDADE DE SANTIAGO DE COMPOSTELA

Table 4. Drug delivery systems of TGF-ß inhibitors

Drug	Nanocarrier	Physicochemical characterization	Tumor model	Outcome	Ref.
Crizotinib + doxorubicin	Polymeric micelles [Polymer: oligo(ethylene glycol) methacrylate-crizotinib]	Size: 244 nm ζpot: ≈ 0 mV	Breast cancer (4T1) *in vitro* / *in vivo* (orthotopic)	77 % tumor volume reduction. Survival of 38 days *vs.* 34 days of free drugs	[97]
Crizotinib + sorafenib	Polymeric NPs [Polymer: PEG-poly(ε-caprolactone)-poly(ethylene glycol)]	Size: 30 ±3 nm PDI: 0.16 ± 0.01 ζpot: −18 ± 1 mV AE: 91 - 93 %	Breast cancer (4T1) *in vitro* / *in vivo* (orthotopic)	86 and 57 % reduction in tumor volume for loaded and free drugs, respectively. Moderate hepatic toxicity for drug-loaded NPs	[98]
Crizotinib + dasatinib	Polymeric micelles [Polymer: poly(styrene-co-maleic acid)]	Size: 121 nm PDI: 0.22 ζpot: −42 mV AE: 81 %	Glioblastoma (GL261) *in vitro* / *in vivo* (subcutaneous)	78 % tumor reduction for dasatinib-loaded micelles. Crizotinib micelles, crizotinib + dasatinib micelles, and free drugs only slowed tumor growth	[99]
Crizotinib	Polymeric nanoparticles (Polymer: PLA-TPGS)	Size: 162 ± 3 nm	Lung cancer (NCIH3122) *in vitro*	Crizotinib-loaded NPs led to 40 % apoptosis compared to 25 % by free drug	[100]
Crizotinib + sildenafil	Polymeric micelles (Polymer: PEG-PLA)	Size: 133 ± 20 nm PDI: 0.19 ± 0.04 ζpot: −16 ± 7 AE: 95 % (crizotinib) and 74 % (sildenafil)	Breast cancer (MCF-7) *in vitro*	4 % viability after crizotinib- and sildenafil-co-loaded micelles *vs.* 10 % viability of free drugs	[101]
Crizotinib + palbociclib + sildenafil	Polymeric micelles (Polymer: PLA-TPGS)	Size: 159 nm PDI: 0.24 nm ζpot: −30 mV	Lung cancer (A549) *in vitro*	Triple drug-loaded micelles led to complete cytotoxicity. Single-loaded micelles at the same concentration had no effect	[102]
Crizotinib + nilotinib	Liposomes (DMPC, DMPG)	n.d.	Healthy rabbits	Reduced cardiac toxicity (almost no QTc-interval prolongation)	[103]
Alectinib	Fe_3O_4 NPs-containing polymeric NPs (TAT-peptide-modified PEG-polyphosphoesters)	Size: 122 nm AE: 45 %	Lung (H2228) *in vitro* / *in vivo* (subcutaneous)	30 % reduction in tumor growth after NPs treatment with magnetic guidance. The free drug slightly slowed tumor growth.	[95]

Table 4. Drug delivery systems of TGF-ß inhibitors (continuation)

Drug	Nanocarrier	Physicochemical characterization	Tumor model	Outcome	Ref.
Brigatinib	SLNPs (Oil: stearic acid)	Size: 476 ± 5 nm PDI: 0.41 ± 0.02 ζpot: −15 ± 1 mV AE: 87 ± 1 %	Lung (A549) *in vitro*	Brigatinib-loaded SLNPs were more cytotoxic, effective in 48.7 % less dose compared to free drug	[104]
	Polymeric NPs [Polymer: chitosan-modified PLGA)]	Size: 406 ± 5 nm PDI: 0.28 ζpot: +30 ± 3 mV AE: 82 %	Lung (A549) *in vitro*	Brigatinib encapsulation reduced 1.3 times the IC_{50} of the free drug	[105]
Galunisertib	Macrophage-membrane-based vesicles with PEG-anti-PD-L1 mAb and loaded with gold nanocages	Size: 57 ± 4 nm PDI: 0.21 ζpot: −18 ± 2 mV AE: 82 %	Colon (CT26) *in vitro* / *in vivo* (subcutaneous)	Drug-loaded vesicles nearly eliminated the primary tumor (+ near-infrared light). Survival of > 50 days *vs*. free drug (32 days) and untreated (21-24 days)	[106]
	Polymeric micelle [Polymer PEG-poly(aspartate hydrazone adriamycin)]	Size: 65 nm	Colon (C26) *in vitro* / *in vivo* (subcutaneous)	Tumor eradication for 50 % of mice. Free drugs killed the mice at lower doses	[107]
		Size: 65 nm	Gastric (OCUM-2MLN) *in vitro* / *in vivo* (orthotopic)	Reduction in tumor growth for drug-loaded micelles. No effect of free drug	[108]
	Polymeric micelles (Polymer: Polygalacturonic acid-polyacrylic acid)	Size: 100 – 200 nm AE: 23 %	Liver (HLF) *in vitro*	No efficacy data	[109]
	Inorganic NPs Composition: diatomite. Decorated with plasmonic gold nanoparticles	Size: 450 ± 50 nm ζpot: −7 ± 8 mV AE: 1 %[112]	Colorectal (LS-174T and SW620) *in vitro*	Loaded NPs caused phenotypic changes related to metastasis inhibition. No reduction in cell growth for all groups	[110]
Galunisertib + PD-L1 siRNA	Polymeric NPs [Polymer: PCL-poly(amidoamine)-g-PCL + PCL + PEG-b-PCL]	Size: 110 nm ζpot: +26 mV	Pancreas (Panc02) *in vitro* / *in vivo* (orthotopic)	88 % reduction in tumor growth compared to PBS. Single treatments caused a 48 – 59 % reduction	[111]

Table 4. Drug delivery systems of TGF-ß inhibitors (continuation)

Drug	Nanocarrier	Physicochemical characterization	Tumor model	Outcome	Ref.
Galunisertib + celastrol	BSA NPs	Size: 119 nm ζpot: −19 mV AE: > 75 %	Glioma (GL261) *in vitro* / *in vivo* (orthotopic)	Extended survival for drug-loaded decorated-NPs (24 days) compared to non-decorated (18 days) and free drugs (17 days)	[113]
	CGREIRTGRAERWSEKF-peptide decorated BSA NPs	Size: 127 nm ζpot: −12 mV AE > 75 %			
LY3200882 + PD-L1 siRNA	MMP2-nonresponsive-decorated solid-core liposome (Protamine, DOPC, cholesterol)	Size: 192 nm ζpot: −3 mV	Breast (4T1) *in vitro* / *in vivo* (orthotopic)	Both MMP2-responsive and MMP2-nonresponsive-decorated liposomes led to almost complete tumor reduction. Liposomal LY3200882 monotherapy showed intermediate efficacy, while liposomal PD-L1 siRNA monotherapy and free drugs exhibited almost no activity.	[96]
	MMP2-responsive-decorated solid-core liposome (Protamine, DOPC, cholesterol)	Size: 194 nm ζpot: −4 mV			

Abbreviations: AE: association efficiency. DMPC: dimyristoylphosphatidylcholine. DMPG: 1,2-dimyristoyl-sn-glycero-3-phosphorylglycerol. DOPE: dioleoyl phosphatidylethanolamine. MMP2: matrix metalloproteinase-2. NPs: nanoparticles. PDI: polydispersity index. PEG: polyethylene glycol. PLA: polylactic acid. PLGA: poly(lactic-co-glycolic) acid. Ref.: reference. TPGS: D-α-tocopherol polyethylene glycol 1000 succinate. TAT-peptide: GRKKRRQRRRPQ. ζpot: ζ-potential. mAb: monoclonal antibody. PD-L1: programmed death-ligand 1. SLNPs: solid lipid nanoparticles. n.d.: no data.

1.5.3. Combination of STAT3 and TGF-β inhibitors in lung cancer treatment

As described in the "1.3.1. STAT3 in cancer" and "1.3.2. TGF-β signaling pathway in cancer" sections, the activation of STAT3 and TGF-β promotes survival, proliferation, and metastasis of cancer cells. However, the effects of these two pathways are not exclusively limited to tumor cells. Phosphorylation of STAT3 and production of TGF-β by TAMs are essential for keeping an immunosuppressive tumor microenvironment and, in the case of the secreted TGF-β, promoting tumor cell growth and metastasis. The interplay of both signaling pathways and the KRAS pathway, which will be relevant for the next chapter, in cancer cells and tumor-associated macrophages is presented in Figure 3. Moreover, as explained in "1.4. Biopharmaceutical limitations of STAT3 and TGF-β inhibitors", the therapeutic use of these drug families is limited by their off-target toxicity.

In this sense, co-encapsulation of a STAT3 inhibitor and a ALK5/ALK2 inhibitor emerges as a promising strategy since (i) the encapsulation of the drugs will lead to a different biodistribution profile, which could limit the off-target effects reported for the free drugs and promote an enhanced accumulation in the tumor due to EPR-related effects or active targeting, which might lead to the reduction of the actual doses needed for achieving the same therapeutic effect, (ii) the co-delivery of the two drugs might end in a synergy, thus, a superior cytotoxicity, as several pathways involved in the tumor growth are targeted at the same time, (iii) both inhibitors not only affect tumor cells but also they promote a pro-inflammatory tumor microenvironment, activating the immune system to destroy the cancer cells, (iv) it will tend to reduce the development of drug resistances, since monotherapy might end selecting the cancer cell sub-clones that are resistant to that treatment,[114] and (v) the use of TGF-β receptor inhibitors are known to promote tumor penetration of NPs, as the inhibition of this pathway in the endothelial cells lead to a higher vascular leakage and allows a higher accumulation of the NPs in the tumor and penetration into their stroma.[115]

Finally, with the aim of exploring the active targeting of the NCs, a prototype including the tLyp-1 was developed. As explained in the general introduction of this thesis, several targeting ligands (i.e., transferrin, methotrexate, HA, and tLyp-1) have been explored as decorating molecules to achieve an active targeting toward cancer cells. tLyp-1 is a member of the CendR family with a high affinity for the NRP1 and NRP2 receptors, which are known to be present in many different tumor cells, including those of lung cancer and lymphatic vessels. Therefore, cancer cell uptake, tumor mass penetration, and vascular permeability could be enhanced with this approach.[116] Moreover, our group conducted extensive research to exploit this targeting ligand and reported a dramatic accumulation of docetaxel (DTX) in lung tumors (37-fold) when this drug was loaded on HA-tLyp-1-coated NCs in comparison with Taxotere®, leading to a significant reduction in tumor growth.

1.6. STATTIC AND GALUNISERTIB

1.6.1. Stattic

As mentioned above, there are many different direct STAT3 inhibitors that, while promising, still have never reached clinical trials. In this sense, we believe that the potent STAT3-specific inhibitor stattic might be an excellent therapeutic agent if administered with adequate combination therapy and in a way that reduces its high toxicity.

USC DE COMPOSTELA

Stattic (2-nitro-1-benzothiophene 1,1-dioxide) is a poorly water-soluble small molecule with an experimental logP value of 0.46 and a molecular weight of 211 $g \cdot mol^{-1}$ (Figure 1). It is soluble in dimethyl sulfoxide (DMSO; up to 10 $mg \cdot mL^{-1}$) and slightly soluble in ethanol (up to 1 $mg \cdot mL^{-1}$). Stattic potently and selectively inhibits the STAT3 signaling pathways by two main mechanisms. First, it hampers the STAT3 activation and dimerization, with an apparent IC_{50} value after one hour of incubation at 37 °C of 5.1 ± 0.8 μM.[117–125] Second, it affects the STAT3 nuclear translocation and DNA-binding activity (IC_{50} of approximately 20 μM). Overall, stattic is an efficient drug in tumor cells with a high level of p-STAT3, with an IC_{50} in those cases of 0.4 to 6 μM for cell growth suppression.

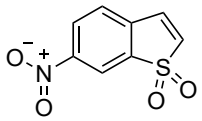


Figure 1. Structure of stattic

1.6.2. Galunisertib

In the case of TGF-β inhibitors, one of the abovementioned most promising drugs is galunisertib, as various clinical trials are ongoing in several cancer types, one of the studies (NCT02008318) in phase II/III in 2019. Galunisertib clinical trials are progressing slowly as a big concern is set on the possible cardiac toxicities that have been observed for this therapeutic family. In this sense, we believe that the ALK5 and ALK2 inhibitor galunisertib might be an excellent therapeutic agent if administered with adequate combination therapy and in a way that reduces its toxicity.

Galunisertib, {4-[2-(6-methylpyridin-2-yl)-5,6-dihydro-4H-pyrrolo[1,2-b]pyrazol-3-yl]quinoline-6-carboxamide} is a poorly water-soluble, non-peptidic small molecule with an experimental logP value of 0.33 and a molecular weight of 369 $g \cdot mol^{-1}$ (Figure 2). It is soluble in DMSO (up to 37 $mg \cdot mL^{-1}$) and slightly soluble in ethanol (up to 7 $mg \cdot mL^{-1}$). Galunisertib potently and selectively inhibits the ALK5 / ALK2 receptors involved in the TGF-β signaling pathways. Galunisertib is a highly selective TGF-β receptor inhibitor with an IC_{50} for the ALK5 kinase domain of 0.172 μM, TGFβ-RII (0.21 μM), and ALK4 (0.08 μM).[126] Overall, galunisertib and other TGF-β receptor inhibitors allow the targeting of a key driver cytokine involved in cancer progression.

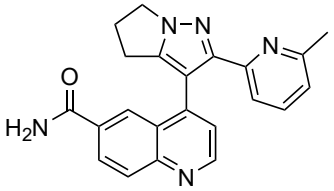


Figure 2. Structure of galunisertib

USC UNIVERSIDADE DE SANTIAGO DE COMPOSTELA

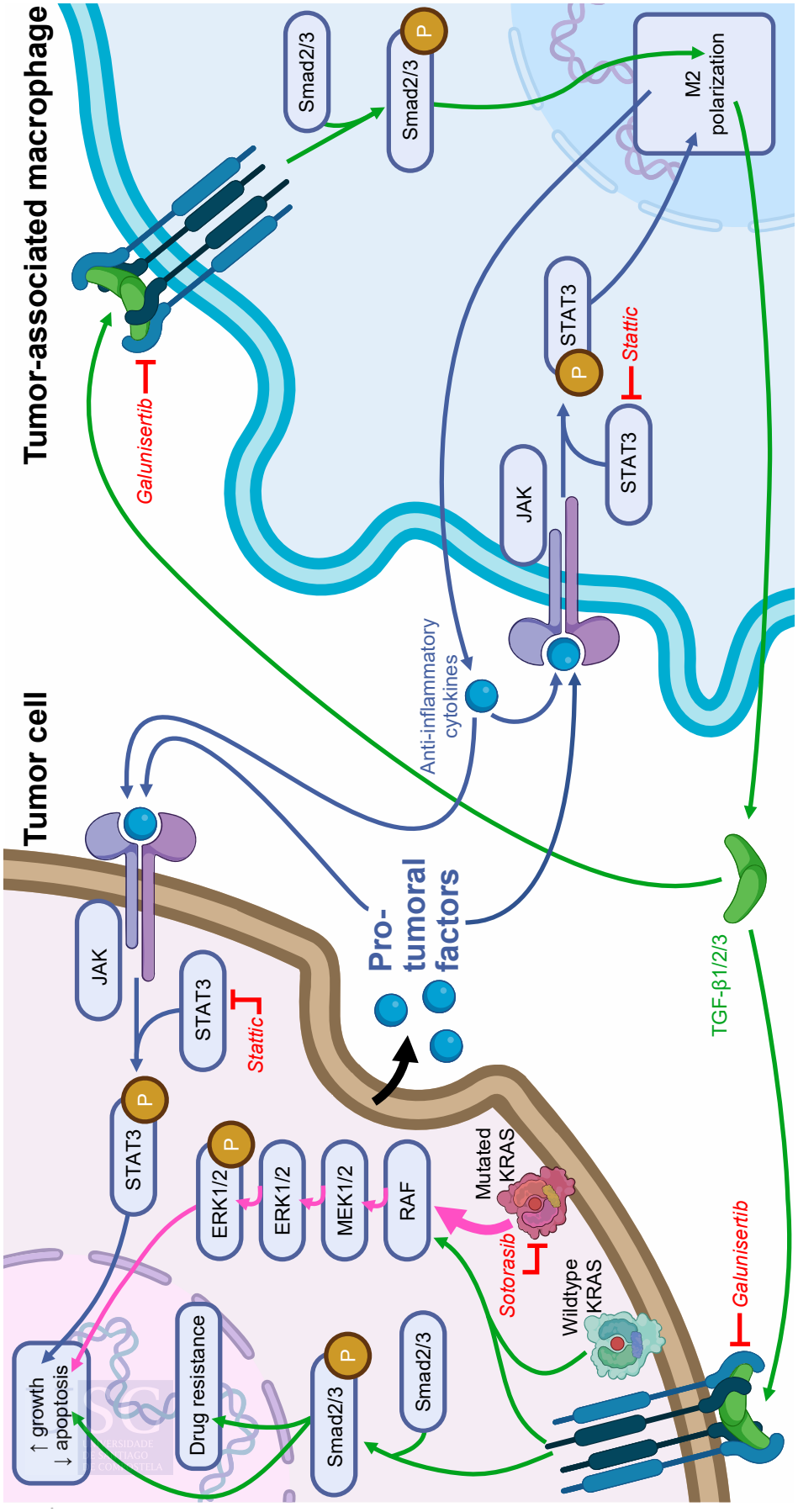


Figure 3. The interplay of STAT3, TGF-ß, and KRAS pathways in tumor cells (left) and tumor-associated macrophages (right)

Pro-tumoral factors produced by tumor cells polarize tumor-associated macrophages to M2. M2 macrophages produce anti-inflammatory cytokines (i.e., IL-10) that can induce tumor growth and reduce tumor cell apoptosis by the STAT3-signaling pathway. TGF-ß produced by M2 macrophages induces more pro-inflammatory cytokine production by immune cells, increases growth, decreases apoptosis, and induces drug resistance in tumor cells. Mutated KRAS continuously activates the MEK/ERK pathway, leading to more tumor growth. **Abbreviations:** ERK: Extracellular signal-regulated kinase. IL: interleukin. JAK: Janus kinase. KRAS: Kirsten rat sarcoma virus protein. MEK: Mitogen-activated protein kinase kinase. RAF: rapidly accelerated fibrosarcoma protein. STAT: signal transducer and activator of transcription. Smad: Suppressor of Mothers against Decapentaplegic. TGF: Transforming growth factor. Adapted from " Blank Pathway (2 Cell Interaction)", by BioRender.com (2022). Retrieved from https://app.biorender.com/biorender-templates

1.7. OBJECTIVES

The objective of this work has been the targeted delivery of a stattic and galunisertib combination with the final goal of reducing their off-target toxicities and achieving a synergistic effect. For this, an NC prototype exhibiting a low protein corona and the possibility of being functionalized with the tLyp-1 peptide will be used with the aim of modifying the biodistribution of the drugs.

2. MATERIALS AND METHODS

2.1. PREPARATION OF NANOCAPSULES

DOTAP, Miglyol® 812N, D-α-tocopherol polyethylene glycol 1000 succinate, DL-α-tocopherol, ethanol absolute, Kolliphor® HS15, phosphate-buffered saline tablets, polyethylene glycol (5 kDa) poly-α-glutamic acid (10 u), and polysorbate 80 were purchased from the companies mentioned in Chapter 1.

Stattic and galunisertib were purchased from MedChemExpress (Monmouth Junction, NJ, USA), DSPE-PEG_{2000} (DPEG) [*N*-(carbonyl-methoxy polyethylene glycol 2000)-1,2-distearoyl-sn-glycero-3-phosphoetanolamine (sodium salt)] (PE 18:0/18:0 – PEG_{2000}) was purchased from Lipoid GmbH (Ludwigshafen am Rhein, Germany), DPSE-PEG_{2000}-maleimide {1,2-distearoyl-sb-glycero-3-phosphoethanolamine-*N*-[maleimide(polyethylene glycol)-2000] (ammonium salt)} was purchased from Avanti Polar Lipids Inc. (Alabaster, CA, USA), and truncated Lyp-1 (tLyp-1, sequence: CGNKRTR, purity = 97 %) was purchased from ChinaPeptides (Shanghai, China).

Glassware, vial caps, spatulas, magnetic stirrers, pipette tips, and endotoxin-free water were autoclaved. Weighting was performed in non-sterile conditions. However, all weighted substances but the polymers were dissolved in ethanol, and the polymer solutions were UV-irradiated for 5 min after weighting. Open vials were placed under a Bunsen burner flame for the formulation of NCs. For solvent evaporation, vials were sealed with a rubber cap and punctured with an 18-gauge needle for exhaust. Next, a 23-gauge needle was connected to a sterile nitrogen tank and inserted into the formulation vial. Nitrogen flow was kept at 1 – 5 psi. The final formulation volume was adjusted with ultrapure water.

2.1.1. Synthesis of DSPE-PEG_{2000}-maleimide-tLyp-1

1 molar equivalent of DSPE-PEG_{2000}-mal at 2 $mg \cdot mL^{-1}$ in 60 % ethanol was incubated with 2 molar equivalents of tLyp-1 at 40 $mg \cdot mL^{-1}$ in 60 % ethanol, first, for 1 h at RT under magnetic stirring and, then, for 23 h at 4 °C without stirring. The resulting solution was placed inside a 7,000 MW cut-off dialysis membrane and initially subjected to dialysis against 0.9 % NaCl for 4 h and then to 3 – 4 cycles against endotoxin-free ultrapure water to remove unreacted tLyp-1. The resulting DSPE-PEG_{2000}-maleimide-tLyp-1 solution was freeze-dried and stored at -20 °C.

For the calculation of the conjugation efficiency, 500 µL of a 2 $mg \cdot mL^{-1}$ DSPE-PEG_{2000}-maleimide-tLyp-1 (DPEG-tLyp-1) solution in DMSO-d_6 were placed in a 5-mm nuclear magnetic resonance (NMR) tube and subjected to ^1H NMR of 500 MHz in a Bruker DRX-500

spectrometer with a magnetic field strength of 11.74 T (Billerica, MA, USA) without presaturation. ^{1}H NMR spectrum was processed and analyzed with MestReNova 14.2.2. Chemical shifts were calculated using DMSO-d_6 (3.33 ppm) as a reference. Auto phase and baseline corrections were applied. The areas under the curve of the peaks at 0.85 and 1.05 ppm, corresponding to the two terminal methyl groups from the DSPE moiety and the methyl group from the tLyp-1 threonine, were recorded. Then, the conjugation efficiencies were calculated as in Equation 1.

$$CE_{DSPE\text{-}PEG_{2000}\text{-}mal\text{-}tLyp\text{-}1}\ (\%) = \frac{\frac{AUC_{1.05\ ppm}}{3}}{\frac{AUC_{0.84\ ppm}}{6}}$$

Where $CE_{DSPE\text{-}PEG_{2000}\text{-}mal\text{-}tLyp\text{-}1}$ is the conjugation efficiency of DSPE-PEG$_{2000}$-mal and tLyp-1. $AUC_{1.05\ ppm}$ is the area under the curve of the hydrogens present in the threonine CH_3 of tLyp-1, with a chemical shift of 1.05 ppm. And $AUC_{0.84\ ppm}$ is the area under the curve of the hydrogens present in the terminal end of the alkyl chains of DSPE, with a chemical shift of 0.85 ppm.

Equation 1. Calculation of the conjugation efficiency of DSPE-PEG$_{2000}$-mal and tLyp-1 based on ^{1}H NMR

2.1.2. Preparation of blank nanocapsules

For SD-noPEG, 1,070 µL of oil phase (25.23 mg·mL^{-1} DL-α-tocopherol and 0.93 mg·mL^{-1} DOTAP in ethanol) were poured directly onto 2.907 mL of water under magnetic stirring at 700 rpm. After 10 min of stirring, 133 µL of PEG·PGA 30 mg·mL^{-1} in water were added to the formulation. Stirring was kept until the NCs volume was lower than 2.0 mL. Then, it was raised to 2 mL using ultrapure water.

For SD-TPGS, 1,070 µL of oil phase (25.23 mg·mL^{-1} DL-α-tocopherol, 7.48 mg·mL^{-1} TPGS, and 0.93 mg·mL^{-1} DOTAP in ethanol) were poured directly onto 2.907 mL of water under magnetic stirring at 700 rpm. After 10 min of stirring, 133 µL of PEG·PGA 30 mg·mL^{-1} in water were added to the formulation. Stirring was kept until the NCs volume was lower than 2.0 mL. Then, it was raised to 2 mL using ultrapure water.

For SD-DPEG, 1,070 µL of oil phase (25.23 mg·mL^{-1} DL-α-tocopherol, 1.72 mg·mL^{-1} DSPE-PEG$_{2000}$, 0.93 mg·mL^{-1} DOTAP in ethanol) were poured directly onto 2.907 mL of water under magnetic stirring at 700 rpm. After 10 min of stirring, 133 µL of PEG·PGA 30 mg·mL^{-1} in water were added to the formulation. Stirring was kept until the NCs volume was lower than 2.0 mL. Then, it was raised to 2 mL using ultrapure water.

For SD-DPEG-tLyp-1, 1,070 µL of oil phase (25.23 mg·mL^{-1} DL-α-tocopherol, 2.28 mg·mL^{-1} DSPE-PEG$_{2000}$-maleimide-tLyp-1, and 0.93 mg·mL^{-1} DOTAP in ethanol) were poured directly onto 2.907 mL of water under magnetic stirring at 700 rpm. After 10 min of stirring, 133 µL of PEG·PGA 30 mg·mL^{-1} in water were added to the formulation. Stirring was kept until the NCs volume was lower than 2.0 mL. Then, it was raised to 2 mL using ultrapure water.

USC UNIVERSIDADE DE SANTIAGO DE COMPOSTELA

2.1.3. Preparation of galunisertib- and stattic-loaded nanocapsules for *in vitro* assays

2.1.3.1. Preparation of DiD-labeled NCs for uptake assays

DiD-labeled NCs were formulated as mentioned in "2.1.2. Preparation of blank nanocapsules", but including DiD in the organic phase to obtain a DiD concentration of 100 ppm in the final formulation.

2.1.3.2. Preparation of galunisertib- and stattic-loaded NCs for cytotoxicity assays

For SD-noPEG, SD-TPGS, SD-DPEG, and SD-DPEG-tLyp-1 NCs were formulated as in "2.1.2. Preparation of blank nanocapsules" but including 0.12 $mg \cdot mL^{-1}$ stattic and 2.34 $mg \cdot mL^{-1}$ galunisertib in their organic phase before formulation.

2.2. CHARACTERIZATION OF NANOCAPSULES

2.2.1. Characterization of the size, ζ-potential, and pH of nanocapsules

Dynamic light scattering (Zetasizer® Nano ZS, Malvern Instruments, Malvern, UK) was used to characterize the nanosystems' hydrodynamic diameter and polydispersity index. ζ-potential was measured by laser Doppler electrophoresis with the same equipment. Unless indicated otherwise, measurements were done after diluting the samples 10 × in ultrapure water, with an automatic run number and length at 25 °C.

pH was measured by Sartorius Docu-pHmeter equipped with a HANNA Instruments HI1330 electrode.

2.2.2. Colloidal stability

The colloidal stability of the different NCs in plasma was evaluated by incubating 10 % of NCs with 90 % of PBS supplemented with 10 % FBS at 37 °C and measuring their hydrodynamic diameter and PDI at different time points by DLS, as indicated in the section "2.2.1. Characterization of the size, ζ-potential, and pH".

In all cases, samples were subjected to mild horizontal shaking during the whole incubation time (300 rpm, Heidolph Titramax/Inkubator 1000, Heidolph Instruments, Schwabach, Germany).

2.2.3. Analysis of the composition of nanocapsules by LC-MS/MS

The LC-MS characterization of all the compounds of the blank NCs was conducted with the same experimental procedure as in Chapter 1. While all the previously developed MS or MS/MS methods were maintained, two more LC-MS/MS ESI(+) quantification methods (for DPEG and DPEG-tLyp-1) were developed (Table 5). Parent and daughter structures are presented in Table 6.

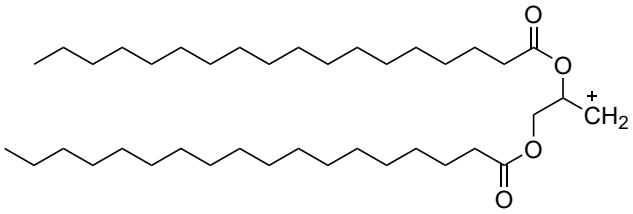
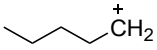
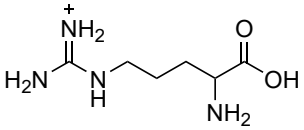
USC UNIVERSIDADE DE SANTIAGO DE COMPOSTELA

Table 5. MS/MS methods for quantifying DSPE-PEG$_{2000}$ and Digested DSPE-PEG$_{2000}$-maleimide-tLyp-1

Substance	Method
DSPE-PEG$_{2000}$	MRM, *m/z* 607.6 → 71.1, DP: 58 V, CE: 30 eV
Digested DSPE-PEG$_{2000}$-maleimide-tLyp-1	MRM, *m/z* 175.1 → 70.1, DP: 25 V, CE: 20 eV

Abbreviations: MRM: multiple reaction monitoring. DP: declustering potential. CE: collision energy. MS: mass spectrometry.

Table 6. Structure of the parent and daughter molecules of each NCs' component

Substance	Parent structure	Daughter structure	Ref.
DPEG			[127]
Digested DPEG-tLyp-1			[128]

Abbreviations: DPEG: *N*-(carbonyl-methoxy polyethylene glycol 2000)-1,2-distearoyl-sn-glycero-3-phosphoetanolamine. DPEG-tLyp-1: tLyp-1-conjugated 1,2-distearoyl-sn-glycero-3-phosphoethanolamine-*N*-[maleimide(polyethylene glycol)-2000].NCs: nanocapsules. Ref.: reference.

The chromatographic method for the PEG·PGA polymer for SD-DPEG remained as described in Chapter 1, as well as for the method of the hydrophobic molecules of SD-DPEG-tLyp-1. In the other cases, the chromatographic methods employed are described in Tables 7-8.

Table 7. Chromatographic method for the analysis of non-polymeric substances by UHPLC-MS/MS

Formulation	Time (min)	Solvent A (%)	Solvent B (%)	Solvent C (%)
SD-DPEG (hydrophobic molecules)	0.00	90	10	0
	0.50	90	10	0
	1.50	0	60	40
	12.90	0	60	40
	13.00	90	10	0
	15.00	90	10	0

Solvent A: 50 mM formic acid and 2 mM ammonium formate in water. Solvent B. 95 % acetonitrile and 5 % 2 mM ammonium formate aqueous solution (v/v) 50 mM formic acid. Solvent C: isopropyl alcohol. The composition of SD-DPEG is shown in Figure 5. **Abbreviations:** UHPLC-MS: ultra-performance liquid chromatography-mass spectrometry.

USC UNIVERSIDADE DE SANTIAGO DE COMPOSTELA

Table 8. Chromatographic method for the analysis of the polymers in SD-DPEG-tLyp-1 by UHPLC-MS/MS

Formulation	Time (min)	Solvent A (%)	Solvent B (%)
SD-DPEG-tLyp-1 (DSPE-PEG_{2000}-maleimide-tLyp-1 and PEG·PGA)	0.00	0	100
	5.00	0	100
	13.00	29.4	70.6
	13.10	0	100
	17.00	0	100

Solvent A: 75 mM formic acid and 5 mM ammonium formate in water. Solvent B: 75 mM formic acid and 5 mM ammonium formate in acetonitrile (90 %) and water (10 %) mixture (v/v). The composition of SD-DPEG-tLyp-1 is shown in Figure 5. **Abbreviations:** UHPLC-MS: ultrahigh-performance liquid chromatography-mass spectrometry.

Except for the PEG·PGA and DSPE-PEG_{2000}-maleimide-tLyp-1, a Kinetex® 1.7 µm C18 100 Å 50 × 2.1 mm column was employed. In the latest cases, a Kinetex® 1.7 µm HILIC 100 Å 50 × 2.1 mm column was used instead (Phenomenex, Torrance, CA, USA), at 50 and 35 °C, respectively. Injection volumes were 5 and 25 µL for the polymers and the SD-DPEG-tLyp-1 and hydrophobic compounds SD-DPEG, respectively. Detector parameters were kept constant from Chapter 1.

2.2.4. Quantification of galunisertib and stattic

In general, galunisertib and stattic association efficiencies were quantified by HPLC-UV-Vis due to simplicity, as both molecules absorb UV light and could be resolved in an 8-minute chromatography. The HPLC-UV-Vis consisted of a Hitachi LaChrom Elite® HPLC system with UV-Vis detectors L-2400, column oven L-2300, ACE Equivalence 5 C18 with dimensions 250 × 2.4 mm column, pump L-2130, autosampler L-2200, and EZChrom Elite V.3.3.1 SP1 software. The mobile phase consisted of an isocratic mixture of acetonitrile (ACN) and ultrapure water 1:1 (v/v) at a flow rate of 1 $mL \cdot min^{-1}$ for 8 min. The injection volume was 50 µL, and the UV-Vis detector was set at 215 nm. The experiment was performed at 30 °C. The retention times of galunisertib and stattic were found to be 3.6 and 4.9 min, respectively. Calibrating solutions were done in acetonitrile in the range of 1 – 12 ppm for galunisertib and 50 – 600 ppb for stattic. An HPLC-UV-Vis chromatogram example can is presented in Supplementary Figure 4.

While the HPLC-UV-Vis quantification was sensitive enough for the calculation of the AEs, we were forced to use an LC-MS/MS method when the release of the drugs in PBS supplemented with 10 % FBS was studied. The LC-MS/MS quantification was carried out by our collaborators from SINTEF AS with a UHPLC coupled to a Triple Quadrupole mass spectrometer (G4226A, G4220A, G1316C, and G6490A. Agilent, Santa Clara, CA, USA) equipped with a C8 column (Ascentis Express C8, 2.1 × 75 mm, 2.7 µm) for Stattic and a C18 (Zorbax Eclipse Plus C18 RR-HD, 2.1 × 50 mm, 1.8 µm) for galunisertib. Both columns were used at 40 °C. The equipment's gas temperature was 150 °C at a flow of 14 $L \cdot min^{-1}$. The nebulizer gas pressure was set at 40 psi. The sheath gas was heated at 400 °C and used at 12 $L \cdot min^{-1}$. Capillary was 3.3 kV for ESI(-) and 4 kV for ESI(+). The injection volume was 3 µL, and the mobile phase flow was set at 0.3 and 0.4 $mL \cdot min^{-1}$ for galunisertib and stattic, respectively. The chromatographic methods are presented in Table 9. Of note, stattic

quantification was carried out in ESI(−), while galunisertib was in ESI(+) (Table 10). Calibration solutions were done in methanol in the range of 1.0 – 1,000.0 ppb for both molecules. The proposed structures of the parent and daughter ions of these molecules can be consulted in Table 11.

Table 9. Chromatographic method for the analysis of galunisertib and stattic by UHPLC-MS/MS

Substance	Time (min)	Solvent A (%)	Solvent B (%)	Solvent C (%)	Solvent D (%)
Galunisertib	0.00	80	20	0	0
	1.00	80	20	0	0
	1.50	65	35	0	0
	4.50	65	35	0	0
	5.00	10	90	0	0
	6.00	80	20	0	0
	7.00	80	20	0	0
Stattic	0.00	0	0	100	0
	0.50	0	0	100	0
	3.00	0	0	0	100
	3.50	0	0	100	0
	7.00	0	0	100	0

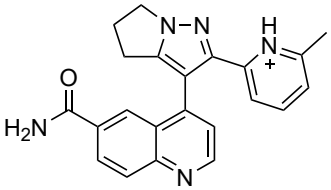
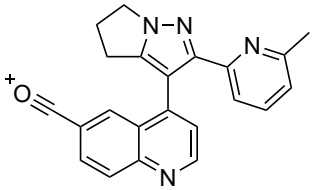
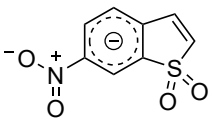
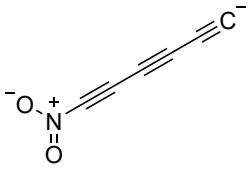
Solvent A: 20 mM ammonium acetate in water. Solvent B: 0.1% formic acid in acetonitrile:methanol (1:1). Solvent C: 13 mM ammonium acetate in water. Solvent D: methanol. **Abbreviations:** UHPLC-MS: ultra-performance liquid chromatography-mass spectrometry.

Table 10. MS/MS methods for galunisertib and stattic

Substance	Method
Galunisertib	MRM, *m/z* 370.4 → 353.2, CE: 20 eV
Stattic	MRM, *m/z* 210.0 → 118.0, CE: 17 eV

Abbreviations: MRM: multiple reaction monitoring. CE: collision energy. MS: mass spectrometry.

Table 11. Structure of the parent and daughter molecules of galunisertib and stattic

Substance	Parent structure	Daughter structure	Ref.
Galunisertib			[129]
Stattic			-

USC UNIVERSIDADE DE SANTIAGO DE COMPOSTELA

Abbreviations: Ref.: reference.

2.2.5. Calculation of the loading capacity and association efficiency of galunisertib and stattic

The drug loading capacity was calculated as in Equation 2:

$$Drug\ loading_{therapeutic\ agent}\ (\%) = \frac{m_{therapeutic\ agent}}{m_{total}} \cdot 100$$

Where $Drug\ loading_{therapeutic\ agent}$ is the loading capacity of a therapeutic agent, $m_{therapeutic\ agent}$ is its mass, and m_{total} is the sum of all the components present in the formulation except for the formulating media.

Equation 2. Calculation of the loading capacity of NCs

The drugs' association efficiencies were calculated indirectly. Galunisertib- and stattic-loaded NCs were ultracentrifuged at an average of 110,000 g (40,000 rpm) for 1 h at 15 °C in an OptimaTM L-90 K Ultracentrifuge equipped with a 70.1 Ti rotor and 10 mL open-top thickwall polycarbonate tubes 16 × 76 mm (Beckman Coulter, Brea, CA, USA). Then, the infranatant was collected using a syringe and analyzed by HPLC-UV-Vis or UPLC-MS/MS by the methods mentioned in "2.2.4. Quantification of galunisertib and stattic".

2.2.6. Release studies

NCs were diluted 10-times in PBS or PBS supplemented with 10 % FBS and incubated for 0, 1, 4, 8, and 24 hours at 37 °C. Then, NCs were submitted to ultracentrifugation at 40,000 rpm, 15 °C, 1 h using a Beckman Coulter (optime L90K) ultracentrifuge equipped with a Beckman type 70.1 Ti rotor. Samples were mixed 1:1 with acetone:acetonitrile (9:1) and centrifuged for 10 min at 8,000 rpm. Then, the protein-free supernatant was collected and diluted 10 × in methanol for stattic quantification and 200 × in the case of galunisertib. After the process, the free galunisertib and stattic content were analyzed by UHPLC-MS/MS.

Extraction yields from the 10 % FBS-supplemented PBS matrix were obtained by quantifying 10 $\mu g \cdot mL^{-1}$ of each drug in the matrix using a calibration curve in the absence of proteins. Calibration curve ranges were 1 – 1000 ppb for both drugs. Extraction yields were found to be 91.69 ± 7.46 and 88.21 ± 3.19 % for galunisertib and stattic, respectively.

The release was calculated based on the AE as in Equation 3:

$$Release_{drug}\ (\%) = \frac{\frac{[drug]_{infranatant} \cdot DF \cdot 100}{[drug]_{theoretical} \cdot EY_{drug}} - (100 - AE_{drug})}{AE_{drug}}$$

Where $[drug]_{infranatant}$ is the drug concentration in the infranatant after the release study, which includes the non-associated and the released fractions. DF is the dilution factor applied during the incubation and sample treatments. $[drug]_{theoretical}$ is the theoretical drug concentration in the original formulation. EY_{drug} is the extraction yield of the drug from the PBS/FBS matrix. And AE_{drug} is the association efficiency of the drug in percentage.

Equation 3. Calculation of the released drug from NCs

USC UNIVERSIDADE DE SANTIAGO DE COMPOSTELA

2.3. CELL COUNTING AND SEEDING

Accutase® or trypsin, PBS, and cell culture media were warmed up to 37 °C in a water bath. Then, the media from the flasks or plates was removed, and cells were washed once with 5 mL of PBS.

1 mL of trypsin or 200 µL of Accutase® was added to the cells and incubated at 37 °C for 5 min. Then, trypsin or Accutase® were inactivated by adding at least the same volume of cell culture medium. Medium containing the cells in suspension was mixed and poured through the walls of the vials to ensure maximum recovery of cells.

Then, cells were centrifuged at 500 g for 5 min at room temperature and resuspended to 1 mL. 10 µL of cell suspension were mixed with 10 µL of trypan blue. 10 µL of this solution was deposited into a Neubauer chamber. Cells present from the four quadrants of the border of the Neubauer chamber were counted. Cell density was estimated as in Equation 4.

$$[Cells]\ (\text{cells}\cdot\text{mL}^{-1}) = mean\ cell\ counting \cdot DF \cdot 10^4$$

Where $[Cells]$ is the cell concentration in cells·mL^{-1}. $Mean\ cell\ counting$ is the mean number of cells in the four quadrants of the Neubauer chamber, and DF is the dilution factor caused by the addition of trypan blue, usually DF = 2.

Equation 4. Calculation of cell concentrations

2.4. *IN VITRO* UPTAKE EXPERIMENTS

50,000 CMT 167 or 100,000 RAW 264.7 cells per well were seeded in 24-well plates containing 500 µL Dulbecco's modified Eagle's medium (DMEM) supplemented with 10 % FBS and 1 × P/S (100 IU·mL^{-1} Penicillin and 100 µg·mL^{-1} of Streptomycin sulfate) [Gibco (Thermo Fisher Scientific), Waltham, MA, USA] (referred as culture medium) and incubated for 24 h at 37 °C. Then different dilutions of the DiD-labeled NCs prototypes were added in culture medium. Cells were incubated at 37 °C and 4 °C. After 4 h, cell supernatants were discarded, and the cells were extensively washed 3 times with cold 1 × PBS, detached by incubation with Accutase® [Gibco (Thermo Fisher Scientific), Waltham, MA, USA] 15 min at 37 °C, and collected in fluorescence-activated cell sorting (FACS) tubes. Cells were washed with 3 mL cold FACS washing buffer (PBS 2 % FBS), pelleted by centrifugation at 1000 rpm for 5 min, fixed with 100 µL 4 % paraformaldehyde [PFA (Sigma-Aldrich, Burlington, MA, USA)] for 30 min, and analyzed in BD FACSCalibur instrument (BD Biosciences, Franklin Lakes, NJ, USA), collecting 10,000 events per sample, and FlowJo 10.8.1 software (BD Bioscience).

2.5. *IN VITRO* CYTOTOXICITY EXPERIMENTS

CMT 167 or RAW 264.7 cells were plated in 96-well plates in 100 µL culture medium and incubated for 24 h at 37 °C. Then prototypes were added at indicated concentrations in culture medium at a final FBS concentration of 10 %. As positive viability control, cells were incubated with culture medium, while Triton™ X-100 (Sigma-Aldrich, Burlington, MA, USA) 0.5 % v/v in culture medium was used as negative viability control. After 24 h, the cell supernatant was discarded, and cells were incubated with 100 µL of 1 % 1.22 mg·mL^{-1} resazurin in Hanks' balanced salt solution (Sigma-Aldrich, Burlington, MA, USA) and 99 % culture medium per

well for 40 min at 37 °C in the dark. Fluorescence was measured in-plate at 590 nm after excitation at 544 nm in a Synergy H1 Hybrid Multi-Mode Reader (BioTek, Winooski, VT, USA). Data were presented as viability percentages setting the control group (DMEM 10 % FBS) to 100 %, as indicated in Equation 5.

$$Viability\ (\%) = \frac{Sample - Triton\ X\text{-}100}{DMEM - Triton\ X\text{-}100} \cdot 100$$

Where $Viability$ is the viability of the treated cells in percentage. $Sample$ is the fluorescence at 590 nm of the sample-treated cells. $Triton\ X\text{-}100$ is the fluorescence at 590 nm of 0.5 % Triton™ X-100 in DMEM supplemented with 10 % FBS-treated cells. And $DMEM$ is the fluorescence at 590 nm of the untreated cells.

Equation 5. Calculation of cell viability

Several cell densities (0, 2,500, 5,000, and 10,000 CMT 167 or RAW 264.7 cells per well) were explored to achieve a good sensitivity in the cytotoxicity assay (Figure 4).

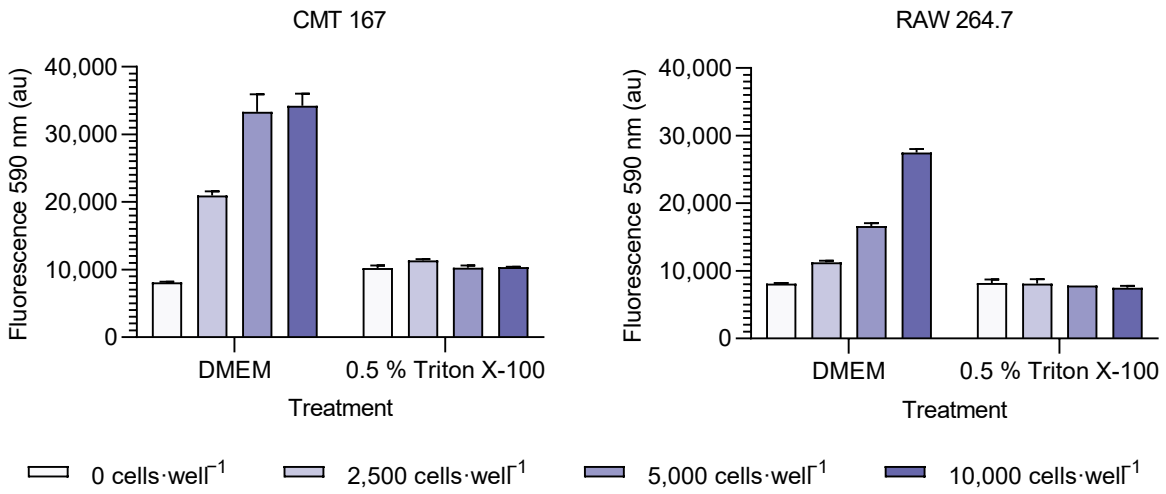


Figure 4. Optimization of the resazurin assay for CMT 167 and RAW 264.7 cell lines

Abbreviations: DMEM: Dulbecco's modified Eagle medium

2,000 CMT 167 cells per well resulted in the optimal cell density for the positive viability control, as the fluorescence values for 5,000 and 10,000 CMT 167 cells per well were similar, suggesting the saturation of the assay. In the case of RAW 264.7, the optimal cell density was found to be 5,000 cells per well. In both CMT 167 and RAW 264.7 selected conditions, fluorescence was significantly higher in the positive viability control compared to the negative viability control, which was Triton™ X-100 (Sigma-Aldrich, Burlington, MA, USA) 0.5 % v/v in culture medium.

Finally, IC_{50} values were calculated with GraphPad Prism 9.4.1. fitting the data to Equation 6:

USC UNIVERSIDADE DE SANTIAGO DE COMPOSTELA

$$y = \frac{100}{1 + \left(\frac{IC_{50}}{x}\right)^{HillSlope}}$$

Where y is the viability of the treated cells in percentage. IC_{50} is the half maximal inhibitory concentration in $\mu g \cdot mL^{-1}$. $HillSlope$ is the unitless slope factor that leads to the best fit of the data. And x is the concentration of the tested drugs in $\mu g \cdot mL^{-1}$.

Equation 6. Dose-response inhibition model for drug concentration *vs*. normalized cytotoxicity with variable slope

2.6. *IN VITRO* STAT3 AND TGF-B PATHWAYS INHIBITION

40,000 RAW 264.7 cells per well were seeded in MW24 plates with 4 mL of culture medium. After 24 h, the medium was replaced with 4 mL of fresh medium containing no treatment, galunisertib (10 $\mu g \cdot mL^{-1}$), stattic (0.5 $\mu g \cdot mL^{-1}$), drug-loaded NCs (with the same galunisertib or stattic concentration as the free drugs), and blank NCs (with the same dilution factor as loaded-NCs). After 1 h, cells were treated with TGF-β and/or IL-10 (10 µL per well; 10 $ng \cdot mL^{-1}$ of each drug in culture medium). 15 min later, LPS was added (10 µL per well; 50 $ng \cdot mL^{-1}$ in culture medium). Cells were incubated for 24 h and then centrifuged at 500 g for 5 min at room temperature. Supernatants were collected, and cells were lysed and collected in 400 µL of TRIzol™ (phenol and guanidinium isothiocyanate). Chemokine release (CCL2 and IL-6) was evaluated by a sandwich enzyme-linked immunosorbent assay (ELISA), and the total production of nitrites was measured through the Griess colorimetric assay.

2.7. DATA PRESENTATION AND STATISTICAL ANALYSIS

Unless indicated otherwise, data are presented as the mean or the mean ± standard deviation of 3 replicates, GraphPad Prism version 9.4.1 (GraphPad, San Diego, CA, USA) was used for data analysis, type I errors (α) were fixed to 0.05, and *p*-values < 0.05 were considered statistically significant (*). Also, (**) if *p*-value < 0.01, (***) if *p*-value < 0.001 and (****) if *p*-value < 0.0001.

For cytotoxicity assays, comparisons were performed by unpaired homoscedastic parametric t-test. For activity studies, one-way ANOVA with a Dunnett posthoc test was performed.

Analyses requiring normally-distributed data were performed after passing the Kolmogorov-Smirnov test, with the Dallal-Wilkinson-Lilliefor corrected *p*-value.

3. RESULTS AND DISCUSSION

In the context of the 2^2-INTRATARGET consortium, it was observed that the combination of a STAT3 inhibitor (stattic) with a TGF-β pathway inhibitor (galunisertib) exhibited a synergistic effect upon intratumoral administration in a subcutaneous CMT 167 lung tumor model. With the aim of reducing the off-target toxicities of galunisertib and stattic combination therapy, both drugs were encapsulated into different NCs prototypes. The design and

development and *in vitro* cellular uptake, cytotoxicity, and efficacy of galunisertib- and stattic-loaded NCs are detailed in the following paragraphs.

3.1. Design and development of nanocapsules containing galunisertib and stattic

As a first step in the development of NCs and based on the results of the protein corona studies, we have selected SD-*l*-PEG-PEG·PGA and SD-noPEG-PEG·PGA as promising candidates for the encapsulation of galunisertib and stattic for treating lung cancers due to their reduced and vitronectin-enriched protein corona, respectively. For simplicity, since both NCs have the same polymer shell, PEG·PGA, they will be named based on the nature of their surfactant, as indicated in Figure 5. Moreover, to explore the possibility of active targeting, we have also developed a tLyp-1-decorated formulation (SD-DPEG-tLyp-1).

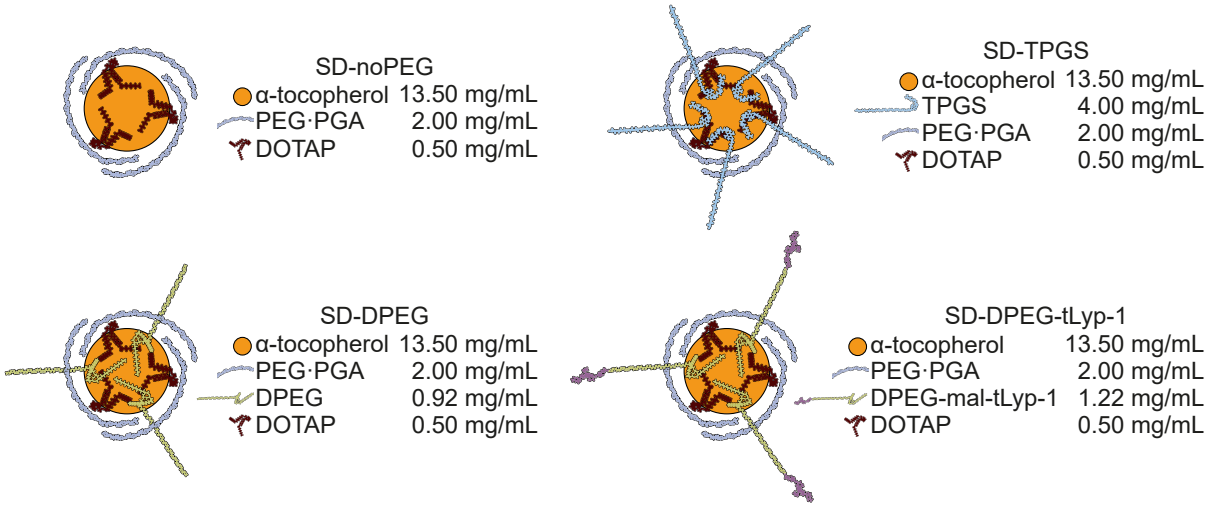


Figure 5. Schematic representation of the expected NCs' compound arrangement and their theoretical composition

SD-noPEG: Formulation prepared by solvent displacement technique and composed of non-PEGylated surfactants (DOTAP) and PEG·PGA shell. **SD-TPGS**: Formulation prepared by solvent displacement technique and composed of lineal PEG (TPGS) and PEG·PGA shell. **SD-DPEG**: Formulation prepared by solvent displacement technique and composed of lineal PEG (DPEG) and PEG·PGA shell. **SD-DPEG-tLyp-1**: Formulation prepared by solvent displacement technique and composed of lineal PEG (DPEG-tLyp-1) and PEG·PGA shell. **Abbreviations**: DOTAP: 1,2-dioleoyl-3-trimethylammoniumpropane. DPEG: DSPE-PEG_{2000} [*N*-(carbonyl-methoxy polyethylene glycol 2000)-1,2-distearoyl-sn-glycero-3-phosphoetanolamine]. DPEG-tLyp-1: DSPE-PEG_{2000}-maleimide-tLyp-1. PEG·PGA: polyethylene glycol polyglutamic acid. TPGS: D-α-tocopherol polyethylene glycol 1000 succinate.

The election of the targeting ligand tLyp-1 was based on previous work from Alonso's group. Indeed, the work of Teijeiro-Valiño *et al.*[116] demonstrated that DTX-loaded and tLyp-1-decorated HA NCs led to an accumulation of the drug in an orthotopic lung cancer model of approximately 37-fold that of Taxotere®. tLyp-1 is a member of the CendR family with a high affinity for the NRP1 and NRP2 receptors. These receptors are known to be present in many different tumor cells, including those of lung cancer and lymphatic vessels. Therefore, cancer cell uptake, tumor mass penetration, and vascular permeability could be enhanced with

this approach.[116] Then, we have decided to conjugate tLyp-1 with a PEGylated surfactant to provide a hydrophilic spacer between the NCs surface and the targeting peptide, which might reduce the hindering of the target by the formation of a protein corona. In this sense, DSPE-PEG_{2000} was selected due to its longer PEG chain length, twice that of TPGS.

The conjugation efficacy of DSPE-PEG_{2000}-mal and tLyp-1 was calculated by ^{1}H NMR and found to be 88 % (Supplementary Figure 2).

Based on the literature, the amount in moles of DSPE-PEG_{2000}-mal-tLyp-1 in SD-DPEG-tLyp-1 was selected to be 1.00 % of the total moles of the components in the blank formulation. DSPE-PEG_{2000} amount in SD-DPEG was calculated based on the SD-DPEG-tLyp-1 NCs to keep the moles of the DSPE-PEG_{2000} moieties constant.

The physicochemical characteristics of the loaded NCs are summarized in Table 12, and examples of the size and ζ-potential distributions can be found in Supplementary Figure 1. The physicochemical characterization of blank prototypes is summarized in Supplementary Table 1, while the one of single-loaded SD-noPEG can be consulted in Supplementary Table 2.

Table 12. Physicochemical characterization of galunisertib- and stattic-loaded SD-noPEG, SD-TPGS, SD-DPEG, and SD-DPEG-tLyp-1

	SD-noPEG	SD-TPGS	SD-DPEG	SD-DPEG-tLyp-1
Final [galunisertib] ($mg \cdot mL^{-1}$)	1.25	1.25	1.25	1.25
Final [stattic] ($mg \cdot mL^{-1}$)	0.0625	0.0625	0.0625	0.0625
Galunisertib loading (%)	7.2	5.9	6.9	6.7
Stattic loading (%)	0.4	0.3	0.3	0.3
Hydrodynamic diameter (DLS) (nm)	118 ± 3	87 ± 9	98 ± 7	106 ± 14
PDI	0.05 ± 0.03	0.19 ± 0.06	0.09 ± 0.02	0.15 ± 0.05
ζ-potential (mV)	−21 ± 1	−3 ± 2	−10 ± 2	+5 ± 7
AE galunisertib (%)	75 ± 11	36 ± 7	71 ± 10	58 ± 12
AE stattic (%)	50 ± 1	26 ± 12	54 ± 12	38 ± 11
pH	5.5 ± 0.1	5.4 ± 0.1	6.6 ± 0.2	6.1 ± 0.1

The compositions of SD-noPEG, SD-TPGS, SD-DPEG, and SD-DPEG-tLyp-1 are shown in Figure 5. **Abbreviations:** AE: association efficiency. DLS: dynamic light scattering. PDI: polydispersity index. Values represent the mean ± standard deviation (n = 3).

Overall, the developed formulations fulfilled the desired properties in terms of particle size (close to 100 nm) and the ζ-potential (close to neutral charge or slightly negative). The highest negative charge observed for the SD-noPEG formulation is easily explained by the lack of PEGylated surfactants. These NCs were found to be stable in storage conditions for up to 1 month (Supplementary Figure 3).

In order to know the amount of the targeting ligand in the SD-DPEG-tLyp-1 formulation and the effect of its incorporation on the NCs composition, an LC-MS/MS study similar to that of Chapter 1 was carried out for the new formulations (Figure 6). Validation of the calibration curves can be consulted in Supplementary Table 3, examples of chromatograms are presented

in Supplementary Table 4, and examples of calibration curves and residual plots are in Supplementary Table 5.

The percentage of DSPE-PEG-mal-tLyp-1 that was incorporated into the targeted formulation resulted in 53 ± 4 % of its theoretical concentration. Moreover, the PEG·PGA amount did not significantly change when the targeting ligand was added.

The association efficiencies of the drugs were between 36 ± 7 and 75 ± 11 % for galunisertib and 26 ± 12 and 54 ± 12 % for stattic. The highest galunisertib and stattic AEs were detected for SD-noPEG and SD-DPEG (Table 12). Of note, the AEs of galunisertib and stattic in the case of SD-DPEG-tLyp-1 were 58 ± 12 and 38 ± 11 %, meanwhile of 71 ± 10 and 54 ± 12 % for SD-DPEG. Finally, SD-TPGS, with the highest free surfactant content (Chapter 1), exhibited the lowest AEs (36 ± 7 % for galunisertib and 26 ± 12 % for stattic). In the case of SD-noPEG, the high AE (75 ± 11 and 50 ± 1 % for galunisertib and stattic, respectively) can be attributed to the absence of PEGylated surfactants, as the free fractions of the PEGylated surfactants do form micellar structures which can solubilize part of the drugs, leading to lower AE results.

Finally, the incorporation of the tLyp-1 moiety into the SD-DPEG-tLyp-1 led to a statistically significantly lower association of DL-α-tocopherol compared to SD-DPEG (unpaired t-test) and a tendency for lower PEGylated polymer as well (Figure 6).

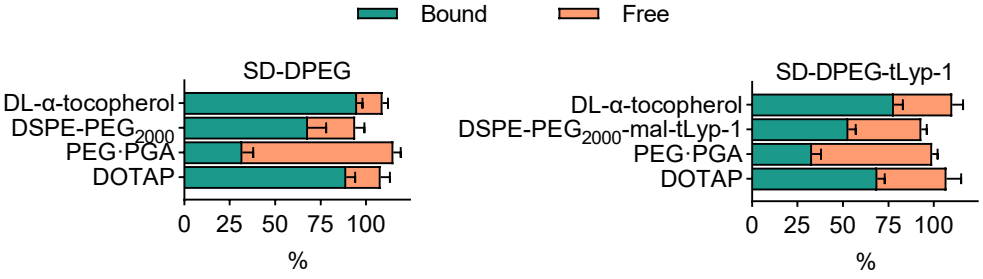


Figure 6. Associated (bound) and non-associated (free) mass percentages referred to the total added mass of each component of the two new NCs (as in Chapter 1).

The compositions of SD-DPEG and SD-DPEG-tLyp-1 are shown in Figure 5. **Abbreviations:** DOTAP: 1,2-dioleoyl-3-trimethylammonium-propane chloride. PEG·PGA: Polyethylene glycol poly-α-glutamic acid. DSPE-PEG_{2000}: *N*-(carbonyl-methoxy polyethylene glycol 2000)-1,2-distearoyl-sn-glycero-3-phosphoetanolamine. DSPE-PEG_{2000}-maleimide-tLyp-1: tLyp-1-conjugated 1,2-distearoyl-sn-glycero-3-phosphoethanolamine-*N*-[maleimide(polyethylene glycol)-2000]. NCs: nanocapsules. Values represent the mean ± standard deviation (n = 3).

The stability of the drug-loaded NCs was assessed in biological-mimicking media (Figure 7). SD-TPGS and SD-DPEG preserved their hydrodynamic size for up to 24 h in PBS supplemented with 10 % FBS. On the contrary, SD-noPEG exhibited a statistically significant increase of ≈ 40 nm in size (two-way ANOVA comparisons *versus* NCs dispersed in water) at the moment of contact with the media that remained constant for 24 h. Besides, the stability of SD-DPEG might be compromised. While the size increase was only significant at early time points (0 and 1 h; ≈ 30 nm), the hydrodynamic diameter of this formulation exhibited high variability between replicates.

Then, the stattic and galunisertib release was assessed after incubation in PBS supplemented with 10 % FBS. As shown in Figure 8, some formulations exhibited a burst release but afterward, no more drug was released.

In general, the burst release was found to be high for galunisertib, between 50 and 100 % depending on the formulation, whereas that of stattic was lower. More detailed, SD-noPEG NCs exhibited a burst release of approximately 80 % for galunisertib and negligible for stattic, while the NCs functionalized with tLyp-1 exhibited a 70 % and a 40 % burst release for galunisertib and stattic, respectively. These different burst releases could be related to the different solubility of both compounds and their tendency to diffuse to the external aqueous medium, a phenomenon that could be augmented due to the ultracentrifugation process.

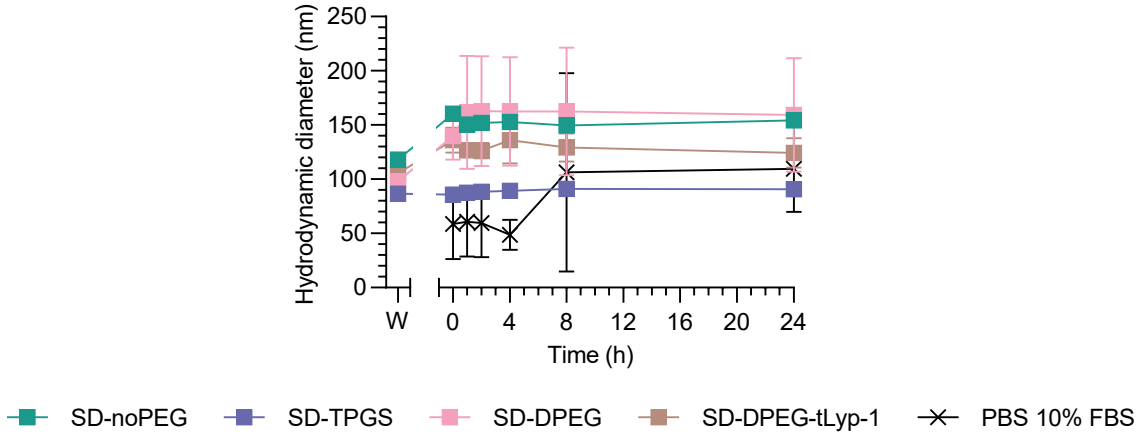


Figure 7. Stability of NCs in relevant simulated biological media (PBS 10 % FBS)

Abbreviations: FBS: fetal bovine serum. PBS: phosphate-buffered saline. W: NCs dispersed in water. The size increase was statistically significant for SD-noPEG for all time points and SD-DPEG-tLyp-1 for 0 and 1h (two-way ANOVA *versus* NCs dispersed in water). However, the hydrodynamic diameter of the last formulation exhibited a high variability. The compositions of SD-noPEG, SD-TPGS, SD-DPEG, and SD-DPEG-tLyp-1 are shown in Figure 5. Values represent the mean ± standard deviation (n = 3).

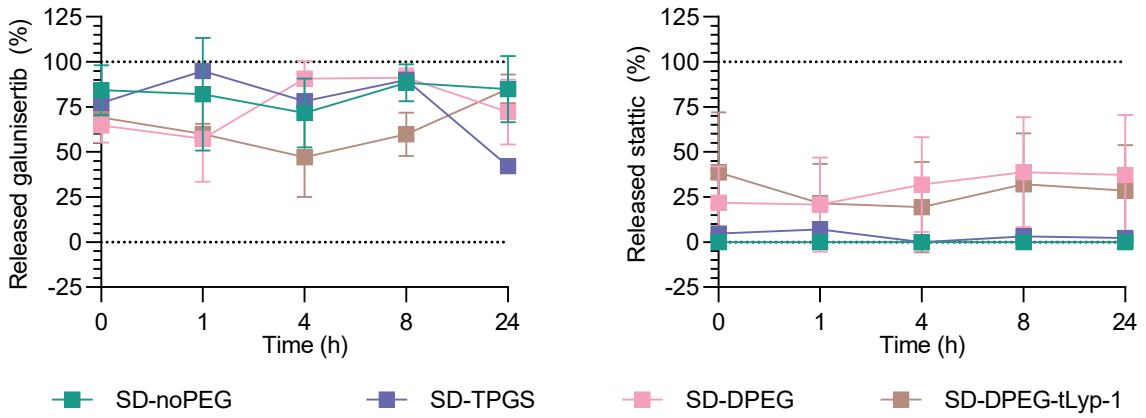


Figure 8. Release of galunisertib (left) and stattic (right) from NCs after 10-× dilution in PBS supplemented with 10 % FBS

The compositions of SD-noPEG, SD-TPGS, SD-DPEG, and SD-DPEG-tLyp-1 are shown in Figure 5. Values represent the mean ± standard deviation (n = 3).

3.2. CELLULAR UPTAKE

Blank NCs were labeled with DiD, and the uptake was studied in the CMT 167 murine cancer cell line and RAW 267.4 murine macrophage cell line. Results from DiD association efficiencies are presented in Table 13.

Table 13. DiD association efficiencies for SD-noPEG, SD-TPGS, SD-DPEG, and SD-DPEG-tLyp-1 NCs

	SD-noPEG	SD-TPGS	SD-DPEG	SD-DPEG-tLyp-1
DiD AE (%)	98 ± 2	69 ± 18	93 ± 8	80 ± 17

The compositions of SD-noPEG, SD-TPGS, SD-DPEG, and SD-DPEG-tLyp-1 are shown in Figure 5. **Abbreviations:** AE: association efficiency. Values represent the mean ± standard deviation (n = 3).

The results of DiD AE are in agreement with those of the drugs. DiD AEs were high for SD-noPEG and SD-DPEG. Also, the lowest DiD AE was found for SD-TPGS. In this sense, DiD might also be partially placed in micelles, leading to that low AE.

The release of DiD from the NCs was checked for SD-TPGS and SD-noPEG upon 10 × dilution in PBS and water, respectively. DiD was found not to be released from the NCs.

However, the use of DiD as a dye for NCs implies important limitations. DiD release profile can completely change in the presence of cells, as the dye can be transferred to the hydrophobic cell membranes independently of the internalization of NCs, leading to an overestimation of the NCs' uptake. Furthermore, the use of the free dye as a control is not suitable since it would label cell membranes when added as a solution. Therefore, the results of the in vitro uptake of DiD-labeled NC should be cautiously considered.

The results from the DiD iMFI in CMT 167 and RAW 264.7 cells at 37 °C compared to 4 °C showed a tendency for temperature-dependent uptake (Figure 9). Also, the results showed a mild tendency for dose-response uptake. SD-DPEG-tLyp-1 exhibited the highest uptake. However, a significant iMFI was detected for this system at 4 °C in RAW 264.7 macrophages, suggesting the extraordinary uptake could be an artifact of a more intense dye transfer to cell membranes.

USC UNIVERSIDADE DE SANTIAGO DE COMPOSTELA

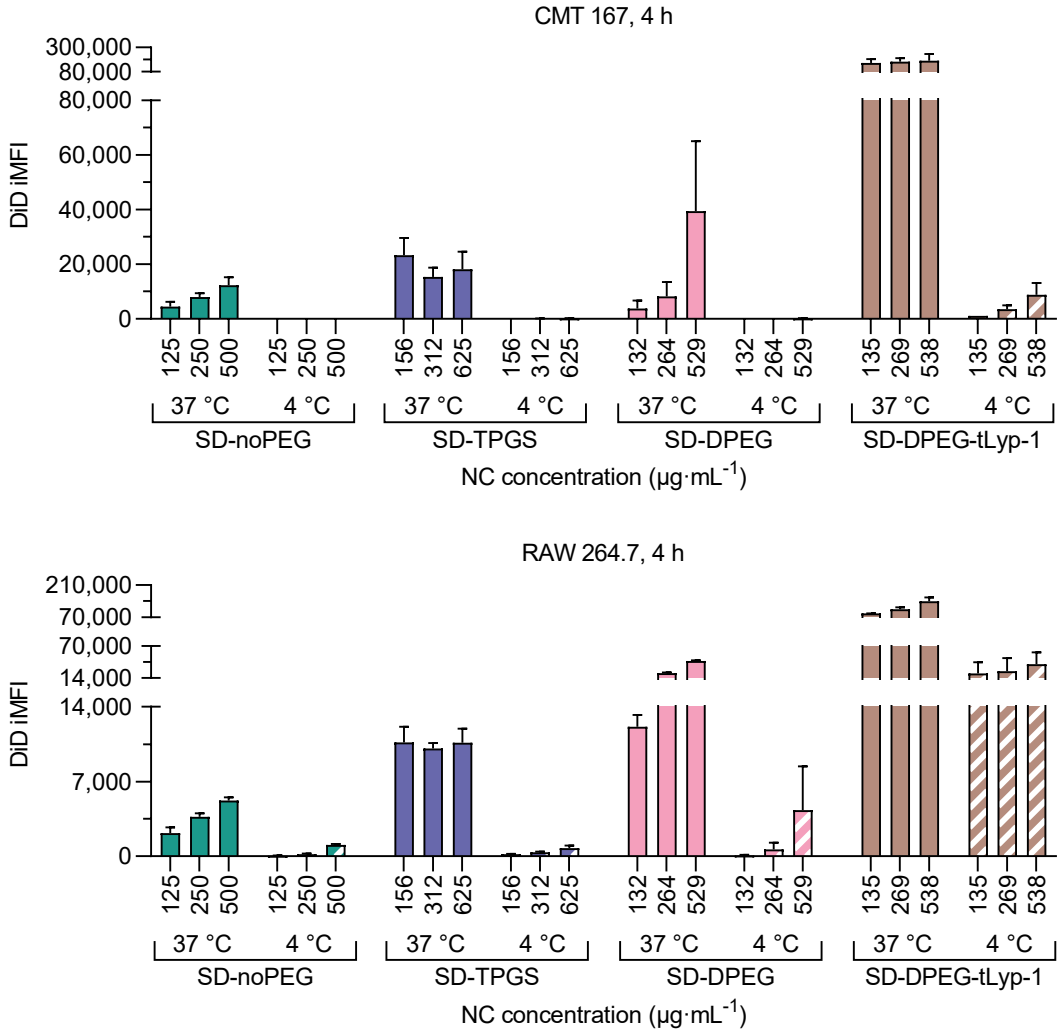


Figure 9. Cellular uptake (DiD iMFI) of DiD-labeled SD-noPEG, SD-TPGS, SD-DPEG, and SD-DPEG-tLyp-1 at 37 ˚C or 4 ˚C in CMT 167 (top) and RAW 264.7 (bottom)

Abbreviations: iMFI: integrated mean fluorescence intensity. The compositions of SD-noPEG, SD-TPGS, SD-DPEG, and SD-DPEG-tLyp-1 are shown in Figure 5. Values represent the mean ± standard deviation (n = 2).

3.3. *IN VITRO* CYTOTOXICITY

The *in vitro* cytotoxicity of the blank and galunisertib and stattic co-loaded NCs was studied in RAW 264.7 macrophages and CMT 167 lung cancer cell lines after 24 h of NCs exposure (Figure 10).

Blank NCs were found not to be toxic in the tested range for CMT 167 cancer cells. However, SD-noPEG, SD-DPEG-tLyp-1, and, to a lesser extent, SD-DPEG led to significant cytotoxicity in RAW 264.7 macrophages (unpaired t-tests *vs.* 100 % viability control, with individual variances computed for each comparison) (Supplementary Figure 8).

With the aim of knowing the effect of the encapsulation of the drugs on their cytotoxicity, the raw viability data (Supplementary Figure 9) were normalized considering the toxicity of the blank NCs.

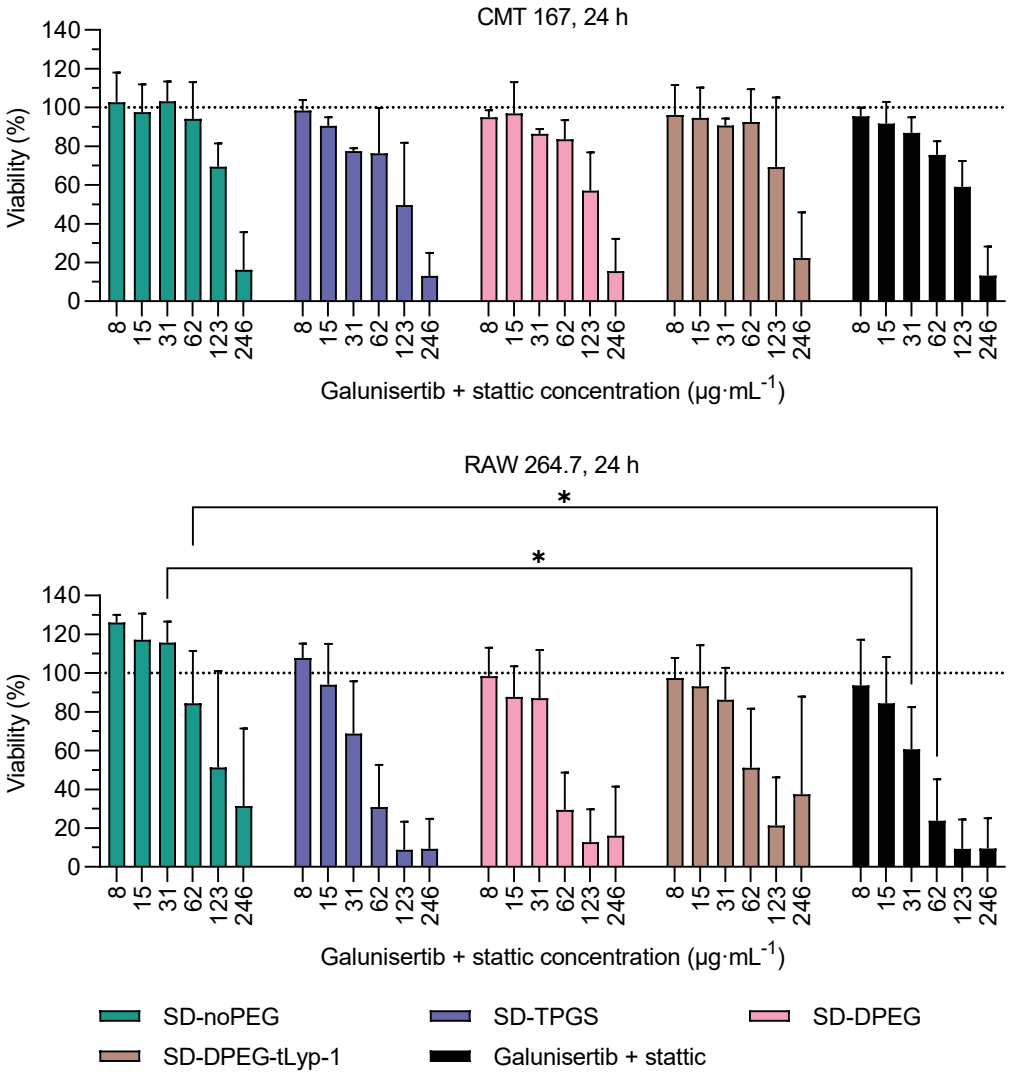


Figure 10. *In vitro* cytotoxicity of galunisertib and stattic loaded NCs and free galunisertib and stattic

Unpaired t-tests of each drug-loaded NCs *vs.* free drugs for each concentration value. *p*-values < 0.05 were considered statistically significant (*). The compositions of SD-noPEG, SD-TPGS, SD-DPEG, and SD-DPEG-tLyp-1 are shown in Figure 5. Values represent the mean ± standard deviation (n = 3).

Dose-dependent toxicity was found for all NCs. The toxicity of all the drug-loaded NCs in CMT 167 was similar to that of the free drugs, meaning their efficacy might be preserved *in vivo* while adverse effects might be reduced due to the differences in biodistribution of the NCs in comparison with the free drugs. The same situation was found for RAW 264.7, except for SD-noPEG, which exhibited a significant toxicity reduction at the concentrations of 31 and 62 $\mu g \cdot mL^{-1}$ of drugs.

The effect of the single drugs was evaluated in the case of SD-noPEG NCs in the RAW 264.7 cell line (Supplementary Figure 10). The toxicity of the co-loaded NCs resulted in being mainly stattic-driven, as viability was not affected even at the highest concentration level (234 $\mu g \cdot mL^{-1}$ of galunisertib) when the NCs were exclusively loaded with galunisertib. In contrast, in the case of the galunisertib and stattic-loaded NCs, complete cytotoxicity was observed for the same NCs concentration.

Then, the IC_{50}s values of the stattic and galunisertib-loaded NCs and free drugs were calculated based on the data from Figure 10. In general, the encapsulation of the drugs preserved the cytotoxicity of the drugs in CMT 167 cancer cell line as all the IC_{50}s were very similar and close to that of the free drug combination (1.3, 1.3, 1.1, and 0.9-fold that of free drugs for SD-noPEG, SD-DPEG-tLyp-1, SD-DPEG, and SD-TPGS, respectively). However, the encapsulation of the drugs led to a more pronounced increase in their IC_{50} value in the case of RAW 264.7 macrophages (approximately 3.92, 2.12, 1.36, and 1.2-fold that of free drugs for SD-noPEG, SD-DPEG-tLyp-1, SD-DPEG, and SD-TPGS, respectively). In this sense, SD-noPEG (in agreement with the statistical significance detected in Figure 10) and SD-DPEG-tLyp-1 were identified as the most promising NCs preserving the cytotoxicity in cancer cells while reducing it in macrophages.

In the literature, the entrapment of stattic had a variable effect on its IC_{50} value, which was dependent both on the nanosystem type and cell line. For example, the cytotoxicity of stattic was enhanced when loaded into PLGA NPs (45 % lower IC_{50}) in 4T1 cells,[72] albumin NPs (60 % lower IC_{50}) in MDA-MB-231 cells,[76] and modified-polyacrylamide polymeric micelles (98 % lower IC_{50}) in MCF7, MDA-MB-231, and 4T1 cell lines. On the contrary, stattic IC_{50} was increased when loaded in albumin NPs in MCF7 cells (37 % increase)[76] and in docosahexaenoic acid-resiquimod micelles in HEK293T cells.[73] Unluckily, no study was carried out in CMT 167 or RAW 264.7 cell lines, making it impossible to establish comparisons with previously published works.

3.4. *IN VITRO* STAT3 AND TGF-B PATHWAYS INHIBITION EFFICACY

After the cytotoxicity studies, the efficacy of the galunisertib-loaded and stattic-loaded SD-noPEG inhibiting the TGF-β and STAT3 pathways of RAW 264.7 macrophages was studied *in vitro*. NO and CCL2 productions were read out in lipopolysaccharides (LPS)-stimulated macrophages exposed to stattic, while NO, IL-6, and CCL2 productions were studied for galunisertib (Figure 11).

Unluckily, while these markers were found to be optimal for the study of the efficacy of both drugs separately, the efficacy of the co-loaded NCs could not be tested as galunisertib and stattic cause opposite effects on these markers.

Stattic-loaded and galunisertib-loaded SD-noPEG NCs were significantly effective in RAW 264.7 macrophages reducing nitrite and CCL2 production and increasing nitrite, IL-6, and CCL2 production, respectively (one-way ANOVA *vs.* LPS + IL-10 or LPS + TGF-β groups with a Dunnett posthoc test). While stattic-loaded SD-noPEG efficacy was lower than that of the free drug, the contrary was observed for galunisertib.

In vivo toxicity studies are being performed to establish the appropriate experimental protocol of administration to assess the efficacy of the formulations.

USC UNIVERSIDADE DE SANTIAGO DE COMPOSTELA

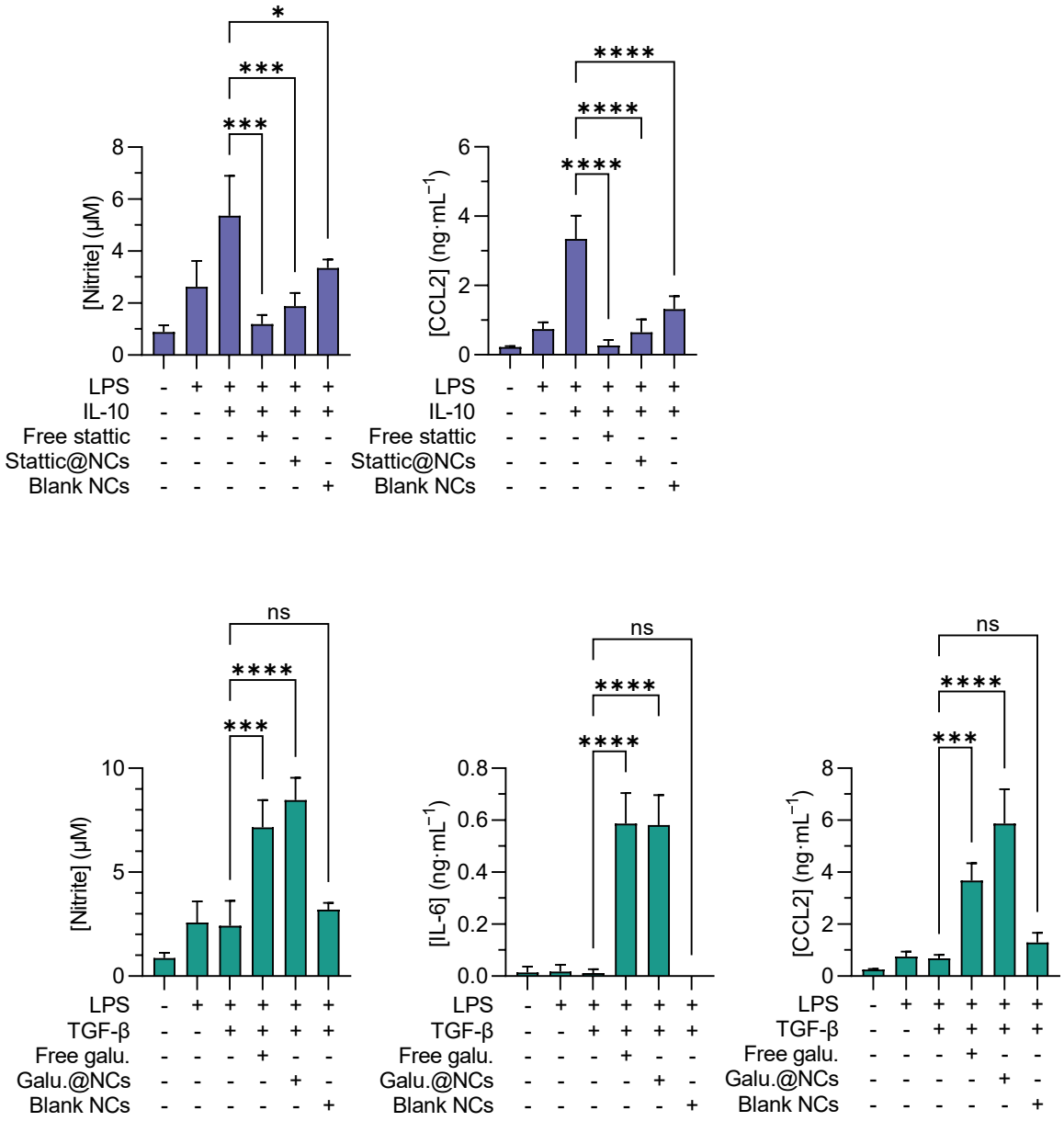


Figure 11. ***In vitro*** **efficacy of stattic-loaded and galunisertib-loaded SD-noPEG NCs in RAW 264.7 macrophages**

For the stattic efficacy study (top), the STAT3 pathway was activated by the addition of LPS + IL-10. Then, free stattic, stattic-loaded SD-noPEG, and blank NCs were added. Reductions in nitrite and CCL2 production were checked. In the case of galunisertib (bottom), the TGF-ß pathway was activated by the addition of LPS + TGF-ß. Then, free galunisertib, galunisertib-loaded SD-noPEG, and blank NCs were added. Increases in nitrite, IL-6, and CCL2 production were checked. Stattic-loaded and galunisertib-loaded SD-noPEG NCs were effective. While stattic-loaded SD-noPEG efficacy was lower than that of the free drug, the contrary was observed for galunisertib. **Abbreviations:** Galu.: galunisertib. IL: interleukin. LPS: lipopolysaccharide. NCs: nanocapsules. TGF-ß: Transforming growth factor-ß. The composition of SD-noPEG is shown in Figure 5. Values represent the mean ± standard deviation of two cell replicates and one NC replicate. One-way ANOVA *vs.* LPS + IL-10 or LPS + TGF-ß groups with a Dunnett posthoc test. *p*-values < 0.05 were considered statistically significant (*). Also, (**) if *p*-value < 0.01, (***) if *p*-value < 0.001 and (****) if *p*-value < 0.0001. ns: not significative.

USC UNIVERSIDADE DE SANTIAGO DE COMPOSTELA

4. CONCLUSIONS

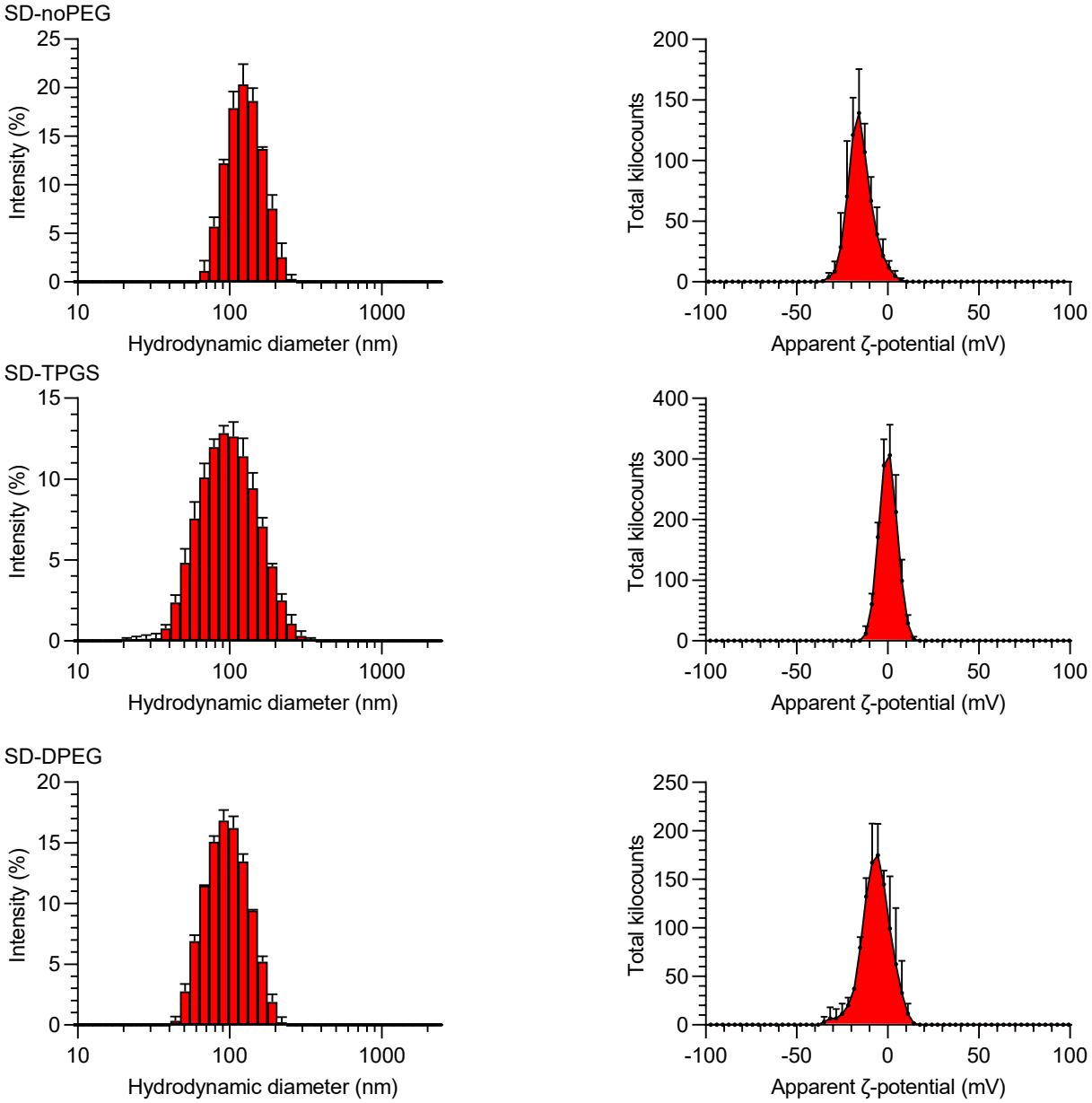
The encapsulation of galunisertib and stattic on NCs preserves the antitumoral activity of the drugs in cancer cells while slightly reducing the toxicity in tumor-associated macrophages.

SD-noPEG loaded with stattic or galunisertib was found to successfully inhibit the STAT3 and TGF-β pathways, respectively, in RAW 264.7 macrophages.

The benefits from their co-encapsulation in terms of synergy and reduction of adverse effects are promising for continuing their evaluation *in vivo*.

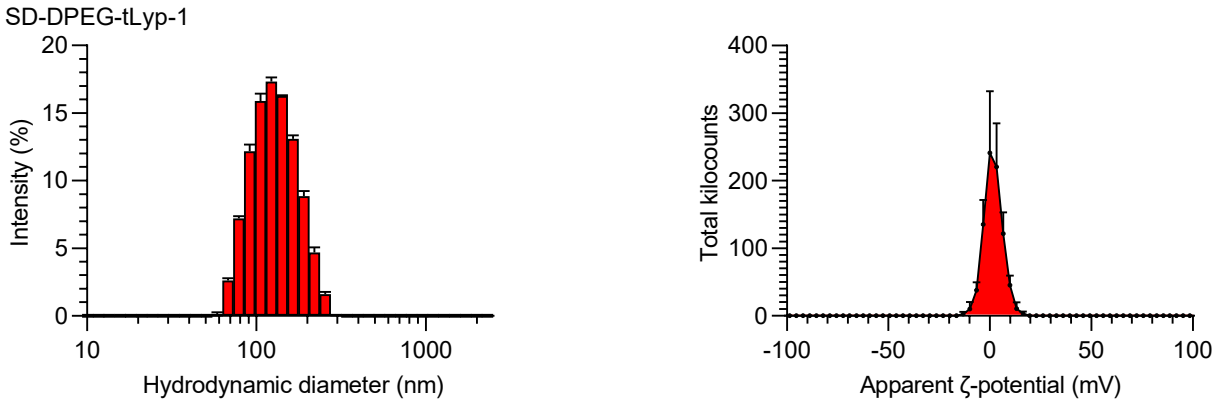
USC
UNIVERSIDADE
DE SANTIAGO
DE COMPOSTELA

5. SUPPLEMENTARY INFORMATION



Supplementary Figure 1. Representative DLS hydrodynamic diameter distributions and ζ-potential of different galunisertib and stattic-loaded NCs

USC
UNIVERSIDADE DE SANTIAGO DE COMPOSTELA



Supplementary Figure 1. Representative DLS hydrodynamic diameter distributions and ζ-potential of different galunisertib and stattic-loaded NCs (continuation)

The compositions of SD-noPEG, SD-TPGS, SD-DPEG, and SD-DPEG-tLyp-1 are shown in Figure 5.

Supplementary Table 1. Physicochemical characterization of the blank SD-TPGS, SD-noPEG, SD-DPEG, and SD-DPEG-tLyp-1 NCs

	SD-noPEG	SD-TPGS	SD-DPEG	SD-DPEG-tLyp-1
Hydrodynamic diameter (DLS) (nm)	149 ± 2	87 ± 1	115 ± 1	118 ±11
PDI	0.09 ± 0.06	0.16 ± 0.01	0.09 ± 0.02	0.12 ± 0.03
ζ-potential (mV)	−21 ± 1	−1 ± 1	−8 ± 1	+1 ± 1
pH	7.1 ± 0.2	7.5 ± 0.1	7.6 ± 0.3	6.9 ± 0.4

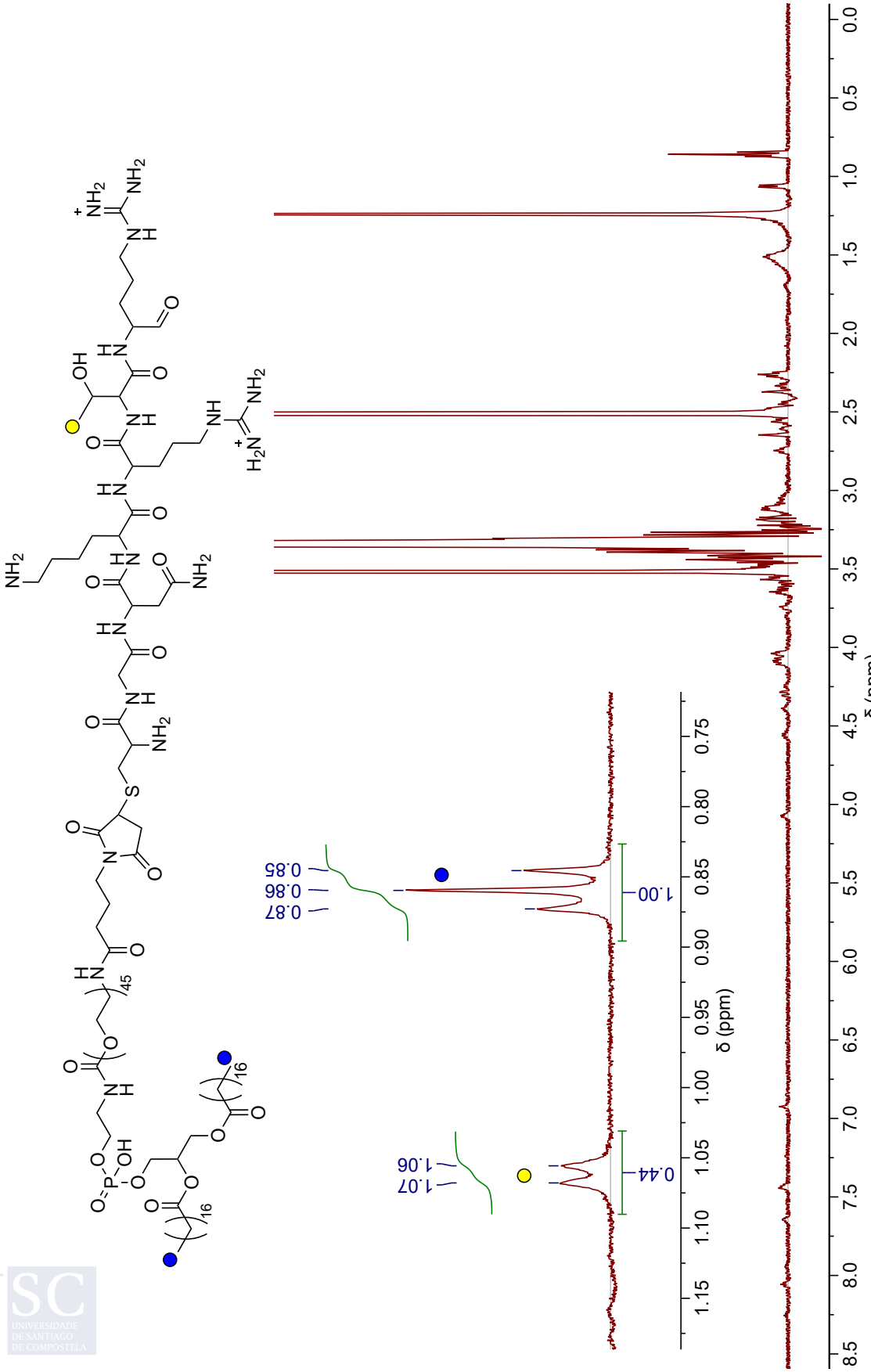
The compositions of SD-noPEG, SD-TPGS, SD-DPEG, and SD-DPEG-tLyp-1 are shown in Figure 5. **Abbreviations:** DLS: dynamic light scattering. PDI: polydispersity index. Values represent the mean ± standard deviation (n = 3).

Supplementary Table 2. Physicochemical characterization of the single-drug loaded (galunisertib or stattic) SD-noPEG

	SD-noPEG (only galunisertib)	SD-noPEG (only stattic)
Hydrodynamic diameter (DLS) (nm)	120 ± 1	121 ± 4
PDI	0.03 ± 0.02	0.04 ± 0.02
ζ-potential (mV)	−16 ± 4	−21 ± 2
AE galunisertib (%)	61 ± 9	-
AE stattic (%)	-	50 ± 8
pH	5.7 ± 0.1	5.6 ± 0.2

The composition of SD-noPEG is shown in Figure 5.

USC UNIVERSIDADE DE SANTIAGO DE COMPOSTELA



Supplementary Figure 2. ^{1}H NMR (500 MHz; d_6-DMSO) spectrum of DSPE-PEG$_{2000}$-maleimide-tLyp-1

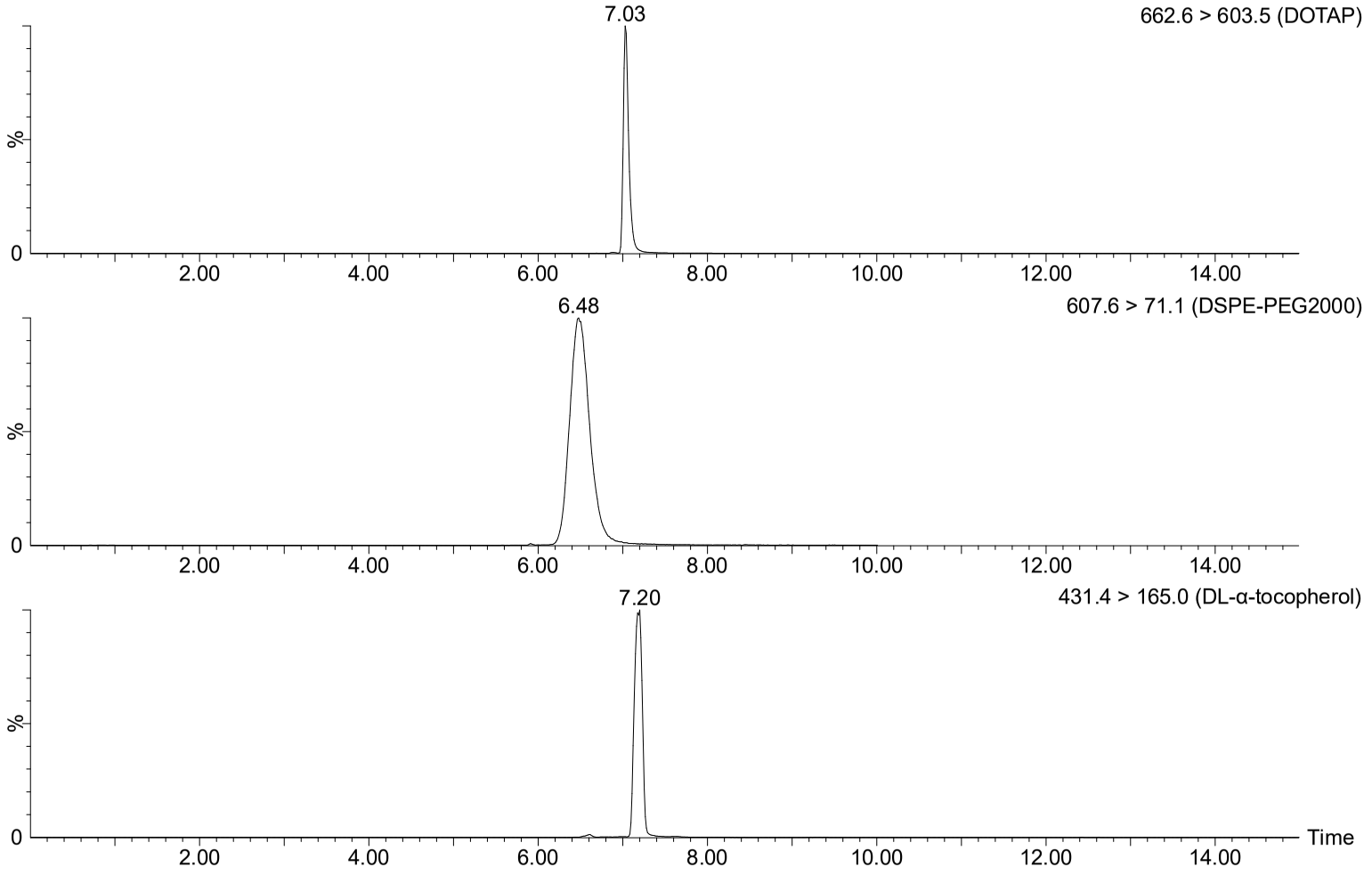
USC UNIVERSIDADE DE SANTIAGO DE COMPOSTELA

Supplementary Table 3. Validation of the calibration curves for each quantified substance and formulation

Formulation	Molecule	Calibration curve range (ppb)	r^2	Precision (pooled RStD%) (%)	Accuracy (RE%) (%) (low; mid; high range)	LoQ (ppb)
SD-DPEG	1,2-dioleoyl-3-trimethylammoniumpropane chloride	30.0 – 65.6	0.9971 ± 0.0025	0.5	0.5; −0.9; −0.7	0.16 ± 0.06
	$DSPE\text{-}PEG_{2000}$	55.2 – 120.8	0.9767 ± 0.0094	0.5	−1.1; −1.1; −1.1	1.19 ± 0.94
	DL-α-tocopherol	810.0 – 1771.9	0.9921 ± 0.0033	1.8	1.5; −1.0; 0.8	0.77 ± 0.10
SD-DPEG-tLyp-1	$DSPE\text{-}PEG_{2000}$-maleimide-tLyp-1 (supernatant)	12,690.0 – 101,500.0	0.9667 ± 0.0354	4.7	−6.3; 11.6; 11.6	1,915.08 ± 1,434.90
	$DSPE\text{-}PEG_{2000}$-maleimide-tLyp-1 (infranatant)	7,120.0 – 56,930.0	0.9850 ± 0.0128	4.0	7.1; 4.1; 4.1	15.42 ± 18.8
	PEG·PGA (supernatant)	41,600.0 – 332,800.0	0.9883 ± 0.0020	2.2	11.0; 4.3; 4.3	2,826.09 ± 3,366.59
	PEG-PGA (infranatant)	11,670.0 – 93,330.0	0.8924 ± 0.1760	18.8	15.3; 16.7; 16.7	3,007.19 ± 968.38
-	Stattic (HPLC-UV-Vis)	50.0 – 600.0	0.9920 ± 0.0017	3.3	−0.1; 5.1; 1.6	35.43 ± 10.04
-	Galunisertib (HPLC-UV-Vis)	1,000.0 – 12,000.0	0.9969 ± 0.0013	1.1	7.8; 3.6; −0.3	127.62 ± 23.74
-	Stattic (UHPLC-MS/MS)	5.0 – 1,000.0	-	-	-	≤ 5.0
-	Galunisertib (UHPLC-MS/MS)	5.0 – 1,000.0	-	-	-	≤ 5.0

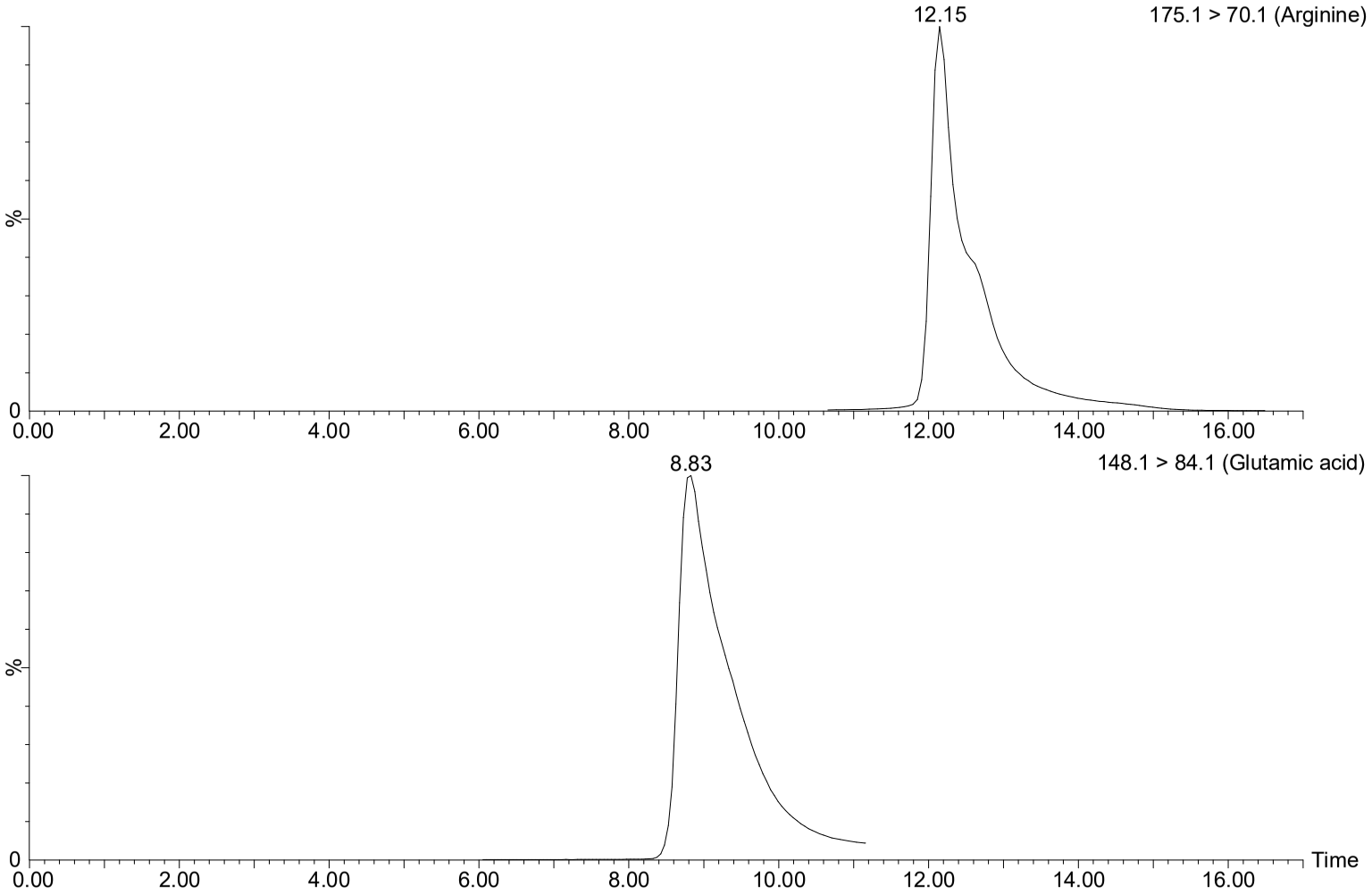
The compositions of SD-DPEG and SD-DPEG-tLyp-1 are shown in Figure 5. **Abbreviations:** StD: standard deviation. RStD%: Relative standard deviation of the responses for each concentration level. RE%: relative differences between the estimated concentrations and the actual standard concentration. LoQ: limit of quantification. TPGS: D-α-tocopherol polyethylene glycol 1000 succinate. Values represent the mean for pooled RStD% and RE% and the mean ± standard deviation for r^2 and LoQ (n = 3).

Supplementary Table 4. Chromatograms of all the chromatographic methods for the NCs

Chromatographic method	Chromatogram
Hydrophobic substances of SD-DPEG	

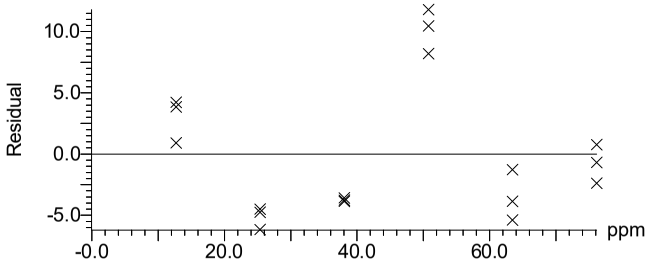
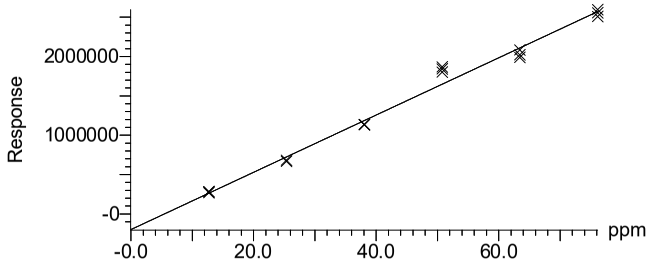
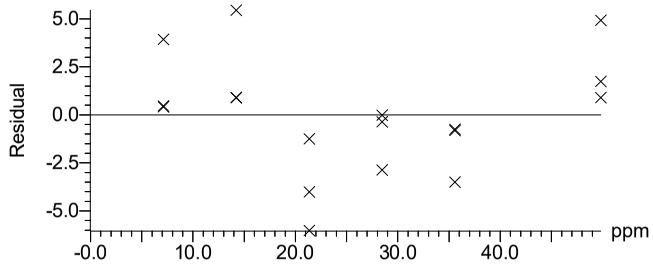
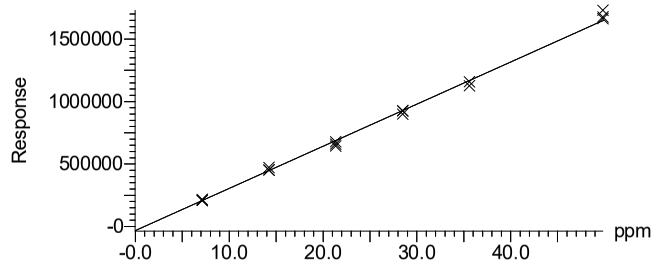
The composition of SD-DPEG is shown in Figure 5.

Supplementary Table 4. Chromatograms of all the chromatographic methods for the NCs (continuation)

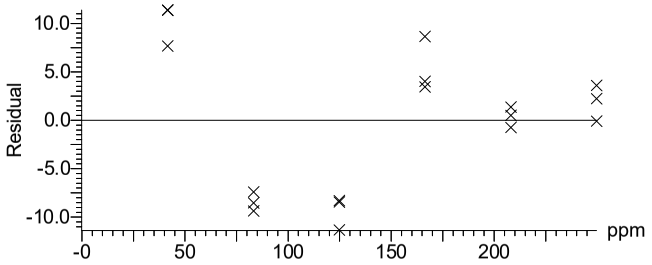
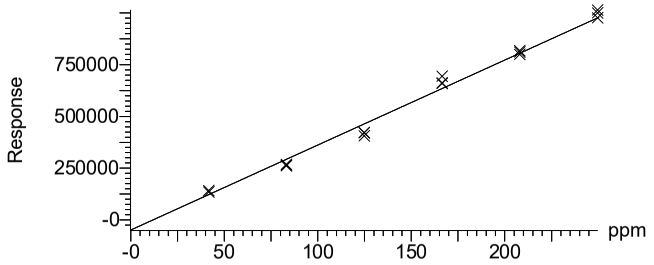
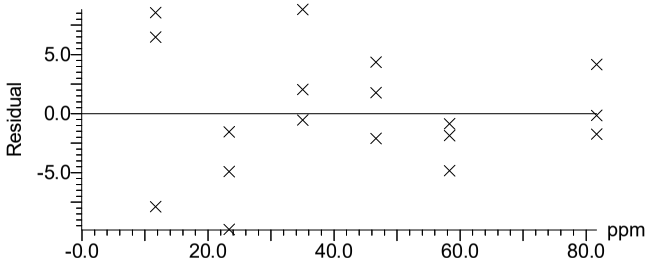
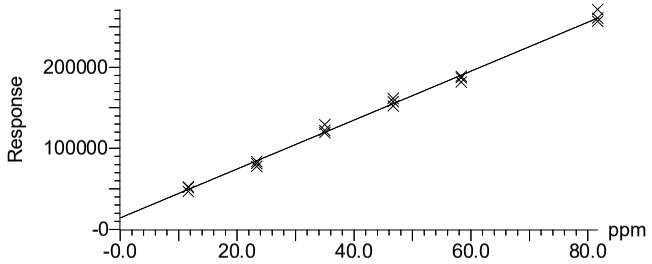
Chromatographic method	Chromatogram
Digested SD-DPEG-tLyp-1	

The composition of SD-DPEG is shown in Figure 5

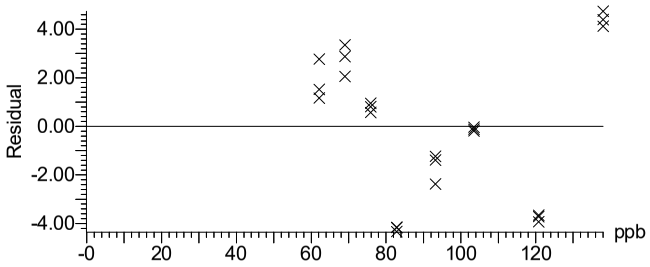
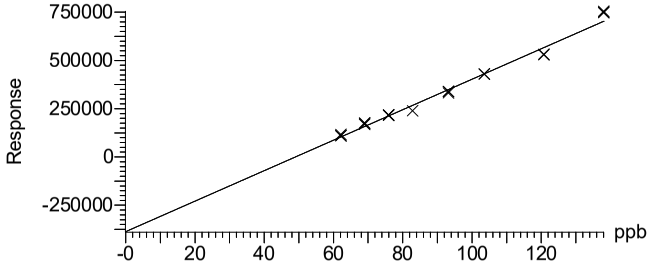
Supplementary Table 5. Calibration curves and residual plots of DSPE-PEG-mal-tLyp-1, PEG·PGA, and DSPE-PEG

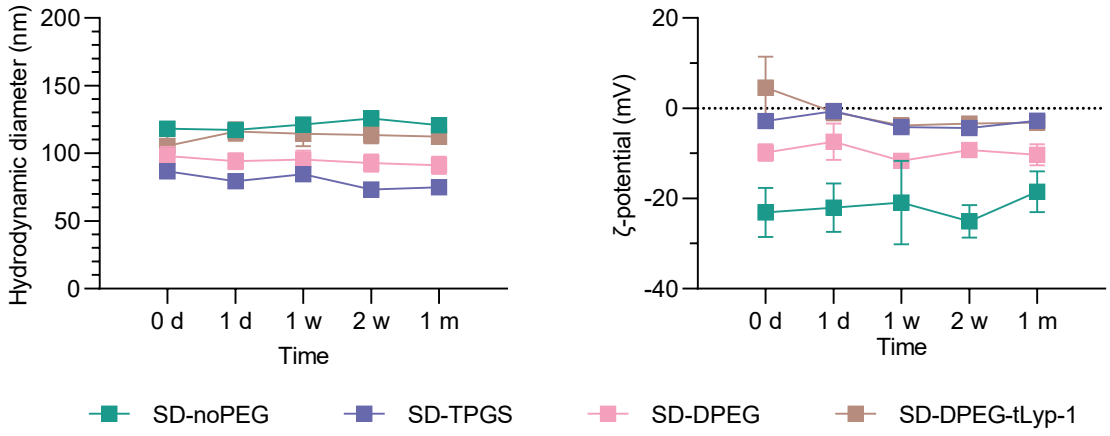
Molecule	Residual plots and calibration curves
Digested DSPE-PEG-mal-tLyp-1 (cream)	Compound name: Digested DSPE-PEG-mal-tLyp-1 Correlation coefficient: r = 0.995142, r^2 = 0.990307 Calibration curve: 36426.9 * x + -199042 Response type: External Std, Area Curve type: Linear, Origin: Exclude, Weighting: 1/x, Axis trans: None  
Digested DSPE-PEG-mal-tLyp-1 (infranatant)	Compound name: Digested DSPE-PEG-mal-tLyp-1 Correlation coefficient: r = 0.998752, r^2 = 0.997506 Calibration curve: 33725.1 * x + -32009.4 Response type: External Std, Area Curve type: Linear, Origin: Exclude, Weighting: 1/x, Axis trans: None  

Supplementary Table 5. Calibration curves and residual plots of DSPE-PEG-mal-tLyp-1 (continuation)

Molecule	Residual plots and calibration curves
Digested PEG·PGA (cream)	Compound name: Digested PEG-PGA Correlation coefficient: r = 0.994532, r^2 = 0.989093 Calibration curve: 4112.08 * x + -48739.6 Response type: External Std, Area Curve type: Linear, Origin: Exclude, Weighting: 1/x, Axis trans: None  
Digested PEG·PGA (infranatant)	Compound name: Digested PEG-PGA Correlation coefficient: r = 0.997552, r^2 = 0.995111 Calibration curve: 3021.15 * x + 14229.1 Response type: External Std, Area Curve type: Linear, Origin: Exclude, Weighting: 1/x, Axis trans: None  

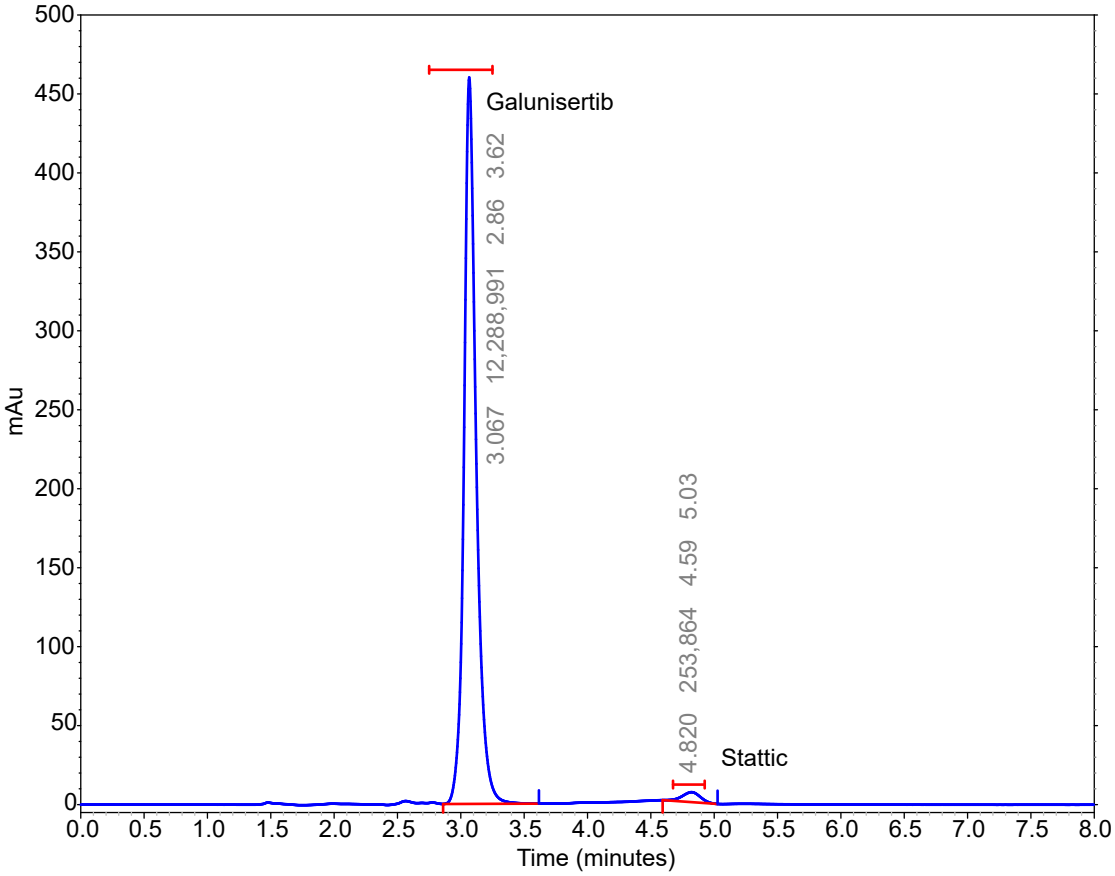
Supplementary Table 5. Calibration curves and residual plots of DSPE-PEG-mal-tLyp-1 (continuation)

Molecule	Residual plots and calibration curves
DSPE-PEG	Compound name: DSPE-PEG Correlation coefficient: r = 0.992754, r^2 = 0.985560 Calibration curve: 7898.65 * x + -386755 Response type: External Std, Area Curve type: Linear, Origin: Exclude, Weighting: 1/x, Axis trans: None  



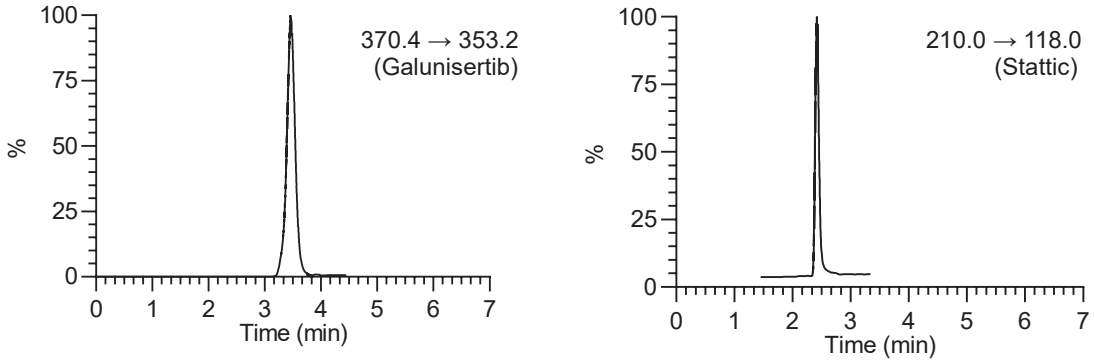
Supplementary Figure 3. Galunisertib and stattic loaded NCs stability in storage conditions (4 °C)

The compositions of SD-noPEG, SD-TPGS, SD-DPEG, and SD-DPEG-tLyp-1 are shown in Figure 5.

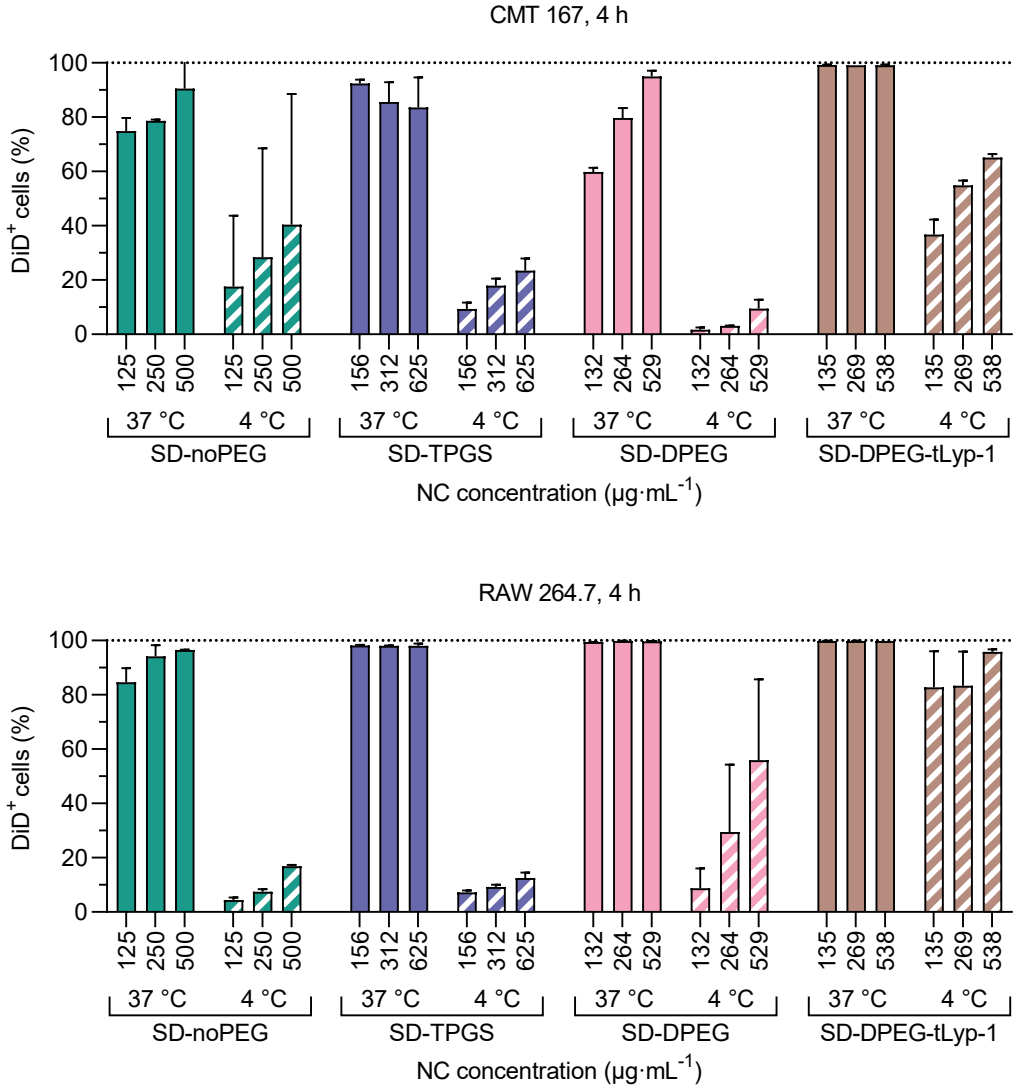


Supplementary Figure 4. Example of galunisertib and stattic HPLC-UV-Vis chromatogram

USC
UNIVERSIDADE DE SANTIAGO DE COMPOSTELA



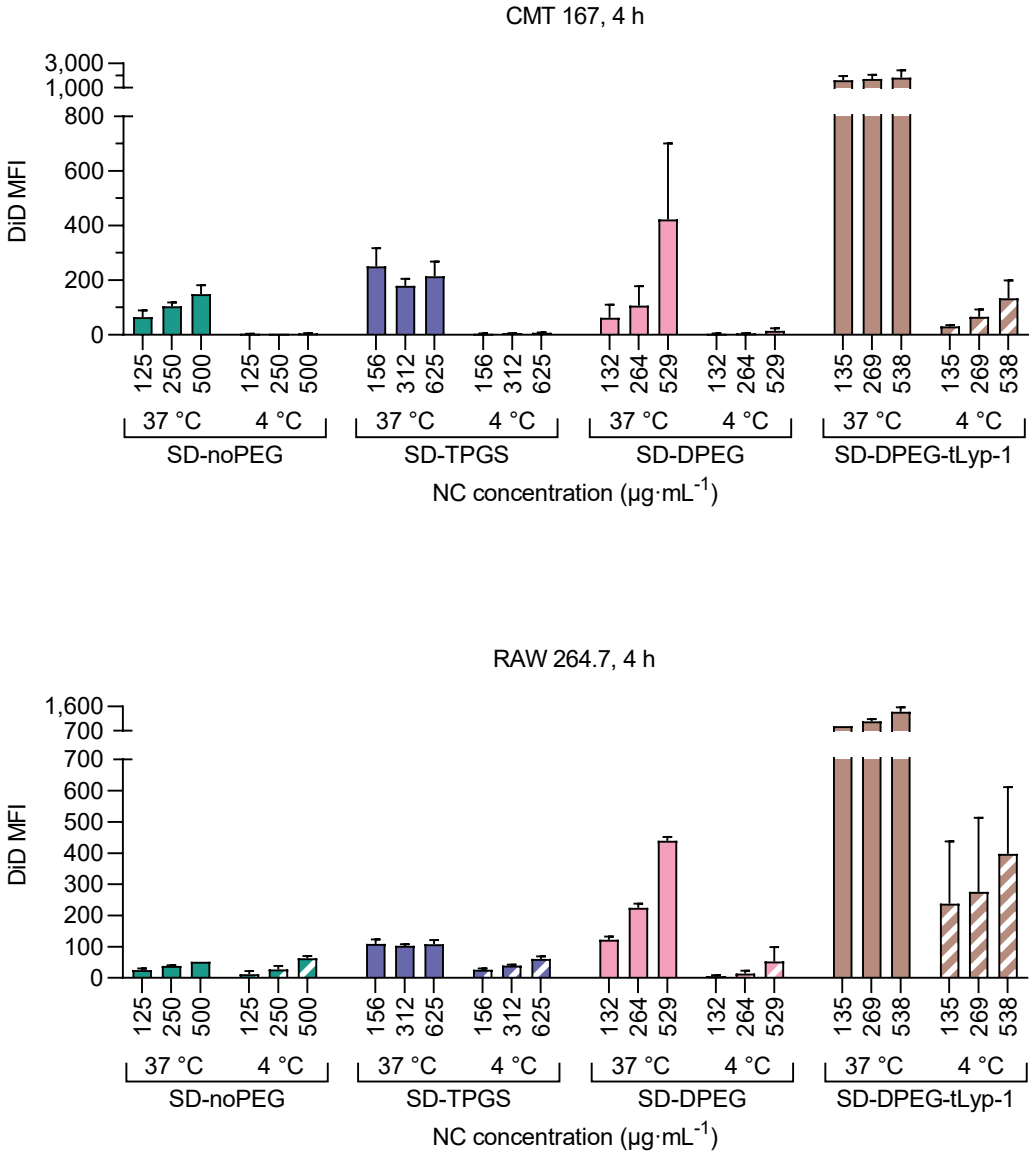
Supplementary Figure 5. Example of galunisertib and stattic UHPLC-MS/MS chromatograms



Supplementary Figure 6. Percentage of DiD-positive CMT 167 (top) and RAW 264.7 (bottom) cells after incubation with DiD-labeled SD-noPEG, SD-TPGS, SD-DPEG, and SD-DPEG-tLyp-1 at 37 ˚C or 4 ˚C

Values represent the mean ± standard deviation (n = 3). The compositions of SD-noPEG, SD-TPGS, SD-DPEG, and SD-DPEG-tLyp-1 are shown in Figure 5.

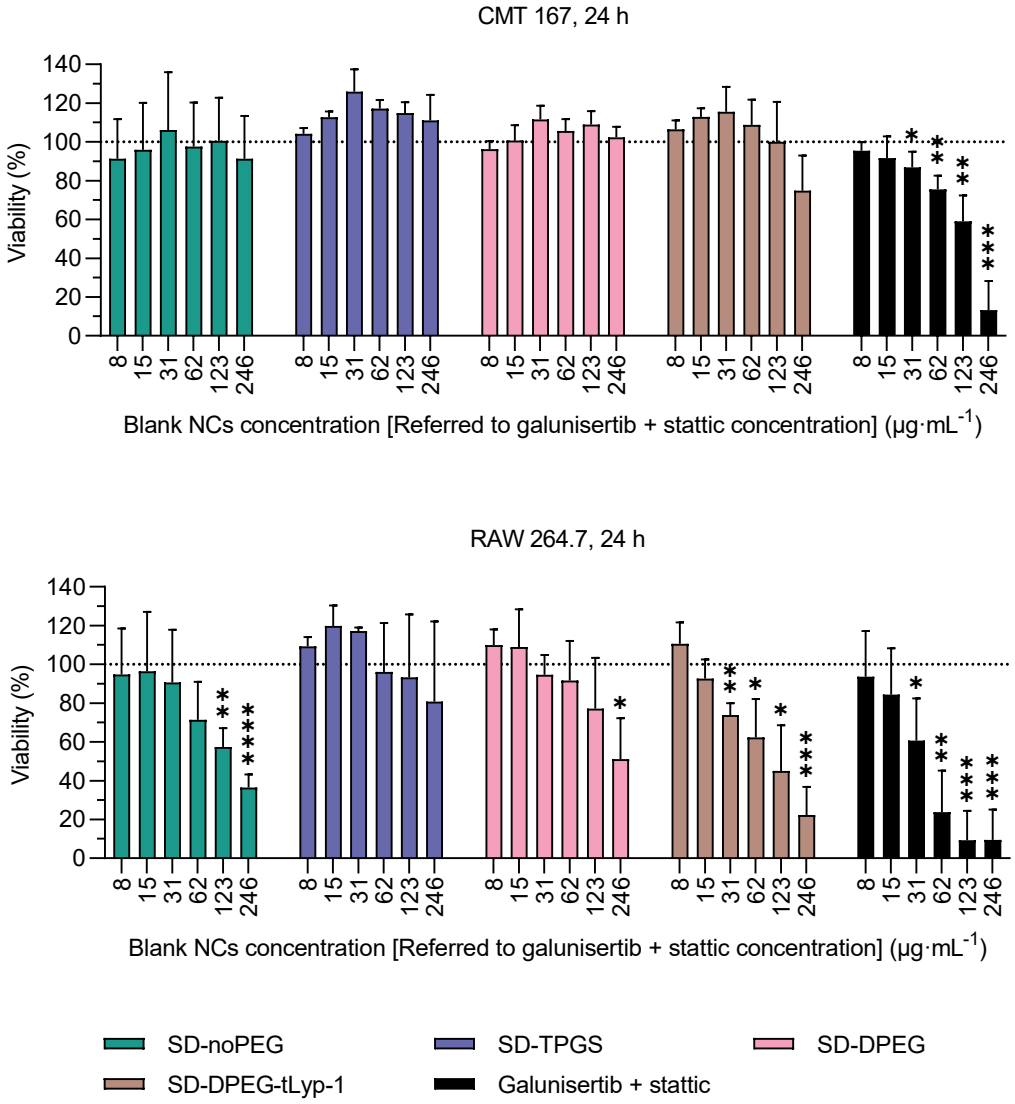
UDC UNIVERSIDADE DE SANTIAGO DE COMPOSTELA



Supplementary Figure 7. Median fluorescence intensity of DiD in CMT 167 (top) and RAW 264.7 (bottom) cells after incubation with DiD-labeled SD-noPEG, SD-TPGS, SD-DPEG, and SD-DPEG-tLyp-1 at 37 °C or 4 °C

Abbreviations: MFI: mean fluorescence intensity. Values represent the mean ± standard deviation (n = 3). The compositions of SD-noPEG, SD-TPGS, SD-DPEG, and SD-DPEG-tLyp-1 are shown in Figure 5.

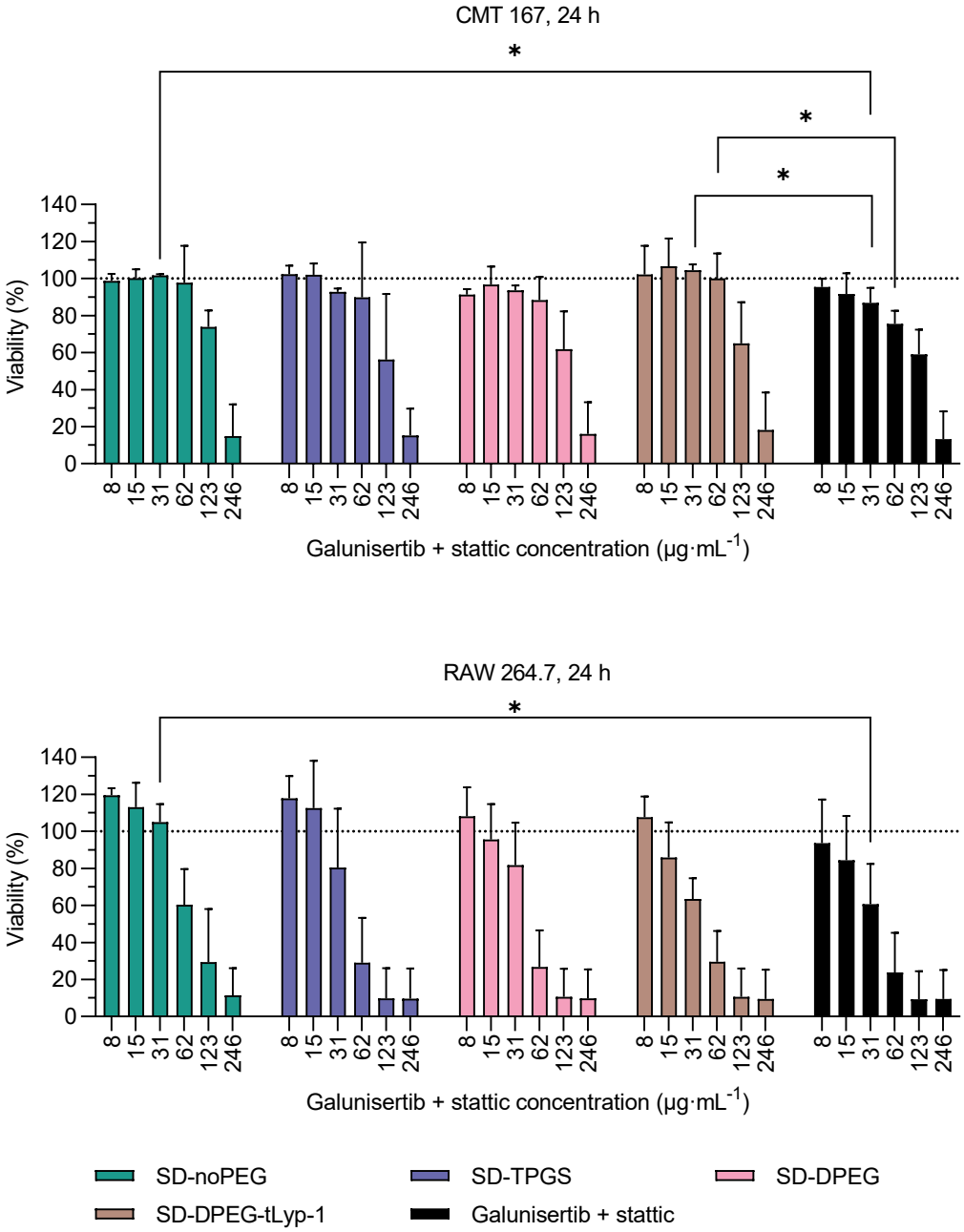
USC UNIVERSIDADE DE SANTIAGO DE COMPOSTELA



Supplementary Figure 8. ***In vitro*** **cytotoxicity blank NCs and free galunisertib and stattic in CMT 167 (top) and RAW 264.7 (bottom) cell lines**

Blank NCs were diluted to the same concentration values as those for the loaded NCs presented in Figure 10. Values represent the mean ± standard deviation (n = 3). Unpaired t-tests of each drug loaded NCs or free drugs *vs.* 100 % viability control for each concentration value. *p*-values < 0.05 were considered statistically significant (*). Also, (**) if *p*-value < 0.01, (***) if *p*-value < 0.001 and (****) if *p*-value < 0.0001. The compositions of SD-noPEG, SD-TPGS, SD-DPEG, and SD-DPEG-tLyp-1 are shown in Figure 5.

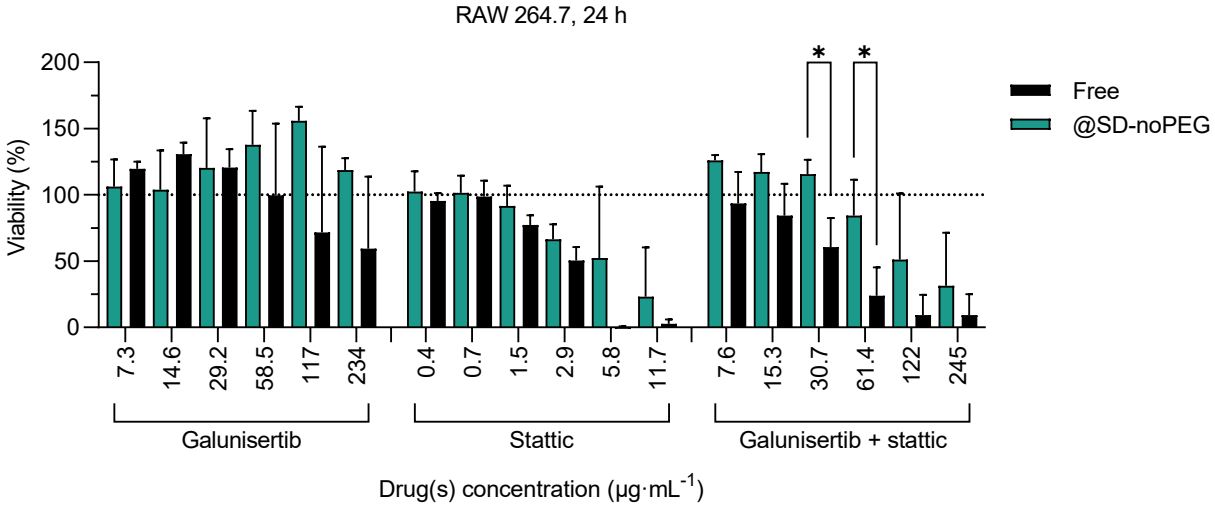
USC UNIVERSIDADE DE SANTIAGO DE COMPOSTELA



Supplementary Figure 9. *In vitro* cytotoxicity of galunisertib and stattic loaded NCs and free galunisertib and stattic in CMT 167 (top) and RAW 264.7 (bottom) cell lines

Values represent the mean ± standard deviation (n = 3). Unpaired t-tests of each drug-loaded NCs *vs.* free drugs for each concentration value. *p*-values < 0.05 were considered statistically significant (*). The compositions of SD-noPEG, SD-TPGS, SD-DPEG, and SD-DPEG-tLyp-1 are shown in Figure 5.

USC UNIVERSIDADE DE SANTIAGO DE COMPOSTELA



Supplementary Figure 10. ***In vitro*** **cytotoxicity of galunisertib, stattic, and galunisertib and stattic free or encapsulated into SD-noPEG in RAW 264.7 cell line**

Values represent the mean ± standard deviation (n = 3). Unpaired t-tests of each drug-loaded NCs *vs.* free drugs for each concentration value. *p*-values < 0.05 were considered statistically significant (*). The composition of SD-noPEG is shown in Figure 5.

6. ACKNOWLEDGMENTS

This work was supported by the Spanish Ministry of Economy and Industry. Project "Nano-Inmunoterapia: Targeting Intracelular de Células Tumorales y Tams" 2-INTRATARGET (Ref.: MINECO- PCIN-2017-129/ AEI), under the frame of EuroNanoMed III" and by the Competitive Reference Groups, Consellería de Educación e Ordenación Universitaria, Xunta de Galicia, Ref: ED431C 2017/09. G. Berrecoso acknowledges the financial support by the Xunta de Galicia through the "Axudas de apoio á etapa predoutoral 2018" grant, co-funded by the European Social Fund "FSE Galicia 2014-2020".

Stattic and galunisertib release studies were carried out in collaboration with SINTEF AS, Norway.

In vitro STAT3 and TGF-β pathways inhibitions were carried out in collaboration with Clément Anfray, Ph.D., at the research group of Paola Allavena (Humanitas Research Hospital, Pieve Emanuele, Milano, 20072, Italy).

7. REFERENCES

[1] D. Liu, M. Furqan, A. Akinleye, N. Mukhi, V. Mittal, Y. Chen. STAT inhibitors for cancer therapy. *Journal of Hematology and Oncology*. 6, 1–11. (2013). doi: 10.1186/1756-8722-6-90.

[2] P. Yue, J. Turkson. Targeting STAT3 in cancer: How successful are we? *Expert Opinion on Investigational Drugs*. 18, 45–56. (2009). doi: 10.1517/13543780802565791.

[3] S. L. Furtek, D. S. Backos, C. J. Matheson, P. Reigan. Strategies and Approaches of Targeting STAT3 for Cancer Treatment. *ACS Chemical Biology*. 11, 308–318. (2016). doi: 10.1021/acschembio.5b00945.

[4] S. Akira, Y. Nishio, M. Inoue, X.-J. Wang, S. We, T. Matsusaka, K. Yoshida, T. Sudo, M. Naruto, T. Kishimoto. Molecular cloning of APRF, a novel IFN-stimulated gene factor 3 p91-related transcription factor involved in the gp130-mediated signaling pathway. *Cell*. 77, 63–71. (1994). doi: 10.1016/0092-8674(94)90235-6.

[5] Z. Zhong, Z. Wen, J. E. Darnell. Stat3: a STAT Family Member Activated by Tyrosine Phosphorylation in Response to Epidermal Growth Factor and Interleukin-6. *Science*. 264, 95–98. (1994). doi: 10.1126/science.8140422.
[6] Y. Verhoeven, S. Tilborghs, J. Jacobs, J. De Waele, D. Quatannens, C. Deben, H. Prenen, P. Pauwels, X. B. Trinh, A. Wouters, E. L. J. Smits, F. Lardon, P. A. van Dam. The potential and controversy of targeting STAT family members in cancer. *Seminars in Cancer Biology*. 60, 41–56. (2020). doi: 10.1016/j.semcancer.2019.10.002.
[7] V. Lifshitz, D. Frenkel. Tgf-B. *Handbook of Biologically Active Peptides*. 1647–1653. (2013). doi: 10.1016/B978-0-12-385095-9.00225-6.
[8] D. S. J. Miller, C. S. Hill. *TGF-β Superfamily Signaling*, Vol. 3, Elsevier Ltd., (2016).
[9] R. Weiskirchen. BMP-7 as antagonist of organ fibrosis. *Frontiers in Bioscience*. 14, 4992. (2009). doi: 10.2741/3583.
[10] S. Zhuang. Regulation of STAT signaling by acetylation. *Cellular Signalling*. 25, 1924–1931. (2013). doi: 10.1016/j.cellsig.2013.05.007.
[11] Y. Liu, S. Liao, S. Bennett, H. Tang, D. Song, D. Wood, X. Zhan, J. Xu. STAT3 and its targeting inhibitors in osteosarcoma. *Cell Proliferation*. 54, 1–15. (2021). doi: 10.1111/cpr.12974.
[12] C. Rébé, F. Ghiringhelli. STAT3, a master regulator of anti-tumor immune response. *Cancers*. 11, 1–24. (2019). doi: 10.3390/cancers11091280.
[13] Z. Yang, X. F. Ming. Functions of arginase isoforms in macrophage inflammatory responses: Impact on cardiovascular diseases and metabolic disorders. *Frontiers in Immunology*. 5, 1–10. (2014). doi: 10.3389/fimmu.2014.00533.
[14] A. Mantovani, S. Sozzani, M. Locati, P. Allavena, A. Sica. Macrophage polarization: tumor-associated macrophages as a paradigm for polarized M2 mononuclear phagocytes. *Trends in Immunology*. 23, 549–555. (2002). doi: 10.1016/S1471-4906(02)02302-5.
[15] S. Zou, Q. Tong, B. Liu, W. Huang, Y. Tian, X. Fu. Targeting STAT3 in Cancer Immunotherapy. *Molecular Cancer*. 19, 145. (2020). doi: 10.1186/s12943-020-01258-7.
[16] R. B. Luwor, S. S. Stylli, A. H. Kaye. The role of Stat3 in glioblastoma multiforme. *Journal of Clinical Neuroscience*. 20, 907–911. (2013). doi: 10.1016/j.jocn.2013.03.006.
[17] X. Hu, J. li, M. Fu, X. Zhao, W. Wang. The JAK/STAT signaling pathway: from bench to clinic. *Signal Transduction and Targeted Therapy*. 6, (2021). doi: 10.1038/s41392-021-00791-1.
[18] U. Bharadwaj, M. M. Kasembeli, D. J. Tweardy. *STAT3 Inhibitors in Cancer: A Comprehensive Update*, (2016).
[19] F. Wang, X.-Y. Cao, G.-Q. Lin, P. Tian, D. Gao. Novel inhibitors of the STAT3 signaling pathway: an updated patent review (2014-present). *Expert Opinion on Therapeutic Patents*. 32, 667–688. (2022). doi: 10.1080/13543776.2022.2056013.
[20] J. Dong, X. D. Cheng, W. D. Zhang, J. J. Qin. Recent Update on Development of Small-Molecule STAT3 Inhibitors for Cancer Therapy: From Phosphorylation Inhibition to Protein Degradation. *Journal of Medicinal Chemistry*. 64, 8884–8915. (2021). doi: 10.1021/acs.jmedchem.1c00629.
[21] M. B. Sonbol, D. H. Ahn, D. Goldstein, T. Okusaka, J. Tabernero, T. Macarulla, M. Reni, C. P. Li, B. O'Neil, E. Van Cutsem, T. Bekaii-Saab. CanStem111P trial: A Phase III study of napabucasin plus nab-paclitaxel with gemcitabine. *Future Oncology*. 15, 1295–1302. (2019). doi: 10.2217/fon-2018-0903.
[22] D. Han, T. Yu, N. Dong, B. Wang, F. Sun, D. Jiang. Napabucasin, a novel STAT3 inhibitor suppresses proliferation, invasion and stemness of glioblastoma cells. *Journal of Experimental and Clinical Cancer Research*. 38, 1–12. (2019). doi: 10.1186/s13046-019-1289-6.
[23] L. MacDonagh, S. G. Gray, E. Breen, S. Cuffe, S. P. Finn, K. J. O'Byrne, M. P. Barr. BBI608 inhibits cancer stemness and reverses cisplatin resistance in NSCLC. *Cancer Letters*. 428, 117–126. (2018). doi: 10.1016/j.canlet.2018.04.008.
[24] G. P. Nagaraju, B. Farran, M. Farren, G. Chalikonda, C. Wu, G. B. Lesinski, B. F. El-Rayes. Napabucasin (BBI 608), a potent chemoradiosensitizer in rectal cancer. *Cancer*. 126, 3360–3371. (2020). doi: 10.1002/cncr.32954.
[25] A. Kawazoe, Y. Kuboki, E. Shinozaki, H. Hara, T. Nishina, Y. Komatsu, S. Yuki, M. Wakabayashi, S. Nomura, A. Sato, T. Kuwata, M. Kawazu, H. Mano, Y. Togashi, H. Nishikawa, T. Yoshino. Multicenter phase I/II trial of napabucasin and pembrolizumab in patients with metastatic colorectal cancer (EPOC1503/SCOOP Trial). *Clinical Cancer Research*. 26, 5887–5894. (2020). doi: 10.1158/1078-0432.CCR-20-1803.
[26] Y. Li, H. A. Rogoff, S. Keates, Y. Gao, S. Murikipudi, K. Mikule, D. Leggett, W. Li, A. B. Pardee, C. J. Li. Suppression of cancer relapse and metastasis by inhibiting cancer stemness. *Proceedings of the National Academy of Sciences of the United States of America*. 112, 1839–1844. (2015). doi: 10.1073/pnas.1424171112.
[27] D. J. Jonker, L. Nott, T. Yoshino, S. Gill, J. Shapiro, A. Ohtsu, J. Zalcberg, M. M. Vickers, A. C. Wei, Y. Gao, N. C. Tebbutt, B. Markman, T. Price, T. Esaki, S. Koski, M. Hitron, W. Li, Y. Li, N. M. Magoski, C. J. Li, J. Simes, D. Tu, C. J. O'Callaghan. Napabucasin versus placebo in refractory advanced colorectal cancer: a randomised phase 3 trial. *The Lancet Gastroenterology and Hepatology*. 3, 263–270. (2018). doi: 10.1016/S2468-1253(18)30009-8.
[28] S. Sau, S. K. Mondal, S. K. Kashaw, A. K. Iyer, R. Banerjee. Combination of cationic dexamethasone derivative and STAT3 inhibitor (WP1066) for aggressive melanoma: a strategy for repurposing a phase I clinical trial drug. *Molecular and Cellular Biochemistry*. 436, 119–136. (2017). doi: 10.1007/s11010-017-3084-z.
[29] J. De Groot, M. Ott, J. Wei, C. Kassab, D. Fang, H. Najem, B. O'Brien, S. P. Weathers, C. K. Matsouka, N. K. Majd, R. A. Harrison, G. N. Fuller, J. T. Huse, J. P. Long, R. Sawaya, G. Rao, T. J. Macdonald, W. Priebe, M. Decuypere, A. B. Heimberger. A first-in-human Phase i trial of the oral p-STAT3 inhibitor WP1066 in patients with recurrent malignant glioma. *CNS Oncology*. 11, (2022). doi: 10.2217/cns-2022-0005.
[30] A. Tolcher, K. Flaherty, G. I. Shapiro, J. Berlin, T. Witzig, T. Habermann, A. Bullock, E. Rock, A. Elekes, C. Lin, D. Kostic, N. Ohi, D. Rasco, K. P. Papadopoulos, A. Patnaik, L. Smith, G. M. Cote. A First-in-Human Phase I Study of OPB-111077, a Small-Molecule STAT3 and Oxidative Phosphorylation Inhibitor, in Patients with Advanced Cancers.

The Oncologist. 23, 658-e72. (2018). doi: 10.1634/theoncologist.2017-0325.

[31] C. Yoo, J. Kang, H. Y. Lim, J. H. Kim, M. A. Lee, K. H. Lee, T. Y. Kim, B. Y. Ryoo. Phase I dose-finding study of OPB-111077, a novel STAT3 inhibitor, in patients with advanced hepatocellular carcinoma. *Cancer Research and Treatment*. 51, 510–518. (2019). doi: 10.4143/crt.2018.226.

[32] D. Genini, L. Brambilla, E. Laurini, J. Merulla, G. Civenni, S. Pandit, R. D'Antuono, L. Perez, D. E. Levy, S. Pricl, G. M. Carbone, C. V. Catapano. Mitochondrial dysfunction induced by a SH2 domain-Targeting STAT3 inhibitor leads to metabolic synthetic lethality in cancer cells. *Proceedings of the National Academy of Sciences of the United States of America*. 114, E4924–E4933. (2017). doi: 10.1073/pnas.1615730114.

[33] A. L. Wong, R. A. Soo, D. S. Tan, S. C. Lee, J. S. Lim, P. C. Marban, L. R. Kong, Y. J. Lee, L. Z. Wang, W. L. Thuya, R. Soong, M. Q. Yee, T. M. Chin, M. T. Cordero, B. R. Asuncion, B. Pang, S. Pervaiz, J. L. Hirpara, A. Sinha, W. W. Xu, M. Yuasa, T. Tsunoda, M. Motoyama, T. Yamauchi, B. C. Goh. Phase I and biomarker study of OPB-51602, a novel signal transducer and activator of transcription (STAT) 3 inhibitor, in patients with refractory solid malignancies. *Annals of Oncology*. 26, 998–1005. (2015). doi: 10.1093/annonc/mdv026.

[34] M. Ogura, T. Uchida, Y. Terui, F. Hayakawa, Y. Kobayashi, M. Taniwaki, Y. Takamatsu, T. Naoe, K. Tobinai, W. Munakata, T. Yamauchi, A. Kageyama, M. Yuasa, M. Motoyama, T. Tsunoda, K. Hatake. Phase I study of OPB-51602, an oral inhibitor of signal transducer and activator of transcription 3, in patients with relapsed/refractory hematological malignancies. *Cancer Science*. 106, 896–901. (2015). doi: 10.1111/cas.12683.

[35] R. Derynck, S. J. Turley, R. J. Akhurst. TGFβ biology in cancer progression and immunotherapy. *Nature Reviews Clinical Oncology*. 18, 9–34. (2021). doi: 10.1038/s41571-020-0403-1.

[36] M. O. Li, Y. Y. Wan, S. Sanjabi, A. K. L. Robertson, R. A. Flavell. Transforming growth factor-β regulation of immune responses. *Annual Review of Immunology*. 24, 99–146. (2006). doi: 10.1146/annurev.immunol.24.021605.090737.

[37] B. A. Teicher. TGFβ-Directed Therapeutics: 2020. *Pharmacology and Therapeutics*. 217, (2021). doi: 10.1016/j.pharmthera.2020.107666.

[38] S. Liu, J. Ren, P. ten Dijke. Targeting TGFβ signal transduction for cancer therapy. *Signal Transduction and Targeted Therapy*. 6, (2021). doi: 10.1038/s41392-020-00436-9.

[39] Y. L. Wu, S. Lu, Y. Lu, J. Zhou, Y. kai Shi, V. Sriuranpong, J. C. M. Ho, C. K. Ong, C. M. Tsai, C. H. Chung, K. D. Wilner, Y. Tang, E. T. Masters, P. Selaru, T. S. Mok. Results of PROFILE 1029, a Phase III Comparison of First-Line Crizotinib versus Chemotherapy in East Asian Patients with ALK-Positive Advanced Non–Small Cell Lung Cancer. *Journal of Thoracic Oncology*. 13, 1539–1548. (2018). doi: 10.1016/j.jtho.2018.06.012.

[40] A. T. Shaw, T. M. Kim, L. Crinò, C. Gridelli, K. Kiura, G. Liu, S. Novello, A. Bearz, O. Gautschi, T. Mok, M. Nishio, G. Scagliotti, D. R. Spigel, S. Deudon, C. Zheng, S. Pantano, P. Urban, C. Massacesi, K. Viraswami-Appanna, E. Felip. Ceritinib versus chemotherapy in patients with ALK-rearranged non-small-cell lung cancer previously given chemotherapy and crizotinib (ASCEND-5): a randomised, controlled, open-label, phase 3 trial. *The Lancet Oncology*. 18, 874–886. (2017). doi: 10.1016/S1470-2045(17)30339-X.

[41] A. Okines, T. Irfan, B. Asare, K. Mohammed, P. Osin, A. Nerurkar, I. E. Smith, M. Parton, A. Ring, S. Johnston, N. C. Turner. Clinical outcomes in patients with triple negative or HER2 positive lobular breast cancer: a single institution experience. *Breast Cancer Research and Treatment*. 192, 563–571. (2022). doi: 10.1007/s10549-021-06432-z.

[42] Y. Li, J. Shi, J. Yang, S. Ge, J. Zhang, R. Jia, X. Fan. Uveal melanoma: progress in molecular biology and therapeutics. *Therapeutic Advances in Medical Oncology*. 12, 1–27. (2020). doi: 10.1177/1758835920965852.

[43] A. Jamieson, T. Bosse, J. N. McAlpine. The emerging role of molecular pathology in directing the systemic treatment of endometrial cancer. *Therapeutic Advances in Medical Oncology*. 13, 1–14. (2021). doi: 10.1177/17588359211035959.

[44] K. T. Flaherty, R. Gray, A. Chen, S. Li, D. Patton, S. R. Hamilton, P. M. Williams, E. P. Mitchell, A. John Iafrate, J. Sklar, L. N. Harris, L. M. McShane, L. V. Rubinstein, D. J. Sims, M. Routbort, B. Coffey, T. Fu, J. A. Zwiebel, R. F. Little, D. Marinucci, R. Catalano, R. Magnan, W. Kibbe, C. Weil, J. V. Tricoli, B. Alexander, S. Kumar, G. K. Schwartz, F. Meric-Bernstam, C. J. Lih, W. McCaskill-Stevens, P. Caimi, N. Takebe, V. Datta, C. L. Arteaga, J. S. Abrams, R. Comis, P. J. O'Dwyer, B. A. Conley, M. Schnall, T. Johnson, F. B. de Abreu, S. J. Deharvengt, T. L. Gallagher, K. Godwin, D. C. Green, C. C. Hain, B. E. Houde, J. D. Peterson, H. B. Steinmetz, G. J. Tsongalis, X. Xiao, B. Giantonio, M. Lou Smith, N. Azad, M. Lambert, L. P. Le, A. Raymond, H. Robinson, K. Vernovsky, D. Hyman, C. Chung, C. Rowe, F. Spina, S. Ansher, J. Cristofaro, P. S. Ivy, I. Lubensky, H. Makhlouf, L. Shankar, J. Wright, L. Yee, L. Lison, M. Anderson, M. Benson, N. Birus, L. Brem, D. Chebattina, H. Donolo, E. Dumene, M. Hammer, M. Hendriksson, S. Kadiyala, J. Lee, A. Lu, T. O'Connor, W. Osman, J. Pumphrey, A. Purkayastha, V. Ramani, J. Scibelli, M. Smith, A. Steinfeld, J. Thompson, S. Vallala, J. Verbeck, C. Winter, S. Yang, Q. Yu, R. Zakharov, C. Bouk, T. C. Chang, A. Fredlock, K. Harper, R. Harrington, C. Karlovich, M. Majano, S. McDermott, E. Mosher, P. Runge, M. Saeed, G. S. Mantha, D. Panditi, K. P. Patel, R. Pepper, L. Rajyalakshmi, N. G. Reddy, R. R. Singh, D. Tripathy, J. Yau, S. Canosa, K. Finberg, J. Huang, K. Ronski, T. Zenta Walther. The molecular analysis for therapy choice (NCI-MATCH) trial: Lessons for genomic trial design. *Journal of the National Cancer Institute*. 112, 1021–1029. (2020). doi: 10.1093/jnci/djz245.

[45] A. S. Mansfield, Z. Wei, R. Mehra, A. T. Shaw, C. H. Lieu, P. M. Forde, A. E. Drilon, E. P. Mitchell, J. J. Wright, N. Takebe, E. Sharon, D. Hovelson, S. Tomlins, J. Zeng, K. Poorman, N. Malik, R. J. Gray, S. Li, L. M. McShane, L. V. Rubinstein, D. Patton, P. M. Williams, S. R. Hamilton, B. A. Conley, C. L. Arteaga, L. N. Harris, P. J. O'Dwyer, A. P. Chen, K. T. Flaherty. Crizotinib in patients with tumors harboring ALK or ROS1 rearrangements in the NCI-MATCH trial. *npj Precision Oncology*. 6, 1–6. (2022). doi: 10.1038/s41698-022-00256-w.

USC UNIVERSIDADE DE SANTIAGO DE COMPOSTELA

[46] J. C. Soria, D. S. W. Tan, R. Chiari, Y. L. Wu, L. Paz-Ares, J. Wolf, S. L. Geater, S. Orlov, D. Cortinovis, C. J. Yu, M. Hochmair, A. B. Cortot, C. M. Tsai, D. Moro-Sibilot, R. G. Campelo, T. McCulloch, P. Sen, M. Dugan, S. Pantano, F. Branle, C. Massacesi, G. de Castro. First-line ceritinib versus platinum-based chemotherapy in advanced ALK-rearranged non-small-cell lung cancer (ASCEND-4): a randomised, open-label, phase 3 study. *The Lancet*. 389, 917–929. (2017). doi: 10.1016/S0140-6736(17)30123-X.

[47] N. Ochi, N. Takigawa. What can we learn from 3 phase III trials of ASCEND-4: Ceritinib vs. platinum/pemetrexed with pemetrexed maintenance, PROFILE 1004: Crizotinib vs. platinum/pemetrexed, and J-ALEX: Alectinib vs. crizotinib? *Translational Cancer Research*. 6, S515–S518. (2017). doi: 10.21037/tcr.2017.04.20.

[48] D. S. W. Tan, S. Geater, C. J. Yu, C. M. Tsai, T. C. Hsia, J. Chen, M. C. Lin, Y. Lu, V. Sriuranpong, C. T. Yang, P. Sen, F. Branle, M. Shi, Y. L. Wu. Ceritinib Efficacy and Safety in Treatment-Naive Asian Patients With Advanced ALK-Rearranged NSCLC: An ASCEND-4 Subgroup Analysis. *JTO Clinical and Research Reports*. 2, 100131. (2021). doi: 10.1016/j.jtocrr.2020.100131.

[49] J. Guan, S. Fransson, J. T. Siaw, D. Treis, J. Van Den Eynden, D. Chand, G. Umapathy, K. Ruuth, P. Svenberg, S. Wessman, A. Shamikh, H. Jacobsson, L. Gordon, J. Stenman, P. J. Svensson, M. Hansson, E. Larsson, T. Martinsson, R. H. Palmer, P. Kogner, B. Hallberg. Clinical response of the novel activating ALK-I1171T mutation in neuroblastoma to the ALK inhibitor ceritinib. *Cold Spring Harbor Molecular Case Studies*. 4, 1–24. (2018). doi: 10.1101/mcs.a002550.

[50] K. W. Nassar, J. D. Hintzsche, S. M. Bagby, V. Espinoza, C. Langouët-Astrié, C. M. Amato, T.-S. Chimed, M. Fujita, W. Robinson, A. C. Tan, R. E. Schweppe. Targeting CDK4/6 Represents a Therapeutic Vulnerability in Acquired BRAF/MEK Inhibitor–Resistant Melanoma. *Molecular Cancer Therapeutics*. 20, 2049–2060. (2021). doi: 10.1158/1535-7163.MCT-20-1126.

[51] K. Hotta, T. Hida, H. Nokihara, M. Morise, Y. H. Kim, K. Azuma, T. Seto, Y. Takiguchi, M. Nishio, H. Yoshioka. Final overall survival analysis from the phase III J-ALEX study of alectinib versus crizotinib in ALK inhibitor-naïve Japanese patients with ALK -positive. *ESMO Open*. 7, 100527. (2022). doi: 10.1016/j.esmoop.2022.100527.

[52] W. Wick, S. Dettmer, A. Berberich, T. Kessler, I. Karapanagiotou-Schenkel, A. Wick, F. Winkler, E. Pfaff, B. Brors, J. Debus, A. Unterberg, M. Bendszus, C. Herold-Mende, A. Eisenmenger, A. Von Deimling, D. T. W. Jones, S. M. Pfister, F. Sahm, M. Platten. N 2 M 2 (NOA-20) phase I/II trial of molecularly matched targeted therapies plus radiotherapy in patients with newly diagnosed non-MGMT hypermethylated glioblastoma. *Neuro-Oncology*. 21, 95–105. (2019). doi: 10.1093/neuonc/noy161.

[53] D. W. Kim, M. Tiseo, M. J. Ahn, K. L. Reckamp, K. H. Hansen, S. W. Kim, R. M. Huber, H. L. West, H. J. M. Groen, M. J. Hochmair, N. B. Leighl, S. N. Gettinger, C. J. Langer, L. G. P. A. Rodríguez, E. F. Smit, E. S. Kim, W. Reichmann, F. G. Haluska, D. Kerstein, D. R. Camidge. Brigatinib in patients with crizotinib-refractory anaplastic lymphoma kinase-positive non-small-cell lung cancer: A randomized, multicenter phase II trial. *Journal of Clinical Oncology*. 35, 2490–2498. (2017). doi: 10.1200/JCO.2016.71.5904.

[54] A. T. Shaw, T. M. Bauer, F. de Marinis, E. Felip, Y. Goto, G. Liu, J. Mazieres, D.-W. Kim, T. Mok, A. Polli, H. Thurm, A. M. Calella, G. Peltz, B. J. Solomon. First-Line Lorlatinib or Crizotinib in Advanced ALK -Positive Lung Cancer. *New England Journal of Medicine*. 383, 2018–2029. (2020). doi: 10.1056/nejmoa2027187.

[55] V. Santini, D. Valcarcel, U. Platzbecker, R. S. Komrokji, A. L. Cleverly, M. M. Lahn, J. Janssen, Y. Zhao, A. Chiang, A. Giagounidis, S. C. Guba, I. Gueorguieva, A. C. Girvan, M. Da Silva Ferreira, T. D. Bhagat, K. Pradhan, U. Steidl, A. Sridharan, B. Will, A. Verma. Phase II study of the ALK5 inhibitor galunisertib in very low-, low-, and intermediate-risk myelodysplastic syndromes. *Clinical Cancer Research*. 25, 6976–6985. (2019). doi: 10.1158/1078-0432.CCR-19-1338.

[56] C. Paller, H. Pu, D. E. Begemann, C. A. Wade, P. J. Hensley, N. Kyprianou. TGF-β receptor I inhibitor enhances response to enzalutamide in a pre-clinical model of advanced prostate cancer. *The Prostate*. 79, 31–43. (2019). doi: 10.1002/pros.23708.

[57] T. Yamazaki, A. J. Gunderson, M. Gilchrist, M. Whiteford, M. X. Kiely, A. Hayman, D. O'Brien, R. Ahmad, J. V Manchio, N. Fox, K. McCarty, M. Phillips, E. Brosnan, G. Vaccaro, R. Li, M. Simon, E. Bernstein, M. McCormick, L. Yamasaki, Y. Wu, A. Drokin, T. Carnahan, Y. To, W. L. Redmond, B. Lee, J. Louie, E. Hansen, M. C. Solhjem, J. Cramer, W. J. Urba, M. J. Gough, M. R. Crittenden, K. H. Young. Galunisertib plus neoadjuvant chemoradiotherapy in patients with locally advanced rectal cancer: a single-arm, phase 2 trial. *The Lancet Oncology*. 23, 1189–1200. (2022). doi: 10.1016/S1470-2045(22)00446-6.

[58] R. K. Kelley, E. Gane, E. Assenat, J. Siebler, P. R. Galle, P. Merle, I. O. Hourmand, A. Cleverly, Y. Zhao, I. Gueorguieva, M. Lahn, S. Faivre, K. A. Benhadji, G. Giannelli. A phase 2 study of galunisertib (TGF-b1 Receptor Type i Inhibitor) and sorafenib in patients with advanced hepatocellular carcinoma. *Clinical and Translational Gastroenterology*. 10, 1–9. (2019). doi: 10.14309/ctg.0000000000000056.

[59] A. A. Brandes, A. F. Carpentier, S. Kesari, J. M. Sepulveda-Sanchez, H. R. Wheeler, O. Chinot, L. Cher, J. P. Steinbach, D. Capper, P. Specenier, J. Rodon, A. Cleverly, C. Smith, I. Gueorguieva, C. Miles, S. C. Guba, D. Desaiah, M. M. Lahn, W. Wick. A Phase II randomized study of galunisertib monotherapy or galunisertib plus lomustine compared with lomustine monotherapy in patients with recurrent glioblastoma. *Neuro-Oncology*. 18, 1146–1156. (2016). doi: 10.1093/neuonc/now009.

[60] T. A. Yap, M. Vieito, C. Baldini, J. M. Sepúlveda-Sánchez, S. Kondo, M. Simonelli, R. Cosman, A. van der Westhuizen, V. Atkinson, A. F. Carpentier, M. Löhr, R. Redman, W. Mason, A. Cervantes, E. Le Rhun, S. Ochsenreither, L. Warren, Y. Zhao, S. Callies, S. T. Estrem, M. Man, L. Gandhi, E. Avsar, D. Melisi. First-In-Human Phase I Study of a Next-Generation, Oral, TGFb Receptor 1 Inhibitor, LY3200882, in Patients with Advanced Cancer.

Clinical Cancer Research. 27, 6666–6676. (2021). doi: 10.1158/1078-0432.CCR-21-1504.

[61] S. Y. Jung, J. S. Yug, J. M. Clarke, T. M. Bauer, V. L. Keedy, S. Hwang, S. J. Kim, E. K. Chung, J. I. Lee. Population pharmacokinetics of vactosertib, a new TGF-β receptor type I inhibitor, in patients with advanced solid tumors. *Cancer Chemotherapy and Pharmacology*. 85, 173–183. (2020). doi: 10.1007/s00280-019-03979-z.

[62] T. A. Yap, N. J. Lakhani, D. V. Araujo, J. Rodon Ahnert, S. R. Chandana, M. Sharma, J.-F. Denis, T. Gruosso, G. Tremblay, M. O'Connor, R. Ghosh, S. Sinclair, D. L. Wood, P. I. Nadler, L. L. Siu. AVID200, first-in-class TGF-beta 1 and 3 selective and potent inhibitor: Safety and biomarker results of a phase I monotherapy dose-escalation study in patients with advanced solid tumors. *Journal of Clinical Oncology*. 38, 3587–3587. (2020). doi: 10.1200/JCO.2020.38.15_suppl.3587.

[63] F. Zhao, Y. Wei, Y. Yan, H. Liu, S. Zhou, B. Ren, R. Liu. Determination of Crizotinib in Mouse Tissues by LC-MS/MS and Its Application to a Tissue Distribution Study. *International Journal of Analytical Chemistry*. 2020, (2020). doi: 10.1155/2020/8837254.

[64] European Medicines Agency. Assessent report: Xalkori. https://www.ema.europa.eu/en/documents/product-information/xalkori-epar-product-information_en.pdf. Accessed: November 1, 2022.

[65] European Medicines Agency. Assessent report: Zykadia. https://www.ema.europa.eu/en/documents/assessment-report/zykadia-epar-public-assessment-report_en.pdf. Accessed: November 1, 2022.

[66] K. C. Cassidy, I. Gueorguieva, C. Miles, J. Rehmel, P. Yi, W. J. Ehlhardt. *Disposition and metabolism of [14C]-galunisertib, a TGF-βRI kinase/ALK5 inhibitor, following oral administration in healthy subjects and mechanistic prediction of the effect of itraconazole on galunisertib pharmacokinetics*, Vol. 48, Taylor & Francis, (2018).

[67] T. Okusaka, H. Ueno, M. Ikeda, S. Mitsunaga, M. Ozaka, H. Ishii, O. Yokosuka, Y. Ooka, R. Yoshimoto, Y. Yanagihara, K. Okita. Phase 1 and pharmacological trial of OPB-31121, a signal transducer and activator of transcription-3 inhibitor, in patients with advanced hepatocellular carcinoma. *Hepatology Research*. 45, 1283–1291. (2015). doi: 10.1111/hepr.12504.

[68] S. Verstovsek, R. Hoffman, J. Mascarenhas, J. C. Soria, R. Bahleda, P. McCoon, W. Tang, J. Cortes, H. Kantarjian, V. Ribrag. A phase I, open-label, multi-center study of the JAK2 inhibitor AZD1480 in patients with myelofibrosis. *Leukemia Research*. 39, 157–163. (2015). doi: 10.1016/j.leukres.2014.11.018.

[69] D. Chen, F. Zhang, J. Wang, H. He, S. Duan, R. Zhu, C. Chen, L. Yin, Y. Chen. Biodegradable nanoparticles mediated Co-delivery of erlotinib (ELTN) and fedratinib (FDTN) toward the treatment of ELTN-resistant Non-small cell lung Cancer (NSCLC) via suppression of the JAK2/STAT3 signaling pathway. *Frontiers in Pharmacology*. 9, 1–9. (2018). doi: 10.3389/fphar.2018.01214.

[70] W. Gao, H. Wen, L. Liang, X. Dong, R. Du, W. Zhou, X. Zhang, C. Zhang, R. Xiang, N. Li. IL20RA signaling enhances stemness and promotes the formation of an immunosuppressive microenvironment in breast cancer. *Theranostics*. 11, 2564–2580. (2021). doi: 10.7150/THNO.45280.

[71] X. Shi, L. Shu, Y. Qiao, J. Yao, H. Xie, L. Zhou, H. Wang, S. Zheng. Synergistic nanoassemblies constructed from a STAT3 inhibitor and a cabazitaxel prodrug with enhanced cancer chemo-immunotherapy. *Materials Today Nano*. 17, 100155. (2022). doi: 10.1016/j.mtnano.2021.100155.

[72] S. S. Fong, Y. Y. Foo, W. S. Saw, B. F. Leo, Y. Y. Teo, I. Chung, B. T. Goh, M. Misran, T. Imae, C. C. Chang, L. Y. Chung, L. V. Kiew. Chitosan-Coated-PLGA Nanoparticles Enhance the Antitumor and Antimigration Activity of Stattic – A STAT3 Dimerization Blocker. *International Journal of Nanomedicine*. 17, 137–150. (2022). doi: 10.2147/IJN.S337093.

[73] L. Zhang, J. Huang, X. Chen, C. Pan, Y. He, R. Su, D. Guo, S. Yin, S. Wang, L. Zhou, J. Chen, S. Zheng, Y. Qiao. Self-assembly nanovaccine containing TLR7/8 agonist and STAT3 inhibitor enhances tumor immunotherapy by augmenting tumor-specific immune response. *Journal for ImmunoTherapy of Cancer*. 9, 1–14. (2021). doi: 10.1136/jitc-2021-003132.

[74] J. Mohammadian, S. Mahmoudi, P. Pourmohammad, M. Pirouzpanah, F. Salehnia, N. F. Maroufi, N. Samadi, M. Sabzichi. Formulation of Stattic as STAT3 inhibitor in nanostructured lipid carriers (NLCs) enhances efficacy of doxorubicin in melanoma cancer cells. *Naunyn-Schmiedeberg's Archives of Pharmacology*. 393, 2315–2323. (2020). doi: 10.1007/s00210-020-01942-x.

[75] Y. C. Kwa, Y. F. Tan, Y. Y. Foo, B. F. Leo, I. Chung, L. V. Kiew, T. Imae, S. ichi Yusa, L. Y. Chung. Improved delivery and antimetastatic effects of Stattic by self-assembled amphiphilic pendant-dendron copolymer micelles in breast cancer cell lines. *Journal of Drug Delivery Science and Technology*. 59, 101905. (2020). doi: 10.1016/j.jddst.2020.101905.

[76] Y. C. Kwa, T. Anasamy, Y. Y. Foo, B. F. Leo, I. Chung, L. V. Kiew, L. Y. Chung. Preparation and Characterization of Stattic-Loaded Albumin Nanoparticles for Antimetastatic Cancer Treatment. *Drug Delivery Letters*. 12, 74–83. (2022). doi: 10.2174/2210303112666220330115110.

[77] C. F. Mu, Y. Xiong, X. Bai, Y. J. Sheng, J. Cui. Codelivery of Ponatinib and SAR302503 by Active Bone-Targeted Polymeric Micelles for the Treatment of Therapy-Resistant Chronic Myeloid Leukemia. *Molecular Pharmaceutics*. 14, 274–283. (2017). doi: 10.1021/acs.molpharmaceut.6b00872.

[78] Z. Ma, J. Li, K. Lin, M. Ramachandran, D. Zhang, M. Showalter, C. De Souza, A. Lindstrom, L. N. Solano, B. Jia, S. Urayama, Y. Duan, O. Fiehn, T. yin Lin, M. Li, Y. Li. Pharmacophore hybridisation and nanoscale assembly to discover self-delivering lysosomotropic new-chemical entities for cancer therapy. *Nature Communications*. 11, (2020). doi: 10.1038/s41467-020-18399-4.

[79] M. I. Confeld, B. Mamnoon, L. Feng, H. Jensen-Smith, P. Ray, J. Froberg, J. Kim, M. A. Hollingsworth, M. Quadir, Y. Choi, S. Mallik. Targeting the Tumor Core: Hypoxia-Responsive Nanoparticles for the Delivery of Chemotherapy

USC UNIVERSIDADE DE SANTIAGO DE COMPOSTELA

to Pancreatic Tumors. *Molecular Pharmaceutics*. 17, 2849–2863. (2020). doi: 10.1021/acs.molpharmaceut.0c00247.

[80] S. Bhunia, V. Vangala, D. Bhattacharya, H. G. Ravuri, M. Kuncha, S. Chakravarty, R. Sistla, A. Chaudhuri. Large Amino Acid Transporter 1 Selective Liposomes of L-DOPA Functionalized Amphiphile for Combating Glioblastoma. *Molecular Pharmaceutics*. 14, 3834–3847. (2017). doi: 10.1021/acs.molpharmaceut.7b00569.

[81] S. Saha, Y. Venu, D. Bhattacharya, S. D. Kompella, K. Madhusudana, S. Chakravarty, S. Ramakrishna, A. Chaudhuri. Combating Established Mouse Glioblastoma through Nicotinylated-Liposomes-Mediated Targeted Chemotherapy in Combination with Dendritic-Cell-Based Genetic Immunization. *Advanced Biosystems*. 1, 1600009. (2017). doi: 10.1002/adbi.201600009.

[82] V. Vangala, V. Vangala, N. V. Nimmu, S. Khalid, M. Kuncha, R. Sistla, R. Sistla, R. Banerjee, R. Banerjee, A. Chaudhuri. Combating Glioblastoma by Codelivering the Small-Molecule Inhibitor of STAT3 and STAT3siRNA with α5β1 Integrin Receptor-Selective Liposomes. *Molecular Pharmaceutics*. 17, 1859–1874. (2020). doi: 10.1021/acs.molpharmaceut.9b01271.

[83] Y. H. Huang, M. R. Vakili, O. Molavi, Y. Morrissey, C. Wu, I. Paiva, A. H. Soleimani, F. Sanaee, A. Lavasanifar, R. Lai. Decoration of anti-CD38 on nanoparticles carrying a STAT3 inhibitor can improve the therapeutic efficacy against myeloma. *Cancers*. 11, (2019). doi: 10.3390/cancers11020248.

[84] F. Zhao, K. Evans, C. Xiao, N. DeVito, B. Theivanthiran, A. Holtzhausen, P. J. Siska, G. C. Blobe, B. A. Hanks. Stromal fibroblasts mediate anti–PD-1 resistance via MMP-9 and dictate TGFb inhibitor sequencing in melanoma. *Cancer Immunology Research*. 6, 1459–1471. (2018). doi: 10.1158/2326-6066.CIR-18-0086.

[85] D. V. F. Tauriello, S. Palomo-Ponce, D. Stork, A. Berenguer-Llergo, J. Badia-Ramentol, M. Iglesias, M. Sevillano, S. Ibiza, A. Cañellas, X. Hernando-Momblona, D. Byrom, J. A. Matarin, A. Calon, E. I. Rivas, A. R. Nebreda, A. Riera, C. S. O. Attolini, E. Batlle. TGFβ drives immune evasion in genetically reconstituted colon cancer metastasis. *Nature*. 554, 538–543. (2018). doi: 10.1038/nature25492.

[86] R. B. Holmgaard, D. A. Schaer, Y. Li, S. P. Castaneda, M. Y. Murphy, X. Xu, I. Inigo, J. Dobkin, J. R. Manro, P. W. Iversen, D. Surguladze, G. E. Hall, R. D. Novosiadly, K. A. Benhadji, G. D. Plowman, M. Kalos, K. E. Driscoll. Targeting the TGFβ pathway with galunisertib, a TGFβRI small molecule inhibitor, promotes anti-tumor immunity leading to durable, complete responses, as monotherapy and in combination with checkpoint blockade. *Journal for ImmunoTherapy of Cancer*. 6, 1–15. (2018). doi: 10.1186/s40425-018-0356-4.

[87] J. van den Bulk, N. F. C. C. de Miranda, P. ten Dijke. Therapeutic targeting of TGF-β in cancer: Hacking a master switch of immune suppression. *Clinical Science*. 135, 35–52. (2021). doi: 10.1042/CS20201236.

[88] J. P. Stevenson, H. L. Kindler, E. Papasavvas, J. Sun, M. Jacobs-Small, J. Hull, D. Schwed, A. Ranganathan, K. Newick, D. F. Heitjan, C. J. Langer, J. M. McPherson, L. J. Montaner, S. M. Albelda. Immunological effects of the TGFβ-blocking antibody GC1008 in malignant pleural mesothelioma patients. *OncoImmunology*. 2, (2013). doi: 10.4161/onci.26218.

[89] A. F. Teixeira, P. ten Dijke, H. J. Zhu. On-Target Anti-TGF-β Therapies Are Not Succeeding in Clinical Cancer Treatments: What Are Remaining Challenges? *Frontiers in Cell and Developmental Biology*. 8, 1–18. (2020). doi: 10.3389/fcell.2020.00605.

[90] F. Vincenti, F. C. Fervenza, K. N. Campbell, M. Diaz, L. Gesualdo, P. Nelson, M. Praga, J. Radhakrishnan, L. Sellin, A. Singh, D. Thornley-Brown, F. V. Veronese, B. Accomando, S. Engstrand, S. Ledbetter, J. Lin, J. Neylan, J. Tumlin. A Phase 2, Double-Blind, Placebo-Controlled, Randomized Study of Fresolimumab in Patients With Steroid-Resistant Primary Focal Segmental Glomerulosclerosis. *Kidney International Reports*. 2, 800–810. (2017). doi: 10.1016/j.ekir.2017.03.011.

[91] N. Díaz-Valdés, M. Basagoiti, J. Dotor, F. Aranda, I. Monreal, J. I. Riezu-Boj, F. Borrás-Cuesta, P. Sarobe, E. Feijoó. Induction of monocyte chemoattractant protein-1 and interleukin-10 by TGFβ1 in melanoma enhances tumor infiltration and immunosuppression. *Cancer Research*. 71, 812–821. (2011). doi: 10.1158/0008-5472.CAN-10-2698.

[92] G. Gallo-Oller, A. Vollmann-Zwerenz, B. Meléndez, J. A. Rey, P. Hau, J. Dotor, J. S. Castresana. P144, a Transforming Growth Factor beta inhibitor peptide, generates antitumoral effects and modifies SMAD7 and SKI levels in human glioblastoma cell lines. *Cancer Letters*. 381, 67–75. (2016). doi: 10.1016/j.canlet.2016.07.029.

[93] I. J. Ezquerro, J. J. Lasarte, J. Dotor, I. Castilla-Cortázar, M. Bustos, I. Peñuelas, G. Blanco, C. Rodríguez, M. D. C. G. Lechuga, P. Greenwel, M. Rojkind, J. Prieto, F. Borrás-Cuesta. A synthetic peptide from transforming growth factor β type III receptor inhibits liver fibrogenesis in rats with carbon tetrachloride liver injury. *Cytokine*. 22, 12–20. (2003). doi: 10.1016/S1043-4666(03)00101-7.

[94] N. A. N. Hanafy, I. Fabregat, S. Leporatti, M. El Kemary. Encapsulating TGF-β1 inhibitory peptides P17 and P144 as a promising strategy to facilitate their dissolution and to improve their functionalization. *Pharmaceutics*. 12, (2020). doi: 10.3390/pharmaceutics12050421.

[95] F. Zeng, B. Xu, H. Zhu, S. Wu, G. Liao, D. Xie, L. Huang, G. Qiao, X. Yang, H. Zhou. A cascade dual-targeted nanocarrier for enhanced alectinib delivery to ALK-positive lung cancer. *Biomaterials Science*. 8, 6404–6413. (2020). doi: 10.1039/d0bm00970a.

[96] P. Zhang, C. Qin, N. Liu, X. Zhou, X. Chu, F. Lv, Y. Gu, L. Yin, J. Liu, J. Zhou, M. Huo. The programmed site-specific delivery of LY3200882 and PD-L1 siRNA boosts immunotherapy for triple-negative breast cancer by remodeling tumor microenvironment. *Biomaterials*. 284, 121518. (2022). doi: 10.1016/j.biomaterials.2022.121518.

[97] Q. Liang, Y. Lan, Y. Li, Y. Cao, J. Li, Y. Liu. Crizotinib Prodrug Micelles Co-Delivered Doxorubicin Synergistic Immunogenic Cell Death Induction for Chemo-Immunotherapy on Breast Cancer. *SSRN Electronic Journal*. 177, 260–272. (2021). doi: 10.2139/ssrn.3979940.

[98] T. Zhong, X. Liu, H. Li, J. Zhang. Co-delivery of sorafenib and crizotinib encapsulated with polymeric nanoparticles

for the treatment of in vivo lung cancer animal model. *Drug Delivery*. 28, 2108–2118. (2021). doi: 10.1080/10717544.2021.1979129.

[99] K. Greish, A. Jasim, N. Parayath, S. Abdelghany, A. Alkhateeb, S. Taurin, H. Nehoff. Micellar formulations of Crizotinib and Dasatinib in the management of glioblastoma multiforme. *Journal of Drug Targeting*. 26, 692–708. (2018). doi: 10.1080/1061186X.2017.1419357.

[100] Z. M. Jiang, S. P. Dai, Y. Q. Xu, T. Li, J. Xie, C. Li, Z. H. Zhang. Crizotinib-loaded polymeric nanoparticles in lung cancer chemotherapy. *Medical Oncology*. 32, 1–8. (2015). doi: 10.1007/s12032-015-0636-5.

[101] J. G. Marques, V. M. Gaspar, D. Markl, E. C. Costa, E. Gallardo, I. J. Correia. Co-delivery of sildenafil (Viagra®) and crizotinib for synergistic and improved anti-tumoral therapy. *Pharmaceutical Research*. 31, 2516–2528. (2014). doi: 10.1007/s11095-014-1347-x.

[102] D. De Melo-Diogo, V. M. Gaspar, E. C. Costa, A. F. Moreira, D. Oppolzer, E. Gallardo, I. J. Correia. Combinatorial delivery of Crizotinib-Palbociclib-Sildenafil using TPGS-PLA micelles for improved cancer treatment. *European Journal of Pharmaceutics and Biopharmaceutics*. 88, 718–729. (2014). doi: 10.1016/j.ejpb.2014.09.013.

[103] G. M. Shopp, L. Helson, A. Bouchard, D. Salvail, M. Majeed. Liposomes ameliorate crizotinib- and nilotinib-induced inhibition of the cardiac IKr channel and QTc prolongation. *Anticancer Research*. 34, 4733–4740. (2014).

[104] M. M. Ahmed, F. Fatima, M. K. Anwer, M. F. Aldawsari, Y. S. M. Alsaidan, S. A. Alfaiz, A. Haque, A. AZ, K. Alhazzani. Development and characterization of Brigatinib loaded solid lipid nanoparticles: In-vitro cytotoxicity against human carcinoma A549 lung cell lines. *Chemistry and Physics of Lipids*. 233, 105003. (2020). doi: 10.1016/j.chemphyslip.2020.105003.

[105] M. Mohammed, M. S. Alnafisah, M. K. Anwer, F. Fatima, B. K. Almutairy, S. M. Alshahrani, A. S. Alshetaili, A. Alalaiwe, M. H. Fayed, A. Z. Alanazi, M. Al Zahrani, M. M. Hailat, R. Al-Shdefat. Chitosan surface modified PLGA nanoparticles loaded with brigatinib for the treatment of non-small cell lung cancer. *Journal of Polymer Engineering*. 39, 909–916. (2019). doi: 10.1515/polyeng-2019-0265.

[106] S. Wang, Y. Song, K. Cao, L. Zhang, X. Fang, F. Chen, S. Feng, F. Yan. Photothermal therapy mediated by gold nanocages composed of anti-PDL1 and galunisertib for improved synergistic immunotherapy in colorectal cancer. *Acta Biomaterialia*. 134, 621–632. (2021). doi: 10.1016/j.actbio.2021.07.051.

[107] Y. Bae, N. Nishiyama, S. Fukushima, H. Koyama, M. Yasuhiro, K. Kataoka. Preparation and biological characterization of polymeric micelle drug carriers with intracellular pH-triggered drug release property: Tumor permeability, controlled subcellular drug distribution, and enhanced in vivo antitumor efficacy. *Bioconjugate Chemistry*. 16, 122–130. (2005). doi: 10.1021/bc0498166.

[108] M. R. Kano, Y. Bae, C. Iwata, Y. Morishita, M. Yashiro, M. Oka, T. Fujii, A. Komuro, K. Kiyono, M. Kaminishi, K. Hirakawa, Y. Ouchi, N. Nishiyama, K. Kataoka, K. Miyazono. Improvement of cancer-targeting therapy, using nanocarriers for intractable solid tumors by inhibition of TGF-β signaling. *Proceedings of the National Academy of Sciences of the United States of America*. 104, 3460–3465. (2007). doi: 10.1073/pnas.0611660104.

[109] N. A. N. Hanafy, A. Quarta, M. M. Ferraro, L. Dini, C. Nobile, M. L. De Giorgi, S. Carallo, C. Citti, A. Gaballo, G. Cannazza, R. Rinaldi, G. Giannelli, S. Leporatti. Polymeric nano-micelles as novel cargo-carriers for LY2157299 liver cancer cells delivery. *International Journal of Molecular Sciences*. 19, (2018). doi: 10.3390/ijms19030748.

[110] S. Managò, C. Tramontano, D. Delle Cave, G. Chianese, G. Zito, L. De Stefano, M. Terracciano, E. Lonardo, A. C. De Luca, I. Rea. SERS Quantification of Galunisertib Delivery in Colorectal Cancer Cells by Plasmonic-Assisted Diatomite Nanoparticles. *Small*. 17, 2101711. (2021). doi: 10.1002/smll.202101711.

[111] Y. Wang, Z. Gao, X. Du, S. Chen, W. Zhang, J. Wang, H. Li, X. He, J. Cao, J. Wang. Co-inhibition of the TGF-β pathway and the PD-L1 checkpoint by pH-responsive clustered nanoparticles for pancreatic cancer microenvironment regulation and anti-tumor immunotherapy. *Biomaterials Science*. 8, 5121–5132. (2020). doi: 10.1039/d0bm00916d.

[112] C. Tramontano, B. Miranda, G. Chianese, L. De Stefano, C. Forestiere, M. Pirozzi, I. Rea. Design of gelatin-capped plasmonic-diatomite nanoparticles with enhanced galunisertib loading capacity for drug delivery applications. *International Journal of Molecular Sciences*. 22, (2021). doi: 10.3390/ijms221910755.

[113] S. Zhu, F. Sun, P. Zhao, G. Liang, X. Sun, L. Zeng, Y. Huang. Brain-targeting biomimetic nanoparticles for codelivery of celastrol and LY2157299 for reversing glioma immunosuppression. *International Journal of Pharmaceutics*. 619, 121709. (2022). doi: 10.1016/j.ijpharm.2022.121709.

[114] L. Xie, P. E. Bourne. Developing multi-target therapeutics to fine-tune the evolutionary dynamics of the cancer ecosystem. *Frontiers in Pharmacology*. 6, 1–5. (2015). doi: 10.3389/fphar.2015.00209.

[115] Z. Q. Zuo, K. G. Chen, X. Y. Yu, G. Zhao, S. Shen, Z. T. Cao, Y. L. Luo, Y. C. Wang, J. Wang. Promoting tumor penetration of nanoparticles for cancer stem cell therapy by TGF-β signaling pathway inhibition. *Biomaterials*. 82, 48–59. (2016). doi: 10.1016/j.biomaterials.2015.12.014.

[116] C. Teijeiro-Valiño, R. Novoa-Carballal, E. Borrajo, A. Vidal, M. Alonso-Nocelo, M. de la Fuente Freire, P. P. P. Lopez-Casas, M. Hidalgo, N. Csaba, M. J. Alonso. A multifunctional drug nanocarrier for efficient anticancer therapy. *Journal of Controlled Release*. 294, 154–164. (2019). doi: 10.1016/j.jconrel.2018.12.002.

[117] J. Schust, B. Sperl, A. Hollis, T. U. Mayer, T. Berg. Stattic: A Small-Molecule Inhibitor of STAT3 Activation and Dimerization. *Chemistry and Biology*. 13, 1235–1242. (2006). doi: 10.1016/j.chembiol.2006.09.018.

[118] S. S. Chung, N. Giehl, Y. Wu, J. V. Vadgama. STAT3 activation in HER2-overexpressing breast cancer promotes epithelial-mesenchymal transition and cancer stem cell traits. *International Journal of Oncology*. 44, 403–411. (2014). doi: 10.3892/ijo.2013.2195.

[119] Z. Han, X. Wang, L. Ma, L. Chen, M. Xiao, L. Huang, Y. Cao, J. Bai, D. Ma, J. Zhou, Z. Hong. Inhibition of STAT3 signaling targets both tumor-initiating and differentiated cell populations in prostate cancer. *Oncotarget*. 5, 8416–

8428. (2014). doi: 10.18632/oncotarget.2314.
[120] P. A. Agudelo-Garcia, J. K. de Jesus, S. P. Williams, M. O. Nowicki, E. A. Chiocca, S. Liyanarachchi, P. K. Li, J. J. Lannutti, J. K. Johnson, S. E. Lawler, M. S. Viapiano. Glioma cell migration on three-dimensional nanofiber scaffolds is regulated by substrate topography and abolished by inhibition of STAT3 signaling. *Neoplasia*. 13, 831–840. (2011). doi: 10.1593/neo.11612.
[121] A. A. Cardoso, Y. Jiang, M. Luo, A. M. Reed, S. Shahda, Y. He, A. Maitra, M. R. Kelley, M. L. Fishel. APE1/Ref-1 Regulates STAT3 Transcriptional Activity and APE1/Ref-1-STAT3 Dual-Targeting Effectively Inhibits Pancreatic Cancer Cell Survival. *PLoS ONE*. 7, (2012). doi: 10.1371/journal.pone.0047462.
[122] T. Ji, D. Gong, Z. Han, X. Wei, Y. Yan, F. Ye, W. Ding, J. Wang, X. Xia, F. Li, W. Hu, Y. Lu, S. Wang, J. Zhou, D. Ma, Q. Gao. Abrogation of constitutive Stat3 activity circumvents cisplatin resistant ovarian cancer. *Cancer Letters*. 341, 231–239. (2013). doi: 10.1016/j.canlet.2013.08.022.
[123] L. Lin, D. Jou, Y. Wang, H. Ma, T. Liu, J. Fuchs, P. K. Li, J. Lü, C. Li, J. Lin. STAT3 as a potential therapeutic target in ALDH+ and CD44+/CD24+ stem cell-like pancreatic cancer cells. *International Journal of Oncology*. 49, 2265–2274. (2016). doi: 10.3892/ijo.2016.3728.
[124] M. Spitzner, B. Roesler, C. Bielfeld, G. Emons, J. Gaedcke, H. A. Wolff, M. Rave-Fränk, F. Kramer, T. Beissbarth, J. Kitz, J. Wienands, B. M. Ghadimi, R. Ebner, T. Ried, M. Grade. STAT3 inhibition sensitizes colorectal cancer to chemoradiotherapy in vitro and in vivo. *International Journal of Cancer*. 134, 997–1007. (2014). doi: 10.1002/ijc.28429.
[125] Y. H. Huang, O. Molavi, A. Alshareef, M. Haque, Q. Wang, M. P. Chu, C. P. Venner, I. Sandhu, A. C. Peters, A. Lavasanifar, R. Lai. Constitutive activation of STAT3 in myeloma cells cultured in a three-dimensional, reconstructed bone marrow model. *Cancers*. 10, (2018). doi: 10.3390/cancers10060206.
[126] J. M. Yingling, W. T. McMillen, L. Yan, H. Huang, J. S. Sawyer, J. Graff, D. K. Clawson, K. S. Britt, B. D. Anderson, D. W. Beight, D. Desaiah, M. M. Lahn, K. A. Benhadji, M. J. Lallena, R. B. Holmgaard, X. Xu, F. Zhang, J. R. Manro, P. W. Iversen, C. V. Iyer, R. A. Brekken, M. D. Kalos, K. E. Driscoll. Preclinical assessment of galunisertib (LY2157299 monohydrate), a first-in-class transforming growth factor-β receptor type I inhibitor. *Oncotarget*. 9, 6659–6677. (2018). doi: 10.18632/oncotarget.23795.
[127] M. R. Schnorenberg, S. P. Yoo, M. V. Tirrell, J. L. Labelle. Synthesis and Purification of Homogeneous Lipid-Based Peptide Nanocarriers by Overcoming Phospholipid Ester Hydrolysis. *ACS Omega*. 3, 14144–14150. (2018). doi: 10.1021/acsomega.8b01772.
[128] P. Zhang, W. Chan, I. L. Ang, R. Wei, M. M. T. Lam, K. M. K. Lei, T. C. W. Poon. Revisiting Fragmentation Reactions of Protonated α-Amino Acids by High-Resolution Electrospray Ionization Tandem Mass Spectrometry with Collision-Induced Dissociation. *Scientific Reports*. 9, 1–10. (2019). doi: 10.1038/s41598-019-42777-8.
[129] M. M. Tibben, S. Huijberts, W. Li, A. H. Schinkel, A. Gebretensae, H. Rosing, J. H. Beijnen. Liquid chromatography-tandem mass spectrometric assay for the quantification of galunisertib in human plasma and the application in a pre-clinical study. *Journal of Pharmaceutical and Biomedical Analysis*. 173, 169–175. (2019). doi: 10.1016/j.jpba.2019.05.037.

USC UNIVERSIDADE DE SANTIAGO DE COMPOSTELA

CHAPTER 3

Polymeric nanocapsules for the intracellular delivery of monoclonal antibodies

USC
UNIVERSIDADE
DE SANTIAGO
DE COMPOSTELA

USC
UNIVERSIDADE
DE SANTIAGO
DE COMPOSTELA

Chapter 3: Polymeric nanocapsules for the intracellular delivery of monoclonal antibodies

This work has been done in collaboration with the research group NanoBiomaterials for Targeted Therapies (i3s, University of Porto, Portugal), Humanitas Research Hospital (Milano, Italy), SINTEF AS (Norway), and University of Navarra (Spain) under the frame of the 2^2-INTRATARGET project. Also, cryo-EM image capture, process, and interpretation have been made in collaboration with Abrescia's Lab (CIC bioGUNE - Centro de Investigación Cooperativa en Biociencias, Derio, Spain).

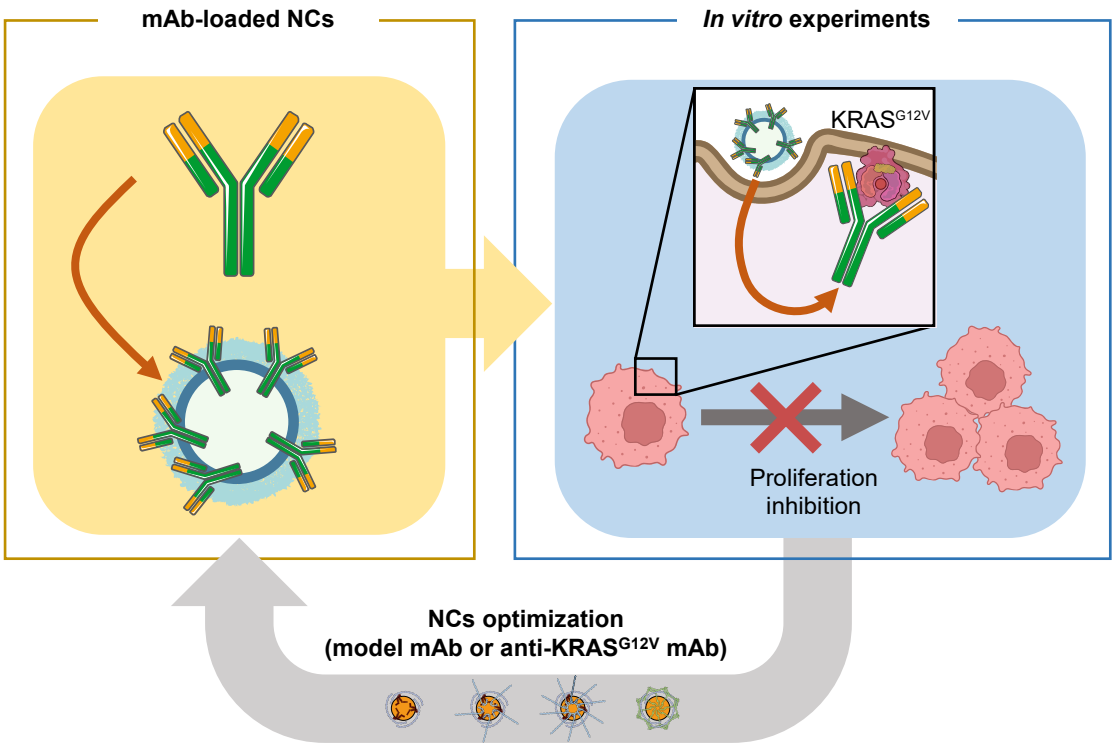
ABSTRACT

The clinical use of monoclonal antibodies (mAb) has become a milestone in cancer therapy strategy due to their high target specificity, long-circulating times, and reduced off-target toxicities compared to classical chemotherapy. Still, more efficient treatments are needed, especially for those tumors whose targets' expression is restricted to the intracellular space. Indeed, highly relevant targets, such as the G12V mutation of Kirsten rat sarcoma viral oncogene homolog ($KRAS^{G12V}$), highly remains untouched due to the inability of mAbs to cross cell membranes. With this critical problem in mind, the objective of the work presented in this chapter has been to assess the feasibility of delivering mAbs inside cancer cells through the application of nanotechnology. For this, first, bevacizumab (BVZ) was used as a model mAb to validate the capacity of polymeric nanocapsules to load mAbs efficiently and to be internalized in cancer cells. Second, the anti-$KRAS^{G12V}$ mAb was loaded into the nanocapsules, and the mechanism of action (target engagement) of the mAb delivered inside the cell was evaluated in $KRAS^{G12V}$-expressing cancer cell lines. Overall, the results showed the potential of the polymeric nanocapsules to efficiently associate and deliver mAbs inside the cancer cells in an active manner.

USC
UNIVERSIDADE DE SANTIAGO DE COMPOSTELA

USC
UNIVERSIDADE
DE SANTIAGO
DE COMPOSTELA

GRAPHICAL ABSTRACT



Created with https://biorender.com.

USC
UNIVERSIDADE
DE SANTIAGO
DE COMPOSTELA

1. INTRODUCTION

1.1. NEW THERAPEUTIC APPROACHES WITH ANTIBODIES AND NANOTECHNOLOGY

The use of monoclonal antibodies (mAbs) for targeting cancer-related extracellular structures has become a successful therapeutic strategy in several tumors, including lung cancer. Currently, 11 different mAb-based therapies against lung cancer have been approved by the FDA or EMA (Table 1).

Table 1. Summary of the monoclonal antibody-based lung cancer therapies approved in the USA/EU

mAb	Trade name (location; year of approval)	Year of first approval (for lung cancer)	Indication	Mechanism of action	Ref.
Amivantamab	Rybrevant™	2021 (FDA and EMA)	NSCLC	Anti-EGF / Anti-MET	[1,2]
Atezolizumab	Tecentriq™	2016 (FDA) 2017 (EMA)	NSCLC and SCLC	Anti-PD-L1	[3,4]
Bevacizumab	Alymsys™, Avastin™, Aybintio®, Oyavas®, Mvasi™, Vegzelma™, and Zirabev®	2004 (FDA) 2005 (EMA)	NSCLC	Anti-VEGF	[5,6]
Cemiplimab	Libtayo™	2021 (FDA and EMA)	NSCLC	Anti-PD-1	[7,8]
Durvalumab	Imfinzi™	2017 (FDA) 2018 (EMA)	NSCLC and SCLC	Anti-PD-L1	[9,10]
Fam-Trastuzumab-deruxtecan	Enhertu™	2022 (FDA)	NSCLC	Anti-HER2 conjugated to a topoisomerase inhibitor	[11,12]
Ipilimumab	Yervoy™	2020 (FDA and EMA)	NSCLC	Anti-CTLA-4	[13,14]
Necitumumab	Portrazza™	2015 (FDA and EMA) Withdrawn in EU in 2021 (lack of demand)	NSCLC	Anti-EGFR	[14,15]
Nivolumab	Opdivo™	2015 (FDA) 2016 (EMA)	NSCLC and SCLC	Anti PD-1	[16,17]
Pembrolizumab	Keytruda™	2015 (FDA) 2016 (EMA)	NSCLC	Anti-PD-1	[18,19]
Ramucirumab	Cyramza™	2014 (FDA) 2015 (EMA)	NSCLC	VEGFR2 antagonist	[20,21]

Abbreviations: CTLA-4: cytotoxic T-lymphocyte antigen-4. EGF: epidermal growth factor. EGFR: epidermal growth factor receptor. EMA: European Medicines Agency. FDA: USA Food and Drug Administration. HER2: human epidermal growth factor receptor 2. mAb: monoclonal antibody. MET: mesenchymal-epithelial transition factor. NSCLC: non-small cell lung cancer. PD-1: programmed cell death protein 1. PD-L1: programmed death-ligand 1. Ref.: reference. SCLC: small cell lung cancer. VEGFR2: vascular endothelial growth factor receptor 2.

UMA

mAbs exhibit a high specificity for their target, however, they have some critical biopharmaceutical limitations. Notably, mAbs do not have the capacity to cross the cell membrane, and hence, they cannot reach intracellular targets. Nanotechnology has been proposed as a strategy to improve the biodistribution profile of mAbs, facilitate their access to intracellular targets and allow for combination therapy. For example, co-encapsulation of the anti-VEGF mAb bevacizumab and the EGFR tyrosine kinase inhibitor in HA-coated phosphatidylcholine-polycaprolactone lipid-hybrid NPs led to a synergistic antitumor effect in a non-small cell lung cancer model.[22]

A complete review of this topic can be found in previous review articles.[23,24]

1.2. INTRACELLULAR DELIVERY OF MONOCLONAL ANTIBODIES

Many of the most relevant oncological targets remain undruggable as they are located intracellularly, meaning that they are inaccessible for mAbs and do not contain specific, well-defined binding pockets for small cytotoxic molecules to bind. The most frequently mutated oncogene family in human cancers, Kirsten rat sarcoma viral oncogene homolog (KRAS), is known as the most relevant target that remains undruggable for the majority of its mutated forms.[25] Other examples of undruggable oncoproteins are the myelocytomatosis proto-oncogene (c-MYC), myeloblastosis proto-oncogene (MYB), nuclear factor-κB (NF-κB), androgen receptor variant 7 (AR-V7), signal transducer and activator of transcription 3 (STAT3), the tumor-suppressor protein p53, and many more.

Interestingly, only a few nanocarriers have been reported in the literature to facilitate the intracellular delivery of mAbs (Table 2).

Table 2. Nanocarriers for the intracellular delivery of antineoplastic monoclonal antibodies with *in vivo* results described in the literature

Nanosystem type and composition	mAb	Mechanism of action	Tumor model and outcome	Ref.
Liposomes (DPPC / Chol / DSPE-PEG_{2000} / DOTAP)	Bevacizumab (combined with benzoporphyrin derivative monoacid A)	Anti-VEGF (extra- and intracellular)	Pancreatic; co-encapsulation efficacy was 5-fold of free drugs	[26]
Polymeric NCs (PLGA)	Bevacizumab	Anti-VEGF (extra- and intracellular)	Glioblastoma; 21 % reduction in the brain VEGF concentration	[27]
Liposomes (DOPC / DSPE / Chol)	Non-commercialized (combined with DOX)	Anti-S100A4	Breast; co-encapsulation efficacy was 2-fold of DOX-loaded liposomes	[28]
Polymeric NCs (HA / P80 / MCT)	Non-commercialized	Anti-Gasdermin B	Breast (orthotopic); efficacy 2-fold of free mAb	[29]
Polymeric NCs (HA / P80 / MCT)	Non-commercialized	Anti-Mutated KRAS	Pancreatic and colorectal (orthotopic); reduction of tumor growth when encapsulated	[30]

Abbreviations: Chol: cholesterol. DOPC: 1,2-dioleoyl-sn-glycero-3-phosphocholine. DOTAP, 1,2-dioleoyl-3-trimethylammonium-propane. DOX: doxorubicin. DPPC: 2-dipalmitoyl-sn-glycero-3-phosphocholine. DSPE: 1,2-distearoyl-sn-glycero-3-phosphoethanolamine. DSPE-PEG_{2000}: 1,2-distearoyl-sn-glycero-3-phosphoethanolamine-*N*-[methoxy(polyethyleneglycol)-2000. HA: hyaluronic acid. KRAS: Kirsten rat sarcoma viral oncogene homolog. MCT: medium-chain triglycerides. P80: polysorbate 80. PLGA: poly(lactic-co-glycolic acid). Ref.: reference. S100A4: S100 calcium binding protein A4. VEGF: vascular endothelial growth factor.

Our laboratory has shown that polymeric NCs could efficiently deliver an anti-gasdermin B mAb inside cancer cells *in vitro* and *in vivo* in an orthotopic breast model. The results from our previous work on the assessment of the potential of anti-gasdermin B mAb-loaded NCs indicated their capacity to reduce tumor size and metastatic spreading to the lungs on that tumor model.[29]

In another study, liposomes were developed containing the fusogenic lipid 1,2-distearoyl-sn-glycero-3-phosphoethanol-amine-*N*-Arg-Arg-Arg-Arg to achieve a non-endocytic uptake.[28] Doxorubicin and anti-S100A4 mAb co-loaded liposomes led to a 50 % reduction in tumor volume in a liver metastasis 4T1 breast tumor model. Moreover, this effect was found to be driven by the reduction in the S100A4 protein levels and activation of caspase 3, which resulted in increased apoptosis processes.

Of note, mAbs that are already commercialized might also benefit from their intracellular delivery, as is the case for bevacizumab (BVZ). Some authors have claimed that BVZ could potentially target the intracellular VEGF pool of cancer cells. Indeed, Tangutoori *et al.*[26] found that the co-encapsulation of the photosensitizer benzoporphyrin and BVZ led to a higher efficacy than the combination of liposomal benzoporphyrin and free BVZ. In this sense, the synergistic effect might come from the interaction of BVZ with VEGF, whose levels usually increase after phototherapy. Moreover, the encapsulation of BVZ into PLGA NPs led to a 21 % reduction in the brain VEGF concentration in comparison to free BVZ in a glioblastoma model, which was hypothesized to be driven by interaction with the intracellular VEGF pool in those cancer cells when loaded into NPs.[27] Finally, the incorporation of BVZ into anti-CD44v6 human antibody fragment-decorated PEG·PLGA NPs led to a 42 % decrease in the intracellular concentration of VEGF *in vitro* in CD44v6-expressing MKN74 colorectal cancer cells, with no effect in the case of free BVZ.[31]

On the other hand, the encapsulation of mAbs such as BVZ was also explored to improve their storage stability, increase their circulation time, and enhance their tumor accumulation. For example, the loading of BVZ into PLGA NPs and subsequent freeze-drying preserved the BVZ activity of the mAb for 6 months with no need for refrigeration.[32] Moreover, its encapsulation into albumin NPs was found to enhance its antiangiogenic effect due to a higher tumor accumulation, as the BVZ tumor concentration and plasmatic concentration, when incorporated into the NPs, were 4-fold and 6 times lower, respectively, than those of free BVZ.[33]

In this chapter, we will study the advantages of nanotechnology to deliver an anti-mutated KRAS mAb intracellularly to cancer cells to inhibit their proliferation. The KRAS pathway physiopathology and KRAS-targeted treatments are discussed in the next section.

1.3. THE KRAS PATHWAY IN LUNG CANCER

RAS proteins, that is, KRAS, neuroblastoma RAS viral (v-ras) oncogene homolog (NRAS), and Harvey rat sarcoma viral oncogene homolog (HRAS), are GTPases that regulate cell signaling. The downstream signaling pathway of KRAS is exhibited in Figure 1.

USC UNIVERSIDADE DE SANTIAGO DE COMPOSTELA

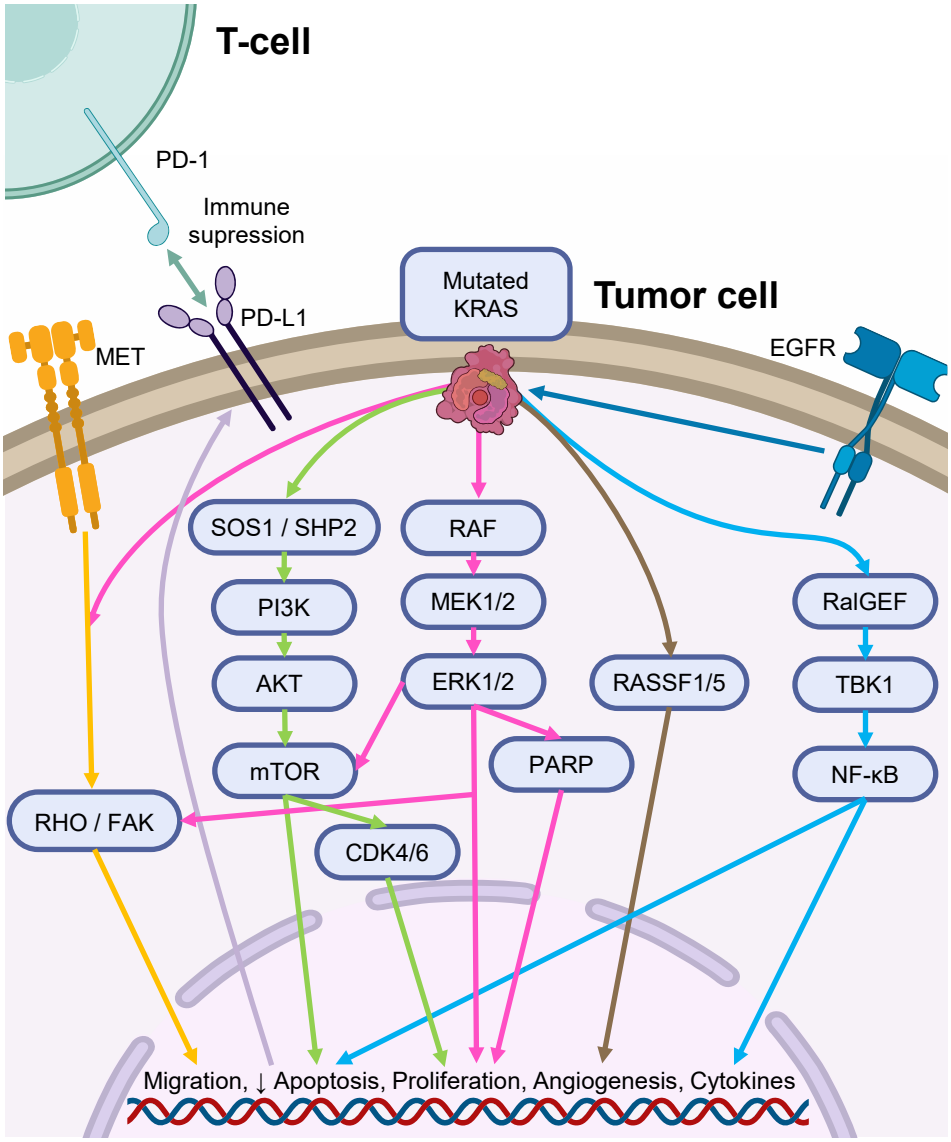


Figure 1. Signaling pathways downstream mutated KRAS and biological implications on tumor cells

Abbreviations: AKT: protein kinase B. ERK: extracellular signal-regulated kinase. KRAS: Kirsten rat sarcoma viral oncogene homolog. MEK: mitogen-activated protein kinase kinase. mTOR: mammalian target of rapamycin. NF-κB: Nuclear factor kappa-light-chain-enhancer of activated B cells. PI3K: phosphoinositide 3-kinase. RalGEF: Ral-selective guanine nucleotide exchange factor. RAF: rapidly accelerated fibrosarcoma kinase. RASSF: Ras-association domain family protein. RHO: Ras homologous GTPase. TBK1: TANK-binding kinase 1. Created with https://biorender.com.

RAS mutations are present in 27 % of all human cancers, 85, 11, and 4 % of those being present in *KRAS*, *NRAS*, and *HRAS*, respectively.[34] The *RAS* mutation prevalence is even higher in the case of NSCLC, as an analysis of 17,095 NSCLC samples revealed that 27.5 % of them harbored *KRAS* mutations.[35] Mutations in the *KRAS* gene usually occur on the second exon and, more precisely, on the codons 12 (83 %) and 13 (14 %), leading to changes in the 12th and 13th amino acids.[34] In NSCLCs, the most frequent mutations in the codon 12 affect the 34th (G) and 35th (G) bases, leading to the substitutions of glycine for cysteine ($KRAS^{G12C}$; ≈ 40 %), valine ($KRAS^{G12V}$; ≈ 20 %), aspartic acid ($KRAS^{G12D}$; ≈ 15 %), and alanine

($KRAS^{G12A}$; ≈ 8 %) in the traduced protein.[35,36] The rates of the different KRAS mutations in lung cancer are summarized in [37].

Wild-type KRAS has 2 switch regions that interact with effector proteins and RAS pathway regulators. These interactions change the conformation of the KRAS protein between its active and inactive form. In this sense, the wild-type KRAS acts as a biological switch of several signaling pathways, ultimately regulating cell migration, decreasing apoptosis, and increasing proliferation, angiogenesis, and the production of several cytokines. On the other hand, mutated KRAS is locked or preferentially disposed on its active conformation, leading to the continuous activation of the signaling pathways downstream of KRAS and promoting tumor growth and invasion. Of note, different *KRAS* mutations also cause different preferential activations of downstream signaling pathways. For example, $KRAS^{G12C}$ or $KRAS^{G12V}$ lead to an increase of Ras-related protein (RAL) A/B and a reduction of PI3K/AKT signaling pathways compared to other KRAS mutant isoforms or the wild-type cell lines.[38] Moreover, $KRAS^{G12V}$, $KRAS^{G12D}$, and $KRAS^{G13C}$ have higher expression of PD-L1 compared with other variants in NSCLC. Consequently, different KRAS mutations led to specific pathological behaviors.

Several therapeutic approaches are being investigated in clinical trials for the treatment of the different KRAS mutations and can be found in the literature.[39]

The highest efforts on the pharmacological treatment of KRAS mutations were carried out for $KRAS^{G12C}$ due to its high incidence. Indeed, tens of $KRAS^{G12C}$ inhibitors have enrolled in clinical trials and, in late 2021 - early 2022, a milestone in KRAS-dependent NSCLC treatment was achieved with the FDA and EMA approval of the irreversible selective inhibitor of the $KRAS^{G12C}$ Lumakras™ (sotorasib). In this sense, Lumakras™ has become the first line of treatment for advanced NSCLC with $KRAS^{G12C}$ mutation that progressed after at least one previous treatment. Sotorasib establishes a covalent bond with the cysteine resulting from the *KRAS* mutation, locking the $KRAS^{G12C}$ in its inactive form while not affecting the wild-type KRAS, leading to minimal off-target activity. Unluckily, 60 % of sotorasib patients develop acquired resistance to the drug after mutation of other *KRAS* codons, implying the necessity for combination therapy when using anti-KRAS drugs.[37]

Combination therapy was proposed with other drugs involved in the KRAS pathway, such as RAF, MEK, ERK, PI3K, AKT, mTOR CDK 4/6, SOS1, SHP2, EGFR, and MET inhibitors, as well as anti-PD-L1 and PD-1 (Figure 1).[40] Initially, anti-KRAS therapies were combined with classical chemotherapy, such as platinum-based, gemcitabine, taxanes, or pemetrexed. Of note, based on these treatment strategies, $KRAS^{G12V}$ was found to be highly resistant to pemetrexed. In clinical trials, special attention was given to the simultaneous inhibition of KRAS and downstream pathways. In this sense, $KRAS^{G12C}$ small-molecule inhibitors are being tested in combination with MEK inhibitors such as trametinib (NCT04185883) and cobimetinib (NCT03989115) and anti-PD-1 mAbs such as pembrolizumab (NCT03785249, NCT04185883, NCT03600883, and NCT04613596).

Finally, much more effort is needed to obtain adequate treatments for $KRAS^{G12V}$ and $KRAS^{G12D}$-mutated NSCLC. In the case of $KRAS^{G12V}$ lung cancer, and excluding T-cell-based therapies, only 3 clinical trials are currently ongoing: VS-6766 (MEK/RAF inhibitor) (Phase I / NCT03875820); VS-6766 + Defactinib (FAK inhibitor) (Phase II / NCT04620330), and carboplatin + paclitaxel + BVZ (Phase III / NCT02743923).

Table 3 summarizes the active clinical trials in the US/EU for the treatment of $KRAS^{G12V}$ and $KRAS^{G12D}$ lung cancers.

Table 3. Summary of the current treatments for $KRAS^{G12D}$ and $KRAS^{G12V}$-mutated tumors undergoing clinical trials in the USA/EU

Drug	Target	Tumor type	Phase/NCT (Last update)	Ref.
anti-$KRAS^{G12V}$ mTCR cells	$KRAS^{G12V}$	Any $KRAS^{G12V+}$ cancer	I/II / NCT03190941 (2022)	-
anti-$KRAS^{G12V}$ mTCR cells	$KRAS^{G12V}$	Any $KRAS^{G12V+}$ cancer	I/II / NCT04146298 (2022)	-
VS-6766	$KRAS^{G12V}$	$KRAS^{G12V+}$ NSCLC	II / NCT04620330 (2022)	[41]
VS-6766	$KRAS^{G12V}$	$KRAS^{G12V+}$ NSCLC	I / NCT03875820 (2022)	-
Carboplatin + paclitaxel + bevacizumab	$KRAS^{G12V/C}$	$KRAS^{G12V/C+}$ NSCLC	III / NCT02743923 (2021)	
HRS-4642	$KRAS^{G12D}$	Any $KRAS^{G12D+}$ cancer	I / NCT05533463 (2022)	-
anti-$KRAS^{G12D}$ mTCR cells	$KRAS^{G12D}$	Any $KRAS^{G12D+}$ cancer	I/II / NCT03745326 (2022)	-
Bortezomib	$KRAS^{G12D}$	$KRAS^{G12D+}$ NSCLC	II / NCT01833143 (2020)	-
Vemurafenib (+ sorafenib)	$KRAS^{G12D}$	$KRAS^{G12D+}$ pancreatic cancer	II / NCT05068752 (2021)	-
ASP3082	$KRAS^{G12D}$	Any $KRAS^{G12D+}$ cancer	I / NCT05382559 (2022)	-
$KRAS^{G12D}$ siRNA (loaded in mesenchymal stromal cells-derived exosomes)	$KRAS^{G12D}$	$KRAS^{G12D+}$ pancreatic cancer	I / NCT03608631 (2022)	[42]
Repotrectinib (+ trametinib)	$KRAS^{G12D}$	Any $KRAS^{G12D+}$ cancer	I/II / NCT05071183 (2022)	-
TAS0612	$KRAS^{G12C/D}$	Any $KRAS^{G12C/D+}$ cancer	I / NCT04586270 (2021)	-

Abbreviations: EU: Europe. KRAS: Kirsten rat sarcoma viral oncogene homolog. NSCLC: non-small cell lung cancer. Ref.: reference. USA: United States of America.

We believe that the encapsulation of an anti-$KRAS^{G12V}$ mAb can be a promising therapeutic approach for reducing the proliferation of $KRAS^{G12V}$-mutated lung cancers. In this chapter, mAb-loaded NCs will be developed by using the anti-VEGF mAb bevacizumab as a model protein. Then, the recognition of the $KRAS^{G12V}$ by the nano-encapsulated mAb will be studied *in vitro*. In this sense, this chapter represents one of the first works on the treatment of lung cancer with an anti-$KRAS^{G12V}$ mAb. However, as abovementioned, combination therapy might still be needed to achieve adequate translatable treatments.

1.4. OBJECTIVES

In this chapter, we aimed to develop new formulations of NCs adapted for the encapsulation and intracellular delivery of an anti-$KRAS^{G12V}$ mAb with the final goal of exploring new personalized therapies for the treatment of lung cancer.

2. MATERIALS AND METHODS

2.1. NANOCAPSULE ELABORATION

DOTAP, Miglyol® 812N, D-α-tocopherol polyethylene glycol 1000 succinate, DL-α-tocopherol, Ethanol absolute, Kolliphor® HS15, phosphate-buffered saline tablets,

polyethylene glycol (5 kDa) poly-α-glutamic acid (10 u), and polysorbate 80 were purchased from the companies mentioned in Chapter 1 and 2.

Lipoid S100 was purchased from Lipoid GmbH (Ludwigshafen am Rhein, Germany), laurylated octaarginine (C_{12}-R_8) was purchased from ChinaPeptides (Shanghai, China), and bevacizumab was kindly gifted by mAbxience (León, Spain).

2.1.1. Blank nanocapsules

Blank SD-noPEG and SD-TPGS were formulated as mentioned in Chapter 2.

For SD-noPEG(+PC), 700 µL of oil phase (38.57 mg·mL^{-1} DL-α-tocopherol, 11.43 mg·mL^{-1} Lipoid S100, and 0.71 mg·mL^{-1} DOTAP in ethanol) was poured directly onto 3.306 mL of aqueous phase (PEG·PGA 2.41 mg·mL^{-1}) under magnetic stirring at 700 rpm. Stirring was kept until NCs volume was lower than 2 mL. Then, it was raised to 2 mL using ultrapure water.

For SD-noPEG(MCT), 1,070 µL of oil phase (25.23 mg·mL^{-1} Miglyol 812N and 0.93 mg·mL^{-1} DOTAP in ethanol) was poured directly onto 3.000 mL of water under magnetic stirring at 700 rpm. After 10 min of stirring, 133 µL of PEG·PGA 30 mg·mL^{-1} in water were added to the formulation. Stirring was kept until NCs volume was lower than 2 mL. Then, it was raised to 2 mL using ultrapure water.

For SD-noPEG(MCT+PC), 1,004 µL of oil phase (23.90 mg·mL^{-1} Miglyol 812N, 3.03 mg·mL^{-1} Lipoid S100, and 2.23 mg·mL^{-1} DOTAP in ethanol) was poured directly onto 3.000 mL of aqueous phase (PEG·PGA 1.33 mg·mL^{-1}) under magnetic stirring at 700 rpm. Stirring was kept until NCs volume was lower than 2 mL. Then, it was raised to 2 mL using ultrapure water.

For SD-TPGS(C_{12}-R_8), 870 µL of oil phase (31.03 mg·mL^{-1} DL-α-tocopherol, 9.20 mg·mL^{-1} TPGS, and 1.15 mg·mL^{-1} C_{12}-R_8 in ethanol) was poured directly onto 2.872 mL of aqueous phase (PEG·PGA 1.39 mg·mL^{-1}) under magnetic stirring at 700 rpm. Stirring was kept until NCs volume was lower than 2 mL. Then, it was raised to 2 mL using ultrapure water.

For SD/SE-P80(MCT), 400 µL of oil phase (100 mg·mL^{-1} Miglyol 812N, 75 mg·mL^{-1} polysorbate 80, and 2.23 mg·mL^{-1} DOTAP in ethanol) was poured directly onto 1.600 mL of aqueous phase (PEG·PGA 2.5 mg·mL^{-1}) under magnetic stirring at 700 rpm. Stirring was kept until NCs volume was lower than 1.5 mL. Then, it was raised to 2 mL using ultrapure water.

For SD-TPGS(↑), 920 µL of oil phase (29.35 mg·mL^{-1} DL-α-tocopherol, 26.09 mg·mL^{-1} TPGS, and 1.09 mg·mL^{-1} DOTAP in ethanol) was poured directly onto 2.908 mL of water under magnetic stirring at 700 rpm. After 10 min of stirring, 133 µL of PEG·PGA 30 mg·mL^{-1} in water were added to the formulation. Stirring was kept until the NCs volume was lower than 2 mL. Then, it was raised to 2 mL using ultrapure water.

For SD-P80, 1,070 µL of oil phase (37.38 mg·mL^{-1} polysorbate 80, 25.23 mg·mL^{-1} DL-α-tocopherol, and 0.93 mg·mL^{-1} DOTAP in ethanol) was poured directly onto 3.040 mL of water under magnetic stirring at 700 rpm. After 10 min of stirring, 133 µL of PEG·PGA 30 mg·mL^{-1} in water were added to the formulation. Stirring was kept until the NCs volume was lower than 2 mL. Then, it was raised to 2 mL using ultrapure water.

USC UNIVERSIDADE

2.1.2. mAb-loaded nanocapsules

In all cases, mAb (BVZ or anti-$KRAS^{G12V}$ mAb) were added to the aqueous phase before emulsification to obtain a mAb concentration of 2 $mg \cdot mL^{-1}$ in the final formulation.

2.2. ISOLATION OF NANOCAPSULES

NCs were ultracentrifuged at ≈ 110,000 g (40,000 rpm) for 1 h at 15 °C as performed in previous chapters.

2.3. CALCULATION OF THE LOADING CAPACITY, ASSOCIATION EFFICIENCIES, AND RELEASE

The loading capacity, association efficiencies (AEs), and release studies were performed as explained in chapter 2. However, the BVZ concentration was calculated by enzyme-linked immunosorbent assay (ELISA) or quantitative sodium dodecyl sulfate-polyacrylamide gel electrophoresis (SDS-PAGE), while the anti-$KRAS^{G12V}$ mAb AE was calculated by quantitative SDS-PAGE.

2.4. ENZYME-LINKED IMMUNOSORBENT ASSAY FOR BEVACIZUMAB QUANTITATION

Association efficiencies of BVZ were performed indirectly by analyzing its unbound fraction, corresponding to its concentration in the infranatant after ultracentrifugation of the NCs containing the free mAb (infranatant when ultracentrifuged). Calibration curves were prepared with the interference of the free compounds present in the infranatant of the blank formulation.

100 µL of antigen solution [0.05 $\mu g \cdot mL^{-1}$ VEGF Protein (Peprotech-Recombinant Human VEGF165) (Cranbury, NJ, USA) in coating buffer (1.59 $mg \cdot mL^{-1}$ Na_2CO_3, 2.94 $mg \cdot mL^{-1}$ $NaHCO_3$, and 0.5 $mg \cdot mL^{-1}$ NaN_3 at pH 9.59)] were added to a high protein-binding capacity polystyrene ELISA plate (MediSorp, ThermoFisher Scientific, Waltham, MA, USA). Then, the plate was covered and incubated overnight at 4°C. Afterward, the plate was inverted and taped on absorbent paper to remove excess liquid, and each well was washed three times by adding 300 µL of washing solution [PBS supplemented with 0.05 % (v/v) polysorbate 20 (Millipore, Burlington, MA, USA)]. Plates were shaken for 5 min under 300-rpm orbital shaking and inverted and tapped on paper. Then, they were dried, and 300 µL of blocking solution [2 % (w/v) skimmed dry milk in washing buffer)] was added to each well. Plates were covered and incubated for 2 h at 37 °C under 300 rpm. Once incubated, the plate was inverted, taped on absorbent paper, washed three times by adding 300 µL of washing solution, shaken for 5 min under 300 rpm, and inverted and tapped on paper. A working BVZ solution containing interference at the same concentration as in the samples was prepared by mixing the stock BVZ solution with PBS and an infranatant of blank NCs. The BVZ calibration points were prepared by diluting the working solution with interference-enriched PBS at the same concentration as in the samples. Calibration curves were pipetted in duplicate, adding 100 µL of solutions with the following BVZ concentrations: 1,000, 750, 500, 250, 125, 100, 75, 50, 25, 12.5, 10, 6.25, 3.10, 1.50, and 0 $ng \cdot mL^{-1}$. Also, 100 µL of PBS-diluted samples were added to the plate. Then, the plate was covered and incubated for 2 h at room temperature or 1 h at 37 °C under 300 rpm. Later, the plate was inverted and taped on absorbent paper, and each well was washed three times by adding 300 µL of washing solution. Then, the plate was shaken for 5 min under

300 rpm and inverted, tapped on paper, and kept open. Once dried, 100 µL of secondary antibody (Ab-HRP; 0.08 µg·mL^{-1} Goat anti-human IgG HRP conjugated; Fcγ Fragment Specific, in PBS) (Thermo Fisher Scientific, Waltham, MA, USA) were added to the wells, followed by incubation of 1 h at 37 °C. After the incubation, the plate was inverted and taped on absorbent paper, and the wells were washed three times by adding 300 µL of washing solution. Then, it was shaken for 5 min under 300 rpm and inverted, and tapped on paper. The plate was dried again, and 50 µL of ABTS (Roche, Basel, Switzerland) was added to each well. The absorbance at 405 nm was recorded in a Synergy H1 Hybrid Multi-Mode Reader (BioTek, Winooski, VT, USA) every 5 min for 30 min. The condition best fit to a sigmoidal four-parameter logistic (4PL) curve was chosen. The equation of the curve, r^2, and interpolation of results were obtained with GraphPad Prism 9 (San Diego, CA, USA).

2.5. QUANTITATIVE SDS-PAGE

Anti-KRAS^{G12V} mAb was quantified by SDS-PAGE. Samples containing the unbound mAb and calibration points were diluted 1:1 in 2 × Laemmli buffer and boiled for 5 min. 20 µL of calibration curves or samples were loaded and resolved in 12 % SDS-polyacrylamide gels under reducing conditions. Calibration points consisted of 2, 1.6, 1, 0.6, and 0.2 µg per lane. Protein gels were fixed with 10 % CH_3OH and 7 % acetic acid in ultrapure water for 45 min and stained by incubation with SYPRO® Ruby in the dark for 18 h in mild agitation. Analysis was performed in a Bio-Rad Gel Doc XR+ instrument. Gels were analyzed with GelAnalyzer 19.1 (www.gelanalyzer.com) by Istvan Lazar Jr., Ph.D., and Istvan Lazar Sr., Ph.D., CSc. A graph representing the intensity of the black-colored bands *vs.* the lane length was built for each lane. The peaks corresponding to the heavy chains were integrated after background subtraction. Sample association efficiency was determined by extrapolation of the area under the curve of the bands from the standard curve of known mAb amounts.

2.6. FLUORESCENT LABEL OF BEVACIZUMAB

2.6.1. Synthesis

467 µL of BVZ 32.11 mg·mL^{-1} were mixed with 53.7 µL of 1 M sodium bicarbonate buffer. Then, 58.6 µL of 10 mg·mL^{-1} of the succinimidyl (NHS) ester of Alexa Fluor™ 488 in DMSO were added to the mixture in the dark and at 4 °C under magnetic stirring at 300 rpm. The reaction was kept overnight. Then, the product was diluted with 10 mL of PBS and subjected to approximately 15 filtration cycles in 15 -Amicon® filters of 30 kDa cut-off at 5,000 g for approximately 30 min each cycle, refilling the solution with PBS to keep a 10 mL volume. Then, it was centrifuged until obtaining approximately 500 µL of the conjugated product.

2.6.2. Characterization of the ^{AF488}BVZ product

The absorbance of 1 mL of 1,000 ×-diluted ^{AF488}BVZ in PBS was measured at 280 and 495 nm in a Beckman Coulter® Du730 UV-Vis spectrophotometer. The protein conjugate concentration was calculated as in Equation 1.

USC DE SANTIAGO DE COMPOSTELA

$$[^{AF488}\text{BVZ}]\ (\text{M}) = \frac{[A_{280} - (A_{495} \cdot CF)] \cdot DF}{l \cdot E_{\text{IgG}}}$$

Where $[^{AF488}\text{BVZ}]$ is the molarity of the ^{AF488}BVZ product, A_{280} is the absorbance of the sample at 280 nm, A_{495} is the absorbance of the sample at 495 nm, CF is a correction factor for the contribution of Alexa Fluor™ 488 to the absorbance at 280 nm, CF = 0.11. DF is the dilution factor, l is the length of the cuvette in cm. l = 1 cm. And E_{IgG} is the molar extinction coefficient of a typical IgG at 280 nm. E_{IgG}=203,000 $cm^{-1} \cdot M^{-1}$.

Equation 1. Calculation of the concentration of ^{AF488}BVZ based on the absorbance of the IgG and AF488

The degree of labeling (DOL) was calculated as in Equation 2.

$$DOL\ (\text{moles of AF488 / mol } ^{AF488}\text{BVZ}) = \frac{A_{495} \cdot DF}{l \cdot E_{\text{AF488}} \cdot [^{AF488}\text{BVZ}]}$$

Where DOL is the degree of labeling in moles of AF488 per mol of ^{AF488}BVZ, A_{495} is the absorbance of the sample at 495 nm, DF is the dilution factor, l is the length of the cuvette in cm. l = 1 cm. E_{AF488} is the molar extinction coefficient of the dye at 495 nm. E_{AF488}=71,800 $cm^{-1} \cdot M^{-1}$. And $[^{AF488}\text{BVZ}]$ is the molarity of the ^{AF488}BVZ product.

Equation 2. Calculation of the degree of labeling of ^{AF488}BVZ

2.6.3. Calculation of the amount of ^{AF488}BVZ product per NC

The amount of ^{AF488}BVZ added to the NCs was established based on the relative fluorescence units (RFU) of 100 ppm of DiD (concentrations used in Chapter 1) to obtain similar signals. To do so, the fluorescence values of solutions of ^{AF488}BVZ and DiD containing the same theoretical moles of fluorochromes were recorded at their maximum excitation/emission wavelengths. Our ^{AF488}BVZ resulted in being 259 times brighter than DiD. Based on this result, a mixture of 98 % unlabeled BVZ and 2 % ^{AF488}BVZ (w/w) was used when formulating the BVZ-loaded NCs.

2.7. IN VITRO ASSAYS

2.7.1. Cell lines

LLC-PK1 and Hep G2 were used to evaluate the general toxicity and membrane disruption by blank NCs. CMT 167 ($KRAS^{G12V}$-mutated) and A549 ($KRAS^{G12S}$-mutated) were used as mice and human lung cancer cells, respectively. DMEM with 10 % FBS and 1 × penicillin-streptomycin was used as the cell culture medium in all *in vitro* experiments.

2.7.2. Toxicity

2.7.2.1. General cytotoxicity in LLC-PK1 and Hep G2

Cytotoxicity in LLC-PK1 and Hep G2 was assessed from the study of the metabolic activity. LLC-PK1 and Hep G2 were seeded at a cell density of 22,000 and 80,000 cells·cm^{-2},

respectively, and kept growing for 24 h. Then, they were exposed to NCs or treatments. After 24 h, media from all plates were discarded. 200 µL of fresh medium and 50 µL of 5 mg·mL^{-1} 3-(4,5-Dimethyl-2-thiazolyl)-2,5-diphenyl-2H-tetrazolium bromide (MTT) in PBS was added to the cells and incubated for 4 h in the dark. During this time, living cells will transform the water-soluble MTT into a water-insoluble, purple-colored formazan derivative. Media from all plates were discarded again. 200 µL of DMSO, 25 µL of 0.1 M glycine, and 0.1 M NaCl buffer (pH 10.5) were added to each well to solubilize the formazan. The plate was shaken for 10 min at room temperature, and absorbance was read at 570 nm (formazan) with a reference wavelength of 680 nm. The percentage of cell viability was calculated following Equation 3.

$$Viability\ (\%) = \frac{Sample - Cell\text{-}free\ blank}{Mean\ media\ control} \cdot 100$$

Where $Sample$ is the absorbance at 570 nm of the NCs-treated cells, the $Cell\text{-}free\ blank$ is the absorbance of a well that did not contain any cell, and the $Mean\ media\ control$ is the mean of the results from subtracting the absorbance of the cell-free sample blank to cell-containing non-NCs-treated wells.

Equation 3. Calculation of cell viability from MTT assay

2.7.2.2. General membrane damage evaluation in LLC-PK1 and Hep G2

Cell membrane integrity in LLC-PK1 and Hep G2 was assessed from the study of leakage of the intracellular enzyme lactate dehydrogenase (LDH). LLC-PK1 and Hep G2 were seeded at a cell density of 22,000 and 80,000 cells·cm^{-2}, respectively, and kept growing for 24 h. Then, they were exposed to NCs. After 24 h, Triton™ X-100 was added to a final concentration of 0.1 % and kept for 10 min at room temperature for the positive control. Then, 100 µL of media from all plates were collected and transferred to another plate. 100 µL of a reaction mixture containing lactate, NAD^+, diaphorase, and 1-(4-Iodophenyl)-5-(4-nitrophenyl)-3-phenylformazan (INT) [Biovision LDH-cytotoxicity assay kit (Biovision, K311-400)] were added to each well and the plate was incubated up to 20 min in the dark. If LDH was leaked, it would catalyze the reaction of lactate into pyruvate, generating an NADH molecule. Then, the diaphorase enzyme would use the produced NADH to transform INT into a red formazan derivative. Absorbance was read at 490 nm (red formazan) with a reference wavelength of 680 nm. The percentage of cell viability was calculated following Equation 4.

$$LDH\ leakage\ (\%) = \frac{(Sample - Cell\text{-}free\ blank) - Mean\ media\ control}{(Triton\ X\text{-}100 - Cell\text{-}free\ blank) - Mean\ media\ control} \cdot 100$$

Where $Sample$ is the absorbance at 490 nm of the NCs-treated cells, the $Cell\text{-}free\ blank$ is the absorbance of a well without cells, the $Mean\ media\ control$ is the mean resulting from subtracting the absorbance of the cell-free sample blank to cell-containing non-treated wells, and the $Triton\ X\text{-}100$ is the absorbance of Triton™ X-100-treated cells.

Equation 4. Calculation of the LDH leakage

USC UNIVERSIDADE DE SANTIAGO DE COMPOSTELA

2.7.2.3. Cytotoxicity by resazurin assay

Cytotoxicity by the resazurin assay was performed as in Chapter 2.

2.7.2.4. Cytotoxicity by 7-AAD staining

7-amino actinomycin D (7-AAD; ThermoFisher Scientific, Waltham, MA, USA) was solubilized in DMSO (20 $mg \cdot mL^{-1}$) and diluted in PBS to a final concentration of 1 $mg \cdot mL^{-1}$. 1 µL of the final 7-AAD solution was added to the washed cells, resuspended to 1 ml with PBS, and analyzed by FACS.

2.7.3. Uptake

Uptake experiments followed by FACS analysis were performed as in Chapter 2.

2.7.3.1. Imaging flow cytometry analysis of DiD- and ^{AF488}BVZ-labeled NCs

500,000 A549 cells per well were seeded in a 6-well plate. After 24 h, media were removed, cells were washed with PBS, and 1937.5 µL of the culture medium and 62.5 µL of NCs were added to the wells. At different time points, media were removed, and cells were washed with PBS. Then cells were incubated with 0.5 mL of trypsin for 5 min, and 1 mL of medium was added to inactivate trypsin. The cell suspension was transferred to 1.5-mL microtubes and centrifuged at 200 g for 5 min at RT. Afterward, the supernatants were collected using micropipettes and discarded. Finally, cell pellets were resuspended in 80 µL of PBS and filtered through 40 µm filters. Cell images were acquired using an Amnis ImageStream^X multispectral imaging flow cytometer (EMD Millipore, Darmstadt, Germany) and the INSPIRE software (Amnis), collecting 10,000 events per sample at a core speed of 60 $mm \cdot s^{-1}$ and 40 × magnification. A 488 nm laser at an intensity of 100 mW was employed to excite the fluorescent labels, and a 785 nm laser at 13.5 mW for side scatter (SSC) imaging. Fluorescence images were collected using a 480 – 560 nm spectral detection channel for ^{AF488}BVZ and 660 – 745 nm for DiD. Single-stained controls consisting of NCs with only one of the fluorophores were used to compensate for crosstalk between channel images on a pixel-by-pixel basis, and non-treated cells were analyzed as negative controls. Moreover, a 785 nm laser at an intensity of 13.5 mW was used for side scatter (SSC) imaging. In that case, the detection range was 745 to 780 nm. Cell suspensions were analyzed twice, first with a regular depth of field and then with the extended depth of field (EDF) option, allowing light from different focal planes to be imaged simultaneously on the detector plane. Cell images were analyzed using IDEAS image-analysis software version 6.2 (Amnis, EDM Millipore, Germany). First, a mask representing the whole cell was created based on the brightfield image. Then, a cytoplasm mask was defined by eroding the whole-cell mask by 4 pixels, equivalent to 2 µm. non-EDF images were used for calculating the percentage of positive cells, internalization score, and co-localization of the dyes. The internalization score (IS) was calculated by comparing the intensity of the eroded mask with the intensity of the whole cell. Internalization is considered to happen when $IS < 0$. In the case of EDF, images were deconvoluted to obtain the final image, and spot counts were studied.

2.7.3.2. Anti-KRAS^{G12V} mAb intracellular staining

50,000 CMT 167 cells per well were plated on 24-well plates with 500 µL of culture medium and incubated at 37 °C for 24 h. Then, cells were treated with blank NCs, anti-

$KRAS^{G12V}$ mAb-loaded NCs, and free mAb in culture medium. Afterward, cells were incubated at 37°C or 4°C for the desired times. Then, the medium was discarded, and wells were rinsed 3 times with 500 µL cold PBS 1 ×. 100 µL of Accutase at 37 °C were added to each well for a maximum of 40 min, and detached cells were collected in FACS tubes. 3 mL of cold FACS washing buffer [2 % FBS in PBS (v/v)] were added per tube, and cells were centrifuged at 1,500 rpm for 5 min at 4 °C. Supernatant was discarded by decantation. Then, cells were fixed by incubating them with 100 µL of 4 % PFA (Sigma-Aldrich, Burlington, MA, USA) aqueous solution per tube at 4 °C for at least 30 min. 3 mL of cold FACS washing buffer were added to each tube and centrifuged at 1,200 rpm for 5 min. Supernatants were discarded by decantation. Then, 100 µL of blocking and permeabilization buffer (0.3 % Triton X-100 and 10 % FBS in PBS 1 ×) was added to each tube. Cells were incubated at 4 °C in the buffer for 1 h. Phycoerythrin (PE)-conjugated anti-mouse antibody [F(ab')2-Goat anti-Mouse IgG (H+L) Secondary Antibody, PE, eBioscience™ (ThermoFisher Scientific, Waltham, MA, USA)] was diluted 100 × in blocking and permeabilization buffer. Then, 100 µL of the diluted fluorescent secondary antibody were added to each tube. Cells were incubated with the secondary antibody for 45 min at 4°C in the dark. Finally, 3 mL of cold FACs washing buffer were added per tube, and tubes were centrifuged at 1,200 rpm for 5 min. The supernatants were discarded by decantation, and the cell pellets were resuspended in 200 µL of PBS and analyzed in BD FACSCalibur instrument (BD Biosciences, Franklin Lakes, NJ, USA), collecting 10,000 events per sample and FlowJo 10.8.1 software (BD Bioscience).

2.7.4. Confocal imaging

For confocal analysis, 2,500 CMT 167 cells or 5,000 A549 per well were plated in an 8-well Millicell EZSlides, in 100 µL of the culture medium and incubated for 24 h at 37 °C. Then NCs were added in the culture medium at a final FBS concentration of 10 % FBS. After incubation, wells were washed with cold PBS 3 times and fixed in PFA 4 %. Slides were analyzed in Leica TCS SP5 X Confocal Laser Scanning Microscope and Leica Application Suite X software (Leica Biosystems, Wetzlar, Germany).

2.7.5. Target engagement

150,000 CMT 167 cells per well were seeded in 6-well plates in the culture medium and incubated for 24 h at 37 °C. Then cells were treated with NCs at 50 nM final mAb concentration (a theoretical amount of 15 µg of mAb per well, 3 wells per condition). After 24, 48, or 72 h, cells were washed twice with PBS 1 ×. 100,000 cells were collected for 7ADD staining and cell mortality analysis by FACS. The remaining cells were centrifuged, and the cell pellet was frozen at -20 °C. Then, the cell pellet was incubated with lysis buffer (Pierce Ip Lysis buffer, ThermoFisher Scientific, Waltham, MA, USA) on ice for 2 h. Cell lysates were centrifuged at 14,0000 rpm for 15 min at 4 °C to remove nuclei and cell debris. Afterward, the supernatant was collected, and protein content was quantified by BCA. To pull down the mAb (with or without its target), 1 mg of total protein (carrying a theoretical amount of 20 µg of mAb) was immunoprecipitated overnight with 40 µL of Protein G PLUS-agarose beads (Santa Cruz Biotechnologies, Santa Cruz, CA, USA) at 4 °C in head-to-tail rotation. For positive target engagement control, 1 mg of CMT 167 cell lysate was incubated for 4 h at 4 °C (head-to-tail rotation) with 5 µg anti-$KRAS^{G12V}$ mAb and then immunoprecipitated as previously mentioned.

Samples were loaded in 12 %-acrylamide PAGE gels. Gels were cast and run by the same methodology mentioned in Chapter 1. Then, a western blot was performed as in Chapter 1 but using a monoclonal anti-KRAS antibody produced in mouse (clone 3B10-2F2, Merck KGaA, Darmstadt, Germany) and an anti-mouse IgG DyLight™ 680 antibody produced in goat (ThermoFisher Scientific, Waltham, MA, USA) as primary and secondary antibodies, respectively. Finally, membranes were scanned in an LI-COR Odyssey Scanner system, and band intensities were quantified with LI-COR Image Studio™ Lite Quantification Software (LI-COR Biosciences, Lincoln, NE, USA).

2.8. DATA PRESENTATION AND STATISTICAL ANALYSIS

Unless indicated otherwise, data are presented as the mean or the mean ± standard deviation of 3 replicates, GraphPad Prism version 9.4.1 (GraphPad, San Diego, CA, USA) was used for data analysis, type I errors (α) were fixed to 0.05, and p-values < 0.05 were considered statistically significant (*****). Also, (******) if p-value < 0.01, (*******) if p-value < 0.001 and (********) if p-value < 0.0001.

For stability studies, two-way ANOVA was performed. For cytotoxicity and uptake assays, comparisons were performed by unpaired homoscedastic parametric t-tests.

Analyses requiring normality were performed after passing the Kolmogorov-Smirnov test, with the Dallal-Wilkinson-Lilliefor corrected p-value.

3. RESULTS AND DISCUSSION

As explained in the introduction, the intracellular targeting of oncoproteins using mAbs-loaded NCs opens a window for further antitumoral drug development. With this goal in mind, we have adapted a previously developed technology platform[30] and explored different compositions for their capacity to associate mAbs and deliver them inside cancer cells. In the first step, bevacizumab (BVZ) was used as a model mAb, and the BVZ-loaded NCs prototypes were characterized in terms of physicochemical properties, toxicity, and cellular uptake. Then, an anti-$KRAS^{G12V}$ mAb was loaded into specific NCs prototypes, and their toxicity, cell uptake, and target engagement were studied *in vitro*.

3.1. DESIGN AND DEVELOPMENT OF BEVACIZUMAB-LOADED NANOCAPSULES

As a first step in the development of NCs for lung cancer treatment, and considering the results obtained in the previous chapters, we selected SD-noPEG and SD-TPGS as starting NCs prototypes and extended the range of their oil and surfactant compositions seeking to improve the physicochemical characteristics and drug loading. In this sense, the incorporation of the non-PEGylated phosphatidylcholines (Lipoid S100) [SD-noPEG(+PC)] and lauric acid-modified octaarginine (C_{12}-R_8) [SD-TPGS(+C_{12}-R_8)] was studied. In addition, we also explored the role of the oily core composition by using Miglyol® 812N instead of Vitamin E [SD-noPEG(MCT) and SD-noPEG(MCT+PC)]. Finally, an NCs prototype formulated with a high surfactant content and a high presence of solvents [SD/SE-P80(MCT)], was also explored.

Several ratios between oil, surfactants, and polymer were tested to obtain stable blank formulations. The ratios (Supplementary Table 1) that led to smaller hydrodynamic diameters (Supplementary Table 2) and storage stability, regarding their particle size, for at least 1 week at 4 °C were selected.

Then, a general study of the tolerability of a panel of NCs was assessed by analyzing the cytotoxicity and membrane damage in the porcine kidney (LLC-PK1) and human cancerous liver (Hep G2) cells, following the standard operating procedures of the European Nanomedicine Characterization Laboratory (EUNCL) EUNCL-GTA-001 and EUNCL-GTA-002 guidelines. In general, formulations affected the viability of LCC-PK1 cells more than Hep G2. More in detail, all prototypes exhibited moderate cytotoxicity in LLC-PK1 (75 % of viability at 1 $mg \cdot mL^{-1}$ of NCs' components), except for SD-noPEG and SD/SE-P80(MCT), which were nontoxic. On the contrary, all NCs exhibited very low toxicity in Hep G2 (Supplementary Figure 1). The integrity of the cellular membrane was explored by the leakage of the intracellular enzyme LDH. In general, NCs did not affect the integrity of the membrane, and only SD/SE NCs and SD-noPEG caused partial membrane damage at concentrations higher than 90 $\mu g \cdot mL^{-1}$ of NCs' components in LLC-PK1, while only SD-noPEG was found to promote LDH leakage in Hep G2 at the same concentration range (Supplementary Figure 2). In this sense, the higher amount of PEGylated surfactant of SD/SE-P80 compared to the other NCs might permeabilize the LLC-PK1 cell membrane. On the other hand, SD-noPEG might interact strongly with cellular membranes. No membrane damage was detected for the other formulations.

After testing their *in vitro* compatibility, the model mAb BVZ was incorporated into all NCs. To do so, BVZ was added to the NCs aqueous phase before the emulsification step to obtain a final BVZ concentration of 2 $mg \cdot mL^{-1}$. Short-term storage stability at 4 °C was performed for the BVZ-loaded NCs. The results showed that, in general, formulations were stable for at least a month in terms of particle size, and only the NCs containing PCs [SD-noPEG(+PC) and SD-noPEG(MCT+PC)], as well as the SD/SE-P80(MCT) formulation exhibited substantial changes and their study was discontinued (Supplementary Figure 3). The physicochemical characteristics of the BVZ-loaded systems are detailed in Table 4.

Table 4. Physicochemical characteristics of BVZ-loaded NCs

	SD-noPEG	SD-noPEG(MCT)	SD-TPGS	SD-TPGS(+C_{12}-R_8)
Hydrodynamic diameter (DLS) (nm)	149 ± 2	118 ± 4	113 ± 5	117 ± 16
PDI	0.02 ± 0.01	0.04 ± 0.01	0.10 ± 0.01	0.13 ± 0.03
Hydrodynamic diameter (NTA) (nm)	100 ± 11	98 ± 4	108 ± 5	-
Concentration ($\times 10^{11}$ particles$\cdot mL^{-1}$)	107.2 ± 6.7	160.7 ± 17.0	77.8 ± 2.1	-
ζ-potential (mV)	−13 ± 1	−15 ± 1	−11 ± 4	−13 ± 10
BVZ loading (%)	11.1	11.1	9.1	7.1
AE BVZ (%)	99 ± 1	99 ± 1	46 ± 15	75 ± 39

SD: solvent displacement. SE: self-emulsifying. PDI: polydispersity index. DLS: dynamic light scattering. AE: association efficiency. LC: loading capacity. The compositions of SD-noPEG, SD-noPEG(MCT), SD-TPGS, and SD-TPGS(+C_{12}-R_8) are shown in Supplementary Table 1. Values represent the mean ± standard deviation (n = 3).

USC UNIVERSIDADE DE SANTIAGO DE COMPOSTELA

The results show NCs with particle sizes below 150 nm, very low PDI, and slightly negative ζ -potential. In addition, the NCs that did not contain any PEGylated surfactant exhibited a high BVZ AE (measured by ELISA) of 99 ± 1 %. On the other hand, the BVZ AE values for TPGS-containing NCs were more moderate [46 ± 15 and 75 ± 39 % in the case of SD-TPGS and SD-TPGS(+C_{12}-R_8), respectively]. Of note, the SD-TPGS(+C_{12}-R_8) exhibited a relevant variability in its BVZ AE.

Then, the biological stability in the presence of plasma proteins was also studied. The results in Figure 2 indicate that SD-noPEG and SD-noPEG(MCT) experienced a significant size increase followed by a shrinking phase that was attributed to their interaction with stabilizing proteins (2-way ANOVA).

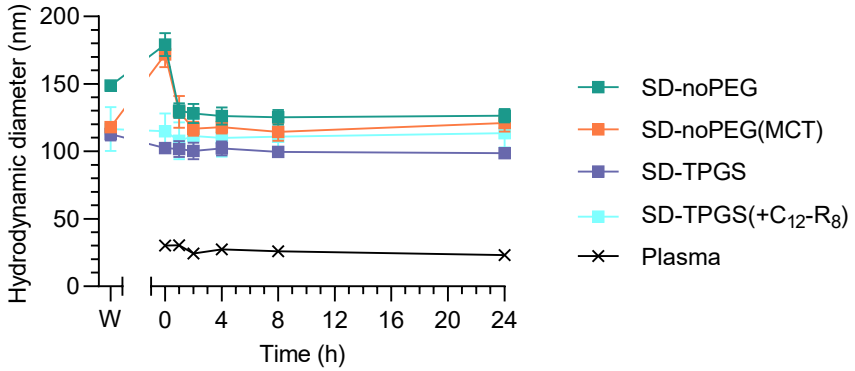


Figure 2. Stability of bevacizumab-loaded NCs in 90 % human plasma

The compositions of SD-noPEG, SD-noPEG(MCT), SD-TPGS, and SD-TPGS(+C_{12}-R_8), are shown in Supplementary Table 1. Size variations were statistically significant for SD-noPEG(MCT) at t = 0 h and SD-noPEG and SD-TPGS for the whole 24 h (two-way ANOVA *versus* NCs dispersed in water). Values represent the mean ± standard deviation (n = 3).

The BVZ release studies were carried out by incubating the formulation in PBS supplemented with 10 % FBS at a 10 × dilution factor at 37 °C. SD-noPEG, SD-noPEG(MCT), and SD-TPGS exhibited no BVZ release (< 1 %) up to 48 h, while SD-TPGS(+C_{12}-R_8) exhibited a very variable release profile. This release behavior indicates a strong interaction of the mAbs with the components of the NCs and suggests that the degradation or disassembling of the NCs may be necessary to achieve the release of their cargo.

Overall, the results from the screening of formulations led us to the conclusion that SD-noPEG, SD-noPEG(MCT), and SD-TPGS fulfilled the product target profile in terms of reduced particle size (< 150 nm) by DLS and NTA, negative or neutral ζ-potential, moderate or high BVZ AE, and no premature release in plasma-containing media. Furthermore, using medium-chain triglycerides instead of Vitamin E did not affect the physicochemical properties of SD-noPEG. Thus, the study of SD-noPEG(MCT) was discontinued.

A schematic representation of the two selected formulations is presented in Figure 3. A summary of the physicochemical properties of BVZ-loaded NCs is detailed in Table 5, and examples of the DLS, LDE, and NTA characterization are presented in Supplementary Figure 4.

USC
UNIVERSIDADE
DE SANTIAGO
DE COMPOSTELA

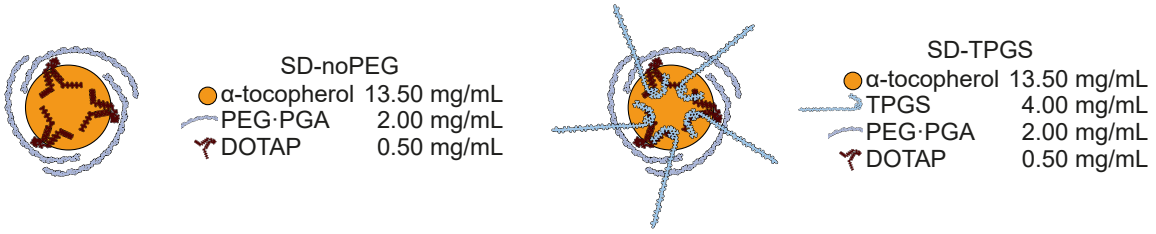


Figure 3. Schematic representation of the expected compound arrangement of the NCs optimized for BVZ-loading and their theoretical composition

SD-noPEG: Formulation prepared by solvent displacement technique and composed of non-PEGylated surfactants (DOTAP) and PEG·PGA shell. SD-TPGS: Formulation prepared by solvent displacement technique and composed of lineal PEG (TPGS) and PEG·PGA shell. **Abbreviations:** DOTAP: 1,2-dioleoyl-3-trimethylammoniumpropane. PEG·PGA: polyethylene glycol polysialic acid. TPGS: D-α-tocopherol polyethylene glycol 1000 succinate.

Table 5. Physicochemical characteristics of the BVZ-loaded NCs

	SD-noPEG	SD-TPGS
Hydrodynamic diameter (DLS) (nm)	149 ± 2	113 ± 5
PDI	0.02 ± 0.01	0.10 ± 0.01
Hydrodynamic diameter (NTA) (nm)	100 ± 11	108 ± 5
Particle size (cryo-EM) (nm)	115 ± 65 (n = 281)	-
Particle concentration (NTA) ($\times 10^{11}$ particles·mL^{-1})	107.2 ± 6.7	77.8 ± 2.1
ζ-potential (mV)	−13 ± 1	−11 ± 4
BVZ loading (%)	11.1	9.1 %
AE BVZ (%)	99 ± 1	46 ± 15
BVZ Release in PBS 10 % FBS	No	No

Abbreviations: BVZ: bevacizumab. DLS: dynamic light scattering. KRAS: Kirsten rat sarcoma viral oncogene homolog. NTA: nanoparticle tracking analysis PDI: polydispersity index. SD: solvent displacement. The compositions of SD-noPEG and SD-TPGS are shown in Figure 3. Values represent the mean ± standard deviation (n = 3) unless stated otherwise.

Finally, SD-noPEG was visualized by cryo-EM (Figure 4). A granular shell, presumably corresponding to BVZ ensembled at the oil/water interphase, was observed. A histogram of the particle distribution of both formulations by cryo-EM can be consulted in Supplementary Figure 5. The incorporation of BVZ decreased the number of particles with a particle size of 40 nm and increased in the 120 – 160 nm range. Overall, cryo-EM results agreed with the other size characterization techniques performed on those NCs.

USC UNIVERSIDADE DE SANTIAGO DE COMPOSTELA

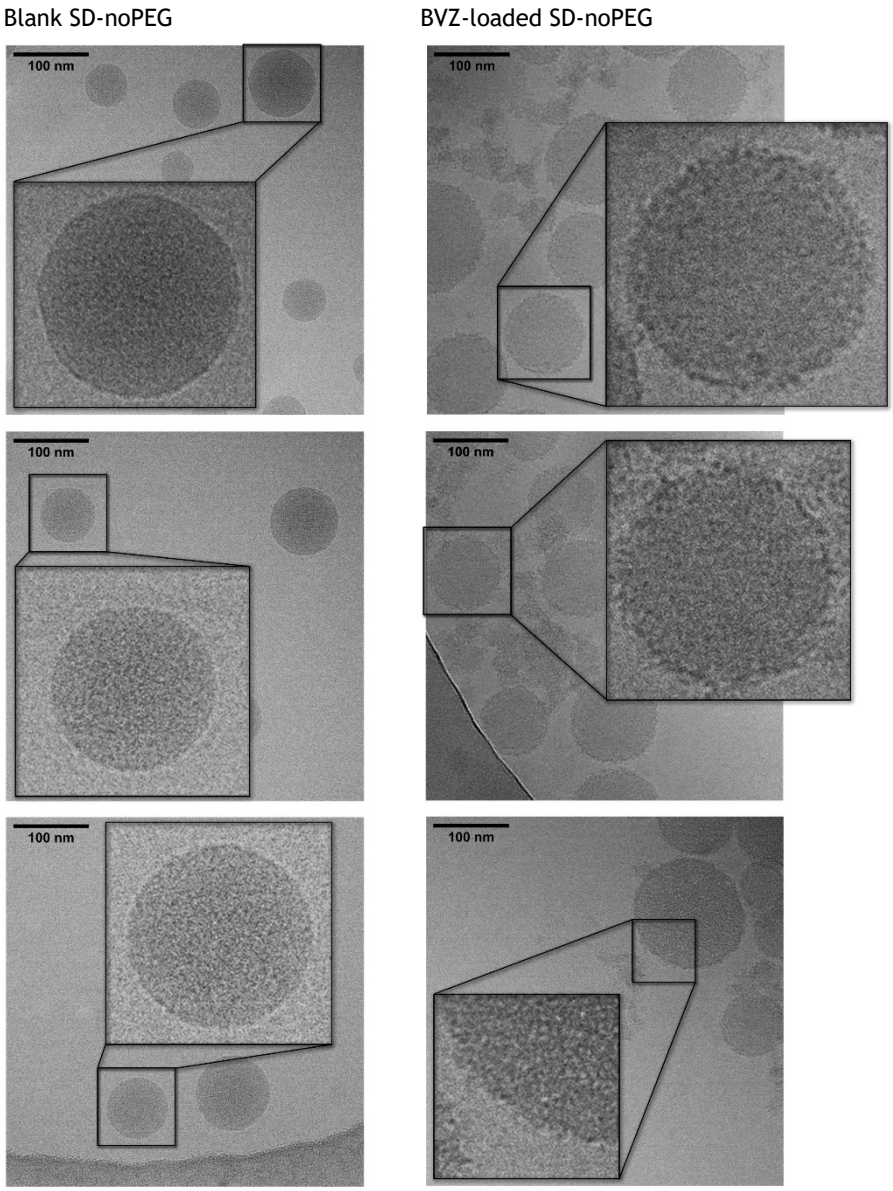


Figure 4. Cryo-EM images of blank SD-noPEG (left) and BVZ-loaded SD-noPEG (right)

The scale bar represents 100 nm. A granular shell can be observed on the oil/water interphase of BVZ-loaded SD-noPEG. The composition of SD-noPEG is shown in Figure 3.

3.2. COMPARISON OF THE CELL INTERNALIZATION OF FLUORESCENTLY LABELED NANOCAPSULES WITH DiD AND NANOCAPSULES LOADED WITH FLUORESCENTLY LABELED BVZ

The two previously selected formulations were labeled using two different approaches: (i) dissolving DiD within their oily core or loading BVZ labeled with Alexa Fluor® 488 (^{AF488}BVZ).

^{AF488}BVZ was synthesized by the *N*-hydroxysuccinimide ester reaction with amines, as explained in the "2. Materials and methods" section. The concentration of the resulting

^{AF488}BVZ was 98.10 mg·mL^{-1}, with a DOL of 4.89 moles of dye per mole of ^{AF488}BVZ. On the other hand, DiD was added to the organic phase to give a final DiD concentration of 100 ppm, as reported in Chapter 2.

The results of the characterization of the fluorescently labeled NCs indicated that the simultaneous incorporation of DiD and ^{AF488}BVZ on SD-noPEG and SD-TPGS did not affect their hydrodynamic diameter and PDI (Supplementary Table 3).

The DiD AEs on DiD-labeled NCs were 88 ± 11 and 52 ± 4 % for SD-noPEG and SD-TPGS, respectively. After 24 h of incubation, the DiD release was only ≈ 1 % for both prototypes. On the other hand, the ^{AF488}BVZ AE in NCs was found to be 83 ± 9 % for SD-noPEG and 82 ± 5 % for SD-TPGS. The ^{AF488}BVZ release from the NCs was explored upon incubation in PBS supplemented with 10 % FBS at the same dilution as in the following *in vitro* studies. The released ^{AF488}BVZ was lower than 5 % for NC-noPEG and approximately 20 % for SD-TPGS up to 48 h (Supplementary Figure 6).

The in vitro cell uptake of SD-noPEG NCs was evaluated in the A549 human lung cancer cell line using imagining flow cytometry with ImageStream^X (Figure 5). Images were taken without the extended depth of focus (EDF) for the detection of the percentage of positive cells, median internalization score, and co-localization of DiD and ^{AF488}BVZ, and with EDF, which provides focused 15 µm deep images of the cells for the quantitative analysis of internalization spots in the entire cell.

First, the internalization profile of the ^{AF488}BVZ- and DiD co-labeled NCs was evaluated. The results in Figure 6A indicate that the uptake of ^{AF488}BVZ was clearly visible after 2 h exposure, and almost all cells became positive after 16 h. Of note, ^{AF488}BVZ was found not to be internalized if not loaded into NCs.

Interestingly, a quite different internalization profile was observed for DiD. The percentage of DiD$^+$ cells was found to be higher than the percentage of AF488$^+$ cells, supporting the hypothesis that part of the DiD is nonspecifically transferred to cell membranes when DiD-loaded NCs are placed in contact with cell cultures. Moreover, the superposition of the AF488$^+$ and the AF488$^+$ and DiD$^+$ curves implies that part of the loaded DiD is still attached to the particles, as we could no detect any AF488$^+$ cell that was not positive for DiD.

Imaging flow cytometry, in contraposition to regular FACS analysis, can determine the location of fluorescent entities on the cells. With the aim of knowing how much the dyes had entered into the cells, internalization scores (IS) were calculated. The IS is defined as the difference between the fluorescence intensity inside the cell and the fluorescence intensity of the whole cell. Fluorescent molecules are considered internalized for positive values of internalization score. The internalization score of ^{AF488}BVZ increased slightly over time, suggesting that the ^{AF488}BVZ arrived at more profound structures in the cell through time. On the other hand, the internalization score of DiD was consistently lower than that of ^{AF488}BVZ, suggesting that part of the DiD might be staining the cell membrane (Figure 6B).

USC UNIVERSIDADE DE SANTIAGO DE COMPOSTELA

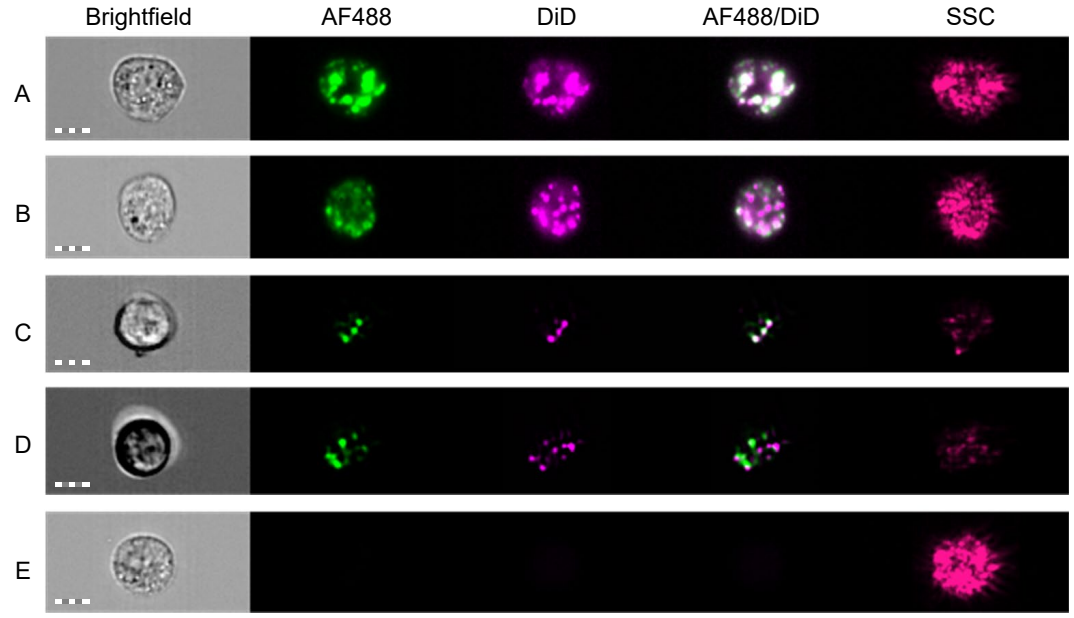


Figure 5. Non-EDF cell image examples of (A) high co-localized AF488 and DiD and (B) low co-localized AF488 and DiD. EDF cell image examples of co-localized AF488 and DiD (C) and non-co-localized (D). A-D images were taken after treatment with ^{AF488}BVZ- and DiD-labeled SD-noPEG. E shows no AF488 signal after treatment with free ^{AF488}BVZ

AF488: green channel; 480 – 560 nm spectral detection channel. DiD: DiD far-red channel; 660 – 745 nm spectral detection channel. AF488/DiD: merge of green and far-red channels. SSC: side scatter. In AF488/DiD, co-localization is represented by white color. The composition of SD-noPEG is shown in Figure 3.

The co-localization of ^{AF488}BVZ and DiD was also investigated (Figure 6C). The fact that there was no initial co-localization of both markers suggests a different interaction of the dyes with the cells. The percentage of cells with co-localized AF488 and DiD increased to 50 % after 16 h. After this time, both markers were again non-colocalized, probably due to the different intracellular fate upon release from the NCs.

Altogether, these results highlight the importance of the labeling process of nanocarriers on the interpretation of their cell internalization. On the other hand, imaging flow cytometry can also be used to detect and count organelles containing a relevant amount of fluorescence. In this sense, this technique has been reported to be able to quantify the number of nanoparticle-containing vesicles (NCVs), that is, endosomes or lysosomes, per cell.[43] Results from AF488 spot count showed that most cells contained 1 NC-containing endosome or lysosome at 4 h. NCVs increased with time and reached their maximum after 16 h post incubation, with most of the cells containing 5 NCVs (Figure 6D).

Overall, imaging flow cytometry confirmed the high internalization of BVZ-loaded SD-noPEG and concluded that ^{AF488}BVZ is a more robust dye than DiD for studying the cellular uptake of NCs. The normalized frequency distribution of the internalization score, bright detail similarity, and the spot count histograms of DiD- and ^{AF488}BVZ-labeled SD-noPEG can be found in Supplementary Figure 7.

USC UNIVERSIDADE DE SANTIAGO DE COMPOSTELA

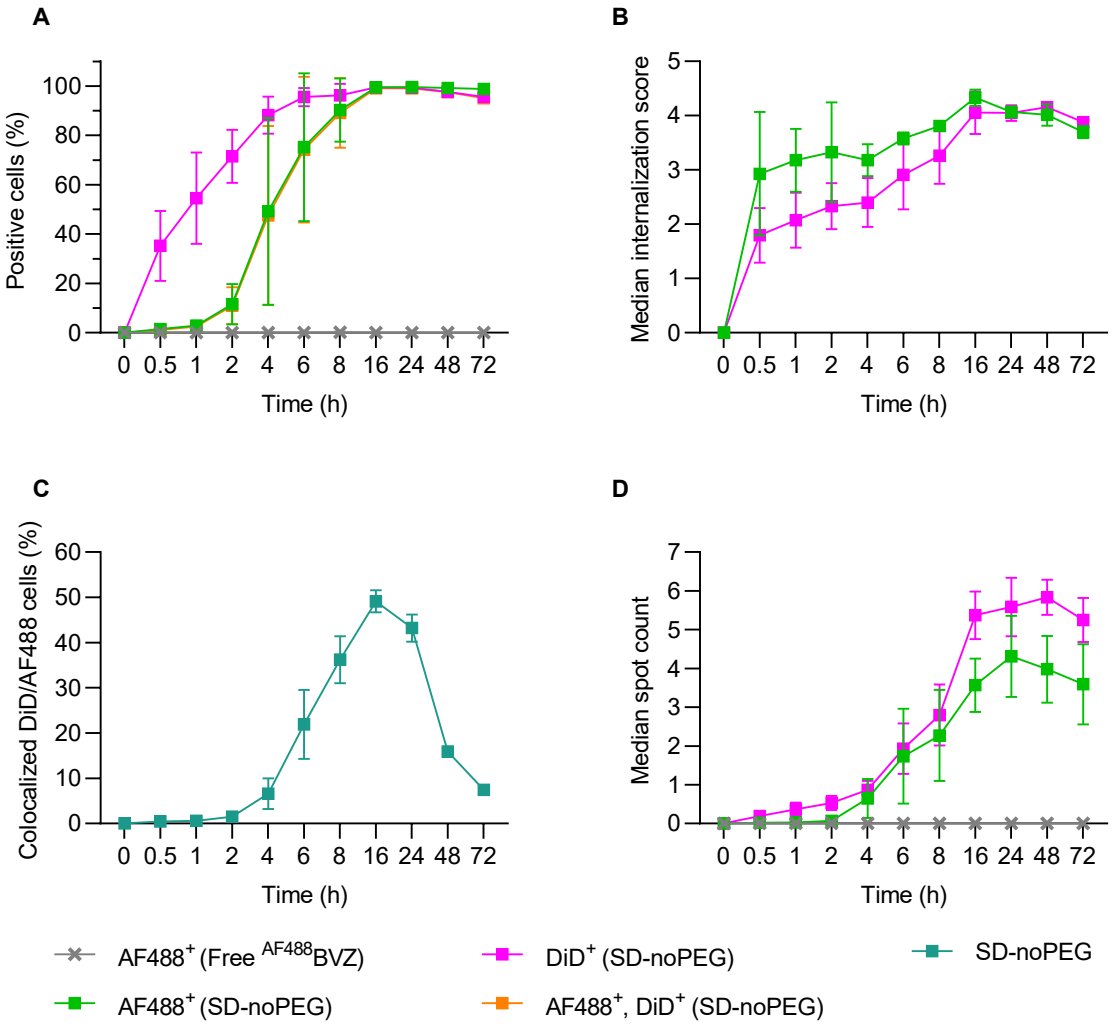


Figure 6. Cellular uptake of ^{AF488}BVZ and DiD-labeled SD-noPEG and free ^{AF488}BVZ

(A) Cells incubated with SD-noPEG started to be positive for DiD at 0.5 h while for AF488 in 2 – 4 h. All cells were positive for both probes at 16 h and higher time points. (B) In general, the DiD exhibited a lower internalization score than ^{AF488}BVZ, probably due to interaction with the cell membrane. (C). Spot count was higher for DiD than AF488, especially at higher points. (D). Co-localization of AF488 and DiD increases in the initial times and reaches its maximum of approximately 50 % at 16 h. Then, the probes are less co-localized, approximately 10 % at 72 h. The composition of SD-noPEG is shown in Figure 3.

3.3. Cellular uptake of fluorescently labeled BVZ-loaded NCs in different cell lines

Based on the previous studies showing the benefits of using ^{AF488}BVZ compared to DiD, NCs were loaded with ^{AF488}BVZ for studying their cellular uptake in several cell lines. The preservation of the physicochemical characteristics of the NCs was checked after the incorporation of ^{AF488}BVZ. SD-noPEG and SD-TPGS exhibited similar hydrodynamic diameter and PDI to the unlabeled systems (Supplementary Table 4).

CMT 167 and A549 were selected as adequate cell lines to study the uptake of mAb-loaded NCs since they harbor KRAS-mutations (G12V and G12S, respectively). First, the cytotoxicity of ^{AF488}BVZ NCs was tested after 24 h of incubation at 37 °C in the selected cell lines

(Supplementary Figure 8). The NCs were found to be nontoxic in the CMT 167 cell line, while moderate toxicity (≈ 60 % viability) was observed in the A549 cell line for SD-noPEG at a blank NC concentration of 750 $\mu g \cdot mL^{-1}$ (equivalent to 93.75 $\mu g \cdot mL^{-1}$ of BVZ). Based on these data, cell uptake experiments were performed at a BVZ concentration of 62.5 $\mu g \cdot mL^{-1}$. As shown in Figures 7 and 8, ^{AF488}BVZ NCs showed statistically significant temperature-dependent uptake (unpaired t-tests). This indicates that the uptake mechanism is mediated by a classical non-specific endocytic process, as previously observed for similar NCs compositions containing anti-gasdermin mAb.

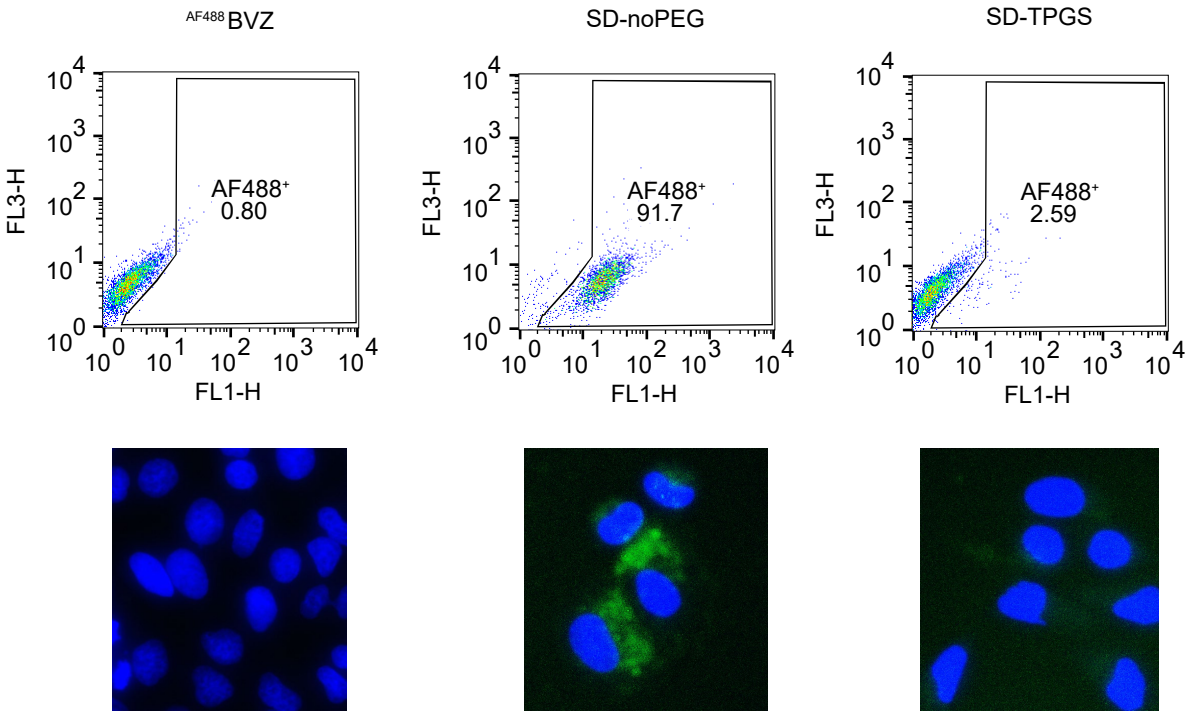


Figure 7. Examples of the percentage of AF488-positive cells by FACS (top) and confocal microscopy (bottom) for free ^{AF488}BVZ and ^{AF488}BVZ-labeled SD-noPEG and SD-TPGS after 4 h at 37 °C in A549

Blue: DAPI. Green: AF488. The compositions of SD-noPEG and SD-TPGS are shown in Figure 3.

On the other hand, it is very notorious that SD-noPEG NCs were much more internalized in both cell lines than SD-TPGS. This effect might be due to the high vitronectin adsorption of the SD-noPEG NCs and/or reduced uptake due to a higher PEG content of SD-TPGS (5-fold PEG mass and 10-fold density compared to SD-noPEG). The percentage of AF488-positive cells follows the same trend as the iMFI (Supplementary Figure 9), and SD-noPEG was more internalized in both cell lines than SD-TPGS. More in detail, the AF488-positive cell percentages were 30 – 57 and 6 – 40 % in CMT 167 and 100 and 52 – 98 % in A549 for SD-noPEG and SD-TPGS, respectively.

Moreover, a dose-response effect was found for all cases except in the punctual case of the AF488-positive cell percentage of SD-noPEG at 37 °C (Supplementary Figure 9), whose higher uptake led to 100 % of positive cells at all the tested concentrations.

USC UNIVERSIDADE DE SANTIAGO DE COMPOSTELA

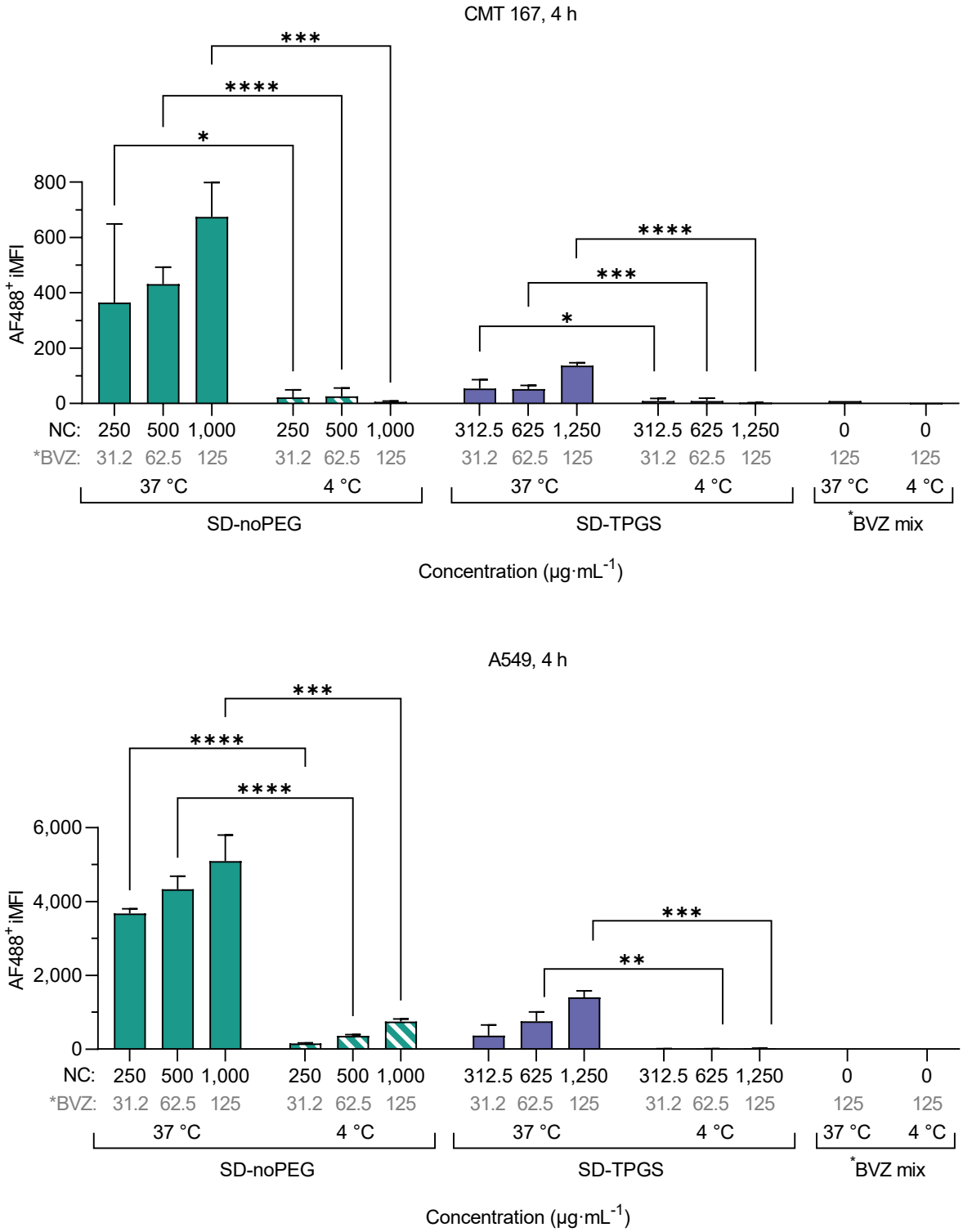


Figure 8. Uptake (iMFI) of ^{AF488}BVZ-labeled SD-noPEG and SD-TPGS in CMT 167 and A549 cell lines after 4 h

^{AF488}BVZ-loaded NCs showed statistically significative temperature-dependent uptake (unpaired t-tests of NCs or *BVZ concentration at 37 °C *vs.* 4 °C. *p*-values < 0.05 were considered statistically significant (*). Also, (**) if *p*-value < 0.01, (***) if *p*-value < 0.001 and (****) if *p*-value < 0.0001. SD-noPEG was more internalized in both cell lines than SD-TPGS. The mixture of 2 % ^{AF488}BVZ and 98 % BVZ (*BVZ) was not taken up by any cell line. **Abbreviations:** *BVZ: fluorescently labeled bevacizumab. iMFI: integrated mean fluorescence intensity. NC: nanocapsule. The compositions of SD-noPEG and SD-TPGS are shown in Figure 3. Values represent the mean ± standard deviation (n = 3).

Regarding the effect of the uptake on different cell lines, A549 exhibited a higher uptake of both systems than CMT 167. This result may be attributed to the intrinsic mechanisms of those different lung cancer cells.

Finally, as expected, the free ^{AF488}BVZ was not internalized by any of the cell lines. Fluorescence by ^{AF488}BVZ internalization was confirmed by confocal microscopy for SD-noPEG and SD-TPGS in A549 cells.

3.4. DESIGN AND DEVELOPMENT OF ANTI-KRAS^{G12V} MAB-LOADED NANOCAPSULES

The SD-noPEG and SD-TPGS NC prototypes were chosen for the formulation of an anti-KRAS^{G12V} mAb at a final concentration of 2 mg·mL^{-1}. However, the translation from the BVZ to the anti-KRAS^{G12V} mAb was not straightforward, and it was necessary to perform further optimizations. Indeed, the incorporation of the anti-KRAS^{G12V} mAb led to problems of aggregation of SD-noPEG and lack of reproducibility in the hydrodynamic size of SD-TPGS during storage. The reproducibility issues of SD-TPGS could be solved by increasing the TPGS content. The resulting formulation was named SD-TPGS(↑). However, since that formulation demonstrated low cellular uptake when loaded with ^{AF488}BVZ, an alternative involving the use of another PEGylated surfactant (polysorbate 80) was explored. As a result, the SD-P80 prototype was also developed (Figure 9).

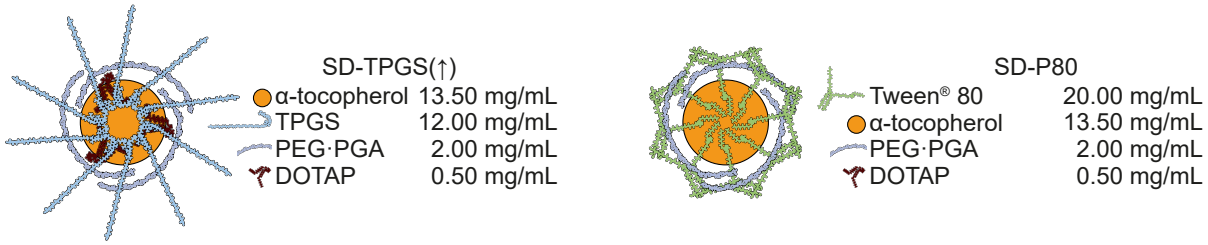


Figure 9. Schematic representation of the expected compound arrangement of the NCs optimized for anti-KRAS^{G12V} mAb-loading and their theoretical composition

SD-TPGS(↑): Formulation prepared by solvent displacement technique and composed of lineal PEG (TPGS; 12 mg·mL^{-1}) and PEG·PGA shell. SD-P80: Formulation prepared by solvent displacement technique and composed of branched PEG (P80) and PEG·PGA shell. **Abbreviations:** DOTAP: 1,2-dioleoyl-3-trimethylammoniumpropane. P80: polysorbate 80. PEG·PGA: polyethylene glycol polysialic acid. TPGS: D-α-tocopherol polyethylene glycol 1000 succinate.

The anti-KRAS^{G12V} mAb-loaded NCs exhibited low hydrodynamic diameters (< 150 nm) and PDI (< 0.3) and neutral ζ-potential (Table 6, Supplementary Figure 9). The anti-KRAS^{G12V} mAb AEs were significantly different between prototypes. SD-TPGS(↑) exhibited a very low AE of ≈ 11 %, whereas the AE of the SD-P80 formulation was 90 %. The main difference between these systems is the nature of their PEGylated surfactant. TPGS exhibits longer PEG chains of 2,000 Da in comparison to the ≈ 250 Da per chain of polysorbate 80. Moreover, while the concentration of TPGS in SD-TPGS(↑) was lower than polysorbate 80 in SD-P80 at the moment of formulating the NCs, the mass of PEGylated surfactants actually incorporated into the systems might be totally different. In this sense, SD-TPGS(↑) might exhibit a higher PEG density that hinders the interaction of the KRAS^{G12V} mAb with the NCs' surface.

Table 6. Physicochemical characteristics of anti-KRAS^{G12V} mAb-loaded NCs

	SD-TPGS(↑)	SD-P80
Hydrodynamic diameter (DLS) (nm)	117 ± 5	143 ± 14
PDI	0.20 ± 0.06	0.21 ± 0.05
ζ-potential (mV)	−5 ± 1	+1 ± 1
anti-KRAS^{G12V} mAb loading (%)	6.67	5.26
anti-KRAS^{G12V} mAb AE (%)	11 ± 19	90 ± 6

Abbreviations: DLS: dynamic light scattering. PDI: polydispersity index. Values represent the mean ± standard deviation (n = 3). The compositions of SD-TPGS(↑) and SD-P80 are shown in Figure 9.

Finally, regarding long-term stability, both prototypes were found to be stable in storage conditions for up to 1 month at 4 °C (Supplementary Figure 10).

Of note, the following *in vitro* experiments with the therapeutic mAb were carried out in CMT 167. CMT 167 cell line was selected to match their KRAS mutation (G12V) with the specificity of our anti-KRAS^{G12V} mAb.

3.5. Toxicity of anti-KRAS^{G12V} mAb-loaded nanocapsules

As shown in Figure 10, the toxicity of the blank and anti-KRAS^{G12V} mAb-loaded NCs was studied in a broad range of NCs concentrations (3,000 to 93.8 μg·mL^{-1}) after incubation with CMT 167 cells for 24 and 48 h. The results showed that the toxicity of NCs started at a concentration of 750 μg·mL^{-1} (unpaired t-tests).

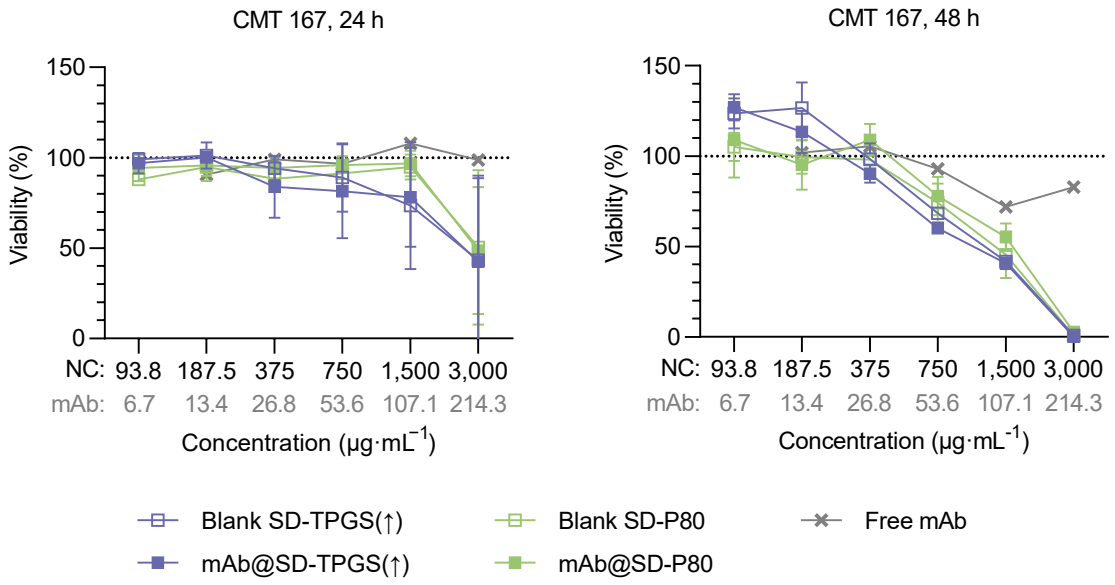


Figure 10. Cytotoxicity of blank and anti-KRAS^{G12V} mAb-loaded NCs in CMT 167 cancer cells for 24 and 48 h at 37 °C

Viability was statistically significantly compromised (unpaired t-tests of each NCs *vs.* 100 % viability control for each concentration value) at concentrations ≥ 750 μg·mL^{-1} after 48 h. The compositions of SD-TPGS(↑) and SD-P80 are shown in Figure 9. Values represent the mean ± standard deviation (n = 3 for NCs at 24 h; n = 2 for NCs at 48 h, n = 1 for free mAb).

USC UNIVERSIDADE DE COMPOSTELA

This toxicity was not relevant for the following *in vitro* experiments, as concentrations of mAbs between 100 and 1,000 nM were tested, that is, in the order of a few tens of $ng \cdot mL^{-1}$ of NCs' components, where the NCs resulted in being totally nontoxic.

3.6. CELLULAR UPTAKE OF ANTI-KRAS^{G12V} MAB-LOADED NANOCAPSULES

The cellular uptake of the anti-KRAS^{G12V} mAb was evaluated for the free protein and the mAb-loaded NCs by intracellular staining. After incubation for 4 h, the cells were washed, fixed, and permeabilized. Then, a fluorescent secondary mAb recognizing the anti-KRAS^{G12V} mAb was added, and cells were analyzed by FACS.

Results from the intracellular staining of anti-KRAS^{G12V} mAb showed a statistically significant and temperature-dependent delivery of the anti-KRAS^{G12V} mAb by SD-P80 compared to the free mAb (Figure 11). However, in the case of SD-TPGS, only a tendency could be observed.

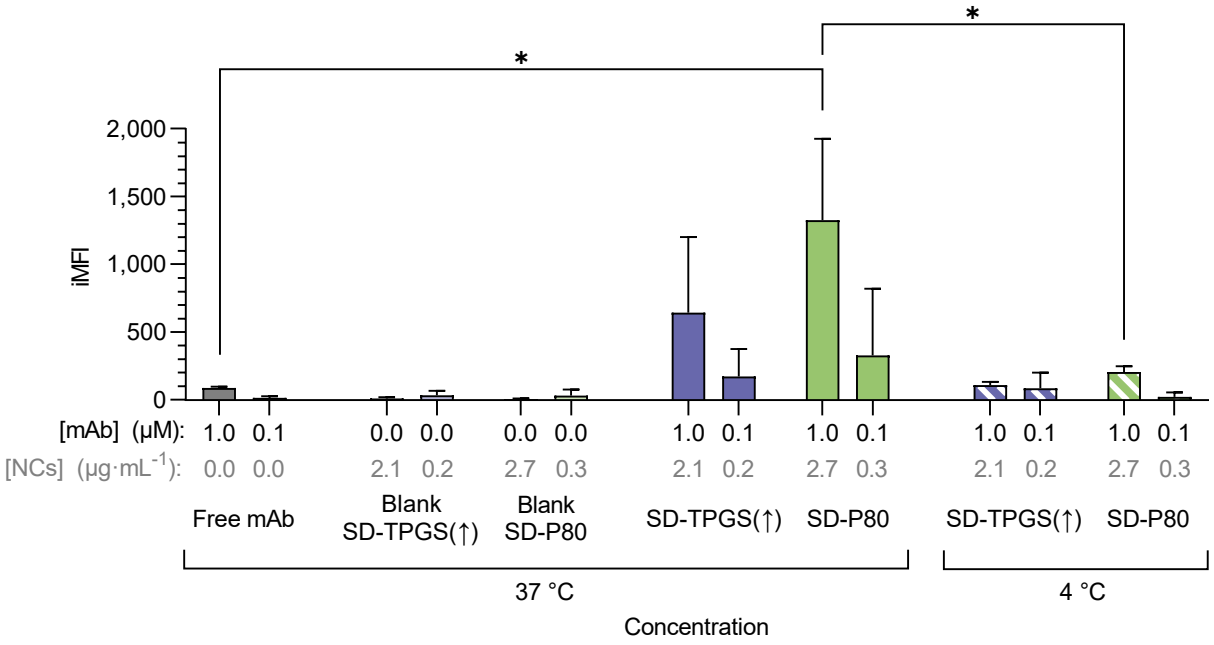


Figure 11. Intracellular staining of anti-KRAS^{G12V} mAb in CMT 167 lung cancer cells after incubation for 4 h at 37 °C

SD-P80 statistically significantly delivered the anti-KRAS^{G12V} mAb to the interior of CMT 167 cells after incubation at a mAb concentration of 1 μM for 4 h at 37 °C. This effect was also temperature dependent (t-tests of mAb-loaded NCs *vs.* free mAb or blank NCs and t-tests of 37 °C vs 4 °C). **Abbreviations:** NCs: nanocapsules. mAb: monoclonal antibody. iMFI: integrated mean fluorescence intensity. The compositions of SD-TPGS(↑) and SD-P80 are shown in Figure 9. Values represent the mean ± standard deviation (n = 3).

USC UNIVERSIDADE DE SANTIAGO DE COMPOSTELA

3.7. *IN VITRO* TARGET ENGAGEMENT OF ANTI-KRAS^{G12V} MAB-LOADED NANOCAPSULES

After demonstrating that the anti-KRAS^{G12V} mAb is taken up significantly by CMT 167 cells when loaded into SD-P80, a preliminary target engagement study was carried out to know if that internalized mAb had successfully bound to its intracellular target.

The evaluation of the toxicity of the NCs is critical when performing the target engagement due to the prolonged time exposure of cells to NCs. Therefore, the mortality of CMT 167 cells was checked at 24, 48, and 72 h by the 7-AAD staining (Supplementary Figure 11). Anti-KRAS^{G12V} mAb-loaded SD-P80 caused no toxicity in CMT 167 cells in the conditions used for the target engagement experiment.

The internalized anti-KRAS^{G12V} mAb was pulled down by immunoprecipitation, and the presence of KRAS^{G12V} was evaluated by Western Blot. KRAS^{G12V} band appeared at approximately 25 kDa, as confirmed by the positive control. Anti-KRAS^{G12V} mAb-loaded SD-P80 demonstrated the delivery and binding of the therapeutic mAb to its target, as the intensity of the 25 kDa band was higher than that of the negative control (Figure 12). A tendency for time-dependent target engagement could be appreciated as well.

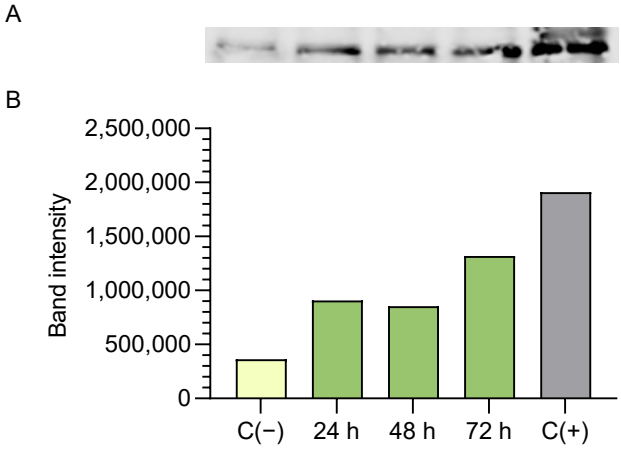


Figure 12. Immunoprecipitation of KRAS^{G12V} protein by anti-KRAS^{G12V} mAb-loaded SD-P80 after incubation at 24, 48, and 72 h in CMT 167 cells

(A) RAW image of the WB membrane. **(B)** Band intensities. For the negative control [C(−)], 1 mg of CMT 167 cell lysate was immunoprecipitated with anti-antibody beads. For the positive control [C(+)], 5 µg of anti-KRAS^{G12V} mAb were added to 1 mg of CMT 167 cell lysate and immunoprecipitated with anti-antibody beads. The composition of SD-P80 is shown in Figure 9. Values represent 1 replicate.

Overall, this result suggests that the SD-P80 NCs can efficiently deliver antibodies to cancer cells, preserving their activity and allowing the intracellular recognition of their target. Of note, while this formulation was based on the SD-noPEG NCs prototype, which exhibited high vitronectin adsorption upon human plasma incubation, its chemical composition was varied notably by the addition of polysorbate 80. In this sense, the analysis of the protein corona fingerprint of SD-P80 would be interesting before its evaluation *in vivo* in order to gather information about its potential biodistribution and interaction with the immune system.

USC UNIVERSIDADE DE SANTIAGO DE COMPOSTELA

4. CONCLUSIONS

Polymeric NCs represent a versatile delivery platform that could be adapted for the formulation of monoclonal antibodies such as BZV and anti-KRAS^{G12V}. Selected formulations were found to have a great capacity for associating monoclonal antibodies and delivering them at the intracellular level. Importantly, a notorious target engagement could be observed for the anti-KRAS^{G12V} mAb released from the NCs inside the cells.

The evaluation of the therapeutic outcomes of the nano-formulated anti-KRAS^{G12V} mAb should be performed in further *in vivo* studies.

5. SUPPLEMENTARY INFORMATION

Supplementary Table 1. Quantitative composition of the new NCs prototypes

Formulation	Concentration (mg·mL^{-1})							
	VitE	MCT	DOTAP	C_{12}-R_8	TPGS	Lipoid S100	P80	PEG·PGA
SD-TPGS	13.5	-	0.5	-	4	-	-	2
SD-noPEG	13.5	-	0.5	-	-	-	-	2
SD-noPEG(+PC)	13.5	-	0.25	-		4		4
SD-noPEG(MCT)	-	13.5	0.5	-	-	-	-	2
SD-noPEG(MCT+PC)	-	12	1.12	-	-	1.52	-	2
SD-TPGS(+C_{12}-R_8)	13.5	-	-	0.5	4	-	-	8
SD/SE-P80(MCT)	-	20	0.5	-	-	-	15	2

SD: solvent displacement. SE: self-emulsifying, DOTAP: 1,2-dioleoyl-3-trimethylammoniumpropane chloride. TPGS: D-α-tocopherol polyethylene glycol 1000 succinate. C_{12}-R_8: lauric acid-modified octaarginine. MCT: medium-chain triglycerides. PEG·PGA: Polyethylene glycol (5 kDa) poly-α-glutamic acid (10 u). VitE: vitamin E.

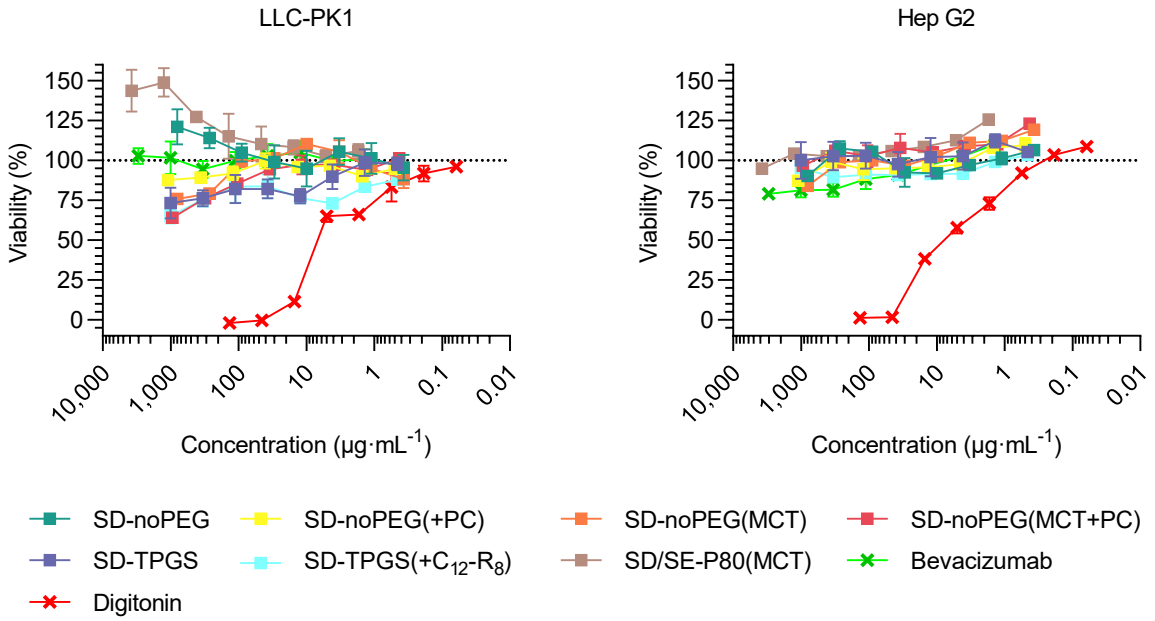
USC UNIVERSIDADE DE SANTIAGO DE COMPOSTELA

USC UNIVERSIDADE DE SANTIAGO DE COMPOSTELA

Supplementary Table 2. Physicochemical characteristics of blank NCs

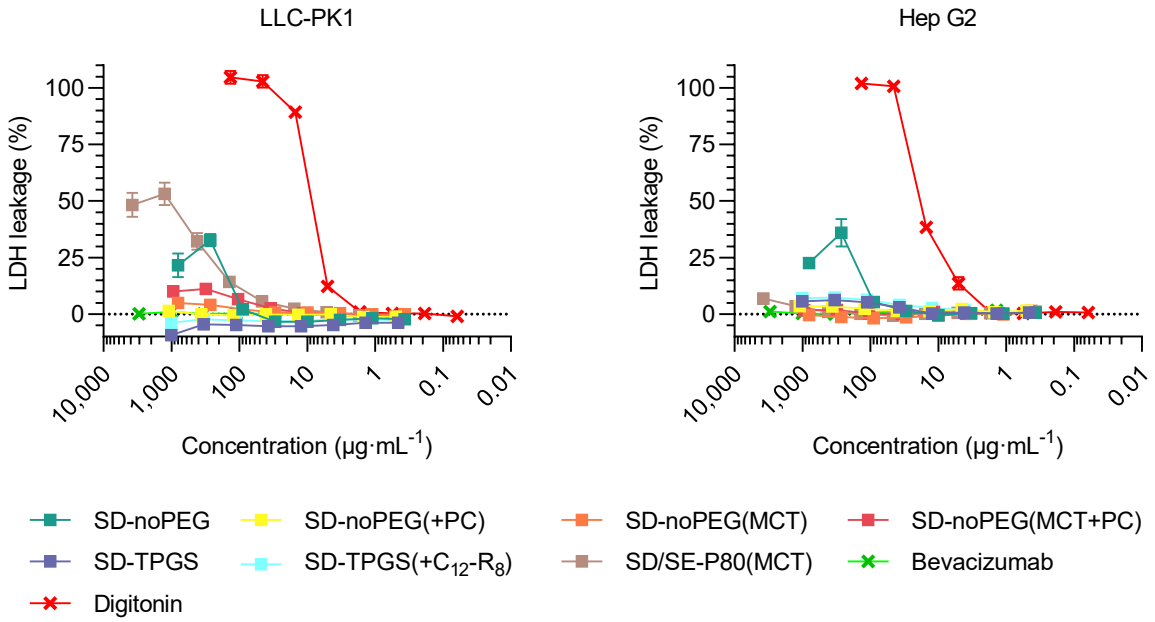
	SD-noPEG	SD-noPEG(MCT)	SD-noPEG(+PC)	SD-noPEG(MCT+PC)	SD-TPGS	SD-TPGS(+C_{12}-R_8)	SD/SE-P80(MCT)
Hydrodynamic diameter (DLS) (nm)	127 ± 6	118 ± 4	194 ± 3	121 ± 1	97 ± 5	129 ± 1	165 ± 1
PDI	0.09 ± 0.06	0.08 ± 0.01	0.04 ± 0.01	0.08 ± 0.01	0.11 ± 0.06	0.11 ± 0.08	0.12 ± 0.02
ζ-potential (mV)	−21 ± 1	−29 ± 6	−9 ± 1	−29 ± 1	−10 ± 1	−6 ± 1	−13 ± 1

Abbreviations: DLS: dynamic light scattering. PDI: polydispersity index. The compositions of SD-noPEG, SD-noPEG(MCT), SD-noPEG(+PC), SD-noPEG(MCT+PC), SD-TPGS, SD-TPGS(+C_{12}-R_8), and SD/SE-P80(MCT) are shown in Supplementary Table 1. Values represent the mean ± standard deviation (n = 3).



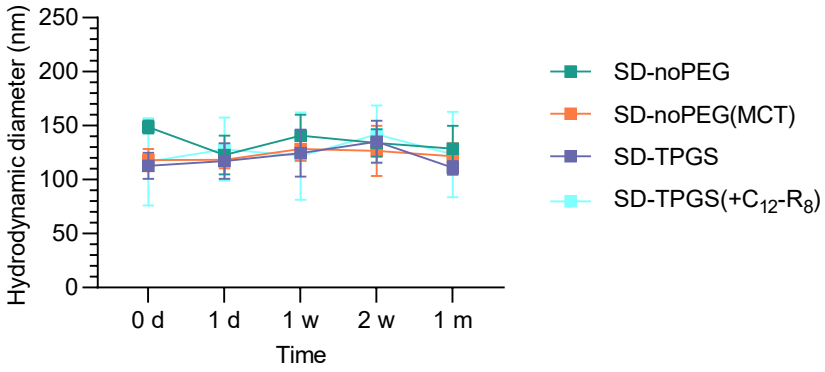
Supplementary Figure 1. Viability of blank NCs prototypes, bevacizumab, and digitonin in LLC-PK1 (left) and Hep G2 (right) cell lines after 24 h

Digitonin, a non-ionic detergent used as a positive control, showed the highest cytotoxicity (100 % viability reduction at doses higher than 45 µg·mL^{-1}). In addition, a slight reduction in viability was observed for SD-TPGS, SD-TPGS(+C_{12}-R_8), and SD-noPEG(MCT) in LLC-PK1. The compositions of SD-noPEG, SD-noPEG(MCT), SD-noPEG(+PC), SD-noPEG(MCT+PC), SD-TPGS, SD-TPGS(+C_{12}-R_8), and SD/SE-P80(MCT) are shown in Supplementary Table 1. Values represent the mean ± standard deviation (n = 3).



Supplementary Figure 2. LDH leakage of blank NCs prototypes, bevacizumab, and digitonin in LLC-PK1 (left) and Hep G2 (right) cell lines after 24 h

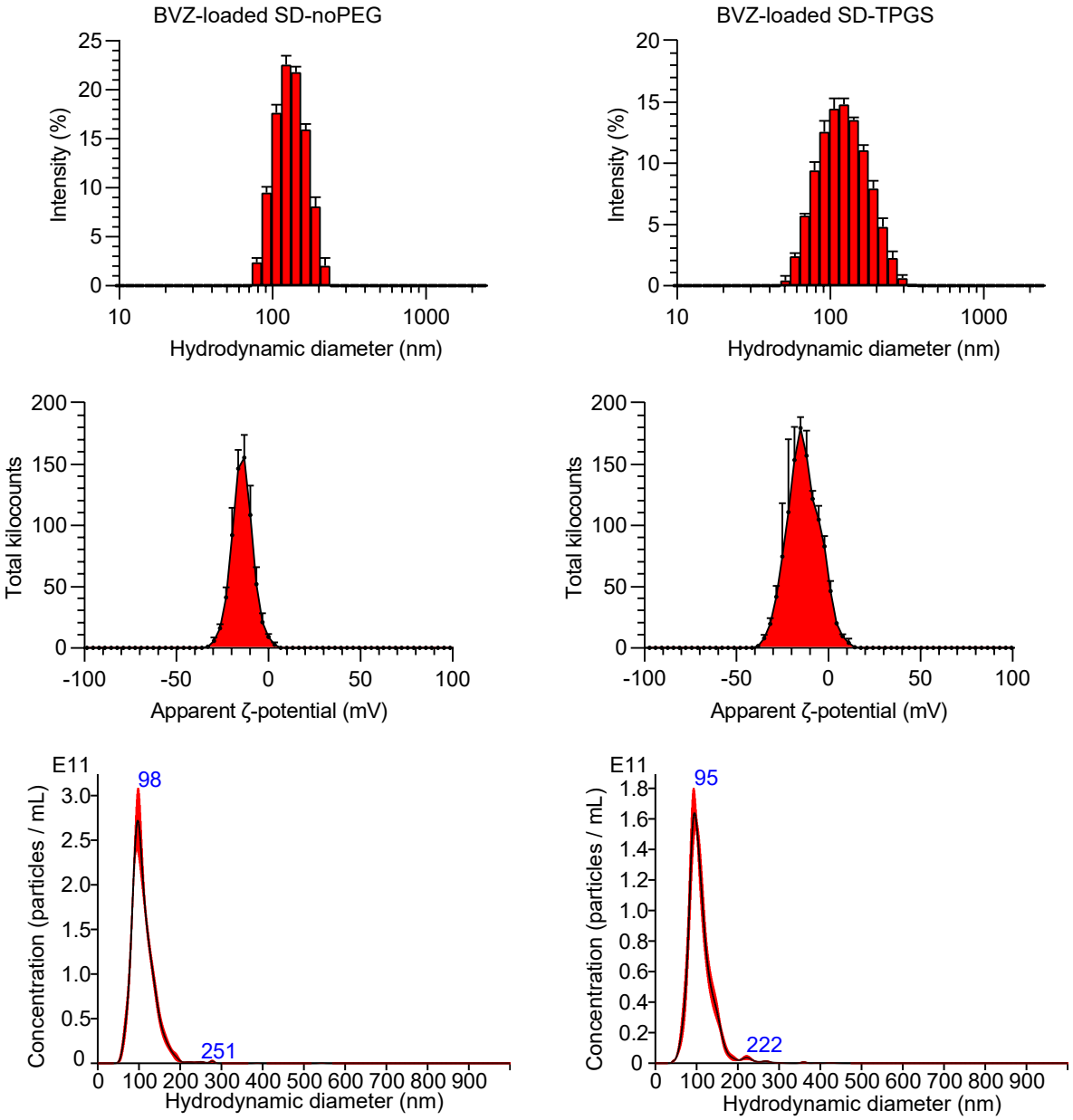
Digitonin, a non-ionic detergent used as a positive control, showed the highest cytotoxicity (100 % LDH leakage at doses higher than 45 µg·mL^{-1}). SD/SE-P80 and SD-noPEG caused partial membrane damage at concentrations higher than 90 µg·mL^{-1}) in LLC-PK1, while only SD-noPEG was found to promote LDH leakage in Hep G2 at the same concentration range. The compositions of SD-noPEG, SD-noPEG(MCT), SD-noPEG(+PC), SD-noPEG(MCT+PC), SD-TPGS, SD-TPGS(+C_{12}-R_8), and SD/SE-P80(MCT) are shown in Supplementary Table 1. Values represent the mean ± standard deviation (n = 3).



Supplementary Figure 3. Long-term stability of BVZ-loaded NCs at 4 °C

The compositions of SD-noPEG, SD-noPEG(MCT), SD-TPGS, and SD-TPGS(+C_{12}-R_8) are shown in Supplementary Table 1. Values represent the mean ± standard deviation (n = 3).

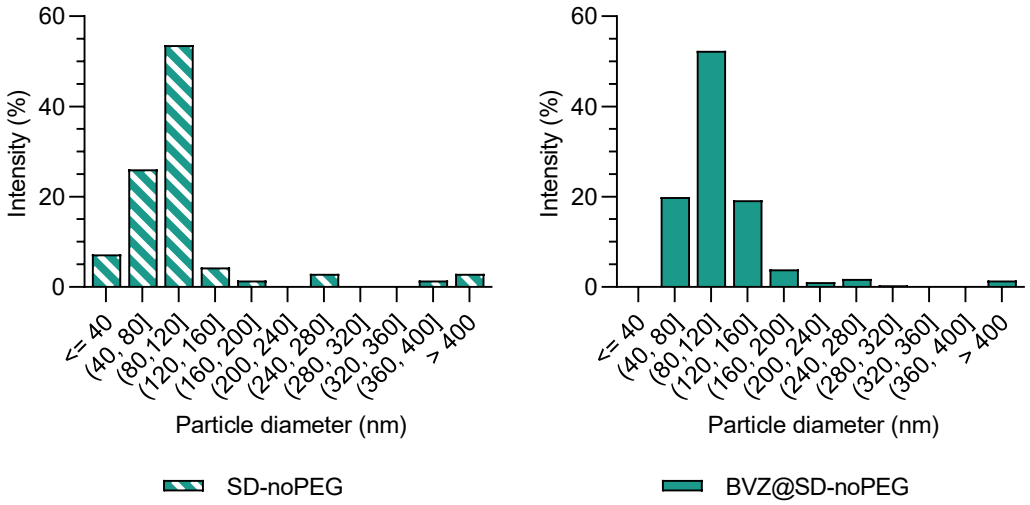
USC
UNIVERSIDADE DE SANTIAGO DE COMPOSTELA



Supplementary Figure 4. DLS (top), LDE (middle), and NTA (bottom) characterization of BVZ-loaded SD-noPEG (left) and SD-TPGS (right)

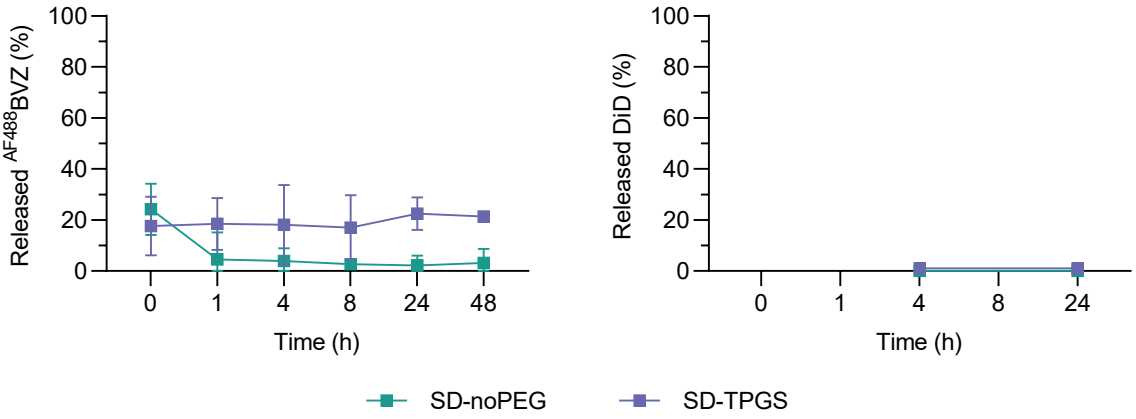
Abbreviations: BVZ: bevacizumab. DLS: dynamic light scattering. LDE: laser Doppler electrophoresis. NTA: nanoparticle tracking analysis. The compositions of SD-noPEG and SD-TPGS are shown in Figure 3. Values represent the mean ± standard deviation of 3 runs (1 measurement).

USC UNIVERSIDADE DE SANTIAGO DE COMPOSTELA



Supplementary Figure 5. Particle diameter histogram of blank SD-noPEG and BVZ-loaded SD-noPEG NCs by cryo-EM

The composition of SD-noPEG is shown in Figure 3. Values represent the intensity of each particle size interval for 69 particles (SD-noPEG) and 281 particles (BVZ-loaded SD-noPEG) (1 NCs replicate).



Supplementary Figure 6. ^{AF488}BVZ release from SD-noPEG and SD-TPGS at 37 °C after a 32 × dilution in PBS supplemented with 10 % FBS

The compositions of SD-noPEG and SD-TPGS are shown in Figure 3. Values represent the mean ± standard deviation (n = 3).

Supplementary Table 3. Physicochemical characteristics of ^{AF488}BVZ and DiD-loaded NCs

	SD-noPEG DiD and ^{AF488}BVZ	SD-TPGS DiD and ^{AF488}BVZ
Hydrodynamic size (nm)	127 ± 1	138 ± 4
PDI	0.03 ± 0.01	0.19 ± 0.02

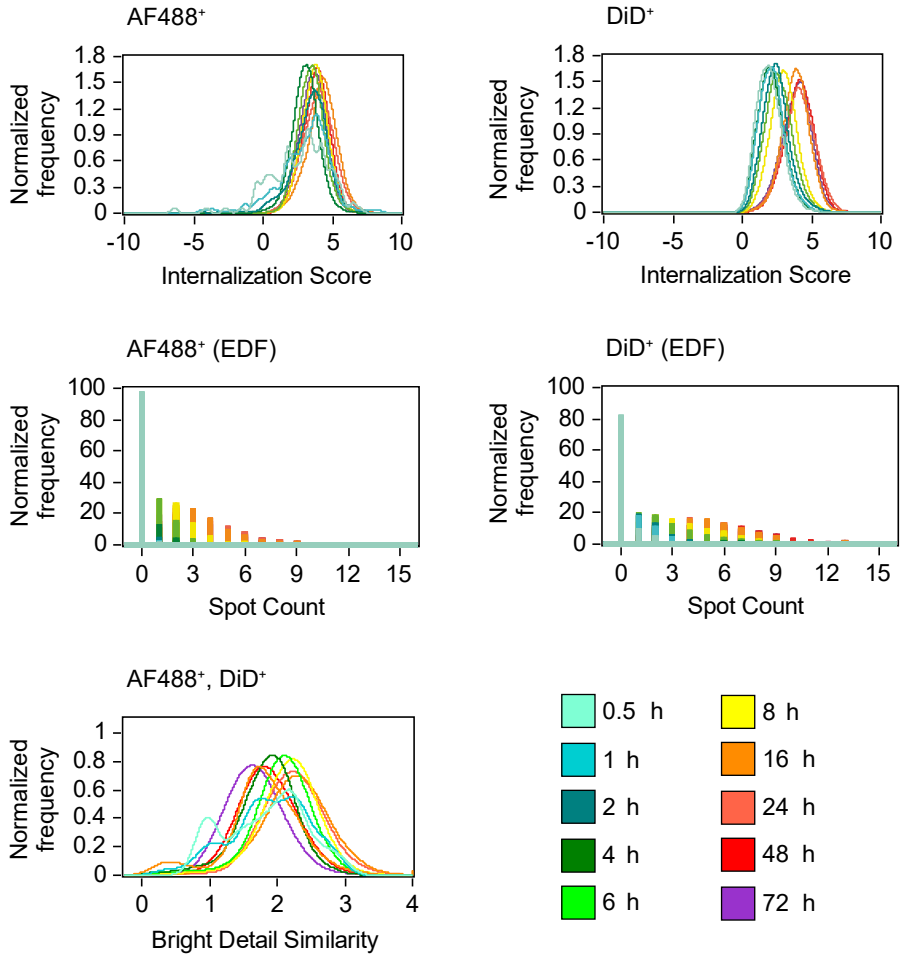
The compositions of SD-noPEG and SD-TPGS are shown in Figure 3. Values represent the mean ± standard deviation (n = 3).

USC
UNIVERSIDADE DE SANTIAGO DE COMPOSTELA

Supplementary Table 4. Physicochemical characteristics of ^{AF488}BVZ-loaded NCs

	SD-noPEG ^{AF488}BVZ	SD-TPGS ^{AF488}BVZ
Hydrodynamic size (nm)	127 ± 1	108 ± 2
PDI	0.11 ± 0.01	0.13 ± 0.02

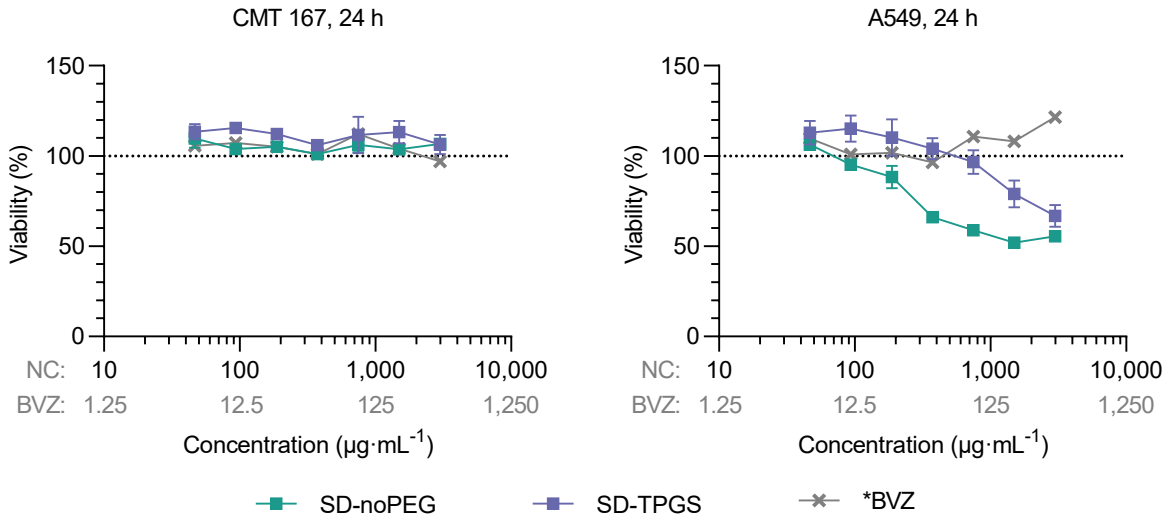
The compositions of SD-noPEG and SD-TPGS are shown in Figure 3. Values represent the mean ± standard deviation (n = 3).



Supplementary Figure 7. Normalized frequency distribution of the internalization score and bright detail similarity and spot count histogram of DiD- and ^{AF488}BVZ-labeled SD-noPEG at different time points (0.5, 1, 2, 4, 6, 8, 16, 24, 48, and 72 h)

Abbreviations: EDF: extended depth field. The composition of SD-noPEG is shown in Figure 3. Values represent the mean of n = 3.

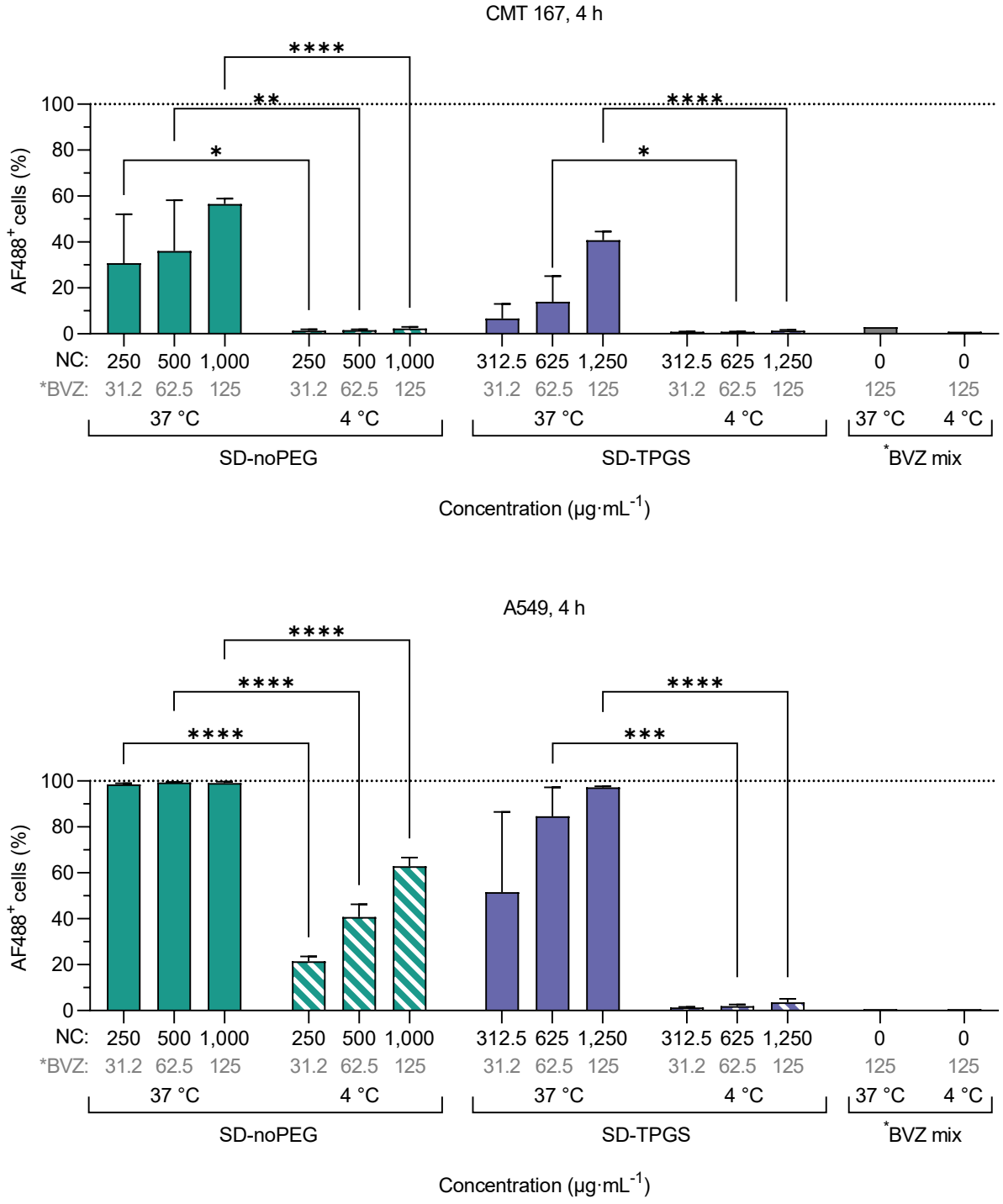
USC UNIVERSIDADE DE SANTIAGO DE COMPOSTELA



Supplementary Figure 8. Cytotoxicity of ^{AF488}BVZ-labeled NCs in CMT 167 and A549 lung cancer cell lines after 24 h incubation at 37 °C

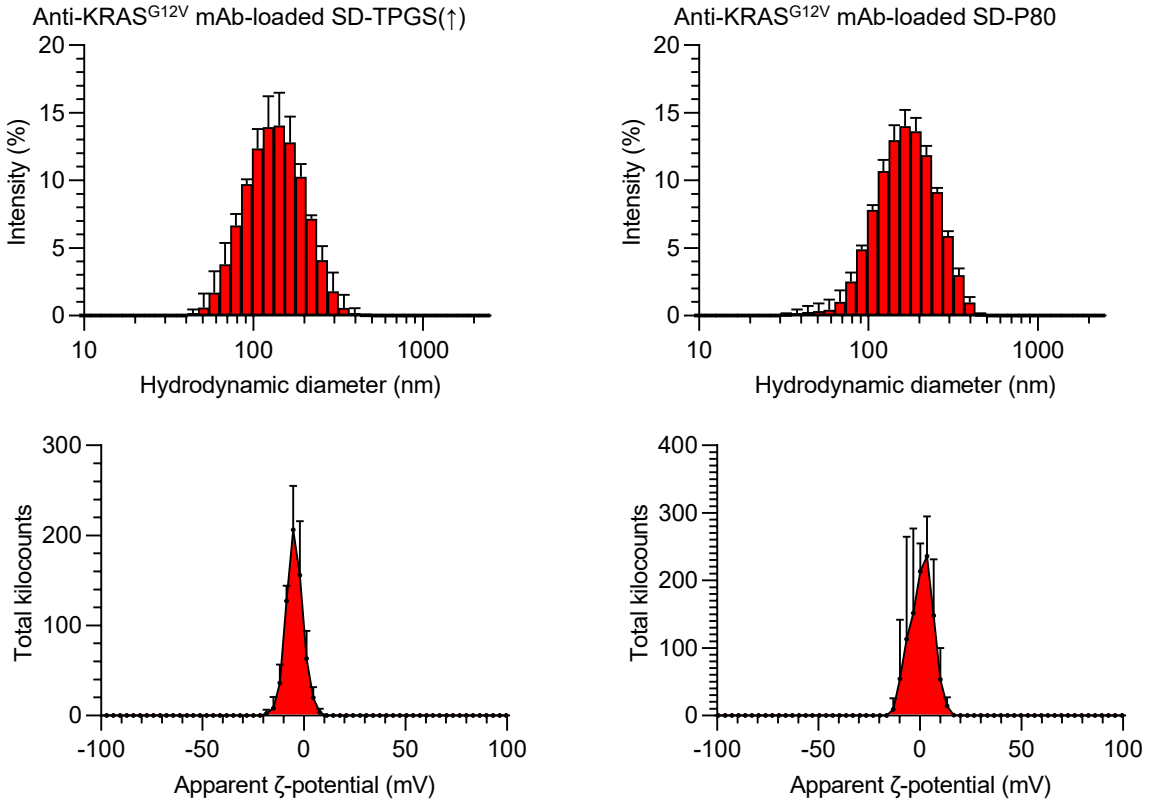
^{AF488}BVZ-labeled NCs were nontoxic in CMT 167. However, SD-noPEG was moderately toxic in A549. Free ^{AF488}BVZ and BVZ mixture were nontoxic in the whole tested concentration range. The compositions of SD-noPEG and SD-TPGS are shown in Figure 3. Values represent the mean ± standard deviation (n = 3).

USC UNIVERSIDADE DE SANTIAGO DE COMPOSTELA



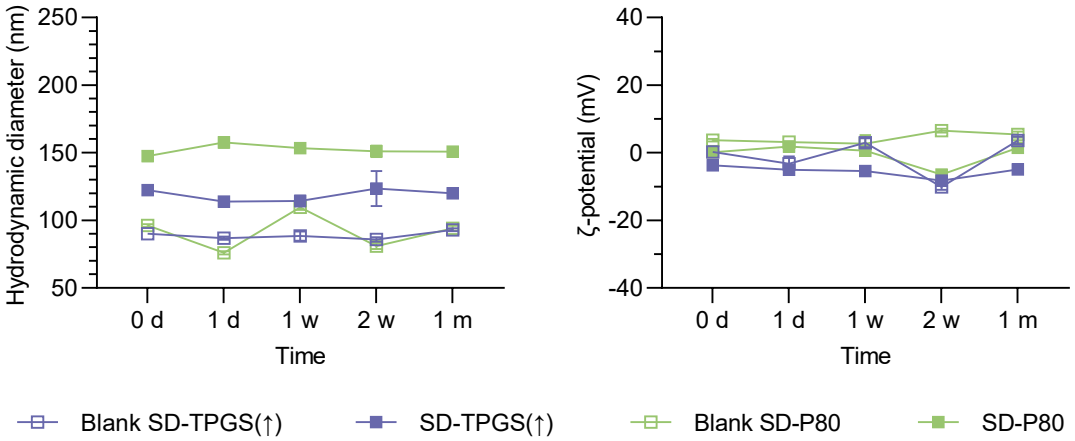
Supplementary Figure 9. Uptake (percentage of AF488-positive cells) of ^{AF488}BVZ-labeled SD-noPEG and SD-TPGS in CMT 167 and A549 cell lines after 4 h

^{AF488}BVZ-loaded NCs showed statistically significative temperature-dependent uptake (unpaired t-tests of NCs or *BVZ concentration at 37 ˚C *vs.* 4 ˚C. *p*-values < 0.05 were considered statistically significant (*). Also, (**) if *p*-value < 0.01, (***) if *p*-value < 0.001 and (****) if *p*-value < 0.0001. SD-noPEG was more internalized in both cell lines than SD-TPGS. The mixture of 2 % ^{AF488}BVZ and 98 % BVZ (*BVZ) was not taken up by any cell line. **Abbreviations:** *BVZ: fluorescently labeled bevacizumab. NC: nanocapsule. The compositions of SD-noPEG and SD-TPGS are shown in Figure 3. Values represent the mean ± standard deviation (n = 3).



Supplementary Figure 10. DLS (top) and LDE (bottom) characterization of anti-KRAS^{G12V} mAb-loaded SD-TPGS(↑) (left) and SD-P80 (right)

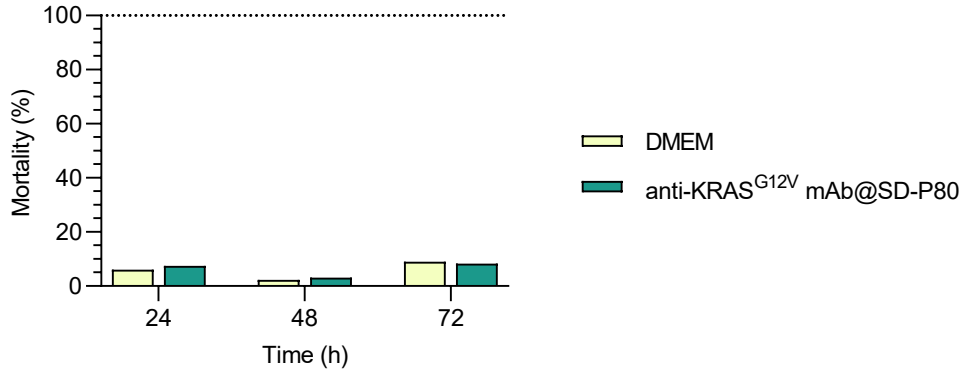
Abbreviations: KRAS: Kirsten rat sarcoma viral oncogene homolog. The compositions of SD-TPGS(↑) and SD-P80 are shown in Figure 9. Values represent the mean ± standard deviation of 3 runs (1 measurement).



Supplementary Figure 11. Stability of blank and anti-KRAS^{G12V} mAb-loaded SD-TPGS(↑) and SD-P80 NCs in storage conditions (4 °C)

The formulations remained stable in terms of particle size and surface charge for up to 1 month at 4 °C. The compositions of SD-TPGS(↑) and SD-P80 are shown in Figure 9. Values represent the mean ± standard deviation (n = 3).

USC UNIVERSIDADE DE SANTIAGO DE COMPOSTELA



Supplementary Figure 12. Mortality of anti-KRAS^{G12V} mAb-loaded SD-P80 in CMT 167 cells during 24, 48, and 72 h by the 7-AAD assay

Abbreviations: 7-AAD: 7-aminoactinomycin D. The compositions of SD-P80 is shown in Figure 9. Values represent the mean of 1 experiment.

6. ACKNOWLEDGMENTS

This work was supported by the Spanish Ministry of Economy and Industry under the grant agreement with reference: MINECO- PCIN-2017-129/ AEI (Project “Nano-Inmunoterapia: Targeting Intracelular de Células Tumorales y TAMs” 2-INTRATARGET) under the frame of "EuroNanoMed III", by the 2^2-INTRATARGET project, which received funding from Instituto de Salud Carlos III (ISCIII) with reference A20/00028 under the umbrella of the ERA NET EuroNanoMed GA N 723770 of the EU Horizon 2020 Research and Innovation Programme, by FEDER/Spanish Ministry of Science, Innovation, and Universities (Ref.: SAF2017-86634-R), and by the Competitive Reference Groups, Consellería de Educación e Ordenación Universitaria, Xunta de Galicia, with Ref: ED431C 2017/09. G. Berrecoso acknowledged the financial support by the Xunta de Galicia through the “Axudas de apoio á etapa predoutoral 2018” grant, co-funded by the European Social Fund “FSE Galicia 2014-2020” (Ref.: ED481A-2018/047).

G. Berrecoso also acknowledges the financial support from the “Agrupación Europea de Cooperación Territorial Galicia-Norte de Portugal (GNP-AECT)” through the “Programa IACOBUS Candidatura Estancias VIII” program (Ref.: 143). Thanks to this financial support, imaging flow cytometry experiments were conducted by G. Berrecoso at the research group of Prof. Paula Pêgo (i3s - Instituto de Investigação e Inovação em Saúde da Universidade do Porto, University of Porto, Porto, 4200, Portugal).

The monoclonal antibody bevacizumab was kindly donated by mAbxience, León.

Cryo-EM images were collected in collaboration with Prof. Nicola G. A. Abrescia (Bizkaia Science and Technology Park, Derio, 48160, Spain).

7. REFERENCES

[1] U.S. Food and Drug Administration. Center for Drug Evaluation and Research. Rybrevant approval letter. https://www.accessdata.fda.gov/drugsatfda_docs/nda/2021/761210Orig1s000Approv.pdf. Accessed: October 26,

2022.
[2] European Medicines Agency. Rybrevant. Summary of product characteristics. https://www.ema.europa.eu/en/documents/product-information/rybrevant-epar-product-information_en.pdf. Accessed: October 26, 2022.
[3] U.S. Food and Drug Administration. Center for Drug Evaluation and Research. Tecentriq approval letter. https://www.accessdata.fda.gov/drugsatfda_docs/nda/2016/761034Orig1s000Approv.pdf. Accessed: October 26, 2022.
[4] European Medicines Agency. Tecentriq. Summary of product characteristics. https://www.ema.europa.eu/en/documents/product-information/tecentriq-epar-product-information_en.pdf. Accessed: October 26, 2022.
[5] U.S. Food and Drug Administration. Center for Drug Evaluation and Research. Avastin approval letter. https://www.accessdata.fda.gov/drugsatfda_docs/nda/2004/STN-125085_Avastin_Approv.pdf. Accessed: October 26, 2022.
[6] European Medicines Agency. Avastin. Summary of product characteristics. https://www.ema.europa.eu/en/documents/product-information/avastin-epar-product-information_en.pdf. Accessed: October 26, 2022.
[7] U.S. Food and Drug Administration. Center for Drug Evaluation and Research. Libtayo approval letter. https://www.accessdata.fda.gov/drugsatfda_docs/nda/2018/761097Orig1s000Approv.pdf. Accessed: October 26, 2022.
[8] European Medicines Agency. Libtayo. Summary of product characteristics. https://www.ema.europa.eu/en/documents/product-information/libtayo-epar-product-information_en.pdf. Accessed: October 26, 2022.
[9] U.S. Food and Drug Administration. Center for Drug Evaluation and Research. Imfinzi approval letter. https://www.accessdata.fda.gov/drugsatfda_docs/nda/2017/761069Orig1s000Approv.pdf. Accessed: October 26, 2022.
[10] European Medicines Agency. Imfinzi. Summary of product characteristics. https://www.ema.europa.eu/en/documents/product-information/imfinzi-epar-product-information_en.pdf. Accessed: October 26, 2022.
[11] U.S. Food and Drug Administration. Center for Drug Evaluation and Research. Enhertu approval letter. https://www.accessdata.fda.gov/drugsatfda_docs/nda/2019/761139Orig1s000Approv.pdf. Accessed: October 26, 2022.
[12] European Medicines Agency. Enhertu. Summary of product characteristics. https://www.ema.europa.eu/en/documents/product-information/enhertu-epar-product-information_en.pdf. Accessed: October 26, 2022.
[13] U.S. Food and Drug Administration. Center for Drug Evaluation and Research. Yervoy approval letter. https://www.accessdata.fda.gov/drugsatfda_docs/nda/2011/125377Orig1s000Approv.pdf. Accessed: October 26, 2022.
[14] European Medicines Agency. Yervoy. Summary of product characteristics. https://www.ema.europa.eu/en/documents/product-information/yervoy-epar-product-information_en.pdf. Accessed: October 26, 2022.
[15] U.S. Food and Drug Administration. Center for Drug Evaluation and Research. Portrazza approval letter. https://www.accessdata.fda.gov/drugsatfda_docs/nda/2015/125547Orig1s000Approv.pdf. Accessed: October 26, 2022.
[16] U.S. Food and Drug Administration. Center for Drug Evaluation and Research. Opdivo approval letter. https://www.accessdata.fda.gov/drugsatfda_docs/nda/2015/125527Orig1s000Approv.pdf. Accessed: October 26, 2022.
[17] European Medicines Agency. Opdivo. Summary of product characteristics. https://www.ema.europa.eu/en/documents/product-information/opdivo-epar-product-information_en.pdf. Accessed: October 26, 2022.
[18] U.S. Food and Drug Administration. Center for Drug Evaluation and Research. Keytruda approval letter. https://www.accessdata.fda.gov/drugsatfda_docs/nda/2014/125514Orig1s000Approv.pdf. Accessed: October 26, 2022.
[19] European Medicines Agency. Keytruda. Summary of product characteristics. https://www.ema.europa.eu/en/documents/product-information/keytruda-epar-product-information_en.pdf. Accessed: October 26, 2022.
[20] U.S. Food and Drug Administration. Center for Drug Evaluation and Research. Cyramza approval letter. https://www.accessdata.fda.gov/drugsatfda_docs/nda/2014/125477Orig1s000Approv.pdf. Accessed: October 26, 2022.
[21] European Medicines Agency. Cyramza. Summary of product characteristics. https://www.ema.europa.eu/en/documents/product-information/cyramza-epar-product-information_en.pdf. Accessed: October 26, 2022.
[22] J. Pang, H. Xing, Y. Sun, S. Feng, S. Wang. Non-small cell lung cancer combination therapy: Hyaluronic acid modified, epidermal growth factor receptor targeted, pH sensitive lipid-polymer hybrid nanoparticles for the delivery of erlotinib plus bevacizumab. *Biomedicine and Pharmacotherapy*. 125, 109861. (2020). doi:

USC UNIVERSIDADE DE SANTIAGO DE COMPOSTELA

10.1016/j.biopha.2020.109861.
[23] T. G. Dacoba, S. Anthiya, G. Berrecoso, I. Fernández-Mariño, C. Fernández-Varela, J. Crecente-Campo, D. Teijeiro-Osorio, F. Torres-Andón, M. J. Alonso. Nano-Oncologicals: A Tortoise Trail Reaching New Avenues. *Advanced Functional Materials*. 31, 1–36. (2021). doi: 10.1002/adfm.202009860.
[24] M. Durán-Lobato, A. M. López-Estévez, A. S. Cordeiro, T. G. Dacoba, J. Crecente-Campo, D. Torres, M. J. Alonso. Nanotechnologies for the delivery of biologicals: Historical perspective and current landscape. *Advanced Drug Delivery Reviews*. 176, (2021). doi: 10.1016/j.addr.2021.113899.
[25] Z.-Y. Zhang. Drugging the Undruggable: Therapeutic Potential of Targeting Protein Tyrosine Phosphatases. *Accounts of Chemical Research*. 50, 122–129. (2017). doi: 10.1021/acs.accounts.6b00537.
[26] S. Tangutoori, B. Q. Spring, Z. Mai, A. Palanisami, L. B. Mensah, T. Hasan. Simultaneous delivery of cytotoxic and biologic therapeutics using nanophotoactivatable liposomes enhances treatment efficacy in a mouse model of pancreatic cancer. *Nanomedicine: Nanotechnology, Biology, and Medicine*. 12, 223–234. (2016). doi: 10.1016/j.nano.2015.08.007.
[27] F. Sousa, H. K. Dhaliwal, F. Gattacceca, B. Sarmento, M. M. Amiji. Enhanced anti-angiogenic effects of bevacizumab in glioblastoma treatment upon intranasal administration in polymeric nanoparticles. *Journal of Controlled Release*. 309, 37–47. (2019). doi: 10.1016/j.jconrel.2019.07.033.
[28] H. Deng, K. Song, X. Zhao, Y. Li, F. Wang, J. Zhang, A. Dong, Z. Qin. Tumor Microenvironment Activated Membrane Fusogenic Liposome with Speedy Antibody and Doxorubicin Delivery for Synergistic Treatment of Metastatic Tumors. *ACS Applied Materials and Interfaces*. 9, 9315–9326. (2017). doi: 10.1021/acsami.6b14683.
[29] Á. Molina-Crespo, A. Cadete, D. Sarrio, M. Gámez-Chiachio, L. Martinez, K. Chao, A. Olivera, A. Gonella, E. Díaz, J. Palacios, P. K. Dhal, M. Besev, M. Rodríguez-Serrano, M. L. García Bermejo, J. C. Triviño, A. Cano, M. García-Fuentes, O. Herzberg, D. Torres, M. J. Alonso, G. Moreno-Bueno. Intracellular Delivery of an Antibody Targeting Gasdermin-B Reduces HER2 Breast Cancer Aggressiveness. *Clinical Cancer Research*. 25, 4846–4858. (2019). doi: 10.1158/1078-0432.CCR-18-2381.
[30] D. Teijeiro-Osorio, C. B. Michalowsky, J. A. Costoya, I. Golán, S. Vicent, M. J. Alonso. In *RAS Targeted Drug Development Summit conference, Boston*. (2019).
[31] A. Baião, F. Sousa, A. V. Oliveira, C. Oliveira, B. Sarmento. Effective intracellular delivery of bevacizumab: Via PEGylated polymeric nanoparticles targeting the CD44v6 receptor in colon cancer cells. *Biomaterials Science*. 8, 3720–3729. (2020). doi: 10.1039/d0bm00556h.
[32] F. Sousa, A. Cruz, I. M. Pinto, B. Sarmento. Nanoparticles provide long-term stability of bevacizumab preserving its antiangiogenic activity. *Acta Biomaterialia*. 78, 285–295. (2018). doi: 10.1016/j.actbio.2018.07.040.
[33] I. Luis de Redín, F. Expósito, M. Agüeros, M. Collantes, I. Peñuelas, D. Allemandi, J. M. Llabot, A. Calvo, J. M. Irache. In vivo efficacy of bevacizumab-loaded albumin nanoparticles in the treatment of colorectal cancer. *Drug Delivery and Translational Research*. 10, 635–645. (2020). doi: 10.1007/s13346-020-00722-7.
[34] G. A. Hobbs, C. J. Der, K. L. Rossman. RAS isoforms and mutations in cancer at a glance. *Journal of Cell Science*. 129, 1287–1292. (2016). doi: 10.1242/jcs.182873.
[35] J. Judd, N. A. Karim, H. Khan, A. R. Naqash, Y. Baca, J. Xiu, A. M. VanderWalde, H. Mamdani, L. E. Raez, M. Nagasaka, S. G. Pai, M. A. Socinski, J. J. Nieva, C. Kim, A. J. Wozniak, C. Ikpeazu, G. de Lima Lopes, A. I. Spira, W. M. Korn, E. S. Kim, S. V. Liu, H. Borghaei. Characterization of KRAS mutation subtypes in non-small cell lung cancer. *Molecular Cancer Therapeutics*. 20, 2577–2584. (2021). doi: 10.1158/1535-7163.MCT-21-0201.
[36] R. Veluswamy, P. C. Mack, J. Houldsworth, E. Elkhouly, F. R. Hirsch. KRAS G12C–Mutant Non–Small Cell Lung Cancer: Biology, Developmental Therapeutics, and Molecular Testing. *Journal of Molecular Diagnostics*. 23, 507–520. (2021). doi: 10.1016/j.jmoldx.2021.02.002.
[37] E. Cekani, S. Epistolio, G. Dazio, M. Cefalì, L. Wannesson, M. Frattini, P. Froesch. Molecular Biology and Therapeutic Perspectives for K-Ras Mutant Non-Small Cell Lung Cancers. *Cancers*. 14, 1–32. (2022). doi: 10.3390/cancers14174103.
[38] M. Shen, R. Qi, J. Ren, D. Lv, H. Yang. Characterization With KRAS Mutant Is a Critical Determinant in Immunotherapy and Other Multiple Therapies for Non-Small Cell Lung Cancer. *Frontiers in Oncology*. 11, 1–17. (2022). doi: 10.3389/fonc.2021.780655.
[39] S. R. Punekar, V. Velcheti, B. G. Neel, K. K. Wong. The current state of the art and future trends in RAS-targeted cancer therapies. *Nature Reviews Clinical Oncology*. 19, 637–655. (2022). doi: 10.1038/s41571-022-00671-9.
[40] A. Spagnuolo, P. Maione, C. Gridelli. The treatment of advanced non-small cell lung cancer harboring KRAS mutation: a new class of drugs for an old target—a narrative review. *Translational Lung Cancer Research*. 11, 1199–1216. (2022). doi: 10.21037/tlcr-21-948.
[41] E. Capelletto, P. Bironzo, L. Denis, A. Koustenis, M. Bungaro, S. Novello. Single agent VS-6766 or VS-6766 plus defactinib in KRAS -mutant non-small-cell lung cancer: the RAMP-202 phase II trial. *Future Oncology*. 18, 1907–1915. (2022). doi: 10.2217/fon-2021-1582.
[42] S. Kamerkar, V. S. LeBleu, H. Sugimoto, S. Yang, C. F. Ruivo, S. A. Melo, J. J. Lee, R. Kalluri. Exosomes facilitate therapeutic targeting of oncogenic KRAS in pancreatic cancer. *Nature*. 546, 498–503. (2017). doi: 10.1038/nature22341.
[43] C. P. Gomes, A. Varela-Moreira, V. Leiro, C. D. F. Lopes, P. M. D. Moreno, M. Gomez-Lazaro, A. P. Pêgo. A high-throughput bioimaging study to assess the impact of chitosan-based nanoparticle degradation on DNA delivery performance. *Acta Biomaterialia*. 46, 129–140. (2016). doi: 10.1016/j.actbio.2016.09.037.

OVERALL DISCUSSION

USC
UNIVERSIDADE
DE SANTIAGO
DE COMPOSTELA

USC
UNIVERSIDADE
DE SANTIAGO
DE COMPOSTELA

1. OVERALL DISCUSSION

Nanotechnology is known as a key enabling technology to enhance the efficacy and reduce the toxicity of a variety of drugs. In the scope of this work, we have focused on polymeric nanocapsules (NCs) as carriers for small-molecule chemotherapeutics and immunomodulators, as well as monoclonal antibodies (mAbs) targeting intracellular oncoproteins. Our group has experience in improving the biodistribution of anti-cancer drugs by their encapsulation in NCs made of chitosan,[1] Polyethylene glycol-polyglutamic acid (PEG·PGA),[2,3] hyaluronic acid (HA),[4–6] and poly(asparagine).[7,8] For example, docetaxel-loaded PEG·PGA NCs showed a significant tumor growth reduction and an increase in survival time in U87 glioma-bearing mice.[2] Moreover, these NCs also significantly reduced lung cancer metastasis, probably due to their accumulation in lymph nodes.[3] Similarly, docetaxel-loaded HA or PEG·PGA NCs were found to reduce tumor size and metastatic burden in orthotopic lung cancer models.[3,5] On the other hand, our group also reported for the first time the intracellular delivery of mAbs targeting intracellular oncoproteins, such as gasdermin B, by using HA NCs. In this case, the results showed the inhibition of cell migration in vitro and, more importantly, the reduction of tumor size and lung metastasis in an orthotopic mammary fat pad tumor model.[6]

Despite the attractive features of the NCs, critical issues remain to be investigated, such as the evaluation of their actual chemical composition and the protein corona formed after their interaction with plasmatic proteins.[9] In this sense, it is clear nowadays that the information about the protein corona is relevant for understanding the biodistribution and, hence, the efficacy of oncological nanomedicine candidates.[10–12] On the other hand, while the majority of efforts have been oriented to the formulation of cytotoxic drugs, we found it important to assess the value of the NCs delivery platform for the formulation of immunomodulatory drugs and mAbs.

Considering this background, we have divided the work of this Ph.D. thesis into three different chapters aimed at investigating:

1. The physicochemical and chemical properties of different prototypes of NCs and their interaction with biological proteins.
2. The potential of the NCs delivery platform for the encapsulation of immunomodulatory drugs and their delivery to cancer cells and macrophages.
3. The potential of the NCs delivery platform for the intracellular delivery of mAbs addressing intracellular oncoproteins.

Below we summarized the main achievements of each of the said chapters.

1.1. CHARACTERIZATION OF POLYMERIC NANOCAPSULES: CHEMICAL COMPOSITION AND PHYSICOCHEMICAL AND BIOLOGICAL PROPERTIES

Based on the knowledge our group has acquired in the last decades about NCs design and their use in the oncology field, seven NCs with negative or neutral surface charge and appropriate

particle size were developed using different preparation techniques [solvent displacement (SD) or self-emulsification (SE)] and containing different surfactants with lineal PEG chains (*l*-PEG; D-α-tocopherol polyethylene glycol 1000 succinate), branched PEG chains (*b*-PEG; polysorbate 80), or without PEG (no-PEG; DOTAP or lecithin) and polymeric coatings [hyaluronic acid (HA), polysialic acid (PSA), and polyethylene glycol-polyglutamic acid (PEG·PGA)] (Figure 1).

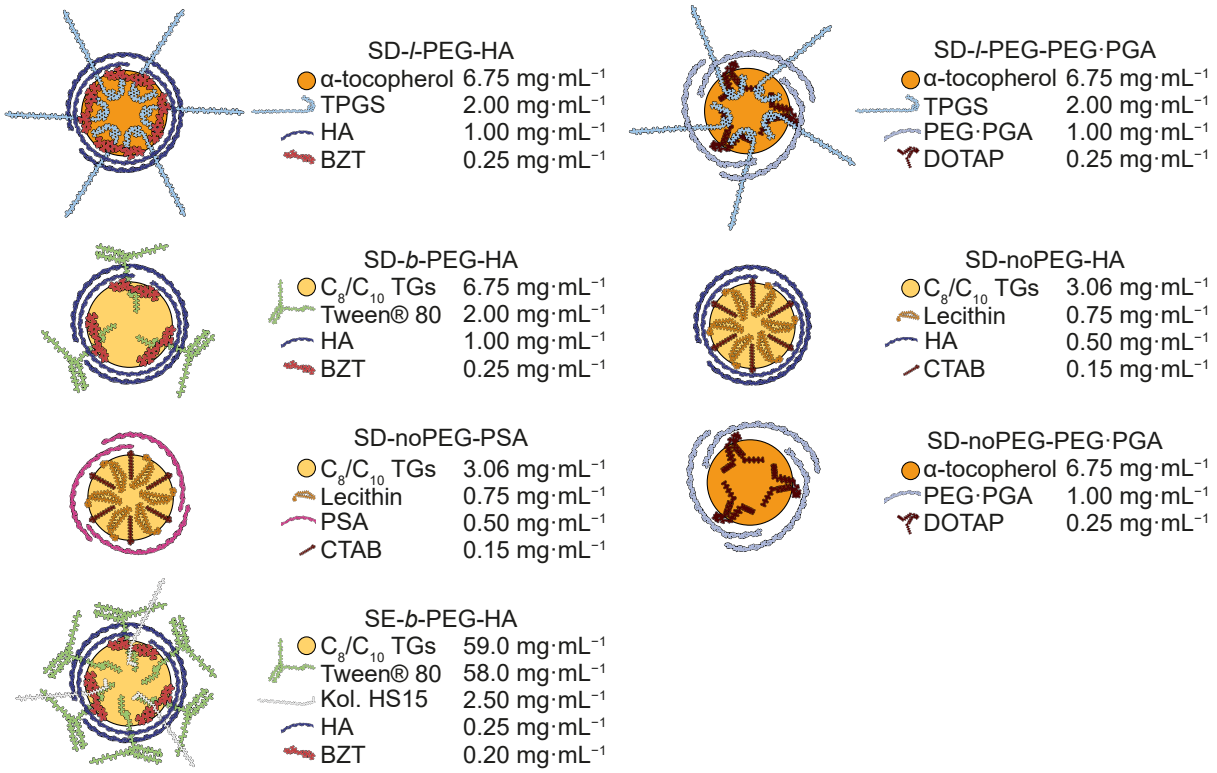


Figure 1. Schematic representation of the expected NCs' compound arrangement and their theoretical composition

SD-*l*-PEG-HA: Formulation prepared by solvent displacement technique and composed of lineal PEG (TPGS), BZT, and hyaluronic acid shell. **SD-*l*-PEG-PEG·PGA**: Formulation prepared by solvent displacement technique and composed of lineal PEG (TPGS), DOTAP, and PEG·PGA shell. **SD-*b*-PEG-HA**: Formulation prepared by solvent displacement technique and composed of branched PEG (polysorbate 80), BZT, and hyaluronic acid shell. **SD-noPEG-HA**: Formulation prepared by solvent displacement technique and composed of non-PEGylated surfactants (lecithin), CTAB, and hyaluronic acid shell. **SD-noPEG-PSA**: Formulation prepared by displacement technique and composed of non-PEGylated surfactant (lecithin), CTAB, and polysialic acid shell. **SD-noPEG-PEG·PGA**: Formulation prepared by solvent displacement technique and composed of non-PEGylated surfactants (DOTAP) and PEG·PGA shell. **SE-*b*-PEG-HA**: Formulation prepared by self-emulsifying technique and composed of branched PEG (polysorbate 80), BZT, and hyaluronic acid shell. **Abbreviations**: BZT: benzethonium chloride. C_8/C_{10} TGs: caprylic/capric triglycerides. CTAB: hexadecyltrimethylammonium bromide. DOTAP: 1,2-dioleoyl-3-trimethylammoniumpropane. HA: hyaluronic acid. Kol. HS15: Kolliphor® HS15. PEG·PGA: polyethylene glycol polyglutamic acid. PSA: polysialic acid. TPGS: D-α-tocopherol polyethylene glycol 1000 succinate. Adaptation from [13] licensed under a Creative Commons CC BY license.

The first screening of the formulations was made to assess the possibility of purifying the selected prototypes using ultracentrifugation or tangential flow filtration. As a result, all prototypes preserved their original properties except for the SD-*b*-PEG-HA prototype, which

exhibited a size increase (> 200 nm) and, therefore, was discontinued. Purified NCs were characterized by dynamic light scattering (DLS), laser Doppler electrophoresis (LDE), and nanoparticle tracking analysis (NTA). Hydrodynamic sizes were between 102 and 156 nm, with polydispersity indexes < 0.3 and ζ-potentials ranging from 0 to –39 mV. NCs were stable when incubated in 90 % human plasma at 37 °C for up to 24 h.

For the actual chemical characterization, an LC-MS/MS methodology was developed for the quantification of every single component of the NCs (2 oils, 7 surfactants, and 3 polymers) and validated following international guidelines. The association efficiencies (AE) of each component of the NCs varied between 14 % and 95 % (Figure 2). These data allowed the calculation of the PEG density (number of PEG chains per 100 nm^2) and their conformation (Table 1). SD-noPEG-PEG·PGA exhibited the lowest PEG density (19 ± 8 PEG chains per 100 nm^2), followed by SD-*l*-PEG-PEG·PGA and SD-*l*-PEG-HA (200 ± 86 and 320 ± 133 PEG chains per 100 nm^2, respectively), whereas the PEG density of SE-*b*-PEG-HA was more than 20-fold that of the others (9,038 ± 3,893 PEG chains per 100 nm^2), probably due to the presence of branched PEG. Moreover, all NCs exhibited a brush PEG conformation, adequate to reduce the interaction with proteins. Finally, results also showed that the polymer association was significantly lower in the SE formulation (2 mg of polymer per g of oil) compared to the SD formulations (from 36 to 57 mg of polymer per g of oil) (Table 2).

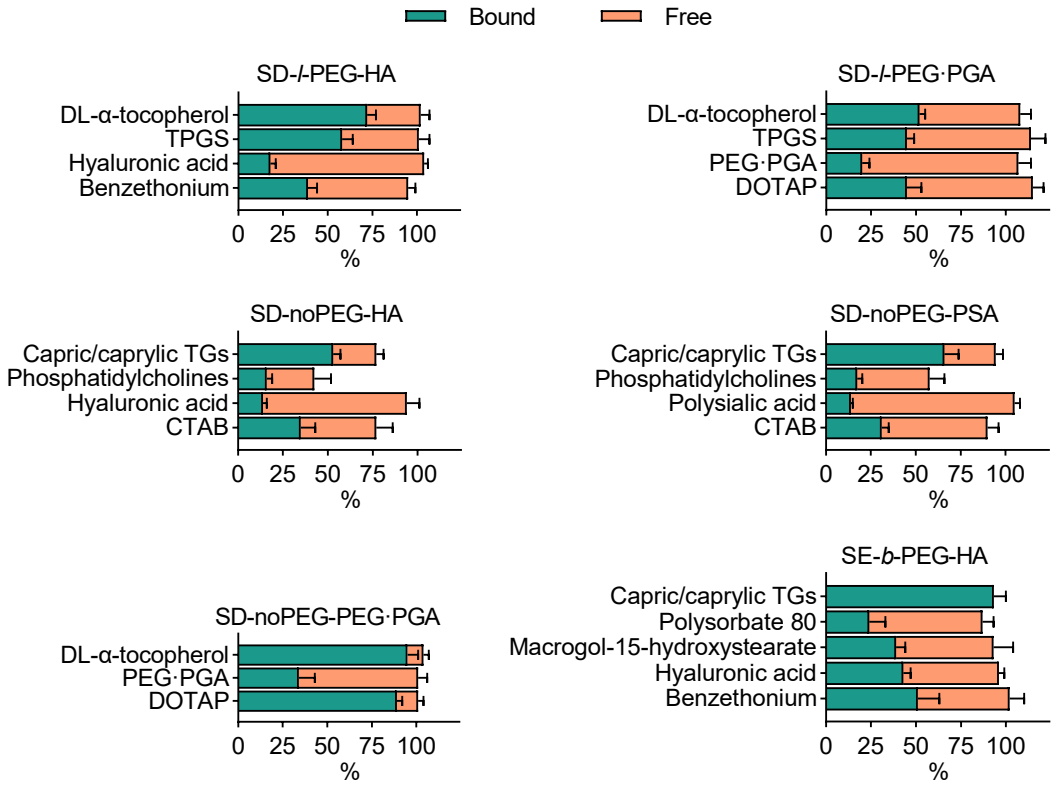


Figure 2. Associated (bound) and non-associated (free) mass percentages referred to the total added mass of each component of the six tested NCs

Abbreviations: TPGS: D-α-tocopherol polyethylene glycol 1000 succinate. TGs: triglycerides. CTAB: Hexadecyltrimethylammonium. DOTAP: 1,2-dioleoyl-3-trimethylammonium-propane chloride. PEG·PGA: Polyethylene glycol poly-α-glutamic acid. The compositions of SD-*l*-PEG-HA, SD-*l*-PEG-PEG·PGA, SD-*b*-PEG-HA, SD-noPEG-HA, SD-noPEG-PSA, SD-noPEG-PEG·PGA, and SE-*b*-PEG-HA are shown in Figure 1. Values represent the mean ± standard deviation (n = 3). Adaptation from [13] licensed under a Creative Commons CC BY license.

Table 1. Total PEG mass, density, and thickness, considering both surfactant and polymer PEG moieties, of the different NCs

Formulation	PEG mass ratio (mg of PEG per g of oil)	Γ (PEG chains / 100 nm^2)	F_R (nm)	A (nm^2)	D (nm)	L (nm)	Configuration
SD-*l*-PEG-HA	159 ± 27	320 ± 133	2.24 (TPGS)	0.5 ± 0.1 (TPGS)	0.83 ± 0.06	4.3 ± 0.2	Brush
SD-*l*-PEG-PEG·PGA	215 ± 35	200 ± 86	2.24 (TPGS) 5.91 (PEG·PGA)	0.6 ± 0.1 (TPGS) 11.1 ± 3.5 (PEG·PGA)	1.19 ± 0.86	4.1 ± 3.4	Brush
SD-noPEG-HA	N/A	N/A	N/A	N/A	N/A	N/A	N/A
SD-noPEG-PSA	N/A	N/A	N/A	N/A	N/A	N/A	N/A
SD-noPEG-PEG·PGA	42 ± 14	19 ± 8	5.91 (PEG·PGA)	11.4 ± 4.6	3.81 ± 0.43	7.9 ± 0.6	Brush
SE-*b*-PEG-HA	188 ± 84	9,038 ± 3,893	3.68 (P80) 1.78 (m15OHSt)	0.6 ± 0.3 (P80) 8.9 ± 3.0 (m15OHSt)	0.97 ± 0.73	3.5 ± 3.3	Brush

Abbreviations: Γ: PEG density. F_R: Flory radius. A: area occupied by each PEG chain. D: distance between PEG molecules. L: PEG layer thickness. TPGS: D-α-tocopherol polyethylene glycol 1000 succinate. m15OHSt: macrogol-15-hydroxystearate. P80: polysorbate 80. The compositions of SD-*l*-PEG-HA, SD-*l*-PEG-PEG·PGA, SD-noPEG-HA, SD-noPEG-PSA, SD-noPEG-PEG·PGA, and SE-*b*-PEG-HA are shown in Figure 1. Values represent the mean ± standard deviation (n = 3).

Table 2. Mass and molar ratios of PEGylated surfactants, non-PEGylated surfactants, and polymers referred to the quantity of oil

Formulation	Mass ratio (mg per g of oil)			Molar ratio (mmol per mol of oil)		
	PEGylated surfactants	Non-PEGylated surfactants	Polymer	PEGylated surfactants	Non-PEGylated surfactants	Polymer
SD-*l*-PEG-HA	238 ± 40	20 ± 4	36 ± 8	68.31 ± 11.48	20.89 ± 4.18	0.27 ± 0.06
SD-*l*-PEG-PEG·PGA	254 ± 37	32 ± 8	57 ± 13	72.86 ± 10.61	20.67 ± 5.17	3.90 ± 0.89
SD-noPEG-HA	N/A	73 ± 20	45 ± 9	N/A	86.64 ± 23.74	0.40 ± 0.08
SD-noPEG-PSA	N/A	58 ± 15	34 ± 7	N/A	64.94 ± 16.79	0.52 ± 0.11
SD-noPEG-PEG·PGA	N/A	35 ± 3	53 ± 18	N/A	22.45 ± 1.92	3.64 ± 1.24
SE-*b*-PEG-HA	265 ± 118	2 ± 1	2 ± 0	105.62 ± 47.03	2.26 ± 1.13	0.02 ± 0.00

Abbreviations: N/A: not applicable. The compositions of SD-*l*-PEG-HA, SD-*l*-PEG-PEG·PGA, SD-noPEG-HA, SD-noPEG-PSA, SD-noPEG-PEG·PGA, and SE-*b*-PEG-HA are shown in Figure 1. Values represent the mean ± standard deviation (n = 3). Adaptation from [13] licensed under a Creative Commons CC BY license.

For the protein corona studies, the different formulations of NCs were diluted to reach the same surface area (0.25 $m^2 \cdot mL^{-1}$) and then incubated in 90 % human plasma for 1 h at 37 °C.[9] Finally, the suspension was subjected to a 3-layer gradient ultracentrifugation process in order to separate the protein-NCs complexes from the unbound proteins.

The adsorbed proteins were visualized by fluorescent polyacrylamide gel electrophoresis and quantified by LC-MS. The highest amount of protein bound to the NCs was found for SD-*l*-PEG-HA (high adsorption of apolipoprotein A-IV). The NCs elaborated without PEGylated surfactants (SD-no-PEG-HA, SD-noPEG-PSA, and SD-noPEG-PEG·PGA) exhibited intermediate protein adsorption. Finally, the lowest protein adsorption was found for SE-*b*-PEG-HA and SD-*l*-PEG-PEG·PGA (Figure 3). These results agree with the PEG length and conformation since the NCs with a greater stealth effect had their PEG in brush conformation and an MW higher than 2 kDa.

With regard to the type of proteins adsorbed to the NCs prototypes, apolipoproteins were particularly relevant in the coronae of SD-*l*-PEG-PEG·PGA, SD-noPEG-HA, SD-noPEG-PSA, SD-*l*-PEG-HA, and SD-noPEG-PEG·PGA, representing 99.82, 84.47, 84.34, 75.27, and 50.71 % of the protein mass, respectively (Figure 4). As abovementioned, apolipoproteins are of great importance for their dysopsonin properties and are expected to facilitate the accumulation of the indicated prototypes in the spleen, liver, and brain. This would be the case mainly for prototypes with a significant amount in their protein corona, especially SD-*l*-PEG-HA.

In this sense, SD-*l*-PEG-HA, which exhibited an extraordinary adsorption of Apo A-IV (more than 3.6 $mg \cdot m^{-2}$), might be the most promising formulation for hepatic targeting due to the high density of Apo A-IV receptors in the liver. On the other hand, SD-*l*-PEG-PEG·PGA NCs are expected to exhibit a very low macrophage uptake due to their very thin protein corona (0.5 $mg \cdot m^{-2}$), mainly composed of Apo A-IV (97 % of its corona).

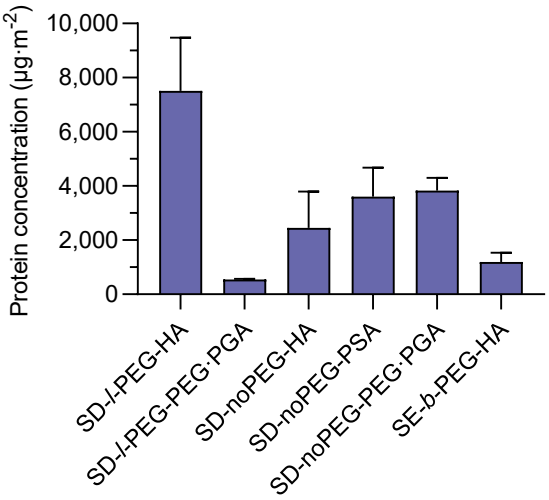


Figure 3. NCs' total adsorbed protein amount

The compositions of SD-*l*-PEG-HA, SD-*l*-PEG-PEG·PGA, SD-noPEG-HA, SD-noPEG-PSA, SD-noPEG-PEG·PGA, and SE-*b*-PEG-HA are shown in Figure 1. Values represent the mean ± standard deviation (n = 3).

In the literature, Apo A-IV was detected as a predominant protein for polyethylene carbonate NPs,[14] cross-linked NPs with acrylic polymers,[15] solid lipid NPs (SLNPs),[16] and PS NPs, to a lesser extent.[14,17] Different attempts were made to correlate the Apo A-IV presence on the corona of polymeric NPs with their physicochemical characteristics.[17] For example, Göppert *et al.* reported an inverse correlation between Apo A-IV adsorption and the poloxamers' PEO length on cetyl palmitate SLNPs. In that study, poloxamer 184, exposing two 13-PEO chains, led to an intense Apo A-IV deposition, representing 22 % of the protein corona, while it was reduced to 7 % when poloxamer 338, with two chains of 128 PEO, was used.[16] A similar correlation between Apo A-IV deposition and PEG presence was also found for SiO_2 NCs.[18] However, in our case, the main parameters driving Apo A-IV adsorption were the formulation methodology and/or the type of PEGylated surfactants rather than the PEG mass, density, or thickness. Namely, Apo A-IV was present in SD and not in the one formulated by SE. Also, high percentages of Apo A-IV were found for *l*-PEG formulations, meaning that TPGS might also promote this adsorption.

Vitronectin, which was highly attached to SD-noPEG-PEG·PGA (39.34 % of its corona), is another relevant protein. Its arginine-glycine-aspartate region allows for its interaction with integrin receptors such as $\alpha_V\beta_3$, which is overexpressed in many tumors.[19,20] In fact, a high *in vitro* uptake by cancer cells was reported for liposomes,[19] DOTAP/DNA lipoplexes,[21] and lipid NPs[21] when coated with a vitronectin-rich protein corona. Vitronectin was also found to be decisive for the interaction between liposomes and HeLa cell membranes,[12,22] and also for the interaction between PS NPs and human mesenchymal stem cells.[23]

The high adsorption of vitronectin in SD-noPEG-PEG·PGA is related to the presence of DOTAP, in agreement with the literature.[24,25] For example. DOTAP-containing lipid NPs exhibited an average vitronectin protein corona abundance of 12.2 %.[26] However, other compositions can also lead to a vitronectin-enriched corona, such as uncoated PS-COOH NPs,

which presented a corona composed of approximately 33 % vitronectin,[27] PLGA NPs,[28,29] and ovalbumin-based polymeric NPs of PEG of high density and MW.[30]

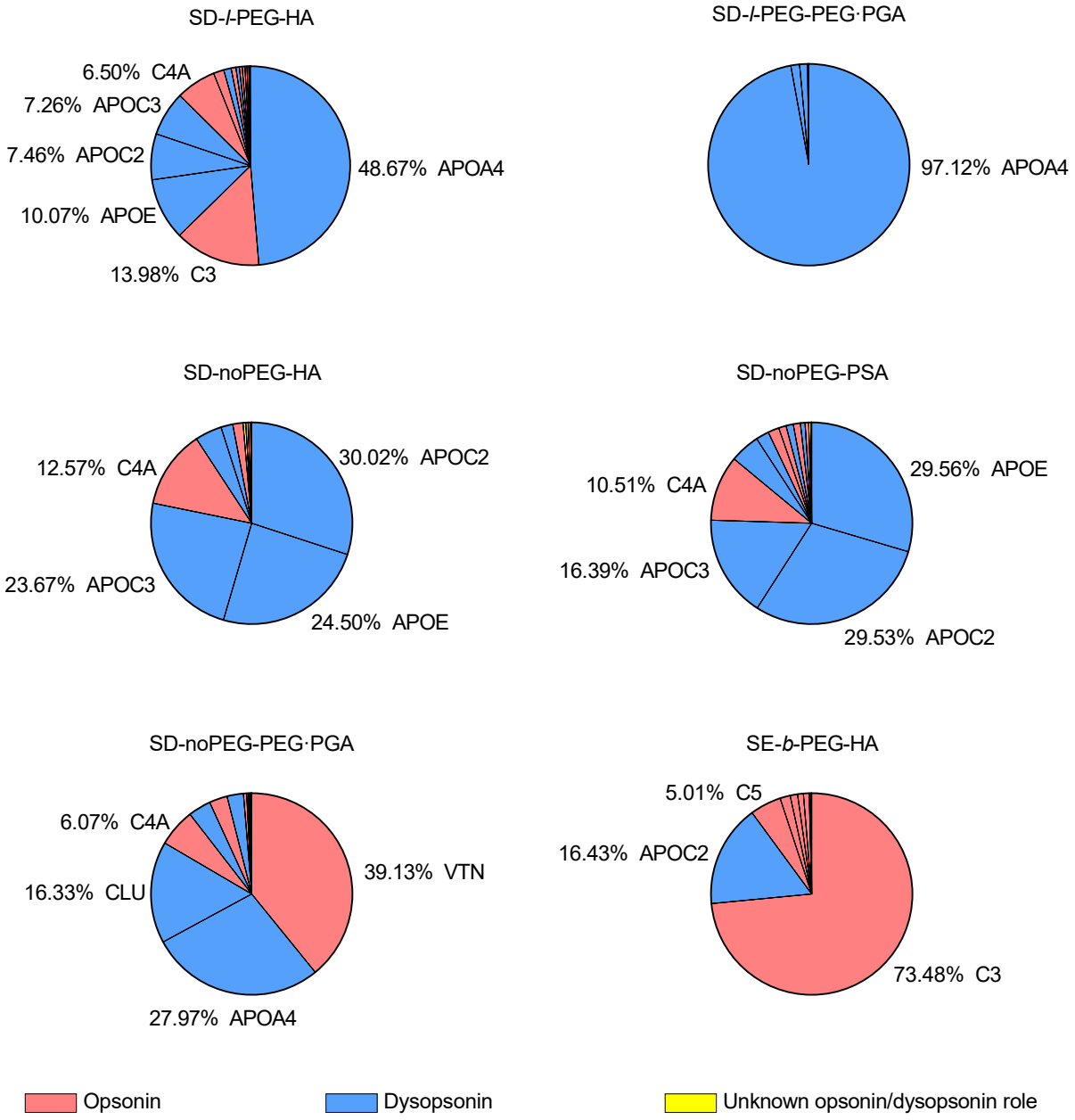


Figure 4. Protein mass percentage of the different proteins detected in the NCs' corona

Abbreviations: APOA4: Apolipoprotein A-IV, APOC2: Apolipoprotein C-II, APOC3: Apolipoprotein C-III, APOE: Apolipoprotein E, C3: Complement C3, C4A: Complement C4-A, C5: Complement C5, CLU: Clusterin, VTN: Vitronectin. The compositions of SD-*l*-PEG-HA, SD-*l*-PEG-PEG·PGA, SD-noPEG-HA, SD-noPEG-PSA, SD-noPEG-PEG·PGA, and SE-*b*-PEG-HA are shown in Figure 1. Values represent the mean of three replicates.

Complement factors were the second most relevant protein family in the coronae of NCs. However, their significance differed across the different prototypes. In fact, the complement protein mass represented 83.52, 24.05, 14.71, 11.82, 7.05, and 0.18 % of the protein corona in

the case of SE-*b*-PEG-HA, SD-*l*-PEG-HA, SD-noPEG-HA, SD-noPEG-PSA, SD-noPEG-PEG·PGA, and SD-*l*-PEG-PEG·PGA, respectively. Therefore, mainly SE-b-PEG-HA would be expected to interact with immune cells. However, the very low amount of these proteins attached would reduce this expected behavior.

The attachment of immunoglobulins to the NCs was only noticeable in the formulations without PEG, representing 3.52 % of the protein corona in the case of SD-noPEG-PSA, 2.90 % in SD-noPEG-PEG·PGA, and 0.39 % in SD-noPEG-HA.

Other protein families were detected in all the NCs except SD-*l*-PEG-PEG·PGA and SE-*b*-PEG-HA. However, these proteins were generally present in low percentages (0.32 – 0.67 %)

Finally, other relationships could be established between the NCs composition and the resulting protein corona. For example, the NCs that contained phosphatidylcholine suffered from intense adsorption of Apo E y Apo C-II.

Overall, based on these results, the NCs SD-noPEG-PEG·PGA and SD-*l*-PEG-PEG·PGA were identified as the most promising prototypes for loading therapeutic entities for treating lung cancer due to their vitronectin adsorption and low protein corona, respectively. In this sense, these formulations were employed as starting points for elaborating galunisertib and stattic-loaded NCs and mAb-loaded NCs.

1.2. GALUNISERTIB AND STATTIC-LOADED NANOCAPSULES FOR LUNG CANCER TREATMENT

STAT3[31,32,41–44,33–40] and TGF-β[45,46,55–60,47–54] inhibitors suffer from biopharmaceutical limitations that compromise their therapeutic efficacy. Indeed, severe hepatic, pancreatic, neurological, and cardiac toxicities were reported using TGF-β inhibitors,[45,46,52–54,57,59,60] while the most significant concerns of STAT3 inhibitors come from their brain toxicities.[61,62] Those off-target toxicities are related to the indiscriminate biodistribution of the drugs after oral administration and the ubiquitous presence of their targets within the body.

With the aim of reducing their off-target toxicities and studying their potential synergistic effect, stattic (STAT3 pathway inhibitor) and galunisertib (TGF-β pathway inhibitor) were loaded on the NCs prototypes selected based on the results of Chapter 1. Moreover, a new NCs prototype was developed with the capacity to be decorated with the tumor-penetrating peptide tLyp-1. For simplicity, since all NCs share the same oil composition (α-tocopherol), positively charged surfactant (DOTAP), and polymeric coating (PEG·PGA), NCs were named based on the nature of their surfactant (Figure 5).

Overall, the developed formulations fulfilled the desired properties in terms of particle size (close to 100 nm) and the ζ-potential (close to neutral charge or slightly negative). The highest negative charge observed for the SD-noPEG formulation is easily explained by the lack of PEGylated surfactants (Table 3). The association efficiencies of the drugs were up to 75 ± 11 % for galunisertib and 54 ± 12 % for stattic. The highest galunisertib and stattic AEs were detected for SD-noPEG and SD-DPEG. SD-TPGS, with the highest free surfactant content (Chapter 1), exhibited the lowest AEs, which was attributed to the solubilization of the drug in micellar structures.

USC UNIVERSIDADE DE SANTIAGO DE COMPOSTELA

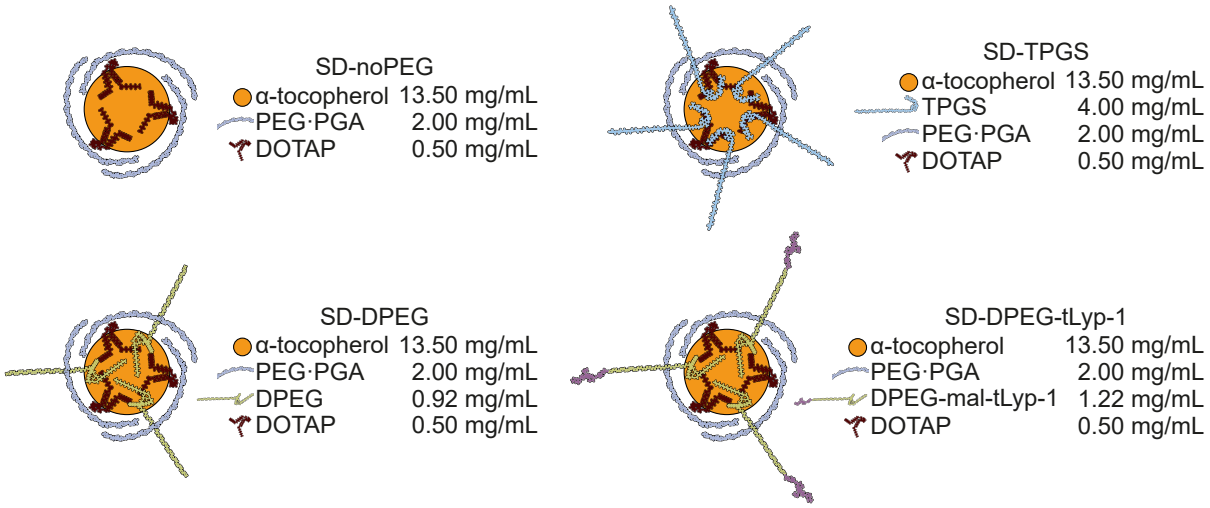


Figure 5. Schematic representation of the expected NCs' compound arrangement and their theoretical composition

SD-noPEG: Formulation prepared by solvent displacement technique and composed of non-PEGylated surfactants (DOTAP) and PEG·PGA shell. **SD-TPGS**: Formulation prepared by solvent displacement technique and composed of lineal PEG (TPGS) and PEG·PGA shell. **SD-DPEG**: Formulation prepared by solvent displacement technique and composed of lineal PEG (DPEG) and PEG·PGA shell. **SD-DPEG-tLyp-1**: Formulation prepared by solvent displacement technique and composed of lineal PEG (DPEG-tLyp-1) and PEG·PGA shell. **Abbreviations**: DOTAP: 1,2-dioleoyl-3-trimethylammoniumpropane. DPEG: DSPE-PEG_{2000} [*N*-(carbonyl-methoxy polyethylene glycol 2000)-1,2-distearoyl-sn-glycero-3-phosphoetanolamine]. DPEG-tLyp-1: DSPE-PEG_{2000}-maleimide-tLyp-1. PEG·PGA: polyethylene glycol polyglutamic acid. TPGS: D-α-tocopherol polyethylene glycol 1000 succinate.

Table 3. Physicochemical characterization of Galunisertib- and Stattic-loaded SD-noPEG, SD-TPGS, SD-DPEG, and SD-DPEG-tLyp-1

	SD-noPEG	SD-TPGS	SD-DPEG	SD-DPEG-tLyp-1
Final [Galunisertib] ($mg \cdot mL^{-1}$)	1.25	1.25	1.25	1.25
Final [Stattic] ($mg \cdot mL^{-1}$)	0.0625	0.0625	0.0625	0.0625
Galunisertib loading (%)	7.2	5.9	6.9	6.7
Stattic loading (%)	0.4	0.3	0.3	0.3
Hydrodynamic diameter (DLS) (nm)	118 ± 3	87 ± 9	98 ± 7	106 ± 14
PDI	0.05 ± 0.03	0.19 ± 0.06	0.09 ± 0.02	0.15 ± 0.05
ζ-potential (mV)	−21 ± 1	−3 ± 2	−10 ± 2	+5 ± 7
AE Galunisertib (%)	75 ± 11	36 ± 7	71 ± 10	58 ± 12
AE Stattic (%)	50 ± 1	26 ± 12	54 ± 12	38 ± 11
pH	5.5 ± 0.1	5.4 ± 0.1	6.6 ± 0.2	6.1 ± 0.1

The compositions of SD-noPEG, SD-TPGS, SD-DPEG, and SD-DPEG-tLyp-1 are shown in Figure 5. **Abbreviations:** AE: association efficiency. DLS: dynamic light scattering. PDI: polydispersity index. Values represent the mean ± standard deviation (n = 3).

The reported AE values are in line with those in the literature for chitosan-coated PLGA NPs (82 % AE for galunisertib and 54 % AE for stattic),[63,64] polygalacturonic acid-polyacrylic acid micelles (23 % AE for galunisertib),[65] and cabazitaxel-docosahexaenoic acid polymeric

NPs (74 % AE for stattic).[66] To the best of our knowledge, the co-encapsulation of these two drugs has not been explored in the literature yet.

The stability of the drug-loaded NCs was assessed in biological-mimicking media. The results showed that all NCs prototypes were stable in PBS supplemented with 10 % FBS at 37 °C for up to 24 h, except SD-DPEG, with exhibited a variable size evolution.

Then, the stattic and galunisertib release was assessed after incubation in PBS supplemented with 10 % FBS. The typical profile showed a burst release, followed by no release afterward (Figure 6). The galunisertib burst release was between 50 and 100 % depending on the formulation, whereas that of stattic was generally lower. Interestingly, the galunisertib burst release was considerably reduced upon functionalization with tLyp-1. The different burst releases observed for both drugs could be related to their different solubility and, hence, the tendency to diffuse to the external aqueous mediums.

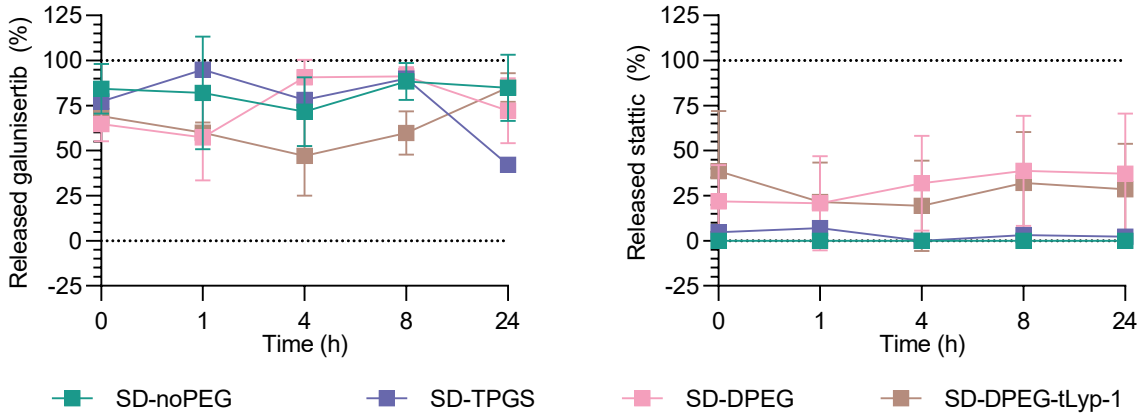


Figure 6. Release of galunisertib (left) and stattic (right) from NCs after 10 × dilution in PBS supplemented with 10 % FBS

The compositions of SD-noPEG, SD-TPGS, SD-DPEG, and SD-DPEG-tLyp-1 are shown in Figure 5. Values represent the mean ± standard deviation (n = 3).

Then, the cellular uptake was evaluated in CMT 167 cancer cells and RAW 264.7 macrophages. The results showed a dose- and temperature-dependent uptake (Figure 7). The toxicity of the stattic and galunisertib-loaded NCs was studied in the same cell lines and was compared to that of the free drugs. The results showed a statistically significant reduction of the drugs' cytotoxicity when loaded into SD-noPEG NCs in the case of RAW 264.7 macrophages (Figure 8). On the other hand, it was found that the cytotoxicity of the drug combination was very similar to that of free static.

Then, the IC_{50}s values of the stattic and galunisertib-loaded NCs and free drugs were calculated based on the data from Figure 8. In general, the encapsulation of the drugs preserved the cytotoxicity of the drugs in CMT 167 cancer cell line as all the IC_{50}s were very similar and close to that of the free drug combination (1.3, 1.3, 1.1, and 0.9-fold that of free drugs for SD-noPEG, SD-DPEG-tLyp-1, SD-DPEG, and SD-TPGS, respectively). However, the encapsulation of the drugs led to a more pronounced increase in their IC_{50} value in the case of RAW 264.7 macrophages (approximately 3.92, 2.12, 1.36, and 1.2-fold that of free drugs for

SD-noPEG, SD-DPEG-tLyp-1, SD-DPEG, and SD-TPGS, respectively). In this sense, SD-noPEG (in agreement with the statistical significance detected in Figure 8) and SD-DPEG-tLyp-1 were identified as the most promising NCs preserving the cytotoxicity in cancer cells while reducing it in macrophages.

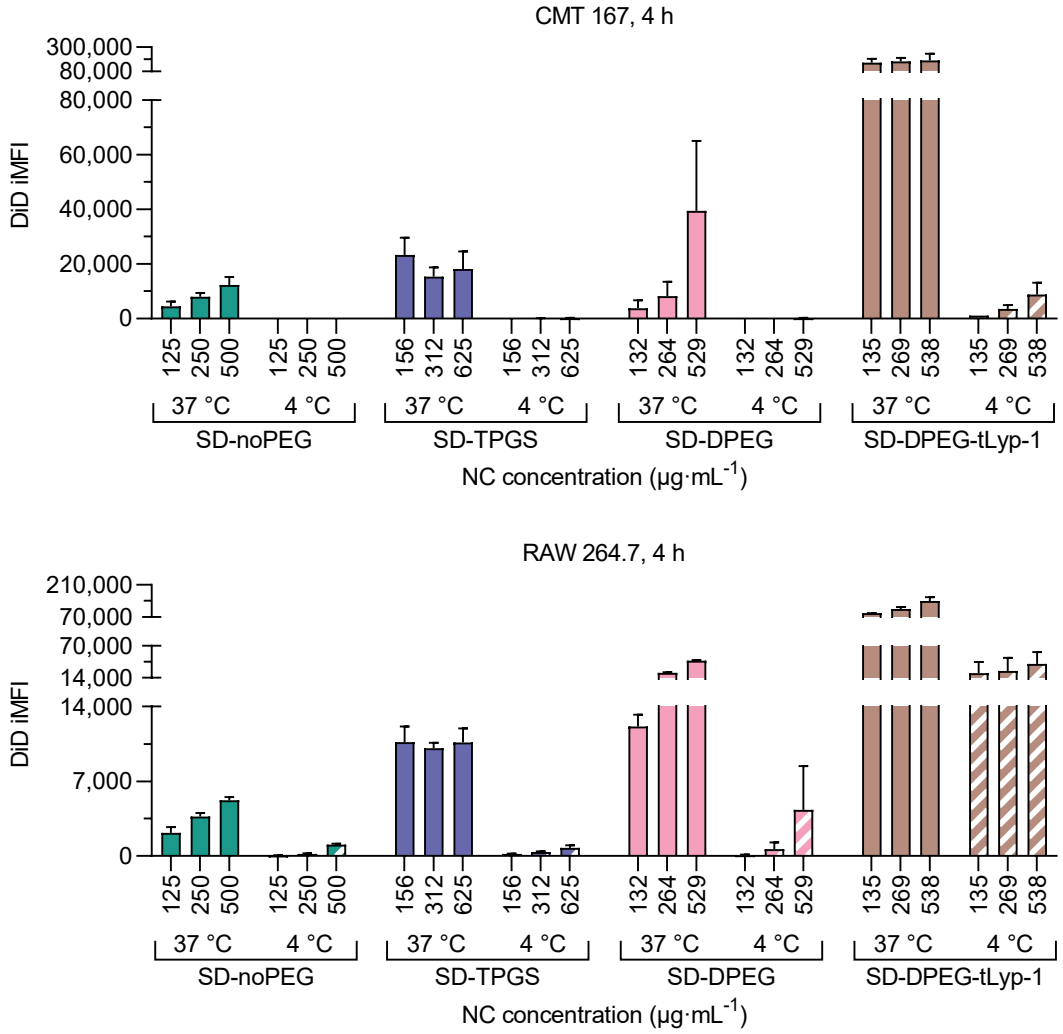


Figure 7. Cellular uptake (DiD iMFI) of DiD-labeled SD-noPEG, SD-TPGS, SD-DPEG, and SD-DPEG-tLyp-1 at 37 ˚C or 4 ˚C in CMT 167 (top) and RAW 264.7 (bottom)

Abbreviations: iMFI: integrated mean fluorescence intensity. The compositions of SD-noPEG, SD-TPGS, SD-DPEG, and SD-DPEG-tLyp-1 are shown in Figure 5. Values represent the mean ± standard deviation (n = 2).

The cytotoxicity of stattic encapsulated in different types of nanocarriers has been reported in the literature. Some reports showed an enhanced cytotoxicity when loaded into PLGA NPs in 4T1 cells,[64] albumin NPs in MDA-MB-231 cells,[67] and polyacrylamide polymeric micelles in MCF7, MDA-MB-231, and 4T1 cell lines. On the contrary, the cytotoxicity of stattic was reduced when loaded into albumin NPs in MCF7 cells[67] and into resiquimod-conjugated docosahexaenoic acid micelles in HEK293T cells.[68] No study was reported for CMT 167 or

USC DE SANTIAGO DE COMPOSTELA

RAW 264.7 cell lines, making it impossible to establish comparisons with previously published works.

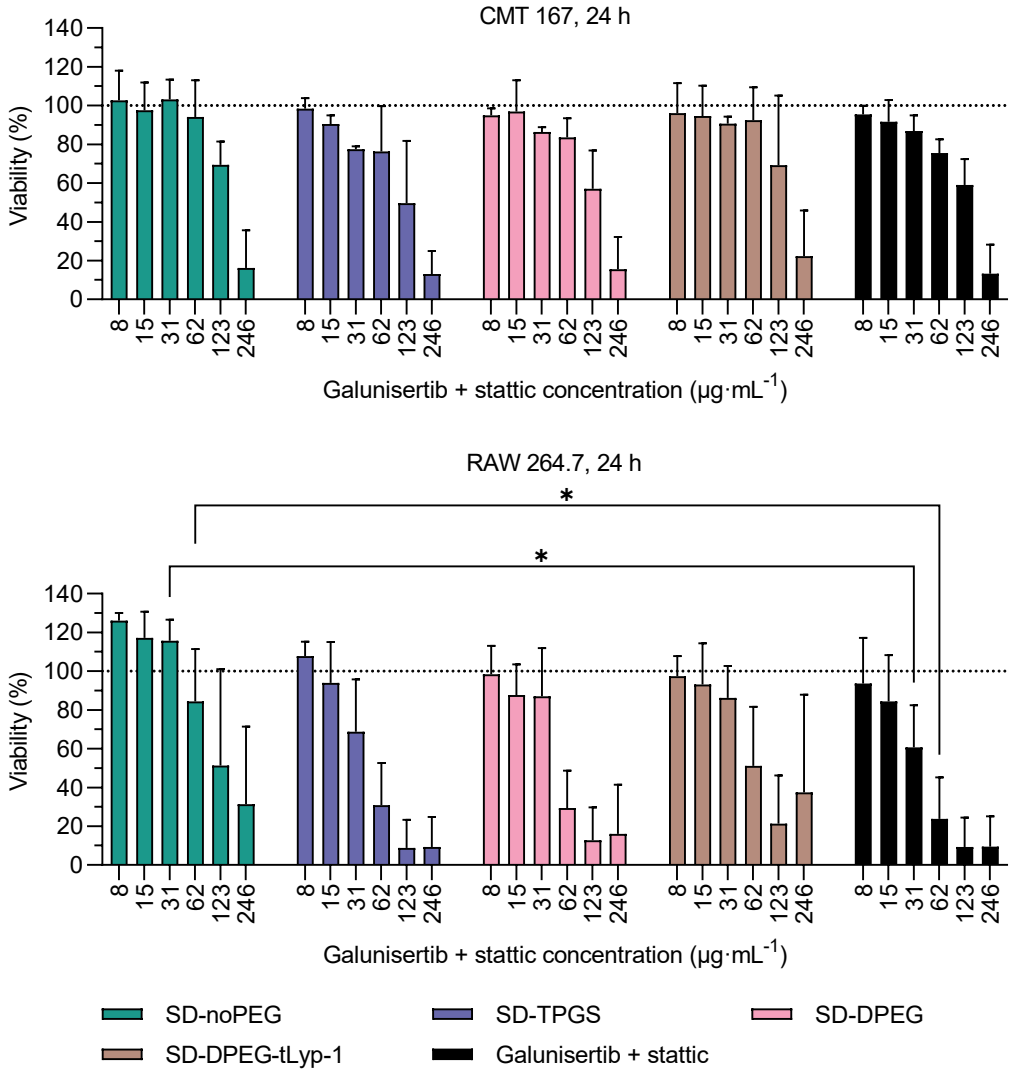


Figure 8. ***In vitro*** **cytotoxicity of galunisertib and stattic loaded NCs and free galunisertib and stattic**

Unpaired t-tests of each drug-loaded NCs *vs.* free drugs for each concentration value. *p*-values < 0.05 were considered statistically significant (*). The compositions of SD-noPEG, SD-TPGS, SD-DPEG, and SD-DPEG-tLyp-1 are shown in Figure 5. Values represent the mean ± standard deviation (n = 3).

Finally, the efficacy of galunisertib-loaded and stattic-loaded SD-noPEG NCs on the polarization of macrophages was evaluated *in vitro* (Figure 9).

The production of NO and pro-inflammatory cytokines were read out in lipopolysaccharides (LPS)-stimulated macrophages exposed to stattic- or galunisertib-loaded NCs.

USC UNIVERSIDADE DE SANTIAGO DE COMPOSTELA

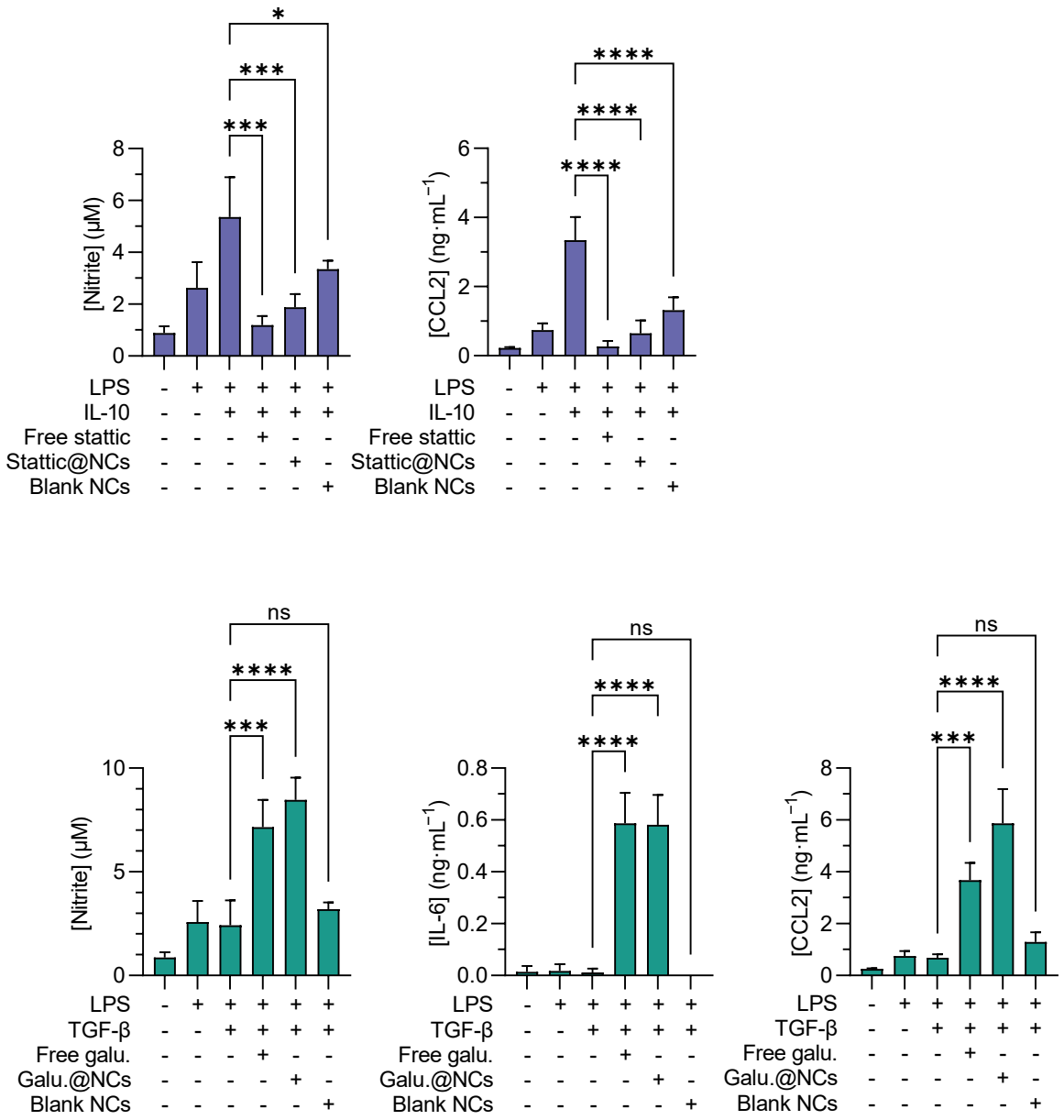


Figure 9. *In vitro* efficacy of stattic-loaded and galunisertib-loaded SD-noPEG NCs in RAW 264.7 macrophages

For the stattic efficacy study (top), the STAT3 pathway was activated by the addition of LPS + IL-10. Then, free stattic, stattic-loaded SD-noPEG, and blank NCs were added. Reductions in nitrite and CCL2 production were checked. In the case of galunisertib (bottom), the TGF-ß pathway was activated by the addition of LPS + TGF-ß. Then, free galunisertib, galunisertib-loaded SD-noPEG, and blank NCs were added. Increases in nitrite, IL-6, and CCL2 production were checked. Stattic-loaded and galunisertib-loaded SD-noPEG NCs were effective. While stattic-loaded SD-noPEG efficacy was lower than that of the free drug, the contrary was observed for galunisertib. **Abbreviations:** Galu.: galunisertib. IL: interleukin. LPS: lipopolysaccharide. NCs: nanocapsules. TGF-ß: Transforming growth factor-ß. The composition of SD-noPEG is shown in Figure 5. Values represent the mean ± standard deviation of two cell replicates and one NC replicate. One-way ANOVA *vs.* LPS + IL-10 or LPS + TGF-ß groups with a Dunnett posthoc test. *p*-values < 0.05 were considered statistically significant (*). Also, (**) if *p*-value < 0.01, (***) if *p*-value < 0.001 and (****) if *p*-value < 0.0001. ns: not significative.

Stattic-loaded and galunisertib-loaded SD-noPEG NCs were significantly effective in inhibiting the STAT3 and TGF-β pathways in RAW 264.7 macrophages, reducing nitrite and CCL2 production in the case of stattic and increasing nitrite, IL-6, and CCL2 production, in the

case of galunisertib (one-way ANOVA *vs.* LPS + IL-10 or LPS + TGF-β groups with a Dunnett posthoc test). While stattic-loaded SD-noPEG efficacy was lower than that of the free drug, the contrary was observed for galunisertib.

Overall, the encapsulation of galunisertib and stattic into SD-noPEG NCs preserved the cytotoxicity of the drugs in CMT 167 cancer cells and slightly reduced it in RAW 264.7 macrophages. Moreover, stattic- and galunisertib-loaded SD-noPEG NCs were found to successfully inhibit the STAT3 and TGF-β pathways of RAW 264.7 macrophages.

1.3. NANOCAPSULES FOR THE INTRACELLULAR DELIVERY OF MONOCLONAL ANTIBODIES

In this section, we aim to optimize a nanotechnology-based platform for the intracellular delivery of mAbs with the final goal of exploring new anti-$KRAS^{G12V}$ personalized therapies for the treatment of lung cancer.

As a first step, considering the results obtained in the previous chapters, we selected SD-noPEG and SD-TPGS as starting NCs prototypes. New compositions were also explored, including two different oils (α-tocopherol and medium-chain triglycerides) and two non-PEGylated surfactants (phosphatidylcholines and lauric acid-modified octaarginine), for the association and delivery of bevacizumab (BVZ), chosen as a model mAb. Afterward, the NCs which exhibited the best physicochemical properties (particle size < 150 nm, PDI < 0.3, and slightly negative ζ-potential), short-term storage stability of at least 1 month at 4 °C, BVZ AE higher than 40 %, stability in relevant biological-media, low BVZ release, and adequate tolerability profile, (Figure 10, Table 4), were selected as promising candidates for the association of the anti-$KRAS^{G12V}$ mAb therapeutic antibody.

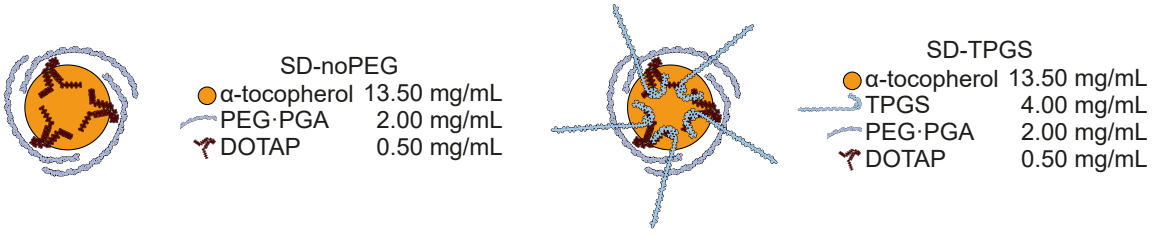


Figure 10. Schematic representation of the expected compound arrangement of the NCs optimized for BVZ-loading and their theoretical composition

SD-noPEG: Formulation prepared by solvent displacement technique and composed of non-PEGylated surfactants (DOTAP) and PEG·PGA shell. SD-TPGS: Formulation prepared by solvent displacement technique and composed of lineal PEG (TPGS) and PEG·PGA shell. **Abbreviations:** DOTAP: 1,2-dioleoyl-3-trimethylammoniumpropane. PEG·PGA: polyethylene glycol polysialic acid. TPGS: D-α-tocopherol polyethylene glycol 1000 succinate.

In a subsequent step, the in vitro uptake of the selected prototypes containing Alexa Fluor® 488-conjugated BVZ (^{AF488}BVZ) was studied in CMT 167 and A549 lung cancer cells (Figure 11). ^{AF488}BVZ-loaded NCs showed statistically significant temperature- and dose-dependent uptake (unpaired t-tests), which indicates that the uptake mechanism is mediated by a classical non-specific endocytic process, as previously observed for similar NCs compositions containing anti-gasdermin mAb.

Table 4. Physicochemical characteristics of the BVZ-loaded NCs

	SD-noPEG	SD-TPGS
Hydrodynamic diameter (DLS) (nm)	149 ± 2	113 ± 5
PDI	0.02 ± 0.01	0.10 ± 0.01
Hydrodynamic diameter (NTA) (nm)	100 ± 11	108 ± 5
Particle size (cryo-EM) (nm)	115 ± 65 (n = 281)	-
Particle concentration (NTA) ($\times 10^{11}$ particles·mL^{-1})	107.2 ± 6.7	77.8 ± 2.1
ζ-potential (mV)	−13 ± 1	−11 ± 4
BVZ loading (%)	11.1	9.1 %
AE BVZ (%)	99 ± 1	46 ± 15
BVZ Release in PBS 10 % FBS	No	No

Abbreviations: BVZ: bevacizumab. DLS: dynamic light scattering. KRAS: Kirsten rat sarcoma viral oncogene homolog. NTA: nanoparticle tracking analysis PDI: polydispersity index. SD: solvent displacement. The compositions of SD-noPEG and SD-TPGS are shown in Figure 10. Values represent the mean ± standard deviation (n = 3) unless stated otherwise.

On the other hand, notoriously, SD-noPEG NCs were much more internalized in both cell lines than SD-TPGS. This effect might be due to the high vitronectin adsorption of the SD-noPEG NCs and/or reduced uptake due to a higher PEG content of SD-TPGS (5-fold PEG mass and 10-fold density compared to SD-noPEG). The percentage of AF488-positive cells (30 – 57 and 6 – 40 % in CMT 167 and 100 and 52 – 98 % in A549 for SD-noPEG and SD-TPGS, respectively) followed the same trend as the iMFI.

Regarding the effect of the uptake on different cell lines, A549 exhibited a higher uptake of both systems than CMT 167. This result may be attributed to the intrinsic mechanisms of those different lung cancer cells.

Finally, as expected, the free ^{AF488}BVZ was not internalized by any of the cell lines. Fluorescence by ^{AF488}BVZ internalization was confirmed by confocal microscopy for SD-noPEG and SD-TPGS in A549 cells.

After the initial screening with bevacizumab, NCs were loaded with the therapeutic anti-KRAS^{G12V} mAb (Figure 12). The resulting NCs exhibited a reduced hydrodynamic diameter (< 150 nm), PDI < 0.3, neutral ζ-potential, and, in the case of SD-P80, a high mAb AE (Table 5). Unexpectedly, SD-TPGS(↑) showed a low anti-KRAS^{G12V} mAb AE, which was attributed to the longer PEG chains of TPGS (2,000 Da MW).

Then, the cellular uptake of the anti-KRAS^{G12V} mAb-loaded NCs was evaluated in the CMT 167 KRAS^{G12V}-mutated lung cancer cell line after 4 h of incubation by the intracellular staining technique. This technique allows the selective label of the therapeutic mAb that was taken up by the cells. The results showed a statistically significant and temperature-dependent delivery of the anti-KRAS^{G12V} mAb by SD-P80 compared to the free mAb (Figure 13). On the contrary, SD-TPGS exhibited a lower uptake, and only a tendency regarding their dose dependency could be observed.

USC UNIVERSIDADE DE SANTIAGO DE COMPOSTELA

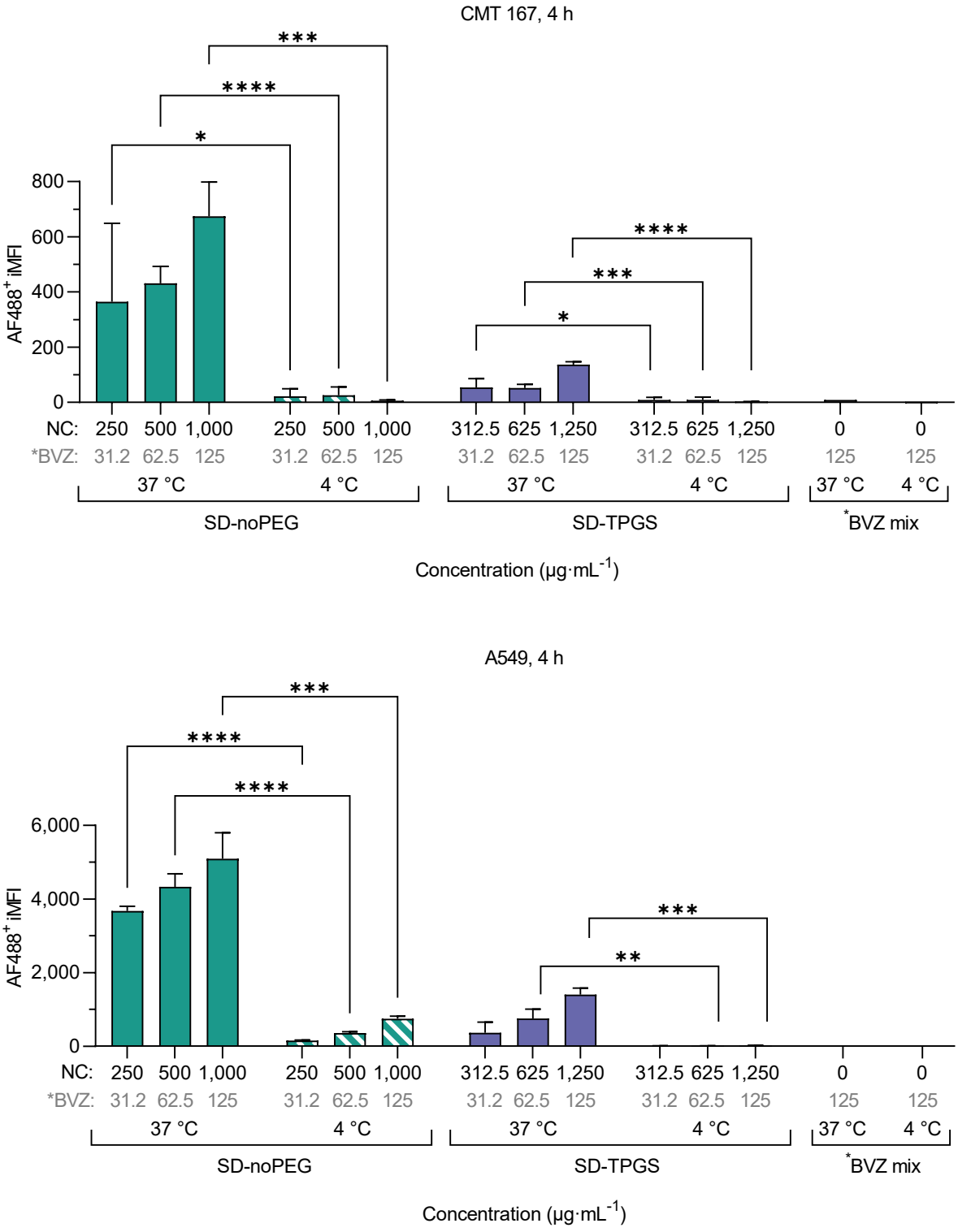


Figure 11. Uptake (iMFI) of ^{AF488}BVZ-labeled SD-noPEG and SD-TPGS in CMT 167 and A549 cell lines after 4 h

^{AF488}BVZ-loaded NCs showed statistically significative temperature-dependent uptake (unpaired t-tests of NCs or *BVZ concentration at 37 °C *vs.* 4 °C. *p*-values < 0.05 were considered statistically significant (*). Also, (**) if *p*-value < 0.01, (***) if *p*-value < 0.001 and (****) if *p*-value < 0.0001. SD-noPEG was more internalized in both cell lines than SD-TPGS. The mixture of 2 % ^{AF488}BVZ and 98 % BVZ (*BVZ) was not taken up by any cell line. **Abbreviations:** *BVZ: fluorescently labeled bevacizumab. iMFI: integrated mean fluorescence intensity. NC: nanocapsule. The compositions of SD-noPEG and SD-TPGS are shown in Figure 10. Values represent the mean ± standard deviation (n = 3).

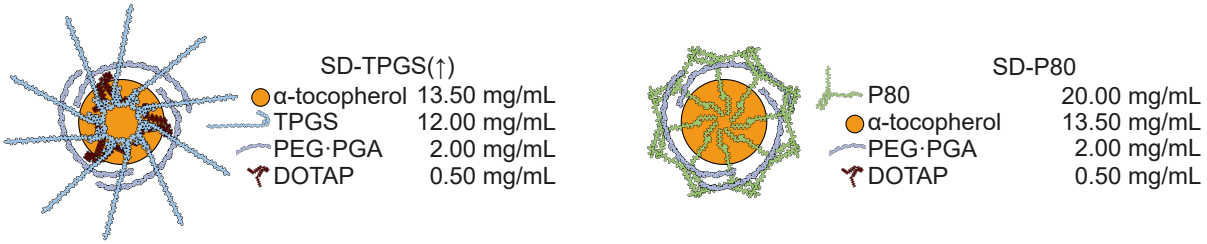


Figure 12. Schematic representation of the expected compound arrangement of the NCs optimized for anti-KRAS^{G12V} mAb-loading and their theoretical composition

SSD-TPGS(↑): Formulation prepared by solvent displacement technique and composed of lineal PEG (TPGS; 12 mg·mL^{-1}) and PEG·PGA shell. SD-P80: Formulation prepared by solvent displacement technique and composed of branched PEG (P80) and PEG·PGA shell. **Abbreviations:** DOTAP: 1,2-dioleoyl-3-trimethylammoniumpropane. P80: polysorbate 80. PEG·PGA: polyethylene glycol polysialic acid. TPGS: D-α-tocopherol polyethylene glycol 1000 succinate.

Table 5. Physicochemical characteristics of anti-KRAS^{G12V} mAb-loaded NCs

	SD-TPGS(↑)	SD-P80
Hydrodynamic diameter (DLS) (nm)	117 ± 5	143 ± 14
PDI	0.20 ± 0.06	0.21 ± 0.05
ζ-potential (mV)	−5 ± 1	+1 ± 1
anti-KRAS^{G12V} mAb loading (%)	6.67	5.26
anti-KRAS^{G12V} mAb AE (%)	11 ± 19	90 ± 6

Abbreviations: DLS: dynamic light scattering. PDI: polydispersity index. Values represent the mean ± standard deviation (n = 3). The compositions of SD-TPGS(↑) and SD-P80 are shown in Figure 12.

Subsequently, a preliminary target engagement study was carried out to know if that internalized mAb was successfully bound to its intracellular target.

The internalized anti-KRAS^{G12V} mAb was pulled down by immunoprecipitation, and the presence of KRAS^{G12V} was evaluated by Western Blot (WB). The KRAS^{G12V} band was confirmed by the positive control (anti-KRAS^{G12V} mAb + untreated cell lysates). Anti-KRAS^{G12V} mAb-loaded SD-P80 demonstrated the delivery and binding of the therapeutic mAb to its target, as the intensity of the KRAS^{G12V} band in the WB was higher than that of the negative control (Figure 14). A tendency for time-dependent target engagement could be appreciated as well.

Overall, these results suggest that polymeric NCs such as SD-P80 NCs represent a versatile delivery platform that can efficiently deliver antibodies such as anti-KRAS^{G12V} mAb to cancer cells, preserving their activity and allowing the intracellular recognition of their target.

USC UNIVERSIDADE DE SANTIAGO DE COMPOSTELA

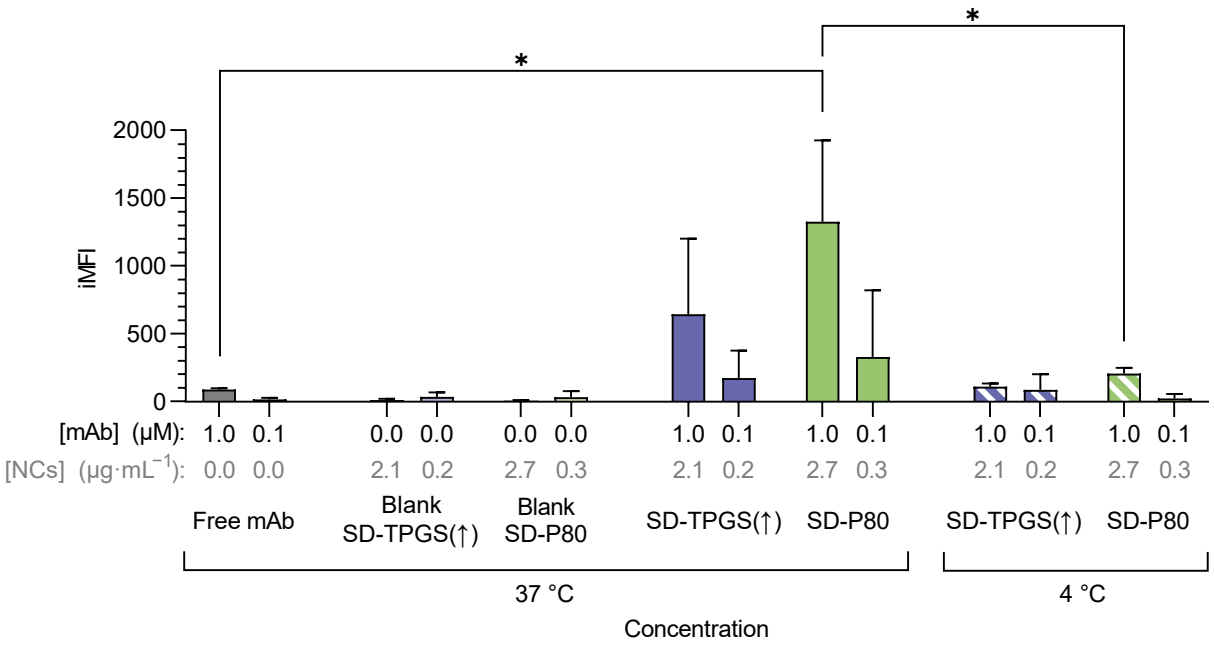


Figure 13. Intracellular staining of anti-KRAS^{G12V} mAb in CMT 167 lung cancer cells after incubation for 4 h at 37 °C

SD-P80 significantly delivered the anti-KRAS^{G12V} mAb to the interior of CMT 167 cells after incubation at a mAb concentration of 1 μM for 4 h at 37 °C. This effect was also temperature dependent (t-test *vs.* free mAb or blank NCs). The compositions of SD-TPGS(↑) and SD-P80 are shown in Figure 12. Values represent the mean ± standard deviation (n = 3).

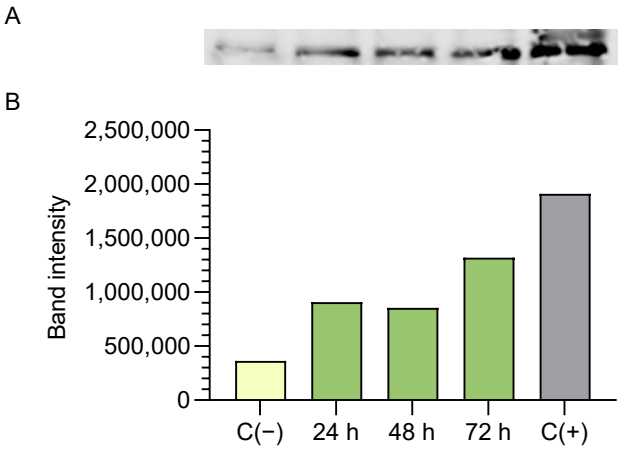


Figure 14. Immunoprecipitation of KRAS^{G12V} protein by anti-KRAS^{G12V} mAb-loaded SD-P80 after incubation at 24, 48, and 72 h in CMT 167 cells

(A) RAW image of the WB membrane. **(B)** Band intensities. For the negative control [C(−)], 1 mg of CMT 167 cell lysate was immunoprecipitated with anti-antibody beads. For the positive control [C(+)], 5 μg of anti-KRAS^{G12V} mAb were added to 1 mg of CMT 167 cell lysate and immunoprecipitated with anti-antibody beads. The composition of SD-P80 is shown in Figure 12. Values represent the mean of 1 replicate.

USC UNIVERSIDADE DE SANTIAGO DE COMPOSTELA

2. REFERENCES

[1] M. V. Lozano, D. Torrecilla, D. Torres, A. Vidal, F. Domínguez, M. J. Alonso. Highly efficient system to deliver taxanes into tumor cells: Docetaxel-loaded chitosan oligomer colloidal carriers. *Biomacromolecules*. 9, 2186–2193. (2008). doi: 10.1021/bm800298u.

[2] G. Lollo, G. R. Rivera-Rodriguez, J. Bejaud, T. Montier, C. Passirani, J. P. Benoit, M. García-Fuentes, M. J. Alonso, D. Torres. Polyglutamic acid-PEG nanocapsules as long circulating carriers for the delivery of docetaxel. *European Journal of Pharmaceutics and Biopharmaceutics*. 87, 47–54. (2014). doi: 10.1016/j.ejpb.2014.02.004.

[3] E. Borrajo, R. Abellan-Pose, A. Soto, M. Garcia-Fuentes, N. Csaba, M. J. M. J. Alonso, A. Vidal. Docetaxel-loaded polyglutamic acid-PEG nanocapsules for the treatment of metastatic cancer. *Journal of Controlled Release*. 238, 263–271. (2016). doi: 10.1016/j.jconrel.2016.07.048.

[4] A. Cadete, A. Olivera, M. Besev, P. K. Dhal, L. Gonçalves, A. J. Almeida, G. Bastiat, J.-P. Benoit, M. de la Fuente, M. Garcia-Fuentes, M. J. Alonso, D. Torres. Self-assembled hyaluronan nanocapsules for the intracellular delivery of anticancer drugs. *Scientific Reports*. 9, 11565. (2019). doi: 10.1038/s41598-019-47995-8.

[5] C. Teijeiro-Valiño, R. Novoa-Carballal, E. Borrajo, A. Vidal, M. Alonso-Nocelo, M. de la Fuente Freire, P. P. P. Lopez-Casas, M. Hidalgo, N. Csaba, M. J. Alonso. A multifunctional drug nanocarrier for efficient anticancer therapy. *Journal of Controlled Release*. 294, 154–164. (2019). doi: 10.1016/j.jconrel.2018.12.002.

[6] Á. Molina-Crespo, A. Cadete, D. Sarrio, M. Gámez-Chiachio, L. Martinez, K. Chao, A. Olivera, A. Gonella, E. Díaz, J. Palacios, P. K. Dhal, M. Besev, M. Rodríguez-Serrano, M. L. García Bermejo, J. C. Triviño, A. Cano, M. García-Fuentes, O. Herzberg, D. Torres, M. J. Alonso, G. Moreno-Bueno. Intracellular Delivery of an Antibody Targeting Gasdermin-B Reduces HER2 Breast Cancer Aggressiveness. *Clinical Cancer Research*. 25, 4846–4858. (2019). doi: 10.1158/1078-0432.CCR-18-2381.

[7] G. R. Rivera-Rodriguez, G. Lollo, T. Montier, J. P. Benoit, C. Passirani, M. J. Alonso, D. Torres. In vivo evaluation of poly-l-asparagine nanocapsules as carriers for anti-cancer drug delivery. *International Journal of Pharmaceutics*. 458, 83–89. (2013). doi: 10.1016/j.ijpharm.2013.09.038.

[8] G. R. Rivera-Rodríguez, M. J. Alonso, D. Torres. Poly-l-asparagine nanocapsules as anticancer drug delivery vehicles. *European Journal of Pharmaceutics and Biopharmaceutics*. 85, 481–487. (2013). doi: 10.1016/j.ejpb.2013.08.001.

[9] G. Berrecoso, J. Crecente-Campo, M. J. Alonso. Unveiling the pitfalls of the protein corona of polymeric drug nanocarriers. *Drug Delivery and Translational Research*. 10, 730–750. (2020). doi: 10.1007/s13346-020-00745-0.

[10] T. A. Faunce, J. White, K. I. Matthaei. Integrated research into the nanoparticle–protein corona: a new focus for safe, sustainable and equitable development of nanomedicines. *Nanomedicine*. 3, 859–866. (2008). doi: 10.2217/17435889.3.6.859.

[11] M. Mahmoudi. Protein corona: The golden gate to clinical applications of nanoparticles. *International Journal of Biochemistry and Cell Biology*. 75, 141–142. (2016). doi: 10.1016/j.biocel.2016.03.016.

[12] V. H. Nguyen, B. J. Lee. Protein corona: a new approach for nanomedicine design. *International Journal of Nanomedicine*. 12, 3137–3151. (2017). doi: 10.2147/IJN.S129300.

[13] G. Berrecoso, J. Crecente-Campo, M. J. Alonso. Quantification of the actual composition of polymeric nanocapsules: a quality control analysis. *Drug Delivery and Translational Research*. 12, 2865–2874. (2022). doi: 10.1007/s13346-022-01150-5.

[14] N. Bege, T. Renette, M. Jansch, R. Reul, O. Merkel, H. Petersen, C. Curdy, R. H. Müller, T. Kissel. Biodegradable poly(ethylene carbonate) nanoparticles as a promising drug delivery system with “stealth” potential. *Macromolecular Bioscience*. 11, 897–904. (2011). doi: 10.1002/mabi.201000496.

[15] T. Cedervall, I. Lynch, M. Foy, T. Berggård, S. C. Donnelly, G. Cagney, S. Linse, K. A. Dawson. Detailed identification of plasma proteins adsorbed on copolymer nanoparticles. *Angewandte Chemie - International Edition*. 46, 5754–5756. (2007). doi: 10.1002/anie.200700465.

[16] T. M. Göppert, R. H. Müller. Protein adsorption patterns on poloxamer- and poloxamine-stabilized solid lipid nanoparticles (SLN). *European Journal of Pharmaceutics and Biopharmaceutics*. 60, 361–372. (2005). doi: 10.1016/j.ejpb.2005.02.006.

[17] A. Gessner, R. Waicz, A. Lieske, B. R. Paulke, K. Mäder, R. H. Müller. Nanoparticles with decreasing surface hydrophobicities: influence on plasma protein adsorption. *International Journal of Pharmaceutics*. 196, 245–249. (2000).

[18] S. Jiang, D. Prozeller, J. Pereira, J. Simon, S. Han, S. Wirsching, M. Fichter, M. Mottola, I. Lieberwirth, S. Morsbach, V. Mailänder, S. Gehring, D. Crespy, K. Landfester. Controlling protein interactions in blood for effective liver immunosuppressive therapy by silica nanocapsules. *Nanoscale*. 12, 2626–2637. (2020). doi: 10.1039/c9nr09879h.

[19] S. Palchetti, D. Caputo, L. Digiacomo, A. Capriotti, R. Coppola, D. Pozzi, G. Caracciolo. Protein corona fingerprints of liposomes: new opportunities for targeted drug delivery and early detection in pancreatic cancer. *Pharmaceutics*. 11, 31. (2019). doi: 10.3390/pharmaceutics11010031.

[20] P. Pande, T. A. Mosleh, A. E. Aust. Role of αvβ5 integrin receptor in endocytosis of crocidolite and its effect on intracellular glutathione levels in human lung epithelial (A549) cells. *Toxicology and Applied Pharmacology*. 210, 70–77. (2006). doi: 10.1016/j.taap.2005.07.017.

[21] G. Caracciolo, D. Pozzi, A. L. Capriotti, C. Cavaliere, F. Cardarelli, F. Salomone, A. Lagana. In *Nanotechnology 2013: Bio Sensors, Instruments, Medical, Environment and Energy*. (2013). pp. 247–250.

[22] S. Palchetti, L. Digiacomo, D. Pozzi, G. Peruzzi, E. Micarelli, M. Mahmoudi, G. Caracciolo. Nanoparticles-cell

USC UNIVERSIDADE DE SANTIAGO DE COMPOSTELA

association predicted by protein corona fingerprints. *Nanoscale*. 8, 12755–12763. (2016). doi: 10.1039/c6nr03898k.

[23] S. Ritz, S. Schöttler, N. Kotman, G. Baier, A. Musyanovych, J. Kuharev, K. Landfester, H. Schild, O. Jahn, S. Tenzer, V. Mailänder. Protein Corona of Nanoparticles: Distinct Proteins Regulate the Cellular Uptake. *Biomacromolecules*. 16, 1311–1321. (2015). doi: 10.1021/acs.biomac.5b00108.

[24] F. Giulimondi, L. Digiacomo, D. Pozzi, S. Palchetti, E. Vulpis, A. L. Capriotti, R. Z. Chiozzi, A. Laganà, H. Amenitsch, L. Masuelli, M. Mahmoudi, I. Screpanti, A. Zingoni, G. Caracciolo. Interplay of protein corona and immune cells controls blood residency of liposomes. *Nature Communications*. 10, 3686. (2019). doi: 10.1038/s41467-019-11642-7.

[25] G. Caracciolo. Clinically approved liposomal nanomedicines: Lessons learned from the biomolecular corona. *Nanoscale*. 10, 4167–4172. (2018). doi: 10.1039/c7nr07450f.

[26] S. A. Dilliard, Q. Cheng, D. J. Siegwart. On the mechanism of tissue-specific mRNA delivery by selective organ targeting nanoparticles. *Proceedings of the National Academy of Sciences*. 118, e2109256118. (2021). doi: 10.1073/pnas.2109256118.

[27] J. Simon, L. K. Müller, M. Kokkinopoulou, I. Lieberwirth, S. Morsbach, K. Landfester, V. Mailänder. Exploiting the biomolecular corona: pre-coating of nanoparticles enables controlled cellular interactions. *Nanoscale*. 10, 10731–10739. (2018). doi: 10.1039/C8NR03331E.

[28] D. J. Sobczynski, P. Charoenphol, M. J. Heslinga, P. J. Onyskiw, K. Namdee, A. J. Thompson, O. Eniola-Adefeso. Plasma protein corona modulates the vascular wall interaction of drug carriers in a material and donor specific manner. *PLoS ONE*. 9, 1–12. (2014). doi: 10.1371/journal.pone.0107408.

[29] G. Caracciolo. Liposome–protein corona in a physiological environment: challenges and opportunities for targeted delivery of nanomedicines. *Nanomedicine: Nanotechnology, Biology and Medicine*. 11, 543–557. (2015). doi: 10.1016/j.nano.2014.11.003.

[30] M. Li, S. Jiang, J. Simon, D. Paßlick, M. L. Frey, M. Wagner, V. Mailander, D. Crespy, K. Landfester. Brush conformation of polyethylene glycol determines the stealth effect of nanocarriers in the low protein adsorption regime. *Nano Letters*. 21, 1591–1598. (2021). doi: 10.1021/acs.nanolett.0c03756.

[31] M. B. Sonbol, D. H. Ahn, D. Goldstein, T. Okusaka, J. Tabernero, T. Macarulla, M. Reni, C. P. Li, B. O'Neil, E. Van Cutsem, T. Bekaii-Saab. CanStem111P trial: A Phase III study of napabucasin plus nab-paclitaxel with gemcitabine. *Future Oncology*. 15, 1295–1302. (2019). doi: 10.2217/fon-2018-0903.

[32] D. Han, T. Yu, N. Dong, B. Wang, F. Sun, D. Jiang. Napabucasin, a novel STAT3 inhibitor suppresses proliferation, invasion and stemness of glioblastoma cells. *Journal of Experimental and Clinical Cancer Research*. 38, 1–12. (2019). doi: 10.1186/s13046-019-1289-6.

[33] L. MacDonagh, S. G. Gray, E. Breen, S. Cuffe, S. P. Finn, K. J. O'Byrne, M. P. Barr. BBI608 inhibits cancer stemness and reverses cisplatin resistance in NSCLC. *Cancer Letters*. 428, 117–126. (2018). doi: 10.1016/j.canlet.2018.04.008.

[34] G. P. Nagaraju, B. Farran, M. Farren, G. Chalikonda, C. Wu, G. B. Lesinski, B. F. El-Rayes. Napabucasin (BBI 608), a potent chemoradiosensitizer in rectal cancer. *Cancer*. 126, 3360–3371. (2020). doi: 10.1002/cncr.32954.

[35] A. Kawazoe, Y. Kuboki, E. Shinozaki, H. Hara, T. Nishina, Y. Komatsu, S. Yuki, M. Wakabayashi, S. Nomura, A. Sato, T. Kuwata, M. Kawazu, H. Mano, Y. Togashi, H. Nishikawa, T. Yoshino. Multicenter phase I/II trial of napabucasin and pembrolizumab in patients with metastatic colorectal cancer (EPOC1503/SCOOP Trial). *Clinical Cancer Research*. 26, 5887–5894. (2020). doi: 10.1158/1078-0432.CCR-20-1803.

[36] Y. Li, H. A. Rogoff, S. Keates, Y. Gao, S. Murikipudi, K. Mikule, D. Leggett, W. Li, A. B. Pardee, C. J. Li. Suppression of cancer relapse and metastasis by inhibiting cancer stemness. *Proceedings of the National Academy of Sciences of the United States of America*. 112, 1839–1844. (2015). doi: 10.1073/pnas.1424171112.

[37] D. J. Jonker, L. Nott, T. Yoshino, S. Gill, J. Shapiro, A. Ohtsu, J. Zalcberg, M. M. Vickers, A. C. Wei, Y. Gao, N. C. Tebbutt, B. Markman, T. Price, T. Esaki, S. Koski, M. Hitron, W. Li, Y. Li, N. M. Magoski, C. J. Li, J. Simes, D. Tu, C. J. O'Callaghan. Napabucasin versus placebo in refractory advanced colorectal cancer: a randomised phase 3 trial. *The Lancet Gastroenterology and Hepatology*. 3, 263–270. (2018). doi: 10.1016/S2468-1253(18)30009-8.

[38] S. Sau, S. K. Mondal, S. K. Kashaw, A. K. Iyer, R. Banerjee. Combination of cationic dexamethasone derivative and STAT3 inhibitor (WP1066) for aggressive melanoma: a strategy for repurposing a phase I clinical trial drug. *Molecular and Cellular Biochemistry*. 436, 119–136. (2017). doi: 10.1007/s11010-017-3084-z.

[39] J. De Groot, M. Ott, J. Wei, C. Kassab, D. Fang, H. Najem, B. O'Brien, S. P. Weathers, C. K. Matsouka, N. K. Majd, R. A. Harrison, G. N. Fuller, J. T. Huse, J. P. Long, R. Sawaya, G. Rao, T. J. Macdonald, W. Priebe, M. Decuypere, A. B. Heimberger. A first-in-human Phase i trial of the oral p-STAT3 inhibitor WP1066 in patients with recurrent malignant glioma. *CNS Oncology*. 11, (2022). doi: 10.2217/cns-2022-0005.

[40] A. Tolcher, K. Flaherty, G. I. Shapiro, J. Berlin, T. Witzig, T. Habermann, A. Bullock, E. Rock, A. Elekes, C. Lin, D. Kostic, N. Ohi, D. Rasco, K. P. Papadopoulos, A. Patnaik, L. Smith, G. M. Cote. A First-in-Human Phase I Study of OPB-111077, a Small-Molecule STAT3 and Oxidative Phosphorylation Inhibitor, in Patients with Advanced Cancers. *The Oncologist*. 23, 658-e72. (2018). doi: 10.1634/theoncologist.2017-0325.

[41] C. Yoo, J. Kang, H. Y. Lim, J. H. Kim, M. A. Lee, K. H. Lee, T. Y. Kim, B. Y. Ryoo. Phase I dose-finding study of OPB-111077, a novel STAT3 inhibitor, in patients with advanced hepatocellular carcinoma. *Cancer Research and Treatment*. 51, 510–518. (2019). doi: 10.4143/crt.2018.226.

[42] D. Genini, L. Brambilla, E. Laurini, J. Merulla, G. Civenni, S. Pandit, R. D'Antuono, L. Perez, D. E. Levy, S. Pricl, G. M. Carbone, C. V. Catapano. Mitochondrial dysfunction induced by a SH2 domain-Targeting STAT3 inhibitor leads to metabolic synthetic lethality in cancer cells. *Proceedings of the National Academy of Sciences of the United States of America*. 114, E4924–E4933. (2017). doi: 10.1073/pnas.1615730114.

[43] A. L. Wong, R. A. Soo, D. S. Tan, S. C. Lee, J. S. Lim, P. C. Marban, L. R. Kong, Y. J. Lee, L. Z. Wang, W. L. Thuya, R. Soong, M. Q. Yee, T. M. Chin, M. T. Cordero, B. R. Asuncion, B. Pang, S. Pervaiz, J. L. Hirpara, A. Sinha, W. W. Xu, M. Yuasa, T. Tsunoda, M. Motoyama, T. Yamauchi, B. C. Goh. Phase I and biomarker study of OPB-51602, a novel signal transducer and activator of transcription (STAT) 3 inhibitor, in patients with refractory solid malignancies. *Annals of Oncology*. 26, 998–1005. (2015). doi: 10.1093/annonc/mdv026.

[44] M. Ogura, T. Uchida, Y. Terui, F. Hayakawa, Y. Kobayashi, M. Taniwaki, Y. Takamatsu, T. Naoe, K. Tobinai, W. Munakata, T. Yamauchi, A. Kageyama, M. Yuasa, M. Motoyama, T. Tsunoda, K. Hatake. Phase I study of OPB-51602, an oral inhibitor of signal transducer and activator of transcription 3, in patients with relapsed/refractory hematological malignancies. *Cancer Science*. 106, 896–901. (2015). doi: 10.1111/cas.12683.

[45] Y. L. Wu, S. Lu, Y. Lu, J. Zhou, Y. kai Shi, V. Sriuranpong, J. C. M. Ho, C. K. Ong, C. M. Tsai, C. H. Chung, K. D. Wilner, Y. Tang, E. T. Masters, P. Selaru, T. S. Mok. Results of PROFILE 1029, a Phase III Comparison of First-Line Crizotinib versus Chemotherapy in East Asian Patients with ALK-Positive Advanced Non–Small Cell Lung Cancer. *Journal of Thoracic Oncology*. 13, 1539–1548. (2018). doi: 10.1016/j.jtho.2018.06.012.

[46] A. T. Shaw, T. M. Kim, L. Crinò, C. Gridelli, K. Kiura, G. Liu, S. Novello, A. Bearz, O. Gautschi, T. Mok, M. Nishio, G. Scagliotti, D. R. Spigel, S. Deudon, C. Zheng, S. Pantano, P. Urban, C. Massacesi, K. Viraswami-Appanna, E. Felip. Ceritinib versus chemotherapy in patients with ALK-rearranged non-small-cell lung cancer previously given chemotherapy and crizotinib (ASCEND-5): a randomised, controlled, open-label, phase 3 trial. *The Lancet Oncology*. 18, 874–886. (2017). doi: 10.1016/S1470-2045(17)30339-X.

[47] A. Okines, T. Irfan, B. Asare, K. Mohammed, P. Osin, A. Nerurkar, I. E. Smith, M. Parton, A. Ring, S. Johnston, N. C. Turner. Clinical outcomes in patients with triple negative or HER2 positive lobular breast cancer: a single institution experience. *Breast Cancer Research and Treatment*. 192, 563–571. (2022). doi: 10.1007/s10549-021-06432-z.

[48] Y. Li, J. Shi, J. Yang, S. Ge, J. Zhang, R. Jia, X. Fan. Uveal melanoma: progress in molecular biology and therapeutics. *Therapeutic Advances in Medical Oncology*. 12, 1–27. (2020). doi: 10.1177/1758835920965852.

[49] A. Jamieson, T. Bosse, J. N. McAlpine. The emerging role of molecular pathology in directing the systemic treatment of endometrial cancer. *Therapeutic Advances in Medical Oncology*. 13, 1–14. (2021). doi: 10.1177/17588359211035959.

[50] K. T. Flaherty, R. Gray, A. Chen, S. Li, D. Patton, S. R. Hamilton, P. M. Williams, E. P. Mitchell, A. John Iafrate, J. Sklar, L. N. Harris, L. M. McShane, L. V. Rubinstein, D. J. Sims, M. Routbort, B. Coffey, T. Fu, J. A. Zwiebel, R. F. Little, D. Marinucci, R. Catalano, R. Magnan, W. Kibbe, C. Weil, J. V. Tricoli, B. Alexander, S. Kumar, G. K. Schwartz, F. Meric-Bernstam, C. J. Lih, W. McCaskill-Stevens, P. Caimi, N. Takebe, V. Datta, C. L. Arteaga, J. S. Abrams, R. Comis, P. J. O'Dwyer, B. A. Conley, M. Schnall, T. Johnson, F. B. de Abreu, S. J. Deharvengt, T. L. Gallagher, K. Godwin, D. C. Green, C. C. Hain, B. E. Houde, J. D. Peterson, H. B. Steinmetz, G. J. Tsongalis, X. Xiao, B. Giantonio, M. Lou Smith, N. Azad, M. Lambert, L. P. Le, A. Raymond, H. Robinson, K. Vernovsky, D. Hyman, C. Chung, C. Rowe, F. Spina, S. Ansher, J. Cristofaro, P. S. Ivy, I. Lubensky, H. Makhlouf, L. Shankar, J. Wright, L. Yee, L. Lison, M. Anderson, M. Benson, N. Birus, L. Brem, D. Chebattina, H. Donolo, E. Dumene, M. Hammer, M. Hendriksson, S. Kadiyala, J. Lee, A. Lu, T. O'Connor, W. Osman, J. Pumphrey, A. Purkayastha, V. Ramani, J. Scibelli, M. Smith, A. Steinfeld, J. Thompson, S. Vallala, J. Verbeck, C. Winter, S. Yang, Q. Yu, R. Zakharov, C. Bouk, T. C. Chang, A. Fredlock, K. Harper, R. Harrington, C. Karlovich, M. Majano, S. McDermott, E. Mosher, P. Runge, M. Saeed, G. S. Mantha, D. Panditi, K. P. Patel, R. Pepper, L. Rajyalakshmi, N. G. Reddy, R. R. Singh, D. Tripathy, J. Yau, S. Canosa, K. Finberg, J. Huang, K. Ronski, T. Zenta Walther. The molecular analysis for therapy choice (NCI-MATCH) trial: Lessons for genomic trial design. *Journal of the National Cancer Institute*. 112, 1021–1029. (2020). doi: 10.1093/jnci/djz245.

[51] A. S. Mansfield, Z. Wei, R. Mehra, A. T. Shaw, C. H. Lieu, P. M. Forde, A. E. Drilon, E. P. Mitchell, J. J. Wright, N. Takebe, E. Sharon, D. Hovelson, S. Tomlins, J. Zeng, K. Poorman, N. Malik, R. J. Gray, S. Li, L. M. McShane, L. V. Rubinstein, D. Patton, P. M. Williams, S. R. Hamilton, B. A. Conley, C. L. Arteaga, L. N. Harris, P. J. O'Dwyer, A. P. Chen, K. T. Flaherty. Crizotinib in patients with tumors harboring ALK or ROS1 rearrangements in the NCI-MATCH trial. *npj Precision Oncology*. 6, 1–6. (2022). doi: 10.1038/s41698-022-00256-w.

[52] J. C. Soria, D. S. W. Tan, R. Chiari, Y. L. Wu, L. Paz-Ares, J. Wolf, S. L. Geater, S. Orlov, D. Cortinovis, C. J. Yu, M. Hochmair, A. B. Cortot, C. M. Tsai, D. Moro-Sibilot, R. G. Campelo, T. McCulloch, P. Sen, M. Dugan, S. Pantano, F. Branle, C. Massacesi, G. de Castro. First-line ceritinib versus platinum-based chemotherapy in advanced ALK-rearranged non-small-cell lung cancer (ASCEND-4): a randomised, open-label, phase 3 study. *The Lancet*. 389, 917–929. (2017). doi: 10.1016/S0140-6736(17)30123-X.

[53] N. Ochi, N. Takigawa. What can we learn from 3 phase III trials of ASCEND-4: Ceritinib vs. platinum/pemetrexed with pemetrexed maintenance, PROFILE 1004: Crizotinib vs. platinum/pemetrexed, and J-ALEX: Alectinib vs. crizotinib? *Translational Cancer Research*. 6, S515–S518. (2017). doi: 10.21037/tcr.2017.04.20.

[54] D. S. W. Tan, S. Geater, C. J. Yu, C. M. Tsai, T. C. Hsia, J. Chen, M. C. Lin, Y. Lu, V. Sriuranpong, C. T. Yang, P. Sen, F. Branle, M. Shi, Y. L. Wu. Ceritinib Efficacy and Safety in Treatment-Naive Asian Patients With Advanced ALK-Rearranged NSCLC: An ASCEND-4 Subgroup Analysis. *JTO Clinical and Research Reports*. 2, 100131. (2021). doi: 10.1016/j.jtocrr.2020.100131.

[55] J. Guan, S. Fransson, J. T. Siaw, D. Treis, J. Van Den Eynden, D. Chand, G. Umapathy, K. Ruuth, P. Svenberg, S. Wessman, A. Shamikh, H. Jacobsson, L. Gordon, J. Stenman, P. J. Svensson, M. Hansson, E. Larsson, T. Martinsson, R. H. Palmer, P. Kogner, B. Hallberg. Clinical response of the novel activating ALK-I1171T mutation in neuroblastoma to the ALK inhibitor ceritinib. *Cold Spring Harbor Molecular Case Studies*. 4, 1–24. (2018). doi: 10.1101/mcs.a002550.

USC UNIVERSIDADE DE SANTIAGO DE COMPOSTELA

[56] K. W. Nassar, J. D. Hintzsche, S. M. Bagby, V. Espinoza, C. Langouët-Astrié, C. M. Amato, T.-S. Chimed, M. Fujita, W. Robinson, A. C. Tan, R. E. Schweppe. Targeting CDK4/6 Represents a Therapeutic Vulnerability in Acquired BRAF/MEK Inhibitor–Resistant Melanoma. *Molecular Cancer Therapeutics*. 20, 2049–2060. (2021). doi: 10.1158/1535-7163.MCT-20-1126.

[57] K. Hotta, T. Hida, H. Nokihara, M. Morise, Y. H. Kim, K. Azuma, T. Seto, Y. Takiguchi, M. Nishio, H. Yoshioka. Final overall survival analysis from the phase III J-ALEX study of alectinib versus crizotinib in ALK inhibitor-naïve Japanese patients with ALK -positive. *ESMO Open*. 7, 100527. (2022). doi: 10.1016/j.esmoop.2022.100527.

[58] W. Wick, S. Dettmer, A. Berberich, T. Kessler, I. Karapanagiotou-Schenkel, A. Wick, F. Winkler, E. Pfaff, B. Brors, J. Debus, A. Unterberg, M. Bendszus, C. Herold-Mende, A. Eisenmenger, A. Von Deimling, D. T. W. Jones, S. M. Pfister, F. Sahm, M. Platten. N 2 M 2 (NOA-20) phase I/II trial of molecularly matched targeted therapies plus radiotherapy in patients with newly diagnosed non-MGMT hypermethylated glioblastoma. *Neuro-Oncology*. 21, 95–105. (2019). doi: 10.1093/neuonc/noy161.

[59] D. W. Kim, M. Tiseo, M. J. Ahn, K. L. Reckamp, K. H. Hansen, S. W. Kim, R. M. Huber, H. L. West, H. J. M. Groen, M. J. Hochmair, N. B. Leighl, S. N. Gettinger, C. J. Langer, L. G. P. A. Rodríguez, E. F. Smit, E. S. Kim, W. Reichmann, F. G. Haluska, D. Kerstein, D. R. Camidge. Brigatinib in patients with crizotinib-refractory anaplastic lymphoma kinase-positive non-small-cell lung cancer: A randomized, multicenter phase II trial. *Journal of Clinical Oncology*. 35, 2490–2498. (2017). doi: 10.1200/JCO.2016.71.5904.

[60] A. T. Shaw, T. M. Bauer, F. de Marinis, E. Felip, Y. Goto, G. Liu, J. Mazieres, D.-W. Kim, T. Mok, A. Polli, H. Thurm, A. M. Calella, G. Peltz, B. J. Solomon. First-Line Lorlatinib or Crizotinib in Advanced ALK -Positive Lung Cancer. *New England Journal of Medicine*. 383, 2018–2029. (2020). doi: 10.1056/nejmoa2027187.

[61] T. Okusaka, H. Ueno, M. Ikeda, S. Mitsunaga, M. Ozaka, H. Ishii, O. Yokosuka, Y. Ooka, R. Yoshimoto, Y. Yanagihara, K. Okita. Phase 1 and pharmacological trial of OPB-31121, a signal transducer and activator of transcription-3 inhibitor, in patients with advanced hepatocellular carcinoma. *Hepatology Research*. 45, 1283–1291. (2015). doi: 10.1111/hepr.12504.

[62] S. Verstovsek, R. Hoffman, J. Mascarenhas, J. C. Soria, R. Bahleda, P. McCoon, W. Tang, J. Cortes, H. Kantarjian, V. Ribrag. A phase I, open-label, multi-center study of the JAK2 inhibitor AZD1480 in patients with myelofibrosis. *Leukemia Research*. 39, 157–163. (2015). doi: 10.1016/j.leukres.2014.11.018.

[63] S. Wang, Y. Song, K. Cao, L. Zhang, X. Fang, F. Chen, S. Feng, F. Yan. Photothermal therapy mediated by gold nanocages composed of anti-PDL1 and galunisertib for improved synergistic immunotherapy in colorectal cancer. *Acta Biomaterialia*. 134, 621–632. (2021). doi: 10.1016/j.actbio.2021.07.051.

[64] S. S. Fong, Y. Y. Foo, W. S. Saw, B. F. Leo, Y. Y. Teo, I. Chung, B. T. Goh, M. Misran, T. Imae, C. C. Chang, L. Y. Chung, L. V. Kiew. Chitosan-Coated-PLGA Nanoparticles Enhance the Antitumor and Antimigration Activity of Stattic – A STAT3 Dimerization Blocker. *International Journal of Nanomedicine*. 17, 137–150. (2022). doi: 10.2147/IJN.S337093.

[65] N. A. N. Hanafy, A. Quarta, M. M. Ferraro, L. Dini, C. Nobile, M. L. De Giorgi, S. Carallo, C. Citti, A. Gaballo, G. Cannazza, R. Rinaldi, G. Giannelli, S. Leporatti. Polymeric nano-micelles as novel cargo-carriers for LY2157299 liver cancer cells delivery. *International Journal of Molecular Sciences*. 19, (2018). doi: 10.3390/ijms19030748.

[66] X. Shi, L. Shu, Y. Qiao, J. Yao, H. Xie, L. Zhou, H. Wang, S. Zheng. Synergistic nanoassemblies constructed from a STAT3 inhibitor and a cabazitaxel prodrug with enhanced cancer chemo-immunotherapy. *Materials Today Nano*. 17, 100155. (2022). doi: 10.1016/j.mtnano.2021.100155.

[67] Y. C. Kwa, T. Anasamy, Y. Y. Foo, B. F. Leo, I. Chung, L. V. Kiew, L. Y. Chung. Preparation and Characterization of Stattic-Loaded Albumin Nanoparticles for Antimetastatic Cancer Treatment. *Drug Delivery Letters*. 12, 74–83. (2022). doi: 10.2174/2210303112666220330115110.

[68] L. Zhang, J. Huang, X. Chen, C. Pan, Y. He, R. Su, D. Guo, S. Yin, S. Wang, L. Zhou, J. Chen, S. Zheng, Y. Qiao. Self-assembly nanovaccine containing TLR7/8 agonist and STAT3 inhibitor enhances tumor immunotherapy by augmenting tumor-specific immune response. *Journal for ImmunoTherapy of Cancer*. 9, 1–14. (2021). doi: 10.1136/jitc-2021-003132.

USC UNIVERSIDADE DE SANTIAGO DE COMPOSTELA

CONCLUSIONS

USC
UNIVERSIDADE
DE SANTIAGO
DE COMPOSTELA

USC
UNIVERSIDADE
DE SANTIAGO
DE COMPOSTELA

The conclusions of the work performed in this thesis have been formulated taking into account the three primary experimental objectives:

1. With regard to the protein corona of nanocapsules:

   The composition of the surface of the nanocapsules determines the type and amount of proteins interacting with them. Compositions with high amounts of PEGylated compounds on their surface have a thin protein corona, whereas those containing an excess of the cationic surfactant DOTAP exhibit intense vitronectin adsorption. The adsorption of these proteins is expected to influence their biodistribution significantly.

2. With regard to the capacity of nanocapsules to load hydrophobic immunomodulators:

   The encapsulation of galunisertib and stattic on NCs preserves the activity of the drugs in cancer cells while slightly reducing the toxicity in tumor-associated macrophages. SD-noPEG was found to successfully inhibit the STAT3 and TGF-β pathways.

3. With regard to the capacity of nanocapsules to load monoclonal antibodies:

   Polymeric NCs represent a versatile delivery platform that could be adapted for the formulation of monoclonal antibodies such as BZV and anti-KRAS. Selected formulations were found to have a great capacity for the association of the mAbs and their delivery at the intracellular level. Importantly, a notorious target engagement could be observed for the anti-$KRAS^{G12V}$ mAb released from the NC inside the cells.

Overall, this work highlights the technological possibilities of polymeric nanocapsules and the importance of their rational design to obtain an adequate protein corona, which ultimately will dictate their biodistribution and interaction with the immune systems. Moreover, it provides some bases for the formulation of immunomodulators and monoclonal antibodies, which could potentially be used for the treatment of lung cancer.

USC UNIVERSIDADE DE SANTIAGO DE COMPOSTELA

USC
UNIVERSIDADE
DE SANTIAGO
DE COMPOSTELA

ETHICAL CONSIDERATIONS

USC
UNIVERSIDADE
DE SANTIAGO
DE COMPOSTELA

USC
UNIVERSIDADE
DE SANTIAGO
DE COMPOSTELA

Human-derived samples

The human plasma used for protein corona experiments and colloidal stability described in this thesis were conducted in the Center for Research in Molecular Medicine and Chronic Diseases (CiMUS) of the Universidade de Santiago de Compostela (Santiago de Compostela, Spain), under Spanish and European law, and with the approval of the Santiago and Lugo research ethic committee (Reference 2019_466). The plasma samples were obtained from anonymous healthy blood donors at an authorized organization (Servizo de Vixilancia da Saúde of the Universidade de Santiago de Compostela, Spain) after the donors had signed an informed consent form.

USC
UNIVERSIDADE
DE SANTIAGO
DE COMPOSTELA

XUNTA DE GALICIA
CONSELLERÍA DE SANIDADE
Secretaría Xeral Técnica

Comité de Ética de la Investigación
Santiago Lugo

galicia

DICTAMEN DEL COMITÉ DE ÉTICA DE LA INVESTIGACIÓN DE SANTIAGO-LUGO

Lorenzo Armenteros del Olmo, Secretario suplente del Comité de Ética de la Investigación de Santiago-Lugo,

CERTIFICA:

Que este Comité evaluó en su reunión del día 22 de octubre de 2019 el estudio:

Título: Estudio de la adsorción de proteínas plasmáticas en nanosistemas
Versión: 2.0
Promotor/a: María José Alonso Marcos
Investigador/a:María José Alonso Marcos
Código de Registro: 2019_466

Y que este Comité, tomando en consideración la pertinencia del estudio, el conocimiento disponible, los requisitos legales aplicables y los Procedimientos Normalizados de Trabajo del Comité, emite un dictamen **FAVORABLE** para la realización del citado estudio.

Documento asinado dixitalmente por:
Lorenzo Armenteros Del Olmo (05/11/2019 14:32)
https://sede.xunta.gal/cve?idcve=SAOC-S4G4-BOAH-OF4Q-TKA6-J157-2960-7383-07

Xacobeo 2021

USC UNIVERSIDADE DE SANTIAGO DE COMPOSTELA

XUNTA DE GALICIA
CONSELLERÍA DE SANIDADE
Secretaría Xeral Técnica

Comité de Ética de la Investigación
Santiago Lugo

galicia

Y HACE CONSTAR QUE:

1.- El Comité Territorial de Ética de la Investigación de Santiago-Lugo cumple tanto en su composición como en sus PNTs los requisitos legales vigentes.

2.- La composición actual del Comité Territorial de Ética de la Investigación de Santiago-Lugo es:

Presidente
Juan Manuel Vázquez Lago. Médico especialista en Medicina Preventiva y Salud Pública. Área de Gestión Integrada de Santiago.

Vicepresidenta
Pilar Rodríguez Ledo. Médico especialista en Medicina Familiar y Comunitaria. Área de Gestión Integrada de Lugo.

Secretaria
Ana Estany Gestal. Licenciada en Farmacia. Fundación Instituto de Investigación Sanitaria de Santiago de Compostela.

Secretario Suplente
Lorenzo Armenteros del Olmo. Médico especialista en Medicina Familiar y Comunitaria. Área de Gestión Integrada de Lugo.

Vocales
María José Alfaro Águila-Real. Paciente experta. Lugo
Francisco Campos Pérez. Biólogo. Fundación Instituto de Investigación Sanitaria de Santiago de Compostela.
Rosana Castelo Domínguez. Farmacéutica de Atención Primaria. Área de Gestión Integrada de Santiago.
Ricardo García Martínez. Licenciado en Derecho. Área de Gestión Integrada de Lugo.
Jaime Gulín Dávila. Farmacéutico especialista en Farmacia Hospitalaria. Área de Gestión Integrada de Lugo.
Guillermo José Prada Ramallal Médico especialista en Farmacología Clínica. Área de Gestión Integrada de Santiago. Fundación Instituto de Investigación Sanitaria de Santiago de Compostela.
Jesús Prego Domínguez. Enfermero. Área de Gestión Integrada de Santiago.
María Mercedes Rodicio García. Médico especialista en Pediatría. Área de Gestión Integrada de Lugo.
Carlos Rodríguez Moreno. Médico especialista en Farmacología Clínica. Área de Gestión Integrada de Santiago.
Sandra Vidal Martínez. Enfermera. Área de Gestión Integrada de Santiago

Para que conste donde proceda, y a petición de quien proceda, en Santiago de Compostela,

El Secretario suplente del Comité Territorial de Ética de la Investigación de Santiago Lugo,

Documento asinado dixitalmente por:
Lorenzo Armenteros Del Olmo (05/11/2019 14:32)
https://sede.xunta.gal/cve?idcve=5AOC-54C4-BOAH-OF4O-TKA6-J157-2960-7383-07

Xacobeo 2021

USC UNIVERSIDADE DE SANTIAGO DE COMPOSTELA

USC
UNIVERSIDADE
DE SANTIAGO
DE COMPOSTELA

PUBLICATIONS DERIVED FROM THIS THESIS

USC
UNIVERSIDADE
DE SANTIAGO
DE COMPOSTELA

USC
UNIVERSIDADE
DE SANTIAGO
DE COMPOSTELA

Publications derived from this thesis

Title: Unveiling the pitfalls of the protein corona of polymeric drug nanocarriers.

Authors: Berrecoso, G., Crecente-Campo, J. & Alonso, M. J.

Drug Delivery and Translational Research. 10, 730–750. (2020).

DOI: https://doi.org/10.1007/s13346-020-00745-0

ISSN: 2190393X, 21903948

Specific contribution to the publication

Literature review. Structuring of information. Manuscript and figure preparation.

Quality indexes

Journal Impact factor: 5.671 (2021 Journal Citation Reports). Journal CiteScore: 8.3 (calculated by Scopus on the 5th of May of 2022). Quartiles: quartile 1 (Q1) in Pharmaceutical Science (SJR 2021 0.808) calculated by Scimago (https://www.scimagojr.com/journalsearch.php?q=19700182043&tip=sid)

Journal authorization

The Journal Drug Delivery and Translational Research, which belongs to the publisher Springer Nature, allowed the partial/whole reproduction of the article by the author for the type of use of thesis/dissertation. (License number: 5420160891385). https://support.springernature.com/en/support/solutions/articles/6000085109

USC UNIVERSIDADE DE SANTIAGO DE COMPOSTELA

SPRINGER NATURE LICENSE TERMS AND CONDITIONS

Nov 02, 2022

This Agreement between Mr. Germán Berrecoso ("You") and Springer Nature ("Springer Nature") consists of your license details and the terms and conditions provided by Springer Nature and Copyright Clearance Center.

License Number	5420160891385
License date	Nov 01, 2022
Licensed Content Publisher	Springer Nature
Licensed Content Publication	Drug Delivery and Translational Research
Licensed Content Title	Unveiling the pitfalls of the protein corona of polymeric drug nanocarriers
Licensed Content Author	Germán Berrecoso et al
Licensed Content Date	Mar 9, 2020
Type of Use	Thesis/Dissertation
Requestor type	academic/university or research institute
Format	print and electronic
Portion	full article/chapter
Will you be translating?	no
Circulation/distribution	1 - 29
Author of this Springer Nature content	yes
Title	Nanocapsules containing immunomodulators and monoclonal antibodies for the treatment of lung cancer
Institution name	University of Santiago de Compostela
Expected presentation date	Dec 2022
Requestor Location	Mr. Germán Berrecoso Av de Barcelona, sn, Edificio CiMUS P6L1 Santiago de Compostela, A Coruna 15706 Spain Attn: Mr. Germán Berrecoso
Total	**0.00 USD**
Terms and Conditions	

Springer Nature Customer Service Centre GmbH
Terms and Conditions

USC UNIVERSIDADE DE SANTIAGO DE COMPOSTELA

This agreement sets out the terms and conditions of the licence (the **Licence**) between you and **Springer Nature Customer Service Centre GmbH** (the **Licensor**). By clicking 'accept' and completing the transaction for the material (**Licensed Material**), you also confirm your acceptance of these terms and conditions.

1. Grant of License

1. 1. The Licensor grants you a personal, non-exclusive, non-transferable, world-wide licence to reproduce the Licensed Material for the purpose specified in your order only. Licences are granted for the specific use requested in the order and for no other use, subject to the conditions below.

1. 2. The Licensor warrants that it has, to the best of its knowledge, the rights to license reuse of the Licensed Material. However, you should ensure that the material you are requesting is original to the Licensor and does not carry the copyright of another entity (as credited in the published version).

1. 3. If the credit line on any part of the material you have requested indicates that it was reprinted or adapted with permission from another source, then you should also seek permission from that source to reuse the material.

2. Scope of Licence

2. 1. You may only use the Licensed Content in the manner and to the extent permitted by these Ts&Cs and any applicable laws.

2. 2. A separate licence may be required for any additional use of the Licensed Material, e.g. where a licence has been purchased for print only use, separate permission must be obtained for electronic re-use. Similarly, a licence is only valid in the language selected and does not apply for editions in other languages unless additional translation rights have been granted separately in the licence. Any content owned by third parties are expressly excluded from the licence.

2. 3. Similarly, rights for additional components such as custom editions and derivatives require additional permission and may be subject to an additional fee. Please apply to Journalpermissions@springernature.com/bookpermissions@springernature.com for these rights.

2. 4. Where permission has been granted **free of charge** for material in print, permission may also be granted for any electronic version of that work, provided that the material is incidental to your work as a whole and that the electronic version is essentially equivalent to, or substitutes for, the print version.

2. 5. An alternative scope of licence may apply to signatories of the STM Permissions Guidelines, as amended from time to time.

3. Duration of Licence

3. 1. A licence for is valid from the date of purchase ('Licence Date') at the end of the relevant period in the below table:

Scope of Licence	Duration of Licence
Post on a website	12 months
Presentations	12 months
Books and journals	Lifetime of the edition in the language purchased

USC UNIVERSIDADE DE SANTIAGO DE COMPOSTELA

4. Acknowledgement

4. 1. The Licensor's permission must be acknowledged next to the Licenced Material in print. In electronic form, this acknowledgement must be visible at the same time as the figures/tables/illustrations or abstract, and must be hyperlinked to the journal/book's homepage. Our required acknowledgement format is in the Appendix below.

5. Restrictions on use

5. 1. Use of the Licensed Material may be permitted for incidental promotional use and minor editing privileges e.g. minor adaptations of single figures, changes of format, colour and/or style where the adaptation is credited as set out in Appendix 1 below. Any other changes including but not limited to, cropping, adapting, omitting material that affect the meaning, intention or moral rights of the author are strictly prohibited.

5. 2. You must not use any Licensed Material as part of any design or trademark.

5. 3. Licensed Material may be used in Open Access Publications (OAP) before publication by Springer Nature, but any Licensed Material must be removed from OAP sites prior to final publication.

6. Ownership of Rights

6. 1. Licensed Material remains the property of either Licensor or the relevant third party and any rights not explicitly granted herein are expressly reserved.

7. Warranty

IN NO EVENT SHALL LICENSOR BE LIABLE TO YOU OR ANY OTHER PARTY OR ANY OTHER PERSON OR FOR ANY SPECIAL, CONSEQUENTIAL, INCIDENTAL OR INDIRECT DAMAGES, HOWEVER CAUSED, ARISING OUT OF OR IN CONNECTION WITH THE DOWNLOADING, VIEWING OR USE OF THE MATERIALS REGARDLESS OF THE FORM OF ACTION, WHETHER FOR BREACH OF CONTRACT, BREACH OF WARRANTY, TORT, NEGLIGENCE, INFRINGEMENT OR OTHERWISE (INCLUDING, WITHOUT LIMITATION, DAMAGES BASED ON LOSS OF PROFITS, DATA, FILES, USE, BUSINESS OPPORTUNITY OR CLAIMS OF THIRD PARTIES), AND
WHETHER OR NOT THE PARTY HAS BEEN ADVISED OF THE POSSIBILITY OF SUCH DAMAGES. THIS LIMITATION SHALL APPLY NOTWITHSTANDING ANY FAILURE OF ESSENTIAL PURPOSE OF ANY LIMITED REMEDY PROVIDED HEREIN.

8. Limitations

8. 1. ***BOOKS ONLY:***Where **'reuse in a dissertation/thesis'** has been selected the following terms apply: Print rights of the final author's accepted manuscript (for clarity, NOT the published version) for up to 100 copies, electronic rights for use only on a personal website or institutional repository as defined by the Sherpa guideline (www.sherpa.ac.uk/romeo/).

USC UNIVERSIDADE DE SANTIAGO DE COMPOSTELA

8. 2. For content reuse requests that qualify for permission under the STM Permissions Guidelines, which may be updated from time to time, the STM Permissions Guidelines supersede the terms and

conditions contained in this licence.

9. Termination and Cancellation

9. 1. Licences will expire after the period shown in Clause 3 (above).

9. 2. Licensee reserves the right to terminate the Licence in the event that payment is not received in full or if there has been a breach of this agreement by you.

Appendix 1 — Acknowledgements:

For Journal Content:
Reprinted by permission from [**the Licensor**]: [**Journal Publisher** (e.g. Nature/Springer/Palgrave)] [**JOURNAL NAME**] [**REFERENCE CITATION** (Article name, Author(s) Name), [**COPYRIGHT**] (year of publication)

For **Advance Online Publication papers:**
Reprinted by permission from [**the Licensor**]: [**Journal Publisher** (e.g. Nature/Springer/Palgrave)] [**JOURNAL NAME**] [**REFERENCE CITATION** (Article name, Author(s) Name), [**COPYRIGHT**] (year of publication), advance online publication, day month year (doi: 10.1038/sj.[JOURNAL ACRONYM].)

For Adaptations/Translations:
Adapted/Translated by permission from [**the Licensor**]: [**Journal Publisher** (e.g. Nature/Springer/Palgrave)] [**JOURNAL NAME**] [**REFERENCE CITATION** (Article name, Author(s) Name), [**COPYRIGHT**] (year of publication)

Note: For any republication from the British Journal of Cancer, the following credit line style applies:

Reprinted/adapted/translated by permission from [**the Licensor**]: on behalf of Cancer Research UK: : [**Journal Publisher** (e.g. Nature/Springer/Palgrave)] [**JOURNAL NAME**] [**REFERENCE CITATION** (Article name, Author(s) Name), [**COPYRIGHT]** (year of publication)

For **Advance Online Publication** papers:
Reprinted by permission from The [**the Licensor**]: on behalf of Cancer Research UK: [**Journal Publisher** (e.g. Nature/Springer/Palgrave)] [**JOURNAL NAME**] [**REFERENCE CITATION** (Article name, Author(s) Name), [**COPYRIGHT**] (year of publication), advance online publication, day month year (doi: 10.1038/sj.[JOURNAL ACRONYM])

For Book content:
Reprinted/adapted by permission from [**the Licensor**]: [**Book Publisher** (e.g. Palgrave Macmillan, Springer etc) [**Book Title**] by [**Book author**(s)] [**COPYRIGHT**] (year of publication)

Other Conditions:

Version 1.3

Questions? customercare@copyright.com or +1-855-239-3415 (toll free in the US) or +1-978-646-2777.

USC UNIVERSIDADE DE SANTIAGO DE COMPOSTELA

Publications derived from this thesis

Title: Asymmetric flow field-flow fractionation as a multifunctional technique for the characterization of polymeric nanocarriers.

Authors: Quattrini, F., Berrecoso, G., Crecente-Campo, J. & Alonso, M. J.

Drug Delivery and Translational Research. 11, 373–395. (2021)

DOI: https://doi.org/10.1007/s13346-021-00918-5

ISSN: 2190393X, 21903948

Specific contribution to the publication

Literature review. Structuring of information. Manuscript review.

Quality indexes

Journal Impact factor: 5.671 (2021 Journal Citation Reports). Journal CiteScore: 8.3 (calculated by Scopus on the 5th of May of 2022). Quartiles: quartile 1 (Q1) in Pharmaceutical Science (SJR 2021 0.808) calculated by Scimago (https://www.scimagojr.com/journalsearch.php?q=19700182043&tip=sid)

Journal authorization

The article is open access and distributed under the terms of the Creative Commons CC BY license, which permits unrestricted use, distribution, and reproduction in any medium, provided the original work is properly cited.

USC UNIVERSIDADE DE SANTIAGO DE COMPOSTELA



Asymmetric flow field-flow fractionation as a multifunctional technique for the characterization of polymeric nanocarriers

Author: Federico Quattrini et al
Publication: Drug Delivery and Translational Research
Publisher: Springer Nature
Date: Jan 31, 2021

Copyright © 2021, The Author(s)

Creative Commons

This is an open access article distributed under the terms of the Creative Commons CC BY license, which permits unrestricted use, distribution, and reproduction in any medium, provided the original work is properly cited.

You are not required to obtain permission to reuse this article.

To request permission for a type of use not listed, please contact Springer Nature

USC UNIVERSIDADE DE SANTIAGO DE COMPOSTELA

Publications derived from this thesis

Title: Nano-Oncologicals: A Tortoise Trail Reaching New Avenues.

Authors: Dacoba, T. G., Anthiya, S., Berrecoso, G., Fernández-Mariño, I., Fernández-Varela, C., Crecente-Campo, J., Teijeiro-Osorio, D., Torres Andón, F., & Alonso, M. J.

Advanced Functional Materials. 31, 1–36. (2021).

DOI: https://doi.org/10.1002/adfm.202009860

ISSN: 1616301X

Specific contribution to the publication

Partial introduction literature review. Literature review on sections "2. Passive and active targeting" and "3. Nanotechnology for the Delivery of Cytotoxic Drugs". Structuring. Writing of the sections "2. Passive and active targeting" and "3. Nanotechnology for the Delivery of Cytotoxic Drugs". Elaboration of "Figure 2. General considerations to achieve an adequate tumor accumulation". Manuscript review.

Quality indexes

Journal Impact factor: 19.924 (2021 Journal Citation Reports). Journal CiteScore: 26.6 (calculated by Scopus on the 5th of May of 2022). Quartiles: quartile 1 (Q1) in Biomaterials, Q1 in Chemistry (miscellaneous), Q1 in Condensed matter physics, Q1 in Electrochemistry, Q1 in Electronic, optical, and magnetic materials, Q1 in Materials science (miscellaneous), and Q1 in Nanoscience and nanotechnology (SJR 2021 5.000) calculated by Scimago (https://www.scimagojr.com/journalsearch.php?q=25143&tip=sid)

Journal authorization

The Advanced Functional Materials, which belongs to the publisher John Wiley and Sons, allowed the partial/whole reproduction of the article by the author for the type of use of thesis/dissertation. (License number: 5420161108133). https://www.wiley.com/en-us/permissions.

USC UNIVERSIDADE DE SANTIAGO DE COMPOSTELA

JOHN WILEY AND SONS LICENSE TERMS AND CONDITIONS

Nov 02, 2022

This Agreement between Mr. Germán Berrecoso ("You") and John Wiley and Sons ("John Wiley and Sons") consists of your license details and the terms and conditions provided by John Wiley and Sons and Copyright Clearance Center.

License Number	5420161108133
License date	Nov 01, 2022
Licensed Content Publisher	John Wiley and Sons
Licensed Content Publication	Advanced Functional Materials
Licensed Content Title	Nano-Oncologicals: A Tortoise Trail Reaching New Avenues
Licensed Content Author	María J. Alonso, Fernando Torres Andón, Desirée Teijeiro-Osorio, et al
Licensed Content Date	Feb 12, 2021
Licensed Content Volume	31
Licensed Content Issue	44
Licensed Content Pages	36
Type of Use	Dissertation/Thesis
Requestor type	Author of this Wiley article
Format	Print and electronic
Portion	Full article
Will you be translating?	No
Title	Nanocapsules containing immunomodulators and monoclonal antibodies for the treatment of lung cancer
Institution name	University of Santiago de Compostela
Expected presentation date	Dec 2022
Requestor Location	Mr. Germán Berrecoso Av de Barcelona, sn, Edificio CiMUS P6L1 Santiago de Compostela, A Coruna 15706 Spain Attn: Mr. Germán Berrecoso
Publisher Tax ID	EU826007151
Total	**0.00 USD**

USC UNIVERSIDADE DE SANTIAGO DE COMPOSTELA

Terms and Conditions

TERMS AND CONDITIONS

This copyrighted material is owned by or exclusively licensed to John Wiley & Sons, Inc. or one of its group companies (each a"Wiley Company") or handled on behalf of a society with which a Wiley Company has exclusive publishing rights in relation to a particular work (collectively "WILEY"). By clicking "accept" in connection with completing this licensing transaction, you agree that the following terms and conditions apply to this transaction (along with the billing and payment terms and conditions established by the Copyright Clearance Center Inc., ("CCC's Billing and Payment terms and conditions"), at the time that you opened your RightsLink account (these are available at any time at http://myaccount.copyright.com).

Terms and Conditions

- The materials you have requested permission to reproduce or reuse (the "Wiley Materials") are protected by copyright.

- You are hereby granted a personal, non-exclusive, non-sub licensable (on a stand-alone basis), non-transferable, worldwide, limited license to reproduce the Wiley Materials for the purpose specified in the licensing process. This license, **and any CONTENT (PDF or image file) purchased as part of your order,** is for a one-time use only and limited to any maximum distribution number specified in the license. The first instance of republication or reuse granted by this license must be completed within two years of the date of the grant of this license (although copies prepared before the end date may be distributed thereafter). The Wiley Materials shall not be used in any other manner or for any other purpose, beyond what is granted in the license. Permission is granted subject to an appropriate acknowledgement given to the author, title of the material/book/journal and the publisher. You shall also duplicate the copyright notice that appears in the Wiley publication in your use of the Wiley Material. Permission is also granted on the understanding that nowhere in the text is a previously published source acknowledged for all or part of this Wiley Material. Any third party content is expressly excluded from this permission.

- With respect to the Wiley Materials, all rights are reserved. Except as expressly granted by the terms of the license, no part of the Wiley Materials may be copied, modified, adapted (except for minor reformatting required by the new Publication), translated, reproduced, transferred or distributed, in any form or by any means, and no derivative works may be made based on the Wiley Materials without the prior permission of the respective copyright owner.**For STM Signatory Publishers clearing permission under the terms of the STM Permissions Guidelines only, the terms of the license are extended to include subsequent editions and for editions in other languages, provided such editions are for the work as a whole in situ and does not involve the separate exploitation of the permitted figures or extracts,** You may not alter, remove or suppress in any manner any copyright, trademark or other notices displayed by the Wiley Materials. You may not license, rent, sell, loan, lease, pledge, offer as security, transfer or assign the Wiley Materials on a stand-alone basis, or any of the rights granted to you hereunder to any other person.

- The Wiley Materials and all of the intellectual property rights therein shall at all times remain the exclusive property of John Wiley & Sons Inc, the Wiley Companies, or their respective licensors, and your interest therein is only that of having possession of and the right to reproduce the Wiley Materials pursuant to Section 2 herein during the continuance of this Agreement. You agree that you own no right, title or interest in or to the Wiley Materials or any of the intellectual property rights therein. You shall have no rights hereunder other than the license as provided for above in Section 2. No right, license or interest to any trademark, trade name, service mark or other branding ("Marks") of WILEY or its licensors is granted hereunder, and you agree that you shall not assert any such right, license or interest with respect thereto

- NEITHER WILEY NOR ITS LICENSORS MAKES ANY WARRANTY OR REPRESENTATION OF ANY KIND TO YOU OR ANY THIRD PARTY, EXPRESS, IMPLIED OR STATUTORY, WITH RESPECT TO THE MATERIALS OR THE ACCURACY OF ANY INFORMATION CONTAINED IN THE MATERIALS, INCLUDING, WITHOUT LIMITATION, ANY IMPLIED WARRANTY OF

MERCHANTABILITY, ACCURACY, SATISFACTORY QUALITY, FITNESS FOR A PARTICULAR PURPOSE, USABILITY, INTEGRATION OR NON-INFRINGEMENT AND ALL SUCH WARRANTIES ARE HEREBY EXCLUDED BY WILEY AND ITS LICENSORS AND W AIVED BY YOU.

- WILEY shall have the right to terminate this Agreement immediately upon breach of this Agreement by you.
- You shall indemnify, defend and hold harmless WILEY, its Licensors and their respective directors, officers, agents and employees, from and against any actual or threatened claims, demands, causes of action or proceedings arising from any breach of this Agreement by you.
- IN NO EVENT SHALL WILEY OR ITS LICENSORS BE LIABLE TO YOU OR ANY OTHER PARTY OR ANY OTHER PERSON OR ENTITY FOR ANY SPECIAL, CONSEQUENTIAL, INCIDENTAL, INDIRECT, EXEMPLARY OR PUNITIVE DAMAGES, HOWEVER CAUSED, ARISING OUT OF OR IN CONNECTION WITH THE DOWNLOADING, PROVISIONING, VIEWING OR USE OF THE MATERIALS REGARDLESS OF THE FORM OF ACTION, WHETHER FOR BREACH OF CONTRACT, BREACH OF WARRANTY, TORT, NEGLIGENCE, INFRINGEMENT OR OTHERWISE (INCLUDING, WITHOUT LIMITATION, DAMAGES BASED ON LOSS OF PROFITS, DATA, FILES, USE, BUSINESS OPPORTUNITY OR CLAIMS OF THIRD PARTIES), AND WHETHER OR NOT THE PARTY HAS BEEN ADVISED OF THE POSSIBILITY OF SUCH DAMAGES. THIS LIMITATION SHALL APPLY NOTWITHSTANDING ANY FAILURE OF ESSENTIAL PURPOSE OF ANY LIMITED REMEDY PROVIDED HEREIN.
- Should any provision of this Agreement be held by a court of competent jurisdiction to be illegal, invalid, or unenforceable, that provision shall be deemed amended to achieve as nearly as possible the same economic effect as the original provision, and the legality, validity and enforceability of the remaining provisions of this Agreement shall not be affected or impaired thereby.
- The failure of either party to enforce any term or condition of this Agreement shall not constitute a waiver of either party's right to enforce each and every term and condition of this Agreement. No breach under this agreement shall be deemed waived or excused by either party unless such waiver or consent is in writing signed by the party granting such waiver or consent. The waiver by or consent of a party to a breach of any provision of this Agreement shall not operate or be construed as a waiver of or consent to any other or subsequent breach by such other party.
- This Agreement may not be assigned (including by operation of law or otherwise) by you without WILEY's prior written consent.
- Any fee required for this permission shall be non-refundable after thirty (30) days from receipt by the CCC.
- These terms and conditions together with CCC's Billing and Payment terms and conditions (which are incorporated herein) form the entire agreement between you and WILEY concerning this licensing transaction and (in the absence of fraud) supersedes all prior agreements and representations of the parties, oral or written. This Agreement may not be amended except in writing signed by both parties. This Agreement shall be binding upon and inure to the benefit of the parties' successors, legal representatives, and authorized assigns.
- In the event of any conflict between your obligations established by these terms and conditions and those established by CCC's Billing and Payment terms and conditions, these terms and conditions shall prevail.
- WILEY expressly reserves all rights not specifically granted in the combination of (i) the license details provided by you and accepted in the course of this licensing transaction, (ii) these terms and

conditions and (iii) CCC's Billing and Payment terms and conditions.

- This Agreement will be void if the Type of Use, Format, Circulation, or Requestor Type was misrepresented during the licensing process.

- This Agreement shall be governed by and construed in accordance with the laws of the State of New York, USA, without regards to such state's conflict of law rules. Any legal action, suit or proceeding arising out of or relating to these Terms and Conditions or the breach thereof shall be instituted in a court of competent jurisdiction in New York County in the State of New York in the United States of America and each party hereby consents and submits to the personal jurisdiction of such court, waives any objection to venue in such court and consents to service of process by registered or certified mail, return receipt requested, at the last known address of such party.

WILEY OPEN ACCESS TERMS AND CONDITIONS

Wiley Publishes Open Access Articles in fully Open Access Journals and in Subscription journals of fering Online Open. Although most of the fully Open Access journals publish open access articles under the terms of the Creative Commons Attribution (CC BY) License only, the subscription journals and a few of the Open Access Journals offer a choice of Creative Commons Licenses. The license type is clearly identified on the article.

The Creative Commons Attribution License

The Creative Commons Attribution License (CC-BY) allows users to copy, distribute and transmit an article, adapt the article and make commercial use of the article. The CC-BY license permits commercial and non-

Creative Commons Attribution Non-Commercial License

The Creative Commons Attribution Non-Commercial (CC-BY-NC)License permits use, distribution and reproduction in any medium, provided the original work is properly cited and is not used for commercial purposes.(see below)

Creative Commons Attribution-Non-Commercial-NoDerivs License

The Creative Commons Attribution Non-Commercial-NoDerivs License (CC-BY-NC-ND) permits use, distribution and reproduction in any medium, provided the original work is properly cited, is not used for commercial purposes and no modifications or adaptations are made. (see below)

Use by commercial "for-profit" organizations

Use of Wiley Open Access articles for commercial, promotional, or marketing purposes requires further explicit permission from Wiley and will be subject to a fee.

Further details can be found on Wiley Online Library http://olabout.wiley.com/WileyCDA/Section/id-410895.html

Other Terms and Conditions:

v1.10 Last updated September 2015

Questions? customercare@copyright.com or +1-855-239-3415 (toll free in the US) or +1-978-646-2777.

USC UNIVERSIDADE DE SANTIAGO DE COMPOSTELA

Publications derived from this thesis

Title: Quantification of the actual composition of polymeric nanocapsules: a quality control analysis.

Authors: Berrecoso, G., Crecente-Campo, J. & Alonso, M.J.

Drug Delivery and Translational Research. 12, 2865–2874. (2022).

DOI: https://doi.org/10.1007/s13346-022-01150-5

ISSN: 2190393X, 21903948

Specific contribution to the publication

Literature review. Experimental design and execution. Data analysis. Supervision and manuscript and figure preparation.

Quality indexes

Journal Impact factor: 5.671 (2021 Journal Citation Reports). Journal CiteScore: 8.3 (calculated by Scopus on the 5th of May of 2022). Quartiles: quartile 1 (Q1) in Pharmaceutical Science (SJR 2021 0.808) calculated by Scimago (https://www.scimagojr.com/journalsearch.php?q=19700182043&tip=sid)

Journal authorization

The article is open access and distributed under the terms of the Creative Commons CC BY license, which permits unrestricted use, distribution, and reproduction in any medium, provided the original work is properly cited.

USC UNIVERSIDADE DE SANTIAGO DE COMPOSTELA

SPRINGER NATURE

Quantification of the actual composition of polymeric nanocapsules: a quality control analysis

Author: Germán Berrecoso et al

Publication: Drug Delivery and Translational Research

Publisher: Springer Nature

Date: Mar 18, 2022

Copyright © 2022, The Author(s)

Creative Commons

This is an open access article distributed under the terms of the Creative Commons CC BY license, which permits unrestricted use, distribution, and reproduction in any medium, provided the original work is properly cited.

You are not required to obtain permission to reuse this article.

To request permission for a type of use not listed, please contact Springer Nature

USC UNIVERSIDADE DE SANTIAGO DE COMPOSTELA

USC
UNIVERSIDADE
DE SANTIAGO
DE COMPOSTELA

USC
UNIVERSIDADE
DE SANTIAGO
DE COMPOSTELA

USC
UNIVERSIDADE
DE SANTIAGO
DE COMPOSTELA

USC
UNIVERSIDADE
DE SANTIAGO
DE COMPOSTELA

USC
UNIVERSIDADE
DE SANTIAGO
DE COMPOSTELA

USC
UNIVERSIDADE
DE SANTIAGO
DE COMPOSTELA

Pharmaceutical nanotechnology has led to the development of innovative anti-cancer nanomedicines. However, challenges associated with the biodistribution of drug nanocarriers and their capacity to load and deliver anti-cancer drugs still exist. Here we have confronted these challenges by making use of a polymeric nanocapsules delivery platform. First, we characterized the chemical composition of a series of nanocapsules and studied their interaction with proteins to anticipate their biodistribution. Second, we loaded the immunomodulators galunisertib and stattic into selected prototypes and studied their interaction with cancer and immune cells. Third, we investigated the potential of this platform for loading an anti-KRAS^{G12V} monoclonal antibody and studied its uptake by cancer cells and engagement with its target.